

OCTOBER 15, 1992

Analytical CHEMISTRY

Acousto- Optical Devices

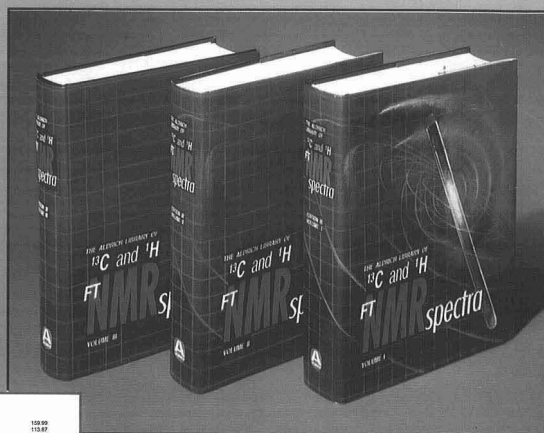
971 A

New Manuscript
Submission
Procedure

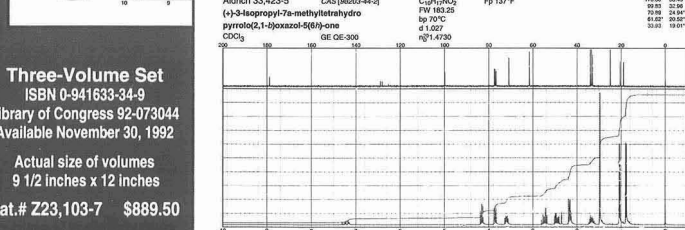
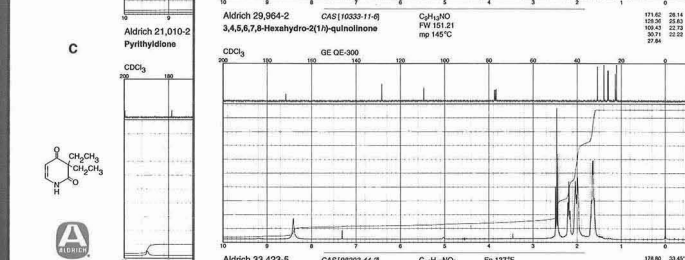
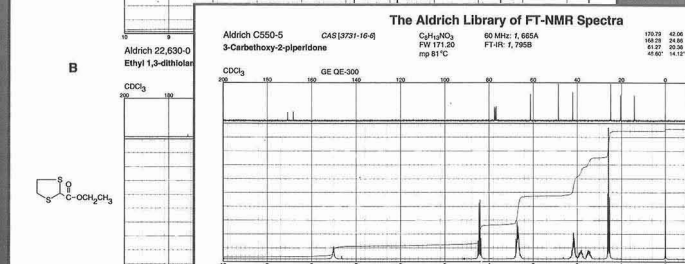
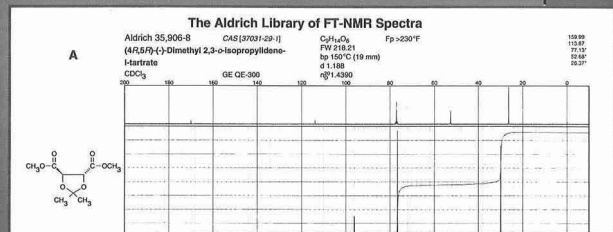
New!

THE ALDRICH LIBRARY OF ^{13}C and ^1H FT-NMR spectra

by Charles J. Pouchert and Jacquelyn Behnke



A three volume set of 4,300 pages of spectra, representing the broad range of organic compounds listed in the 1992-1993 Aldrich Catalog Handbook of Fine Chemicals.



A

B

C

12,000 300 MHz ^1H spectra

12,000 75 MHz ^{13}C spectra

^{13}C Peak Listings with
Attached Proton Test (APT)
data

Proton signal integration

Sequenced by functionality
and molecular complexity

Chemical structure

Physical constants

CAS number

Other Aldrich spectral
references

Indexed by name, molecu-
lar formula, and CAS
number

Three-Volume Set
ISBN 0-941633-34-9
Library of Congress 92-073044
Available November 30, 1992

Actual size of volumes
9 1/2 inches x 12 inches

Cat.# Z23,103-7 \$889.50



chemists helping chemists in research & industry

aldrich chemical co.

TO ORDER

Telephone 800-558-9160 414-273-3850
FAX 800-962-9591 414-273-4979
Mail P.O. Box 2060 Milwaukee, WI 53201 USA

Phone (800)228-4250 and discover new solutions to your analysis problems

Capillary Electrophoresis

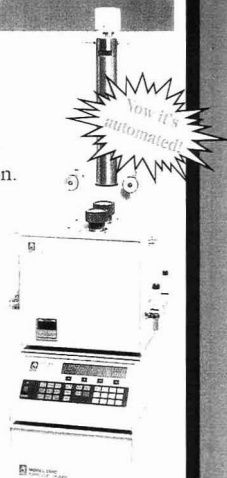
CE is a powerful tool for separation and analysis of proteins, peptides, organic acids, nucleotides, and other samples. Now put this power on your own bench with a compact "personal CE." For less-than-HPLC prices, a Model 3850 Electrophograph™ gives you fast, quantitative analysis of nanoliter samples. Or if you prefer to build your own modular CE system, our top performing CV⁴ detector is the best way to get started.



Circle No. 48 on Reader Service Card

SFE Sample Prep

High speed supercritical fluid extraction has no solvent disposal problems. These new Isco SFX™ systems give you all the advantages of SFE with automated, hands-off operation. Extract two samples at a time — in minutes — with low-cost, non-toxic CO₂. Snap-in sample cartridges with finger-tight caps speed up loading and increase throughput. Programmed, precise modifier addition lets you tailor solvating power for the results you want.



Circle No. 49 on Reader Service Card

Prep LC

Get no-miss collection of your LC or HPLC peaks with a space-saving Isco fraction collector.

All-new Retriever® 500 is the smallest 100-tube fraction collector — and the most affordable.



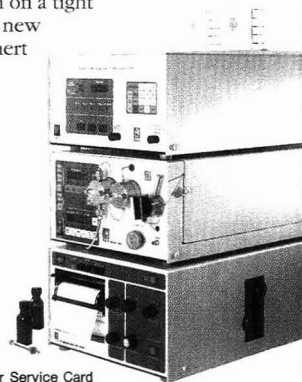
Super-smart Foxy® 200 makes it easy to collect just the peaks you want. Sort and group fractions to get the most out of any separation.



Circle No. 50 on Reader Service Card

Bio-inert HPLC

Robust, reliable HPLC systems give you modular flexibility and programmability at a fair price — so you can still get great HPLC value even on a tight budget. And the new ProTeam LC™ Inert option assures maximum bio-compatibility — including metal-free columns for biopolymer separations.



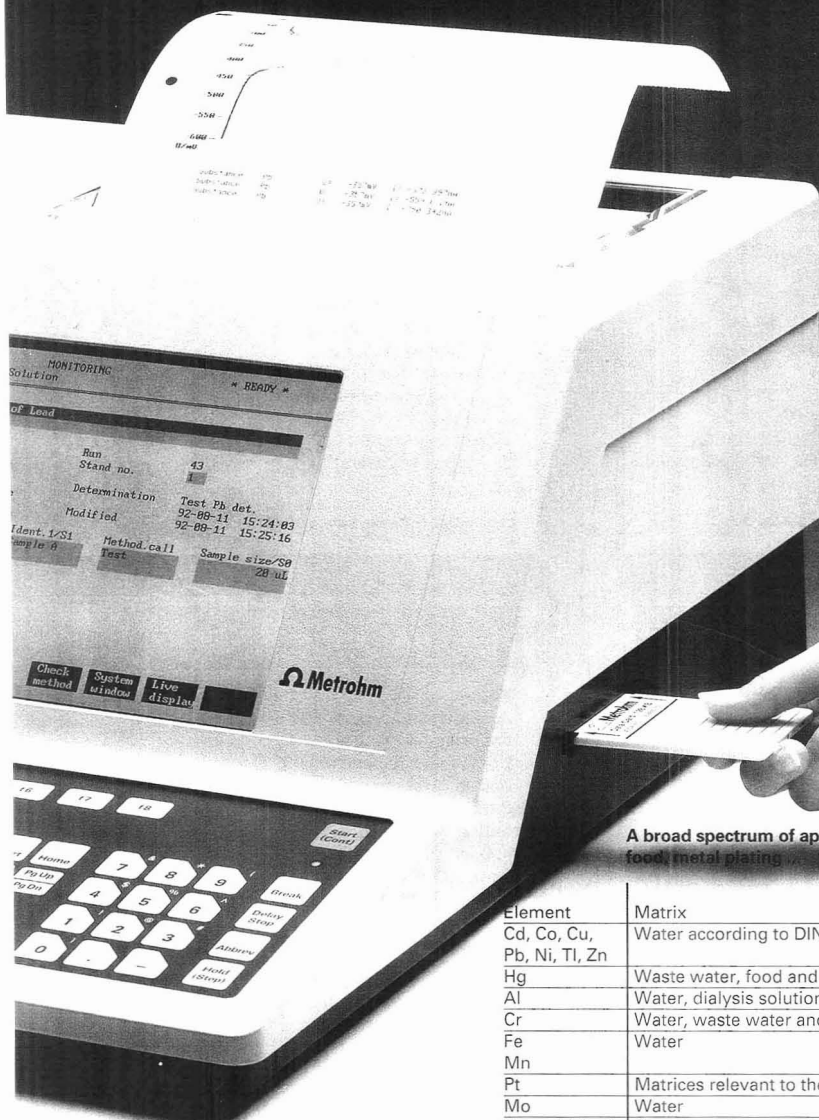
Circle No. 51 on Reader Service Card

**Call toll-free today and find out how
Isco quality and reliability mean
more research, less problems.**

Isco, Inc., P.O. Box 5347
Lincoln NE 68505 U.S.A.
Tel. (402)464-0231
Fax (402)464-0318

VA Trace Analyzer from Metrohm

Your key to trace analysis



The alternative in trace analysis: The 693 VA Processor

- Application specific software is user-friendly
- Analysis of individual substance peaks assures accuracy and flexibility
- Wide dynamic measuring range – ppb to g/L
- Real time display of curves and results
- Memory cards allow quick and easy loading and storage of methods

A broad spectrum of applications, in water, environment, food, metal plating ...

Element	Matrix	Determination limit (ppb)
Cd, Co, Cu, Pb, Ni, Ti, Zn	Water according to DIN 38406	0.05 ... 1
Hg	Waste water, food and pharmaceuticals	1
Al	Water, dialysis solutions and salt solutions	5
Cr	Water, waste water and biologic materials	0.02
Fe	Water	0.2
Mn		2
Pt	Matrices relevant to the environment	0.0001
Mo	Water	0.05
Formaldehyde	Samples relevant to the environment, plastics, film, textiles and food	200
NTA, EDTA	Water and waste water	50
Ti, V, Sb, Bi, Fe, Cu	Water, waste water and samples relevant to the environment	1 0.5 0.05
Pb, Sn	In the presence of each other in samples relevant to the environment	1
Sulphide	Pharmaceuticals, waste water, flue gas	10
Sulphite	scrubber, water and photographic solutions	100

BRINKMANN

Quality products for research and control.
Westbury, NY 11590 9974
800-645-3050
In Canada
800-263-8715

CIRCLE 72 ON READER SERVICE CARD

Metrohm
Ion analysis

METROHM Ltd
CH-9101 Herisau
Tel. 071 538 585
Fax 071 538 901

Registered in U.S. Patent and Trademark Office;
©Copyright 1992 by the American Chemical Society

EDITOR: ROYCE W. MURRAY, University of North Carolina

ASSOCIATE EDITORS: Catherine C. Fenselau, University of Maryland Baltimore County, William S. Hancock, Genentech, James W. Jorgenson, University of North Carolina, Robert A. Osteryoung, North Carolina State University, Edward S. Yeung, Iowa State University/Ames Laboratory

Editorial Headquarters, research section
Department of Chemistry
Venable and Kenan Laboratories
University of North Carolina
Chapel Hill, NC 27599-3290
Phone: 919-962-2541
Fax: 919-962-2542

E-mail: Murray @ uncwv1.olt.unc.edu

Editorial Headquarters, A-page section

1155 Sixteenth St., N.W.
Washington, DC 20036
Phone: 202-872-4570
Fax: 202-872-4574

E-mail: rmh96 @ acs.org

Managing Editor: Mary Warner

Senior Editor: Louise Voress

Associate Editor: Grace K. Lee

Assistant Editors: Julie Poudrier Skinner, Felicia Wach

Contributing Editor: Marcia Vogel

Director, Operational Support: C. Michael Phillippe

Head, Production Department: Leroy L. Corcoran

Art Director: Alan Kahan

Composition Systems Administrator: Vincent L. Parker

Designers: Peggy Corrigan, Robert Sargent

Production Editor: Elizabeth Wood

Circulation: David Schulbaum

LabGuide

Managing Editor of Directories and Databases: Kathleen Strum

Associate Editor: Joanne Mullican

Journals Dept., Columbus, Ohio

Associate Head: Marianne Brogan

Editorial Office Manager: Mary E. Scanlan

Journals Editing Managers: Kathleen E. Duffy,

Joseph E. Yuvati

Assistant Editors: Stephanie R. Harrell,
Diane E. Needham

Advisory Board: Michelle V. Buchanan, M. Bonner Denton, Joel M. Harris, Timothy D. Harris, Franz Hillenkamp, Dennis C. Johnson, Richard A. Keller, Philip D. LaFleur, Alan G. Marshall, John F. Rabolt, Geraldine Richmond, Ralph Riggan, Debra R. Rolison, Shigeru Terabe, Michael Thompson

Ex Officio: Charles L. Wilkins

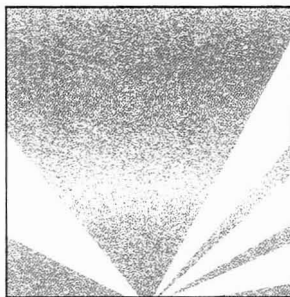
Instrumentation Advisory Panel: Daniel W. Armstrong, Anna Brajer-Toth, Thomas L. Chester, Raymond E. Clement, Norman J. Dovichi, Jack D. Henion, John W. Olesik, Dallas L. Rabenstein, Brenda R. Shaw

Publications Division

Director: Robert H. Marks

Head, Special Publications: Anthony Durniak

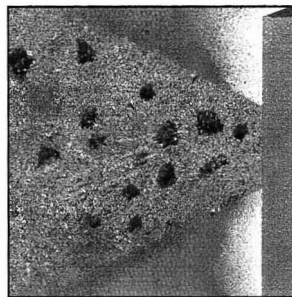
Head, Journals: Charles R. Bertsch



INSTRUMENTATION

971 A

On the cover. Acousto-optic devices. Seventy years ago, Brillouin theorized that light could be diffracted by an acoustic wave. Chieu D. Tran of Marquette University describes the theory of isotropic and anisotropic acousto-optic diffraction and emphasizes the principles and applications of devices such as light deflectors, mode lockers, and acousto-optical tunable filters



REPORT

964 A

Solids analysis by GFAAS. Direct analysis of solids can provide analysts with special information that is not obtainable by conventional techniques that require dissolution. Nancy J. Miller-Ihli of USDA discusses historical perspectives, describes potential problems, and compares solid sampling to slurry sampling

Effective immediately, all manuscripts submitted for consideration for publication in AC RESEARCH should be sent to Editor Royce Murray, Department of Chemistry, Venable and Kenan Laboratories, University of North Carolina, Chapel Hill, NC 27599-3290

UPCOMING RESEARCH

959 A

NEWS

963 A

Joseph Jordan, former Advisory Board member, passes away. • Real-time blood glucose monitor using near-IR light. • Hydrocarbon emission from trees. • New DNA SRM available

BOOKS

983 A

Volumes on fluorescence, immunoassays, and biosensors are reviewed

NEW PRODUCTS & MANUFACTURERS' LITERATURE

986 A

Delivery...What You Expect From the World Leader.

(800) 544-1658

Scrubbers

Purifiers

Regulators

Gas Detection

Assembled in Minutes, Available When You Need It!

Matheson has 48,000 square feet of gas handling equipment and components in stock. All of it is available for delivery as fast as you need it.

Getting the **right** equipment for your needs is just as important as getting it quickly. Matheson understands the chemical and physical properties of gases; this translates to being able to recommend the best product for any application.

When your needs are special, trust Matheson for expert recommendations and the skill to assemble custom gas handling equipment properly. With over 600 components in stock for

regulators alone, you can rely on Matheson to get it right, and get it to you fast.

To learn more about our delivery from stock, send for free information on the Matheson Gas Equipment Technology Center. Circle the Reader Service Number below - or call our Technical Help Line at 1-800-544-1658 (8 a.m.-7:30 p.m. EST).

Matheson®
Gas Products
World Leader in Specialty Gases & Equipment
30 Seaview Drive, Secaucus, NJ 07096-1587

CIRCLE 74 ON READER SERVICE CARD

ANALYTICAL CHEMISTRY (ISSN 0003-2700) is published semimonthly by the American Chemical Society, 1155 Sixteenth St., N.W., Washington, DC 20036. Second-class postage paid at Washington, DC, and additional mailing offices. Postmaster: Send address changes to ANALYTICAL CHEMISTRY, Member & Subscriber Services, P.O. Box 3337, Columbus, OH 43210. Canadian GST Reg. No. R127571347.

Copyright Permission: An individual may make a single reprographic copy of an article in this publication for personal use. Reprographic copying beyond that permitted by Section 107 or 108 of the U.S. Copyright Law is allowed, provided that the appropriate per-copy fee is paid through the Copyright Clearance Center, Inc., 27 Congress St., Salem, MA 01970. For reprint permission, write Copyright Administrator, Publications Division, ACS, 1155 Sixteenth St., N.W., Washington, DC 20036.

Registered names and trademarks, etc., used in this publication, even without specific indication thereof, are not to be considered unprotected by law.

Subscription and Business Information

1992 subscription rates include air delivery outside the U.S., Canada, and Mexico. Canadian subscriptions are subject to 7% GST.

	Members	Nonmembers (personal)	Nonmembers (institutional)
U.S.	\$ 33	\$ 76	\$ 373
Canada and Mexico	69	112	409
Europe	117	233	457
Other countries	150	266	490

Nonmember rates in Japan: Rates above do not apply to nonmember subscribers in Japan, who must enter subscription orders with Maruzen Company Ltd., 3-10, Nihonbashi 2-chome, Chuo-ku, Tokyo 103, Japan. Tel: (03) 272-7211.

For multi-year and other rates, call toll free 800-227-5558 in the U.S. and Canada; in the Washington, DC, metropolitan area and outside the U.S., call 202-872-4363; fax 202-872-4615.

Single issues, current year, \$16.00 except review issue, \$40.00, and LabGuide, \$50.00; **back issues and volumes and microform editions** available by single volume or back issue collection. For information or to order, call the number listed for subscription orders by phone; or write the Microform & Back Issues Office at the Washington address.

Subscription orders by phone may be charged to VISA, MasterCard, or American Express. Call toll free 800-333-9511 in the continental U.S.; in the Washington, DC, metropolitan area and outside the continental U.S., call 202-872-8065. Mail orders for new and renewal subscriptions should be sent with payment to American Chemical Society, Department L-0011, Columbus, OH 43268-0011.

Changes of address must include both old and new addresses with ZIP code and a recent mailing label. Send all address changes to the ACS Columbus address. Please allow 6 weeks for change to become effective. **Claims for missing numbers** will not be allowed if loss was due to failure of notice of change of address to be received in the time specified; if claim is dated (a) North America—more than 90 days beyond issue date, (b) all other foreign—more than 180 days beyond issue date. Hard copy claims are handled at the ACS Columbus address.

ACS membership information: Lorraine Bowlin (202-872-4567)

Articles

- Rapid Screening for Taxanes by Tandem Mass Spectrometry **2313**
Steven H. Hoke II, Joe M. Wood, R. Graham Cooks, Xiao-Hua Li, and Ching-er Chang**
- Application of a Trochoidal Electron Monochromator/Mass Spectrometer System to the Study of Environmental Chemicals **2316**
*J. A. Laramée, C. A. Kocher, and M. L. Deinzer**
- High-Performance Liquid Chromatographic Assay of Taxol **2323**
Steven L. Richheimer, David M. Tinnermeier, and Daniel W. Timmons*
- Molecular Transformation in Hydrotreating Processes Studied by On-Line Liquid Chromatography/Mass Spectrometry **2327**
*Kunngan Qian and Chang S. Hsu**
- Cloud Point Preconcentration and High-Performance Liquid Chromatographic Analysis with Electrochemical Detection **2334**
*Carmelo García Pinto, José Luis Pérez Pavón, and Bernardo Moreno Cordero**
- High-Resolution Determination of ^{147}Pm in Urine Using Dynamic Ion-Exchange Chromatography **2339**
Steve Elchuk, Charles A. Lucy, and Kerry I. Burns*
- Carboxylated Starburst Dendrimers as Calibration Standards for Aqueous Size Exclusion Chromatography **2344**
Paul L. Dubin, Shun L. Edwards, Jerome I. Kaplan, Mamta S. Mehta, Donald Tomalia, and Jiulin Xia*
- Enhanced Separation of DNA Restriction Fragments by Capillary Gel Electrophoresis Using Field Strength Gradients **2348**
András Guttman, Bart Wanders, and Nelson Cooke*
- Collection Efficiency of Solid Surface and Sorbent Traps in Supercritical Fluid Extraction with Modified Carbon Dioxide **2352**
*L. J. Mulcahey and L. T. Taylor**
- Processing Analytical Data Obtained from Second-Order Reactions by Using Continuous Reagent Addition **2359**
*Antonio Velasco, Manuel Silva, and Dolores Pérez-Bendito**
- Use of Spherical Targets To Minimize Effects of Neutron Scattering by Hydrogen in Neutron Capture Prompt γ -Ray Activation Analysis **2366**
Elizabeth A. Mackey, Glen E. Gordon, Richard M. Lindstrom, and David L. Anderson*
- Steady-State Voltammetry of Strong and Weak Acids with and without Supporting Electrolyte **2372**
*Malgorzata Ciszowska, Zbigniew Stojek, Susan E. Morris, and Janet G. Osteryoung**
- Data-Processing Method To Reduce Error Coefficients for Membrane-Based Analytical Systems. 1. Amperometric-Based Sensor Evaluated for Quantification of Oxygen **2378**
*Christopher E. Uhegbu and Harry L. Pardue**
- Recognition of Chemical Markers in Chromatographic Data by an Individual Feature Reliability Approach to Classification **2383**
*Rachhpal S. Sahota and Stephen L. Morgan**
- Flow Determination of Dissolved Inorganic Carbon Using the Alternate Washing System Equipped with a Potentiometric Gas Electrode **2393**
Hirokazu Hara, Yohzoh Okabe, and Tomoko Kitagawa*

*Corresponding author

continued on p. 957 A

Guaranteed Reproducibility Reversed Phase HPLC from EM SEPARATIONS

**Consistent, accurate results - sample after sample,
column after column, year after year
...and then scale up to prep. We guarantee it.**

LiChrospher® RP-18, RP-8, and RP-select B Guaranteed Reproducibility Reversed Phases

E. Merck LiChrospher Guaranteed Reproducibility Reversed Phase HPLC Packings are produced to exacting specifications from the base silica gel through the bonded phases with special testing procedures to assure precise selectivities.

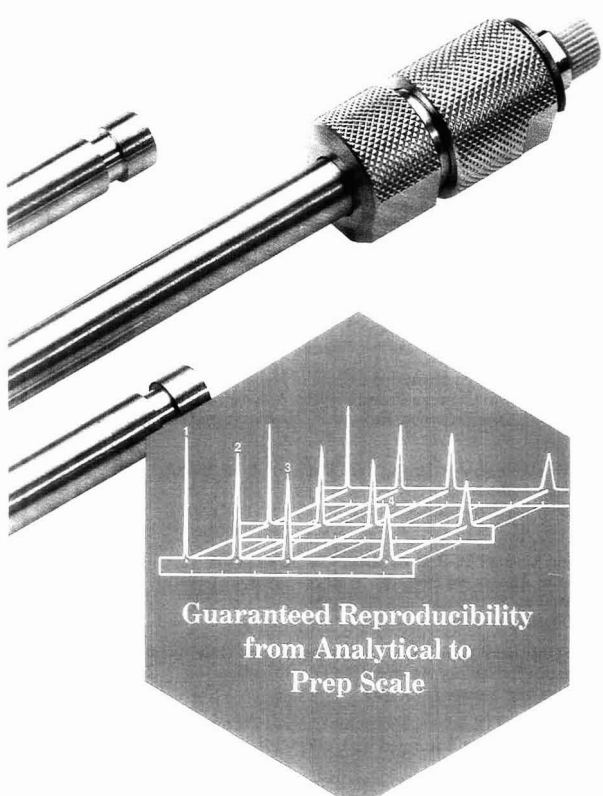
Available in Economical LiChroCART® Cartridge Columns

LiChrospher Reversed Phases are available packed in LiChroCART Cartridge Columns. This newest innovation in HPLC column design from E. Merck provides the highest degree of flexibility and cost saving advantages. Column cartridges are available in three packs at considerable savings.

Introducing Aluspher™ RP-select B For Basic Pharmaceutical Compounds

Aluspher RP-select B is the newest Reversed Phase from E. Merck, which provides a unique selectivity for basic pharmaceutical compounds. As an added advantage Aluspher RP-select B can be used with high pH mobile phases with no detrimental effects on column life.

**Order E. Merck Chromatography
Products directly from EM Separations**



**Guaranteed Reproducibility
from Analytical to
Prep Scale**



EM SEPARATIONS

A Division of EM Industries, Inc.

480 Democrat Road • Gibbstown, New Jersey 08027
(609) 224-0742 • (800) 922-1084 • FAX: (609) 423-4389

CIRCLE 30 ON READER SERVICE CARD

RP-select B • RP-18 • RP-8 • RP-18e • RP-8e

Editorial Information

Instructions for authors of AC RESEARCH are published in the January 1 issue, p. 107. Guidelines for the INSTRUMENTATION, REPORT, ANALYTICAL APPROACH, and A/C INTERFACE features are available from the Washington editorial office. Please consult these instructions and guidelines prior to submitting a manuscript for consideration for publication.

Manuscripts for publication in AC RESEARCH (4 copies of text and illustrative material) should be submitted to the Editor at the University of North Carolina address. Please include a signed copyright status form; a copy of this document appears on p. 111 of the January 1 issue. Manuscripts for publication in the A-page section should be submitted to the Washington editorial staff.

For individual reprints of AC RESEARCH or A-page articles, please contact the authors directly. Bulk reprints of individual articles are available from ACS. For information, write or call the Distribution office at the ACS Washington address (202-872-4539; fax 202-872-4615).

ACS Division of Analytical Chemistry
Chair, Joseph L. Glajch (508-671-8413)
Secretary, Sarah Rutan (804-367-1298)

ACS Information

Library Services	202-872-4515
Education Division	202-872-4388
Meetings Dept.	202-872-4397
Member Services	202-872-4414
Employment Services	202-872-6120
Public Outreach	202-872-4091

Supplementary material is noted in the table of contents with a ■. It is available as photocopy (\$10.00 for up to 3 pages and \$1.50 per page for additional pages, plus \$2.00 for foreign postage) or as 24X microfiche (\$10.00, plus \$1.00 for foreign postage). Canadian residents should add 7% GST. See supplementary material notice at end of journal article for number of pages. Orders must state whether for photocopy or for microfiche and give complete title of article, names of authors, journal, issue date, and page numbers. Prepayment is required and prices are subject to change. Order from Microforms & Back Issues Office at the ACS Washington address.

The paper used in this publication meets the minimum requirements of American National Standard for Information Sciences—Permanence of Paper for Printed Library Materials, ANSI Z39.48-1984.

Journals Department

American Chemical Society
2540 Olentangy River Road
P.O. Box 3330
Columbus, OH 43210
614-447-3600, Ext. 3171
TELEX 6842086; Fax 614-447-3745

Member & Subscriber Services

American Chemical Society
P.O. Box 3337
Columbus, OH 43210
614-447-3776
800-333-9511

Advertising Office: Centcom, Ltd., 1599 Post Road East, P.O. Box 231, Westport, CT 06881

The American Chemical Society and its editors assume no responsibility for the statements and opinions advanced by contributors. Views expressed in the editorials are those of the editors and do not necessarily represent the official position of the American Chemical Society.

Theory of the Interfacial Potential Distribution and Reversible Voltammetric Response of Electrodes Coated with Electroactive Molecular Films

*Christopher P. Smith and Henry S. White**

2398

Voltammetric Sensor for Determination of Water in Liquids

*Huilang Huang and Purnendu K. Dasgupta**

2406

Use of a Laser/Photodiode Array Detector System To Study Mass Transport across Membranes

*Shu-Ling Liao, Richard A. Couch, and Carter L. Olson**

2413

Refractory Behavior of Lead in a Graphite Furnace When Palladium Is Used as a Matrix Modifier

Robert W. Dabeka

2419

Determination of Inorganic Halogen Species by Liquid Chromatography with Inductively Coupled Argon Plasma Mass Spectrometry

*Valeri V. Salov, Jun Yoshinaga, Yasuyuki Shibata, and Masatoshi Morita**

2425

Photoacoustic Spectroscopy and the Effect of Amplified Spontaneous Emission

*Gregory L. Klunder, Robert J. Silva, and Richard E. Russo**

2429

Acrylamide Polymerization Kinetics in Gel Electrophoresis Capillaries. A Raman Microprobe Study

*Tracey L. Rapp, Will K. Kowalchuk, Kevin L. Davis, Elizabeth A. Todd, Kei-Lee Liu, and Michael D. Morris**

2434

Fiber-Optic Ammonia Sensor for Measuring Synaptic Glutamate and Extracellular Ammonia

*Satyajit Kar and Mark A. Arnold**

2438

Speciation of Mercury and Lead Compounds by Microbore Column Liquid Chromatography—Inductively Coupled Plasma Mass Spectrometry with Direct Injection Nebulization

*Sam C. K. Shum, Ho-ming Pang, and R. S. Houk**

2444

Selective Detection of Brominated Hydrocarbons by the Photodetachment-Modulated Electron Capture Detector

*J. A. Bognar, W. B. Knighton, and E. P. Grimsrud**

2451

Correspondence

Determination of Amide Hydrogen Exchange Rates in Peptides by Mass Spectrometry

*Géraldine Thévenon-Emeric, John Kozlowski, Zhongqi Zhang, and David L. Smith**

2456

Outline of a Theory of Focusing in Linear Chromatography

Leonid M. Blumberg

2459

Technical Notes

Cellulose Acetate-Coated Porous Polymer Joint for Capillary Zone Electrophoresis

Chen-Wen Whang and I-Chih Chen*

2461

Synchronization of Timing in Chemiluminescence Thin-Layer Chromatographic Systems by Coupling Pneumatic Nebulization with Optical Fiber-Based Detection

*Nian Wu and Carmen W. Huie**

2465

Tissue Bioreactor for Eliminating Interferences in Flow Analysis

Joseph Wang and Najih Naser*

2469

Author Index

2472

Choice Offerings.

Choice of injector.

Rheodyne's Series-25 line of injectors for HPLC offers you four models:

1. For biotechnology and ion chromatography, the Model 9125.
2. For low-dispersion and microbore chromatography, the 8125.
3. For general applications, the widely used 7125 or the new 7725.

Choice of loading.

Each injector offers two ways of loading sample:

1. You can partially fill the loop. The syringe sets the volume without wasting sample.
2. Or you can completely fill the loop. The loop sets the volume without need to read syringe calibrations. There are ten loop sizes from 5 μ L to 5 mL.

A new choice.

Rheodyne's new model 7725 has all the capabilities of the 7125 plus five advanced features:

1. Continuous flow during switching.
2. Front-end pressure screw for easy maintenance.
3. Wide port angles for improved access to fittings.
4. 2- μ L loop accessory.
5. Optional internal position switch.

For information phone your Rheodyne dealer. Or contact Rheodyne, Inc., P.O. Box 996, Cotati, California 94931, U.S.A. Phone (707) 664-9050. Fax (707) 664-8739.



Circle Reader
Service Card No. 95

RHEODYNE

Tandem Mass Spectrometry of Peptides Using a Magnetic Sector/Quadrupole Hybrid—The Case for Higher Collision Energy and Higher Radio-Frequency Power

Operation of a hybrid mass spectrometer at a laboratory collision energy of 500 eV results in enhanced fragmentation for peptides of RMM > 1 kDa that resembles the fragmentation achieved on four-sector instruments.

Caroline D. Bradley, Jonathan M. Curtis*, and Peter J. Derrick, Institute of Mass Spectrometry and Department of Chemistry, University of Warwick, Coventry CV4 7AL, England and **Barry Wright**, Kratos Analytical, Barton Dock Road, Urmston, Manchester M31 2LD, England

All-Solid-State Sodium-Selective Electrode Based on a Calixarene Ionophore in a Poly(vinyl chloride) Membrane with a Polypyrrole Solid Contact

An all-solid-state sodium-selective electrode is constructed. A polypyrrole membrane doped with NaBF₄ is the charge transfer mediating layer between the sodium-selective PVC membrane and the platinum substrate.

Aodhmar Cadogan, Zhiqiang Gao, Andrzej Lewenstam, and Ari Ivaska*, Laboratory of Analytical Chemistry, Åbo Akademi University, SF-20500 Turku-Åbo, Finland and **Dermot Diamond**, School of Chemical Sciences, Dublin City University, Dublin 9, Ireland

Spike-Correction of Weak Signals from Charge-Coupled Devices and Its Application to Raman Spectroscopy

A multiple missing point fitting method is developed for the correction of spectra that have been contaminated by spikes due to cosmic events, other outliers, or missing points.

Wieland Hill* and Dirk Rogalla, Institut für Spektrochemie und Angewandte Spektroskopie (ISAS), P.O. Box 101352, W-4600 Dortmund 1, Germany

Application of Neutral Networks To Identify Two-Dimensional Fluorescence Spectra

Because of the high noise resistivity of the formal neural network, it can be used to identify two-dimensional fluorescence spectra in cases where classical methods are unsuccessful. This new approach is general and reliable enough to be used as an automatic method for spectra identification.

A. L. Allanic, J. Y. Jézéquel*, and J. C. André, GRAPP-DCPR-UA 328 du CNRS, ENSIC-INPL, BP 451, 54001 Nancy Cedex, France

Scanning Electrochemical Mass Sensitivity Mapping of the Quartz Crystal Microbalance in Liquid Media

A scanning electrochemical method is used to obtain mathematical descriptions of the spatially resolved frequency response to mass changes on the surface of a quartz crystal microbalance immersed in liquid media. The role of the crystal contour, solution properties, and electrode mass on the sensitivity distribution and field fringing is revealed.

A. C. Hillier and M. D. Ward*, Department of Chemical Engineering and Materials Science, University of Minnesota, 421 Washington Avenue Southeast, Minneapolis, MN 55455

Effect of Source 1/f Noise on Optical Polarimeter Performance

An optical polarimeter is modeled using optical calculus computer simulations that accurately account for the effects of the polarizer extinction ratio, the polarization modulation frequency, the analyte concentration, and preamplifier noise.

Edward Voigtman, LGRT-102 (Chemistry), University of Massachusetts at Amherst, Amherst, MA 01003-0035

Quartz Crystal Detector for Microrheological Study and Its Application to Phase Transition Phenomena of Langmuir-Blodgett Films

The resonant frequency and the change in resonant resistance of a quartz crystal is used for the rheological study of thin films. The method is applied to the characterization of the phase transition phenomena of Langmuir-Blodgett films of 1,3-diocetadecyl-*rac*-glycero-2-ol.

Hiroshi Muramatsu* and Kazuhiko Kimura, Technology Center, Seiko Instruments Inc., 563 Takatsuka-shinden, Matsu-do-shi, Chiba 271, Japan

On-Line Coupling of in Vivo Microdialysis with Tandem Mass Spectrometry

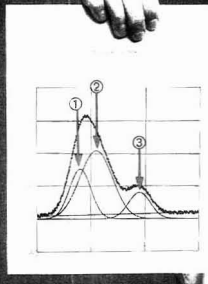
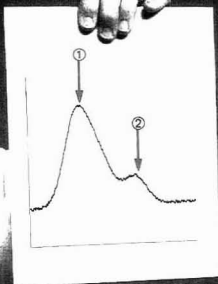
In vivo microdialysis is coupled with MS using a coaxial continuous-flow FAB interface. By using MS/MS, changes in blood levels of xenobiotics in dosed rats can be monitored in real time.

Leesa J. Deterding, Kelly Dix, Leo T. Burka, and Kenneth B. Tomer*, Laboratory of Molecular Biophysics and Experimental Toxicology Branch, National Institute of Environmental Health Sciences, P.O. Box 12233, Research Triangle Park, NC 27709

These articles are scheduled to appear in AC RESEARCH in the near future.

*Corresponding author

Dr. Smith
found
two peaks...



Using PeakFit™,
Dr. Jones found
three peaks...

Guess who got the grant?

Because PeakFit™ uses sophisticated non-linear curve fitting techniques, it is far more effective than other data analysis tools in reducing noise and separating unresolved peaks! In fact, PeakFit is one of the most powerful software packages available today for chromatography and spectroscopy data analysis. For chromatographers, PeakFit extracts important system suitability information such as peak areas, asymmetries, and resolutions – plus column efficiency (number of theoretical plates) from raw data. For spectroscopists, PeakFit calculates peak amplitudes, areas, centers and widths – with complete uncertainty analysis, too!

Use PeakFit's 30 built-in peak functions (including Gaussian, Exponentially-Modified Gaussian, Voigt and many others specifically suited for chromatography and spectroscopy) or input and use your own! Output both graphs and data to over 150 printers, including PostScript™. Of course we can't promise that PeakFit will win you a grant (your competition may already be using PeakFit!), but we can promise that PeakFit will enhance your current analysis methods. Order PeakFit today and see just how many peaks there really are in your data!

Manufacturers: Call for OEM info!

CIRCLE 56 ON READER SERVICE CARD

New Version 3.0!
PeakFit™
Peak Analysis Software
for the IBM PC™



For free brochure:
800-874-1888 (U.S.)
415-453-6700 FAX 415-453-7769

From the makers of SigmaPlot!

Jandel
SCIENTIFIC

2591 Kerner Blvd
San Rafael, CA 94901
Europe: Schmelbuschstr. 25
4006 Erkath, Germany



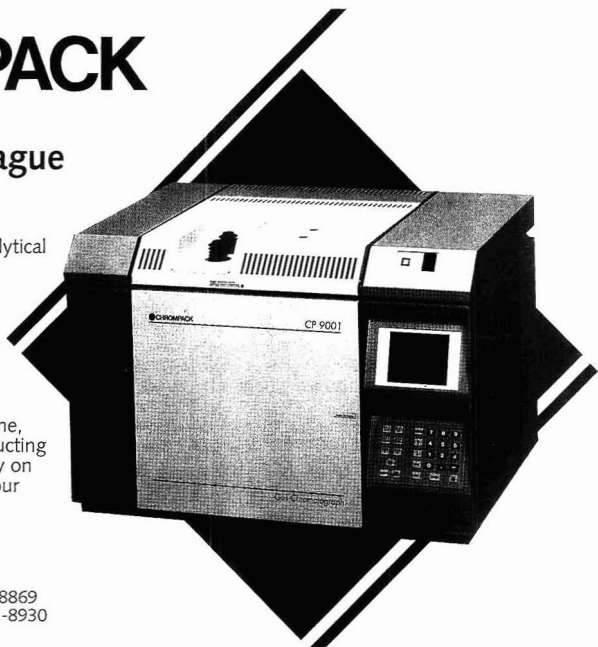
CHROMPACK

Your favorite colleague

- CP-9001 GC - the colleague that:
 - is really easy to work with
 - helps you develop the right analytical methods
 - never holds anything back; all information you want is visible at any time
 - will always work hard for you, while never loudly proclaiming the fact

Whether you are performing routine, around-the-clock analysis or conducting fundamental research, you can rely on your local CP-9001 GC to be at your side for many years to come.

CHROMPACK, Inc
1130 Route 202 South - Raritan, NJ 08869
Tel: 1-800-526-3687 - Fax: (908) 722-8930



FROM CHROMATOGRAPHERS - FOR CHROMATOGRAPHERS

CIRCLE 20 ON READER SERVICE CARD

Quantitative Determination of Glucose in Blood Plasma and in Fruit Juices by Combined WATR-CPMG ^1H NMR Spectroscopy

The method is applied to the determination of total glucose in blood plasma, and the results are compared with those obtained using the standard glucose oxidase method. The accuracy of the results obtained with the WATR-CPMG method is generally within 5% of those obtained with the glucose oxidase method.

Shiyan Fan, W. Y. Choy, S. L. Lam, and S.C.F. Au-Yeung*, Department of Chemistry, The Chinese University of Hong Kong, Shatin, New Territories, Hong Kong and **L. Tsang and C. S. Cockram**, Department of Medicine, Prince of Wales Hospital, The Chinese University of Hong Kong, Shatin, New Territories, Hong Kong

Impact of Polycation Adsorption on Efficiency and Electroosmotically Driven Transport in Capillary Electrophoresis

Cationic polymer adsorption on CZE has an impact on electroosmotically driven transport, peak symmetry, recovery, and efficiency. Polycation fouling of as little as 2% at the inlet of the capillary reduces efficiency by 50% due to nonuniform axial distribution of ζ potential.

John K. Towns, Eli Lilly and Company, Lilly Research Laboratories, Indianapolis, IN 46285 and **Fred E. Regnier***, Department of Chemistry, Purdue University, West Lafayette, IN 47907

Effects of Redox System Structure on Electron-Transfer Kinetics at Ordered Graphite and Glassy Carbon Electrodes

The electron transfer kinetics for 13 redox systems on low-defect highly ordered graphite and laser-activated glassy carbon electrodes are described. The dramatic differences in rate are attributed to several factors, including varying homogeneous self-exchange rates and the physical properties of ordered graphite.

Kristin R. Kneten and Richard L. McCreery*, Department of Chemistry, The Ohio State University, 120 West 18th Ave., Columbus, OH 43210

High-Performance Capillary Electrophoresis of SDS-Protein Complexes Using UV-Transparent Polymer Networks

The application of UV-transparent polymer networks to the separation of SDS-protein complexes on the basis of molecular weight is demonstrated.

Katalin Ganzler, K. S. Greve, A. S. Cohen, and B. L. Karger*, Barnett Institute, Northeastern University, Boston, MA 02115 and **Andras Guttman and N. C. Cooke**, Beckman Instruments, Inc., 2500 Harbour Blvd., Fullerton, CA 92634

Use of Capillary Zone Electrophoresis To Evaluate the Binding of Anionic Carbohydrates to Synthetic Peptides Derived from Human Serum Amyloid P Component

CZE is used to quantitate the binding of peptides to anionic carbohydrates by measuring the amount of unbound peptide that is electrophoretically separated from peptide-carbohydrate complexes.

Niels H. H. Heegaard* and Frank A. Robey, Peptide and Immunochemistry Unit, Laboratory of Cellular Development and Oncology, National Institute of Dental Research, National Institutes of Health, Bethesda, MD 20892

Unsymmetrical Calix[4]arene Ionophore/Silicone Rubber Composite Membranes for High-Performance Sodium Ion-Sensitive Field-Effect Transistors

High-performance sodium ISFETs are fabricated using a calix[4]arene derivative that is highly soluble in silicone rubber. The ISFETs show high sodium ion selectivity and durability.

Keiichi Kimura*, Tasushi Matsuba, Yutaka Tsujimura, and Masaaki Yokoyama, Chemical Process Engineering, Faculty of Engineering, Osaka University, Yamada-oka, Suita, Osaka 565, Japan

Predictive Mode of Kinetic Analysis and Transient Detection Responses. Evaluation of a Recursive Algorithm

The suggested algorithm can be used to extrapolate transient responses when the explicit mathematical function is unknown. It is tested on the responses of ion-selective electrodes and evaluated for a wide range of parameters. The algorithm performs better than least-square fitting.

Israel Schechter, Max-Planck-Institut für Quantenoptik, D-8046 Garching, Germany

Fluorescence Imaging of Electrode-Solution Interfacial Processes

Fluorescein fluorescence generated through electrochemical production of hydroxide is collected with a microscopic imaging system and used to spatially resolve electrochemical activity at the micrometer level.

Royce C. Engstrom*, Shahrokh Ghaffari, and Hongwei Qu, Department of Chemistry, University of South Dakota, Vermillion, SD 57059

Evidence for a Water-Rich Surface Region in Poly(vinyl chloride)-Based Ion-Selective Electrode Membranes

Optical imaging and gravimetric desorption methods demonstrate the presence of a water-rich surface region in poly(vinyl chloride) based on ion-selective electrode membranes and allow estimation of water concentration and diffusion coefficients.

Andy D. C. Chan, Xizhong Li, and D. Jed Harrison*, Department of Chemistry, University of Alberta, Edmonton, Alberta, Canada T6G 2G2

Laser Two-Photon Ionization Detection of Aromatic Molecules on a Metal Surface in Ambient Air

Sensitive and selective ionization of aromatic molecules on a metal surface is demonstrated using laser two-photon ionization. The detection limit is 10^{-13} mol/cm².

Teiichiro Ogawa* and To-oru Yasuda, Department of Molecular Science and Technology, Kyushu University, Kasuga-shi, Fukuoka 816, Japan and **Hirofumi Kawazumi**, Division of Science, Kitakyushu University, Kitakata, Kokura-Minami, Kitakyushu 802, Japan

For a much-needed, molecular focus
on the toxicological effects of chemical agents

Chemical Research in Toxicology

Published bimonthly by the American Chemical Society

Editor: Lawrence J. Marnett, Vanderbilt University

Associate Editors: Fred P. Guengerich, Vanderbilt University
Paul F. Hollenberg, Wayne State University

Chemical
Research in
Toxicology

Chemical
Research
in Toxicology

In primary research reports, *Chemical Research in Toxicology* covers:

- Structure elucidation of novel toxic agents;
- Chemical and physical studies on chemical agents that provide insight into their mode or mechanism of action;
- Experimental and theoretical investigations of the interaction of toxic chemicals with biological macromolecules and other biological targets;
- A range of topics which includes toxicity, teratogenicity, mutagenicity, carcinogenicity, neurotoxicity, and immunotoxicity.

Guided by an esteemed, international editorial advisory board, *Chemical Research in Toxicology* delivers peer-reviewed articles and invited reviews, communications and perspectives, such as these:

A Metabolically Competent Human Cell Line Expressing Five cDNAs Encoding Procarcinogen-Activating Enzymes: Application to Mutagenicity Testing. C.L. Crespie, F.J. Gonzalez, D.T. Steimel, T.R. Turner, H.V. Gelvoine, B.W. Penman, and R. Langenbach.

Carbamoylation of Peptides and Proteins In Vitro by S-(N-Methylcarbamoyl) glutathione and S-(N-Methylcarbamoyl) cysteine, Two Electrophilic S-Linked Conjugates of Methyl Isocyanate. P.G. Pearson, J.G. Slatter, M.S. Rashed, D.H. Han, and T.A. Billie.

Identification of Epoxide and Quinone-Derived Bromobenzene Adducts to Protein Sulfur Nucleophiles. D.E. Slaughter and R.P. Hanzlik.

Mass Spectrometric Analysis of Tobacco-Specific Nitrosamine-DNA Adducts in Smokers and Nonsmokers. P.G. Foiles, S.A. Akerkar, S.G. Carmella, M. Kagan, G.D. Stoner, J.H. Resau, and S.S. Hecht.

Submit Your Papers Now!

CRT reviews all articles promptly, and upon acceptance, publishes in a timely manner.

For complete information on manuscript submission, please contact Lawrence J. Marnett, Department of Biochemistry & Center for Molecular Toxicology, School of Medicine, Vanderbilt University, Nashville, TN 37232-0146. Phone: 615-343-7328. Fax: 615-343-7534.

Here's what *Nature* says about this prestigious, essential resource for any scientist involved in toxicological research.

"As would be expected of a journal of the American Chemical Society, it [*Chemical Research in Toxicology*] has been able to sustain publication of quality research papers, particularly in chemical analysis and reactive intermediates. The invited reviews and perspectives have been particularly well chosen and are of high quality."

Reprinted by permission from *Nature* Vol. 341 pp. 356
Copyright © 1989 Macmillan Magazines Ltd.

1992 Subscription Information

Chemical Research in Toxicology is published by the American Chemical Society. One volume per year.
1992 Volume 4 ISSN 0893-228X

	Canada and U.S.	Europe and Mexico	Air Service Included	All Other Countries Air Service Included
ACS Members				
One Year	\$ 46	\$ 54	\$ 63	\$ 69
Two Years	\$ 82	\$ 98	\$ 116	\$ 128
Nonmembers	\$296	\$304	\$313	\$319

Member rates are for personal use only. For nonmember rates in Japan, contact Maruzen Co., Ltd. This publication is available on microfilm, microfiche, and online through CJO on STN International.

ACS members and nonmembers send your order to:
ACS, Department L-0011, Columbus, OH 43268-0011,
or call 1-800-333-9511 (toll free) or 614-447-3776.

Joseph Jordan



The JOURNAL regrets to report the death of Joseph Jordan on Aug. 14. Jordan, a professor of chemistry at The Pennsylvania State University for more than 30 years, was a pioneer in bioelectrochemistry and the study of heat effects in chemical reactions. He served on the Advisory Board of ANALYTICAL CHEMISTRY from 1968 to 1970.

Blood Glucose and IR Light

Sandia National Laboratories and the University of New Mexico (UNM) School of Medicine have combined IR spectroscopy and chemometrics to develop a painless, real-time blood glucose monitoring system for diabetics.

Near-IR light, which has slightly longer wavelengths than visible light, can penetrate tissue—in this case, a finger inserted into the monitor. The various wavelengths are absorbed by the tissues of the finger, the light is dispersed into a spectrum, and the data are analyzed for glucose-specific absorptions to determine glucose concentration. The algorithm used takes into account variations in skin coloring, blood chemistry, and finger thickness.

Sandia and UNM are looking for an industrial partner to help them develop a commercial monitor. The eventual goal of those working on glucose monitors is a programmable insulin pump and monitor system that would act as an artificial pancreas, replacing the daily, self-administered injections of insulin. Diabetes, the leading cause of blindness in people aged 25–74, is estimated to contribute \$20 billion annually to health care costs.

Hydrocarbons from Trees

Most of us are aware that trees replenish the oxygen in the atmosphere, but our beloved trees may also be polluters.

According to the National Center for Atmospheric Research (NCAR) in Boulder, CO, the Environmental Protection Agency has found that reducing hydrocarbon emissions from cars has not helped to reduce ozone concentrations in rural and urban areas. NCAR hypothesizes that nonmethane hydrocarbon emissions, such as isoprene and terpenes from vegetation, may be promoting ozone formation.

NCAR will monitor isoprene emissions from trees at Oak Ridge National Laboratory through the use of a chemiluminescence detector (*Anal. Chem.* **1990**, *62*, 1055–60) and an existing 33-m tower equipped with leaf en-

closures as well as light and temperature sensors at four levels in the forest canopy. They will also gather data from various instrument packages suspended at different levels on a tethered line hung from a balloon 1 km in the air. This project will be the first opportunity researchers have had to take measurements of this type from several acres of trees at the same time.

DNA SRM

DNA fingerprint matching is the latest weapon in law enforcement's arsenal against crime. It is also used in paternity cases, and the Army is beginning a new program to use it as "dog tags" for soldiers. However, because it is relatively new, attorneys have not always had an easy time getting the results introduced as evidence.

The National Institute of Standards and Technology's newly formed Biotechnology Division, with support from the National Institute of Justice, hopes to help change that by making available Standard Reference Material 2390. This new QA standards set is the first developed by the division. It contains male and female DNA molecules extracted from living cells; pre-cut fragments of a viral DNA that can be used as a genetic ruler; and tubes, each containing 3 million human cells from which DNA can be extracted and tested. Laboratories that use FBI protocols for DNA profiling can effectively use the SRM to check their performance at each step of the procedure.

DNA molecules are cut at specific points, using enzymes separated by electrophoresis, and transferred onto a nylon membrane. The fragments are tagged with radioactive probes and photographed. The DNA fingerprint appears as lines in specific positions, much like the bar coding used in grocery stores. A combination of five probes is used to discern an individual's unique DNA pattern. The chance of two unrelated individuals having the same pattern is less than about one in hundreds of thousands.

SRM 2390 costs \$374 and can be obtained from the Standard Reference Materials Program, Rm. 205, Bldg. 202, Gaithersburg, MD 20899 (301-975-6776; fax 301-948-3730).

For Your Information

A new, Canadian-based, bimonthly publication entitled *Scientific Exchange* is designed to provide a venue for the advertising of surplus and used scientific equipment. The vendor supplies a brief description of the item for sale or exchange or the item that is wanted, along with a point of contact. For subscription, classified, and advertising rates, contact *Scientific Exchange*, P.O. Box 484, Osgoode, Ontario, Canada K0A 2W0 (613-826-0742; fax 613-826-0489).

SOLIDS ANALYSIS BY GFAAS

Nancy J. Miller-Ihli

U.S. Department of Agriculture
Nutrient Composition Laboratory
Beltsville, MD 20705

Graphite furnace atomic absorption spectrometry (GFAAS) is one of the most cost-effective, sensitive techniques available. GFAAS provides sub-part-per-billion detection capability using microliter-sized samples and has been used extensively for metal determinations in a wide variety of sample matrices. Most analysts dissolve the sample so that it is in a liquid form for injection and analysis, but there are benefits to direct solids analysis by GFAAS.

Advantages of solid sampling over conventional sample preparation procedures, such as acid digestion or fusion, include reduced sample preparation time, decreased analyte loss through volatilization before analysis, reduced analyte loss related to retention by an insoluble residue, reduced sample contamination, increased sensitivity (because samples are not diluted), elimination of hazards associated with the use of acids, and easier selective analysis of microamounts of sample. Unlike nebulization techniques, GFAAS does not suffer significantly from particle size effects because it offers longer residence times. As a result, samples may be placed directly in the graphite furnace atomizer and, in most instances, are completely atomized.

Direct analysis of solids can provide analysts with special information that is not obtainable by conventional techniques requiring sample

dissolution. In addition, direct solids analysis is important when only small amounts of sample are available or when there is interest in the distribution of analyte. Forensic applications, including analyses of gunshot residues, are well suited for solid sampling. Environmental monitoring often can be accomplished with direct solid sampling.

The two principal methods for analyzing solids by GFAAS are to introduce the solid material directly into the furnace and to prepare a slurry or a suspension, then inject the sam-

REPORT

ple by using conventional liquid sample delivery techniques. The merits of each technique will be compared. Because both methods provide for the analysis of solids, the following definitions apply: Direct solids analysis means that the solid is placed directly in the furnace; slurry analysis means that the sample is prepared as a slurry or a suspension.

Historical perspective

Several reviews have focused on solid sampling using GFAAS (1-5). The most comprehensive of these is a recent paper by Bendicho and de Loos-Vollebregh (5), which includes more than 250 references. The idea of doing direct solids analysis was first reported by L'vov, who introduced the concept of graphite furnace determinations in the 1950s (6). Early pioneers included Kerber (7), who in 1971 reported the use of the first

commercial tube-type furnace to determine gold in polyester fibers.

Much of the early work was done with specially built atomizers or modified commercial graphite furnaces. Both resistively and inductively heated furnaces were used. A variety of commercial and noncommercial atomizers, some of which were specially designed for solid sampling, have been reported in the literature. Solid sample analyses have been performed with the following types of atomizers: Massman-type graphite tube, Hitachi's cup-cuvette, platform, Grün-Optiks' boat system, Thermo Jarrell Ash's microboat, Perkin Elmer's cup-in-tube, Varian's transversely heated carbon rod, graphite probes, Schmidt and Falk's ring chamber, and Rettberg and Holcombe's second surface atomizer.

The only commercial graphite furnace AA spectrometers designed specifically for direct solids analysis are the systems built in Germany by Grün-Optiks. More recently, Analyte Corporation has produced the Atom-source system, which is a commercial glow discharge AA system.

Although each of the above-mentioned systems offers special advantages for solid sampling, a general improvement in graphite furnace technology probably had a more significant impact on the direct analysis of solids. A noteworthy improvement during the past decade was the introduction of the stabilized-temperature platform furnace (STPF) concept by Slavin et al. (8, 9), which provided conditions leading to reproducible, high-accuracy determi-



nations that were not significantly affected by matrix effects.

The STPF approach strives for more isothermal conditions for atomization using a conventional Massman-style furnace that is known to have a longitudinal temperature gradient. This concept facilitated the direct analysis of solid samples and also encouraged the use of aqueous standards for calibration. The key points of this approach include using good background correction (such as the Zeeman effect), platform atomization, and integrated absorbance measurements for quantitation.

As Bendicho and de Loos-Vollebregt (5) point out, the annual number of solid-sampling applications reported has increased since 1970. The STPF concept was introduced in 1982, and in 1987 a record was set, when more than 20 papers on direct solid sampling were published. Interestingly enough, the average number of publications on direct solid sampling between 1970 and 1992 has been approximately 10 per year.

Potential problems

Although it seems obvious that solid-sampling GFAAS is a powerful technique, it is rather limited for direct solids analysis. Many authors have reported disadvantages such as calibration, microweighing, and sample introduction difficulties; lack of solid standards; problems attributable to sample inhomogeneity; increased background (requiring good background correction); residue buildup; sample-dependent peak shapes; problems with refractory elements and with automation of sample intro-

duction; too much sensitivity; poor precision; and limited sample size.

Admittedly, some of these problems justify serious consideration; successful determinations may be impeded if certain criteria are not met. However, many problems can be avoided by using state-of-the-art technology and equipment. Calibration can be successfully performed in most instances with aqueous calibration standards, thereby avoiding the need for solid standards for each sample matrix of interest. Sample inhomogeneity can be a problem if one is trying to get an accurate estimate of the mean concentration of analyte in the bulk sample; however, direct solid sampling can provide detailed information and facilitate homogeneity characterization of materials at milligram and submilligram levels.

Use of Zeeman effect or Smith-Hieftje background correction provides adequate compensation for background in most instances. The buildup of residual material can often be avoided by using oxygen ashing during the char step in the furnace program. The fact that solid sampling produces signals with sample-dependent peak shapes is typically unimportant as long as quantification is done using integrated absorbance measurements.

Poor precision is usually the result of inhomogeneous distribution of analyte in the solid material. Precision can be improved by reducing the particle size of the material being analyzed and by increasing the number of samples analyzed. Limited sample size can be a physical restriction, or it can be attributable to the analyti-

cal signal relative to the working range. In the latter case, larger amounts of material may be used when an alternate, less sensitive wavelength is available.

The two disadvantages related to sample introduction are not easily dismissed. Analysts agree that microweighing is difficult and time consuming, and that transport of milligram quantities of material requires special care—even if the sample is weighed directly on a boat, a platform, or a cuvette that can be directly inserted into the furnace.

Grün-Optiks developed a partially automated commercial solid sampler consisting of a powder sampler, a balance, and a transport system to be used with its Grün Zeeman AAS instruments (10). Powdered sample is transferred, using a piston and vibration, onto a graphite boat that is subsequently weighed and inserted inside the graphite tube. As one might expect, several factors affect the amount of material placed on the platform: particle size, moisture content, fat content, and specific gravity. Obviously, such a system works best with dried powders consisting of particles of uniform size and density. An alternative approach to the automation of direct solid sample introduction is the preparation of a slurry or a suspension that facilitates using conventional liquid sample-handling technology. This approach will be discussed later in this REPORT.

Solid-sampling applications

Table I lists 15 references in which direct solid sample insertion into the

graphite furnace is used. These fairly recent references typically report data based on calibration against aqueous standards (11–25). Table I highlights the suitability of this approach for the successful determination of many elements in a wide variety of sample matrices. Some other applications have been reported that indicate that strong matrix interferences have been observed, necessitating the method of additions or calibration against matrix-matched reference materials.

One serious problem with the use of reference materials for calibration is that analysts treat the mean reference value as absolute, ignoring the uncertainty. The certified concentration of Cd in Standard Reference Material 1568 Rice Flour is $0.029 \pm 0.004 \mu\text{g/g}$ (26). Thus the uncertainty is $\pm 14\%$ compared with the mean concentration. If calibration is performed by using this material, then by definition, the computed analytical concentrations can have no smaller uncertainty than $\pm 14\%$. This level of uncertainty is not uncommon in commercial reference materials, and some uncertainties are as high as 25%. Also typically, minimum recommended amounts for commercial materials are on the order of 250 mg. When using these materials for direct solids sampling, 0.5–5.0 mg is commonly used. The use of small amounts creates the possibility that the analyte will not be sufficiently homogeneously distributed to be representative of the bulk material.

If analysts want to use solid materials for calibration, special materials must be developed that are well characterized with small elemental concentration uncertainties. In addition, these materials must be characterized at milligram and submilligram levels. These concerns strongly support the benefit of calibration with aqueous standards whenever possible.

Calibration using aqueous standards for direct solids analysis requires absolute accuracy of the liquid sample delivery system, because the accuracy of the determination will depend on the volume delivered by the autosampler or the pipet. This method differs from digest analyses in which both samples and standards are pipetted and the absolute volumes delivered do not affect calibration accuracy.

Slurry sampling

As mentioned earlier, a convenient way to introduce solid material into the graphite furnace is to prepare a

Table I. Solid-sampling applications

Sample	Element	Reference	Comments
Ni alloys	Ti, Bi, Te, Se, Pb	11	STPF, cup-in-tube
Plastics	Cd, Cu, Mn, Rb	12	Cup-in-tube
Wheat	Cd	13	Milled
Biological samples	Pb, Cd	14	Special platform
Biological samples	Cu	15	Ringed chamber, integrated absorbance
Biological samples	Al	16	Constant-temperature furnace
Bovine liver	Pb	17	Wall, probe, platform, oxygen ashing
Airborne particles	Cd, Pb, Ni, Cu, Mn	18	Probe
Coal, fly ash	Cd, Ni	19	Cup-in-tube, oxygen ashing, alternate wavelength
Inorganic materials	Se	20	Graphite dilution, nickel powder modifier
Filter material	Cd	21	Ground, punched
Waterborne suspended matter	Cd, Pb, Cu	22	Filtered
Biological samples	As, Cd, Zn, Pb, Mn	23	Minicup
Fly ash, ash, filter paper	Cd, Pb, Ti, Cu, Mn, Ag	24	Second surface atomizer
Coal, fly ash	As, Cd, Cr, Hg	25	Graphite dilution

slurry or a suspension. Conventional liquid sample-handling devices such as autosamplers and pipets may then be used to inject material into the furnace for analysis.

Because of the ease of sample introduction, Stephen and co-workers (27) concluded that slurry sampling combines the benefits of both solid and liquid sampling. To ensure that a representative aliquot is injected into the furnace, the slurry must be either stabilized or homogenized. Stabilization has been attempted with the use of thixotropic agents such as viscalex (27) and glycerol (28). In each instance, the authors reported difficulty with reproducible autosampler pipetting because of material adherence to the exterior of the autosampler capillary. Problems with incomplete delivery of the sample with more viscous solutions were also reported. Such results suggest that sample homogenization using agitation, such as a magnetic stir bar (29), vortex mixing (30), gas bubbling (31), or ultrasonic agitation, is preferable.

Reports of magnetic stirring of slurries followed by manual pipetting are frequently found in the literature. Many researchers have reported good results, but this approach is limited because manual pipetting provides poorer precision than that which can be achieved with

an autosampler, and most modern laboratories require automated GFAAS analyses. Lynch and Littlejohn (32) developed a miniature stir bar mixing method that was used with an autosampler to facilitate automatic mixing of food slurries in the autosampler cup before analysis. Hinds and Jackson (33) found magnetic stir bar mixing inadequate for some applications, because soil samples often contain particles that adhere to the stir bar due to their magnetic properties.

Vortex mixing can provide adequate agitation of slurries before analysis, but sample aliquots removed for injection must be hand-pipetted directly into the furnace to avoid rapid sedimentation of larger, dense particles that may occur when vortexed samples are subsequently placed in an autosampler cup (28). Because automated sample introduction using an autosampler is virtually impossible when using vortex mixing, this mixing technique has limited applicability for modern slurry analyses.

Workers in our lab tried gas bubbling for slurry mixing and found that this method typically provided low analyte concentrations when the analyte of interest was associated with larger, dense particles. Bendicho and de Loos-Vollebregt (31) also reported poor homogenization when

using argon mixing for glass slurries containing particles in the 82–341- μ m range, but they found that the argon bubbling method could be used to extract analyte from glass slurries into a 3% HF solution (34).

Mixing with the use of a compact portable ultrasonic processor provides superior agitation of slurry preparations (28). High-power ultrasound depends on cavitation and its secondary effects. Ultrasound can be effective in dislodging mechanically interlocked particles, dispersing solids, and wetting particles; and the effectiveness often increases with decreasing particle size (35). In addition, ultrasonic agitation can increase the extraction of analyte into the liquid phase of the slurry. Commercial 40–50-W units designed to process small samples (100 μ L–25 mL) effectively disaggregate and disperse particles. The titanium ultrasonic probe may be mounted on the autosampler tray and its operation synchronized with that of the autosampler, providing fully automated slurry analyses (36, 37). Perkin Elmer has commercialized this concept and sells an ultrasonic mixing device (USS-100) (38) as an autosampler accessory to facilitate automated slurry analyses.

Slurry-sampling applications

Table II lists 13 references in which slurry graphite furnace determinations were made. Like the applications cited in Table I, these references contain data based on calibration

against aqueous standards (28, 30, 32, 33, 39–47). Table II illustrates the utility of this approach and suggests that a wide range of samples can be accurately analyzed by using aqueous standards and modern furnace technology. All applications in Table II use one of the mixing methods discussed previously. The only mixing methods that have been automated are the minibar (32) and ultrasonic agitation (28, 30, 44–46).

In some instances, matrix modifiers have been used. Oxygen ashing to avoid buildup of carbonaceous material has also been used successfully in some studies. Bradshaw and Slavin (45) reported a method that omitted both the pyrolysis step and use of a matrix modifier, providing rapid furnace analyses. Such a method requires the use of an efficient background correction system such as the Zeeman effect.

Comparison of techniques

Direct solids sampling and slurry sampling each have advantages and disadvantages. Both may require some sample pretreatment, such as grinding, if the sample is not in the proper form or if the analyte is not homogeneously distributed.

Direct solids sampling is desirable when only a small amount of sample is available or when there is interest in the distribution of analyte in the solid. Most solid-sampling insertion devices are manual and require skill to obtain reasonable precision. Direct solids sampling may require the use

of matrix-matched standards or the method of standard additions for calibration. Direct solids sampling can easily handle alloys, pure metals, and plastics. Slurry sampling is best suited for powdered samples such as sediments or soils.

Slurry sample introduction is straightforward when using conventional liquid autosamplers and allows matrix modifiers to be used easily because they are miscible with the liquid phase. Slurry mixing can be automated by using the mini-stir bar method or ultrasonic agitation. Calibration using aqueous standards may be applicable for a wide range of samples for both solid and slurry sampling. Slurry samples may be diluted easily to facilitate analysis in the linear range; solid samples can be diluted only with graphite powder, increasing the risk of sample contamination. Both techniques, however, may take advantage of other methods for reducing sensitivity, such as selecting an alternate absorption line.

Analysts using slurry sampling must have some knowledge of the analyte distribution in the solid and liquid phases of the slurry to derive maximum benefit from the technique. If a large percentage of the analyte is extracted into the liquid phase, the precision will approach that obtainable with a conventional liquid digest. If, on the other hand, none of the analyte is extracted into the liquid phase, slurry sampling can provide an easy and reproducible method for the introduction of microgram amounts of solid into the graphite furnace.

Factors of interest in optimizing either direct solids analysis or slurry sampling include homogeneity of the solid material, distribution of analyte in the solid, density, and particle size. Density and particle size should be used to calculate the number of particles in a mass. A large number of particles will reduce sampling errors (48). Both techniques offer the unique opportunity for homogeneity characterizations of materials at milligram and submilligram levels. When working with inhomogeneous samples, both direct solids analysis and slurry sampling will benefit from smaller particle sizes.

Several authors have reported a preference for either direct solids analysis or slurry analysis. In my opinion, slurry sample introduction should be used whenever possible because it is easy, it uses liquid sample-handling technology, and it provides both accurate and precise

Table II. Slurry-sampling applications

Sample	Element	Reference	Comments
Soil	Pb	33	Vortex mixing
Airborne particulates	V, Cd, Ni, Cu, Pb, Fe, Mn	39	Ultrasonic mixing
Biological RMs	Cr, Co, Pb, Mn	40, 41	Manual agitation, oxygen ashing, zirconium beads
Iron oxide	As, Pb	42	Magnetic stirring, manual pipetting, nickel modifier
Glass	Cu, Co, Cr, Mn, Fe, Ni	43	3% HF, argon bubbling
Spinach RM	Mn, Fe, Cu, Cr, Al	44	Ultrasonic mixing, homogeneity study
Coal, fly ash	As, Ti, Pb	45	Ultrasonic mixing
Sediment	As, Fe, Mn, Pb	30	Ultrasonic and vortex mixing
Biological samples	Mn	46	Ultrasonic mixing
Milk powder	Zn, Cu, Mo, Pb	47	Magnetic stirring
Food	Pb	32	Minibar mixing, palladium modifier
Biological samples	Mn, Zn, Fe, Cu, Pb, Cr, Ni, Mo, Al, Ca	28	Ultrasonic mixing

results with calibration using aqueous standards. Bendicho and de Loos-Vollebregt (5) state that the slurry technique gives better analytical performance than direct solid sampling. Brady and co-workers (49) also endorse the use of slurries because of the ease of sample introduction. Schmiedel and co-workers (50) support slurry GFAAS and state that ultrasonic mixing provides optimum homogenization of the slurry before analysis.

A generalized approach

Compared with other techniques for direct solids analysis, GFAAS clearly offers the analyst a unique combination of excellent sensitivity and simplicity at moderate cost. Modern methods must address the need for increased sample throughput, necessitating faster analyses. This requires minimizing chemical sample pretreatment, including decomposition procedures. Analysis of solids by either direct analysis or slurry sample introduction facilitates rapid analyses.

Regardless of whether the analyst chooses direct solids or slurry analysis, a systematic approach can be identified. Calibration with aqueous standards represents the most sensible approach for identifying generalized procedures for solids and slurry sampling. Calibration with aqueous standards does, however, require that the absorption signal be independent of the bulk matrix and be dependent only on the concentration of the analyte (5). Using peak area measurements for calibration is therefore imperative, because peak area measurements minimize the effect of varying vaporization rates (attributable to matrix differences).

The analyst must also be concerned with sample homogeneity, because results will be affected by the distribution of analyte in the solid. If increased homogeneity is desirable, samples may be ground to a small (<10 µm) particle size before analysis (48). All samples should be weighed on an electronic microbalance, and care must be taken to avoid sample contamination. Analytical conditions must be optimized for each sample type. Wavelength selection will depend on analyte concentration, and less sensitive nonresonance wavelengths may prove useful.

GFAAS conditions must be systematically optimized, because analyte volatilities may be affected by the sample matrix. Charring and atomization optimization studies must be performed to identify optimum

conditions. The use of matrix modifiers or oxygen ashing may prove useful to avoid carbonaceous buildup in the furnace. Modern furnace technology should be used, including good background correction, platform atomization, and calibration with aqueous standards using peak area measurements. Optimized furnace conditions make it possible to obtain accurate and precise analytical determinations by using either direct solids analysis or slurry analysis.

References

- (1) Headridge, J. B. *Spectrochim. Acta* **1980**, *35B*, 785.
- (2) Langmyhr, F. J.; Wibetoe, G. *Prog. Anal. At. Spectrosc.* **1985**, *8*, 193.
- (3) Van Loon, J. C. *Anal. Chem.* **1980**, *52*, 955A.
- (4) Langmyhr, F. J. *Analyst* **1979**, *104*, 993.
- (5) Bendicho, C.; de Loos-Vollebregt, M.T.C. *J. Anal. At. Spectrom.* **1991**, *6*, 353.
- (6) Lvov, B. V. *Spectrochim. Acta (Engl. Transl.)*, **1984**, *39B*, 159; *Inzh. Fiz. Zh.* **1959**, *2*(2), 44.
- (7) Kerber, J. D. *At. Absorpt. Newsl.* **1971**, *10*, 104.
- (8) Slavin, W.; Manning, D. C. *Spectrochim. Acta* **1982**, *37B*, 955.
- (9) Slavin, W.; Carnrick, G. R.; Manning, D. C.; Pruszkowska, E. *At. Spectrosc.* **1983**, *4*, 69.
- (10) Kurfürst, U.; Kempeneer, M.; Stoeppler, M.; Schuier, O. *Fresenius J. Anal. Chem.* **1990**, *337*, 245.
- (11) Irwin, R.; Mikkelsen, A.; Michel, R. G.; Dougherty, J. P.; Pirelli, F. R. *Spectrochim. Acta* **1990**, *45B*, 903.
- (12) Vollkopf, U.; Lehmann, R.; Weber, D. *J. Anal. At. Spectrom.* **1987**, *2*, 455.
- (13) Horner, E.; Kurfürst, U. *Fresenius Z. Anal. Chem.* **1987**, *328*, 386.
- (14) Brown, A. A.; Lee, M.; Küllemer, G.; Rosopulo, A. *Fresenius Z. Anal. Chem.* **1987**, *328*, 354.
- (15) Schmidt, K. P.; Falk, H. *Spectrochim. Acta* **1987**, *42B*, 431.
- (16) Frech, W.; Baxter, D. C. *Fresenius Z. Anal. Chem.* **1987**, *328*, 400.
- (17) Chakrabarti, C. L.; Karwowska, R.; Hollebone, B. R.; Johnson, P. M. *Spectrochim. Acta* **1987**, *42B*, 1217.
- (18) Chakrabarti, C. L.; Xiuren, H.; Shaole, W.; Schroeder, W. H. *Spectrochim. Acta* **1987**, *42B*, 1227.
- (19) Schlemmer, G.; Welz, B. *Fresenius Z. Anal. Chem.* **1987**, *328*, 405.
- (20) Dürnberger, R.; Esser, P.; Janßen, A. *Fresenius Z. Anal. Chem.* **1987**, *327*, 543.
- (21) Schothorst, R. C.; Geron, H.M.A.; Spitsbergen, D.; Herber, R.F.M. *Fresenius Z. Anal. Chem.* **1987**, *328*, 393.
- (22) van Son, M.; Muntau, H. *Fresenius Z. Anal. Chem.* **1987**, *328*, 390.
- (23) Atsuya, I.; Itoh, K.; Akatsuka, K. *Fresenius Z. Anal. Chem.* **1987**, *328*, 338.
- (24) Rettberg, T. M.; Holcombe, J. A. *Anal. Chem.* **1986**, *58*, 1462.
- (25) Esser, P. *Fresenius Z. Anal. Chem.* **1985**, *322*, 677.
- (26) Standard Reference Material 1568 Rice Flour, National Bureau of Standards Certificate of Analysis; National Institute of Standards and Technology; Gaithersburg, MD, 1978.
- (27) Stephen, S. C.; Littlejohn, D.; Ottaway, J. M. *Analyst* **1985**, *110*, 573.
- (28) Miller-Ihli, N. J. *J. Anal. At. Spectrom.* **1988**, *3*, 73.

- (29) Karwowska, R.; Jackson, K. W. *J. Anal. At. Spectrom.* **1987**, *2*, 125.
- (30) Epstein, M. S.; Carnrick, G. R.; Slavin, W.; Miller-Ihli, N. *J. Anal. Chem.* **1989**, *61*, 1414.
- (31) Bendicho, C.; de Loos-Vollebregt, M.T.C. *Spectrochim. Acta* **1990**, *45B*, 679.
- (32) Lynch, S.; Littlejohn, D. *J. Anal. At. Spectrom.* **1990**, *4*, 157.
- (33) Hinds, M. W.; Jackson, K. W. *At. Spectrosc.* **1991**, *12*, 109.
- (34) Bendicho, C.; de Loos-Vollebregt, M.T.C. *Spectrochim. Acta* **1990**, *45B*, 695.
- (35) *Ultrasonics, Encyclopedia of Chemical Technology*, 3rd ed.; John Wiley and Sons: New York, 1983; Vol. 23.
- (36) Miller-Ihli, N. J. *J. Anal. At. Spectrom.* **1989**, *4*, 295.
- (37) Miller-Ihli, N. J. U.S. Patent 4,930,898, 1990.
- (38) Carnrick, G. R.; Daley, G.; Fotinopoulos, A. *At. Spectrosc.* **1989**, *10*, 170.
- (39) Fernandez, A.; Fernandez, R.; Carrion, N.; Loreto, D.; Benzo, Z.; Fraile, R. *At. Spectrosc.* **1991**, *12*, 111.
- (40) Ebdon, L.; Fisher, A. S.; Parry, H.G.M.; Brown, A. A. *J. Anal. At. Spectrom.* **1990**, *5*, 321.
- (41) Ebdon, L.; Fisher, A. S.; Parry, H.G.M.; Brown, A. A. *J. Anal. At. Spectrom.* **1988**, *3*, 131.
- (42) Garcia, I. L.; Cordoba, M. H. *J. Anal. At. Spectrom.* **1990**, *5*, 647.
- (43) Bendicho, C.; de Loos-Vollebregt, M.T.C. *Spectrochim. Acta* **1990**, *45B*, 695.
- (44) Miller-Ihli, N. J. *Fresenius J. Anal. Chem.* **1990**, *337*, 271.
- (45) Bradshaw, D.; Slavin, W. *Spectrochim. Acta* **1989**, *44B*, 1245.
- (46) Jordan, P.; Ives, J. M.; Carnrick, G. R.; Slavin, W. *At. Spectrosc.* **1989**, *10*, 165.
- (47) Wagley, D.; Schmiedel, G.; Mainka, E.; Ache, H. *J. At. Spectrosc.* **1989**, *10*, 106.
- (48) Miller-Ihli, N. J. *At. Spectrosc.* **1992**, *1*, 1.
- (49) Brady, D. V.; Montalvo, J. G.; Glowacki, G.; Pisciotto, A. *Anal. Chim. Acta* **1974**, *70*, 448.
- (50) Schmiedel, G.; Mainka, E.; Ache, H. *J. Fresenius Z. Anal. Chem.* **1989**, *335*, 195.



Nancy J. Miller-Ihli is a research chemist in the Nutrient Composition Laboratory at the USDA. She received her B.A. degree in chemistry in 1977 from Shippensburg University (PA) and her Ph.D. in analytical chemistry in 1982 from the University of Maryland under the direction of T. C. O'Haver. Her research interests include GFAAS, multielement AAS, slurry sampling, sample preparation, plasma emission spectrometry, and the development of quality control materials. She has published approximately 35 papers and is the author of a patent describing the use of ultrasonic agitation for slurry mixing.

Intelligent Particle Sizing



with integrated SMART OPTICS

Malvern's MasterSizer X, top of its class in laser diffraction particle sizing, now has a new and unique smart optics module. A dedicated microprocessor takes care of instrument control settings and data storage, leaving the system computer free to concentrate on its own specialist subjects. More sophisticated background subtraction, accurate triggering and measurement cycles up to 250 Hz, are some of the new features.

To learn more, be **SMART** contact Malvern Instruments.....



Malvern Instruments Inc.
10 Southville Rd, Southborough, MA 01772, USA
Telephone: (508) 480 0200 Fax: (508) 460 9692

CIRCLE 70 ON READER SERVICE CARD

Keep Important Microsamples From Getting More Micro

Wheaton V-Vials® Provide A Better Way To Handle Microsamples...And The Best Way To Get Them Back

Conical interior ensures maximum retrieval

Multipurpose vials can be used for microscale reactions, centrifugation, storage, and shipping

Available with a variety of closures including screw cap, crimp seals, and liners

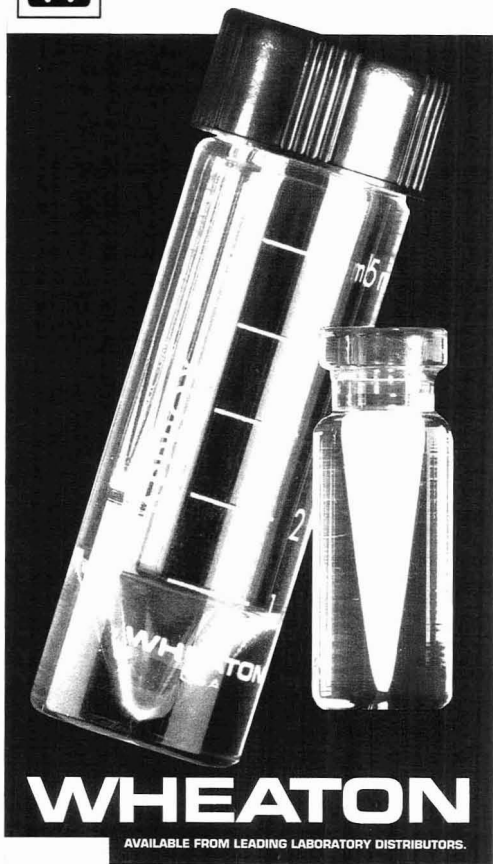
Specify Wheaton V-Vials...because not all V-Vials are alike.

For more product information and a list of the dealers nearest you call 1-609-825-1100 or FAX: 1-609-825-1368.



WHEATON

Manufacturers Since 1888
1000 N 10TH STREET MILLVILLE NJ 08332-2092 USA



WHEATON

AVAILABLE FROM LEADING LABORATORY DISTRIBUTORS.

Circle 114 for Demonstration. Circle 115 for Literature.

Providing Quality, Excellence, Innovation and Service to exhibitors and conferees for 44 years:

- Outstanding Technical Program
- Plenary Sessions with world-renowned speakers
- Symposia organized by experts in their field
- Poster symposia
- "PC&E Interactions" – informal sessions
- Quality short courses
- Unique showcase for new instrumentation
- On-floor sales
- Vendor-sponsored seminars & demonstrations
- Employment bureau
- Social activities for conferees and their families and much more

If you value "Quality, Excellence, Innovation and Service," you will want to attend the world's largest scientific exposition and technical program — PITTCO'93.

For more information contact:

Dept. 60, Suite 332, Penn Center Blvd.

Pittsburgh, PA 15235-5503

Phone: (412) 825-3220 Fax: (412) 825-3224

Toll Free: 1-800-825-3221



Georgia World Congress Center March 8-12, 1993

CIRCLE 88 ON READER SERVICE CARD

From pesticides/residues to food and feed processing

Journal of Agricultural and Food Chemistry

Published monthly!

EDITOR:
Irvin E. Liener
University of Minnesota

ASSOCIATE EDITORS:
G. Wayne Ivie
USDA
Marshall Phillips
USDA

Let the **Journal of Agricultural and Food Chemistry** (JAFC) keep you up to date on the production and safety of foods, feeds, fibers, and other agricultural products, as well as the chemical, biochemical, and nutritional aspects of foods and feeds.

Published monthly, JAFC is the leading international journal of basic research into the application of chemistry to foods and agricultural products. Read wide-ranging reports and original research used by your colleagues virtually every working day!

1992 Rates ISSN 0021-8561	ACS Members**		Nonmembers 1 Year
	1 Year	2 Years	
U.S.	\$ 30	\$ 54	\$303
Canada & Mexico	\$ 48	\$ 90	\$321
Europe*	\$ 70	\$134	\$343
All Other Countries*	\$ 85	\$164	\$358

*Includes Air Service **Member rates are for personal use only
For nonmember rates in Japan, contact Maruzen Co., Ltd.

For more information or to subscribe contact:
American Chemical Society
Member and Subscriber Services
P.O. Box 3337, Columbus, OH 43210

In a hurry? Call Toll Free 1-800/333-9511 (U.S. only).
Outside the U.S.: (614) 447-3776.
Fax your order: (614) 447-3671



Acousto-Optic Devices

Optical Elements for Spectroscopy

Chieu D. Tran
Department of Chemistry
Marquette University
Milwaukee, WI 53233

Seventy years ago, Brillouin theorized that light could be diffracted by an acoustic wave (1). This prediction was based on the fact that when an acoustic wave is propagated in a transparent material, it produces a periodic modulation of the index of refraction. The perturbation in the refractive index arises from the change in the number density of the acoustic medium induced by the compression and rarefaction of the traveling sound wave. As a consequence, the propagating acoustic wave produces a moving grating that will diffract portions of an incident light beam.

This sound-light interaction phenomenon, which is called the acousto-optic interaction, was initially observed by Debye and Sears in 1932 (2). Early studies were limited to interactions of low-frequency acoustic

waves with incoherent light sources in liquids and gases. As a result, the phenomenon had an impact primarily on the academic community; experimental results provided a basic understanding of the thermal and acoustic properties of liquids and gases.

The first applications of the acousto-optic interaction did not appear until the 1960s. Since then, significant scientific and technological advances have occurred in optics, electronics, and materials chemistry.

for the deflection, temporal and amplitude modulation, and spectral tuning of light. Today, acousto-optic devices are used in applications ranging from sophisticated scientific instruments such as astronomical spectrophotometers and picosecond laser systems to the commonplace neighborhood supermarket scanner.

Diffraction by acoustic waves may lead to a change in the amplitude, frequency, direction, or wavelength of the incident light. Optical properties of the medium where the acous-

INSTRUMENTATION

The advent of the laser, the development of new piezoelectric materials with high coupling factors that facilitate high-frequency (GHz) acoustic techniques, and the development of new crystals that have low acoustic loss at high frequencies and require low radio frequency (rf) drive power made it possible to realize practical applications of acousto-optic devices

to-optic interaction occurs usually dictate the type of transformation of the diffracted light. Acousto-optic interactions, when observed in an optical isotropic medium, lead to a change in the frequency, direction, and amplitude of the light. The diffraction in this case can be explained by using the classical Bragg diffraction principle. Acousto-optic devices

such as light modulators, deflectors, scanners, and mode lockers are based on this type of interaction.

Interesting results are observed when acousto-optic interactions occur in an anisotropic medium. This type of interaction leads to a change not only in the frequency and direction of the incident beam but also in its wavelength. Here the diffraction process cannot be explained by the normal Bragg diffraction principle. This so-called abnormal Bragg diffraction process has been successfully exploited to develop devices such as the acousto-optic tunable filter (AOTF). The AOTF is a compact, solid-state monochromator that can be tuned electronically in a matter of microseconds over a wide spectral range encompassing the UV and IR regions. This device has been called the "new generation monochromator" and provides a unique means for the development of spectroscopic instruments.

In this INSTRUMENTATION article the theory of isotropic and anisotropic acousto-optic diffraction will be described. Emphasis will be placed on the principles and applications of specific devices such as light deflectors, mode lockers, and AOTFs.

Acousto-optic interactions in an optical isotropic medium

Theory. The diffraction of a light beam by an acoustic wave can be explained in terms of wave interactions or particle collisions. In the former case, the acoustic wave produces a change in the refractive index of the optical medium and generates a traveling pressure disturbance that

includes regions of compression and rarefaction in the crystal. This effect can be considered as generating a diffraction grating that moves at the speed of sound and comprises periodic changes in the optic phase.

The diffraction process can be explained by the optical wavefronts illustrated in Figure 1. Because the velocity of light is about 5 orders of magnitude greater than the velocity of sound, the acoustic wave is considered to be stationary during the time required for the optical beam to travel through the crystal. Suppose that the half-wavelength region labeled $n + \Delta n$ is under compression, and the region labeled $n - \Delta n$ is under rarefaction. The portion of the optical wave passing through the compression will be slowed (relative to the undisturbed material of index n), whereas the portion passing through the rarefaction will be accelerated. The emerging optical wavefront will be "corrugated" and, if the corrugations are joined by a continuous plane, its direction will be tilted relative to that of the incident wavefronts.

Depending on the interaction length l between the acoustic wave and the light wave, the diffraction process can be divided into two different types: Raman-Nath diffraction (sometimes called Debye-Sears diffraction) and Bragg diffraction. The diffraction is in the Raman-Nath region when the interaction length l is relatively short or when the Raman-Nath parameter Q , defined as

$$Q = 4l\lambda/\Lambda^2 \quad (1)$$

(where λ and Λ are the wavelength of the optical wave and the sound wave, respectively), is less than one (3-5). The diffraction process (Figure 2a) has multiple orders, because the interaction length is relatively short and can be approximated as a thin grating (i.e., the diffraction spreading of the light between adjacent compression and rarefaction regions overlaps).

When the interaction length l is large (or when $Q \gg 1$), the diffraction is in the Bragg region (3-5). In this case, only first-order diffraction is observed (Figure 2b). Because the thin grating approximation is no longer valid, higher diffraction orders will undergo complete destructive interference if the incident light beam is normal to the sound beam. For constructive interference to take place, the angle of incidence must be tilted with respect to the acoustic beam direction.

Consider the collisions of photons and phonons, as shown by Yariv (5). From a quantum theoretical point of view, the interaction of sound and light can be treated as a collision of photons and phonons. The incident light beam with a wave vector \mathbf{k}_i and the frequency ω_i can be considered as consisting of a stream of particles (photons) with momentum $\hbar\mathbf{k}_i$ and energy $\hbar\omega_i$. Similarly, the sound wave can be thought of as particles (phonons) with momentum $\hbar\mathbf{k}_a$ and energy $\hbar\omega_a$.

As illustrated in Figures 2b and 2c, the diffraction of light by the acoustic beam involves a series of collisions, each consisting of the annihilation of one incident photon at frequency ω_i and one phonon (ω_a) as well as the simultaneous creation of a new (diffracted) photon at a frequency ω_d . For these collisions to occur, conservation of energy and momentum must be observed. Conservation of momentum requires that the momentum $\hbar(\mathbf{k}_i + \mathbf{k}_a)$ of the colliding particles be equal to the momentum $\hbar\mathbf{k}_d$ of the diffracted photon. Therefore

$$\mathbf{k}_d = \mathbf{k}_i + \mathbf{k}_a \quad (2)$$

Conservation of energy dictates that

$$\omega_d = \omega_i \pm \omega_a \quad (3)$$

It is evident from Equation 3 that the diffracted beam is shifted in frequency by an amount equal to the sound frequency. These relationships facilitate the use of propagation of the applied acoustic wave to either increase or decrease the frequency of the diffracted beam by an amount equal to ω_a . Figure 2b illustrates the upshift case in which the conservation of energy requires addition of the phonon energy to that of the annihilated (incident) photon to form a new (diffracted) photon. As a consequence, $\omega_d = \omega_i + \omega_a$. If the direction of the sound wave in Figure 2b is reversed (as shown in Figure 2c), the diffraction process is the one in which a new (diffracted) photon and a new phonon are generated while the incident photon is annihilated. In this case, conservation of energy yields

$$\omega_d = \omega_i - \omega_a \quad (4)$$

This process is generally known as downshift Bragg diffraction.

Because the energy of the acoustic waves is much smaller than that of the photons, $\mathbf{k}_i = \mathbf{k}_d$ may be assumed. The momentum-matching triangle is isosceles; thus, the incident and diffracted angles are the same ($\theta_i = \theta_d$) and are related to the wavelength of

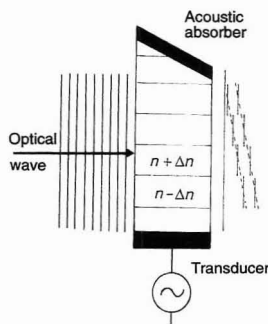


Figure 1. Diffraction of optical wavefronts by an acoustic wave.

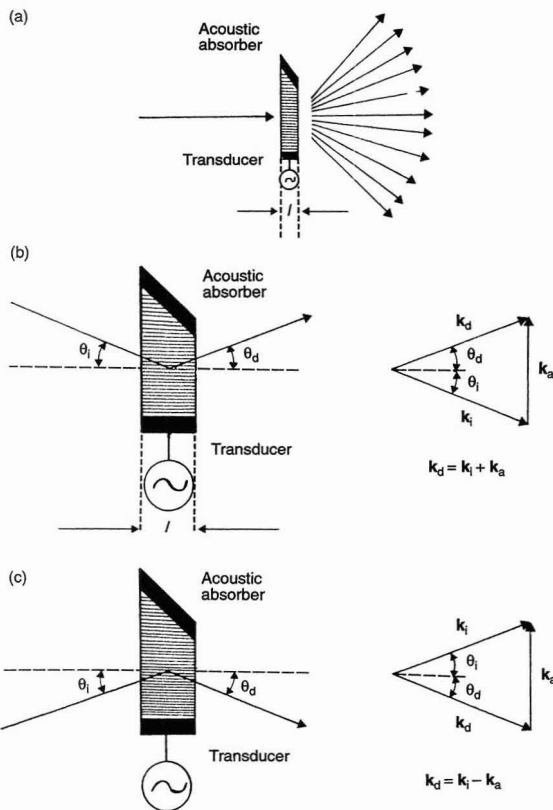


Figure 2. Diffraction of light by an acoustic wave in an isotropic medium.

(a) Raman-Nath diffraction into multiple orders, (b) upshift Bragg diffraction, and (c) downshift Bragg diffraction.

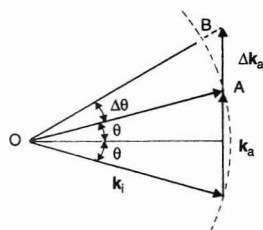


Figure 3. Wavevector diagram illustrating the deflection of light from θ to $\theta + \Delta\theta$ when the frequency of the acoustic wave changes from f_a to $f_a + \Delta f_a$.

the light λ and of the sound Λ by the well-known Bragg equation

$$\sin \theta = \mathbf{k}_a / 2\mathbf{k}_d = \lambda / 2\Lambda \quad (5)$$

Applications

Deflectors. Acousto-optic deflectors are based on the deflection of light by a propagating acoustic wave in an optical isotropic medium. Incident light is deflected in one or more directions by periodic variations in the refractive index produced by the propagating ultrasound wave. A change in the deflection angle (defined as the angle between the transmitted and the diffracted beam) is achieved by changing the applied acoustic frequency. This change can be accomplished only if the operation is near the Bragg diffraction condi-

tion (i.e., the laser beam is oriented at the Bragg angle of incidence θ in relation to the acoustic beam of frequency ω_a). Because the Bragg condition is satisfied, diffraction is optimized and the momentum vector diagram shown in Figure 3 is closed. After being diffracted by the sound wave, all light rays emerge in phase at an angle θ and interfere constructively.

The sound frequency is then varied from f_a to $f_a + \Delta f_a$ while the incident angle is kept constant at θ . Because $k_a = 2\pi f_a / v_s$ (where v_s is the acoustic velocity), this frequency variation causes a change $\Delta k_a = 2\pi \Delta f_a / v_s$ in the magnitude of the sound wave vector, as shown in Figure 3. To satisfy the conservation of momentum, all diffracted wave vectors must lie on the circle through A and B, with O as the center. Because the incident angle θ and the magnitude of the diffracted wave vector remain unchanged, the tip of the diffracted wave vector, as previously explained, must lie on the circle. The momentum diagram cannot be closed, and the momentum therefore is not strictly conserved. The beam will diffract in the direction that gives the least violation (i.e., along the direction OB), causing a change of $\Delta\theta$ in the diffraction angle. The value of $\Delta\theta$ is calculated from the figure as (5)

$$\Delta\theta = \Delta k_a / k_i = \lambda \Delta f_a / n v_s \quad (6)$$

Thus the deflection angle is proportional to the change of the sound frequency.

Another important parameter is the number of resolvable spots N or the factor by which $\Delta\theta$ exceeds the beam divergence angle. If the diffraction angle θ_{dif} is assumed to be λ / nD where D is the beam diameter, the number of resolvable spots is

$$N = \theta / \theta_{\text{dif}} = (\lambda / v_s) \Delta f_a / (\lambda / D) = \Delta f_a (D / v_s) = \Delta f_a \tau \quad (7)$$

where $\tau = D / v_s$ is the time it takes the sound to cross the optical beam diameter.

It is evident from Equations 6 and 7 that materials with low acoustic velocity v_s will provide a large angle of deflection and a large number of resolvable spots. However, such materials cannot be used in high-speed operation and in the high-frequency region because they have high acoustic attenuation. Usually, a compromise must be made in designing such devices. This type of acousto-optic device has been used not only as a deflector but also as an optical scanner, an intracavity Q switch, and a cavity dumper (6-8).

Modulators and mode lockers. In addition to modulating direction and frequency as in the deflector, an acousto-optic device can be used to modulate the diffracted beam amplitude. Two types of modulators are possible, depending on whether the applied acoustic wave is a propagating wave or a standing wave.

When the applied acoustic wave is a propagating wave, the modulator consists of a combination of an acousto-optic deflector and a spatial filter, a device with a lens and a pinhole. The filter is aligned so that it will reject the deflected beam and pass the undeflected beam. The deflected beam will be turned on and off as the wave propagates across the crystal, and the amplitude of the beam emerging from the spatial filter will be modulated (3, 4).

The second type of modulator is different from other acousto-optic devices in that it has no damper to absorb the propagating acoustic wave. Thus the acoustic wave generated by the transducer will be reflected by the opposite face of the crystal. Interference between the propagating and the reflected waves produces standing waves inside the crystal. The diffraction of light by standing waves produces some interesting phenomena, notably the locking of the longitudinal modes of the laser or mode locking (5).

A mode locker is an acousto-optic modulator placed inside a laser cavity. An acoustic standing wave is produced inside the modulator when an rf signal is applied to the crystal through the transducer. According to Bragg diffraction, the modulator will introduce a periodic loss into the laser cavity at twice the frequency of the acoustic standing wave. As a consequence of the loss, the energy inside the laser cavity is compressed to very short pulses. These compressed pulses must travel at the same frequency and in phase (i.e., the longitudinal modes have to be locked together) to produce a very short output pulse.

To mode lock a laser, the frequency of the modulator must be in synchronization with the traveling time of the compressed pulse inside the cavity. To make a round trip in the laser cavity, a pulse requires a time of $2L/c$ (where L is the cavity length and c is the speed of light). Thus the frequency of the standing wave inside the modulator must be $c/4L$ if mode locking is to be achieved. This condition enables the modulator (the mode locker) to act as a very fast shutter that is in synchronization

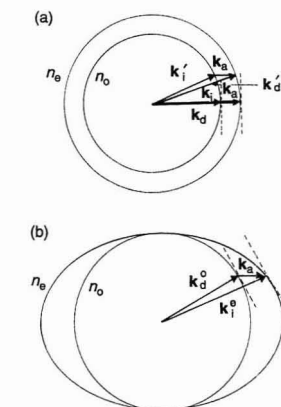


Figure 4. Wavevector diagrams for diffraction of light by an acoustic wave in an anisotropic medium.

(a) collinear acousto-optic interaction and
(b) noncollinear acousto-optic interaction.

with the pulse. It will open only once per round-trip transit time to allow passage of the pulse; the shutter is closed at all other times, and the only light that can circulate between the output coupler and the high reflector is the mode-locked pulse. Because this pulse experiences minimum loss and maximum gain, it will be amplified. Light traveling in the cavity when the mode locker is closed will be attenuated and cannot reach threshold.

The output of a mode-locked laser is, therefore, a train of very short pulses. The time separation between pulses is the time it takes for each pulse to make one round trip inside the cavity, $2L/c$; and the frequency of the mode-locked pulses is therefore $c/2L$. For example, a laser that has a distance of 30 cm between the high reflector and the output coupler will produce a mode-locked pulse train at 500 MHz.

Acousto-optic interactions in an optical anisotropic medium

Theory. For acousto-optic diffraction to occur in an isotropic medium, the phonon vector is normal to the bisector of k_d and k_i and

$$[k_d] = [k_i] \quad (8)$$

Because $[k_d] = 2\pi n_d/\lambda$ and $[k_i] = 2\pi n_i/\lambda$, Equation 8 is valid only when the refractive index for the incident and diffracted waves is iden-

tical (i.e., $n_i = n_d$). However, this is not true when the light is diffracted by shear acoustic waves in an optical anisotropic medium. In a shear acoustic wave, the displacement of matter is perpendicular to the direction of its propagation. A light beam propagating as an extraordinary ray (e-ray) is converted into an ordinary ray (o-ray) by interaction with and diffraction from the shear acoustic wave propagating in the same medium. This 90° rotation of the polarization stems from the fact that the disturbance caused by the shear wave induces a birefringence that acts on the incident light as a birefringent plate (3, 4, 9, 10). Thus the plane of polarization of light is rotated. Because the crystal is birefringent, the rotation of the plane of polarization results in a significant change in refractive index ($n_i \neq n_d$), and a change in momentum and wavelength must occur.

The associated momentum vector diagram is no longer symmetric as it was in Figures 2b and 2c. Instead, it appears as shown in Figures 4a and 4b, where θ_d may be significantly different from θ_i . The same effect also occurs in isotropic crystals. However, in isotropic materials, the wavevector for the incident and diffracted beams is the same (because $n_i = n_d$); thus, there is no effect on the diffraction processes (3, 4, 9, 10).

Consider Figure 4, where the incident light is an e-ray and the diffracted light is an o-ray. The associated wavevectors are

$$k_i = (2\pi n_e/\lambda_o) \quad \text{and} \quad k_d = (2\pi n_o/\lambda_o) \quad (9)$$

As expected, $\theta_i \neq \theta_d$. The angles θ_i and θ_d are related (10) to the acoustic frequency f_a , the refractive indices for the incident and diffracted light polarizations n_i and n_d , and the acoustic velocity v_s by

$$\sin \theta_i = \left(\frac{1}{2n_i} \right) \left(\frac{\lambda_o f_a}{v_s} \right) \times \left[1 + \left(\frac{v_s}{\lambda_o f_a} \right)^2 (n_i^2 - n_d^2) \right] \quad (10)$$

and

$$\sin \theta_d = \left(\frac{1}{2n_d} \right) \left(\frac{\lambda_o f_a}{v_s} \right) \times \left[1 + \left(\frac{v_s}{\lambda_o f_a} \right)^2 (n_i^2 - n_d^2) \right] \quad (11)$$

In Figure 5, θ_i and θ_d are plotted against the acoustic frequency for paratellurite (TeO_2) at $\lambda = 632.8$ nm, $n_i = 2.45$, $n_d = 2.26$, and $v_s = 6.17 \times 10^4$ cm/s. The minimum frequency at which an interaction may occur corresponds to $\theta_i = 90^\circ$ and $\theta_d = -90^\circ$. At

these angles, the three wavevectors \mathbf{k}_i , \mathbf{k}_d , and \mathbf{k}_a are collinear, as shown in Figure 4a, and the conservation of momentum can be written as

$$|\mathbf{k}_i| + |\mathbf{k}_a| = |\mathbf{k}_d| \quad (12)$$

The frequency for which collinear diffraction takes place is

$$f_a = [v_s (n_i - n_d)] / \lambda_o \quad (13)$$

Because of this collinearity, the interaction between the incident and acoustic waves is relatively long and the bandwidth of the diffracted light is narrow (high resolution). The acceptance angle is relatively large: When the incident wavevector changes from \mathbf{k}_i to \mathbf{k}_i' , the diffracted wavevector becomes \mathbf{k}_d' and the momentum matching condition is still approximately maintained ($\mathbf{k}_d' = \mathbf{k}_i' + \mathbf{k}_a$; see Figure 4a).

If the incident light were an o-ray rather than an e-ray, the direction of the acoustic wave in Figure 4a would be reversed. In fact, the roles of the two curves in Figure 5 would be reversed by interchanging n_i and n_d .

Collinear acoustic diffraction can only be achieved in a uniaxial crystal where the incident and diffracted light are normal to the optical axis of the crystal. Because of the symmetry of crystals, it is sometimes not possible to have this type of interaction. The common type of interaction is noncollinear, as shown in Figure 4b, where the incident and diffracted wavevectors and the acoustic wavevector are not collinear. To satisfy the momentum-matching condition, it is necessary to select the

acoustic wavevector so that the tangents to the incident and diffracted wavevector loci are parallel. Figure 4b shows the incident e-beam (whose wavevector is \mathbf{k}_i^e) diffracted by the acoustic wave (\mathbf{k}_a) to a diffracted o-beam (whose wavevector is \mathbf{k}_d^o). The two optical beams do not separate until they exit the crystal, at which time the diffracted beam is separated from the transmitted beam (i.e., the zero-order diffracted beam). This separation facilitates isolation of the diffracted beam by an aperture (9, 10).

The relationship between the acoustic frequency f_a and the incident angle θ is given by

$$f_a = [v_s (n_i - n_d)] (1/\lambda_o) (\sin^4 \theta_i + \sin^2 2\theta_i)^{1/2} \quad (14)$$

When $\theta_i = 90^\circ$, Equation 14 reduces to Equation 13, the collinear case.

In an anisotropic crystal in which the phase-matching requirement is satisfied, diffraction occurs only under optimal conditions. These conditions are defined by the frequency of the acoustic waves and the type of crystal. For a particular crystal and at a given acoustic frequency f_a , only light whose wavelength satisfies either Equation 13 or 14 is diffracted from the crystal. The crystal can, therefore, be spectrally tuned by changing the frequency of the acoustic wave.

The acousto-optic interaction in an anisotropic medium has led to the development of AOTFs (9, 11–19). As indicated previously, an AOTF is an electronically driven optical dispersion device capable of performing spectral analysis of optical signals. It is constructed from a birefringent crystal, such as quartz or TeO_2 , onto which an array of piezoelectric transducers (e.g., LiNbO_3 , LiTaO_3 , LiIO_3) is bonded. When an rf signal is applied to the transducer, acoustic waves are generated in the crystal. The propagating acoustic waves produce a periodic moving grating that will diffract a portion of the incident beam. For a fixed acoustic frequency and sufficiently long interaction length, only a very narrow band of optical frequencies can approximately satisfy the phase-matching conditions necessary for diffraction. The narrow spectral bandpass of the filter can thus be tuned over large optical regions simply by changing the frequency of the applied rf signal.

Based on the configuration of the optical and acoustic wavevectors, the AOTFs can be divided into two different types: collinear and noncollinear (9, 11–19). In collinear AOTFs,

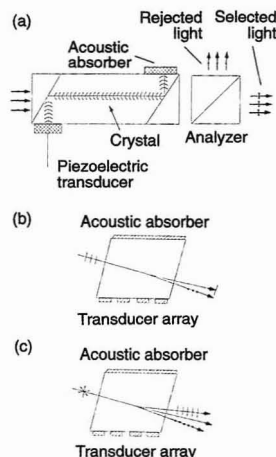


Figure 6. Types of acousto-optic tunable filters: (a) collinear, (b) noncollinear with linear polarized incident light, and (c) noncollinear with unpolarized incident light.

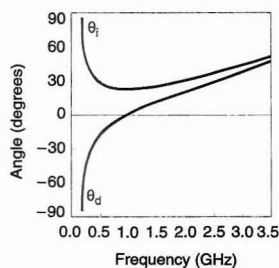


Figure 5. Angles of (extraordinary) incident (θ_i) and (ordinary) diffraction (θ_d) as a function of acoustic frequency for diffraction of 632.8-nm light by an acoustic wave in an anisotropic crystal (TeO_2) with $n_i = 2.45$, $n_d = 2.26$ and acoustic velocity of 6.17×10^4 cm/s.

the acoustic wave is brought in as a longitudinal wave, which is then converted to a shear wave upon reflection at the input face of the crystal (Figure 6a). The acoustic wave and the input optical beam then propagate collinearly down the crystal along which the acousto-optic interaction occurs. The diffracted wave, whose polarization is orthogonal to that of the incident beam, also propagates down the crystal collinearly with the incident beam and the acoustic wave. The transmitted (or zero-order diffraction) and diffracted beams also emerge collinearly from the AOTF. Because polarization of the diffracted beam is orthogonal to that of the transmitted beam, it is separated from the latter not by a pinhole but rather by a polarizer (Figure 6a). The interaction length between the incident wave and the acoustic wave is relatively long in this type of filter. AOTFs fabricated from birefringent crystals that have relatively small acoustic figures of merit (e.g., quartz and MgF_2) are often of the collinear type.

As explained in the previous section, it is sometimes impossible to construct collinear AOTFs because of crystal structure. Noncollinear AOTFs have been reported. Figures 6b and 6c illustrate the case where

the incident, diffracted, and acoustic waves are noncollinear. In Figure 6b, the acoustic wave diffracts the vertically polarized incident beam into a horizontally polarized beam. Because the transmitted and diffracted beams are well separated, the latter can be readily isolated by an aperture. Because of the birefringence of the crystal and the noncollinearity of the transmitted and diffracted beams, an incident horizontal polarized light beam will be diffracted into a vertical polarized light beam, and an incident unpolarized light beam will be diffracted into two beams that have orthogonal (vertical and horizontal) polarization propagated in different directions (see, e.g., Figure 6c). AOTFs of this type are often reserved for crystals that have relatively high acousto-optic figures of merit, such as TeO_2 (9, 11–19).

A typical spectral profile of diffracted light as a function of the applied rf for a noncollinear TeO_2 AOTF is shown in Figure 7 (12). The incident light in this case is a multiline argon ion laser beam that was a mixture of six different wavelengths: 514.5, 501.7, 496.5, 488.0, 476.5, and 457.9 nm. As indicated in Equation 14, the wavelength of the diffracted light depends on the frequency of the applied rf signal. Light with relatively shorter wavelengths will be diffracted from the AOTF when the filter is applied with a higher rf signal. For example, 514.5-nm light is diffracted when a 64.3115-MHz rf signal is applied to the AOTF. Increasing the frequency to 75.8522 MHz changes its wavelength to 457.9 nm.

As illustrated, the intensity of the diffracted light is very sensitive to the frequency of the applied rf signal. A very small change in the frequency may result in a large change in the intensity of the diffracted light (12). The power of the applied rf signal also affects the intensity of the diffracted light, I , because it is a function of the acoustic power density P_a . I is given by (9, 10)

$$I = I_0 \sin^2(\Delta k l / 2\pi) \quad (15)$$

where Δk is the wavevector mismatch; l is the interaction length between the acoustic and the optical beams; and \sin is defined as $\sin(x) = \sin(\pi x / \pi \lambda)$. I_0 is a function of acoustic power density P_a , the acousto-optic figure of merit M_2 , and the interaction length l , and is given by

$$I_0 = \sin^2(\pi^2 M_2 P_a l^2 / 2\lambda_0) \quad (16)$$

Figure 8 shows the intensity of the light diffracted by the TeO_2 AOTF

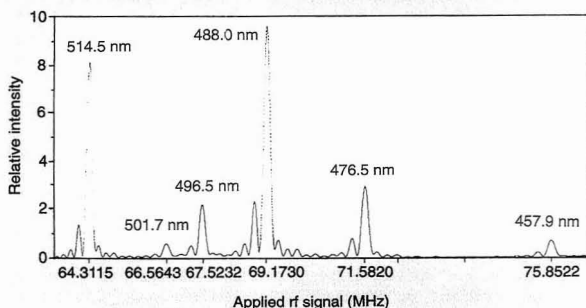


Figure 7. Spectral profile of the light diffracted from a noncollinear TeO_2 acousto-optic tunable filter as a function of the frequency of the applied rf signal.

The incident light is the multiline output of an argon ion laser. (Adapted with permission from Reference 12.)

plotted in three dimensions against the frequency and the acoustic power of the applied rf signal (20). The intensity of the diffracted light can be controlled by controlling either the frequency or the power of the applied rf signal.

Other characteristics of the AOTF include its resolution, spectral tuning range, and response time. The filter resolution, defined as the full width at half maximum, is given by

$$\Delta\lambda = \lambda_0^2 / 2\Delta n \sin^2 \theta_i \quad (17)$$

where $\Delta n = n_e - n_o$ and λ_0 is the wavelength of observation (9). The resolution of a noncollinear TeO_2 AOTF with $l = 1$ cm and $\Delta n = 2.45 - 2.26 = 0.19$ is calculated as 3 Å at 632.8 nm (3). It is evident from Equation 17 that the AOTF resolution is dependent on the wavelength. The resolution is higher at shorter wavelengths and becomes degraded as the wavelength increases. Other factors such as increasing the interaction length l can also be exploited to enhance the resolution. For a particular AOTF, l can be increased by increasing the number of acoustic waves in the optical aperture of the crystal. To achieve good performance, the acoustic frequency should be high and the aperture should be large. Finite aperture and attenuation of the acoustic waves at high frequencies (through absorption by the AOTF) determine the final resolution. AOTFs with resolutions of a few angstroms are commercially available from Brimrose Corp. (Baltimore, MD) and Matsushita Electronic Components (Kodama, Osaka, Japan).

Important criteria for selecting birefringent materials for AOTFs include the acousto-optic figure of merit M_2 and the high-frequency acoustic loss. According to Equation 16, materials with high M_2 values will provide diffracted light with higher intensity. Higher resolution AOTFs will be achieved when the filter is constructed from material that can tolerate acoustic waves with higher frequency (i.e., low absorption loss). A relatively large number of materials with the required transmission range and optical quality are available.

Quartz is used to construct collinear AOTFs that operate over the 240–400-nm wavelength region (13), MgF_2 is used for noncollinear AOTFs for the 200–700-nm region (21), CaMoO_4 for collinear AOTFs for the 510–670-nm region (22), TeO_2 for noncollinear AOTFs for the visible range from 370 nm to the IR region of 4.5 μm (12, 14–20, 23), and LiNbO_3 for noncollinear AOTFs for 1.23–17 μm (9). TeO_2 is perhaps the most widely used material because, in addition to its high M_2 value, low acoustic attenuation, and good transmission range, it is available in large quantities and has good optical quality. The spectral tuning range for an AOTF is limited not by the transmission of the crystal but by the bandwidth of the acoustic transducer. A piezoelectric crystal (LiNbO_3) is bonded to the AOTF crystal on a specific crystal face to inject an acoustic wave in the required direction. A single transducer provides one or two octaves of scan range. Multiple

transducers have been bonded to AOTFs to enhance the scan range and/or to increase the interaction length. For example, two arrays of transducers are employed to provide the MgF_2 AOTF with a spectral tuning range of 200–700 nm (13).

In selecting a material for an AOTF, one must remember that a polarizer is needed to separate the diffracted light from the transmitted light for the collinear AOTF. Noncollinear AOTFs should be used in the short-wavelength region of the UV and in the IR region, where no suitable polarizers are available.

The scanning speed of an AOTF is controlled by the transit time of an acoustic wave across an optical beam. In the case of the TeO_2 AOTF, because the acoustic velocity in the crystal is known to be 6.17×10^3 m/s (13), it takes an acoustic wave 1.6 μs to travel across an optical beam of 1 mm diameter. It is thus evident that the tuning speed of the filter can be as fast as a few microseconds. Of course, rapid scanning of the filter may lead to degradation of the filter resolution.

The demand for rapid scanning and the requirement for materials with high optical and acoustic homogeneity often limit the aperture of AOTFs to a few millimeters (e.g.,

5 mm \times 5 mm). However, an AOTF as large as 25 mm \times 25 mm has been constructed (24). Such a large AOTF is quite expensive because not only does it employ a large crystal and a large number of transducers, but it also requires an extensive scheme to dissipate the heat generated. The required acoustic power density (or the power of the applied rf signal) increases as the aperture and as the square of the wavelength increase (24). Thus long-wavelength and large-aperture AOTFs generate a considerable amount of heat that must be dissipated quickly for the filter to remain in operation. However, small-aperture AOTFs are suitable for almost all applications because they have acceptance angles as large as 20° .

Collectively, when compared with other dispersive devices (such as a grating or a prism), the advantages of the AOTF include the following: a compact, solid-state design that is rugged and contains no moving parts, a wide angular field (i.e., wide acceptance angle), a wide tuning range (from the UV through the visible to the IR regions), high spectral resolution (bandwidth of light diffracted by the filter is about 1–6 Å), rapid scanning ability (on the order of a few microseconds), high-speed

random or sequential wavelength access, and imaging ability.

Applications

The advantages of the AOTF allow development of novel instruments that could not otherwise be easily accomplished. In initial applications, AOTFs were used mainly as rapid-scanning dispersive devices. Examples of novel AOTF-based instruments include rapid-scanning UV-vis (22), near-IR (18), and mid-IR (25) spectrophotometers; a circular dichroism spectropolarimeter (19); a fluorescence spectrophotometer (11); a near-IR microscope (14); and an astronomical photometer (26) and polarimeter (24).

In addition to dispersive and scanning capabilities, AOTFs can serve as electronic shutters for amplitude modulation of the diffracted beam (12, 23). This function is possible because the wavelength of the diffracted light is dependent on the frequency of the applied rf signal: No light will be diffracted from the AOTF when the applied frequency does not correspond to any wavelengths in the input beam. Therefore, by controlling the frequency duration and the scanning speed of the applied rf signal, spectral scanning and amplitude modulation of the diffracted light can be readily achieved.

This feature makes the AOTF particularly suited for the development of multiwavelength photothermal and photoacoustic spectrophotometers that require a dark period following each excitation period for a sample to relax to its original state. In fact, an AOTF-based multiwavelength thermal lens spectrophotometer has been developed (23).

The intensity of the diffracted light is dependent on the frequency and the power of the acoustic wave. Thus the AOTF provides a unique way to maintain the intensity of light of different wavelengths at a constant level. By incorporating a feedback system into the driver, either the frequency (12) or the power (20) of the rf signal can be controlled. Two systems based on controlling one of these elements have been reported (12, 20). The capability of the AOTF to stabilize the amplitude of the diffracted light is important in optical spectroscopic techniques—particularly in the IR region. Even though other devices can stabilize the amplitude of the light (e.g., an electro-optical modulator or a Pockels cell driven by a feedback driver [27]), they can only be used in the UV-vis region. These devices lack a suitable

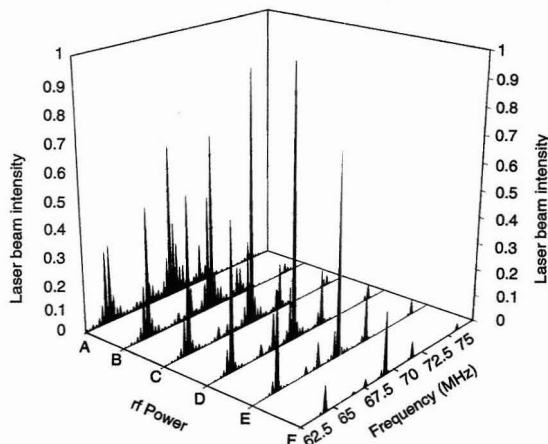


Figure 8. Plot of the intensity of light diffracted from a noncollinear TeO_2 acousto-optic tunable filter as a function of the power and frequency of the applied rf signal.

Powers of the applied rf are A: 122.5 mW, B: 90.0 mW, C: 62.5 mW, D: 40.0 mW, E: 22.5 mW, and F: 8.1 mW. (Adapted with permission from Reference 20.)

electrooptic crystal for the IR region, a compact, low-extinction IR polarizer, and a compact, sensitive IR detector. The AOTF, which can be used in the UV-vis and the IR regions, is not limited by restrictions such as stabilizers based on Pockels cells.

The AOTF can also be used to generate images of a sample. The AOTF-based imaging spectrometer usually has one of two possible configurations. In the first, the AOTF is placed in front of a broadband light source to select the wavelength. Normally, the filter sweeps through hundreds of nanometers at predetermined wavelength intervals, recording one frame with the focal plane array detector at each wavelength interval. Hundreds or even thousands of frames may be collected to generate images of the sample. This method of imaging is particularly suited for transmission measurements, and an AOTF-based near-IR imaging microscope has been described (14).

Alternatively, the AOTF can be placed in front of the imaging detector, and the sample directly excited by a broadband light source. This configuration is often used for techniques such as fluorescence and Raman scattering. An AOTF-based fluorescence imaging spectrometer that employs this configuration has been developed (11).

The IR region is perhaps the most scientifically and industrially important region for spectral and/or chemical imaging, and IR imaging sensors based on the use of the AOTF have been reported. Difficulties such as the requirement of operating the filter at cryogenic temperature, the mismatch in the thermal expansion of the crystal and the transducer material, and problems associated with heat assimilation impede progress in this field. However, a cryogenic AOTF device that can operate in the 2.3–5.2- μm range has been reported by Tracy (28).

Applications of the AOTF are not limited to rapid-scanning electronic gratings. In conventional systems, at any given time only a single rf signal is applied into the filter to diffract out a single-wavelength beam. It is possible to apply several rf signals simultaneously into the filter. This capability was investigated recently in a study in which a TeO_2 AOTF was used (29).

Previously it was determined that this filter provided diffracted light at 514.5 or 488.0 nm when an rf signal of 64.310 or 69.200 MHz was applied individually. When these two rf signals are simultaneously applied, the

filter diffracts light that has two different wavelengths: 514.5 and 488.0 nm. The total number of wavelengths in the diffracted light is determined by the total power of the applied rf signals that the AOTF can tolerate and the relationship (for each wavelength) between the applied rf signal and diffraction efficiency. Thus it is dependent on the type of crystal and the construction of the filter. Specifically, it is known that the maximum rf power that an AOTF can tolerate is dependent on its construction. This is normally on the order of a few watts. For a given wavelength, the relationship between the applied rf power and the diffraction efficiency is a parabolic curve.

For crystals such as TeO_2 , which have high acoustic figures of merit, 20-mW rf power can provide diffraction efficiency as high as 90% (3, 9). Therefore up to 100 different wavelengths can be diffracted simultaneously from a TeO_2 AOTF filter. The AOTF can be used not only as a monochromator but also as a polychromator. Compared with a conventional grating polychromator, the AOTF polychromator can provide an output beam that has unique features such as being well collimated (all wavelengths will be diffracted from the filter at approximately the same angle) and being individually and differently amplitude-modulated.

The latter feature is accomplished by modulating the amplitude of each applied rf signal at the desired frequency. For the TeO_2 AOTF described above, when the applied 64.310- and 69.200-MHz signals were individually and sinusoidally modulated at 100 and 66 Hz, respectively, the diffracted light was a mixture of the 514.5-nm light modulated at 100 Hz and the 488.0-nm light modulated at 66 Hz. There was no cross talk (there was neither a modulated component at 66 Hz in the 514.5-nm light nor a 100-Hz modulated component in the 488.0-nm light). This feature should allow the use of an AOTF to develop a multidimensional fluorometer (29).

Conventional multidimensional fluorometers such as those based on the (grating) polychromator and multichannel detector (e.g., diode array, vidicon, charge-coupled device, or charge-injection device) use the ability of the polychromator to spatially focus different wavelengths of light. For instance, in the first videofluorometer, the polychromator was set on its side to provide excitation wavelengths in the vertical plane (30). Two-dimensional spectra can be

acquired because the emission is detected by use of a diode array detector in the horizontal plane.

Because the AOTF-based polychromator diffracts all wavelengths of light to approximately the same point, the same principle could not be used to develop an AOTF-based multidimensional fluorometer. In such an instrument, each excitation (and emission) wavelength is differentiated from another wavelength not by spatial resolution but by the frequency of the amplitude modulation. In the example above, if the sample is excited by the light diffracted from the TeO_2 AOTF, the fluorescence signal detected at 100 Hz is attributable only to the 514.5-nm excitation, whereas the 488.0-nm excitation leads to the fluorescence component modulated at 66 Hz (29). This AOTF-based multidimensional fluorometer has been used successfully to simultaneously analyze two-component samples (29). In the AOTF-based multidimensional fluorometer, the AOTF is used as a polychromator to disperse excitation and emission. Only a single-channel detector such as a photomultiplier is needed; thus, the sensitivity of the instrumentation is increased and the cost is lowered.

Descriptions of the AOTF applications have thus far been limited to the (laser) extracavity use of this device. The extracavity use may, in some cases, lead to a waste of laser power and the need to operate the laser at high current. For instance, because the 457.9-nm line is a weak output line of an argon ion laser, when the AOTF is used as an extracavity device and this line is selected from the multiline output, the laser must be operated at a higher current to achieve adequate power for this line. Stronger lines such as 514.5, 488.0, and 476.5 nm transmit through the filter and are wasted. This can be eliminated by inserting the AOTF into the laser cavity. In fact, when used inside the cavity of a standing wave dye laser, a TeO_2 AOTF can provide scanning from 560 to 610 nm in as little as 50 μs . The output beam has a power output as high as 130 mW and a bandwidth of 0.3 nm (31). In another example, the AOTF constructed from Te_3AsSe_3 and inserted in the cavity of a pulsed CO_2 laser provided rapid scanning from 9 to 11 μm (32). An intracavity AOTF tuning device for solid-state lasers such as Ti:sapphire was recently reported (33).

Because of the relationship between the applied rf and the dif-

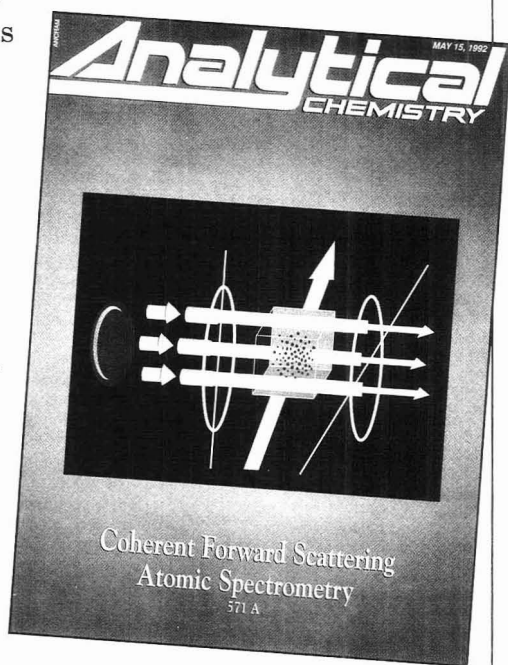
When you're confronted
with a specific "need to know"...

Analytical CHEMISTRY

Every chemist knows having the most up-to-date information is essential for success. And, in the vital field of measurement science, ANALYTICAL CHEMISTRY is the one publication you cannot do without. For over sixty years, ANALYTICAL CHEMISTRY has proven to be a useful problem-solving resource, no matter what your specialty.

Publishing information that will help you deal skillfully with problems such as sampling, data analysis and methodology—the papers in today's twice monthly ANALYTICAL CHEMISTRY cover real world problems involving trace analysis of air, water, soil, materials, drugs, and biopolymers.

Call now to order your subscription. Your order includes the LABGUIDE and Annual Reviews issue!



Volume 64 (1992) ISSN: 0003-2700

	U.S.	Canada & Mexico	Europe**	All Other Countries**
ACS Member – 1 year	\$ 33	\$ 69	\$117	\$150
2 years	\$ 56	\$128	\$224	\$290
Nonmember Personal – 1 year	\$ 76	\$112	\$233	\$266
Nonmember Institutional – 1 year	\$373	\$409	\$457	\$490

Member and Nonmember Personal subscriptions are for personal use only.

** Air service included.

Subscriptions may start any month of the year and expire one year later. Foreign payment must be made in U.S. currency by international money order, UNESCO coupons, or U.S. bank draft, or order through your subscription agency. For nonmember rates in Japan, contact Maruzen Co., Ltd. This publication is available on microfilm or microfiche, and the full text is available online on STN International.

**Call Toll-Free
1-800/333-9511**
Outside the continental U.S.
call 614-447-3776
TWX: 810-482-1608
FAX: 614-447-3671
or write:
American Chemical Society
Member and Subscriber Services
P.O. Box 3337
Columbus, OH 43210

GRANDMA CALLED IT *Roughage*

Fiber Facts and Fallacies

Robert L. Ory



Grandma Called It *Roughage*

Fiber Facts and Fallacies

This semi-technical volume, written specifically for non-scientists, is must-reading for anyone concerned about health and nutrition. With scientific facts to support the statements made about the known health benefits of fiber, Dr. Ory offers an interesting, sometimes humorous, approach that will appeal to the general reader.

Although not intended to be the final word on dietary fiber (research goes on continually), the book is intended to quell rumors about dietary fiber and to inform those who don't understand enough about fiber's benefits and limitations.

The author also offers some of his own recipes for simple and tasty high-fiber foods, including Bread Pudding, New Orleans Style Red Beans, and Eggplant Lasagna.

Contents

- Fibermania and How It Began
- What Is Fiber and Where Do We Find It?
- Fiber and Metabolism vs. Fat and Cholesterol
- Can Fiber Fight Fat?
- Fiber and the Big "C"—Constipation!
- Can Fiber Cure Cancer, Diabetes, or Other Diseases?
- Fiber and Mineral Nutrition
- Is Fiber an Essential Nutrient?
- Breakfast Cereals: The Battle of the Brans
- Fiber in Fruits and Vegetables
- Can Fiber Be Good for You and Still Taste Good?

Robert L. Ory, Ph.D.

160 pages (1991)
Clothbound: ISBN 0-8412-1749-1

\$22.95

Paperbound: ISBN 0-8412-1764-5

\$12.95

ORDER FROM

American Chemical Society
Distribution Office, Dept. 21
1155 Sixteenth St., N.W.
Washington, DC 20036

or CALL TOLL FREE

800-227-5558

(In Washington, D.C. 872-4363) and use your credit card!

INSTRUMENTATION

fracted wavelength, the AOTF can, in principle, be exploited in both directions. Thus far, only one facet of applications has been described: the application of different rf signals into the AOTF to disperse and/or analyze optical signals. The AOTF can also be used to analyze the frequency distribution of rf signals (34). In this case rf signals collected through an antenna and processed by an amplifier are fed into the filter (34). A stable, well-characterized light source is then introduced into the AOTF. Because of the applied rf signals, the filter will diffract the incident light beam into different wavelengths. The frequency distribution of rf signals is then calculated from the rf optical wavelength relationship and from wavelengths of the diffracted light. An rf spectrum analyzer based on this principle has been recently constructed and reportedly can measure rf signals with bandwidths as large as 5 GHz (34).

Future prospects

It would be misleading to conclude this discussion with the idea that acousto-optic devices have reached technological maturity and that they do not have disadvantages and defects. In fact, the field has not been fully developed. Disadvantages and defects do exist, and much fundamental as well as technological research needs to be performed. Furthermore, some improvements have been proposed in theory but have not been experimentally realized. Some of these are discussed below.

TeO₂ remains the best material for devices operated in the visible and near-IR regions (up to 5 μ m). In the UV region, where the absorption of many compounds of interest occurs, there are very few birefringent crystals suitable for acoustic devices. Those currently available (quartz, MgF₂) have low acoustic figures of merit and small photoelastic tensors. AOTFs fabricated from these materials are usually collinear or noncollinear, but with very small deflection angles. A polarizer is needed to isolate the diffracted light. Because polarizers in this region are currently unavailable, it is essential to find new materials with better acousto-optic properties for the UV region. The situation is better for AOTFs in the mid-IR region. Several new birefringent materials that have relatively good acousto-optic properties and are transparent up to 17 μ m were recently described (9).

As mentioned earlier, acousto-optic materials must have low acous-

tic attenuation. It is possible to reduce the acoustic attenuation of a given crystal by cooling it, as demonstrated in a recent report of the acoustic attenuation of a TeO₂ crystal, which was reduced sixfold when the crystal was cooled to 4 K (35).

As shown in Equation 15, the intensity of the diffracted light is a sinc² function. It is, therefore, similar to that of the diffraction grating. That is, for each specific diffracted wavelength, there are several side bands in addition to the main band. An example of this was shown in Figure 7. Because the incident beam was a multiline output from an argon ion laser, side bands and the main band have the same spectral purity (i.e., they have exactly the same wavelength). Therefore, their presence does not degrade the filter resolution.

The same cannot be said when an incoherent continuous light source such as an incandescent or a xenon arc lamp is used. In this case, side bands of one wavelength may overlap with those of another wavelength and hence degrade the filter resolution. Several methods may be used to depress these side bands. For example, appropriate adjustment of the power of the applied rf signal may substantially reduce the side bands (36). As an example, it was found that the diffraction efficiency (and hence the intensity of the diffracted light) of a noncollinear TeO₂ AOTF is proportional to the power of the applied rf signal (36). The proportional constants are, however, different for the main band and the side bands.

Appropriate selection of the power will lead to a substantial reduction of the side bands. For 488.0-nm light at a 10-mW applied rf signal, the ratio of the main band to the first side band is 9.0. An increase in rf power to 35 mW, which is the optimal power for maximum diffraction efficiency (for the main band), will increase the main band and will also increase the side bands (36). Because the side bands increase more than the main band in this region, the ratio of the main band to the first side band decreases to 4.5 (36). Alternatively, the side bands can also be reduced by apodizing the acoustic profile. It has been reported that by using the apodization method based on the Hamming window, the first side bands were reduced 30 dB below the main band (37).

The resolution of an AOTF filter can, in principle, be improved substantially by using the filter in the

wavelength region close to the absorption edge of the crystal. This prediction is based on the fact that, according to Equation 17, the resolution of the AOTF is inversely proportional to the dispersive constant Δn , and Δn is known to be wavelength dependent. It becomes very large near the absorption band edge of the crystal.

The resolution of the AOTF, as shown in Equation 17, also depends on the wavelength. This dependency makes it somewhat difficult to use the AOTF to develop a spectrophotometer based on a continuous white light source. Efforts are being made to develop an AOTF that has constant resolution and spectral bandwidth (38).

This article is limited to the subject of acousto-optic interactions in bulk materials and their applications in optical spectrometry. Other areas of acousto-optic interactions, including integrated optics and surface acoustics, are also important—particularly in the fields of electronics, communications signal processing, and sensing (39), where intense investigations are under way.

I am grateful to my co-workers, whose work is cited in the references; and I also acknowledge the National Institutes of Health, National Center for Research Resources, Biomedical Research Technology Program for financial support of some of the work reported here.

References

- (1) Brillouin, L. *Ann. Phys. (Paris)* **1922**, 17, 88.
- (2) Debye, P.; Sears, F. W. *Proc. Nat. Acad. Sci. (USA)* **1932**, 18, 409.
- (3) Sapriel, J. *Acousto-Optics*; John Wiley and Sons: New York, 1976.
- (4) Korpel, A. *Acousto-Optics*; Marcel Dekker, Inc.: New York, 1988.
- (5) Yariv, A. *Optical Electronics*, 3rd ed.; Holt, Rinehart, and Winston: New York, 1985.
- (6) Skogerboe, K. J.; Yeung, E. S. *Anal. Chem.* **1986**, 58, 1014.
- (7) Huie, C. W.; Yeung, E. S. *Appl. Spectrosc.* **1986**, 40, 863.
- (8) Erskine, S. R.; Foley, C. M.; Bobbitt, D. R. *Appl. Spectrosc.* **1987**, 41, 1189.
- (9) Chang, I. C. *Proc. Soc. Photo Opt. Instrum. Eng.* **1976**, 90, 12.
- (10) Dixon, R. W. *IEEE J. Quant. Elect.* **1967**, QE-3, 85.
- (11) Kurtz, I.; Dwelle, R.; Katzka, P. *Rev. Sci. Instrum.* **1987**, 58, 1996.
- (12) Tran, C. D.; Bartelt, M. *Rev. Sci. Instrum.* **1992**, 63, 2932.
- (13) Katzka, P.; Chang, I. C. *Proc. Soc. Photo Opt. Instrum. Eng.* **1979**, 202, 753.
- (14) Treado, P. J.; Levin, I. W.; Lewis, E. N. *Appl. Spectrosc.* **1992**, 46, 553.
- (15) Hallikainen, J.; Parkkinen, J.; Jaaskelainen, T. *Rev. Sci. Instrum.* **1988**, 59, 81.
- (16) Bates, B.; Findlay, D.; Halliwell, D. *Proc. Soc. Photo Opt. Instrum. Eng.* **1982**, 369, 315.
- (17) Yan, C.; Tang, J. *Proc. Soc. Photo Opt. Instrum. Eng.* **1990**, 1230, 38.

- (18) Jaenisch, H. M. et al. *Proc. Soc. Photo Opt. Instrum. Eng.* **1990**, 1379, 162.
- (19) Hatano, M. et al. *Rev. Sci. Instrum.* **1981**, 52, 1311.
- (20) Tran, C. D.; Furlan, R. J. *Appl. Spectrosc.* **1992**, 46, 1092-95.
- (21) Katzka, P., AOTF Technology, Sunnyvale, CA, personal communication, 1992.
- (22) Shipp, W. S.; Biggins, J.; Wade, C. W. *Rev. Sci. Instrum.* **1976**, 47, 565.
- (23) Tran, C. D.; Simianu, V. *Anal. Chem.* **1992**, 64, 1419-25.
- (24) Kradjel, C. *Fresenius Z. Anal. Chem.* **1991**, 339, 65.
- (25) Smith, W. H. *Publ. Astron. Soc. Pac.* **1987**, 99, 1344.
- (26) Smith, W. H.; Smith, K. M. *Experimental Astronomy* **1991**, 1, 329.
- (27) Goldstein, R. *Laser Appl.* **1986**, 4, 67.
- (28) Tracy, J. *Opt. Eng.* **1981**, 20, 716.
- (29) Tran, C. D.; Furlan, R. J. *Anal. Chem.*, in press.
- (30) Warner, I. M. et al. *Anal. Lett.* **1975**, 8, 665.
- (31) Richter, P. I. et al. *Opt. Comm.* **1991**, 84, 159.
- (32) Denes, L. J. et al. *Proc. SPIE "Gas Laser Technology"* **1988**, 894, 78.
- (33) Lambert, J. L. *NASA Tech. Briefs* **1991**, 6, 52.
- (34) Chang, I. C. *Proc. SPIE Vol. 1476 "Optical Technology for Microwave Applications V"* **1991**, V, 257.
- (35) Fuss, I.; Smart, D. *Appl. Opt.* **1991**, 30, 4526.
- (36) Tran, C. D.; Furlan, R. J., unpublished results.
- (37) Chang, I. C. *Opt. Eng.* **1981**, 20, 824.
- (38) Sivanayagam, A.; Findlay, D. *Appl. Opt.* **1984**, 23, 4601.
- (39) *Guided-Wave Acousto-Optics*; Tsai, C. S., Ed.; Springer-Verlag: New York, 1990.



A native of Vietnam, Chieu D. Tran is an associate professor of analytical chemistry at Marquette University. He received his B.S. degree from Kumamoto University in Japan and his Ph.D. from Texas A&M University. Following postdoctoral research at the Royal Institution of Great Britain, he joined Brookhaven National Laboratory as a staff scientist. In 1986 he joined the faculty of Marquette University. He is the recipient of the 1992 Perkin-Elmer International Liquid Chromatography Technical Paper Award. His research interests include colloid chemistry; development and applications of acousto-optic devices; and applications of lasers to chemical analysis, specifically the use of the thermal lens effect to develop novel instruments and methods for trace chemical analysis and chromatographic detection.

THE WORLD'S LEADING COMMERCIAL PRODUCER OF STABLE ISOTOPES



Isotec is the world's leading commercial producer of enriched stable isotopes, with a large inventory of labelled starting materials, intermediates, and final products to meet our customers' varied needs. We are capable of producing large volumes, and Long Term Blanket Agreements are available.

- NMR Solvents & Reagents
- Noble Gas Isotopes
- Metal Stable Isotopes
- Cyclotron Target Materials
- Environmental Pollutant Standards

Quality Products • Excellent Service
Competitive Prices

ISOTEC INC.
A Matheson, USA Company

Stable Isotopes For Research & Industry
3858 Benner Road, Miamisburg, OH 45342
(513) 859-1808 (800) 448-9760
Telex: 288278 FAX: (513) 859-4878

CIRCLE 54 ON READER SERVICE CARD



NEW RELEASES

FROM THE ACS SYMPOSIUM SERIES

Chiral Separations by Liquid Chromatography

Presenting state-of-the-art information, this volume covers all the major modes of separation and offers contributions from the leading researchers who developed these techniques. It provides a detailed review of the commonly used columns: brush type, cyclodextrin, polysaccharide carbonate, and protein. In addition, the volume provides significant discussion on the use of chiral discriminators or selectors.

Satinder Ahuja, Editor
ACS Symposium Series No. 471
240 pages (1991) Clothbound
ISBN 0-8412-2116-2
\$59.95

Particle Size Distribution II Assessment and Characterization

This compendium of current work in the field features the latest technology now in use for particle size distribution assessment. Among the new techniques discussed are capillary hydrodynamic fractionation, field flow fractionation, disc centrifuge photosedimentometry, on-line measurements, fractals, electrophoretic characterization, image analysis, and electric sensing zone. A review chapter examines turbidimetry, an old technique that has been revitalized with new mathematical approaches.

Theodore Provder, Editor
ACS Symposium Series No. 472
400 pages (1991) Clothbound
ISBN 0-8412-2117-0
\$89.95

Food and Packaging Interactions II

The most comprehensive and current information available on food packaging interactions, including presentations on migration, scalping, permeability, and microwave susceptor packaging products. A valuable resource for food product development scientists and engineers who need to understand what can happen to foods in different types of packages and regulatory agencies who must keep pace with new developments and maintain appropriate regulations. Includes information on regulations of packaging for the United States, United Kingdom, and the European Community.

Sara J. Risch and Joseph H. Hotchkiss, Editors
ACS Symposium Series No. 473
270 pages (1991) Clothbound
ISBN 0-8412-2122-7
\$59.95

Brassinosteroids Chemistry, Bioactivity, and Applications

With contributions from all over the world, this volume presents an accurate and comprehensive picture of the present state of research and development in brassinosteroids. Provides a survey of the chemistry, synthesis, physiology, and practical applications of brassinosteroids, in experimental and agricultural references alike. Presents results of large-scale field trials in China, which strongly indicate the economic potential of these compounds as environmentally benign agricultural chemicals to significantly increase crop yields.

Horace G. Cutler, Takao Yokota, and Günter Adam, Editors
ACS Symposium Series No. 474
358 pages (1991) Clothbound
ISBN 0-8412-2126-X
\$84.95

Radiation Effects on Polymers

Reviews the fundamental chemistry and physics of polymer-radiation interaction and examines recent progress in most major areas of the field. Covers fundamentals of polymer radiation chemistry, technological applications of radiation to polymers (including radiation processing, radiation curing, sterilization, cross-linking, polymerization, grafting, X-ray resists, and others), and degradation and stabilization of irradiated polymers (including nuclear plants, scintillation detectors for particle physics, and others).

Roger L. Clough and Shalaby W. Shalaby, Editors
ACS Symposium Series No. 475
640 pages (1991) Clothbound
ISBN 0-8412-2165-0
\$109.95

Emerging Technologies for Materials and Chemicals from Biomass

As nonrenewable chemical feedstocks are depleted, new sources of materials and chemicals must be developed to fill the need.

Radiation Effects on Polymers

This new volume examines the technologies now emerging for the use of biomass as an environmentally friendly and sustainable solution to the problem. Its 25 chapters are divided into three sections covering: lignocellulosic materials and composites; biopolymers (alloys, derivatives, and blends), and chemicals and fuels from biomass and wastes. Each section opens with review chapters summarizing potentials and opportunities.

Roger M. Rowell, Tor P. Schultz, and Ramani Narayan, Editors
ACS Symposium Series No. 476
480 pages (1992) Clothbound
ISBN 0-8412-2171-5
\$99.95

Expression Systems and Processes for rDNA Products

This fascinating volume provides a wealth of information on developments in expression system technologies. Among the topics covered in its nine chapters are bacterial hosts (*E. coli*), yeast (*Saccharomyces cerevisiae*), and insect cells. In addition, the book examines process technologies, including high cell density bacterial fermentations, biocatalysis, and process issues with recombinant microorganisms.

Randolph T. Hatch, Charles Gooch, Anthony Moreira, and Yair Alroy, Editors
ACS Symposium Series No. 477
130 pages (1992) Clothbound
ISBN 0-8412-2172-3
\$34.95

Order from:

American Chemical Society
Distribution Office, Dept. 23
1155 Sixteenth St., N.W.
Washington, DC 20036
or CALL TOLL FREE 800-227-5558
or in Washington DC 202-872-4363
and use your credit card!

Fluorescence, Immunoassays, and Biosensors

Applications of Fluorescence in Immunoassays. Ilkka A. Hemmila. xi + 343 pp. John Wiley & Sons, 605 Third Ave., New York, NY 10158. 1991. \$85

Reviewed by E. P. Diamandis, Department of Clinical Biochemistry, The Toronto Hospital (TW Division), 399 Bathurst St., Toronto, Ontario M5T 2S8 Canada

A number of books on immunological techniques have been published in the past couple of years. This new book concentrates on fluorescence immunoassay and its applications in various areas, especially in diagnostic medicine.

The 11 chapters cover more than the title reveals. The first four chapters present general aspects of immunoassays that are applicable to any detection technology. Although brief, these introductory chapters can be useful to readers whose background in immunoassay techniques is limited. Chapter 5 deals with general aspects of photoluminescence spectroscopy. The instrumentation for fluorescence immunoassay is covered in Chapter 6, which contains a useful compilation of available fluorometric readers as well as more integrated instruments that perform mechanized functions and random access analysis. The latter is an area of intense activity, and Table 5 may well be obsolete by now.

Various fluorescent probes, including fluorescein, rhodamines, coumarins, and phycobiliproteins, are described in Chapter 7. Major emphasis is placed on the fluorescent lanthanide chelates (the fluorophores used in time-resolved fluorometric immunoassay), which is the author's primary area of expertise. Fluorescence immunoassay techniques are discussed in Chapter 8. Homogeneous and heterogeneous assays are covered, and applications for each method are assembled in tables with numerous references. Again, time-resolved fluorometric assays are

prominent. A short Chapter 9 covers enzymatically labeled fluorescence immunoassay.

Chapter 10, which is also short, covers nonimmunological assay, with some emphasis on nucleic acid hybridization. Chapter 11 covers multi-analyte immunoassay principles, a concept that is now drawing attention, although some advances made this year are not discussed.

The book has an impressive list of references, an invaluable source of primary information. The 1991 citations account for more than 20% of the pages. The index is satisfactory.

The major strength of this book is the concise description of fluorescence immunoassay and its applications, especially in the field of clinical chemistry. The book should be suitable for analytical chemists interested in using immunological assay and for clinical chemists, medical technologists, graduate students, and diploma candidates in clinical chemistry programs.

Practical Fluorescence, 2nd ed. George G. Guilbault, Ed. 812 pp. Marcel Dekker, 270 Madison Ave., New York, NY 10016. 1990. \$155

Reviewed by Linda B. McGown, Department of Chemistry, P. M. Gross Chemical Laboratory, Duke University, Durham, NC 27706

The second edition of *Practical Fluorescence* expands and updates topics covered in the previous edition and provides new information on photobiosensors and process applications. The book includes 13 chapters written by 10 contributors. This volume is a worthwhile investment as a basic source of information on fluorescence techniques and their applications to measurements of chemical, biological, and environmental systems.

The first chapter is an introduction to luminescence and its applications. The tables of quantum yields and lifetimes are interesting, although

some of the values—which are taken from older literature—provide oversimplified views of complex systems. Chapter 2, on instrumentation, is the least current chapter; it covers only the most basic types of traditional instruments. No mention is made of modern innovations such as lasers or array detectors, which are available on many commercial instruments. Fortunately, some of these topics are discussed in other chapters.

The chapters on the effects of molecular structure and molecular environment on luminescence cover basic concepts of fundamental photophysical processes, structural factors favoring luminescence, types of compounds that luminesce, solvent relaxation, polarity, temperature, hydrogen bonding, and pH, and provide excellent discussions of measurements in supersonic expansions, solid surfaces, and organized media. Chapters on organic, inorganic, and enzymatic determinations follow the format of the previous edition; they are organized by groups of compounds. These chapters provide quick answers to questions about which compounds luminesce, the characteristics of their luminescence, and optimal conditions for their measurement. Although many of the methods and references are from older literature, these chapters provide a good starting point for identifying possible applications.

The chapter on environmental analysis is particularly good, not only for its excellent coverage of this topic but also for its introduction of synchronous luminescence, low-temperature techniques, time-resolved luminescence, room-temperature phosphorescence, optical sensors, and laser-based techniques. The chapter on phosphorescence analysis is written as a review and is somewhat out of step with the instructional format of the rest of the book. This chapter will be most useful to researchers already familiar with the subject. A chapter on pesticides and enzyme-related substrates

on solid surfaces is somewhat outdated; it contains photographs and descriptions of instruments that are no longer modern.

Chapters on chemiluminescence, photobiosensors, and enzymology are good sources of information about general approaches and specific applications. The chapter on proteins and peptides is excellent; it provides important concepts of fluorescence probe techniques and areas of application ranging from characteristics of fluorescent amino acids and proteins to measurements of antigen-antibody binding. Fluorescence anisotropy, lifetime, dynamic depolarization, and quenching are explained; and both extrinsic and intrinsic probe techniques are discussed. The final chapter, on monitoring bioprocesses, emphasizes *in situ* sensors. The discussion focuses on measurement of coenzyme F₄₂₀ in methanogens, measurement of microbial ATP by bioluminescence, and application of NADH-dependent sensors in the control of bioprocesses. This is an interesting chapter that illustrates the important role of luminescence in process monitoring and control.

Numerous references are provided at the end of each chapter (except for the chapter on instrumentation, which has no references), and most extend through the mid-1980s. Several chapters can provide the basis for advanced courses on luminescence; others will be most useful for identifying groups of fluorescent compounds and methods for their determination. The book is weakest in its coverage of modern instrumentation. There are also small annoyances, such as photographs of outdated instruments and incorrect usage of terms such as "assay." These points aside, this book will be a valuable resource for analytical laboratories and researchers.

Immunochemical Assays and Biosensor Technology for the 1990s. R. M. Nakamura, Y. Kasahara, and G. A. Rechnitz, Eds. 411 pp. American Society for Microbiology, 1325 Massachusetts Ave., N.W., Washington, DC 20005. 1992. \$51

Reviewed by Susan R. Mikkelsen, Department of Chemistry and Biochemistry, Concordia University, 1455 de Maisonneuve Blvd. West, Montreal H3G 1M8, Canada

The preface states that this book is intended to summarize current technology in immunochemical assays

and to show how the use of nonradioactive labels has aided the development of biosensor technology. It is directed toward intermediate-level students. More than 40% of the cited works were published after 1986, and many from early 1991 are included. The book is divided into three parts: Concepts of Immunochemical Assays, Nonisotopic Immunochemical Assays, and Biosensors.

Part I contains five contributed chapters: "General Principles of Immunoassays" (Nakamura; 61 references), "Nonisotopic Immunoassay Labels" (Howanitz; 16 references), "Use of Different Labels in Immunoassays" (Kricka; 76 references), "Advances in Monoclonal Antibody Technology" (McCormack, Ludwig, and Wolfert; 125 references), and "Evaluation and Validation of Immunoassays" (Feldkamp; 36 references).

The first chapter describes the general nature of antibodies and introduces kinetic and equilibrium con-

cepts. Immunoassays" (Nakamura; 60 references), "Enzyme Immunoassays with Chemiluminescent Detection" (Bronstein and Sparks; 94 references), and "Time-Resolved Fluorescence Immunoassays" (Diamandis and Christopoulos; 70 references).

Within each chapter, the authors present fundamental research and descriptions of commercially available systems. The chapter by Ritchie includes sections that underline the importance of sample collection and storage conditions. Kasahara's discussion of particle immunoassay includes a theoretical section on agglutination kinetics and a survey of particles used as solid phases. Ishikawa's chapter on ultrasensitive enzyme immunoassay considers non-competitive systems for antigen and antibody detection at attomole levels. Bronstein and Sparks review both luminescent labels and luminogenic enzyme substrates. Diamandis and Christopoulos describe immunoassays that measure long-lived fluorescence emission from Eu³⁺ chelates.

Part III contains seven chapters: "An Introduction to Biosensors" (Ho and Rechnitz; 110 references), "Immunoassay with Electrochemical Detection" (Xu, Halsall, and Heinemann; 41 references), "Fiber-Optic Biosensors" (Arnold; 51 references), "Amperometric Biosensors" (Yacynych; 116 references), "Polymeric Membrane Anion-Selective Electrodes" (Wotring, Johnson, Daunert, and Bachas; 51 references), "Native Chemoreceptor-Based Sensors" (Belli; 21 references), and "Pharmacological Biosensors" (Eldefrawi, Eldefrawi, Rogers, and Valdes; 72 references).

The introductory chapter reviews potentiometric biosensors and surveys a variety of biochemical recognition elements. It would have been more appropriate to include the chapter by Xu and co-workers in Part II, because the excellent coverage of electrochemically detectable immunoassay labels complements the reviews of optically detectable labels. Arnold's summary of optical sensors states that fundamental advances are required for miniaturization and for the prevention of biomolecule photodegradation. Yacynych's chapter is a thorough review of amperometric enzyme electrodes, although immunosensors are not discussed. The final chapter, by Eldefrawi and co-workers, considers sensors based on acetylcholine receptors.

“...Summarizes current technology in immunochemical assays.”

cepts, immunologic reactions, monoclonal and polyclonal antibodies, and a classification system for immunoassays. The contribution by Kricka is a thorough overview of enzyme, fluorescent, particle, and secondary labels, with and without amplification systems; extralaboratory applications also are considered. McCormack and co-workers discuss general properties of antibodies, the production of monoclonals, and engineered reagents for immunoassays. The final chapter by Feldkamp introduces statistical rigor for the quantitative evaluation of immunoassays and provides useful material for student training as well as for clinical immunoassay validation.

Part II includes eight contributions and is organized according to label type: "Light-Scattering Immunoassay" (Ritchie; 42 references), "Particle Immunoassay" (Kasahara; 31 references), "Heterogeneous Enzyme Immunoassays" (Nakamura and Kasahara; 61 references), "Homogeneous Enzyme Immunoassays" (Kasahara; 28 references), "Ultrasensitive Enzyme Immunoassay" (Ishikawa; 17 references), "Fluores-

Books Received

Factor Analysis in Chemistry, 2nd ed. Edmund R. Malinowski. xii + 350 pp. John Wiley & Sons, 605 Third Ave., New York, NY 10158. 1991. \$55

Topics in this 10-chapter book include the basic steps of factor analysis, mathematical formulation of target factor analysis, effects of experimental error, special chemometric methods based on factor analysis, the application of factor analysis to qualitative and quantitative analyses of various analytical methods, and the applicability of factor analysis to other chemistry problems. The appendices contain a discussion of pseudoinverse and computer programs that can be used for factor analysis. Author and subject indexes are also included.

High Pressure NMR. P. Diehl, E. Fluck, H. Gunther, R. Kosfeld, J. Seelig, and J. Jonas, Eds. 263 pp. Springer-Verlag New York, 175 Fifth Ave., New York, NY 10010. 1991. \$98

This book, volume 24 of the NMR Series, has six chapters on the following topics: high-pressure solid-state NMR studies; motion and phase transitions in molecular systems; dynamics in liquids and complex systems; studies of water and aqueous solutions; high-resolution variable-pressure NMR for chemical kinetics; and the glass-cell method for high-pressure, high-resolution NMR measurements. An author index for volumes 21-24 is included.

Applications of Plasma Source Mass Spectrometry. Grenville Holland and Andrew N. Eaton, Eds. viii + 222 pp. Royal Society of Chemistry, Distribution Center, Blackhorse Rd., Letchworth, Herts SG6 1HN, U.K. 1991. \$95

This 21-chapter volume is based on the Second Durham International Conference on Plasma Source Mass Spectrometry. Among the wide range of topics are glow discharge MS and analyses using ICP-MS, including analyses of thermal waters, drinking water, terrestrial water, gold in humus, ion formation, whole blood and body fluids, and environmental samples. Various sampling and detection techniques are also discussed.

Sequential Simplex Optimization: A Technique for Improving Quality and Productivity in Research, Development, and Manufacturing. Frederick H. Walters, Lloyd R. Parker, Jr., Stephen L. Morgan, and Stanley

N. Deming. xix + 325 pp. CRC Press, 2000 Corporate Blvd., N.W., Boca Raton, FL 33431. 1991. \$50

One of the Chemometrics Series books, this volume describes three sequential simplex methods used in evolutionary operation. The book discusses in detail the logic behind sequential simplex optimization and the calculations of simplex algorithms. Worksheets, a glossary, a bibliography of sequential simplex applications, and a subject index are included.

Introduction to Stereochemistry and Conformational Analysis. Eusebio Juaristi. xv + 331 pp. John Wiley & Sons, 605 Third Ave., New York, NY 10158. 1991. \$50

Designed to provide an understanding of the principles of stereochemical phenomena, this textbook covers a variety of topics and includes references to both historical and recent literature. The 18 chapters discuss the following subjects: chirality, absolute configuration, stereochemical and conformational descriptors, chiroptic properties, stereochemistry of organic reactions,

prochirality, asymmetric syntheses, enantiomeric purity, resolution of racemates, methods for the control of stereochemistry, conformational analysis, the anomeric effect, and attractive and repulsive gauche effects. Bibliographies are provided at the end of each chapter, and author and subject indexes are included.

Analysis of Substances in the Gaseous Phase. E. Smolkova-Keulemansova and L. Feltl. xiv + 480 pp. Elsevier Science Publishing Co., P.O. Box 882, Madison Square Station, New York, NY 10159. 1991. \$205

Current and future methods for the analysis of gaseous substances are described. The theoretical basis, instrumentation, analytical steps, and areas of application of each analytical method are discussed. Topics include the history of the chemistry of gases; characteristics of gas analysis; temperature, pressure, and volume determination; qualitative, semiquantitative, quantitative, chemical, physicochemical, and physical methods of analysis; and GC. A bibliography and a subject index are included.

NEW
Fast, Easy
to Use
ZetaPlus

Zeta Potential



The **ZetaPlus** uses electrophoretic light scattering to determine the zeta potential of colloidal-sized material suspended in water or polar solvents.

- ✓ **Easy to Use:** Simple cell design: one piece, easy fill and throwaway.
- ✓ **Automatic:** Single push-button operation: pre-aligned optics and no cell calibration.
- ✓ **Compact:** Small footprint: integral powerful 386/387 computer.

Particle sizing by Dynamic Light Scattering is available as an option. Ideal for use in QC and R & D labs. The **ZetaPlus** has the best price/performance ratio of any zeta potential analyzer.

For free technical literature contact:



BROOKHAVEN INSTRUMENTS CORP.
750 BLUE POINT ROAD
HOLTSVILLE, NY 11742 USA
TEL: (516) 758-3200 • FAX: (516) 758-3255
TWX: WU16852252 BRKHVN INSTR

CIRCLE 12 ON READER SERVICE CARD

NEW PRODUCTS

Instrumentation

Laser. Model 6102 continuously tunable diode laser, with output centered at 670 nm, has 10–100-kHz bandwidth and tunability over more than 12 nm. Stability of the laser is ± 5 mK, and front panel modulation to 1 MHz is possible without affecting the frequency noise. New Focus 401

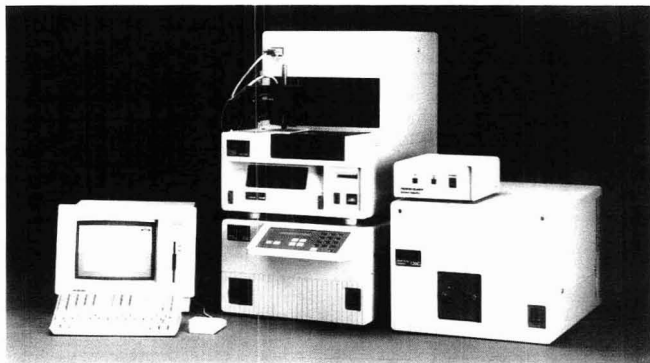
Ammonia measurement. Model 404 Colorimetric On-Line Analyzer uses the phenate analysis method to determine ammonia in water and wastewater without using toxic reagents such as mercury and zinc. Ammonia can be measured in 0–1- and 1–10-ppm ranges. Ionics 402

Ion chromatography. Integrated ion chromatography system consists of the Model 320 conductivity detector, the Model 325 digital HPLC pump, the Model 330 column heater, and the Model 9125 Rheodyne injection valve. The system is metal-free and can be used for the determination of anions, cations, transition metals, amines, organic acids, and surfactants. Alltech 403

CCD detector. InstaSpec IV detector features a direct link between the detector head and the PC interface board and software that allows the acquisition of up to 256 spectra at effective rates of up to 74,500 spectra per second. The detector is 100 times more sensitive than linear diode array detectors. Data are displayed as 2D, overlaid, stacked, or 3D plots. Oriol 404

HPLC. Glass-lined Develosil microbore and semimicrobore columns feature low consumption of mobile phase and increased mass sensitivity. The columns, which are available in 0.3-, 0.5-, 1.0-, 1.5-, and 2.0-mm diameters, can also be used for MS or SFC applications. JM Science 405

Sulfur detection. Courier Model 10-S, designed to help petroleum refiners meet EPA regulations on sul-



Model 1020 LC Plus controller provides system control and chromatography monitoring for the Model 250 pump, the ISS-200 autosampler, and the LC-135C/235C diode array detector. Perkin Elmer 406

fur in diesel fuel, measures sulfur in the 50 ppm–10% range with an X-ray fluorescence method that is similar to the ASTM D4294 technique. Outokumpu Electronics 407

FT-IR spectroscopy. Model 74-5041 self-contained FT-IR purge-gas generator is designed to produce a purified carbon dioxide-free gas from compressed air. The gas contains no suspended impurities larger than 0.1 μm . Balston 408

TEM. Model CM10-BioTWIN, designed to increase contrast and sharpness of electron images, incorporates a large pole-piece gap in the objective lens design. The specimen can be tilted $\pm 80^\circ$; a high-tilt goniometer provides enhanced eucentricity and positional reproducibility; and switching between TEM imaging, low-dose operation, and the small-probe mode for microanalysis does not require realignment. Philips Analytical 409

TOC measurement. Model TOC-5000/5050 on-line process analyzer, designed to withstand adverse environmental conditions, measures total carbon, inorganic carbon, and total organic carbon concentrations from

40 ppb to 4000 ppm. Optional features include a module that can be used to measure suspended particles up to 800 μm . Shimadzu 410

Magnetic separation. Beadprep-96 separation system, designed to accommodate a 96-well microplate or other flexible microplates, has two shaking speeds and uses uniformly sized paramagnetic particles as well as a series of rare-earth magnets to pelletize or move the magnetic beads. Applications include immunoassays, nucleic acid assays, cell sorting, and other bioprocesses. Techné 411

Trace metal analysis. AMEL Model 433A Trace Analyzer for polarographic analysis consists of a potentiostat and an electrode housed in a single cell stand. An onboard computer synchronizes operations, acquires data, ensures a precise dropping (or static) mercury electrode, and drives the potentiostat. Software allows the use of a range of voltammetry and polarography techniques. ElectroSynthesis 412

Radiochromatography. Flow-Count detectors count gamma, positron, and high-energy beta emitters over a range of 10^2 – 10^{12} dpm.

The detectors are compatible with all recorders, integrators, and chromatography data systems. Applications include monoclonal antibody research, protein labeling and purification, and nuclear medicine. Bioscan 413

Formaldehyde monitoring. Model TGM 555 air monitor measures formaldehyde levels in the part-per-billion range. The monitor uses the pararosaniline procedure, which correlates with the NIOSH chromatographic acid technique within $\pm 3\%$. The instrument can be run from a battery or an ac and can be used for continuous atmospheric monitoring of workplaces where formaldehyde may be produced. CEA Instruments 414

Protein chemistry. HP G1004A automated benchtop protein chemistry station concentrates, purifies, fragments, and modifies protein before HPLC or sequence analysis. Samples can be loaded directly onto the column; sample solutions containing contaminants such as salts, nonvolatile buffers, detergents, and surfactants will not interfere with the reactions; and chemistries are performed in a closed, inert environment. Hewlett Packard 415

Moisture measurement. Model DL37KF titrator uses the Karl Fischer coulometric titration method to measure moisture in the 10 μg –100 mg range in solid, liquid, and gaseous samples. The instrument features an automatic start mode; a built-in printer; and display of set-up menus, test conditions, and self diagnostics. Mettler 416

Software

Chromatography. EZChrom software revision 2.0 aids laboratories with GLP compliance and includes system log-in, audit trail, multipoint calibration, and standard bracketing. A multiple-document interface mode allows viewing, analysis, comparison, and interpretation of chromatograms. Shimadzu 418

X-ray microanalysis. Sorcerer, which is available on Macintosh platforms, performs data acquisition, analysis, and report generation. The software identifies and quantifies spectra in real time and provides autocalibration, image analysis (including fast Fourier transform feature analysis), elemental distribution mapping, and principal component analysis. Horiba Instruments 419

Manufacturers' Literature

Surface analysis. Product guide describes instrumentation for surface analysis, including instruments for industrial quality control applications; XPS and AES instrumentation; a SIMS system; and the ECLIPSE data system, which runs in a Windows environment and consists of software applications that support all surface analysis techniques. 8 pp. Fisons 420

Coatings. "Metal Soaps, Specialty Additives, and Biocides for the Coatings Industries" describes typical use levels, performance expectations, applications, and incorporation procedures for a variety of coatings additives.

A problem-solving chart lists the appropriate products for correcting problems in conventional and high-solids solvent-based coatings as well as in waterborne coatings systems. 8 pp. Hüls America 421

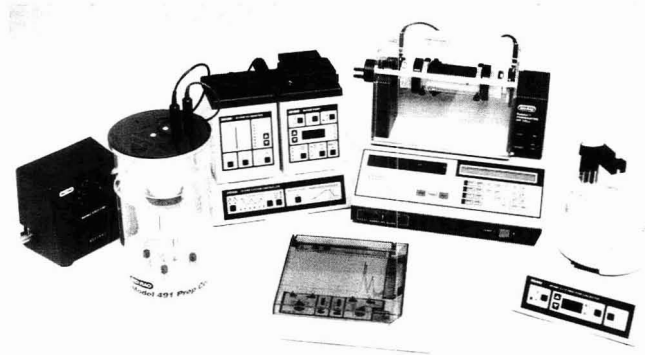
Newsletter. "The Supelco Reporter," Vol. XI, No. 3, contains articles on carbon layer open tubular capillary columns, separation of oxygenated compounds in complex hydrocarbon matrices, monitoring oxygenated and polar volatile compounds in wastewater, quantifying benzene and other hydrocarbons in environmental systems using thermal extraction, and analytical reference standards for monitoring disinfection byproducts in drinking water. 16 pp. Supelco 422

Polyphosphates. Application note describes the use of the PRP-X100 anion-exchange column to separate polyphosphates in fertilizer, water, and detergents. An 8-min gradient separation allows the determination of triphosphate, phosphate, pyrophosphate, and sulfate. The column works with most ion chromatographs and high-performance liquid chromatographs. 2 pp. Hamilton 423

Catalogs

Reflectance products. Catalog describes reflectance standards and targets, integrating spheres and integrating sphere sources, photometers, radiometers, and reflectometers. Technical information on properties of reflectance materials, comparative properties of reflective materials and coatings, and illuminance from uniform lambertian sources is also included. 112 pp. Lab-sphere 424

Inorganic spectroscopy. "Tools of the Trade" includes QC samples for environmental analysis; organometallic oil standards; solution standards for plasma emission spectroscopy; multielement solution standards for the Superfund contract laboratory program and for environmental analysis; instrument check standards for ion chromatography; and solution standards for AAS, optical emission spectroscopy, and X-ray spectroscopy. 44 pp. Spex 425



Preparative 2D electrophoresis system combines the Rotofor preparative isoelectric focusing cell with the Model 491 preparative cell to purify proteins from crude preparations such as cell culture media, tissue homogenates, whole cell lysates, sera, plasma, and plant or fungal extracts. Bio-Rad 417

For more information, please circle the appropriate numbers on one of our Readers' Service Cards.

LABORATORY SERVICE CENTER

DL- α -Alanine • Allyl Isovalerate • 1-Amino-2-naphthol-4-sulfonic Acid
Ammonium Pyrrolidinedithiocarbamate • Aniline Sulfate • Benzoic Anhydride
Brilliant Green • Bromosulphophthalein • 3,3'-Diaminobenzidine Tetra HCl
Dihydroxyacetone • Dimethylamine HCl • 2,2'-Dipyridyl • Gentisic Acid
Glycolic Acid • Hematoxylin • Levulinic Acid • Melibiose • Neocuproine
Polyacrylonitrile • Propyl Iodide • Pyromellitic Acid • Succinimide
Sodium Diethyldithiocarbamate • Suberic Acid • Sulfosalicylic Acid
Thymolphthalein • Triphenylphosphine • iso-Valeraldehyde • Wright's Stain

Write for our Products List of over 3,000 chemicals

Tel: 516-273-0900 • TOLL FREE: 800-645-5566

Telefax: 516-273-0858 • Telex: 497-4275

EASTERN CHEMICAL
A Division of UNITED-GUARDIAN, INC.

P.O. Box 2500
DEPT. AC
SMITHTOWN, N.Y. 11787

NMR ANALYSIS

Multinuclear Multifield
Liquid or Solid State
GLP Compliance

Spectral Data Services, Inc.
818 Pioneer, Champaign, IL 61820
(217) 352-7084 Fax (217) 352-9748

FREE DATA, FAST

To quickly amass data on all of the products you need, consult the Lab Data Service Section on our Analytical Chemistry reader reply card insert.

HELP WANTED ADS

ROP display at ROP rates. Rate based on number of insertions within contract year. Cannot be combined for frequency.

Unit	1-Ti	6-Ti	12-Ti
1" (25 mm)	\$210	\$190	\$180
	24-Ti	48-Ti	72-Ti
	\$170	\$160	\$150

ANALYTICAL CHEMISTRY

1599 Post Road East
P.O. Box 231
Westport, CT 06881
203-256-8211/FAX: 203-256-8175

LABORATORY SERVICE CENTER

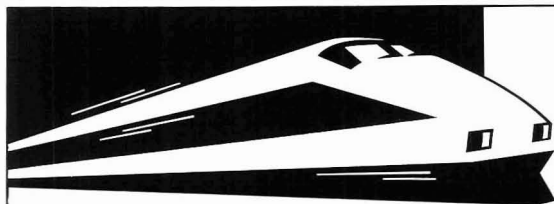
(Equipment, Materials, Services, Instruments for Leasing), Maximum space — 4 inches per advertisement. Column width, 2-3/16"; two column width, 4-9/16". Artwork accepted. No combination of directory rates with ROP advertising. Rates based on number of inches used within 12 months from first date of first insertion.

Per inch: 1" — \$185; 12" — \$180; 24" — \$175; 36" — \$170; 48" — \$165.

CALL OR WRITE JANE GATENBY

ANALYTICAL CHEMISTRY

1599 Post Road East
P.O. Box 231
Westport, CT 06881
203-256-8211
FAX: 203-256-8175



STN Express®
Version 3.1
now available



Easy connection to STN®

Step aboard STN Express (for the IBM® AT and PS/2 and Apple® Macintosh), the software that will quickly log you on to STN International® and help you prepare your questions *offline*, before online charges are incurred. Then you can upload and execute your search and produce *print-quality output of both text and graphics*.

Easy structure searching

You can draw structures freehand or with templates or venture into molecular modeling. Once you've defined the structure the way you pictured it, *search for it among the 10 million structure diagrams in the CAS Registry file*. Was there a match? If so, that's a valuable piece of information. No match? Knowing that could be *invaluable*.

New features of version 3.1 include support of network communications, easy drawing of reaction queries, and much more.

YES! Please send me the FREE STN Express evaluation package.

Name _____
Position _____
Address _____
Phone _____

STN International, c/o CAS, Marketing, Dept 33392, P.O. Box 3012, Columbus, Ohio 43210-0012
FOR FASTER SERVICE call 614-447-3731, 800-933-4350, or FAX this completed coupon to 614-447-3713.

INDEX TO ADVERTISERS IN THIS ISSUE

Advertising Management for the American Chemical Society Publications

CIRCLE INQUIRY NO.	ADVERTISERS	PAGE NO.
1	Aldrich Chemical Company, Inc. Advertising Design Studios, Inc.	IFC
12	*Brookhaven Instruments Corporation	985A
20	*Chrompack, Inc.	960A
30	EM Separations Scientific Marketing Services, Inc.	956A
45, 46	*Hewlett-Packard Company Brooks Communications, Inc.	OBC
48-51	*Isco, Inc. Farneaux Associates	951A
54	*Isotec, Inc.	981A
56	Jandel Scientific	960A
70	*Malvern Instruments, Inc.	969A
74	*Matheson Gas Products Kenyon Hoag Associates	954A
72	*Metrohm, Ltd. Ecknauer + Schoch Werbeagentur ASW	952A
88	PITTCO '93 The Pittsburgh Conference	970A
95	Rheodyne, Inc. Bonfield Associates	958A
114, 115	*Wheaton The Wheaton Agency	969A

CENTCOM, LTD.

President

James A. Byrne

Executive Vice President

Benjamin W. Jones

Robert L. Voepel, Vice President

Joseph P. Stenza, Production Director

1599 Post Road East
P.O. Box 231
Westport, Connecticut 06881-0231
(Area Code 203) 256-8211
Fax No. 203-256-8175

DIRECTOR, ADVERTISING SALES, LABORATORY PRODUCTS

Bruce E. Poorman

ADVERTISING PRODUCTION MANAGER

Jane F. Gatenby

SALES REPRESENTATIVES

Philadelphia, Pa. . . . CENTCOM, LTD. GSB Building, Suite 405, 1 Belmont Ave., Bala Cynwyd, PA. 19004. Telephone: 215-667-9666, FAX: 215-667-9353

New York/New Jersey . . . Dean A. Baldwin, John F. Rafferty, CENTCOM, LTD., Schoolhouse Plaza, 720 King Georges Post Road, Fords, NJ 08863, Telephone: 908-738-8200, FAX: 908-738-6128

Westport, CT/Boston, MA. . . . Edward M. Black, CENTCOM, LTD., 1599 Post Road East, P.O. Box 231, Westport, CT 06881-0231. Telephone: 203-256-8211, FAX: 203-256-8175

Cleveland, OH/Atlanta, GA. . . . Bruce E. Poorman, CENTCOM, LTD., 325 Front St., Suite 2, Berea, OH 44017. Telephone: 216-234-1333, FAX: 216-234-3425

Chicago, IL/Houston, TX. . . . Michael J. Pak, CENTCOM, LTD., 540 Frontage Rd., Northfield, IL. 60093. Telephone: 708-441-6383, FAX: 708-441-6382

West Coast/Denver, CO. . . . Paul M. Butts, Jay S. Francis, CENTCOM, LTD., Suite 808, 2672 Bayshore Parkway, Mountain View, CA 94043. Telephone: 415-969-4604, FAX: 415-969-2104

United Kingdom, Scandinavia and Europe (Except: Germany, Switzerland, Austria) . . . Malcolm Thiele, Technomedia Ltd., Wood Cottage, Shurlock Row, Reading RG10 0QE, Berkshire, England. Telephone: 0734-343302, FAX: 0734-343848

France, Belgium, The Netherlands, Spain, and Italy . . . Ivonne Melcher, Bel Air Building 331A, 58 Rue Pottier, 78150, Le Chesnay, France. Telephone: (1)34-62-00-03, FAX: (1)34-62-95-07

Germany, Switzerland, Austria . . . InterMedia Partners, GmbH, Katernberger Strasse 247, 5600 Wuppertal #1, Germany. Telephone: (0202) 711091, FAX: (0202) 712431

Tokyo, Japan . . . Sumio Oka, International Media Representatives Ltd., 1-11-5-502, Tamazutsumi, Setagaya-ku, Tokyo 158 Japan. Telephone: 502-0656, Telex #22633, FAX: 5706-7349

Asia (Except Japan) . . . Bruce E. Poorman, CENTCOM, LTD., 325 Front St., Suite 2, Berea, OH 44017. Telephone: 216-234-1333, FAX: 216-234-3425

South America . . . Bruce E. Poorman, CENTCOM, LTD., 325 Front St., Suite 2, Berea, OH 44017. Telephone: 216-234-1333, FAX: 216-234-3425

Directory section, see page 988A.

* See ad in ACS LabGuide.

ACCOUNTS OF CHEMICAL RESEARCH announces BUCKMINSTERFULLERENES issue now on SALE!

Dedicated to "Buckyballs", this issue offers the most comprehensive, up-to-date review of the C_{60} molecule and its fullerene relatives.

Articles by the most prominent scientists in the field report on buckyballs and their family of molecules, from discovery to characterization of their structural, physical, and chemical properties.

This versatile C_{60} molecule is pushing researchers into unexplored areas, demanding attention from scientists in all fields.

MUST READ "BUCKYBALL" Articles:

Self-Assembly of the Fullerenes

R.E. Smalley

A Postbuckminsterfullerene View of Carbon in the Galaxy

J.P. Hare and H.W. Kroto

Solid-State Chemistry of Fullerene-Based Materials

J.E. Fischer, P.A. Heiney, and A.B. Smith III

Beyond C_{60} : The Higher Fullerenes

F. Diederich and R.L. Whetten

Electronic Structure, Conductivity, and Superconductivity of Alkali Metal Doped C_{60}

R.C. Haddon

Metal Complexes of Buckminsterfullerene (C_{60})

P.J. Fagan, J.C. Calabrese, and B. Malone

Fullerenes and Fullerides:

Photoemission and Scanning Tunneling Microscopy Studies

J.H. Weaver

Osmylation of C_{60} : Proof and Characteri- zation of the Soccer-Ball Framework

J.M. Hawkins

The Chemical Properties of Buckminsterfullerene (C_{60}) and the Birth and Infancy of Fulleroids

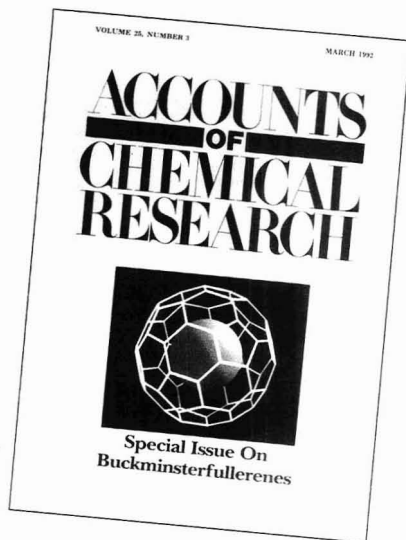
F. Wudl

Characterization of Fullerenes by Mass Spectrometry

S.W. McElvany, M.M. Ross, and J.H. Callahan

Fullerene Structure and Dynamics: A Magnetic Resonance Potpourri

R.D. Johnson, D.S. Bethune, and C.S. Yannoni



UP TO THE MINUTE RESEARCH

"This special issue was put together in a record three-month period and it promises an up-to-date review of the research in the field."

Fred McLafferty, Editor

ACCOUNTS OF CHEMICAL RESEARCH

GET YOUR RESEARCH NOTICED

Over the past ten years ACR was either the most cited or the second most cited journal of ninety primary chemistry journals.*

Join your colleagues in publishing your research where it will get the attention it deserves, with no page charges and timely manuscript review.

For author guidelines write the editor, or check the appropriate box on the order form below.

*SCI Journal Citation Reports. Scientific Citation Index, Institute of Scientific Information.

PURCHASE YOUR OWN "BUCKYBALL" SPECIAL ISSUE

Simply fill out the coupon below and enclose with your payment of \$15 OR SUBSCRIBE now to ACCOUNTS OF CHEMICAL RESEARCH and receive all 1992 issues, including the "Buckyball" and "Special 25th Anniversary" issues, at the low rate of \$26 (U.S.). International rates listed below. Please use coupon below to start your subscription.

- ☐ **Yes.** I want my own copy of the special ACR "Buckminsterfullerenes" Issue Number 3, Volume 25, March 1992.

U.S.

Foreign Includes Postage Via Air Service

☐ \$15

☐ \$18

- ☐ **Yes.** I want to begin my subscription to ACR, which includes the "Buckminsterfullerenes" issue and the "25th Anniversary Issue".

U.S.

Canada & Mexico

Europe

All Other Countries

ACS Members 1 year

☐ \$26

☐ \$33

☐ \$37

☐ \$41

Nonmembers 1 year

☐ \$170

☐ \$177

☐ \$181

☐ \$185

This publication is available on microfilm, microfiche, and online through CJO on STN International.

Name

Address

City State Zip

- ☐ Please send author guidelines to me at the above address.

Please Select Your Method of Payment:

- ☐ Payment Enclosed (Payable to the American Chemical Society)

- ☐ Bill Me

- Charge my ☐ Visa/MasterCard or ☐ American Express

Acct. #

Exp. Date

Signature

Print Name

Mail this coupon to:

ACCOUNTS OF CHEMICAL RESEARCH, American Chemical Society
Marketing Communications, Rm. 609

1155 16th Street, N.W., Washington, D.C. 20036

Or Call: 1-800/333-9511 (U.S. only) or 614/447-3776

FAX: 614/447-3671

To place your "Buckyball" issue order by phone call:
1-800/227-5558 and press 2.

Foreign payment must be made in U.S. dollars by international money order, UNESCO coupons, or U.S. bank draft. Orders accepted through your subscription agency. For nonmember rates in Japan, contact Maruzen Co., Ltd., 3-10 Nihonbashi 2-chome, Chuo-ku, Tokyo, 103, Japan.

AC RESEARCH

Rapid Screening for Taxanes by Tandem Mass Spectrometry

Steven H. Hoke II, Joe M. Wood,[†] and R. Graham Cooks*

Department of Chemistry, Purdue University, West Lafayette, Indiana 47907-1393

Xiao-Hua Li and Ching-je Chang*

Department of Medicinal Chemistry and Pharmacognosy, Purdue University, West Lafayette, Indiana 47907-1333

A highly specific and sensitive method is described for determining taxol, cephalomannine, and baccatin III in crude plant extracts. Radical anions of the taxanes are formed by desorption chemical ionization, and a parent tandem mass spectrometric scan is used to recognize these compounds by their characteristic dissociations. The limit of detection of the individual taxanes in typical plant matrices is less than 500 pg when all three species are screened simultaneously. Because of the sensitivity of the method, extraction times can be shortened to 30 min and crude extracts can be examined at the rate of 6/h. Detection of all three taxanes extracted from a single *Taxus cuspidata* needle in a combined extraction/analysis time of less than 1 h is demonstrated.

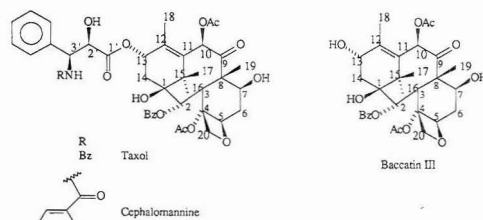
INTRODUCTION

The clinical trials of the natural product taxol have shown extremely promising results for treatment of ovarian, breast, and skin cancers.¹⁻³ Taxol is isolated from the bark of the Pacific yew tree, *Taxus brevifolia*;⁴ however, the yield of taxol is only approximately 1 g/10 kg of bark⁵ and it has been estimated that this natural supply of taxol will be consumed within the next 5-10 years.⁶ In addition, many of the trees are located in areas where logging is prohibited to protect the habitat of the spotted owl.⁷ It is this dilemma which led Bruce Chabner of the National Cancer Institute to call the procurement of taxol "the ultimate confrontation between medicine and the environment".⁷

As a result of this natural shortage, alternative methods of taxol production are being explored. Production of taxol by

culturing plant tissues in a laboratory setting has been accomplished on a small scale.⁸ Total synthesis of taxol has not been achieved because of the number of asymmetric centers and the complexity of the diterpene skeleton.⁹⁻¹¹ However, a method of partial synthesis of taxol which couples the simpler diterpenoid, baccatin III, with the synthetic carboxylic acid side chain has been developed.¹²

Because of the potential usefulness of taxol analogs in the partial synthesis of taxol, methods which screen various plant materials for taxol and other taxanes such as cephalomannine and baccatin III are highly desirable. High-performance



liquid chromatography (HPLC) is widely used to determine taxane concentrations,¹³⁻¹⁵ but it is not suited for rapidly screening numerous samples at low levels. Recently, enzyme-linked immunosorbent assays (ELISA) have been used to screen plant extracts for taxanes, but with current technology cephalomannine cross reacts with taxol.¹⁶ Other methods of taxane analysis including multimodal thin-layer chromatog-

[†] Present address: Vistakon Johnson and Johnson Vision Products, P.O. Box 10157, Jacksonville, FL 32247.

(1) McGuire, W. P.; Rowinsky, E. K.; Donehower, R. C. In *Accomplishments in Cancer Research-1990*; Fortner, J. G., Rhoads, J. E., Eds.; J. B. Lippincott: Philadelphia, 1991; pp 276-283.

(2) Borman, S. *Chem. Eng. News* 1991, Sept 2, 11-18.

(3) Suffness, M.; Cordell, G. A. In *The Alkaloids, Chemistry and Pharmacology*; Broggi, A., Ed.; Academic Press: Orlando, FL, 1985; Vol. XXV, pp 280-288.

(4) Wani, M. C.; Taylor, H. L.; Wall, M. E.; Coggon, P.; McPhail, A. T. *J. Am. Chem. Soc.* 1971, 93, 2325-2327.

(5) Vidensek, N.; Lim, P.; Campbell, A.; Carlson, C. J. *Nat. Prod.* 1990, 53, 1609-1610.

(6) Kingston, D. G. I. *Pharmacol. Ther.* 1991, 52, 1-34.

(7) Chase, M. A. New Cancer Drug May Extend Lives-At Cost of Rare Trees. *Wall St. J. [Three Star] East Ed.* 1991, April 9, pp A1, A8.

(8) Lansing, A.; Haertel, M.; Gordon, M.; Floss, H. G. *Program and Abstracts of the 32nd Annual Meeting of the American Society of Pharmacognosy*; Chicago, 1991; p-109.

(9) Holton, R. A. *J. Am. Chem. Soc.* 1984, 106, 5731-5732.

(10) Guéritte-Voegelein, F.; Guénard, D.; Potier, P. *J. Nat. Prod.* 1987, 50, 9-18.

(11) Holton, R. A.; Joo, R. J.; Kim, H. B.; Williams, A. D.; Harusawa, S.; Lowenthal, R. E.; Yogai, S. *J. Am. Chem. Soc.* 1988, 110, 6558-6560.

(12) Denis, J.-N.; Greene, A. E.; Guénard, D.; Guéritte-Voegelein, F.; Mangatal, L.; Potier, P. *J. Am. Chem. Soc.* 1988, 110, 5917-5919.

(13) Witherup, K. M.; Look, S. A.; Stasko, M. W.; McCloud, T. G.; Issaq, H. J.; Muschik, G. M. *J. Liq. Chromatogr.* 1989, 12, 2117-2132.

(14) Harvey, S. D.; Campbell, J. A.; Kelsey, R. G.; Vance, N. C. *J. Chromatogr.* 1991, 587, 300-305.

(15) Cardellina, J. H., II. *J. Liq. Chromatogr.* 1991, 14, 659-665.

(16) Jaziri, M.; Diallo, B. M.; Vanhaelen, M. H.; Vanhaelen-Fastre, R. J.; Zhiri, A.; Becu, A. G.; Homes, J. *J. Pharm. Belg.* 1991, 46, 93-99.

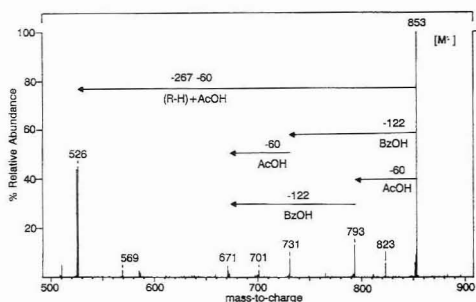


Figure 1. MS/MS product ion spectrum of the taxol radical anion produced by collision-induced dissociation using an argon target and a collision energy of 24 eV. The loss of the neutral species, R, corresponds to cleavage of the acyl-oxygen bond of the C13 side chain.

raphy (TLC),¹⁷ fast atom bombardment mass spectrometry,¹⁸ and combinations of techniques such as HPLC and thermospray mass spectrometry,¹⁹ do not provide both rapid analysis of crude extracts and low limits of detection.

Tandem mass spectrometry (MS/MS) is particularly well suited for trace analysis of target compounds in complex matrices.²⁰⁻²⁴ This report presents a highly specific and extremely sensitive parent tandem mass spectrometric method for screening plant extracts for taxol, cephalomannine, and baccatin III using a triple quadrupole mass spectrometer. A preliminary account of this result has been given elsewhere.²⁵

EXPERIMENTAL SECTION

Extraction Procedure. Plant needle and bark samples were collected, dried, ground, and extracted in 95% ethanol overnight. The resulting solution was filtered and evaporated to dryness. After partitioning between methylene chloride and water (1:1), the methylene chloride fraction was dried and partitioned between hexane and (90%) methanol and the methanol fraction was analyzed using the MS/MS parent scan.

Analysis Procedure. A Finnigan triple-stage quadrupole (TSQ) 700 was used for the analysis of samples. Radical anions of the taxanes were generated in an ammonia chemical ionization plasma by electron attachment²⁶⁻²⁸ after sample molecules had been thermally desorbed from a direct evaporation probe. Under the ionization conditions used during these experiments, some $[M-H]^-$ was also produced but was not utilized in the screening procedure.

(17) Stasko, M. W.; Witherup, K. M.; Ghiorzi, T. J.; McCloud, T. G.; Look, S.; Muschik, G. M.; Issa, H. J. *J. Liq. Chromatogr.* **1989**, *12*, 2133-2143.

(18) McClure, T. D.; Reimer, M. L. J.; Schram, K. H. *Proceedings of the 38th ASMS Conference on Mass Spectrometry and Allied Topics*; Tucson, 1990; pp 1008-1009.

(19) Auriola, S. O. K.; Lepistö, A.-M.; Naaranlahti, T.; Lapinjoki, S. P. *J. Chromatogr.* **1992**, *594*, 153-158.

(20) Roush, R. A.; Cooks, R. G. *J. Nat. Prod.* **1984**, *47*, 197-214.

(21) Busch, K. L.; Glush, G. L.; McLuckey, S. A. *Mass Spectrometry/Mass Spectrometry*; VCH: New York, 1988.

(22) Fetterolf, D. D.; Yost, R. A. *Int. J. Mass Spectrom. Ion Processes* **1984**, *62*, 33-49.

(23) Lau, B. P.-Y.; Scott, P. M. *Proceedings of the 32nd ASMS Conference on Mass Spectrometry and Allied Topics*; San Antonio, 1984; pp 789-790.

(24) Plattner, R. D.; Bennett, G. A.; Stubblefield, R. D. *J. Assoc. Off. Anal. Chem.* **1984**, *67*, 734-738.

(25) Wood, J. M.; Hoke, S. H.; Cooks, R. G.; Chang, C.-j.; Heinsteins, P. F. *Proceedings of the 39th ASMS Conference on Mass Spectrometry and Allied Topics*; Nashville, 1991; pp 1679-1680.

(26) von Ardenne, M.; Steinfelder, K.; Tummeler, R. *Elektronen-anlagerungs-massenspektrometrische Organische Substanzen*; Springer: Berlin, 1971.

(27) Hunt, D. F.; Sethi, S. K. *J. Am. Chem. Soc.* **1980**, *102*, 6953-6963.

(28) Dillard, J. G. *Chem. Rev.* **1973**, *73*, 589-643.

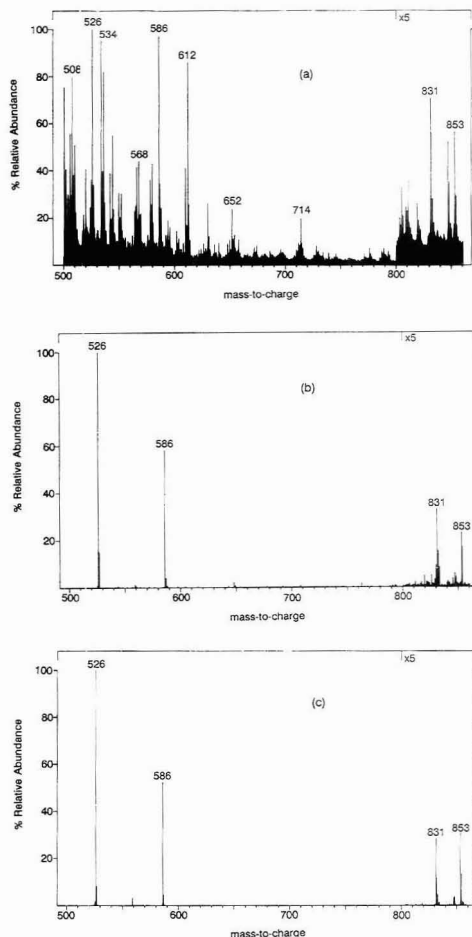


Figure 2. (a) Full-scan, single-stage, mass spectrum of a plant extract containing less than 10 ng of each of the taxanes. (b) Parent ion spectrum of m/z 526 of the same plant extract. (c) Parent ion spectrum of a mixture of taxol, cephalomannine, and baccatin III standards. Spectra in (b) and (c) were produced by collision-induced dissociation on an argon target at 40 eV. Taxol (m/z 853), cephalomannine (m/z 831), and baccatin III (m/z 586) are represented in all three spectra.

Collisional activation was generally achieved with 30-eV collisions upon an argon target gas at 0.5 mTorr in quadrupole 2 during the parent ion scan of m/z 526. To decrease the limit of detection, multiple reaction monitoring was performed in which a 10-Da window around the molecular ion regions of taxol, cephalomannine, and baccatin III was scanned in 0.05 s. Quantitation data were taken in the profile mode.

Analysis of each plant extract required two measurements. First, 1 μ L of the plant extract (1 mg/mL) was placed on the filament and the ion current for each of the taxanes was recorded. Second, 1 μ L of the sample was spiked with taxol, cephalomannine, and baccatin III and reexamined. The spike was typically 1, 5, or 10 ng depending on the ion current recorded from the sample alone. This entire process took approximately 10 min. The concentration of each of the taxanes in the sample was then determined from a plot of the ion abundance versus the amount of taxane added.

RESULTS AND DISCUSSION

The MS/MS product ion spectrum of taxol (Figure 1) is recorded by mass-selecting the radical anion in quadrupole 1, effecting collision-induced dissociation in quadrupole 2, and scanning quadrupole 3 to determine the masses of the fragment ions. This spectrum shows several neutral losses which are characteristic of taxol including the loss of acetic and benzoic acids. A prominent peak at m/z 526 is observed in this spectrum and also in the MS/MS product ion spectra of cephalomannine and baccatin III.

Because the ion m/z 526 is common to the product ion spectra of these three taxanes, a parent ion scan was utilized to screen for all three taxanes simultaneously. With this type of scan, the ion current recorded by the electron multiplier results from ions that lose a neutral species and form m/z 526; therefore, the method is selective for molecules containing the same diterpene skeleton as taxol.

To illustrate the selectivity of the method for the target compounds, the parent ion spectrum (Figure 2b) is compared to a conventional single-stage mass spectrum (Figure 2a) of the same plant extract. Note the presence of ions representative of the three species of interest, taxol (m/z 853), cephalomannine (m/z 831), and baccatin III (m/z 586) in both spectra. However, there are many unknown ions present in the mass spectrum and the signal to noise ratio is poor compared to the parent scan. Figure 2c is a parent scan of a mixture of the three standard compounds. All three taxanes have been recognized in plant extracts at levels less than 500 pg; however, the ion current recorded for the taxanes is expected to decrease in matrices containing high concentrations of species with positive electron affinities.

The parent ion scan of m/z 526 was tested as a rapid screening method for taxanes by examining needle and bark extracts from a variety of *Taxus* species. Table I displays the weight percentages of each of the taxanes in various plant samples as determined by the MS/MS methodology. The *Taxus brevifolia* bark extract contained the largest percentage of taxol, as expected.^{5,16} A *Taxus cuspidata* fresh bark extract was run four times with the concentrations of the taxanes determined as 3.70 ± 1.15 ng/ μ L for taxol, 3.15 ± 1.01 ng/ μ L for cephalomannine, and 0.56 ± 0.11 ng/ μ L for baccatin III, with the 90% confidence interval displayed. The reproducibility of the method is adequate, but its main value is in rapidly screening large numbers of plant extracts to determine approximate taxane concentrations.

Table I. Weight Percentages of Taxol, Cephalomannine, and Baccatin III in Various *Taxus* Species As Determined by MS/MS

sample	plant part	% taxol	% cephalomannine	% baccatin III
<i>T. cuspidata</i> (dry)	needle	0.0050	0.0015	0.00022
	twig bark	0.0065	0.0023	0.00042
<i>T. cuspidata</i> (fresh)	needle	0.0069	0.0066	0.00035
	twig bark	0.0030	0.0025	0.00045
<i>T. brevifolia</i>	needle	0.0036	0.00054	0.00078
	bark	0.084	0.0096	0.021
<i>T. floridana</i>	needle	0.012	0.0054	0.00067
	old bark	0.0046	0.0013	0.00090
<i>T. canadensis</i>	needle	0.019	0.0043	0.00073
	bark	0.0029	0.0013	0.00022
<i>T. baccata</i>	needle	0.0070	0.0020	0.00040
	old bark	0.0026	0.0011	0.00059

Because intense ion signals were recorded for most of the samples analyzed, a *T. cuspidata* fresh needle sample was extracted using an abbreviated procedure. The sample was ground and extracted for 30 min in 95% ethanol. The taxanes were determined as 0.0046% (wt %) for taxol, 0.0017% for cephalomannine and 0.00031% for baccatin III. Using this 30-min extraction procedure, 5.0 mg of extract was obtained from a single *T. cuspidata* needle. This extract was dissolved in ethanol (1 mg/mL), and 1 μ L of the resulting solution was analyzed. The presence of these three taxanes in a single needle was confirmed in less than 1-h combined extraction and analysis time. These results demonstrate the great potential of tandem mass spectrometry for rapid selection of high taxane producing species from hybrid yews cultivated by numerous nurseries or from plant tissue culture specimens.

ACKNOWLEDGMENT

The authors thank Dr. Richard Spjut of World Botanical Associates for collection of the *T. brevifolia*, *T. baccata*, *T. canadensis*, and *T. floridana* samples and for identification of the *Taxus* species at Purdue University from which the *T. cuspidata* extracts were taken. This work was supported by the National Cancer Institute, R01 CA55118. S.H.H. acknowledges support from BASF Corp.

RECEIVED for review July 20, 1992. Accepted August 20, 1992.

Application of a Trochoidal Electron Monochromator/Mass Spectrometer System to the Study of Environmental Chemicals

J. A. Laramée,[†] C. A. Kocher,[‡] and M. L. Deinzer^{*†}

Department of Agricultural Chemistry, Environmental Health Sciences Center, and Department of Physics, Oregon State University, Corvallis, Oregon 97331

A trochoidal electron monochromator has been interfaced to a mass spectrometer to perform electron capture negative ion mass spectrometric (ECNIMS) analyses of environmentally relevant chemicals. The kinetic energy of the electron beam can be varied from 0.025 to 30 eV under computer control. No reagent gas is used to moderate the electron energies. An electron energy spread of ± 0.1 to ± 0.4 eV full width at half-maximum (fwhm) can readily be obtained at a transmitted current of 2×10^{-8} A, improving to ± 0.07 eV at 5×10^{-7} A. Comparisons of ECNIMS results from the electron monochromator/mass spectrometer system with those from a standard instrument that uses a moderating gas show similar spectra for heptachlor but not for the s-triazine herbicides, as for example, atrazine. This compound shows numerous adduct ions by standard ECNIMS that are eliminated by using the electron monochromator to generate the mass spectra. Isomeric tetrachlorodibenzo-*p*-dioxins show distinct differences in the electron energies needed to produce the maximum amount of parent and fragment anions. Multiple resonance states resulting in stable radical anions ($M^{\cdot-}$) are easily observed for nitrobenzene and for polycyclic aromatic hydrocarbons. Ionic products of dissociative electron capture invariably occur from several resonance states.

INTRODUCTION

Standard electron capture negative ion mass spectroscopy (ECNIMS) is a sensitive and selective method for the analysis of electrophilic compounds,^{1,2} but the requirement for a buffer gas in the ion source to moderate the electron energy introduces additional variables that are difficult to control. Differences in the reagent gas pressure cause changes in the electron energies and in the resulting relative ion intensities.^{3,4} Various ions and neutral molecules in the source can react to give unpredictable spurious product ions,^{5,6} making it difficult to interpret the spectra. Thus, the advantages in sensitivity and specificity in ECNIMS for the analysis of electronegative compounds often are negated by poor precision and inaccurate results.

The need for a reliable but general and simple analytical device for electronegative compounds remains an important goal in environmental research. An ion source with the

sensitivity and specificity of the ECNIMS method but one that is not dependent on a reagent gas to moderate the electron energies can be envisioned. This device, the electron monochromator, uses a magnetic field to confine the very low energy electrons and crossed electric and magnetic fields to disperse the electrons of different energies. A series of lenses collimates and focuses the energy-selected electrons to increase the electron beam brightness. The device has the further advantage of being tunable to give just the right energy for ionizing specific isomers. This should be particularly advantageous for environmental chemicals of concern, since they derive from compound classes that are highly isomeric.

The trochoidal electron monochromator was first brought to practice by Stamatovic and Schultz⁷ and has been used since by several investigators.⁸ The design adapted here follows closely that of Illenberger⁹ and essentially involves interfacing the monochromator to a quadrupole mass filter.^{10,11} We discuss the utility of the instrument for environmental chemical analysis.

EXPERIMENTAL SECTION

Instrument Design and Calibration. An electron monochromator/mass spectrometer system has been assembled via a modified design of Illenberger.⁹ The electron monochromator was interfaced to a Hewlett-Packard 5982A (Palo Alto, CA) mass spectrometer (Figure 1). The system is pumped by 6-in. and 4-in. oil diffusion pumps, which give a base pressure of 1×10^{-8} Torr. To minimize surface charging problems, the electron optic components in the monochromator were made of 99.999% pure molybdenum. Other components and the entire high-vacuum manifold were constructed from 303 stainless steel, and the filament holder was made of oxygen-free high conductivity (OFHC) copper. Electrodes and deflectors, 1.6 and 19 mm in thickness, respectively, were machined with six equally spaced holes, each of 1.2-mm diameter, on a 13-mm bolt center diameter. These holes serve as seats for 1.6-mm diameter sapphire balls (General Ruby and Sapphire, New Port Richey, FL) which function as insulators and spacers between the components. The electron monochromator and filament are held together by two end-plates; four bolts join the upper and lower end-plates. The entire assembly is spring-mounted on three supports to a 6-in. flange which houses a 20-pin feedthrough (Ceramaseal, New Lebanon, NY). The other end of the assembly fits into the ion source of the mass spectrometer via two off-axis asymmetrical pins. This arrangement allows for rapid and reproducible realignment after cleaning. The rest of the ion optic components and mass analyzer are as supplied by the instrument manufacturer.

(7) Stamatovic, A.; Schultz, G. J. *Rev. Sci. Instrum.* **1970**, *41* (3), 423-427.

(8) Christophorou, L. G. *Electron-Molecule Interactions and Their Applications*; Academic Press, Orlando: 1984; Vols. 1 and 2 and references therein.

(9) Illenberger, E.; Scheunemann, H.-U.; Baumgärtel, H. *Chem. Phys.* **1979**, *37*, 21-31.

(10) Laramée, J. A.; Mahiou, B.; Deinzer, M. L. *The 39th Conference on Mass Spectrometry and Allied Topics* May 19-24, 1991, p 170.

(11) Laramée, J. A.; Deinzer, M. L. *The 40th Conference on Mass Spectrometry and Allied Topics* May 31-June 5, 1992.

* Corresponding author.

[†] Department of Agricultural Chemistry and Environmental Health Sciences Center.

[‡] Department of Physics.

(1) Dougherty, R. C. *Anal. Chem.* **1981**, *53*, 625-636A.

(2) Hunt, D. F.; Crow, F. W. *Anal. Chem.* **1978**, *50*, 1781-1784.

(3) Laramée, J. A.; Arbogast, B. D.; Deinzer, M. L. *Anal. Chem.* **1986**, *58*, 2907-2912.

(4) Laramée, J. A.; Chang, Y.-S.; Arbogast, B. C.; Deinzer, M. L. *Biomed. Environ. Mass Spectrom.* **1988**, *17*, 63-67.

(5) Stöckl, D.; Budzikiewicz, H. *Org. Mass Spectrom.* **1982**, *17* (10), 470-474.

(6) Stöckl, D.; Budzikiewicz, H. *Org. Mass Spectrom.* **1982**, *17* (8), 376-381.

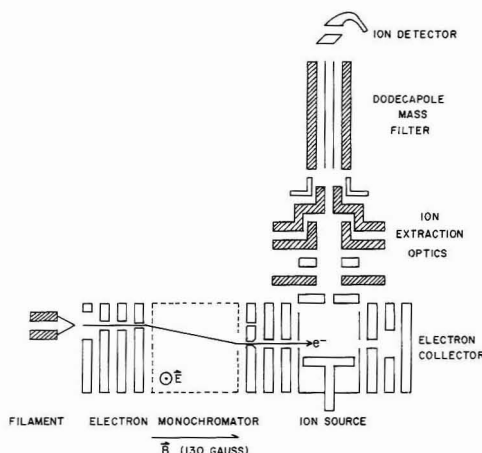


Figure 1. Schematic diagram of the trochoidal electron monochromator/mass spectrometer system.

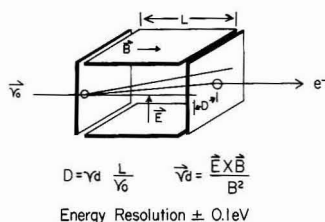


Figure 2. Operating principle of the trochoidal electron monochromator.

Operating Principle. Electrons emitted by a rhenium filament outside the monochromator are collimated and focused by four electrodes into a magnetic field produced by a pair of Helmholtz coils located outside the vacuum system. The filament and the apertures of the first four electrodes are offset 3.18 mm from the ion chamber center. The apertures in the electrodes have diameters of 3.18, 0.99, 0.99, and 0.51 mm, in sequence. A small electric field of about 0.4 V/cm is established between a pair of vertical deflecting plates, oriented perpendicular to the electron beam. The applied potentials, referenced to the filament center, create a transverse electric field E . This field, together with a magnetic field B parallel to the initial beam direction, results in the trochoidal motion of the electrons. The electrons then move trochoidally until they reach the exit aperture, which is funnel-shaped (0.51–1.00-mm diameter) to prevent reflection of electrons from the aperture walls.

Electrons are deflected in a direction perpendicular to both the magnetic and electric fields and disperse according to their initial kinetic energies, v_0 . The transverse displacement depends on the number of trochoids completed by the electrons during their residence time in the crossed field region (Figure 2). Calculations for the geometry used in this design show that the transverse displacement is given by $D = v_d L (m/2v_0)^{1/2}$, where the trochoidal drift velocity is given by $v_d = (E \times B)/B^2$ in SI units.⁷ Energy selection results from the electron's time-of-flight.¹² A special feature of the exit electrode is its dual apertures: one on-center and funnel-shaped to pass a narrow range of electron energies, and the other (0.24-mm diameter) in line with the filament for alignment of the magnetic field, which is accomplished by switching off the deflectors and maximizing the electron current measured at the next electrode on the stack. This set of three electrodes before the ion source functions as an Einzel lens to focus the electrons from the monochromator into the ion source. The assembly of electron optic components produces an intense electron beam even at thermal energies.

Ion Formation and Detection. Ions formed in the ion chamber are extracted by a small electric field (~ 0.7 V/cm) and are focused onto the entrance aperture of an HP 5982A dodecapole mass spectrometer by a six-component ion-extraction system. The extraction potential is applied so that the potential on the axis of the electron beam has a potential equal to that of the entrance and exit apertures of the ion source, thereby establishing a uniform potential along the electron's path through the ion chamber (Figure 1). The electron beam is undisturbed by the ion extraction optics since the current measured at the electron collector does not change when the lenses are energized. Either negative or positive ions can be analyzed. The ion detector consists of a Spiraltron (DeTech 450, Brookfield, MA) operated in a pulse-counting mode at 2 kV, preceded by a conversion dynode at +5 kV for anion detection or -5 kV for cation detection. Thus two 5-kV power supplies are required (Bertin PMT-50A, Hicksville, NY). Three additional electrodes are located at the electron exit side of the ion source and serve a dual function for monitoring beam intensity or for determining the total scattered-electron cross section.^{13,14} An electrometer (Keithley 600A, Cleveland, OH) monitors the electron beam intensity at the electron collector (Figure 1).

Helmholtz Coils. The magnetic field is produced by a pair of series-connected Helmholtz coils (Western Transformer, Portland, OR) external to the vacuum system. The Helmholtz geometry, with two parallel circular coils having a separation equal to their radius R , provides a nearly uniform axial magnetic field at its center, where the monochromator is located. In this central region the field magnitude, B , in the thin-coil limit, is related to the current i by $B = (4/5)^{1/2} \mu_0 N i / R$ in SI units, where N is the number of turns per coil and μ_0 is the permeability of free space. With $R = 22.7$ cm and $N = 96$ turns of double-stranded no. 4 copper wire, the cross section of each coil is approximately a square having dimensions of 4.8 cm. The thin-coil calculation must, therefore, be generalized by integration over the coil cross section. The results of this calculation yield a calibration $B/i = 3.794$ G/A, in agreement with direct gaussmeter measurements of B .

The coil windings are constructed for continuous operation at fields to 400 G. Total dissipation in both coils is about 300 W at the usual operating value of $B = 130$ G. Since the resulting increase in temperature causes the resistance of the windings to increase, the magnetic-field power supply (Hewlett-Packard 6296B) is operated in a current-regulated mode.

Data Acquisition. Pulses from the Spiraltron detector are counted and stored in a multichannel analyzer. The data acquisition system consists of a fast preamplifier (Ortec 9305), a main amplifier/discriminator (Ortec 9302) which has been modified by the addition of a very fast NIM-to-TTL pulse-shape converter (Paulus Engineering Co., Knoxville, TN), a ratemeter (Ortec 9349), and a multichannel analyzer (ACE-MCS) which is housed in an IBM-XT computer with 20 MB hard drive; data are displayed on a Princeton HX-12E monitor and printed on an IBM Proprinter II XL. The electron energy potential is generated by converting the channel number from the multichannel analyzer (ACE-MCS option 1) into an analogous voltage signal which is buffered and reshaped by an operational amplifier (B&B 3627) and then connected via a Wheatstone bridge to a 10A filament power supply (Power-ONE, Inc., Camarillo, CA). This arrangement allows a linear conversion between channel number and electron energy.

Electron Energy Calibration and Energy Resolution. The electron energy distribution was measured using several compounds with generally accepted electron attachment energies. Thermal energy electrons (0.025 eV) were defined with sharply peaked resonances for the capture of electrons by sulfur hexafluoride to produce the molecular radical anion viz. $\text{SF}_6 + e^- \rightarrow \text{SF}_6^-$ with a natural line width of 6 meV.¹⁵ Sulfur hexafluoride

(13) Jordan, K. D.; Burrow, P. D. *Chem. Rev.* 1987, 87, 557–588.

(14) Sanche, L.; Schultz, G. J. *J. Chem. Phys.* 1973, 58, 479–493.

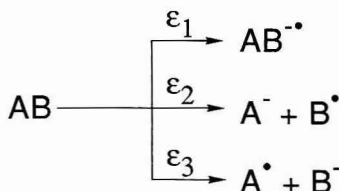
(15) Hickam, W. M.; Fox, R. E. *J. Chem. Phys.* 1956, 25, 642–647.

(16) Stamatovic, A.; Schultz, G. J. *Rev. Sci. Instrum.* 1968, 39, 1752–1753.

(17) Brion, C. E. *Int. J. Mass Spectrom. Ion Phys.* 1969, 3, 197–202.

(18) Foster, M. S.; Beauchamp, J. L. *Chem. Phys. Lett.* 1975, 31, 482–486.

Scheme I



tends to produce memory effects in the instrument; therefore 0.025 eV electrons were more often defined using nitrobenzene²⁰ and hexafluorobenzene.²¹ The process $\text{SF}_6 + e^- \rightarrow \text{SF}_5^- + \text{F}^{\bullet}$ was used to calibrate at 0.37 eV;²² $\text{C}_6\text{F}_6 + e^- \rightarrow \text{C}_6\text{F}_5^- + \text{F}^{\bullet}$ (first resonance) to calibrate at 4.5 eV;²¹ and $\text{CO} + e^- \rightarrow \text{O}^-(^2\text{P}) + \text{C}^+(^3\text{P})$ at 9.62 eV.²³

The fractional electron energy distribution, $\Delta W/W$, is approximately constant over the range of energies employed in the experiment (0–10 eV), as predicted by Stamatovic and Schultz.⁷ Our electrostatic lens configurations were chosen to give a flat transfer function over the energy range in these experiments.²⁴ Peak centroids were used to assign the electron energy scale; thus the electron energy scale corresponds to the median energy. Calibration is performed immediately before and after data acquisition to check for drifts in the energy scale, which sometimes result from contamination of the electrode surfaces by the sample. Using the deviation of the pre- and postcalibration data versus their accepted resonance values, we estimate the absolute accuracy to be ± 0.07 eV at the 99% confidence level. Trade-offs between the energy resolution and energy-resolved electron currents were used to obtain optimum results. Most spectra were obtained at ± 0.1 – 0.4 eV (fwhm) energy distributions at 2×10^{-6} A.¹⁰ The narrowest energy spread obtained thus far is ± 0.07 eV at 5×10^{-7} A (fwhm). All electron optic components were maintained at 105 °C. Samples were introduced into the ion source using a 1.8-mm (o.d.) \times 21-mm Pyrex capillary tube on the end of a direct insertion probe.

Gas-Moderated ECNIMS. In addition to the trochoidal electron monochromator/mass spectrometer system, mass spectra were obtained on a Finnigan 4023 mass spectrometer operating under ECN conditions using methane as buffer gas at 0.6 Torr.³⁴

Chemicals. The chemicals were obtained from commercial sources. Pyrene (99%), chrysene (95%), fluoranthene, and hexachlorobenzene were obtained from Aldrich Chemical Co.; zone-refined pyrene of 99+ % purity was a gift from M. M. Labes, Temple University. Hexachlorobenzene was recrystallized three times and was more than 99% pure. Anthracene was obtained from MC&B Co., and naphthalene (99%) and nitrobenzene (ACS grade) were obtained from Baker Chemical Co. Heptachlor (1,4,5,6,7,8-heptachlor-3a,4,7,7a-tetrahydro-4,7-methanoindene) (99.5%) was obtained from Veliscol and 1,2,3,4-tetrachloro (99%) and 1,3,6,8-tetrachlorodibenzo-*p*-dioxins (99%) were obtained from Ultra Scientific Co. Atrazine (98%) was obtained from Ciba Geigy Co.

RESULTS

Two ionic processes which are of concern in this study are resonance electron capture to form the molecular radical anion and dissociative electron capture to produce fragment ions with the charge residing on either of the two fragments (Scheme I). These processes are distinguished by their energy requirements (ϵ_1 , ϵ_2 , ϵ_3) which can be defined in several ways,

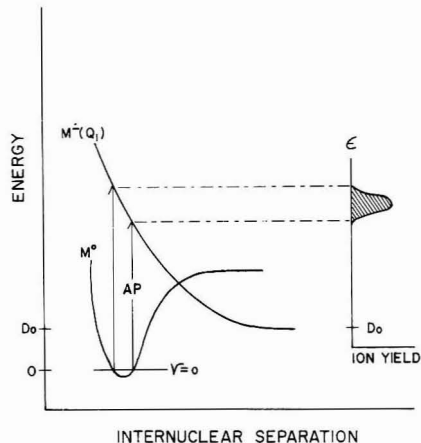


Figure 3. Potential energy surfaces for electron capture with subsequent electronic dissociations. The effect of observed peak shape is illustrated for a dissociation limit (D_0) lying below the energy of the anion in the Franck-Condon region. $M^-(Q_1)$ represents a specific molecular motion in the molecular radical anion which leads to formation of the product ion.

but the minimum energy required for ion formation is the appearance potential (AP). Within the Born-Oppenheimer formalism, the AP is the energy difference from the ground vibrational state of the neutral molecule to the anionic surface (Figure 3). The energy associated with maximum ion production (ϵ_{max}) is manifest as the topmost position in the ion yield curve measured as a function of electron energy (Figure 3, RHS). A useful operational variant for peak shape identification is the centroid energy ($\epsilon_{\text{centroid}}$) which is defined as the energy with 50% of the ion current below $\epsilon_{\text{centroid}}$ and 50% above $\epsilon_{\text{centroid}}$. Regardless of the criteria used to describe the peak, its energetic position and shape are governed by Franck-Condon factors which as a function of electron energy simply reflect the wave function of the ground vibrational state in the neutral molecule (Figure 3). This is true regardless of the mechanism responsible for producing the fragment ion as long as the dissociation limit (D_0) lies below the energy of that portion of the anionic surface which is located within the Franck-Condon region. An additional though less likely violated condition is that the potential energy along the reaction coordinate also must lie below the Franck-Condon region. An experimental consequence of these conditions is that the measured peak widths can be much wider than the width of the electron energy distribution.

Heptachlor (1,4,5,6,7,8-Heptachloro-3a,4,7,7a-tetrahydro-4,7-methanoindene). Heptachlor was analyzed using the electron monochromator/mass spectrometer instrument tuned to transmit monoenergetic electrons at 0.3 eV (Figure 4) or with a broad range of electron energies from 0 to 3 eV. The spectra were essentially identical under these two conditions. A comparison of data produced by buffer gas generated thermal electrons at 0.6 Torr of pressure on a Finnigan 4023 instrument shows the same ions, but with different ion intensities. Mass scans from both systems yield spectra showing $(M - 2\text{HCl})^-$, Cl_2^- , and Cl^- ion peaks. A small molecular anion cluster at m/z 370 is observed in the spectrum produced by the buffer-gas-moderated electrons. This ion cluster is probably stabilized against autodetachment of the electron by the buffer gas because it is not observed with the electron monochromator/mass spectrometer system even with scale expansion.

(19) Chutjian, A.; Alajajian, S. H. *Phys. Rev. A* 1985, 31, 2885–2892.

(20) Christophorou, L. G.; Compton, R. N.; Hurst, G. S.; Reinhardt, P. W. *J. Chem. Phys.* 1966, 45, 536–547.

(21) Fenzlaff, H.-P.; Illenberger, E. *Int. J. Mass Spectrom. Ion Proc.* 1984, 59, 185–202.

(22) Johnson, J. P.; Christophorou, L. G.; Carter, J. G. *J. Chem. Phys.* 1977, 67, 2196–2215.

(23) Sanche, L.; Schultz, G. J. *Phys. Rev. A* 1972, 6, 69–86.

(24) Harting, E.; Read, F. H. *Electrostatic Lenses*; Elsevier: Amsterdam, 1976.

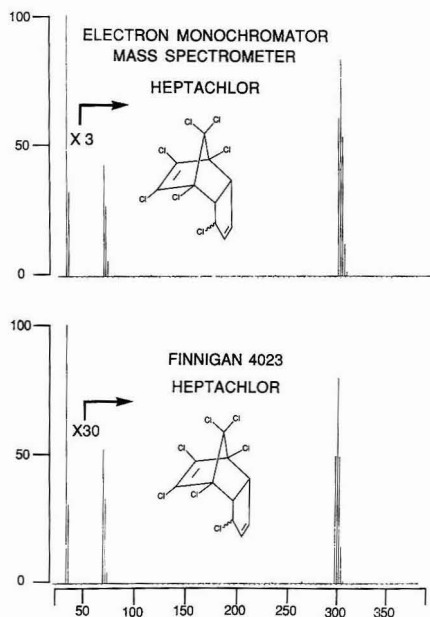


Figure 4. Comparison of ECNI mass spectra of heptachlor obtained on the electron monochromator/mass spectrometer system using electrons with energies of 0.3 eV and on a Finnigan 4023 GC/MS using methane as buffer gas. The data in the top figure were obtained by scanning the rf and dc voltages of the quadrupole at fixed electron energy and then plotting the resulting peak areas using commercial software. Data in the bottom figure were obtained using the standard INCOS software package.



Figure 5. Raw data mass spectrum of the molecular ion region of hexachlorobenzene beginning at mass 282 using 0.5 eV electrons.

Hexachlorobenzene and Carbon Tetrachloride.

Hexachlorobenzene was used in this study to test the capacity of the electron monochromator system to reproduce a complex string of peak shapes derived from isotopes of ^{12}C , ^{13}C , ^{35}Cl , ^{37}Cl . Peak shape analysis on the raw data spectrum (Figure 5) reveals a moment coefficient of skewness 0.04 which compares well with an expected value of zero, and a moment coefficient of kurtosis 2.2 which compares very well with the value of 2.35 for a triangular peak. Mass resolution (Figure 5) also is excellent. The fragment anion abundances from carbon tetrachloride were used to test the ability of the instrument to reproduce chlorine isotope clusters accurately. Excellent agreement has been observed between measured and theoretical²⁵ relative probability of occurrence of the isotopes (Figure 6) with a relative error of $\pm 1.4\%$ at the 99% confidence level.

Polyaromatic Hydrocarbons. Isomeric polycyclic aromatic hydrocarbons (PAHs) are difficult to distinguish by mass spectrometry. Certain isomers, however, capture low-energy electrons and form stable radical anions. In this case the electron affinities (EA) have been calculated to be greater

CHLORINE ISOTOPE ACCURACY MEASUREMENT

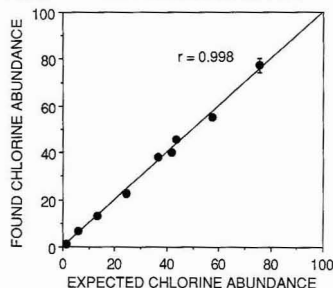


Figure 6. Isotope accuracy performance test. Relative error between expected and observed isotope occurrence probability is $\pm 1.4\%$ (99% confidence level).

than 0.5 eV.²⁶ Several PAHs were analyzed to determine whether they show molecular radical anions on the basis of their calculated EAs and if so whether their energy distributions could be used for their identification. Anthracene has a calculated EA of 0.49 eV and shows a molecular radical anion with m/z 178 at energy centroid values of 0.17 ± 0.04 and 7.3 ± 0.3 eV. The isomers pyrene and fluoranthrene with EA's of 0.45 and 0.63 eV²⁷ show maximum M^- production at 0.21 ± 0.04 and 0.26 ± 0.03 eV, respectively. These results are in contrast to the results obtained under ECNI conditions using methane as buffer gas²⁸ where no molecular ion was observed for anthracene or pyrene. Experimental electron affinities have been reported recently for pyrene at 0.50 and 0.59 eV²⁸ and bracket the value 0.53 eV which was obtained from our predictive model.²⁹

It is assumed the ionizing electrons enter the lowest unoccupied molecular orbitals (LUMOs), which for PAHs would be π orbitals. Under standard ECNIMS conditions stabilization of the radical anion is achieved by the buffer gas in the ion source. This appears not to be necessary in the present case, although sensitivity might very well be enhanced with buffer gas present. The energy spectra of anthracene, pyrene, and naphthalene also show ion signals around 7.7 eV (Figure 7). These higher-energy signals can be nicely explained as ions resulting from capture of electrons by σ orbitals with concomitant breaking of an inner sp^2 bond and loss of the aromatic stabilization energy in two rings. Indeed the LUMO +2 orbital has two very strong antibonding nodes located at the innermost C-C bond. The energy requirements for these processes are ~ 116 kcal/mol for dissociation of a carbon-carbon bond³⁰ and 54.5 kcal/mol³¹ for loss of half of the resonance energy from pyrene. This amounts to 7.4 eV. Some additional energy requirements, such as repulsion of the radical site from the charge site which will occur during electron capture to give an sp^3 -hybridized carbon in the aromatic system,³² could account for the remaining 0.3 eV to bring the total to 7.7 eV.

Nitrobenzene. Nitrobenzene provides an interesting substrate for analysis by electron capture mass spectrometry.

(26) Buchanan, M. V.; Olerich, G. *Org. Mass Spectrom.* 1984, 19 (10), 486-489.

(27) Zander, M. In *Handbook of Polycyclic Aromatic Hydrocarbons*; Bjørseth, A., Ed.; Marcel Dekker: New York, 1983; pp 1-26.

(28) Lias, S. G.; Bartmess, J. E.; Leibman, J. F.; Holmes, J. L.; Levin, R. D.; Mallard, W. G. *J. Phys. Chem. Ref. Data* 1988, 17, suppl. 1, NSRDS.

(29) Laramée, J. A.; Arbogast, B.; Deinzer, M. L. *Anal. Chem.* 1989, 61, 2154-2160.

(30) Benson, S. W. *Thermochemical Kinetics*; Wiley-Interscience: New York, 1976.

(31) Streitwieser, A. *Molecular Orbital Theory for Organic Chemists*; Wiley: New York, 1961.

(32) Chang, Y.-S.; Laramée, J. A.; Dienzer, M. L. *Anal. Chem.* 1991, 63, 2715-2718.

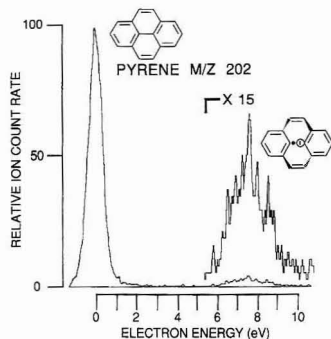


Figure 7. Anion yield curve for the molecular radical anion of pyrene. The ion of mass 202 is energy-resolved into two major components with energy centroids at 0.21 ± 0.04 and 7.7 ± 0.2 eV.

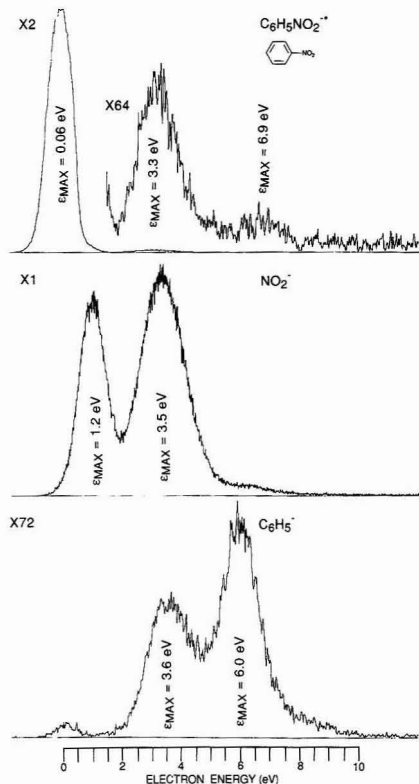


Figure 8. Anion yield curves with respect to electron energy for nitrobenzene molecular anion ($C_6H_5NO_2^-$) and its two major fragment ions, viz. NO_2^- and $C_6H_5^-$.

It has a high EA (ca. 1.0 eV) (28) and clearly shows three distinct negative ion resonance states for the molecular radical anion with m/z 123 and two states each for the phenyl ion with m/z 77 and NO_2^- with m/z 46 (Figure 8). The molecular ion shows maximum production at energies of 0.06, 3.3, and 6.9 eV. The electron energies for maximum nitrobenzene radical anion production have been reported to be 3.8 and 7.2

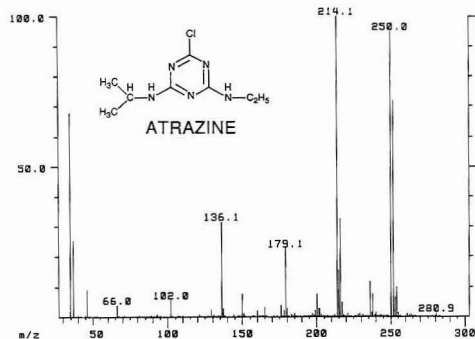


Figure 9. ECNI mass spectrum of atrazine (MW = 215) obtained on the Finnigan 4023 GC/MS. Buffer gas pressure of methane is 0.6 Torr.

eV³³ as measured by an electron-swarm technique;⁸ a technique whereby the rate of electron removal in the swarm is monitored as a function of density-reduced electric field. The values are in reasonable agreement with those measured in this study. It should be pointed out that the electron-swarm technique does not allow the observation of ion production below 1 eV,⁸ at least not very well. And since the values obtained for the measured variables are averaged over the electron energy distribution,⁹ the dependence of the attachment process on electron energy is difficult to determine accurately. The first and second resonances are assumed to be π^* states and the third because of the high energy, a σ^* state. The maximum amount of phenyl anion is produced at energies of 3.56 and 6.02 eV, whereas the NO_2^- ion appears at 1.20 and 3.53 eV. These electron energies for production of the nitro group ion agree well with those reported, i.e. 1.06 and 3.53 eV, in a study using the swarm technique.³³ It is of special interest that the nitro group ion arises from a relatively low energy resonance state, i.e. at 1.2 eV. If this represents a π^* state then the high electron affinity of the NO_2^- group (~ 3.1 eV) and the energy gained by rearomatization of the ring system from the molecular radical anion must be the driving force for cleavage of the nitro group.

s-Triazine Herbicides. s-Triazine herbicides represent a class of environmental chemicals with a large number of derivatives whose gas-moderated ECNIMS spectra are especially complex. Numerous adduct ions with masses corresponding to $(M+1)^-$, $(M+2)^-$, $(M+14)^-$, $(M+28)^-$, and $(M+35)^-$ are reported to have significant ion intensity.³⁴ Relative abundances of these species, however, vary widely and in a complex fashion depending on ion source temperature, cleanliness, and pressure.³⁴ Thus, atrazine with a molecular weight of 215 shows an abundant $(M+35)^-$ ion at m/z 250 when ionized under gas-moderated ECNIMS conditions (Figure 9). Likewise, the 2-(alkylthio)-s-triazines, ametryne, for example, reportedly show $(M+1)^-$, $(M+13)^-$, and $(M+25)^-$ ions.³⁴ These ions are not observed in the spectra of s-triazine herbicides when ionized with the electron monochromator. The energy spectra of these derivatives, however, are rich in information. Atrazine, for example, produces an $(M-H)^-$ ion with m/z 214, $(M-HCl)^-$, and Cl^- with intensities to be observable from just one resonance state each (Figure 10), whereas ametryne produces each fragment ion with high abundance from several resonance states (Table I). Although a systematic study has not yet been carried out,

(33) Jäger, K.; Henglein, A. Z. *Naturforsch.* 1967, 22a, 700.

(34) Huang, L. Q.; Mattina, M. J. I. *Biomed. Environ. Mass Spectrom.* 1989, 18, 828-835.

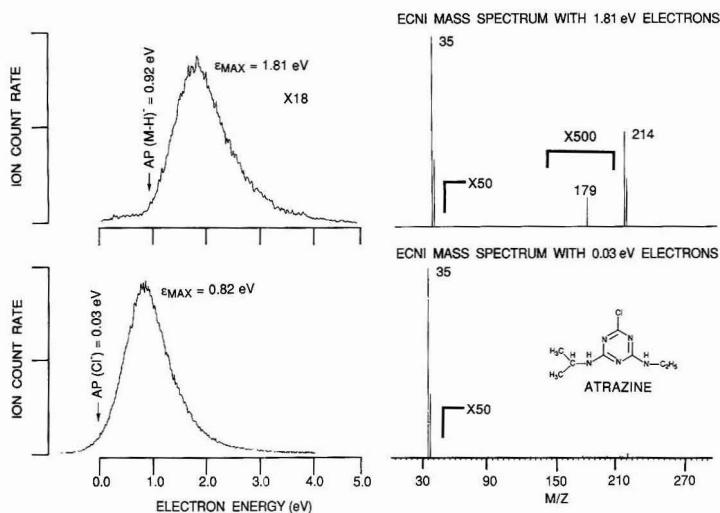


Figure 10. Anion yield curves for $(M-H)^-$ and Cl^- from atrazine, together with mass spectra obtained at a peak production energy of 1.8 and 0.03 eV. At 0.03 eV there are some noise peaks in the mass spectrum which do not correspond to fragment ion peaks.

Table I. Electron Energy Centroids (eV) Producing Ions from *s*-Triazine Herbicides under ECNIMS Conditions

<i>s</i> -triazine herbicide	M^-	$(M-H)^-$	$(M-HCl)^-$	Cl^-	$(M-CH_3)^-$	$(M-SCH_3)^-$	$(M-HSCH_3)^-$
<chem>CC1=NC2=C(N1)N=CN=C2NCC</chem> atrazine	0.21 1.98	1.97	0.97	0.95			
<chem>CC1=NC2=C(N1)N=CN=C2NCC</chem> ametryne	0.30 2.07	0.35 2.05 5.63 9.20			1.15 5.00 7.22	~0 4.82	4.75

it appears from initial examination that other 2-chloro-*s*-triazines and 2-(alkylthio)-*s*-triazines show similar behavior with respect to single versus multiple resonance states from which these ions arise. With the electron energy set at 0.03 eV, which is the appearance energy for production of the chloride ion, no other ions with any intensity are observed in the spectrum. With the electron monochromator set to transmit electrons of 1.81 eV, which is the electron energy for maximum production of $(M-H)^-$, the chloride ion peak is still the most intense one in the spectrum. Scale expansions, however, allow both the $(M-H)^-$ and the $(M-HCl)^-$ ion peaks to be observed (Figure 10).

In a separate experiment the mass spectrometer was set to transmit m/z 215 ions which consists of M^- and $^{13}C(M-H)^-$ species,³⁴ and the electron energy was scanned. Two peaks in the energy-resolved spectrum were found with ϵ_{max} 0.38 and 1.78 eV (Figure 11). The latter value must be the ϵ_{max} for $^{13}C(M-H)^-$ production. This value is within the experimental error (± 0.07 eV) of ϵ_{max} for production of the $^{12}C(M-H)^-$ ion peak with m/z 214 (Figure 10), and there is no reason to believe that the electron energy needed to ionize the carbon-13 isotope will be significantly different from that producing the carbon-12 isotope. The lower energy resonance at 0.38 eV therefore must be due to M^- production. The mass resolution required for separation of M^- from $(M-H)^-$ with one carbon-13 is 48 000, but their separation on an energy basis can be achieved with a resolution of about 50. The

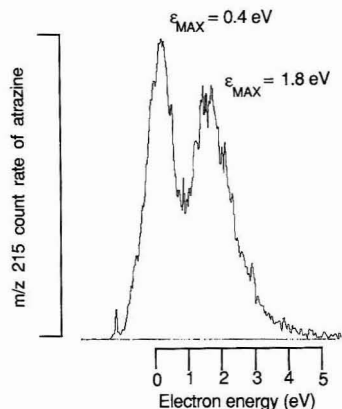
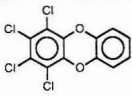
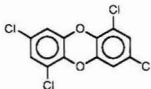


Figure 11. Separation of M^- from $^{13}C(M-H)^-$ on the basis of their molecular orbital energy differences for m/z 215 of atrazine.

electron monochromator could be advantageous for using energy rather than mass discrimination as a basis for separation and identification of certain ions.

Tetrachlorodibenzo-*p*-dioxins. Polychlorodibenzo-*p*-dioxins are uniquely suited for analysis by ECNIMS. These

Table II. Centroided Electron Energies for Producing Ions from Tetrachlorodibenzo-*p*-dioxins under ECNI MS Conditions

	M ^{•-}	Cl ⁻	(M - Cl) ^{•-}
	0.23	0.78 3.75	0.43
	0.38	0.66 3.81	0.64 3.81

compounds absorb electrons and yield molecular radical anions if the electron affinities are sufficiently high.³ More highly chlorinated dioxins produce (M^{•-}), and the lower chlorinated ones produce (M - H)^{•-}.⁴ Electron energy scanning with the electron monochromator shows energy maxima for production of molecular ions from isomeric 1,2,3,4-TCDD and 1,3,6,8-TCDD of 0.23 and 0.38 eV, respectively (Table II). These electron attachment energies follow the same ordering as their calculated lowest unoccupied orbital energies, 0.96 and 1.59 eV, respectively, obtained by CNDO³⁵ calculations and their ratios are almost identical. The 1,2,3,4-tetrachlorodibenzo-*p*-dioxin isomer shows the production of chloride ion from two states at 0.78 and at 3.75 eV and the loss of a chlorine atom at 0.43 eV. These different energy states for the loss of chlorine atom and chloride ion are in marked contrast with the results for 1,3,6,8-tetrachlorodibenzo-*p*-dioxin which show identical energies from which these fragmentations occur.

DISCUSSION

There are advantages in using the electron monochromator as an electron source in ECNIMS experiments. First, the need for using a moderating gas to generate electrons with thermal or epi-thermal energies is eliminated. This helps to remedy a recurring problem in standard ECNI experiments which is the spontaneous and most often undesirable ion/molecule reactions between sample ions and buffer gas molecules or ions. Sensitivity is enhanced in the negative ion mode because electron capture is an on-resonance phenomenon and the electron kinetic energy can be tuned to that resonance. Also the discrete energy of the electron prevents simultaneous formation of positive and negative ions due to

the wide energy separation of electron affinities (ca. 0–3 eV) from molecular ionization potentials (ca. 8–15 eV). Thus, sensitivity reducing anion/cation charge neutralization is eliminated. Stabilization of radical anions to prevent auto-detachment is an important function of the buffer gas in ECNI experiments, and the effects of not having the buffer gas for this purpose still must be evaluated. Sensitivity may be compromised, but this may be corrected by introducing a buffer gas whose only purpose is to stabilize the molecular ion. Such a gas would have a high ionization potential and a negative electron affinity.

Ions are generated at specific electron energies, and this information is potentially valuable for determining positional isomers in a given class of compounds. The unique energetic position and shape of the ion yield curve for isomeric polycyclic aromatic hydrocarbons, polychlorinated dibenzo-*p*-dioxins and dibenzofurans, and other halogenated environmental chemicals could be beneficial in the analytical chemistry of these compounds, particularly when standards are not available. This information could complement or supplement general GC/MS data in confirmation studies. Moreover, the ability to produce ions at specific electron energies will facilitate investigations of the energies and electronic states involved in dissociative electron capture processes. Illenberger and co-workers³⁶ have used the electron monochromator extensively to study the attachment of low-energy electrons to hexafluorobenzene, haloalkyl compounds, van der Waals' complexes, and other electron-absorbing compounds. The electron monochromator should have an impact on such theoretical studies as well as on the practical aspects in the analysis of many other environmental chemicals. Presently we cannot accurately assess the sensitivity of our system because an ordinary insertion probe is used to introduce samples. A GC inlet will allow meaningful comparisons of sensitivity. These modifications have been initiated.

ACKNOWLEDGMENT

This work was supported by the National Institutes of Health (NIEHS 40 and NIEHS 210) and is Technical Report No. 9775 from the Oregon Agricultural Experiment Station.

Received for review January 10, 1992. Accepted July 17, 1992.

Registry No. Heptachlor, 76-44-8; hexachlorobenzene, 118-74-1; carbon tetrachloride, 56-23-5; pyrene, 129-00-0; fluoranthrene, 206-44-0; anthracene, 120-12-7; nitrobenzene, 98-95-3; atrazine, 1912-24-9; ametryne, 834-12-8; 1,2,3,4-tetrachlorodibenzo-*p*-dioxin, 30746-58-8; 1,3,6,8-tetrachlorodibenzo-*p*-dioxin, 33423-92-6.

(36) Oster, T.; Kuhn, A.; Illenberger, E. *Int. J. Mass Spectrom. Ion Proc.* 1989, 89, 1–72.

(35) Laramée, J. A.; Arbogast, B. C.; Deinzer, M. L. *Anal. Chem.* 1988, 60, 1937–1943.

High-Performance Liquid Chromatographic Assay of Taxol

Steven L. Richheimer,* David M. Tinnermeier, and Daniel W. Timmons

Hauser Chemical Research, Inc., Boulder, Colorado 80301

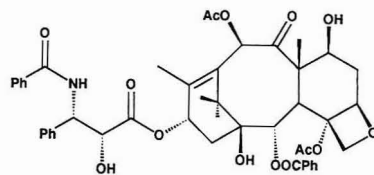
A reversed-phase high-performance liquid chromatographic (HPLC) method for assaying taxol bulk drug or process samples is described. The method utilizes a commercially available pentafluorophenyl (PFP) packing material that has greater selectivity for taxol and related taxanes than other reversed-phase media tested. The method has been shown to be accurate, linear, precise, specific, and rugged, and can be used to assay the bulk drug and determine its chromatographic purity as well as to assay taxol in process and biomass samples.

INTRODUCTION

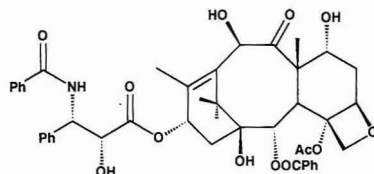
Taxol (I) is isolated in large quantities from the bark of the Pacific yew tree, *Taxus brevifolia*. It is a unique antitumor drug that appears to exert its activity as a result of interference with microtubular structure and function.¹ Several other HPLC assays for taxol using reversed-phase media have appeared in the literature.²⁻⁹ However, these methods have focused on the separation of taxol (I) from the closely eluting analog cephalomannine (III) and tend to be long and tedious. None of the published methods separate taxol from another closely eluting taxane: 7-epi-10-deacetyl taxol (II), which tends to elute between I and III on reversed-phase columns. This report describes a new reversed-phase liquid chromatographic (HPLC) method that adequately separates I from II and III and from other closely eluting compounds that occur naturally in the bark and leaves of *Taxus* species.

EXPERIMENTAL SECTION

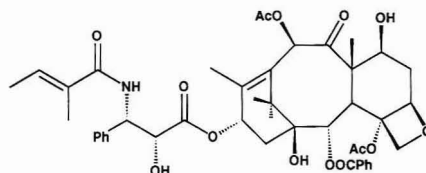
Reagents and Materials. Acetonitrile and water (HPLC grade) and methanol (reagent grade) were purchased from Fisher Scientific Co. (Fair Lawn, NJ). Reagent-grade phosphoric acid (ca. 85%), hydrochloric acid, glacial acetic acid, and methylene chloride were purchased from Baxter Scientific Products (McGraw Park, IL). I and II were isolated in-house from bark of the Pacific yew tree. Taxol was shown to be over 99% pure by chromatography. 7-Epitaxol (XII) was prepared by heating taxol at 140 °C for 70 h. Cephalomannine (III), baccatin III (VII), and 10-deacetyl baccatin III (X) were obtained from the National Cancer Institute (Bethesda, MD). Phenyl HPLC columns (4.6 mm × 250 mm), packed with 5-μm diphenyl material, were purchased from Supelco, Inc. (Bellefonte, PA) and Metachem Technologies, Inc. (Redondo Beach CA). Pentafluorophenyl (PFP) HPLC columns (4.6 mm × 250 mm, 5 μm, 60 Å) were purchased from



I: Taxol



II: 7-Epi-10-deacetyl taxol



III: Cephalomannine

ES Industries (Marlton, NJ) and Metachem Technologies. A 4.6-mm × 20-mm phenyl guard column (Jones Chromatography, Lakewood, CO) was used for all analyses. Crude extracts were filtered through 0.2-μm, 13-mm PVDF filters (Baxter Scientific Products).

Apparatus. The HPLC system consisted of a Model L-6200 pump, Model AS-4000 autosampler equipped with a 100-μL loop, and a Model L-4000 or L-3000 UV/VIS/DAD detector (Hitachi Instruments, Inc., Fremont, CA). The system was equipped with an NEC 286 computer with 40M hard drive (Boxborough, MA) and Lab Manager HPLC software (Hitachi Instruments, Inc.). Chromatographic reports were printed on a Star Micronics Model NX-1000 dot matrix printer (New York, NY) or a Panasonic Model KX-P4450i laser printer (Chicago, IL). Partial loop fill method of injection was used.

Phenyl Column Conditions. The mobile phase for elution of taxanes on diphenyl columns was a linear gradient beginning with 25:75 MeCN/water at a flow rate of 1 mL/min, reaching 60:40 after 35 min.

PFP Column Conditions. The mobile phase for isocratic elution on PFP columns consisted of a 45:55 (v/v) mixture of acetonitrile (MeCN) and water or 0.1% phosphoric acid solution (1 mL of phosphoric acid/L of solution). The flow rate was 1.5 mL/min. Under these conditions, I eluted in about 10 min. For chromatographic purity testing with the PFP column, the initial isocratic conditions were 36–39% MeCN with the remainder water or 0.1% phosphoric acid solution; this was held for 35 min at a flow of 2 mL/min. This was followed by a linear gradient to

- (1) Schiff, P. B.; Faut, J.; Horwitz, S. B. *Nature* 1979, 277, 665.
- (2) Harvey, S. D.; Campbell, J. A.; Kelsey, R. G.; Vance, N. C. *J. Chromatogr.* 1991, 587, 300.
- (3) Witherup, K. M.; Look, S. A.; Stasko, M. W.; McCloud, T. G.; Issaq, H. J.; Muschik, G. M. *J. Liq. Chromatogr.* 1989, 12 (11), 2117.
- (4) Longnecker, S. M.; Donehower, R. C.; Cates, A. E.; Chen, T. L.; Brundrett, R. B.; Grochow, L. B.; Ettinger, D. S.; Colvin, M. *Cancer Treat. Rep.* 1987, 71, 53.
- (5) Magri, N. F.; Kingston, D. G. *J. Org. Chem.* 1986, 51, 797.
- (6) Senih, V.; Bleichert, S.; Colin, M.; Guenard, D.; Picot, F.; Potier, P.; Varenne, P. *J. Nat. Prod.* 1984, 47, 131.
- (7) Hamel, E.; Lin, C. M.; Johns, D. G. *Cancer Treat. Rep.* 1982, 66, 1381.
- (8) Miller, R. W.; Powell, R. G.; Smith, C. R., Jr.; Arnold, E.; Clardy, J. *J. Org. Chem.* 1981, 46, 1469.
- (9) Wani, M. C.; Taylor, H. L.; Wall, M. E.; Coggon, P.; McPhail, A. T. *J. Am. Chem. Soc.* 1971, 93, 2325.

60:40 MeCN/water at 50 min. Under these conditions, I eluted in about 30 min. Detection was at 227 nm throughout, and 10 μ L of sample was injected for all samples except for chromatographic purity testing, where 15 μ L was injected.

Sample and Standard Preparation. Pure I (100 mg) was dissolved in 100.0 mL of methanol containing approximately 100 μ L (0.1%) of acetic acid. Acetic acid was used to neutralize traces of alkali present in the methanol and increase the shelf-life of the standard solution. Crude extracts of *T. brevifolia* biomass were obtained by exhaustive soxhlet extraction with methanol followed by dilution to known volume with methanol.

Assay Procedure. Standard and sample preparations (1 mg/mL) were injected on the PFP column under isocratic conditions (45:55, 1.5 mL/min). Either peak areas or peak heights were measured. Taxol was quantitated by comparing the average peak response of the sample to that of the standard.

Ultraviolet Spectra. UV spectra of taxol and related taxanes were obtained in the range of 200–360 nm with the Model L-3000 diode array detector and DAD Manager software (Hitachi Instruments, Inc.). All spectra were normalized.

NMR Spectra. Proton NMR spectra were obtained on a Varian EM-390 operating at 90 MHz for or on a Bruker ACP-300 operating at 300.13 MHz. Spectra were acquired at ambient temperature using a 5-mm probe in deuterated chloroform at approximately 20 mg/mL. All chemical shifts are reported relative to tetramethylsilane.

RESULTS AND DISCUSSION

Identification of 7-Epi-10-deacetyltaxol (II). II was first described by McLaughlin.¹⁰ II was isolated from a crude methanolic extract of *T. brevifolia* bark by silica column chromatography followed by crystallization from ethyl acetate. The UV spectrum of II was identical to that of 10-deacetyltaxol (IV), and heating IV at 120 °C converted it partially to II. It has been previously reported that epimerization at C-7 decreases the polarity of the epimer, probably due to intramolecular hydrogen bonding between the 7 α -hydroxyl and the carbonyl oxygen of the 4 α -acetoxy group.¹⁰ Hence, 7-epitaxol (XII) eluted after I by reversed-phase chromatography, and similarly, II eluted after IV. The structure of II was confirmed by two-dimensional proton NMR.

Preparation and Identification of Taxol Acid Side. Taxol acid side chain [β (S)-(benzoylamino)- α (R)-hydroxybenzenepropanoic acid, XI] was prepared by treating I, dissolved in a 1:1 mixture of methanol and water, at room temperature with concentrated ammonium hydroxide. XI was extracted from the acidified solution with methylene chloride. The methyl ester of the taxol acid side chain (IX) was prepared similarly in the absence of water. NMR, UV, and HPLC retention times were consistent with the assigned structures.

Chromatography and Comparison to Other Methods. Witherup et al. reported good separation of I and III using a phenyl column and a mobile-phase mixture of acetonitrile, methanol, and water.³ We found that when methanol was eliminated from the mobile phase, the chromatographic separation of I and III improved on a phenyl column. However, II still coeluted with I under these conditions. Several brands of phenyl columns were tried with mixed results. However, we found that a high carbon load diphenyl column (Supelco or Metachem Technologies), using a methanol-free gradient, could achieve baseline separation of these closely eluting taxanes (see Figure 1). In comparison, a pentafluorophenyl column was found to better separate these closely eluting taxanes (see Figure 2). The PFP column appeared to be more selective for I, II, and III and could achieve baseline separation of I, II, and III under isocratic conditions (45% MeCN and 55% H₂O at 1.5 mL/min) in less

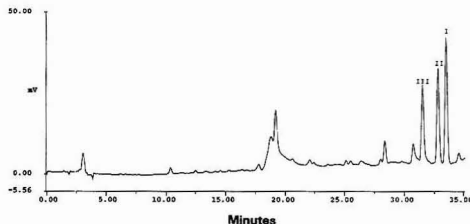


Figure 1. Chromatogram of a mixture of taxol (I), 7-epi-10-deacetyltaxol (II), and cephalomannine (III) on a phenyl column. Chromatographic conditions: linear gradient at 1 mL/min starting at MeCN/H₂O (25:75) and going to MeCN/H₂O (60:40) after 35 min.

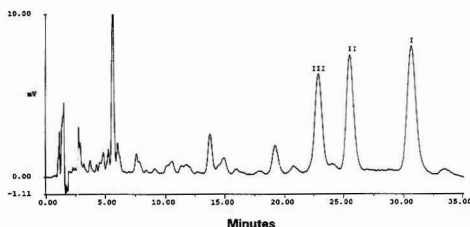


Figure 2. Chromatogram of a mixture of taxol (I), 7-epi-10-deacetyltaxol (II), and cephalomannine (III) on a PFP column. Chromatographic conditions: isocratic for 35 min at 2 mL/min with MeCN/H₂O (37:63), followed by a linear gradient to MeCN/H₂O (60:40) at 50 min.

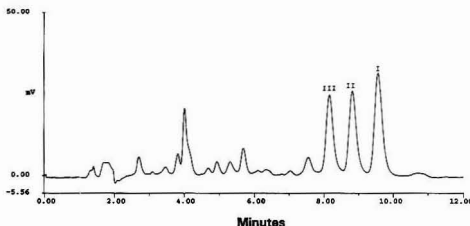


Figure 3. Chromatogram of a mixture of taxol (I), 7-epi-10-deacetyltaxol (II), and cephalomannine (III) on a PFP column. Chromatographic conditions: isocratic for 1.5 mL/min with MeCN/H₂O (45:55).

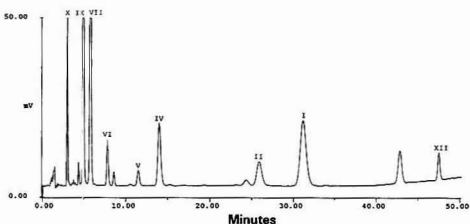


Figure 4. Chromatogram of a sample of degraded taxol standard on a PFP column. Chromatographic conditions: isocratic for 35 min at 2 mL/min with MeCN/H₂O (37:63), followed by a linear gradient to MeCN/H₂O (60:40) at 50 min. I = taxol; II = 7-epi-10-deacetyltaxol; IV = 10-deacetyltaxol; V = 7-epibaccatin III; VI = methylbenzoate; VII = baccatin III; IX = methyl α (S)-(benzoylamino)- β (R)-hydroxybenzenepropanoate; X = 10-deacetylbenzoylamine; XII = 7-epitaxol.

than 10 min (see Figure 3). These chromatographic conditions were found suitable for assaying both I bulk drug, and I in crude *Taxus* extracts. Figure 4 shows the chromatogram obtained on a sample of alkali-degraded I using the PFP column. Figure 5 illustrates the chromatogram obtained on the same sample using the diphenyl column. The phenyl

(10) McLaughlin, J. L.; Miller, R. W.; Powell, R. G.; Smith Jr., C. R. *J. Nat. Prod.* 1981, 44, 312.

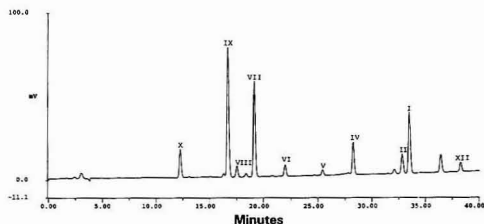


Figure 5. Chromatogram of a sample of degraded taxol standard on a Metachem Intersil 5- μ m phenyl column. Chromatographic conditions: linear gradient at 1 mL/min starting with MeCN/H₂O (25:75) and going to MeCN/H₂O (60:40) after 35 min. I = taxol; II = 7-*epi*-10-deacetyltaxol; IV = 10-deacetyltaxol; V = 7-*epi*baccatin III; VI = methyl benzoate; VII = baccatin III; VIII = 7-*epi*-10-deacetyl-baccatin III; IX = methyl α -(benzoylamino)- β -(*R*)-hydroxybenzene-propanoate; X = 10-deacetylbaccatin III; XII = 7-*epi*taxol.

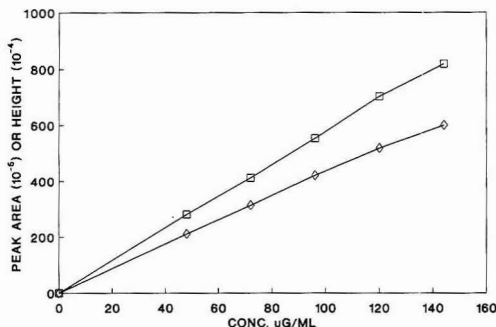


Figure 6. Taxol standard linearity curve. Chromatographic conditions: isocratic at 1.5 mL/min at MeCN/H₂O (45:55); (□) area counts; (◇) height counts.

column was superior in separating naturally occurring taxanes from one another, while the PFP column was more selective for I and was superior in separating I from closely eluting taxanes. Most of the base-catalyzed degradation products have been described previously¹⁰ and were identified by their relative retention time and UV spectra, and in some cases by spiking with known standards. II tailed on new PFP columns. This tailing could be eliminated by adding phosphoric acid (1:1000) to the mobile phase. The addition of phosphoric acid had no effect on the chromatography of other taxanes, and after such treatment, water could be substituted for the dilute phosphoric acid and the tailing did not return.

Linearity. The linear peak response for I was determined over the range of 0.25–1.5 mg/mL. The standard curve was linear ($r = 0.9999$) for both peak area and peak height. The standard curves are shown in Figure 6.

Precision. The injection precision was measured by performing 10 replicate injections of both 5 and 10 μ L of a standard preparation (1 mg/mL). The standard error (2 σ %) was 0.8% for a 5- μ L injection and 0.6% for a 10- μ L injection. The overall assay variability was determined by performing five separate assays on a sample of bulk I (concentration 0.9–1.1 mg/mL). The ratio of milligrams of I to peak area was calculated; the standard error was 2.0%.

Stability of the Bulk Drug. Heating pure, previously dried I at 80 °C or higher converted it primarily to XII. An Arrhenius plot (see Figure 7) was generated for the conversion of I to XII. Extrapolation of the curve to 25 °C indicated that about 0.02% would degrade per year. An Arrhenius plot was also generated for the degradation of I in solution.

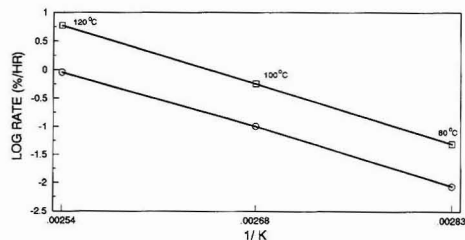


Figure 7. Arrhenius plots for the degradation of taxol: (□) in isobutanol; (○) dry state.

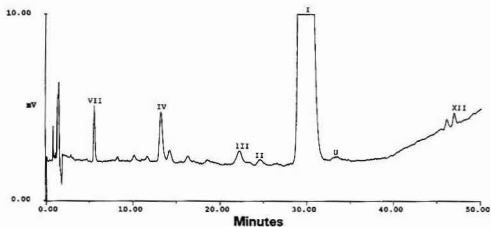


Figure 8. Chromatogram of a sample of taxol bulk drug. Peak assignments are the same as in Figure 1. The closely eluting unknown compound (U) is separated from I by the method. Chromatographic conditions: isocratic for 35 min at 2 mL/min with MeCN/H₂O (37:63), followed by a linear gradient to MeCN/H₂O (60:40) at 50 min. I = taxol; II = 7-*epi*-10-deacetyltaxol; III = cephalomannine; IV = 10-deacetyltaxol; VII = baccatin III.

The plot has approximately the same slope, but the rate of degradation was approximately 5–6 times faster in solution than in the dry state (see also Figure 7).

Stability of Standard and Sample Solutions. Taxol underwent hydrolysis and transesterification in methanolic solutions. A standard consisting of reagent- or HPLC-grade methanol typically lost about 30% of the taxol peak area after storage for 2 weeks at room temperature (see also Figure 1). A sample with 0.1% acetic acid added to the methanol showed no sign of degradation. The preservation effect of acetic acid appeared to be due to its ability to neutralize traces of alkali (probably ammonia) present in methanol. Experiments indicated that taxol standards containing 0.1% acetic acid showed no detectable degradation when stored 7 weeks at room temperature or 3 months at 4 °C.

Chromatographic Purity Testing. The PFP column run under isocratic conditions with less MeCN achieved separation of I from other closely eluting compounds such as the closely eluting taxane U (see also Figure 8). No peak corresponding to U was seen in the chromatogram of the same sample using a phenyl column, and presumably U co-elutes with I under these conditions. Isocratic conditions of approximately 37:63 MeCN/water on the PFP column were found to separate I from impurities and degradation products that might normally be encountered in process samples and bulk drug. Less polar compounds such as XII, which elute after I, were eluted by increasing the MeCN to 60% after the completion of the isocratic phase. This chromatographic method is suitable for performing chromatographic purity testing of the bulk drug.

Degradation of Taxol by Alkali. In aqueous or methanolic alkaline solution, I was destroyed rapidly and totally. In aqueous solution, the acid side chain (XI) and benzoic acid were isolated. In methanolic solution, IX was produced in addition to VII and X. Other deacetylated and debenzoylated derivatives of VII were probably also produced by alkaline hydrolysis, but debenzoylated derivatives of VII

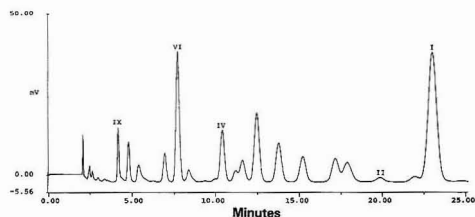


Figure 9. Chromatogram of a sample of taxol subjected to degradation for 9 min in a 1:1 mixture of methanol and concentrated HCl. Chromatographic conditions: isocratic at 2 mL/min at MeCN/H₂O (39:61). I = taxol; II = 7-epi-10-deacetyltaxol; IV = 10-deacetyltaxol; VI = methyl α -(benzoylamino)- β -(R)-hydroxybenzene propanoate.

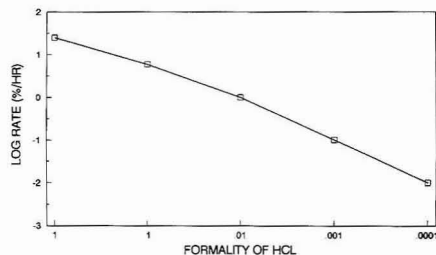


Figure 10. log/log plot of the rate of degradation of taxol in methanolic HCl solution vs the formality of the solution.

would be poorly retained on the column and have weak UV absorbance at 227 nm, and none were observed.

Degradation of Taxol by Acid. Taxol was degraded rapidly at room temperature in a 1:1 mixture of methanol and concentrated HCl. Several polar degradation products were produced, including II, IV, VI, and IX (see also Figure 9). However, unlike base-catalyzed degradation of I, the chromatographic and UV data indicated that no derivatives of VII formed. In contrast to weakly alkaline solutions, I was stable in methanol containing 0.1% acetic acid. In dilute methanolic HCl solutions, the rate of degradation of I was dependent on the concentration of acid (see Figure 10).

Usefulness of the Method for Analyzing Crude Biomass Extracts. The phenyl column method was superior to the PFP method for separating polar taxanes such as baccatin III (VII) and 10-deacetylbaccatin III (X) from other

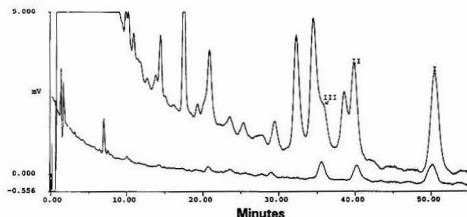


Figure 11. Chromatogram of a crude methanolic extract of *Taxus brevifolia* leaf. Chromatographic conditions: isocratic at 2 mL/min at MeCN/H₂O (35:65). I = taxol; II = 7-epi-10-deacetyltaxol; III = cephalomannine.

polar material occurring in methanol extracts of *Taxus*. Methanolic extracts of *T. brevifolia* bark were found to contain only traces of II and could be analyzed by either the phenyl column method or the PFP column method. On the other hand, some *Taxus* leaf samples had several non-taxane compounds that eluted between I and III, and near II (see also Figure 11). Using the PFP column, these unknown compounds were separated from I, while they interfered with the analysis of I using the phenyl column method. Even after multiple analyses of crude methanolic *Taxus* extracts neither the PFP columns nor the phenyl columns developed high back pressure. Both columns showed long lifetimes when protected with a standard phenyl guard column. Therefore, preliminary cleanup steps appear to be unnecessary when using these columns, and crude methanolic extracts of *Taxus* can be analyzed directly.

ACKNOWLEDGMENT

We thank Thomas H. Warden for suggesting that we try using the PFP column for analyzing *Taxus* extracts. We thank the National Cancer Institute (NCI) taxane standards; Bernard J. Floor of Bristol-Myers Squibb Co., Pharmaceutical Research and Development Division, Syracuse, NY, for his contribution toward developing conditions for the chromatographic purity test; Jeff T. Beckvermit of Hauser Chemical Research for obtaining crystalline 7-epi-10-deacetyltaxol; and Chris Rithner of Colorado State University for running the 300-MHz NMR spectra.

RECEIVED for review February 18, 1992. Accepted June 24, 1992.

Molecular Transformation in Hydrotreating Processes Studied by On-Line Liquid Chromatography/Mass Spectrometry

Kuangnan Qian[†] and Chang S. Hsu^{*}

Exxon Research and Engineering Company, Route 22 East, Clinton Township, Annandale, New Jersey 08801

On-line liquid chromatography/mass spectrometry (LC/MS), in combination with low-voltage electron-impact ionization (LVEI)/medium-resolution mass spectrometry (MRMS, resolution $\sim 10\,000$) and advanced data analysis procedures, provides us with an opportunity for in-depth molecular level characterization of high-boiling petroleum or synthetic fuel fractions. This combined technique has been applied to the studies of molecular transformation of a petroleum hydrotreating process on different levels: overall changes of hydrocarbons and heteroatom-containing hydrocarbons, compositional changes in terms of compound series, and changes in carbon number distribution within individual compound series. The usefulness of LC/LVEI/MRMS for unraveling some of the complex chemistry associated with heavy hydrocarbon processes has been demonstrated.

INTRODUCTION

Many technical challenges are present in the characterization of high-boiling petroleum fractions due to the complexity of these fractions and limitations in analytical technology.¹ Recent endeavors in combining liquid chromatography and mass spectrometry (LC/MS) enable us to address important science issues and obtain previously unattainable results in petroleum fractions boiling between 650 and 1050 °F. Using a moving-belt interface and low-voltage electron-impact ionization (LVEI) medium-resolution mass spectrometry, on-line LC/MS takes advantage of the unique characteristics associated with LC and MS to differentiate between aromatics and naphthoenaromatics (hydroaromatics) and between aromatic hydrocarbons and hard-to-resolve sulfur compounds. The combination of LC and MS reduces the resolution requirement for accurate mass measurements of aromatic and sulfur compounds.²

To effectively process enormous amounts of high-resolution mass spectral data obtained from on-line LC/MS, we developed an innovative data analysis procedure including the use of the Kendrick mass scale ($CH_2 = 14.000\,000$), indigenous mass calibrants, and nominal mass series groupings for the determination of compound type distributions at each LC/MS scan. Higher speed and accuracy than can be obtained by conventional methods are achieved by presorting, grouping, and using statistically averaged mass defects for the determination of the elemental composition of each compound class. Thus, the elution characteristics of individual compound classes within each LC peak can be delineated.³

In this paper, we report our studies of molecular transformation occurring in an important petroleum refining process, hydrotreating, using on-line LC/MS operated at LVEI medium-resolution MS mode. As discussed later, hydrotreating greatly alters the molecular composition of the hydrotreated product from its precursor. Our results suggest several reaction pathways taking place in the hydrotreating process. The study demonstrates the roles of on-line LC/MS in the molecular-level understanding of complex chemistry associated with heavy petroleum processes.

EXPERIMENTAL SECTION

A thermally cracked petroleum distillate (8.5% 430–650 °F and 91.5% 650–1050 °F) was hydrotreated at mild conditions to yield a product containing 1.5% naphtha (430 °F), 14.5% 430–650 °C, and 91.6% 650–1050 °F fractions. The 650–1050 °F fractions of the distillate before (containing 2.77 wt % of sulfur and 0.45 wt % of nitrogen) and after (containing 0.34 wt % of sulfur and 0.23 wt % of nitrogen) hydrotreating were subjected to combined LC/MS analysis with instrumental conditions described in our previous paper.² In brief, each sample was separated by high-performance liquid chromatography (HPLC) into elution regions of saturates, monoaromatics, diaromatics, triaromatics, tetraaromatics, and polars. An Applied Chromatography Model 750/14 evaporative mass detector (EMD) was used to determine the weight percent of all components in each LC region.⁴ The EMD outputs of the distillates before and after hydrotreating are shown in Figure 1. In the LC/MS experiments, the LC eluents were continuously transported into the ion source of a VG-70 VSE double-focusing mass spectrometer by a moving-belt interface. Low-energy electron-impact ionization was used to selectively ionize aromatic hydrocarbons with minimal fragmentation for obtaining the distribution of molecular ions. The resolution of the mass spectrometer was set at 10 000 (medium resolution).

RESULTS AND DISCUSSION

The 650–1050 °F fractions of the thermally cracked distillate before and after hydrotreating were characterized using a moving belt LC/MS. The moving-belt interface is particularly suitable for analysis of 650–1050 °F fractions because the low-boiling fractions are evaporated along with the solvent during sample transport by the belt and high-boiling fractions cannot be completely evaporated by a nose heater located inside the ion source of the mass spectrometer. For fractions with boiling points greater than 1000 °F a different type of LC/MS interface, such as particle beam or thermospray, would be needed to evaporate high-boiling components.

Table I compares the overall compound distributions of the distillates before and after hydrotreating, determined by low-voltage electron-impact ionization mass spectrometry (LVEIMS) and an evaporative mass detector (EMD), in each LC elution regions. The LVEIMS values of aromatics and

[†] Present Address: W. R. Grace & Co.-Conn, Washington Research Center, 7379 Route 32, Columbia, MD 21044.

(1) Boduszynski, M. M. *Energy Fuels* 1988, 2, 597–612.

(2) Hsu, C. S.; McLean, M. A.; Qian, K.; Aczel, T.; Blum, S. C.; Olmstead, W. N.; Kaplan, L. H.; Robbins, W. K.; Schulz, W. W. *Energy Fuels* 1991, 5, 395–398.

(3) (a) Qian, K.; Chen, Y. C.; Hsu, C. S. *Proceedings of the 39th ASMS Conference on Mass Spectrometry and Allied Topics*, Nashville, TN, May 19–24, 1991; pp 1115–1116. (b) Hsu, C. S.; Qian, K.; Chen, Y. C. *Anal. Chim. Acta* 1992, 264, 79–89.

(4) VanderMeeren, P.; Vanderdeelen, J.; Baret, L. *Anal. Chem.* 1992, 64, 1056–1062 and references cited therein.

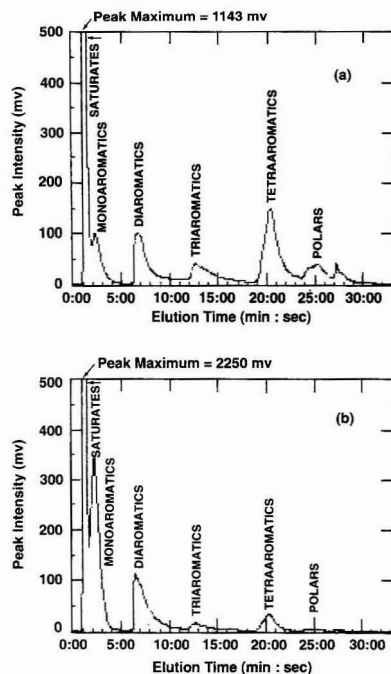


Figure 1. HPLC EMD chromatograms of 650–1050 °F distillates (a) before and (b) after hydrotreating.

Table I. Comparison of Compound Distributions Determined by Low-Voltage Electron-Impact Ionization Mass Spectrometry with Evaporative Mass Detector^a

LC elution region	before hydrotreating		after hydrotreating	
	EMD	LVEIMS	EMD	LVEIMS
saturates	24.2	(24.2)	36.7	(36.7)
monoaromatics	13.5	12.4	21.9	18.6
diaromatics	13.2	11.5	14.9	15.7
triaromatics	14.8	12.7	11.9	10.0
tetraaromatics	19.4	23.1	9.9	12.3
polars	14.9	16.1	4.7	6.7
total	100.0	100.0	100.0	100.0

^a Note: The LVEIMS values are normalized to the total of aromatics and polars determined by EMD. The percentage values from EMD are weight percent, while those from LVEIMS are percent of total ionization.

polars shown in the table are normalized to the total of aromatics and polars (excluding saturates) as determined by EMD. The percentage values from EMD are weight percents, while those from LVEIMS are percents of total ionization. The sensitivity of each individual component determined by LVEIMS is dependent on its isomeric structure and molecular weight.⁵⁻¹⁰ However, sensitivity measurement of the heavy compounds boiling in the range of 650–1050 °F (mainly

aromatic hydrocarbons and thiophenes) is difficult because very few of the compounds needed for the measurement, especially those which are alkyl substituted and naphthenoaromatic, are available commercially. It is not unreasonable to assume that sensitivities among heavy hydrocarbon isomers are averaged out and almost equal among various compound series (molecular types),¹⁰ thus the percent of ionization can be regarded as weight percent. Table I shows a fairly good agreement in compound distributions determined by LVEIMS and EMD. The LVEIMS values are slightly lower than those of EMD for smaller aromatic cores and higher for more condensed aromatic compounds which have relatively higher ionization cross sections than less condensed aromatic compounds.

Table I also illustrates that upon hydrotreating there was a dramatic increase in monoaromatics accompanied by decreases in tetraaromatics and polars. Some increase in diaromatics and decrease in triaromatics are also observed. The table only represents gross changes in compound distribution observed in the LC separation and does not provide any insight into compositional changes in corresponding LC peaks. As discussed later, a detailed LC/MS analysis revealed upon hydrotreating an increase in naphthenoaromatics and a decrease in heteroatom-containing compounds occur in all of the LC elution regions. The observation of gross changes by LC alone does not unravel the complex chemistry occurring in the hydrotreating process.

Figure 2 exhibits mass spectra integrated over the LC peaks corresponding to monoaromatics, diaromatics, triaromatics, tetraaromatics, and polars (including 4+ ring aromatics) of the distillate before hydrotreating, while Figure 3 shows those after hydrotreating. A general feature of these two figures is that the more polar (or aromatic) the LC region, the lower the average molecular weight. However, direct comparison between the mass spectra of the corresponding LC elution regions before and after hydrotreating is difficult because the hydrotreating process converts compounds in one LC region with their products appearing in another LC region. For example, dibenzothiophenes appear in the triaromatic region before hydrotreating. Their products, biphenyls, are present in the diaromatic region after hydrotreating. It is therefore necessary to analyze these spectra in more detail in order to realize how the molecules transform during the process.

Figures 2 and 3 also show complexity of the spectra. When operated at a medium/high-resolution mode, multiple peaks appear at each nominal mass, resulting in hundreds of mass peaks at each LC/MS scan. To process these enormous amounts of data, we have developed an effective data processing procedure to sort out and group the components in each compound series according to their nominal mass series and Kendrick mass defects and then used the averaged mass defect of the group for the identification of compound series. Thus, this procedure provides a rapid and convenient means of scan-to-scan qualitative and quantitative analysis for the determination of compound series distributions. The elution characteristics of each compound class appearing in the LC peaks can then be delineated.³

We used the new procedure outlined above to analyze the mass peaks appearing in Figures 2 and 3 to obtain the distributions of major compound series in the distillate before and after hydrotreating, as illustrated in Figures 4–13. Figures 4–8 exhibit the hydrocarbon series present in the monoaromatic, diaromatic, triaromatic, tetraaromatic, and polar regions of the LC chromatograms, respectively, and Figures 9–13 show the monosulfur compound series present in each of these LC elution regions.

- (5) Lumpkin, H. E. *Anal. Chem.* 1958, 30, 321–325.
- (6) Crabbe, G. F.; Kearns, G. L.; Norris, M. S. *Anal. Chem.* 1960, 32, 13–17.
- (7) Lumpkin, H. E.; Aczel, T. *Anal. Chem.* 1964, 36, 181–184.
- (8) Schulz, J. L.; Sharkey, A. G., Jr.; Brown, R. A. *Anal. Chem.* 1972, 44, 1486–1487.
- (9) Schiller, J. E. *Anal. Chem.* 1977, 49, 1260–1262.
- (10) Severin, D.; Deymann, H.; Glinzer, O. *Anal. Chem.* 1982, 54, 824–825.

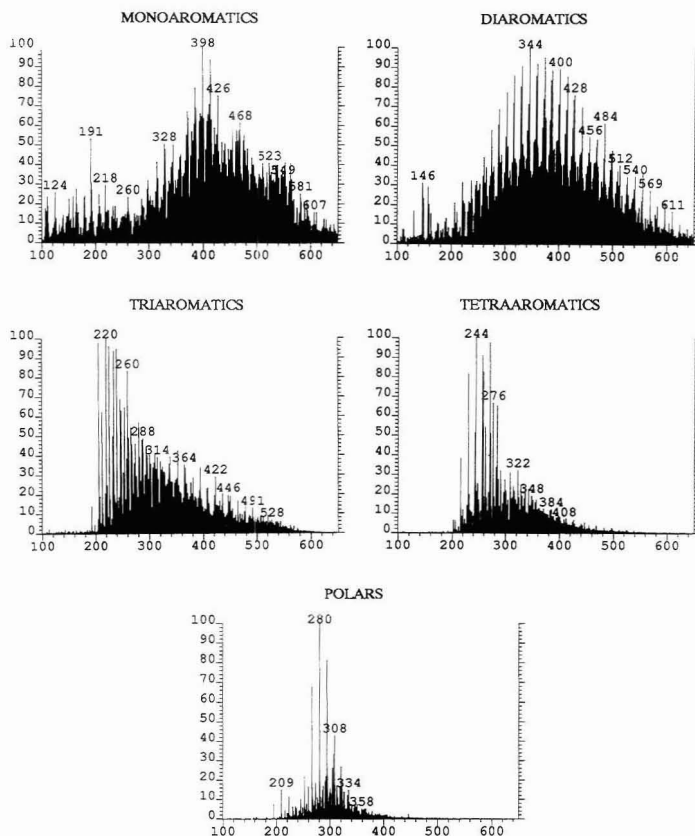


Figure 2. Mass spectra of monoaromatics, diaromatics, triaromatics, tetraaromatics, and polars before hydrotreating.

Scheme I



Let us examine Figure 4 which represents the distribution of compound series in the monoaromatic region before and after hydrotreating. The numbers shown in the abscissa are the z numbers, as in $\text{C}_n\text{H}_{(2n+z)}\text{X}$ where X stands for the heteroatoms (S, N, O, S₂, SO, etc.) in the molecules. In Figure 4, the $z = -6$ series are benzenes. There is a difference between "compound series" and "compound class". A compound series can contain several compound classes. For example the $z = -12$ and -18 series in the monoaromatic region are not naphthalenes, and phenanthrenes; they are actually trinaphthenobenzenes and hexanaphthenobenzenes with typical structures shown in the figure. At this point, we would like to introduce a new nomenclature system for aromatics and naphthenes. The trinaphthenobenzenes contain four rings with only one of them being aromatic; they are denoted as 4R1A. Similarly, hexanaphthenobenzenes, naphthalenes, and perhydrochrysenes are denoted as 7R1A, 2R2A, and 4R0A, respectively. Therefore, the $z = -18$ series in the monoaromatic, diaromatic, and triaromatic regions are 7R1A, 5R2A, and 3R3A, respectively. This coded system would be con-

venient in describing molecular types present in mixtures containing large numbers of hydroaromatics.

In the monoaromatic region, the compound series on the right of the $z = -6$ series are hydroaromatic compounds. Similarly, the compound series on the right of the $z = -12, -18, -22/-24, \dots$ series in the diaromatic, triaromatic, tetraaromatic, \dots regions are hydroaromatics as well. Although there are no clear cuts in many cases, the suggested boundaries between aromatics and hydroaromatics are indicated in Figures 4-13.

For hydrocarbons as shown in Figures 4-8, compound type distributions change dramatically in the monoaromatic, diaromatic, and triaromatic regions, smaller changes are found in the tetraaromatic and polar regions. Before hydrotreating, the most abundant compound series in the monoaromatic, diaromatic, and triaromatic regions are $\text{C}_n\text{H}_{2n-6}$ (benzenes, 1R1A), $\text{C}_n\text{H}_{2n-16}$ (acenaphthenes, dinaphthenonaphthalenes, or vinylbiphenyls; 2R2A), and $\text{C}_n\text{H}_{2n-18}$ (phenanthrenes, 3R3A), respectively. After hydrotreating, the most abundant series in these regions are $\text{C}_n\text{H}_{2n-14}$ (tetranaph-

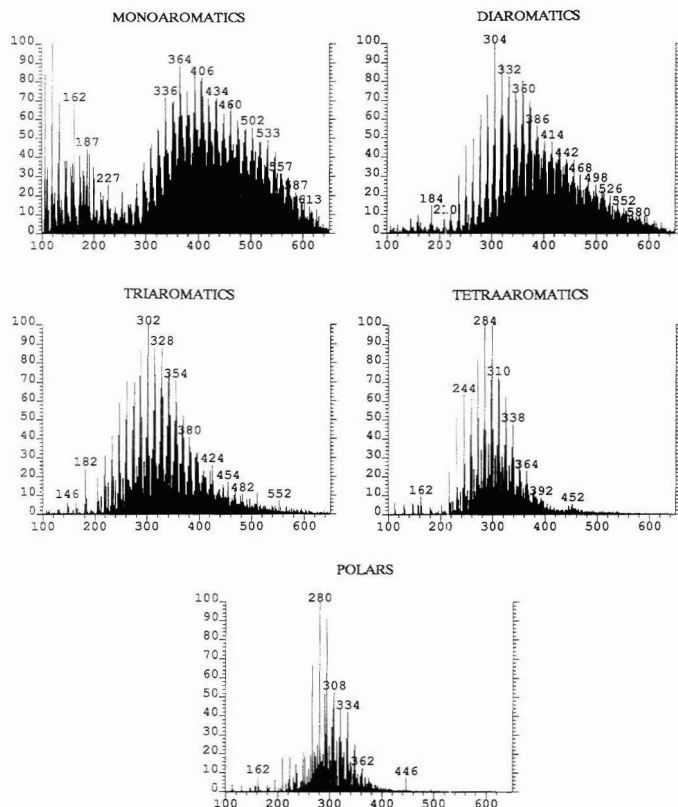
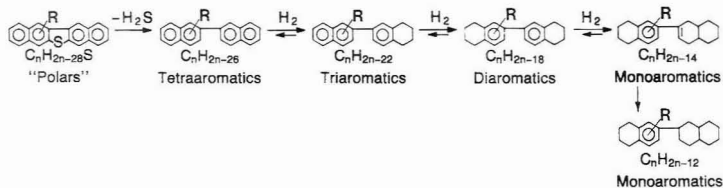


Figure 3. Mass spectra of monoaromatics, diaromatics, triaromatics, tetraaromatics, and polars after hydrotreating.

Scheme II



thenobenzenes, 5R1A), C_nH_{2n-18} (trinaphthenonaphthalenes, 5R2A), and C_nH_{2n-22} (dinaphthenophenanthrenes, 5R3A). These series may contain molecular types representing various degrees of benzopyrene (C_nH_{2n-28}) hydrogenation, shown in Scheme I. Another possible molecular type represented by these series is derived from the hydrogenolysis of dinaphthalenothiophenes and their isomers ($C_nH_{2n-28}S$), shown in Scheme II. Evidently, these simplified schemes do not account for all of the complicated reaction pathways responsible for the molecular transformation in the hydrotreating process. The total decrease in highly condensed aromatic hydrocarbons and thiophenes is less than the total increase in naphthenoaromatics. Some of naphthenoaromatics are possibly formed from cyclization of side chain of alkyl aromatics,^{11,12} which can be further hydrogenated to form naphthenoaromatics with larger numbers of naphthenic rings.

With LC/MS, aromatic hydrocarbons and thiophenes with different aromatic ring numbers can be differentiated via the LC ring type¹² separation. However, some ambiguities still exist for resolving overlapping aromatic hydrocarbons from thiophenes that elute in the same LC region.² The mass differences between the difficult-to-resolve compound series are typically 3.4 millimass units.^{3,13} It would require a mass resolution of over 100 000 to resolve them for compounds in the boiling ranges beyond 650 °F (molecular weights >340). For samples containing rather high concentrations of sulfur compounds, such as the distillate before hydrotreating, the identification of sulfur compounds can be corroborated by

(11) Sullivan, R. F.; Egan, C. J.; Longlois, G. E. *J. Catal.* 1964, 3, 183-195.

(12) Sullivan, R. F.; Boduszynski, M. M.; Fetzer, J. C. *Energy Fuels* 1989, 3, 603-612.

(13) Lumpkin, H. E.; Aczel, T. *ACS Symp. Ser.* 1978, 70, 261-273.

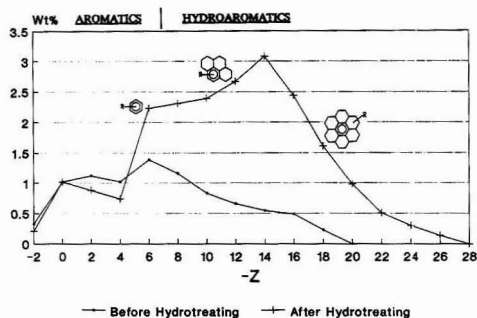


Figure 4. Distributions of hydrocarbon series in the monoaromatic regions before and after hydrotreating.

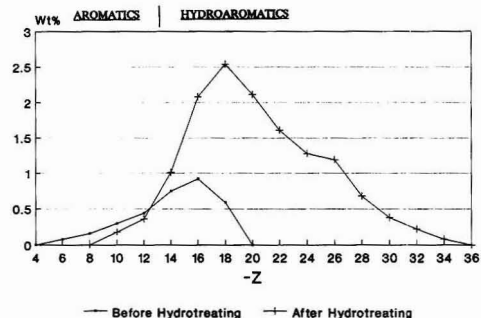


Figure 5. Distributions of hydrocarbon series in the diaromatic regions before and after hydrotreating.

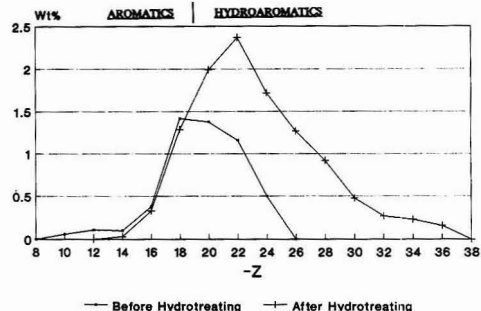


Figure 6. Distributions of hydrocarbon series in the triaromatic regions before and after hydrotreating.

the use of ^{34}S -containing peaks that are 2 mass units higher than the corresponding compounds of interest.¹⁴ However, for samples containing sulfur compounds in low concentrations, such as hydrotreated distillates, the overlapping compounds can only be resolved by using a high-resolution mass spectrometer with resolving power greater than 100 000 because of the difficulties of detecting insignificant amounts of ^{34}S -containing peaks. Therefore, at 10 000 resolution it is necessary to split the overlapping hydrocarbon and sulfur compound series in the hydrotreated distillate based on the sulfur value determined by elemental analysis.

For the monosulfur compound series shown in Figures 9–13, the major series before hydrotreating are in the diaromatic, triaromatic, and tetraaromatic regions, with the most

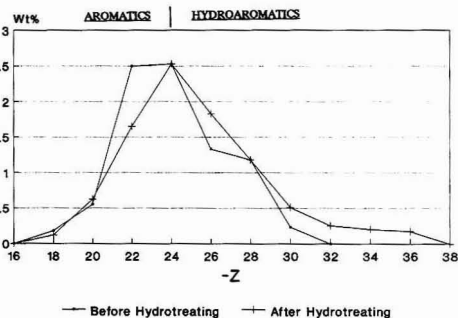


Figure 7. Distributions of hydrocarbon series in the tetraaromatic regions before and after hydrotreating.

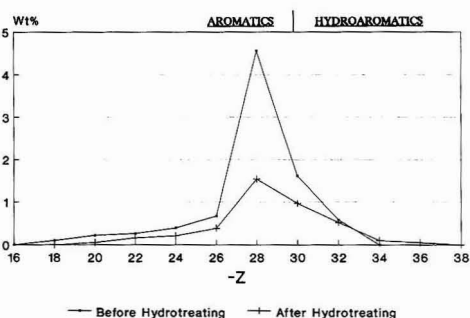


Figure 8. Distributions of hydrocarbon series in the polar regions before and after hydrotreating.

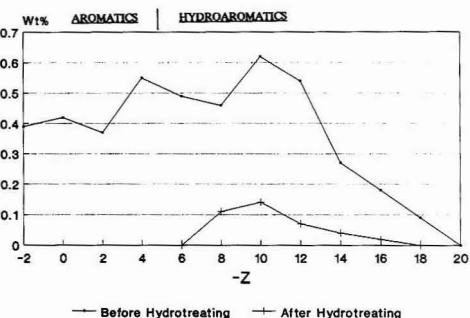


Figure 9. Distributions of sulfur compound series in the monoaromatic regions before and after hydrotreating.

abundant series in each region to be $\text{C}_{18}\text{H}_{22-10}\text{S}$ (benzothiophenes, 2R2A), $\text{C}_{18}\text{H}_{22-16}\text{S}$ (dibenzothiophenes, 3R3A), and $\text{C}_{18}\text{H}_{22-22}\text{S}$ (benzonaphthalenothiophenes, 4R4A), respectively. Upon hydrotreating, all of the monosulfur series are reduced in significant amounts. Thiophenes are more effectively removed than naphthenothiophenes. For example, the $\text{C}_{18}\text{H}_{22-16}\text{S}$ series (dibenzothiophenes) is reduced in a larger extent than the $\text{C}_{18}\text{H}_{22-18}\text{S}$ (naphthenodibenzothiophenes, 4R3A) and $\text{C}_{18}\text{H}_{22-20}\text{S}$ (dinaphthenodibenzothiophenes, 5R3A) series.

The carbon number distribution of each compound series can also be studied in great detail. Figures 14 and 15 show the carbon number distribution for the $\text{C}_{18}\text{H}_{22-18}$ (phenanthrenes) and $\text{C}_{18}\text{H}_{22-16}\text{S}$ (dibenzothiophenes) in the triaromatic region. The distribution of phenanthrenes maximizes at C_{17} and C_{18} (C_3 - and C_4 -substituted) before hydrotreating,

(14) Johnson, B. H.; Aczel, T. *Anal. Chem.* 1967, 39, 682–685.

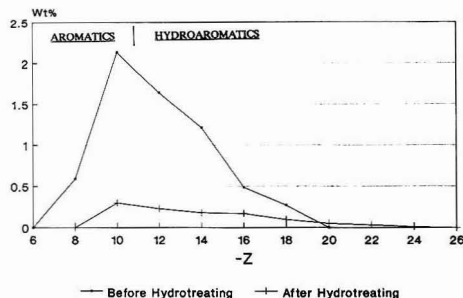


Figure 10. Distributions of sulfur compound series in the diaromatic regions before and after hydrotreating.

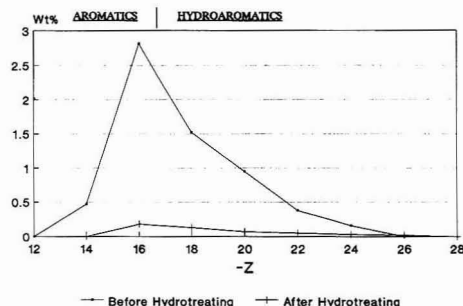
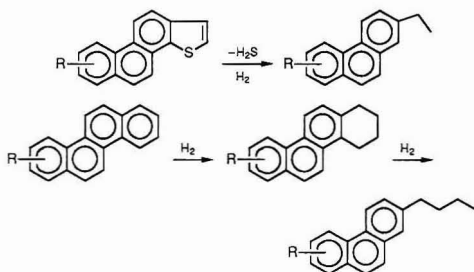


Figure 11. Distributions of sulfur compound series in the triaromatic regions before and after hydrotreating.

but at C_{20} and C_{21} (C_6 - and C_7 -substituted) after hydrotreating. This indicates that the least-substituted and shortest side chain phenanthrenes are most effectively converted into hydrophenanthrenes. The additional C_{20} and C_{21} phenanthrenes after hydrotreating come from many different sources, such as hydrogenolysis of phenanthrenethiophenes and hydrogenation of aromatics followed by ring opening:



In the $C_nH_{2n-16}S$ series, more effective removal of dibenzothiophenes occurs among lower members of the series that have low alkyl substituents. The less effective removal of dibenzothiophenes with higher carbon numbers is possibly due to the presence of more isomers with steric hindrance around the sulfur center. The sterically hindered thiophenes are known to be refractory to hydrodesulfurization and referred to as "hard" sulfur compounds. In both C_nH_{2n-18} and $C_nH_{2n-16}S$ series, there is no evidence of hydrocracking from the carbon number distributions observed before and after the hydroprocessing. In fact, the average carbon number is shifted to a higher rather than a lower value after hydro-

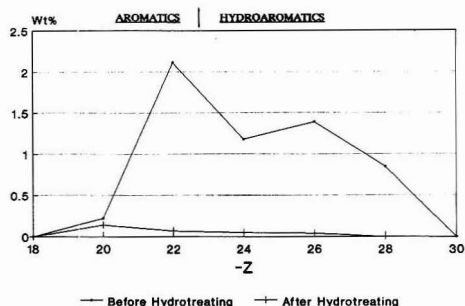


Figure 12. Distributions of sulfur compound series in the tetraaromatic regions before and after hydrotreating.

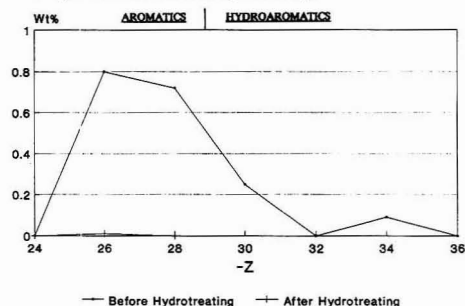


Figure 13. Distributions of sulfur compounds series in the polar regions before and after hydrotreating.

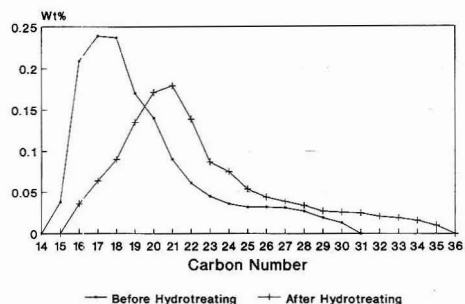


Figure 14. Carbon number distributions of the C_nH_{2n-18} (phenanthrenes) series in the triaromatic region before and after hydrotreating.

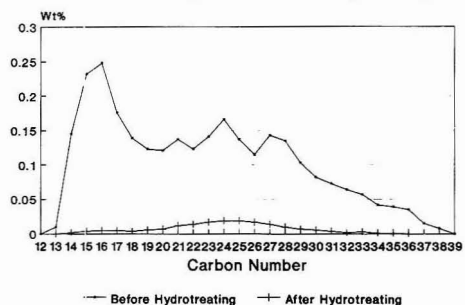


Figure 15. Carbon number distributions of the $C_nH_{2n-16}S$ (dibenzothiophenes) series in the triaromatic region before and after hydrotreating.

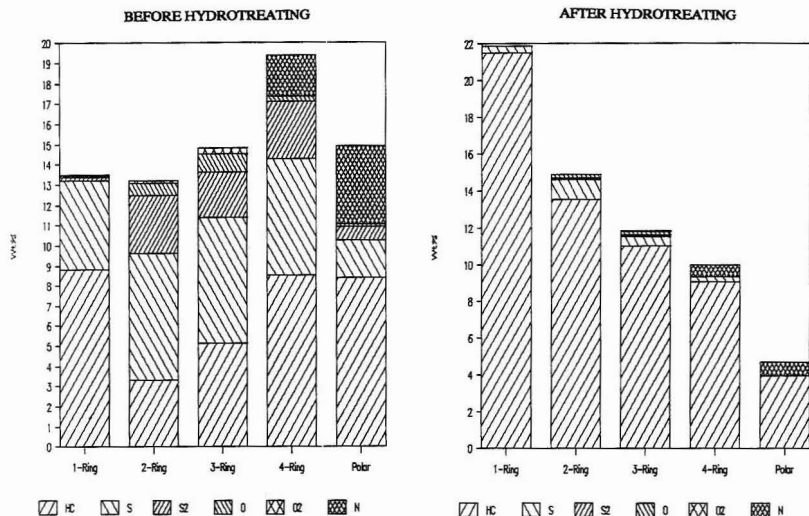


Figure 16. Overall compound type distributions of the distillate in each LC aromatic ring regions before and after hydrotreating.

treating. This is reasonable considering the short side chain nature of thermally cracked distillates and mild hydrotreating conditions used. On the other hand, hydrocracking is an important refining process for residuum-derived vacuum gas oils (VGO's) that are rich in aromatic compounds with long alkyl substituents.¹³

The overall compositional changes in the LC aromatic ring regions of the distillate before and after hydrotreating can be summarized in Figure 16. The relative abundances of different compound types are normalized to the largest LC peaks (in peak area) found in each sample. Six compounds types, i.e., hydrocarbons, monosulfur, disulfur, monooxygen, dioxxygen, and mononitrogen, are identified in the thermally cracked petroleum distillate. As intended, the hydrotreating substantially reduces the amounts of monosulfur compounds in all LC regions, accompanied by a large increase in the amounts of hydroaromatic hydrocarbons. The other heterocompounds in the feed are more narrowly distributed with oxygen compounds mostly in the diaromatic and triaromatic regions and nitrogen compounds abundant in the tetraaromatic and polar regions. Further studies showed that the nitrogen compounds are mainly 5-membered nitrogen heterocyclics (pyrrolic nitrogen compounds, such as carbazoles) and 6-membered nitrogen heterocyclics (basic nitrogen compounds, such as quinolines) with the z -distributions ranging from $-15N$ to $-27N$. Upon hydrotreating, most of the hydroaromatic hydrocarbons formed are in the monoaromatic and diaromatic regions. Disulfur and oxygenated compounds are almost completely removed, while certain amounts of monosulfur and nitrogen compounds survive from hydrotreating. Disulfur compounds appear to contain external thiophene rings which are less sterically hindered and more susceptible to hydrogenolysis than monosulfur compounds. Partial conversion of disulfur compounds could account for some of the monosulfur compounds remaining after hydrotreating.

CONCLUSION

On-line LC/MS in combination with low-voltage EI/medium-resolutions MS provides us with an unprecedented opportunity for the in-depth molecular level characterization of high-boiling petroleum or synthetic fuel fractions without the need of using high-resolution mass spectrometry. With an advanced data analysis procedure to process medium/high-resolution data, the compositional changes within each LC peak can be studied in great detail. This combined technique has been applied to study molecular transformation of a hydrotreating process on different levels: (1) overall changes of hydrocarbons and heterocompounds, (2) compositional changes in terms of compound series, and (3) changes in carbon number distribution of individual compound series. The combination of LC and MS enhances either technique to obtain previously unattainable results in the characterization of heavy hydroaromatics and heteroaromatics, thus demonstrating the value of on-line LC/MS for detailed molecular transformation studies to unravel complex chemistry associated with heavy hydrocarbons refining processes.

ACKNOWLEDGMENT

We would like to acknowledge Saul Blum for his valuable discussions of the work, Win Robbins and Larry Kaplan for their assistance in establishing the liquid chromatographic system, Bill Olmstead, Ed Ellis, and Marty Poole for providing thermally cracked distillates, Y. Charles Chen for his assistance in computer programming, and Marilyn Brownawell for her comments during the preparation of the manuscript. This paper is dedicated to the memory of Thomas Aczel.

RECEIVED for review March 3, 1992. Accepted June 26, 1992.

Cloud Point Preconcentration and High-Performance Liquid Chromatographic Analysis with Electrochemical Detection

Carmelo García Pinto, José Luis Pérez Pavón, and Bernardo Moreno Cordero*

Departamento de Química Analítica, Nutrición y Bromatología, Facultad de Química, Universidad de Salamanca, 37008 Salamanca, Spain

One of the major disadvantages of cloud point preconcentration prior to HPLC analysis is the high absorbance background due to the surfactant that, in many cases, despite the optimum performance of the separation step, makes this methodology useless when optical detection is used. In this paper electrochemical detection is proposed for the first time to overcome this problem due to the electrochemical inactivity of commercially available surfactants as Triton X-114. Vitamins A and E and the pesticide parathion have been used in order to test the suitability of electrochemical detection after the cloud point preconcentration-chromatographic analysis of important biological and environmental compounds.

INTRODUCTION

Organized molecular assemblies (aqueous and reversed micelles, microemulsions, vesicles, bilayers, etc.) have been used in practically all fields of analytical chemistry in order to improve existing methods and to develop new analytical procedures.¹⁻⁶ During the last 10 years many separation processes mediated by organized media have been developed;⁷⁻⁹ in particular, applications including high-performance liquid chromatography, extraction, gel filtration, ultracentrifugation, and electrokinetic capillary chromatography have opened new possibilities for the separation of molecules in certain research areas such as analytical biotechnology, public health, or the study of environmental pollutants.

The use of ordered media in separation processes also allows the direct injection of untreated biological fluids (plasma, urine, or saliva) or waste water samples in any hydrodynamic analytical system (i.e. HPLC or flow injection analysis) which, in turn, will facilitate sample preparation and reduce the analysis time.

In addition, in several instances, the use of appropriate surfactants allows for the improvement of the analytical signal in chromatographic detection.^{8,10}

It is well-known that aqueous micellar solutions of nonionic surfactants such as *n*-alkylsulfinyl alcohols, alkyl methyl sulfone dimines, dimethylalkylphosphine oxides and alkyl (or aryl) poly(oxyethylene) ethers are capable of undergoing

a phase separation (i.e. temperature changes) known as the cloud point phenomenon;¹¹⁻¹⁵ that is, when the aqueous solution of surfactant is heated above a critical temperature the solution suddenly becomes turbid (cloud point) due to the diminished solubility of the surfactant in water. At higher temperatures than the cloud point and after some time interval (centrifugation can speed up this step) the solution separates into two transparent liquid phases: a surfactant-rich phase and an aqueous solution in equilibrium with a surfactant concentration close to the cmc (critical micelle concentration). This surfactant-rich phase can be used for the preconcentration of some analytes prior to gas or liquid chromatographic analysis with the obvious benefits (safety, cost, compatibility with micellar and hydroorganic mobile phases, etc.).

The cloud point methodology has been used in different applications: Watanabe et al.¹⁶⁻¹⁹ have reported the use of poly(oxyethylene) nonylphenyl ether (PONPE 7.5) as a nonionic surfactant for the preconcentration of several metal ions after converting them into sparingly water-soluble chelates. Bordier²⁰ has described the separation of peripheral membrane proteins using Triton X-114. Hinze et al.²¹ have reported the preconcentration of polynuclear aromatic hydrocarbons, and Pramauro²² has studied the separation of different chloroaromatic pollutants from aqueous solutions using equal amounts of poly(oxyethylene) (4.5) dodecyl ether and poly(oxyethylene) (8) dodecyl ether.

When cloud point extraction prior to HPLC analysis is used, two important disadvantages arise: a high background absorbance at UV detection (no optical transparency) and the lengthy operating time (up to several hours) required for total elution of the surfactant injected. These two drawbacks clearly affect the use of this methodology in chromatographic determinations with optical detection.

When the analytes under study are species of very low polarity, these problems may be overcome owing to the fact that for the elution of such molecules, in analytically reasonable times, mobile phases with a high content in organic

- (1) Hinze, W. L. In *Solution Chemistry of Surfactants*; Mittal, K. L., Ed.; Plenum Press: New York, 1979, pp 79-127.
- (2) Pelizzetti, E.; Pramauro, E. *Anal. Chim. Acta* 1985, 169, 1-29.
- (3) Hinze, W. L.; Sing, H.; Baba, Y.; Harvey, N. G. *Trends Anal. Chem.* 1984, 3, 193-199.
- (4) Moreno Cordero, B.; Pérez Pavón, J. L.; Hernández Méndez, J. *Quim. Anal.* 1989, 8, 231-240.
- (5) Moreno Cordero, B.; Pérez Pavón, J. L.; Hernández Méndez, J. *Anal. Chim. Acta* 1990, 234, 239-245.
- (6) McIntire, G. L. *Crit. Rev. Anal. Chem.* 1990, 4, 257-274.
- (7) Armstrong, D. W. *Sep. Purif. Methods* 1985, 14, 213-304.
- (8) Hinze, W. L. *Ann. Chim.* 1987, 77, 167-207.
- (9) Hinze, W. L. In *Ordered Media in Chemical Separations*; Hinze, W. L., Armstrong, D. W., Eds.; ACS Symposium Series 342; American Chemical Society: Washington, DC, 1987.
- (10) Xia, F. Cassidy, R. M. *Anal. Chem.* 1991, 63, 2883-2887.

- (11) Kjellander, R. *J. Chem. Soc. Faraday Trans.* 1982, 2, 78-81.
- (12) Corti, M.; Minero, C.; Degiorgio, V. *J. Phys. Chem.* 1984, 88, 309.
- (13) Degiorgio, V.; Piazza, R.; Corti, M.; Minero, C. *J. Chem. Phys.* 1985, 82, 1025-1031.
- (14) Degiorgio, V. In *Physics of Amphiphilic: Micelles, vesicles, and Microemulsions*; Degiorgio, V., Corti, M., Eds.; North-Holland: Amsterdam, 1985; pp 303-335.
- (15) Goldstein, R. E. *J. Phys. Chem.* 1986, 84, 3367-3378.
- (16) Watanabe, H. In *Solution Behaviour of Surfactants*; Mittal, K. L., Fendler, E. F., Eds.; Plenum Press: New York, 1982; Vol. 2, pp 1305-1313.
- (17) Kwamoris, S.; Watanabe, H.; Haraguchi, K. *Anal. Sci.* 1985, 1, 41-45.
- (18) Watanabe, H.; Tanaka, H. *Talanta* 1978, 25, 585-589.
- (19) Saitoh, T.; Kimura, Y.; Kamidate, T.; Watanabe, H.; Haraguchi, K. *Anal. Sci.* 1989, 5, 577-581.
- (20) Bordier, C. *J. Biol. Chem.* 1981, 256, 1604.
- (21) Hinze, W. L.; Sing, H. N.; Fu, Z. S.; Williams, R. W.; Kippenberger, D. J.; Morris, M. D.; Sadek, F. S. In *Chemical Analysis of Polycyclic Aromatic Compounds*; Vo-Dinh, T., Ed.; John Wiley & Sons: New York, 1989; Chapter 5, pp 155-157.
- (22) Pramauro, E. *Ann. Chim.* 1990, 80, 101-109.

modifier (i.e. >95% methanol) are needed, thus enabling rapid elution of the injected surfactant.

For analytes of intermediate polarity, mobile phases with lower organic content are used and the problems of high absorbance due to the slowly eluted surfactant can be circumvented in two different ways:

(1) By using surfactant species that display the cloud point phenomenon and do not show high absorbance at the customary working wavelengths in HPLC (254–280 nm). Recently Hinze et al.²³ have used this alternative with two synthesized zwitterionic surfactants: 3-(nonyldimethylammonium)propyl sulfate (C_9 APSO₄) and 3-(decyldimethylammonium)propyl sulfate (C_{10} APSO₄). These new surfactants undergo phase separation like nonionic surfactants but do not appreciably absorb in the UV zone of the spectrum, thereby permitting their use in cloud point preconcentration methodology prior to HPLC analysis. Both surfactants have been employed for the preconcentration of several hydrophobic organic compounds (steroidal hormones, vitamin E) and the extraction of the membrane protein bacteriorhodopsin from the hydrophilic cytochrome c protein.

(2) By using detectors that under certain conditions will make the surfactants employed in the surfactant-mediated phase separations transparent. In the present work we propose for the first time the use of electrochemical detection as a simple and cheap alternative for solving the problem of the lack of optical transparency of many nonionic surfactants in cloud point extractions prior to HPLC determination.

This alternative has three clear advantages. Firstly, its applicability is high because of the number of both biologically and environmentally interesting species that can undergo oxidation or reduction processes on an electrode.²⁴ Secondly, electrochemical detection is more sensitive (50–100-fold) and more selective than UV detection; thus, electrochemical detection in HPLC has become a useful method for the determination of analytes in complex samples such as biological fluids, natural products or pharmaceutical products. Thirdly, many commercially available nonionic surfactants that show a cloud point close to room temperature (Triton X-114 or PONPE 7.5), and hence suitable for the separation of molecules of biological interest, do not contain any functional groups subject to electrochemical reactions.

The nonionic surfactant Triton X-114 was chosen owing to its favorable characteristics regarding price, toxicity, and commercial availability; additionally its cloud point (23–26 °C) permits its use in the extraction/preconcentration of a large number of molecules, even though these are thermolabile. In order to prove the suitability of electrochemical detection for cloud point preconcentration prior to HPLC analysis, two types of molecules of different polarity were chosen. As highly hydrophobic molecules, the liposoluble vitamins A and E, which require mobile phases with high methanol or acetonitrile concentrations for elution, were chosen. As an analyte of intermediate polarity, the organophosphorus pesticide parathion was chosen as a representative of molecules of considerable environmental interest. In view of its higher polarity as compared with those of vitamins A and E, for elution this latter molecule requires mobile phases with lower proportions of organic modifier, thus hindering rapid elution of the surfactant injected.

EXPERIMENTAL SECTION

Reagents. The nonionic surfactant Triton X-114 was obtained from Fluka and used without further purification, the pesticide

parathion was purchased from Riedel-de Haen (Seelze-Hannover, Germany), vitamin A was obtained from Sigma, and vitamin E was obtained from Fluka. All other reagents were of analytical grade.

Mobile phases were 99:1 (v/v) mixture of methanol/water (flow rate = 1.0 mL/min) to which 0.1 M LiClO₄ had been added as supporting electrolyte for vitamins and 70:30 (v/v) mixture of methanol/water (flow rate = 1.25 mL/min) to which 0.0025 M acetic acid + sodium acetate has been added as supporting electrolyte for parathion.

All solvents and analytes were filtrated through 0.45-μm nylon membrane filters (Millipore) and ultra-high-quality water obtained from an Elgastat UHQ water purification system was used.

Apparatus. A modular component liquid chromatographic system was used consisting of a Spectra Physics SP 8800 ternary pump, an SP 8450 UV detector, an EG&G PARC 400 electrochemical detector, and an SP 4290 integrator. The electrodes were as follows: Ag/AgCl/0.1 M KCl reference electrode, gold auxiliary electrode, and single glassy carbon electrode MP 1305 and dual glassy carbon electrode MP 1304 for the detection of vitamins and parathion, respectively. The two detectors were connected in series, the electrochemical one being the later. In all experiments, a Rheodine 7125 injection valve, with a 10-μL sample loop and an 224 × 4.6-mm Spheri 5 ODS-224 stationary phase column from Brownlee labs were used.

Procedures. *Cloud Point Determination.* The cloud point for Triton X-114 was determined by observing the appearance of the two phases on heating different previously cooled aqueous solutions of surfactant in a thermostatted bath. Within the concentration range studied (1–5%) the cloud point remained constant at 25 °C. This value is consistent with that reported by other authors.²¹

Ratio of Phases. The volumes of the respective phases were measured in tubes calibrated for different amounts of surfactant under the same experimental conditions as those used for the phase separation (heating at 40 °C and centrifuging at 3500 rpm).

Cloud Point Preconcentration. Aliquots of 15.0 mL of the cold solutions containing the analytes in 1.3% Triton X-114 for the vitamins and in 1.0% Triton X-114 for parathion were kept for 5 min in a thermostatic bath at 40 °C. Separation of the two phases was achieved by centrifugation for 5 min at 3500 rpm. From the surfactant-rich phase, 60 μL was collected in a Hamilton syringe, and 10 μL of this was injected into the chromatographic system.

Electrochemical Detection and Electrode Pretreatment. The detection of vitamins A and E was performed by oxidation on a single glassy carbon electrode at +800 and +1150 mV respectively. This electrode was electrochemically pretreated daily by applying for 10 min a potential of -600 mV followed by 30 min at +1300 mV;²⁵ after that the potential was set at the appropriate working value for the vitamin studied.

The detection of parathion was carried out with a dual glassy carbon electrode in the series configuration (reductive-oxidative mode); the working potentials were $E_1 = -1500$ mV (generating electrode) and $E_2 = +400$ mV, the intensity at E_2 being the analytical signal. The electrodes were electrochemically pretreated as follows:²⁶ E_1 was kept for 10 min at -1500 mV and then 10 min at +1500 mV, and finally it was set at the working potential (-1500 mV); meanwhile E_2 was kept for 10 min at +1000 mV and then 10 min at -1000 mV, and after that another 10 min at +1000 mV, and finally it was set at the measuring potential (+400 mV).

RESULTS AND DISCUSSION

Cloud Point Preconcentration-HPLC of Vitamins A and E. Figure 1 shows the signal obtained with a UV detector at 260 nm and the signals at different applied potentials when 10 μL of a surfactant-rich phase containing only Triton X-114 is injected after cloud point separation. When spectrophotometric detection is employed, the baseline is not recovered

(25) EG&G Princeton Applied Research Model 400 Electrochemical Detector. User's Manual, p 13.

(26) Hernández Méndez, J.; Carabias Martínez, R.; Rodríguez Gonzalo, E.; Garay García, F. Presented at the Symposium on Fungicides, Herbicides and Insecticides, London, 1992.

(23) Saitoh, T.; Hinze, W. L. *Anal. Chem.* 1991, 63, 2526–2525.

(24) Hart, J. P. *Electroanalysis of Biologically Important Compounds*. Ellis Horwood, New York 1990.

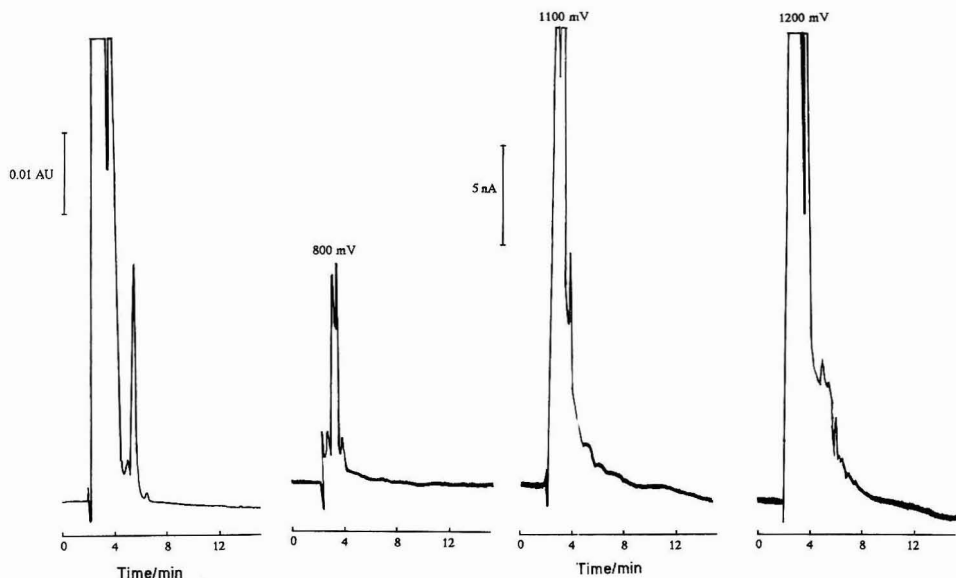


Figure 1. Chromatograms obtained for the injection of a surfactant-rich phase after cloud point separation with UV detection at 260 nm (first on the left) and electrochemical detection (applied potentials on the peaks). Chromatographic conditions as described in the text.

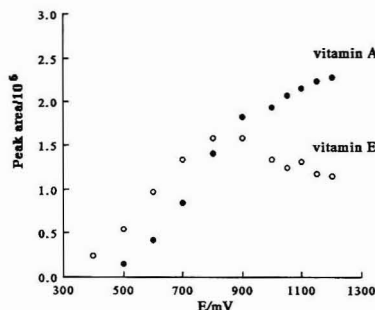


Figure 2. Hydrodynamic voltammograms for vitamins A and E. Chromatographic conditions as described in the text.

until at least 8 min have elapsed. This indicates that analytes with elution times shorter or close to this value would yield chromatograms that would be very difficult to quantify.

Under these experimental elution conditions, the electrochemical signal afforded by Triton X-114 strongly depends on the potential applied owing to the different adsorption capacity shown by the surfactant on the working electrode at different potentials. Thus, for example, when detection was carried out at +800 mV, the baseline needs approximately 4 min to recover, while if detection is performed at +1200 mV, at least 10 min are required for the recovery. The choice of the optimum potential for detection depends on the retention time and hydrodynamic voltammogram of the species chromatographed.

As an example, Figure 2 shows the hydrodynamic voltammograms corresponding to vitamins A and E (whose retention times are close to 4 and 13 min, respectively) when 10 μ L of a solution containing 3.7 ng of vitamin A and 5.8 ng of vitamin E is injected. The results obtained show that both vitamins can be detected in the range of potentials between

+800 and +1200 mV. However, in view of the retention time and the signal provided by Triton X-114 (see Figure 1) a working potential of +800 mV should be chosen for the detection of vitamin A, at which the signal afforded by the surfactant is small and there is no appreciable loss of sensitivity, although its quantification, if necessary, could be carried out at higher potentials.

The chromatograms shown in the upper part of Figure 3 correspond to the injection of 10 μ L of a solution containing 0.37 ppm of vitamin A (3.7 ng injected) by both electrochemical and UV detection. In the lower chromatograms of Figure 3, the signals for the injection of the cloud point preconcentrated solution are shown. As can be seen, electrochemical detection offers much greater sensitivity in addition to a perfectly defined peak while UV detection can be considered absolutely inadequate for the quantification of vitamin A after the preconcentration step. The preconcentration factor P was calculated from the ratio of the signals obtained with the preconcentrated and unconcentrated samples; this value was 20 by both electrochemical and UV detection for vitamin A. The recovery attained in the preconcentration process was calculated by the expression $R = P/PR$, where PR is the volume phase ratio; the obtained value was 67%.

If the molecules under study are eluted at times longer than 10 min, quantification with both UV and the electrochemical technique is adequate, although electrochemical detection is more sensitive. As an example, Figure 4 (upper part) shows the chromatograms obtained for the injection of 10 μ L of a solution containing 0.57 ppm of vitamin E (5.7 ng injected) both with electrochemical and UV detection; the lower part of the figure shows the chromatograms obtained for the injection of the cloud point preconcentrated solution. The potential used (+1150 mV) was higher than that necessary for vitamin E, but it was selected to show that for analytes eluting at these times there is no influence of the surfactant signal even at these high potential values. The increase of sensitivity obtained with electrochemical detection is obvious and for the nonpreconcentrated solution the analyte is not

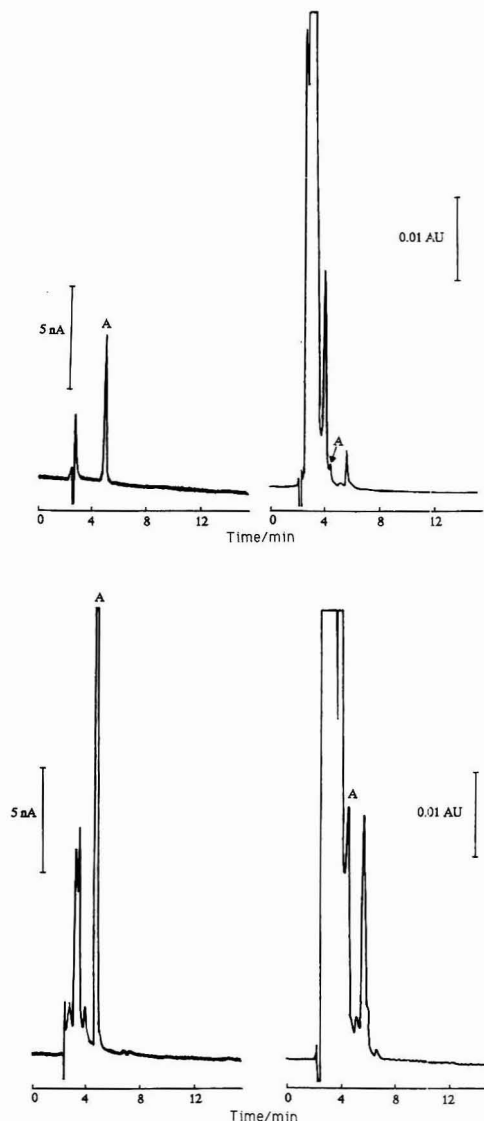


Figure 3. Upper chromatograms: electrochemical (left, $E = +1150$ mV) and UV (right, 260 nm) detection of 0.37 ppm of vitamin A (10 μ L injected). Lower chromatograms: electrochemical (left) and UV (right) detection of the surfactant-rich phase obtained after the cloud point preconcentration of 15 mL of the same solution.

detected. The calculated values for P and R were 30 and 100%, respectively; they are higher than those obtained for vitamin A due to the less hydrophobic character of vitamin A.

It can be concluded that when mobile phases with high organic modifier content are used, both electrochemical and UV detection are suitable after cloud point preconcentration with Triton X-114 for analytes eluted at long times, electrochemical detection being, in general, more sensitive. However, under the same experimental conditions, electrochemical detection permits the detection and quantification

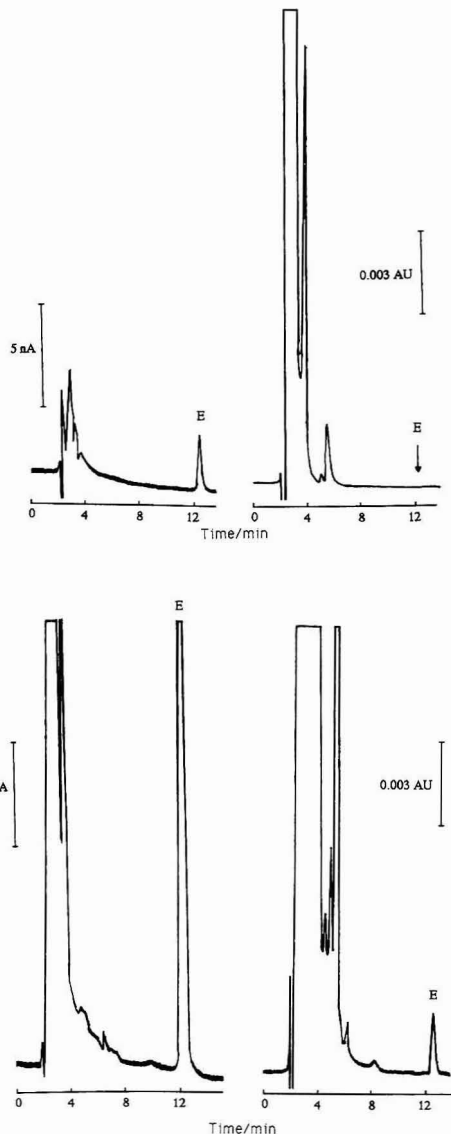


Figure 4. Upper chromatograms: electrochemical (left, $E = +800$ mV) and UV (right, 260 nm) detection of 0.57 ppm of vitamin E (10 μ L injected). Lower chromatograms: electrochemical (left) and UV (right) detection of the surfactant-rich phase obtained after the cloud point preconcentration of 15 mL of the same solution.

of analytes at shorter elution times for which UV detection is not suitable as shown for vitamin A.

Cloud Point Preconcentration-HPLC of Parathion.

When it is desired to determine molecules of intermediate polarity, the amount of organic modifier should be lower than that used when strongly hydrophobic molecules are eluted. Under these experimental conditions, if the surfactant-rich phase is injected, the mobile phase is unable to completely elute the surfactant in a short time. Accordingly, if spectrophotometric detection is used, the surfactant signal can be seen for several hours; this time depends on the relative

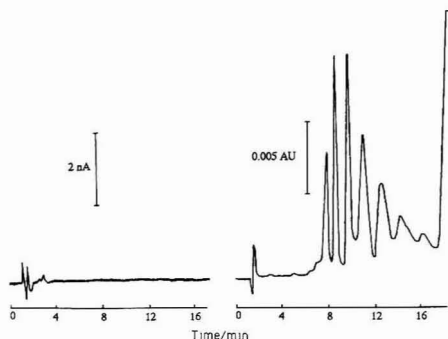


Figure 5. Electrochemical (left, $E_1 = -1500$ mV and $E_2 = +400$ mV) and UV (right, 260 nm) chromatograms obtained for the injection of a surfactant-rich phase of Triton X-114 alone after cloud point separation.

amount of organic modifier in the mobile phase. In most cases, this prevents suitable quantification of the species chromatographed.

The electrochemical behavior of parathion, the species chosen for chromatographic conditions of mobile phase with low organic content, has been previously described.²⁷ It can undergo electrochemical reduction processes, but no oxidation waves are obtained on glassy carbon electrodes. As the oxidative mode is the preferred one for detection in chromatography, a dual glassy carbon electrode was used in which the reduction products generated on the upstream electrode are reoxidized on the downstream electrode. This latter oxidation intensity is the signal being monitored.

Figure 5 shows the comparative chromatograms obtained when 10 μ L of a surfactant-rich phase of Triton X-114 is injected after cloud point separation with UV detection at 260 nm and with the dual glassy carbon electrode. For UV detection, the signal obtained displays three perfectly distinguishable zones; during the first 5 min, no signal of the Triton X-114 is observed because the surfactant, at this composition of mobile phase, is not eluted; this would permit quantification of a species whose retention times are lower than this value. The second zone ranges between 5 and 18 min in which the surfactant affords a set of perfectly reproducible peaks, probably due to the presence of impurities in it, and then a pronounced broad peak is obtained due to the elution of most of the surfactant injected. Detection and quantification of species whose retention times are longer than 6 min is practically impossible with UV detection.

However, under the same experimental conditions but using electrochemical detection, the surfactant does not yield any signal. This electrochemical inactivity allows detection and quantification of species for which UV detection would be impossible. Even though no signal is obtained for Triton X-114, it is obvious that most of the surfactant injected remains in the column and, in order to obtain reproducibility in the chromatographic process, a washing cycle of 5 min with 100% methanol was included at the end of every run (run time 15 min). This time was enough to elute the surfactant injected as proved by following the signal provided by the UV detector; no electrode pretreatment was needed in between runs. The retention time stability, measured as its relative standard deviation for 10 consecutive injections, was 2.7% when no washing cycle was used and 0.5% if the 5-min methanol cycle was included.

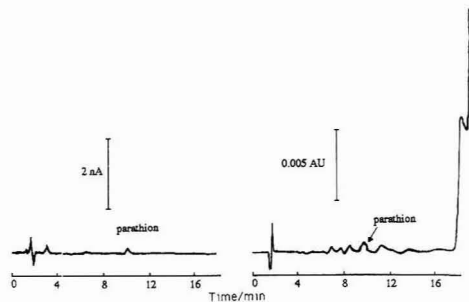


Figure 6. Upper chromatograms: electrochemical (left, $E_1 = -1500$ mV and $E_2 = +400$ mV) and UV (right, 260 nm) detection of 0.50 ppm of parathion (10 μ L injected). Lower chromatograms: electrochemical (left) and UV (right) detection of the surfactant-rich phase obtained after the cloud point preconcentration of 15 mL of the same solution.

Figure 6 (upper part) shows the chromatograms obtained with electrochemical and UV detection when 10 μ L of a solution containing 0.50 ppm of the pesticide parathion in 1% Triton X-114 is injected. The lower chromatograms are obtained following the cloud point preconcentration step after which 10 μ L of the surfactant-rich phase is injected in the chromatographic system. With electrochemical detection the chromatogram is perfectly well defined and it is possible to quantify the pesticide. However, with spectrophotometric detection, quantification of parathion is almost impossible. The calculated values for *P* and *R* were 47 and 94% respectively.

CONCLUSIONS

The main advantage of electrochemical detection after cloud point preconcentration arises from the fact that it allows the use of commercially available surfactants as Triton X-114 owing to its electrochemical transparency, thus making this methodology useful for the determination of important compounds at very low concentration levels.

ACKNOWLEDGMENT

We want to thank Dr. Carabias Martínez and Dr. Delgado Zamarreño for useful information and helpful discussions on the electrochemical detection. C.G.P. acknowledges the financial support by the Spanish Government (PFP). This work was supported by DGICYT (project no. PB91-0185).

High-Resolution Determination of ^{147}Pm in Urine Using Dynamic Ion-Exchange Chromatography

Steve Elchuk, Charles A. Lucy,^{*,†} and Kerry I. Burns

AECL Research, General Chemistry Branch, Chalk River Laboratories, Chalk River, Ontario, Canada K0J 1J0

A procedure has been developed for measuring ^{147}Pm in bioassay samples, based on the separation and preconcentration of ^{147}Pm from the urine matrix by adsorption onto a conventional cation-exchange column with final separation and purification by HPLC using dynamic ion-exchange chromatography. The concentration of ^{147}Pm is determined by collecting the appropriate HPLC fraction and measuring the ^{147}Pm by liquid scintillation counting. The limit of detection is 0.1 Bq (3 fg) ^{147}Pm based on a 500-mL sample of urine and a counting time of 30 min with a background of 100 cpm. Ten samples can be processed in 1.5–2 days.

INTRODUCTION

Within CANDU reactors, ^3H and volatile, long-lived fission products such as ^{137}Cs and $^{90}\text{Sr}/^{90}\text{Y}$ are the radionuclides which are most closely monitored to ensure the health and safety of personnel. However, in the production of separated radionuclides for radiopharmaceutical applications or during the maintenance of reactor components, rare-earth nuclides such as ^{147}Pm and ^{144}Ce can be of concern as well. If ingested or inhaled, only a small fraction of the rare-earth inventory is absorbed, however that portion is translocated to the liver and skeleton where it is retained with a biological half-life of 3500 days.¹ These long biological residence times can lead to significant radiation doses, thus making it necessary to regularly monitor personnel who come in contact with these radionuclides.

Monitoring of personnel for internal exposure can be based on the following approaches: direct in vivo monitoring of the radionuclides, measurement of radionuclides in excreta, or estimation of intake based on a personal air sampler. The choice of measurement approach is dictated by the mode of decay of the radionuclide (i.e., α , β , or γ -ray), its metabolic behavior, and the sensitivity, availability, and convenience of the appropriate measurement facilities.² Direct monitoring of the whole body or specific organs provides a reliable means to measure the retained activity within the body following an intake. "Whole-body scanning" is usually performed using γ spectrometers³ and is the method of choice for γ -emitting radionuclides such as ^{144}Ce and ^{137}Cs .² Whole-body scanning, however, is of little value in assessing retained activity of pure β -emitters such as ^{147}Pm and $^{90}\text{Sr}/^{90}\text{Y}$, except when there is high internal contamination and when the body burden of other radionuclides is very low.^{3–5}

At levels appropriate to routine internal dose monitoring, internal contamination by pure β -emitting radionuclides is

determined by measuring their concentration in urine. The Dosimetric Research Branch at the Chalk River Laboratories (CRL) routinely screens personnel for radiologically significant β contaminants by coprecipitating the radionuclides with calcium oxalate from buffered urine (pH 3.8). The dried precipitate is measured with a low background gas flow proportional counter.⁶ Although this technique is satisfactory for detecting high-energy β emitters such as $^{90}\text{Sr}/^{90}\text{Y}$, it has poor counting efficiencies for low-energy β emitters due to attenuation in the precipitate. Thus while this procedure may be useful as a screening test, it cannot be readily used to identify the contaminant, determine the level of intake, or establish the committed dose equivalent.²

To determine the committed dose equivalent, it is necessary to know the identity and concentration of each radionuclide contributing to the total body burden. Previously, if the screening indicated possible contamination, a solvent extraction procedure based on bis(2-ethylhexyl) phosphoric acid (HDEHP) in *n*-heptane was used to separate ^{90}Sr , ^{90}Y , ^{147}Pm , and ^{144}Ce from urine.⁷ However, a number of difficulties were encountered when this procedure was used to measure ^{147}Pm : formation of precipitate in the liquid scintillation cocktail; poor precision in the results because of variability in the recovery; interference due to the presence of other radionuclides in the ^{147}Pm fraction; long sample preparation times.

In this work, chromatographic procedures have been developed for the determination of rare-earth radionuclides, most notably ^{147}Pm , in urine. Urine is a complex solution containing an array of inorganic salts and organic constituents, and its composition varies considerably depending on the dietary habits of the individual. In this matrix, the concentration of the radionuclides of interest will be at femtogram levels, because of their long biological half-life. Therefore a cation-exchange sample preparation step was used to minimize the interference from the inorganic salts in the urine matrix and to preconcentrate the rare earths. The resultant rare-earth sample was then analyzed by dynamic ion-exchange chromatography. Previous studies have shown that dynamic ion-exchange chromatography, when coupled with postcolumn reaction detection, enables precise and accurate determinations of nanogram amounts of lanthanides in complicated matrices.^{8–10} It has also been used as a rapid and convenient procedure for separation and determination of lanthanides for nuclear fuel burnup measurements^{11,12} and in the separation of actinides prior to their measurement by α spec-

[†] Present address: Department of Chemistry, University of Calgary, 2500 University Drive NW, Calgary, Alberta, Canada T2N 1N4.

(1) ICRP. Limits for Intakes of Radionuclides by Workers. Publication 30; Pergamon Press: Oxford, U.K., 1981.

(2) ICRP. Individual Monitoring for Intakes of Radionuclides by Workers: Design and Interpretation. Publication 54; Pergamon Press, Oxford, U.K., 1988.

(3) IAEA. Directory of Whole-Body Radioactivity Monitors; STI/PUB/213; IAEA: Vienna, 1970.

(4) Johnson, J. R.; Lamothe, E. S.; Kramer, G. H. *Radiat. Prot. Dosim.* 1987, 20, 267–269.

(5) Johnson, J. R. Report AECL-5854; Atomic Energy of Canada Ltd.: Chalk River, Ontario, 1977.

(6) Mawson, C. A.; Fischer, I. Report CRM-455; National Research Council, Research Division: Chalk River, Ontario, 1950.

(7) Kramer, G. H.; Davies, J. M. *Anal. Chem.* 1982, 54, 1428–1431.

(8) Knight, C. H.; Cassidy, R. M.; Recoskie, B. M.; Green, L. W. *Anal. Chem.* 1984, 56, 474–478.

(9) Cassidy, R. M.; Elchuk, S.; Elliot, N. L.; Green, L. W.; Knight, C. H.; Recoskie, B. M. *Anal. Chem.* 1986, 58, 1181–1186.

(10) Barkley, D. J.; Blanchette, M.; Cassidy, R. M.; Elchuk, S. *Anal. Chem.* 1986, 58, 2222–2226.

(11) Elliot, N. L.; Green, L. W.; Recoskie, B. M.; Cassidy, R. M. *Anal. Chem.* 1986, 58, 1178–1181.

rometry.^{12,13} In this work, ¹⁴⁷Pm is separated from other rare-earth elements by dynamic ion-exchange chromatography and determined off-line by liquid scintillation counting of the appropriate HPLC fraction.

EXPERIMENTAL SECTION

HPLC System. The HPLC system consisted of a Spectra Physics pump (Model 8700, Spectra Physics, Santa Clara, CA), a Rheodyne sampling valve (Model 7125, Rheodyne, Berkeley, CA) fitted with a 1.0-mL sample loop, a 150-mm- \times 4.6-mm-i.d. Supelco column packed with 5- μ m C₁₈ reversed-phase particles, a Rheodyne switching valve (Model 7000), a fixed-wavelength (658-nm) detector (Model 441, Waters Associates, Milford, MA), and a Spectra Physics Computing Integrator (SP4100). The eluted metal ions, except for promethium, were measured colorimetrically by a postcolumn reaction with 3,6-bis[(*o*-arsenophenyl)azo]-4,5-dihydroxy-2,7-naphthalenedisulfonic acid (Arsenazo III). The postcolumn reagent was added to the eluate downstream of the fraction collection valve via a screen-tee reactor,¹⁴ using a syringe pump (ISCO M314, Lincoln, NE).

Reagents and Standards. α -Hydroxyisobutyric acid (HIBA) (Aldrich Chemical Co., Milwaukee, WI) was purified by passage through a 3- \times 200-cm AG 50W-X8 cation-exchange column and filtered through a 0.8- μ m/0.45- μ m cartridge filter (Nalgene Co.). The modifier used for the reversed-phase column was 1-octanesulfonate (Regis Chemical Co., Martin Grove, TN). All other reagents were reagent grade, and all aqueous solutions were prepared from quartz double-distilled and deionized water (Milli-Q system). All eluents were filtered through 0.45- μ m Millipore filters before use to remove any particulate and to degas the solvent.

Dilute solutions of lanthanide standards were prepared from Spex Industries standard solutions. The ¹⁴⁷Pm standard was from Amersham Canada (Oakville, ON, Canada) and had an activity of 651.3 Bq mg⁻¹ at reference time 87-Nov-23 @ 12h EST, based on calibration by $4\pi\beta$ counting with ⁶⁰Co as an efficiency tracer. A half-life of 958.18 \pm 0.15 days was used to calculate the concentration of ¹⁴⁷Pm at the time of use.

Sample Preparation. To aid in the development of this procedure, a number of rare-earth tracers (¹⁴⁷La, ¹⁴⁷Nd, ^{149,151}Pm, and ¹⁴¹Ce) were prepared by irradiating the appropriate lanthanides (10 μ g of La, 2.0 mg of Nd, and 1 mg of Ce) in the NRU reactor (Chalk River Laboratories, Chalk River, Ontario) for a period of 19 h at a flux of 2×10^{14} n cm⁻² s⁻¹. In initial studies, a 100- μ L aliquot of each tracer containing 8 ng of Nd, 4 ng of Ce, 40 pg of La, and ~20 pg of Pm was added to 500 mL of urine, while in subsequent recovery studies 100 ng of U, 11 Bq of ¹⁴⁷Pm (0.32 pg), and 10⁴ Bq of ¹⁴¹Ce tracer were added to the sample. In all cases, 100 ng of Y and Sm carrier were added to the 500-mL urine samples. The urine samples were not pooled, so that the effect of variability in the urine matrix on the analysis procedure could be assessed.

Initial experiments with urine spiked immediately before processing indicated that acidifying the urine to 0.5 M HNO₃ and heating to 80 °C resulted in complete recovery of the tracer lanthanides on a 10-mL cation-exchange column. However, when this same procedure was applied to urine samples which had been spiked and then allowed to equilibrate for 4 days, only 40–50% of the tracer inventory was retained on the cation resin. The poor recovery was attributed to incomplete destruction of organic lanthanide complexes that had formed in the urine and which were not retained on the ion-exchange column. Additional experiments using urine which had been spiked and allowed to equilibrate for 4 days indicated that acidifying the sample to 0.5 M HNO₃ and boiling for 1 h successfully destroyed any complexes which had formed and resulted in complete adsorption of the lanthanides on the cation column. In all subsequent experiments the urine specimens were acidified to 0.5 M HNO₃ and boiled for

a period of 1 h before processing. The samples were then cooled to room temperature, filtered by gravity using Whatman No. 41 filter paper and passed through a 10-mL bed of AG 50W-X8 cation-exchange resin (100–200 mesh). The resin was washed in turn with 25 mL of water and 250 mL of 1.0 M NH₄Cl (pH 5.0) and again with 25 mL of water, and the lanthanides were eluted from the resin with 35 mL of 0.03 M citric acid (pH 5.0).

The citrate solution was evaporated to dryness and then ignited at 520–550 °C for 30 min. The lanthanides were converted to the nitrate form by dissolving the residue in 3–4 mL of concentrated HNO₃/2% HF and evaporating to dryness. Finally, the lanthanide nitrates were dissolved in 1.0 mL of HIBA solution (0.05 M at pH 3.5) containing 1-octanesulfonic acid (0.01 M).

Sample Analysis by HPLC. The 1.0-mL sample loop was flushed with distilled-deionized water, the sample was loaded into the loop through a 0.45- μ m syringe cartridge filter, and then valved "in-line" with the eluent. The solvent for the gradient elution was varied from 0.05 M HIBA to 0.25 M HIBA over 15 min at a flow rate of 1.5 mL/min; for both eluents the pH was 4.6. The concentration of 1-octanesulfonate was constant throughout a given gradient, and ranged from 7.5×10^{-3} to 1×10^{-2} M in the various studies. The eluted fractions of ¹⁴⁷Pm and ¹⁴¹Ce were collected using a manually operated switching valve, for subsequent determination by liquid scintillation counting and γ spectrometry, respectively. The elution times required for collecting the fractions were determined prior to the analysis using lanthanide standards and were verified during the sample runs using the Sm peak as a marker.

Radiochemical Analysis. Two milliliters of the ¹⁴⁷Pm fraction were mixed with 18.0 mL of Scintiverse liquid scintillation cocktail (Fisher Chemical Co.) and counted on a Beckman LS 2800 counter (Beckman Instruments Inc., Nuclear Systems Operation, Irvine, CA) for 30 min. Calibration of the liquid scintillation counter using a ¹⁴⁷Pm standard gave a counting efficiency of $91 \pm 3\%$ for ¹⁴⁷Pm under these conditions. The background for the liquid scintillation counter was 100 cpm.

The ¹⁴¹Ce fraction (2.0 mL) was counted on a EG&G Ortec PopTop high-purity germanium γ spectrometer (30% relative efficiency). The recovery of the ¹⁴¹Ce was determined relative to 2.0 mL of eluent containing the same quantity of ¹⁴¹Ce as spiked into the urine.

ICP Analyses. Samples from initial cation-exchange studies were analyzed with an Applied Research Laboratories 3520 B inductively coupled plasma-atomic emission spectrometer using a 1.0-m Paschen-Runge vacuum monochromator with a 1080 lines/mm grating. The specific conditions were rf power 1.5 kW, torch viewing height 14 mm above the load coil, nebulizer uptake rate ~3.0 mL/min, integration time 5 s/step, and argon flow rates (nebulizer) 1.5 L/min, (plasma) 1.0 L/min, and (coolant) 10 L/min. The lines used for each element were Sm 359.260 nm, Nd 430.357 nm, Sr 407.771 nm, Ca 317.933 nm, and Y 371.030 nm.

RESULTS AND DISCUSSION

Cation-Exchange Pretreatment. The recovery of the rare-earth elements from the cation exchange pretreatment was determined by adding ¹⁴⁰La, ¹⁴⁷Nd, ^{149,151}Pm, and ¹⁴¹Ce tracers to urine specimens obtained from seven individuals, along with 100 ng of Y and Sm carrier. The lanthanide-amino acid complexes were destroyed by acidification and boiling, and then the metals were preconcentrated on a 10-mL bed of AG50W-X8 cation-exchange resin. Monitoring of the eluting urine matrix by γ spectrometry indicated that less than 1% of the lanthanide tracers were lost during the preconcentration step.

The bulk of the inorganic urine matrix retained on the cation exchanger was calcium. It was determined that citric acid quantitatively elutes the lanthanides while leaving calcium on the column. Best removal was achieved at pH < 4, but even at pH 9 only 1.5 μ g/mL of Ca was present in the citric acid. The pH of the citric acid eluent also affects the elution of the lanthanides (Figure 1), with only a minor portion of the lanthanides being eluted below a pH of 5. However, as the pH is increased above pH 5, the lanthanide recovery

(12) Cassidy, R. M.; Miller, F. C.; Knight, C. H.; Roddick, J. C.; Sullivan, R. W. *Anal. Chem.* 1986, 58, 1389–1394.

(13) Elchuk, S.; Burns, K. L.; Cassidy, R. M.; Lucy, C. A. *J. Chromatogr.* 1991, 558, 197–207.

(14) Cassidy, R. M.; Elchuk, S.; Dasgupta, P. K. *Anal. Chem.* 1987, 59, 85–90.

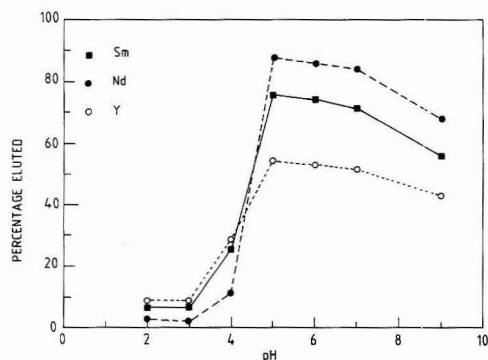


Figure 1. Effect of pH on elution of lanthanides and yttrium in urine from AG50W-X8 cation-exchange resin by 0.03 M citric acid. Experimental conditions are as described in the Sample Preparation. The sample was spiked with 1 mg each of Sm, Nd, and Y, and their concentrations in the eluate were determined by ICP-AES.

gradually decreases. Based on Figure 1, a pH of 5 was used to elute the lanthanides. Initial studies were conducted using a citrate concentration of 0.3 M, however a reduced concentration of 0.03 M was found to elute the lanthanides equally well and reduced the subsequent combustion time to 30 min.

Tracer studies and ICP analyses indicate that 70–90% of the lanthanides and 55% of the yttrium are recovered from this procedure. However, as can be seen in Figure 1, there are significant differences in the recoveries of the lanthanides. This will impact on the internal standard, as discussed below.

Dynamic Ion-Exchange Separation of Lanthanides.

The chromatographic conditions used in this work were based on those previously developed for the separation of lanthanides in spent thorium-uranium dioxide fuels.⁴ Figure 2 shows the separation of an aqueous standard containing 100 ng/mL of the lanthanides, uranium, and yttrium and 8 μ g/mL of Ca. The peak at 1.4 min is composed of transition-metal impurities from the HF.

If calcium is not removed from the urine sample prior to the dynamic ion-exchange chromatography, the large concentration of calcium will overload the column and alter the elution times of the lanthanides, resulting in incorrect fraction collection and erroneous determination of the radioisotopes present.

Determination of ^{147}Pm and ^{144}Ce in Urine. Thirteen urine samples were spiked with 11.0 Bq of ^{147}Pm , 10⁴ Bq of ^{141}Ce tracer, and 100 ng of inactive Sm carrier and processed through the full separation and detection protocol. These samples were not pooled so that the effect of variations in the urine matrix on the analysis could be assessed. The final seven samples were spiked with a further 100 ng each of Y and U. The results for Y and U will be discussed below.

A typical sample chromatogram is shown in Figure 3, where the peak at 1.4 min is attributed to the presence of transition metals in the urine. The baseline shift at the retention times corresponding to Pm and Ce results from the diversion of the eluent from the column to a collection vial at these points. The Pm and Ce fractions were analyzed by liquid scintillation counting and γ spectrometry, respectively.

The recoveries of ^{147}Pm , ^{141}Ce , and the inactive Sm carrier are reported in Tables I and II. Sample 5 of Table I represents a "catastrophic" sample preparation incident, wherein the sample was spilled after the cation-exchange pretreatment resulting in the loss of approximately one-third of the sample solution. Nevertheless, the recovery of ^{147}Pm is equivalent at the 95% confidence interval to that of Sm for this sample

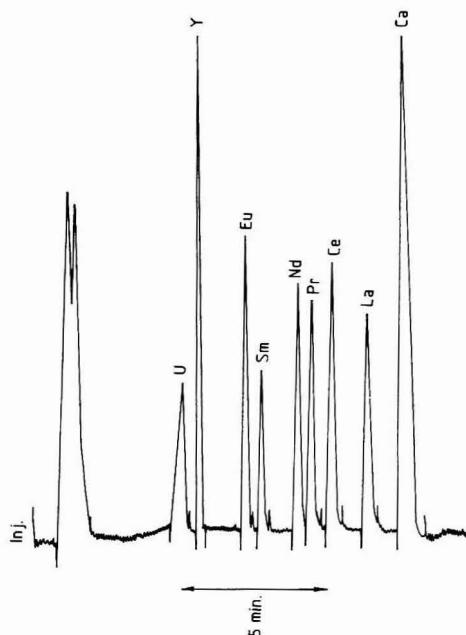


Figure 2. Dynamic ion-exchange separation of a standard solution containing 100 ng of each lanthanide, yttrium, and uranium and 8 μ g of Ca. The standard solution was processed as described in the Experimental Section.

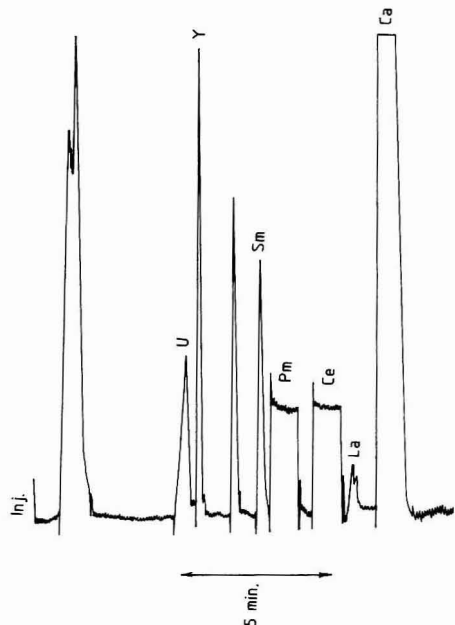


Figure 3. Dynamic ion-exchange separation of a urine sample spiked with 100 ng of Sm, Y, and U. Conditions are as described in the Experimental Section.

and for all other samples. Whereas the ^{141}Ce and ^{147}Pm recoveries differed at the 95% confidence interval for 3 of the

Table I. Recovery of Lanthanide Spikes from Urine Samples^a

sample	Sm yield (HPLC) ^b	¹⁴⁷ Pm yield (LSC) ^b	¹⁴¹ Ce Yield (γ spec) ^b
1	80 ± 3	85 ± 5	82 ± 2
2	90 ± 3	79 ± 5	73 ± 3
3	93 ± 3	91 ± 5	82 ± 3
4	91 ± 3	90 ± 5	82 ± 3
5 ^c	50 ± 4	60 ± 5	67 ± 3
6	71 ± 3	68 ± 5	64 ± 4
av ^d	85 ± 9	83 ± 9	77 ± 8

^a A 500-mL aliquot of each urine sample was spiked with 11.0 Bq of ¹⁴⁷Pm, 10⁴ Bq of ¹⁴¹Ce, and 100 ng of Sm and handled as described in the Experimental Section. ^b Errors are the standard deviations (at 1s level) associated with the peak area measurement (HPLC) or the counting statistics (liquid scintillation counting and γ spectroscopy). ^c Sample was accidentally spilled, resulting in the loss of about one-third of the sample volume. ^d Sample number 5 is excluded from the average.

Table II. Recovery of Lanthanide, Yttrium, and Uranium Spikes from Urine Samples^a

sample	Sm yield (HPLC) ^b	¹⁴⁷ Pm yield (LSC) ^b	¹⁴¹ Ce yield (γ spec) ^b	Y yield (HPLC) ^b	U yield (HPLC) ^b
7	70 ± 3	67 ± 5	84 ± 3	50 ± 4	77 ± 6
8	70 ± 3	67 ± 5	79 ± 3	63 ± 4	73 ± 6
9	81 ± 3	87 ± 4	90 ± 3	80 ± 3	60 ± 7
10	67 ± 3	70 ± 5	76 ± 3	50 ± 4	81 ± 6
11	83 ± 3	85 ± 4	90 ± 3	72 ± 4	81 ± 6
12	92 ± 3	89 ± 4	91 ± 3	86 ± 4	85 ± 5
13	82 ± 3	83 ± 4	93 ± 3	78 ± 4	85 ± 5
av	78 ± 9	78 ± 10	86 ± 7	68 ± 14	77 ± 9

^a A 500-mL aliquot of each urine sample was spiked with 11.0 Bq of ¹⁴⁷Pm, 10⁴ Bq of ¹⁴¹Ce, and 100 ng of Sm, U, and Y and handled as described in the Experimental Section. ^b Errors are the standard deviations (1s) associated with the peak area measurement (HPLC) or counting statistics (liquid scintillation counting and γ spectroscopy).

13 samples. Therefore the internal standard should be as chemically similar to promethium as possible—i.e. samarium or neodymium.

An additional urine sample was spiked with ¹⁴⁷Nd and ¹⁴¹Ce, and passed through the cation-exchange and HPLC separation stages. The resultant Pm fraction was analyzed by γ spectrometry, and contained undetectable quantities of these radionuclides. Thus, on the basis of the minimum detectable activity for ¹⁴⁷Nd, the decontamination factor for adjacent lanthanides is ≥790.

On the basis of an average recovery of 80% and a counting efficiency of 91%, the limit of detection for ¹⁴⁷Pm in 500 mL of urine is 0.1 Bq for a 30-min count on a liquid scintillation counter with a background of 100 cpm. Use of a low-background liquid scintillation counter or a longer count time would further improve the sensitivity of the method; however the current sensitivity was sufficient for our application.

Determination of Other Radionuclides. Preliminary studies were also performed on two other radionuclides, U and Y. Uranium and yttrium were separated from the bulk cations of the urine matrix using a cation-exchange column in the same fashion as for the lanthanides. Tracer studies determined that U recoveries from this initial step were comparable to those of the lanthanides. However ICP-AES analyses showed that Y had significantly lower recoveries (Figure 1).

To improve the dynamic ion-exchange separation between U and Y, the octanesulfonate concentration was reduced to 7.5 × 10⁻³ M. Yttrium and the lanthanides are retained solely by ion exchange with the octanesulfonate, whereas the uranium forms a much more hydrophobic complex with HIBA

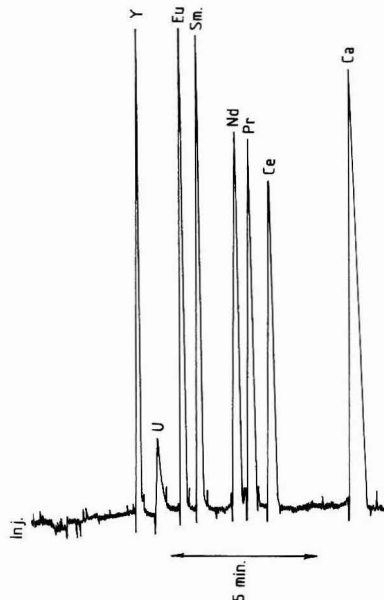


Figure 4. Dynamic ion-exchange separation of a standard solution of urine containing 100 ng of each lanthanide, uranium, and yttrium and 8 μg of Ca. Conditions are as described in the Experimental Section, except that the 1-octanesulfonic acid concentration is 7.5 × 10⁻³ M.

and so is less affected by changes in the ion-exchange capacity of the column.^{8,15,16} Thus by decreasing the concentration of 1-octanesulfonate, the retention of uranium on the column can be adjusted so that it does not coelute with any of the lanthanides or yttrium (Figure 4).

Table II shows the recoveries of each of the radionuclides in the urine samples. The results for the lanthanides were discussed above. The standard deviation for the U recovery is greater than that of Sm, which was also determined using postcolumn reaction with Arsenazo III, because the U peak tends to tail, making peak area determinations less precise. For all cases except sample 3, the U recoveries were equivalent to those of Sm, ¹⁴⁷Pm, and ¹⁴¹Ce within the 95% confidence interval. Sample 3 was within the 99% confidence interval. Therefore, it is concluded that a lanthanide carrier can be used as a recovery marker for U as well as ¹⁴⁷Pm. The limit of detection for U in urine by HPLC separation and postcolumn reaction detection with Arsenazo-III is 10 ng in a 500-mL urine sample. This is much more sensitive than the 1-μg detection limit achieved by using anion-exchange purification followed by spectrophotometric determination of the uranium-Arsenazo III complex,¹⁷ or the 1 μg/L U detection limit of the fluorometric method.¹⁸

The recoveries observed for yttrium for the cation-exchange pretreatment and overall process were consistently lower than those obtained for the rare-earth elements (Figure 1 and Table II). Therefore inactive Y would be the only accurate internal standard which could be used to assess the recovery of ⁹⁰Y.

(15) Cassidy, R. M.; Elchuk, S.; Green, L. W.; Knight, C. H.; Miller, F. C.; Reoscio, B. M. *J. Radioanal. Nucl. Chem., Art.* **1990**, *139*, 55-64.

(16) Kerr, A.; Kupferschmidt, W.; Attas, M. *Anal. Chem.* **1988**, *60*, 2729-2733.

(17) Kressin, I. K. *Anal. Chem.* **1984**, *56*, 2269-2271.

(18) Kramer, G. H.; Johnson, J. R.; Green, W. Report AECL-8251; Atomic Energy of Canada Ltd.: Chalk River, Ontario, 1984.

This would preclude collection of the Y fraction prior to the addition of the Arsenazo III postcolumn reagent, and so it would be necessary to decolorize the solution by wet ashing with HNO_3 prior to analysis by liquid scintillation counting.

Thorium could not be determined using this procedure, since it was lost during filtration (most likely as an insoluble phosphate) prior to the initial cation exchange.

ACKNOWLEDGMENT

Robert Martin performed the calibration of the ^{147}Pm standard. Helpful discussions with Stan Linauskas are

gratefully acknowledged. This work was presented in part at the International Ion Chromatography Forum, September 17-19, 1989, Boston, MS.

RECEIVED for review March 20, 1992. Accepted July 15, 1992.

Registry No. ^{147}Pm , 14380-75-7; ^{140}La , 13981-28-7; ^{147}Nd , 14269-74-0; ^{141}Ce , 13967-74-3; U, 7440-61-1; Y, 7440-65-5.

Carboxylated Starburst Dendrimers as Calibration Standards for Aqueous Size Exclusion Chromatography

Paul L. Dubin,^{*,†} Shun L. Edwards,[†] Jerome I. Kaplan,[‡] Mamta S. Mehta,[§] Donald Tomalia,^{||} and Jiulin Xia[†]

Departments of Chemistry and Physics, Indiana University-Purdue University at Indianapolis, Indianapolis, Indiana 46205, and Department of Chemistry and Macromolecular Architecture, The Michigan Molecular Institute, Midland, Michigan 48640

Standards commonly employed to calibrate size exclusion chromatography columns usually do not themselves have well-defined sizes. Carefully characterized spherical solutes in the appropriate size range are therefore of considerable interest. The chromatographic behavior of carboxylated starburst dendrimers—characterized by quasielastic light scattering and viscometry—on a Superose size exclusion column has been explored. Carboxylated starburst dendrimers appear to behave as noninteracting spheres during chromatography in the presence of an appropriate aqueous mobile phase. The dependence of the retention time on solute size seems to coincide with data collected on the same column for Ficoll, an uncharged, quasi-spherical polysaccharide. Chromatography of the dendrimers yields a remarkable correlation of the chromatographic partition coefficient with the generation number; this result is in part a consequence of the exponential relationship between the generation number and the molecular volume of the dendrimers.

INTRODUCTION

Size exclusion chromatography (SEC) is often referred to as a relative molecular weight (MW) method, in the sense that a chromatographic system must be calibrated with standards of known molecular weight. There are in fact three aspects to the problem of obtaining correct MW values from SEC. The first is the determination of the relationship between the solutes' molecular sizes and the retention time for the column in use. This can be carried out in principle with almost any well-characterized set of solutes, preferably of narrow molecular weight distribution. However, we must recognize at the outset that the molecular size relevant to SEC may not be well-defined (strong convictions exist in the biochemical community that this size is the Stokes radius¹ and in the polymer community that it is the viscosity radius,^{2,3a} but this matter is unresolved⁴ at the present time). The second requirement is that of knowing the relationship between the

molecular dimension and the molecular weight for the solute of interest. Such relationships are often available, e.g. via the Mark-Houwink equation for flexible chain macromolecules.⁵ The third consideration is the question of solute-packing interactions; if the analyte or the reference compounds are adsorbed onto or partitioned into the stationary phase, the separation is not based on size alone, and attempts to determine either molecular dimensions or mass are probably useless. In practice, the first two questions are usually answered simultaneously: if the calibration is done with compounds similar in structure to the analyte, it is assumed that the empirical relationship between MW and retention time so established is valid for the unknown. The third step is usually not studied explicitly, but the absence of significant interactions is commonly assumed on the basis of prior experience with a given class of solutes on a particular column.

It should be evident from the preceding comments that the ideal calibration standards would fulfill the following requirements: (a) their MW distributions should be negligibly small; (b) it should be possible to determine their molecular dimensions in an unambiguous manner; (c) they should not adsorb to the packing in question. Few solutes satisfy these criteria, and the situation is particularly problematic in the area of aqueous SEC. Proteins, which are commonly used for calibration standards, fulfill item (a) but are less satisfactory with regard to (b) and (c). Typically, one finds deviations around the best common curve for any calibration curve constructed with proteins, and it is difficult to know whether these deviations arise from variations of geometry for the different solutes (some of which are more spherical than others) or from differences in solute-packing interactions, due to differences in protein charge character or hydrophobicities. Nonionic polysaccharides, such as dextrans or pullulans, are representative of the class of flexible-chain water-soluble polymers. These are structurally uniform and do not interact with any stationary phase, but the interpretation of measured dimensions—such as radius of gyration or viscosity radius—in terms of the molecular volume controlling SEC is problematic. We have previously utilized in this regard fractions of Ficoll, a densely branched nonionic polysaccharide which may more closely approach a noninteracting sphere. However, its molecular weight polydispersity and its deviation from full compactness both impose difficulties in interpretation of SEC partition coefficients measured at chromatographic peaks vis-a-vis dimensional measurements, which themselves correspond to different averages over the distributions of molecular weights and conformations.

Carboxylated starburst dendrimers⁶ would appear to embody several of the features sought for aqueous SEC standards. While these materials are not yet commercialized,

[†] Department of Chemistry.

[‡] Department of Physics.

[§] Current address: Department of Chemistry, University of Illinois, Urbana-Champaign, IL 61820.

^{||} Department of Chemistry and Molecular Architecture.

(1) Cantor, C. R.; Schimmel, P. R. *Biophysical Chemistry. Part II. Techniques for the Study of Biological Structure and Function*; W. H. Freeman: New York, 1980; p 675.

(2) See, for example: Rosen, S. L. *Fundamental Principles of Polymeric Materials*; John Wiley & Sons: New York, NY, 1982; p 70.

(3) The term "hydrodynamic radius" is inexact because either the intrinsic viscosity or the diffusion coefficient may be used to obtain an "equivalent sphere" radius for any solute, the former via the Einstein relation and the latter via Stokes' equation. Although both of these are hydrodynamic measurements, the radii so obtained will not be identical for a highly asymmetric solute, since the first arises from energy transfer among adjacent solvent layers, and the latter from the frictional solute-solvent interface. Therefore, we follow Potschka^{3b} in referring to R_h as the viscosity radius. (b) Potschka, M. *Anal. Biochem.* 1987, 162, 47.

(4) Potschka, M. *Macromolecules* 1991, 24, 5023.

(5) Brandrup, J.; Immergut, G. H., Eds. *Polymer Handbook*, 2nd ed.; John Wiley: New York, 1975; Chapter 4.

(6) Tomalia, D. A.; Naylor, R. M.; Goddard, W. A., III. *Angew. Chem., Int. Ed. Engl.* 1990, 29, 138.

Table I. Hydrodynamic and Chromatographic Characterization of Carboxylated Starburst Dendrimers

generation	10^{-3} MW	$[\eta]$, cm ³ /g	R_h , nm ^a	$10^6 D$, cm ² /s	R_s , nm ^b	K_{SEC}^c
0.5	0.92			2.66	0.92	0.74
1.5	2.17			1.91	1.28	0.68
2.5	4.67	4.15	1.45	1.67	1.47	0.62
3.5	9.67	4.58	1.92	1.00	2.45	0.56
4.5	19.7	4.77	2.46	0.79	3.10	0.51
5.5	39.7	4.88	3.13	0.67	3.65	0.45
6.5	79.6	5.16	4.03	0.54	4.50	0.39
7.5	160.	5.87	5.30	0.41	5.95	0.34

^a From data in columns 2 and 3, via eq 4. ^b From data in column 5, via eq 3. ^c From measured peak retention volumes, via eq 5.

their uses in many areas of research have been explored. With regard to SEC, their compact and symmetrical structures could make them rather close to rigid spheres so that the dimensions obtained by a variety of scattering or hydrodynamic techniques could be unambiguously identified with the dimension controlling SEC migration. The mode of synthesis guarantees that they are monodisperse. Lastly, the negative charge on the distal groups would prevent adsorption, since nearly all commonly used aqueous SEC packings have some negative surface charge.⁷ With regard to repulsion effects, one would expect some decrease in retention times at higher pH's and low ionic strength, under which conditions the negative charge on typical SEC stationary phases would enhance the exclusion of these solutes. These effects become essentially negligible at moderate ionic strength and pH on most columns.

In the current work we evaluate carboxylated starburst dendrimers (hereinafter referred to simply as dendrimers) as calibration standards on a Superose column. For this stationary phase, we know that electrostatic repulsive forces are negligible, even for, e.g., highly charged DNA fragments, in a 0.38 M pH 5.8 phosphate mobile phase⁸ and furthermore that proteins of various isoelectric points elute along a common curve in this same medium.⁹ In order to properly characterize the dendrimers, we obtained the Stokes radius by quasielastic light scattering (QELS) and the viscosity radius from the known MW and intrinsic viscosity (all measurements made in the SEC mobile phase solvent). The nature of the calibration curve obtained with these solutes is discussed vis-a-vis current understanding of the SEC separation mechanism.

EXPERIMENTAL SECTION

Materials. Carboxylated starburst dendrimers were prepared by methods described elsewhere.¹⁰ These molecules are synthesized by a series of stepwise condensation reactions on an initial trifunctional amine, and consequently molecular size grows in three dimensions with each subsequent step (called a "generation").¹⁰ The samples employed in these studies are described in Table I. All measurements were made in a 9:1 mixture of NaNO₃:NaH₂PO₄, pH = 5.5, 0.38 M, which had been previously shown to minimize electrostatic interactions between a variety of proteins and this stationary phase.⁹ This solvent is referred to below as the "standard mobile phase".

Methods. Quasielastic Light Scattering (QELS). Light-scattering measurements were made using one of two systems. With a Brookhaven (Holtville, NY) system equipped with a 72-channel digital correlator (BI-2030 AT) and using a Jodon 15-mW He-Ne laser (Ann Arbor, MI), QELS measurements were

made at scattering angles from 30 to 150°. Dendrimer samples at concentrations of ca. 2 mg/mL were filtered through 0.20- μ m Acrodisc filters (Gelman) prior to analysis. Counts were typically collected for 1 h. We obtained the homodyne intensity-intensity correlation function $G(q,t)$, with q , the amplitude of the scattering vector, given by $q = (4\pi n/\lambda) \sin(\theta/2)$, where n is the refractive index of the medium, λ is the wavelength of the excitation light in a vacuum, and θ is the scattering angle. $G(q,t)$ is related to the time correlation function of concentration fluctuations $g(q,t)$ by

$$G(q,t) = A(1 + bg(q,t)^2) \quad (1)$$

where A is the experimental baseline and b is the fraction of the scattered intensity arising from concentration fluctuations.

The diffusion coefficients were calculated using

$$D = \Gamma \lambda^2 / 16 \pi^2 \sin^2(\theta/2) \quad (2)$$

where Γ is the reciprocal of the diffusion time constant, which is obtained from the slope of $\ln g^2(q,t)$ vs t plots. The diffusion coefficient, D , is directly related to the Stokes radius, R_s , by Stokes' equation

$$D = kT/6\pi\eta R_s \quad (3)$$

where k is Boltzmann's constant, T is the absolute temperature, and η is the viscosity of the solvent.

QELS was also carried out with an Oros (Biotage Co. Charlottesville, VA) Model 801 "Molecular Weight Detector" which employs a 30-mW solid-state 780-nm laser and an avalanche photodiode detector. Samples were introduced into the 7- μ L scattering cell (maintained at 26.5 ± 0.4 °C) through 0.2- μ m Anotec filters. Scattering data (90°) were analyzed via cumulants. There were no significant differences between the results obtained using the two instruments. (General discussions of QELS data analysis may be found in ref 11.)

Viscometry. Measurements were made with a Schott AVSN automatic viscometer equipped with a 10-mL capacity glass Type 531 capillary viscometer, at 25.0 ± 0.02 °C. Dendrimer samples were dissolved in our standard mobile phase at concentrations ranging from 6 to 17 mg/mL and filtered through 0.45- μ m Gelman filters. Efflux times were obtained with precisions of ± 0.05 s. However, the very low viscosities of these materials made it difficult to obtain $[\eta]$ with better than 2% precision. The viscosity radius was obtained as¹²

$$R_\eta = \{3[\eta]M/10\pi N_A\}^{1/3} \quad (4)$$

where the units of R_η and $[\eta]$ are cm and cm³/g, respectively.

Chromatography. The chromatographic system was a Beckmann "system Gold" HPLC equipped with refractive index (ri) and UV detectors and a Superose 12 column (Pharmacia Fine Chemicals, Uppsala, Sweden). This last component consists of 10.5- μ m-mean-diameter cross-linked 12% agarose particles packed into a 30- \times 1-cm-i.d. column. The initial column efficiency was ca. 10 000 theoretical plates, but during the period of use described here declined to ca. 3500. The average pore size was 170 Å, as determined by the slope of a plot of $1 - K_{SEC}^{1/2}$ (for definition of K_{SEC} , see below) vs R_h for the nearly spherical solute Ficoll.¹³ The characteristics of Superose 12 packings and columns are described in detail in ref 14. Flow rates were determined by weighing of collections of timed eluent and were precise to better than $\pm 0.2\%$. Peak retention volumes, V_e , were determined by triplicate injections with a repeatability of $\pm 0.5\%$. The chromatographic partition coefficient then could be determined according to

$$K_{SEC} = (V_e - V_0)/(V_t - V_0) \quad (5)$$

where V_0 is the exclusion volume (interstitial packing volume), determined as 8.05 mL from the elution of DNA, and V_t is the total column liquid volume, determined as 21.82 mL from the

(7) Dubin, P. L. In *Aqueous Size Exclusion Chromatography*; Dubin, P. L., Ed.; Elsevier: Amsterdam, 1988; Chapter 5.

(8) Dubin, P. L.; Principi, J. M. *Macromolecules* 1989, 22, 1891.

(9) Dubin, P. L.; Principi, J. M. *J. Chromatogr.* 1989, 479, 159.

(10) Tomalia, D. A.; Berry, V.; Hall, M.; Hedstrand, D. M. *Macromolecules* 1987, 20, 1164.

(11) Phillies, G. D. J. *Anal. Chem.* 1990, 62, 1049A.

(12) Flory, P. J. *Principles of Polymer Chemistry*; Cornell University Press: Ithaca, NY, 1953; p 606.

(13) Dubin, P. L.; Kuntz, M. Manuscript in preparation.

(14) Andersson, T.; Carlsson, M.; Hagel, L.; Pernemalm, P.-A.; Jansson, J.-A. *J. Chromatogr.* 1985, 326, 33.

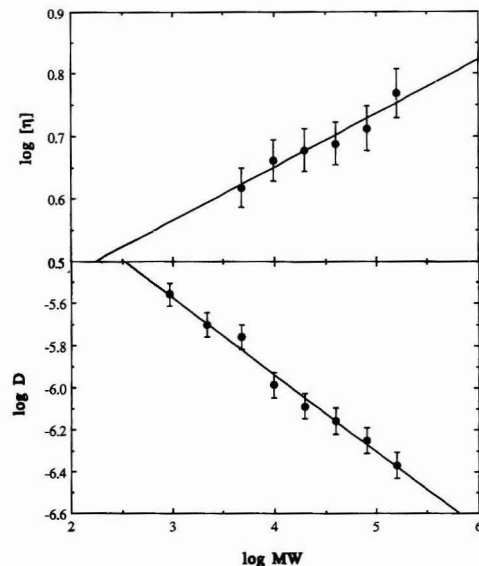


Figure 1. Double-logarithmic plots of the MW-dependence of intrinsic viscosity (upper) and diffusion coefficient (lower) of dendrimers, in standard mobile phase solution.

elution of acetone. K_{SEC} could thus be measured with a relative precision of about 2%.

Dendrimer samples typically exhibited a number of peaks in both RI and UV detection. That these were not chromatographic artifacts was established by collection and reinjection of the individual peaks. However, only the earliest eluting (and largest) peak changed with generation number, G . Furthermore, all other peaks had retention times too large to be consistent with the expected MWs or either R_g or R_h . We therefore conclude that these peaks are low-MW impurities, likely to be synthetic precursors of the final products. While the nature of these impurities is clearly of concern, there are a number of findings that support the conclusion that these species may be neglected in the evaluation of $[\eta]$, R_g , or K_{SEC} . First, the plot of $\log [\eta]$ vs $\log MW$ (Mark-Houwink plot) is quite linear (correlation coefficient of 0.98), whereas an abundance of low-MW impurities would be expected to produce more erratic error in the intrinsic viscosities. Furthermore, when the values of R_g obtained from $[\eta]$ were plotted against R_h , a regression coefficient of 0.99 was obtained. (It is noteworthy that because the values of $[\eta]$ are small and do not vary much (as one would expect for spherical solutes), the effect of errors in $[\eta]$ tend to be overwhelmed by the much larger and more variable MW term). The parameter R_h , obtained by light scattering, may be assumed to be relatively insensitive to the less massive, hence weakly scattering, impurities. We therefore suggest that the presence of the chromatographically detectable low-MW subspecies does not contribute significantly to either measurements of dimension. Consequently, their elution was neglected in the determination of K_{SEC} .

RESULTS AND DISCUSSION

Table I contains the results of viscometry and QELS for the dendrimers in the standard mobile phase, along with the chromatographic partition coefficients, measured in the same solvent. The dependences of the intrinsic viscosity and the diffusion coefficients on the MW are shown in the double-logarithmic plots in Figure 1. From the exponents of the equations $[\eta] = KM^a$ and $D = K'M^a$, namely $a = 0.086$ and $a' = -0.36$, it is evident that the dendrimers approach the compactness of an impenetrable sphere, for which $a = 0$ and

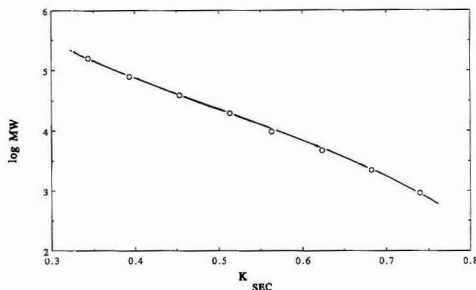


Figure 2. Dendrimer calibration curve, as log molecular weight vs chromatographic partition coefficient, on Superose 12.

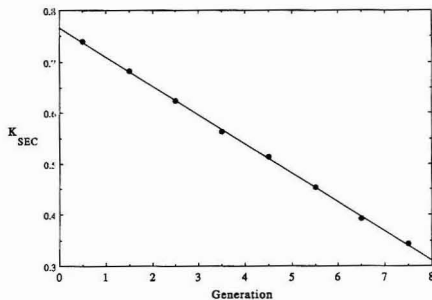


Figure 3. Dependence of chromatographic partition coefficient on generation number.

$a' = -0.33$. The relationship between the Stokes radius and the viscosity radius is given by $R_h = 1.15R_g$. For hard spheres, we would expect $R_h = R_g$ for flexible chains, $R_h/R_g = 0.5-0.8$.¹⁵ The somewhat greater value for R_h in the present case may arise from the highly charged nature of the dendrimer, so that it diffuses along with a number of counterions. In an analogous system, we have found that the effective charge of anionic micelles measured by electrophoretic light scattering is far smaller than the formal charge.¹⁶ This means that the diffusing species encompasses a large number of counterions, i.e. that the electrophoretic shear plane is some distance from the average micellar ionic headgroup. The relevance to the present case is that the mutual diffusion coefficient is reduced by the counterion cloud, leading to somewhat elevated values for R_h .

Figures 2-4 show calibration curves for the dendrimers, presented in several ways: as K_{SEC} vs $\log MW$ in Figure 2, as K_{SEC} vs generation number in Figure 3, and as K_{SEC} vs solute dimensions— R_g or R_h —in Figure 4. Figure 4 also includes data for another compact, spherically symmetric solute, Ficoll, eluted under identical conditions, which were reported elsewhere.¹⁷

The coincidence of the Ficoll and dendrimer curves in Figure 4 is compelling evidence that both behave as spheres of radius R , i.e. that Ficoll and dendrimer samples of the same R_g or R_h are chromatographically indistinguishable. Since the former solutes are uncharged, these results also suggest that solute-substrate interactions are negligible for the latter. It is certainly possible that early elution of the dendrimers might be observed at higher pH and lower ionic

(15) Doi, M.; Edwards, S. F. *The Theory of Polymer Dynamics*; Oxford Science Press: Oxford, U. K., 1986.

(16) Xia, J.; Dubin, P. L.; Kim, Y. *J. Phys. Chem.* 1992, 96, 6805.

(17) Hussain, S.; Mehta, M. S.; Kaplan, J. L.; Dubin, P. L. *Anal. Chem.* 1991, 63, 1132.

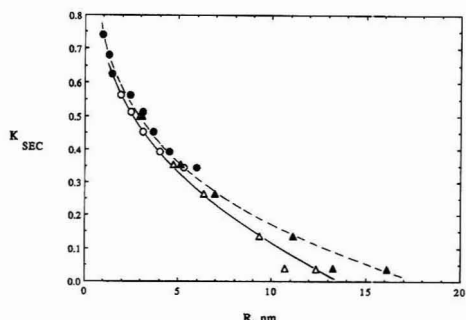


Figure 4. Dependence of chromatographic partition coefficient on solute radius, for dendrimers (circles) and for Ficolls (triangles). Open symbols are for viscosity radii; filled symbols are for the Stokes radii. Ficoll data are taken from ref 17.

strength. The somewhat greater divergence for the R_S plots of Figure 4 may arise from the effect of the electrical double layer of the dendrimers on their diffusion coefficients, without a parallel effect on their permeation behavior.

The values of R_S are consistently larger than R_η for Ficolls as well as for dendrimers. As suggested above, the surface charge and concomitant electrical double layer of the dendrimers may contribute to this effect. The Ficoll fractions are uncharged but differ from the dendrimers also in being polydisperse with respect to MW. Since the Stokes radius from QELS corresponds to the z-average component of the distribution, it must exceed the viscosity radius, which corresponds to the (smaller) viscosity average of the distribution. This is not a consideration for the monodisperse dendrimers and is unlikely to be very important for the viscosity radius plots for Ficolls, because for polymers with low α values, such as the value of ca. 0.35 found for Ficolls,¹⁸ the MW weight of the component corresponding to the measured viscosity radius is unlikely to diverge much from the MW of the component eluting at the chromatographic peak. However, these small uncertainties preclude any assertions about whether the effective dimension controlling SEC is the viscosity radius or the Stokes radius, based on the current data alone.

The dependence of K_{SEC} on generation number, G , is seen in Figure 3 to be strikingly linear; the correlation coefficient for this plot is found to be $r > 0.995$. This remarkable correlation deserves further analysis. We observed that the dependence of R_η on K_{SEC} and on G , respectively, is fit very well by the two empirical equations

$$R_\eta = 24.77 \times 10^{-1.97K_{SEC}} \quad (6a)$$

$$R_\eta = 0.7737 \times 10^{0.111G} \quad (6b)$$

Since the value of R_η is strongly influenced by the MW value for each dendrimer, which in turn is not a measured quantity but is rather a calculated one based on the synthetic procedure and some indirect evidence,⁶ we chose to verify the relationships of eqs 6a and 6b by examining the logarithmic forms of these two equations using measured values for R_S as well

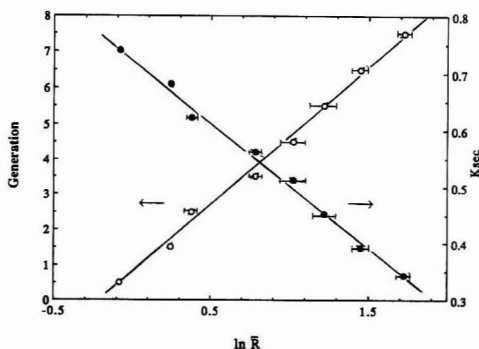


Figure 5. Dependence on solute radius of generation number (left axis) and chromatographic partition coefficient (right axis). \bar{R} is the mean of the Stokes and viscosity radii. The horizontal bars indicate the difference between these two dimensions: the left end of each bar corresponds to R_η , and the right end to R_S .

as R_η . This is done in Figure 5 in which we plot the dependence of both K_{SEC} and G on $\ln \bar{R}$, where \bar{R} is the mean of the radii measured by viscometry and QELS. The horizontal bars in this figure indicate the discrepancy between R_η and R_S . We observe that both K_{SEC} and G are linear functions of the logarithm of the solute radius.

The structure of the dendrimers ensures⁶ that the solute volume increases exponentially with G ; and since solute volume varies as R^3 , the linear relationship between $\ln R$ and G is not surprising. The observed dependence of K_{SEC} on $\ln R$ was not expected and does not conform to any of the commonly cited theoretical expressions for size exclusion,¹⁹⁻²² although experimental calibration curves often display a roughly linear dependence of, e.g., $\ln \{[\eta]M\} \sim \ln R_\eta$ on K_{SEC} in the region of intermediate K_{SEC} prior to the sigmoidal inflections at small and large permeation. In the present case, it is the exact linear relationship between K_{SEC} and $\ln R$ that leads to the remarkable correlation of K_{SEC} with G shown in Figure 3. The theoretical significance of this behavior merits further attention.

CONCLUSION

Carboxylated starburst dendrimers appear to behave as noninteracting spheres during chromatography on Superose size exclusion columns, in the presence of an appropriate aqueous mobile phase. The dependence of the retention time on solute size coincides with data collected on the same column for Ficoll, an uncharged, quasi-spherical polysaccharide. Chromatography of the dendrimers yields a remarkable correlation of the chromatographic partition coefficient with the generation number; this result is in part a consequence of the exponential relationship between the generation number and the molecular volume of the dendrimers.

ACKNOWLEDGMENT

This work was supported by Grant CHE-9021484 from the National Science Foundation. D.T. also acknowledges support from the U.S. Army Chemical Research Development and Engineering Center.

(18) Lavrenko, P. N.; Mikryukova, O. I.; Didenko, S. A. *Polym. Sci. U.S.S.R. (Engl. Transl.)* 1986, 28, 576; *Vysokomol. Soed.* 1986, A28, 517.

(19) Giddings, J. C.; Kucera, E.; Russell, C. F.; Meyers, M. N. *J. Phys. Chem.* 1968, 72, 4397.

(20) Waldmann-Meyer, H. *J. Chromatogr.* 1985, 350, 1.
(21) (a) Laurent, T. C.; Bjork, L.; Pietruszkievicz, A.; Persson, H. *Biochim. Biophys. Acta* 1983, 83, 351. (b) Laurent, T. C.; Killander, J. *J. Chromatogr.* 1984, 14, 317.

(22) Ackers, G. K. *Adv. Protein Chem.* 1970, 24, 343.

Enhanced Separation of DNA Restriction Fragments by Capillary Gel Electrophoresis Using Field Strength Gradients

András Guttman,* Bart Wanders, and Nelson Cooke

Beckman Instruments Inc., Fullerton, California 92634

The effect of electric field strength gradients on the separation of DNA restriction fragments was investigated. As reported in our earlier work, the mobility of different size double-stranded DNA molecules is a function of the applied electric field which suggests that the use of a nonuniform (time varying) electric field may increase the resolving power. We demonstrate that in capillary gel electrophoresis enhanced separation of DNA restriction fragments up to 1353 base pairs (bp) in size can be achieved by employing the field strength gradient method. The shape of the gradient can be continuous or stepwise over time. Both methods can be used to increase separation efficiency and resolution in capillary gel electrophoresis of double-stranded DNA molecules.

INTRODUCTION

Recently, there has been a great deal of activity in DNA analysis by capillary electrophoretic methods.¹⁻³ Using this new and powerful technology, results have been published on the separation of single-stranded DNA molecules, such as in synthetic DNA analysis⁴ as well as in the separation of double-stranded DNA molecules, particularly concerning PCR products and restriction fragments.⁵ It was also demonstrated that high-efficiency, fast separations of DNA molecules can be achieved by the use of linear polyacrylamide gel-filled capillary columns.^{6,7} Even fragments of the same chain length with different sequences were separated by this method due to differences in molecular conformation.⁸

Different field operation techniques have been described recently to achieve better separation of different size DNA molecules, mainly with slab gel electrophoresis. Dennison et al.⁹ employed conical or wedge-shaped slab gels to linearize the logarithmic distribution of bands (nonlinear voltage gradient method). Biggin et al.¹⁰ studied the usefulness of a high ionic strength anode buffer where the resistance of the gel in the direction of the anode decreases and creates a negative field strength gradient along the DNA's migration path. They concluded that this particular method is not practical for ultrathin gels, as is also the case for capillary gel

electrophoresis.¹¹ Ansorge et al. tried using an increasing cross-sectional area of the slab gels, producing a field gradient to achieve enhanced sharpening of bands, thereby increasing the number of resolvable bases per gel.¹² Cantor et al.¹³ introduced the pulsed-field method (changing the direction and magnitude of the field in an oscillating manner), that takes advantage of the elongated and oriented configuration of large DNA (>50 kbp) molecules in gels. Heiger et al.⁶ described the capillary gel electrophoretic separation of double-stranded DNA molecules up to 23 kbp in size using the pulsed-field technique with very low gel concentrations. Although in slab gel operation there are some mechanical difficulties involved in handling low-concentration gels,¹⁴ this does not present a problem in capillary electrophoresis techniques. Demana and co-workers¹⁵ used an analyte velocity modulation method to increase separation power in capillary gel electrophoresis of DNA restriction fragments.

In this paper, a simple field strength gradient method is described that provides enhanced resolution of double-stranded DNA molecules in capillary polyacrylamide gel electrophoresis.

EXPERIMENTAL SECTION

Apparatus. In all of the experiments, the P/ACE System 2100 capillary electrophoresis apparatus (Beckman Instruments, Inc., Fullerton, CA) was used with the cathode on the injection side and the anode on the detection side. Therefore, the negatively charged DNA molecules migrate toward the anode in the gel (i.e., polymer network) filled capillary column. The separations were monitored on column at 254 nm. The temperature of the capillary column was kept constant at 20 ± 0.1 °C by the liquid cooling system of the P/ACE instrument. The electropherograms were acquired and stored on an Everex 386/33 computer.

Chemicals. The ϕ X174 DNA *Hae*III digest and the pBR322 DNA *Msp*I digest restriction fragment mixtures (New England Biolabs, Beverly, MA) were diluted with deionized water to a concentration of 25 µg/mL before injection and were stored at -20 °C. Ultrapure grade acrylamide, Tris, boric acid, EDTA, ammonium persulfate, and tetramethylethylenediamine (TEMED) were used in the experiments (Schwarz/Mann Biotech, Cambridge, MA). All buffer and acrylamide solutions were filtered through a 0.2-µm-pore-size filter (Schleicher and Schuell, Keene, NH) and carefully vacuum degassed.

Procedures. Polymerization of the linear polyacrylamide gel was initiated by ammonium persulfate and catalyzed by TEMED in 100 mM Tris-borate, 2 mM EDTA buffer (pH 8.35) prior to inserting the reaction mixture into the 0.1-mm-i.d. fused-silica capillary tubing (DB-225, J&W, Inc., Sacramento, CA). The polymerization reaction mixture was injected into the capillary by means of a gastight syringe (Dynatech, Balton Rouge, LA).

* To whom correspondence and reprint requests should be addressed.

(1) Cohen, A. S.; Najarian, D. R.; Paulus, A.; Guttman, A.; Smith, J. A.; Karger, B. L. *Proc. Natl. Acad. Sci. U.S.A.* 1988, 85, 9660-9663.

(2) Paulus, A.; Gassmann, E.; Field, M. J. *Electrophoresis* 1990, 11, 702-708.

(3) Yin, H. F.; Lux, J. A.; Shomberg, G. J. *High Resolut. Chromatogr.* 1990, 13, 624-627.

(4) Guttman, A.; Cohen, A. S.; Heiger, D. N.; Karger, B. L. *Anal. Chem.* 1990, 62, 2038-2042.

(5) Schwartz, H. E.; Ulfelder, K.; Sunzer, F.; Busch, M.; Brownlee, M. G. *J. Chromatogr.* 1991, 559, 287-293.

(6) Heiger, D. N.; Cohen, A. S.; Karger, B. L. *J. Chromatogr.* 1990, 516, 33-48.

(7) Guttman, A.; Cooke, N. J. *Chromatogr.* 1991, 559, 285-294.

(8) Guttman, A.; Nelson, R. J.; Cooke, N. J. *Chromatogr.* 1991, 593, 297-303.

(9) Dennison, C.; Linder, W. A.; Phillips, N. C. K. *Anal. Biochem.* 1982, 120, 12-18.

(10) Biggin, M. D.; Gibson, T. J.; Hong, G. F. *Proc. Natl. Acad. Sci. U.S.A.* 1983, 80, 3963-3965.

(11) Guttman, A. Beckman Instruments, Inc., Research and Development. Unpublished results, 1991.

(12) Ansorge, W.; Labeit, S. J. *Biochem. Biophys. Methods* 1984, 10, 237-243.

(13) Cantor, C. R.; Smith, C. L.; Mathew, M. K. *Annu. Rev. Biophys. Biophys. Chem.* 1988, 17, 287-304.

(14) Fangman, W. L. *Nucl. Acids Res.* 1978, 5, 653-665.

(15) Demana, T.; Lanan, M.; Morris, M. D. *Anal. Chem.* 1991, 63, 2795-2797.

The use of low-viscosity linear polyacrylamide, not bound to the capillary wall, permits replacement of the gel-buffer system in the capillary column by means of the rinse operation mode of the P/ACE apparatus. The total length of the gel-filled capillary column was 470 and 670 mm (400 and 600 mm to the detection point), respectively. The samples were injected by the pressure injection mode of the P/ACE system, typically 5 s, 0.5 psi (estimated injection amount: 0.1 ng of DNA).

Field strength gradients were programmed in the P/ACE apparatus with continuously increasing or decreasing voltage separation modes. In the stepwise field gradient separation mode, constant voltages were used for different time periods as specified in the corresponding figure.

The relative standard deviation (RSD) of the migration time was less than 2% ($n = 12$) when the temperature of the gel-filled capillary column was maintained within $\pm 0.1^\circ\text{C}$. The same capillary column could be used for approximately 100 runs with or without replacement of the separation gel-buffer system.

RESULTS AND DISCUSSION

By the use of a low concentration gel (less than 5% linear polyacrylamide) in capillary electrophoresis, it is possible to achieve good separation of a wide size range of double-stranded DNA molecules. Separations are comparable to or better than those achieved with agarose in slab gel operation.⁵ Using a relatively high electric field, DNA molecules can be separated with high resolution in a relatively short time. However, at high field strengths, the electrophoretic mobility of DNA molecules becomes field-dependent.¹⁶ Furthermore, it is known that chain entanglement plays a significant role in the separation of DNA molecules in a gel of a given pore size;¹⁷ this entanglement is a function of the molecular size and the applied electric field.¹⁵ The main challenge is to find the appropriate field for the optimal separation of a mixture of DNA molecules with different chain lengths in a given gel matrix. At low field strengths a sieving effect applies and an inversely proportional relationship between mobility and molecular size is observed.¹⁸ With higher field strengths, a different phenomenon appears. The DNA chain becomes more oriented because the field biases the direction of the leading end of the molecule.¹⁸ This leads to an increase in mobility with increasing field strength, particularly for the larger size molecules. In other words, by application of a high electric field, the longer chain length DNA molecules might be partially or completely stretched along the alignment of the field. Thus the electrophoretic mobilities of these big molecules become size-independent causing poor separation at high field strengths.¹⁹ It should be noted that in capillary polyacrylamide gel electrophoresis this effect appears to occur with fragment lengths longer than 1000 bp. Interestingly, for very short chain length fragments (<300 bp) the separation power might be increased by using a high applied electric field.^{6,19}

Figure 1 compares the separations of a ϕ X174 DNA *Hae*III restriction fragment mixture using different constant field strengths. Figure 1A shows the electropherogram of the test mixture when 100 V/cm electric field is applied to the gel-filled capillary column. At this low field strength DNA molecules act more like random coils, so good separation can be achieved even for fragments above 10^3 bp (sieving effect¹⁸). This separation of the larger fragments is attained at the cost of longer separation time (>50 min). However, some of the smaller fragments are not fully resolved. As Figure 1A shows,

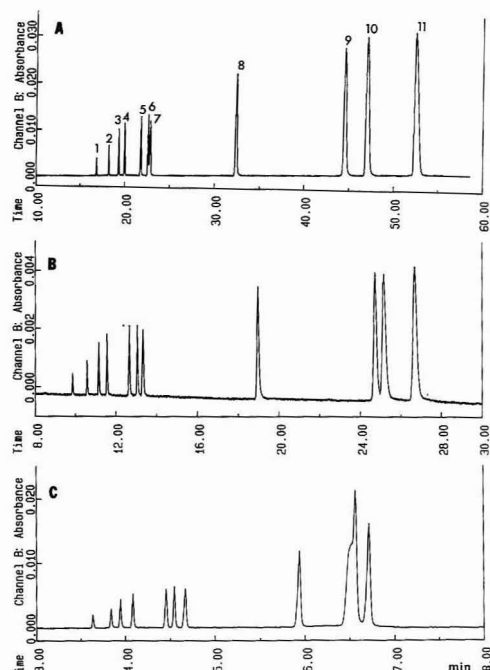


Figure 1. Separation of the ϕ X174 DNA restriction fragment mixture by capillary gel electrophoresis using constant applied electric field (isoelectrostatic): (A) 100, (B) 200, (C) 500 V/cm. Peaks were identified by their increasing area, which correlates to the chain lengths: 1 = 72, 2 = 118, 3 = 194, 4 = 234, 5 = 271, 6 = 281, 7 = 310, 8 = 603, 9 = 872, 10 = 1078, 11 = 1353 bp. Conditions: replaceable polyacrylamide gel column, effective length to detector 40 cm, total length 47 cm; buffer, 0.1 M Tris-borate, 2 mM EDTA (pH 8.35).

there is an incomplete separation between peak 6 and peak 7 (271- and 281-bp fragments). Similar results have been attributed by Karger and co-workers⁶ to diffusional band broadening due to the long separation time in very diluted gel-filled capillary columns. Increasing the applied electric field to 200 V/cm completes separation of all 11 fragments in 27 min (Figure 2B). The larger DNA molecules probably start to align with the electric field, and therefore resolution in the large-size range is not as complete as in Figure 1A. A further increase in field strength to 500 V/cm (Figure 1C), causes stronger alignment²⁰ of the larger fragments with a concomitant loss of resolution, since the sieving matrix can no longer separate some of the aligned molecules (peaks 9 and 10). However, the separation time decreases to 7 min and the lower molecular weight fragments (peaks 6 and 7) are separated completely due to the high applied electric field.¹⁹

On the basis of the results shown above we reasoned that enhanced separation of DNA molecules could be achieved by applying a nonuniform electric field (field strength gradient) at time. In this way all the different molecular weight range DNA molecules can be exposed to the electric field strength that is optimal for their separation.

In capillary polyacrylamide gel electrophoresis of DNA, when a uniform electric field (E) is applied to a charged polyanion under steady-state conditions,⁷ the electrophoretic velocity (v) can be expressed by the product of the electric field and

(16) Flint, D. H.; Harrington, R. E. *Biochemistry* 1972, 11, 4858-4864.

(17) Smizek, D. L.; Hoegland, D. A. *Science* 1990, 248, 1221-1223.

(18) De Gennes, P. G. *Scaling Concepts in Polymer Physics*; Cornell University Press: Ithaca, NY, 1979; Chapter 3.

(19) Lumpkin, O. J.; Dejardin, P.; Zimm, B. H. *Biopolymers* 1985, 24, 1573-1593.

(20) Slater, G. W.; Noolandi, J. *Biopolymers* 1986, 25, 431-454.

the electrophoretic mobility of the DNA molecule at the given field strength (μ):

$$v = \mu E \quad (1a)$$

However, this basic equation should be modified when a nonuniform field is applied [$E(t)$] since then the applied electric field is changed with respect to time (t), causing a change in the electrophoretic velocity of the polyion. We also should consider that the electrophoretic mobility of the DNA molecule is a function of the electric field [$\mu(E)$], as we reported earlier,²¹ so we can write

$$v(t) = \mu(E)E(t) \quad (1b)$$

Equation 1b states that the actual velocity, $v(t)$, of a DNA molecule is influenced by the field strength in use at a given time and by the mobility, which is also a function of the field strength. Thus, when a nonuniform electric field is applied, the electrophoretic acceleration (a) can be expressed as the change in electrophoretic velocity, i.e. the product of the electrophoretic mobility and the field strength at a given time:

$$a = dv/dt = d(\mu E)/dt \quad (2)$$

where dv and dt are the electrophoretic velocity and the time increments, respectively. On the basis of our earlier results,²¹ as a first approximation we can consider that the mobility of the double-stranded DNA molecules has a field-independent (μ_0) and a field-dependent component:

$$\mu = \mu_0 + S_1 E \quad (3)$$

where μ_0 is an extrapolated value of the electric field vs the mobility plot to zero field strength for a given chain length DNA molecule and S_1 is the slope value of the same plot ($r^2 = 0.987$). Since this slope values show a linear relationship with the chain length of the DNA molecules in the range we examined,¹¹ the following equation will hold:

$$S_1 = A + S_2 n \quad (4)$$

where A is a constant for a given gel-buffer system, S_2 is the slope of the S_1 versus n plot ($r^2 = 0.992$), and n is the chain length (base pair number) of the DNA molecule. Combining eqs 1-4 we obtain

$$a = dv/dt = d[\mu_0 + (A + S_2 n)E]/dt \quad (5)$$

thus

$$a = \mu_0 dE/dt + (A + S_2 n) dE^2/dt \quad (6)$$

where term I is the field strength only and term II is the field- and chain-length-dependent component. As an example, when the electric field strength is a linear function of time

$$E = B + Ct \quad (7)$$

where B and C are constants, then the electrophoretic acceleration of the polyion can be simply expressed as in eq 6:

$$a = \text{const}_1 + t \text{const}_2 \quad (8)$$

Peak efficiency (N) and resolution (R_s) are also affected by the momentary field strength.²² Thus, we conclude that after the proper substitutions, the change in the theoretical plate number is a linear function of the acceleration

$$\frac{dN}{dt} = \frac{d}{dt} \left(\frac{al}{2D} \right) = \frac{d}{dt} \left(\frac{\mu_0 + (A + S_2 n)E}{2D} l \right) \quad (9)$$

where l is the effective length of the capillary and D is the diffusion coefficient of the solute. The change in resolution

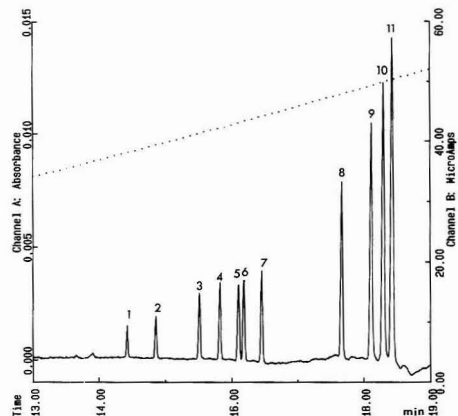


Figure 2. Separation of the ϕ X174 DNA restriction fragment mixture by capillary polyacrylamide gel electrophoresis using an increasing voltage gradient. The dotted line represents the current output. Conditions: continuous field strength gradient, 0–400 V/cm in 20 min; other conditions as in Figure 1.

is proportional to the square root²² of the acceleration, $dR_s/dt \sim d(a^{1/2})/dt$, when a linear field strength gradient is used.

Since different applied electric fields are optimal for the separation of different size DNA fragments,^{13–16,19–21} the use of a field strength gradient gives the opportunity to increase significantly the resolving power of the technique. Field strength gradients can be used in increasing, decreasing, or stepwise modes or in any combination thereof, if necessary.

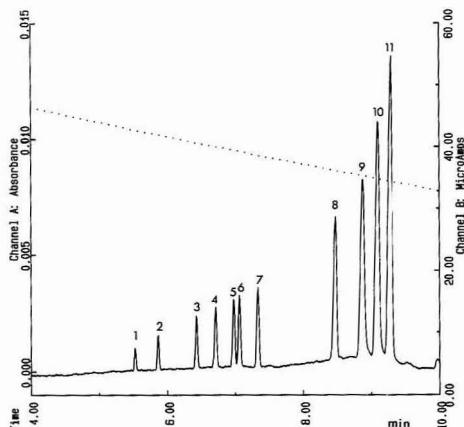
Figure 2 shows a separation of the ϕ X174 DNA restriction fragment mixture using increasing electric field strength over time (0–400 V/cm in 20 min). Full separation of all the test mixture components was achieved in less than 19 min. As Figure 2 shows, the apparent efficiency (i.e., theoretical plate number⁷ of the last several peaks (9–11) is greater compared to Figure 1B, where full separation of all the sample components was also attained. In this example, these fragments migrate faster past the detector window due to the higher field strength applied at the last part of the separation. Thus, consistent with the above, the apparent theoretical plate value N (eq 9, Table I), seems to be higher. (It is important to note here that the effect of the same phenomenon should be considered in peak area quantitation). Separation time was decreased by one-third by using the increasing field strength gradient method (compare to Figure 1B).

Conversely, the applied electric field can be decreased over time, as shown in Figure 3. Here, a decreasing field strength gradient of 400–100 V/cm in 20 min was applied to the linear polyacrylamide-filled capillary column. Baseline separation of all 11 components of the ϕ X174 restriction fragment mixture was achieved in less than 10 min, which is comparable to the separation time shown in Figure 1C. In the case of Figure 3, the larger fragments migrated past the detector window slower due to the lower field strength at the end of the separation. This causes an apparent loss in efficiency (eq 9, Table I) and resolution, particularly for the last three peaks.

In some instances the continuous ramping does not give sufficient separation between very closely related compounds (e.g., same chain length but different sequence DNA fragments). During continuous ramping, the time the DNA molecules are exposed to the field that is optimal for their separation may be too short. In this case a stepwise field

Table I. Theoretical Plate Number Values (RSD < 5%, $n = 9$) of the Peaks on Figures 1–4, Calculated by Using the System Gold Software Package (Beckman Instruments, Inc., Fullerton, CA)

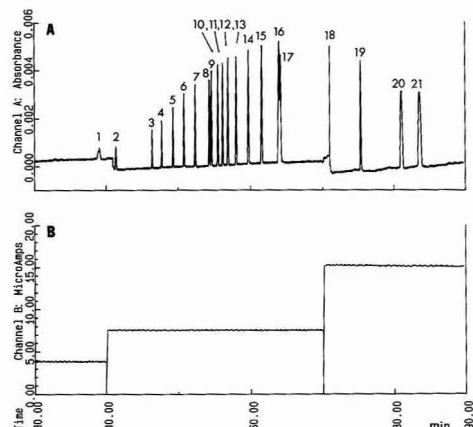
peak no.	no. of base pairs	100 V/cm (Figure 1A)	200 V/cm (Figure 1B)	500 V/cm (Figure 1C)	0–400 V/cm (Figure 2)	400–100 V/cm (Figure 3)
1	72	267 315	285 570	231 663	2 238 505	233 525
2	118	314 173	296 041	225 221	1 659 932	207 590
3	194	295 187	288 121	233 902	1 585 342	215 614
4	234	266 028	296 556	226 452	1 555 559	207 910
5	271	234 530	286 551	201 401	1 274 003	189 650
6	281	244 754	294 239	255 325	1 380 669	197 177
7	310	143 187	191 084	146 538	1 483 281	204 222
8	603	147 648	194 253	164 707	1 411 394	145 678
9	872	110 304	149 061		1 325 371	101 351
10	1078	86 257	100 610		1 162 954	113 796
11	1353	61 032	88 550	147 018	1 131 967	116 819

**Figure 3.** Separation of the ϕ X174 DNA restriction fragment mixture by capillary polyacrylamide gel electrophoresis using decreasing voltage gradient. The dotted line represents current output. Conditions: continuous field strength gradient, 400–100 V/cm in 20 min; other conditions as in Figure 1.

strength gradient is better because closely related molecules are exposed to their optimal separation field strength for a longer period of time, resulting in better resolution. Figure 4 shows the separation of a pBR322 DNA restriction fragment mixture employing a stepwise voltage gradient method in a longer capillary column (effective column length: 60 cm). The method consisted of three consecutive steps, 100 V/cm from 0 to 30 min, 200 V/cm from 30 to 70 min, and 400 V/cm from 70 to 100 min. In this way, full separation of almost all the components was attained. It is worth noting the baseline separation of peaks 8 and 9 (147-mers) and peaks 10 and 11 (160-mers), since these components have the same chain lengths but different sequences. These fragments could have been separated previously only by means of capillary affinity gel electrophoresis using ethidium bromide as an intercalating affinity ligand.²¹

CONCLUSION

A simple field strength gradient method was introduced in order to increase the resolving power in capillary polyacrylamide gel electrophoresis separation of DNA restriction fragment mixtures. The use of increasing, decreasing, or stepwise voltage gradient techniques showed that the resolving power can be optimized for a given DNA chain length range, and separation time can be significantly reduced. In our study on the separation of the ϕ X174 DNA restriction fragments by capillary polyacrylamide gel electrophoresis, the best separation with minimum time requirement was achieved by

**Figure 4.** Separation of the pBR322 DNA restriction fragment mixture by capillary polyacrylamide gel electrophoresis using an increasing stepwise gradient field. Channel B represents current output. Conditions: field strengths, 100 V/cm for 0–40 min, 200 V/cm for 40–70 min, 400 V/cm for 70–100 min; effective column length, 60 cm; other conditions as in Figure 1. Peaks: 1 = 26, 2 = 34, 3 = 67, 4 = 76, 5 = 90, 6 = 110, 7 = 123, 8 = 147, 9 = 147, 10 = 160, 11 = 160, 12 = 180, 13 = 190, 14 = 201, 15 = 217, 16 = 238, 17 = 242, 18 = 309, 19 = 404, 20 = 527, 21 = 622 bp.

using a continuously decreasing applied electric field. It is important to note that with the use of field strength gradient methods, the apparent peak efficiency and resolution may be misleading since the different size components migrate past the detector window with a velocity that is determined by the voltage in use at that point in time. Other types of gradients may be employed, such as current, power, and temperature, and the combination of those can also be used to optimize capillary gel electrophoretic separations of a given sample mixture.

ACKNOWLEDGMENT

We gratefully acknowledge Barry L. Karger for his stimulating discussions. We further thank Judy Nolan, Herb E. Schwartz, and Tom van de Goor for reviewing the manuscript before submission. The help of Phyllis Browning in the preparation of the manuscript is also highly appreciated.

RECEIVED for review April 16, 1992. Accepted July 14, 1992.

Collection Efficiency of Solid Surface and Sorbent Traps in Supercritical Fluid Extraction with Modified Carbon Dioxide

L. J. Mulcahey and L. T. Taylor*

Department of Chemistry, Virginia Polytechnic Institute and State University, Blacksburg, Virginia 24061

The effect of modifier on solid-phase trapping efficiency in off-line supercritical fluid extraction was studied. Two types of traps—solid surface (stainless steel) and sorbent (octadecyl silica)—were studied with pure carbon dioxide and 1%, 2%, 4%, and 8% methanol-modified carbon dioxide. The trapping efficiency of a polarity test mix consisting of *N,N*-dimethylaniline, acetophenone, naphthol, decanoic acid, and *n*-tetracosane was studied at trap temperatures ranging from 5 to 80 °C with each fluid. For low concentrations of methanol and the ODS sorbent, trap temperatures below 20 °C were necessary for volatile (bp < 200 °C) analytes. With less volatile analytes, trapping was near 100% regardless of the trap temperature. To achieve maximum recovery at high (>2%) methanol concentrations, elevated trap temperatures were required. At 8% methanol, efficiency was less than 50% for all analytes regardless of the temperature, except tetracosane. Stainless steel trapping was less satisfactory since analytes boiling less than 200 °C yielded approximately 15% recovery with 100% CO₂. With 1% methanol-modified CO₂, collection efficiency was actually improved to near 50% because trapping was believed to be via a thin layer of methanol absorbed on the stainless steel surface. Higher concentrations of methanol, however, resulted in essentially no trapping. For the less volatile analytes collection efficiency was quantitative with 1% methanol-modified CO₂ for trap temperatures 50–80 °C. Higher concentrations of methanol resulted in less efficient trapping.

INTRODUCTION

There are two general requirements that must be met in order to successfully perform off-line analytical supercritical fluid extraction (SFE). First, the extraction parameters must be chosen correctly, given that the analyte is soluble in the extraction fluid. Even at this point strong matrix interactions may preclude direct extraction of the analyte. Second, the trapping system used must perform efficiently. Two basic trapping philosophies have been espoused: liquid solvent and solid matrices. The majority of reports to date have utilized trapping in liquid solvents. SFE collection efficiencies of 66 compounds with a wide range of volatility and polarity have recently been reported.¹ Greater than 90% trapping of all test analytes with 100% CO₂ was attained by controlling the trap temperature at 5 °C with methylene chloride as the solvent (e.g. 2–10 mL of solvent maintained by small additions during SFE). A systematic evaluation of several sorbent traps and a solid surface trap has recently been presented with a five-component polarity mix and with a series of both hydrocarbons and phenols.² In all of this work only pure carbon dioxide was used. The effect of modifiers on solid

phase and solvent traps has not been seriously studied. If the trap is maintained above the boiling point of the modifier, the modifier should vaporize upon contact with the trap and vent to waste. However, the analytes of interest may not trap effectively at the temperatures required to vaporize the modifier. On the other hand, if the trap temperature is maintained at temperatures below the boiling point of the modifier the modifier may condense on the stationary phase and influence the trapping efficiency. It should be noted, however, that there are a number of reports that describe the quantitative collection (and extraction) of both more and less volatile and more and less polar analytes using modified CO₂ by liquid trapping.^{3–5} Data describing collection of analytes into liquid solvents under identical pressure/temperature/flow conditions employing modified fluids are however not available. Instances employing solid matrix trapping and modified fluids have been less numerous in quantitative SFE studies.⁶

The goal of the work reported here was to determine what effect modifier has on the efficiency of solid surface and sorbent traps. Stainless steel beads were investigated as the solid surface trap and octyldecyl bonded silica (ODS) was used for the sorbent trap. The effect of modifier on the trap is an extremely important parameter. Often modifier is added to a fluid in an attempt to improve extraction recoveries or decrease extraction time. However, if modifier is causing the trap to perform less efficiently than it would with a pure fluid, the benefit of adding the modifier may be reduced or lost. A search of the literature resulted in no studies regarding the influence of modifier on trapping efficiency for off-line SFE with sorbent or solid-phase traps.

EXPERIMENTAL SECTION

A Hewlett Packard (Avondale, PA) 7680A supercritical fluid extractor was used for all work reported here. This instrument was modified so that a reproducible amount (50 µL) of sample could be introduced into the system. A six-port external loop injection valve (Valco, Houston, TX) was plumbed in-line between the extraction vessel and the pressure isolation valve. A 0.5-mL dead volume (i.e. empty extraction vessel) was introduced after the injection valve so that mixing of the injected components and the extraction fluid would occur.

The trapping system on the 7680A consists of a temperature-controlled stainless steel housing with frits on both ends. Approximately 1 mL of either 100-µm stainless steel beads or 40-µm silica-based ODS chromatographic packing material (Hypersil) filled the trap. The trap temperature during the extraction step varied from 5 to 80 °C. After the SFE simulation step (no matrix) was completed, analytes were recovered from the trap by rinsing with methylene chloride, wherein the trap temperature and solvent rinse volume were controlled. The trap temperature was maintained at 30 °C during rinsing, and 2.6 mL

(1) Langenfeld, J. J.; Burford, M. D.; Hawthorne, S. B.; Miller, D. J. *J. Chromatogr.* 1992, 594, 297.

(2) Mulcahey, L. J.; Hedrick, J. L.; Taylor, L. T. *Anal. Chem.* 1991, 63, 2225.

(3) Wheeler, J. R.; McNally, M. E. *J. Chromatogr. Sci.* 1989, 27, 534.

(4) Janda, V.; Steenbeke, G.; Sandra, P. *J. Chromatogr.* 1989, 479, 200.

(5) Hawthorne, S. B.; Miller, D. J. *Anal. Chem.* 1987, 59, 1705.

(6) Howard, A. L.; Taylor, L. T. *Supercritical Fluid Extraction of Chlorsulfuron and Sulfometuron Methyl From Aqueous Matrices*. Pittsburgh Conference and Exposition on Analytical Chemistry and Applied Spectroscopy, New Orleans, LA, March 1992; Paper No. 308.

Table I. Percent Recovery and RSD's for Selected Volatile Compounds with Pure Carbon Dioxide on the ODS Trap

trap temp (°C)	acetophenone ^a		<i>N,N</i> -dimethylaniline ^b	
	% rec	RSD	% rec	RSD
5	96.3	1.7	94.7	2.7
10	102.3	2.1	100.4	2.8
20	102.2	2.8	100.4	2.8
30	58.2	3.4	61.5	3.7
40	23.6	0.6	19.2	0.8
50	27.3	0.7	21.8	0.6
65	15.4	0.6	15.1	0.7
80	9.6	0.6	10.8	0.4

^a Acetophenone: 120.15 amu, mp = 20 °C, bp = 202 °C. ^b *N,N*-Dimethylaniline: 121.18 amu, mp = 2 °C, bp = 193 °C.

Table II. Percent Recovery and RSD's for the Nonvolatile Compounds with Pure Carbon Dioxide on the ODS Trap

trap temp (°C)	<i>n</i> -decanoic acid ^a		2-naphthol ^b		<i>n</i> -tetracosane ^c	
	% rec	RSD	% rec	RSD	% rec	RSD
5	75.1	3.0	94.8	2.0	97.5	1.6
10	78.2	3.4	99.8	2.5	100.7	2.7
20	76.4	3.4	99.2	2.5	99.5	1.7
30	76.7	4.8	96.6	1.6	97.7	1.1
40	80.1	3.9	94.9	1.8	98.0	2.0
50	83.4	4.9	93.4	1.5	97.7	1.1
65	85.3	4.0	92.6	5.6	97.4	1.1
80	90.1	4.6	91.3	2.4	97.1	1.7

^a *n*-Decanoic acid: 172.26 amu, mp = 31.4 °C, bp = 270 °C. ^b 2-Naphthol: 144.16 amu, mp = 122 °C, bp = 285 °C. ^c *n*-Tetracosane: 398.63 amu, mp = 125 °C, bp = 300 °C.

of rinse solvent was passed through the trap (two 1.3-mL fractions) to collect the sample. Any irreproducibility in rinse solvent volume was eliminated through the use of an internal standard (anthracene) that was added to each 2-mL autosampler rinse vial before rinsing so that analyte/anthracene peak area ratios and not absolute peak areas could be used.

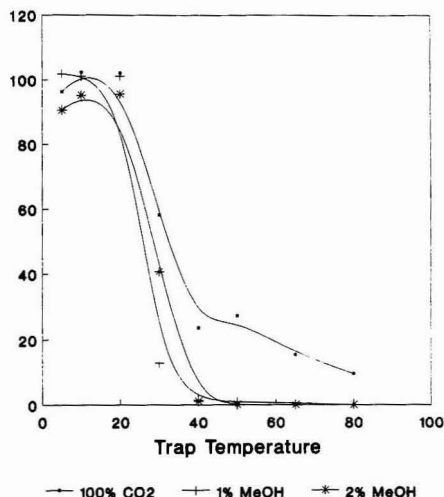
The compounds used to evaluate trapping efficiency consisted of a mixture of acetophenone, *N,N*-dimethylaniline, *n*-decanoic acid, 2-naphthol, and *n*-tetracosane dissolved in methylene chloride at approximately 1 mg of component/mL. Since CH₂Cl₂ has a density of 1.317 g/mL at 25 °C, each component was present in solution at approximately 0.07% (w/w). The molecular weights and melting and boiling points for these compounds are listed in Tables I and II. The test mix components were all obtained from Aldrich Chemical Co. (Milwaukee, WI). Carbon dioxide was obtained from Air Products (Allentown, PA) while the 1%, 2%, 4%, and 8% methanol-modified carbon dioxide was provided by Scott Specialty Gases (Plumsteadville, PA). Methanol-modified tanks were supplied with 1500 psi of helium headspace, while the pure carbon dioxide had no headspace.

The specific protocol for trap evaluation with the previously stated polarity mix was as follows. Analytes were transferred to the trap by placing the filled sample loop (50 μ L) in line with the fluid path for a period of 10 min at a liquid flow rate of 2 mL/min at 340 bar with an oven temperature of 75 °C and a nozzle temperature (variable restrictor) of 50 °C. Recovery of analyte was monitored at trap temperatures of 5, 10, 20, 30, 40, 50, 65, and 80 °C. Three replicate "extractions" were done at each trap temperature. The extracts were analyzed by gas chromatography on a Hewlett Packard (Avondale, PA) 5890 Series II GC equipped with an autosampler. The column used was an HP-5 (5% phenylmethylsiloxane) and was 25 m \times 0.2 mm with a film thickness of 0.33 μ m. A 1- μ L purged splitless injection was used. The initial column temperature was held at 75 °C for 0.5 min and ramped to 300 °C at 25 °C/min.

Peak area ratios representing complete recovery were obtained as follows. The injection valve was plumbed so that the 50- μ L loop was filled in the load position with the sample of interest through a needle port. Once the loop was filled the position of the valve was changed from load to inject. The loop was then rinsed with methylene chloride into a 2-mL vial where anthracene

Table III. Percent Recovery and RSD's for the Volatile Compounds with 1% and 2% Methanol-Modified CO₂ on the ODS Trap

trap temp (°C)	acetophenone				<i>N,N</i> -dimethylaniline			
	1%		2%		1%		2%	
	% rec	RSD	% rec	RSD	% rec	RSD	% rec	RSD
5	101.9	1.8	90.6	3.8	100.7	1.8	90.2	3.6
10	101.2	1.7	95.3	1.8	100.4	1.7	94.7	1.8
20	101.3	2.0	95.7	3.5	101.6	1.9	93.6	3.6
30	12.9	1.0	40.8	1.1	84.8	3.7	88.0	1.4
40	1.4	0.3	1.1	0.2	7.4	1.2	10.1	0.4
50	0.9	0.1	0		4.6	0.4	4.9	0.4
65	0.6	0.1	0		1.9	0.1	2.4	0.4
80	0		0		1.3	0.1	1.0	0.4

**Figure 1. Acetophenone recovery versus trap temperature for 100% CO₂, 1% methanol, and 2% methanol.**

(200 μ L of 1 mg/mL) was added as an internal standard, and then the mixture was analyzed by GC. The values for peak area ratios obtained (peak area of compound/peak area of internal standard) for five replicate experiments were used for 100% numbers. The relative standard deviations obtained for the peak area ratios were typically in the range 1–2%.

RESULTS AND DISCUSSION

Experimental Considerations. With neat sample introduction through a sample loop the kinetics of extraction are eliminated in this study since an actual extraction (i.e. no matrix) is not occurring. On the basis of the known structure/solubility data⁷ and the absence of any clogging of the extraction system after more than 150 injections of the "test mix", it is safe to assume that all of the components of the test mixture are sufficiently soluble in carbon dioxide. Furthermore, the weight percent ratio of compound to trapping phase was low (0.3%), indicating that analyte breakthrough was very unlikely (i.e. 1 μ g/ μ L \times 50- μ L injection volume \times 5 components = 250 μ g loaded onto 100 mg of sorbent material).

Because there are residual silanol groups present on the ODS trapping material used in this work, two types of sorptive

(7) *Analytical Supercritical Fluid Chromatography and Extraction*; Lee, M. L., Markides, K. E., Eds.; Chromatography Conferences Inc.: Provo, UT, 1990; p 320.

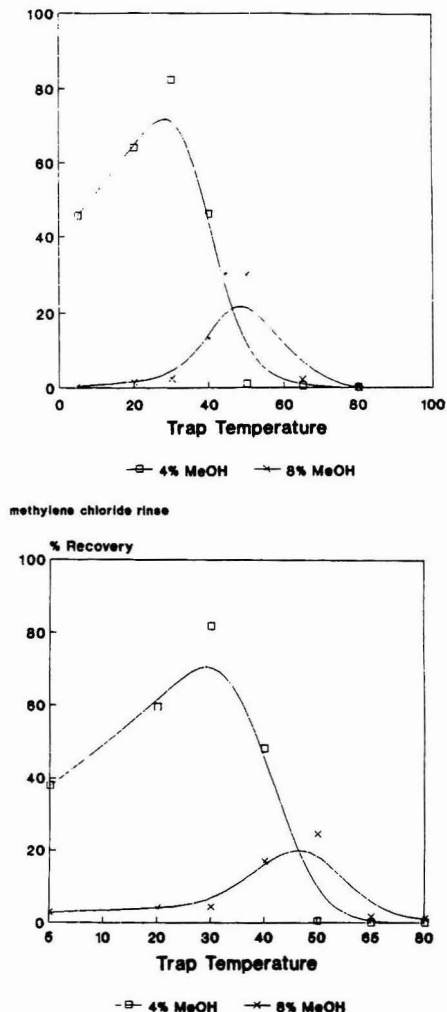
Table IV. Percent Recovery and RSD's for the Nonvolatile Compound with 1% and 2% Methanol-Modified CO₂ on the ODS Trap

trap temp (°C)	decanoic acid				2-naphthol				n-tetracosane			
	1%		2%		1%		2%		1%		2%	
	% rec	RSD	% rec	RSD	% rec	RSD	% rec	RSD	% rec	RSD	% rec	RSD
5	91.2	8.2	75.6	13.5	99.8	2.9	95.4	4.6	102.5	2.5	93.7	5.8
10	87.9	2.0	75.9	1.4	99.6	2.5	94.0	1.3	100.3	2.1	90.1	1.8
20	91.1	2.1	76.1	4.9	98.9	2.9	93.2	4.2	100.7	2.4	90.4	4.6
30	83.2	2.9	77.6	2.0	94.2	2.6	87.7	1.8	92.8	2.0	88.3	2.3
40	86.4	3.5	74.6	2.0	95.3	4.3	91.3	1.3	97.2	2.4	94.4	1.8
50	87.0	2.4	74.9	2.0	94.9	2.6	90.8	1.8	94.5	2.3	93.9	2.4
65	92.3	3.0	78.0	4.2	97.9	3.5	92.6	3.4	97.4	2.6	96.5	3.5
80	91.4	2.1	75.2	1.4	95.7	2.5	90.3	1.3	96.7	2.2	94.7	1.8

interactions can occur.⁸ There can be sorptive interactions between the solutes and the ODS phase (dispersive forces) and there can be sorption between the silanol groups and the analytes (hydrogen bonding or forces stronger than dispersive). At the trap temperatures used in this work (5–80 °C) the ODS phase should be stable since there is flow of carbon dioxide passing through it when it is heated (i.e. the phase is not being "baked") and the temperatures used were not high enough to remove any physically adsorbed water.⁹ It is unlikely that carbon dioxide at 80 °C would be able to dehydrate the stationary phase since the solubility of water in supercritical carbon dioxide is low¹⁰ (0.1%). The stainless steel beads used in this work were 100- μ m 316 stainless steel with high nickel content. These beads have low carbon content and are not subjected to acid or heat pretreatment. The mechanism of action for analyte trapping on stainless steel beads is supposed to be cryotrapping only. However, there may be an oxide layer present that could lead to appreciable adsorption of either methanol or other analytes.

ODS Trap Studies. Table I shows the percent recoveries and their associated relative standard deviations for the two most volatile components of the test mixture, acetophenone and *N,N*-dimethylaniline. At trap temperatures of 5, 10, and 20 °C high recoveries and low relative standard deviations were obtained. At a trap temperature of 30 °C, however, the recoveries of the volatiles dropped to approximately 60%. At trap temperatures of 40 and 50 °C recoveries of both compounds dropped even further to 20–25%, and finally at temperatures above 50 °C recoveries of 10–15% were obtained. For efficient solid-phase trapping of volatile compounds (bp < 200 °C) it therefore appears that two trapping mechanisms are required—cryotrapping and absorption. Table II shows the percent recoveries and relative standard deviations obtained for *n*-decanoic acid, 2-naphthol, and *n*-tetracosane on the ODS trap with 100% CO₂. As can be seen from the table the behavior of these less volatile (bp > 200 °C) analytes is drastically different from the more volatile analytes. Decanoic acid yielded the lowest recovery (75–80%) at low trap temperatures (5–40 °C). However, as the trap temperature was increased above 40 °C, decanoic acid recovery surprisingly improved until it reached 90% at a trap temperature of 80 °C. Since the rinse conditions were constant at all trap temperatures, it can be assumed that any variation in recoveries was due to the trapping portion of the experiment. Trapping of 2-naphthol and *n*-tetracosane was statistically unaffected by trap temperature.

Table III shows the percent recoveries obtained for acetophenone and *N,N*-dimethylaniline over 5–80 °C with 1% and 2% methanol as the fluid phase. The recoveries (>90%) and RSD's (<4%) of the volatiles were very good at

**Figure 2.** Recovery versus trap temperature for acetophenone (top) and *N,N*-dimethylaniline (bottom) on the ODS trap with 4% and 8% methanol in carbon dioxide.

trap temperatures from 5 to 20 °C. As was the case when pure carbon dioxide was used, recoveries of the volatiles dropped drastically when a trap temperature of 30 °C was

(8) Janssen, J. G. M.; Schoenmakers, P. J.; Cramers, C. A. *HRC & CC* 1989, 12, 645.

(9) Snyder, L. R.; Kirkland, J. J. *Introduction to Modern Liquid Chromatography*; John Wiley & Sons, Inc.: New York, 1979; p 276.

(10) Hedrick, J. L.; Taylor, L. T. *HRC & CC* 1990, 13, 312.

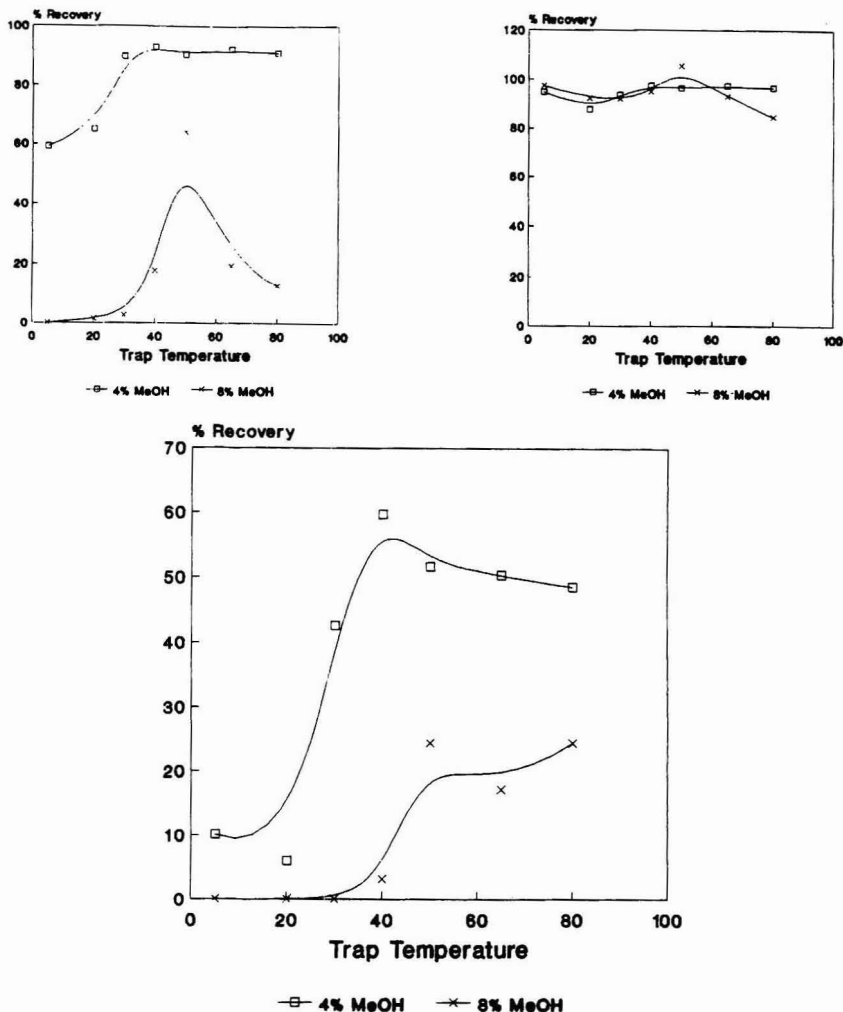


Figure 3. Recovery versus trap temperature for decanoic acid, (bottom), 2-naphthol (left), and *n*-tetracosane (right) on the ODS trap with 4% and 8% methanol in carbon dioxide.

used (Figure 1). Acetophenone recovery at a trap temperature of 30 °C with 1% methanol was 12.9%, while *N,N*-dimethylaniline recovery was 84.8%. This disparity in recovery was also observed with 2% methanol. At trap temperatures of 40 °C and above the recoveries of both compounds were low, with the recovery of acetophenone generally being the lowest of the two. The disparity in recovery of acetophenone and *N,N*-dimethylaniline at 30 °C can be explained by examining the interactions of each compound with the stationary phase. Both compounds are soluble in CH_2Cl_2 , and their boiling points are similar. However, *N,N*-dimethylaniline would be expected to have stronger interactions with the stationary phase, especially the silanol sites, than acetophenone would, since *N,N*-dimethylaniline is basic. It should also be more difficult for the CH_2Cl_2 rinse to remove *N,N*-dimethylaniline from the stationary phase than to remove acetophenone, which is not held as strongly.

Table IV shows recoveries versus trap temperature for the nonvolatile components of the test mixture with 1% and 2%

methanol in carbon dioxide. Upon first examination of the figure it appears that there is little effect on recovery for the nonvolatiles when methanol is present relative to pure CO_2 over the entire temperature range. However, when pooled *t*-tests were performed, differences at the 95% confidence level were revealed. For example, recoveries of decanoic acid were statistically higher at low trap temperatures (5–40 °C) when 1% methanol was used as the mobile phase as compared to recoveries obtained with pure carbon dioxide. The role of the methanol at this concentration may be to form a thin film on the ODS phase, thereby providing an additional trapping mechanism in the polar methanol. As the trap temperature increases, the amount of methanol on the stationary phase decreases so that recoveries do not differ significantly between pure carbon dioxide and 1% methanol at trap temperatures above 40 °C.

When 2% methanol was added to the mobile phase the recoveries of decanoic acid dropped in comparison to those obtained with 1% methanol over the entire temperature range.

There are three possible explanations for this behavior. First, methanol could again be forming a film on the surface of the bonded phase. However, with the greater concentration of methanol the film may be thick and not mechanically stable. Therefore, as decompressed carbon dioxide passes through the trap at flow rates from 200 to 2000 mL/min, analyte and methanol could be mechanically pushed through the trap. The second way that 2% methanol could cause a decrease in recovery relative to 1% methanol is by forming a film over the ODS stationary phase and preventing some of the dispersive interactions to occur that lead to the efficient trapping. The third way that 2% methanol could be causing a decrease in decanoic acid recovery relative to 1% methanol is by increasing the strength of the fluid phase and causing more decanoic acid to partition into it.

When 2-naphthol and *n*-tetracosane recoveries obtained with pure carbon dioxide and 1% methanol were compared, no statistical difference was found over the entire temperature range. When the recoveries of both analytes with pure carbon dioxide were compared to those obtained with 2% methanol it was found that recoveries were statistically higher when pure carbon dioxide was used over the 5–40 °C temperature range. At temperatures above 40 °C there was no difference in recovery.

Figure 2 shows the results obtained for acetophenone and *N,N*-dimethylaniline over the 5–80 °C range with 4% and 8% methanol. As can be seen by comparing Table III and Figure 2, the trend observed with 1% and 2% methanol is no longer observed. Instead of the high recoveries at low trap temperatures and low recoveries at high trap temperatures, a maximum recovery was obtained at a temperature that is dependent on the methanol concentration. With 4% methanol in the fluid phase maximum recoveries were obtained at 30 °C, while a trap temperature of 5 °C resulted in recovery maxima for 8% methanol. The shape of the percent recovery versus trap temperature curves for the volatile components is believed to be a result of two competing mechanisms. At low trap temperatures methanol condenses on the stationary phase where *N,N*-dimethylaniline and acetophenone dissolve in it. These components are then mechanically removed from the trap by the decompressed carbon dioxide. As the trap temperature is increased, methanol begins to vaporize, and the amount of methanol on the stationary phase decreases. The decreased amount of methanol on the stationary phase allows the acetophenone and *N,N*-dimethylaniline to more strongly interact with the stationary phase, leading to an increase in recovery. Above the maximum recovery temperature the percent recovery curves followed the same trend seen with 100% carbon dioxide, 1% methanol, and 2% methanol for the volatiles (i.e. as trap temperature increases the vapor pressure of the analytes increases and recovery decreases).

Figure 3 shows the recovery versus trap temperature curves for the nonvolatile compounds with 4% and 8% methanol. The percent recovery versus trap temperature curves for decanoic acid and 2-naphthol are similar to what was seen for the volatiles at low temperatures (i.e. recoveries increased as trap temperature was increased). Since the boiling points of these analytes and the volatile components of the test mix are so different, their similar behavior may be due to the fact that decanoic acid and 2-naphthol are very soluble in methanol. Unlike the volatile components, the recovery of both compounds did not decrease at temperatures above 40 °C. Instead, recovery remained constant, although statistically lower than what was obtained with 2% methanol. When methanol concentration was increased to 8% the same trend as was seen with 4% methanol was observed, but with lower recoveries. Recoveries obtained for *n*-tetracosane with 4%

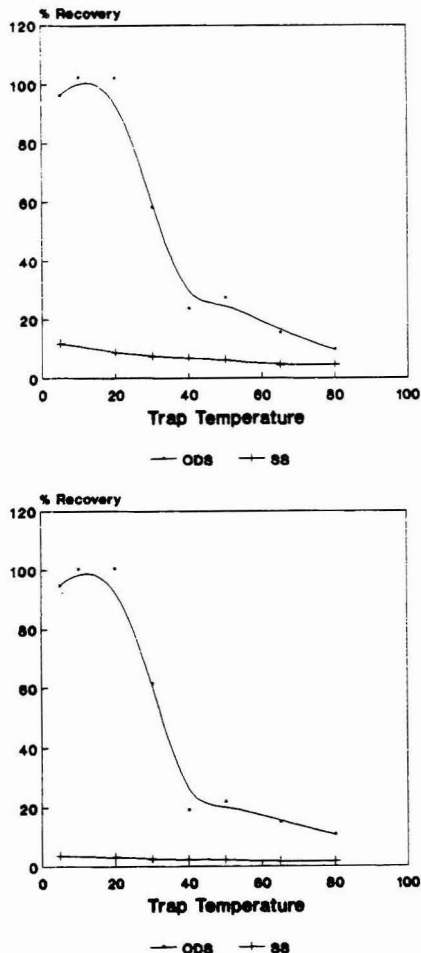


Figure 4. Recovery versus trap temperature for acetophenone (top) and *N,N*-dimethylaniline (bottom) on stainless steel and ODS traps with pure carbon dioxide.

and 8% methanol were not statistically different from those obtained with 2% methanol.

Stainless Steel Trap Studies. Figure 4 shows the percent recovery versus trap temperature curves obtained over 5–80 °C for the volatile components of the test mixture with pure CO₂ by employing singly ODS and stainless steel traps. Neither of the trends that were observed with the ODS trap was observed on the stainless steel trap. Acetophenone recovery at 5 °C was 11.7%, while *N,N*-dimethylaniline recovery was 3.6%. Obviously a lower trap temperature is needed for these two polar compounds. The difference in recoveries of these compounds at low trap temperatures reflects the slight differences in volatility of these compounds. Figure 5 shows the recoveries versus trap temperature for the nonvolatile components with 100% CO₂ employing ODS and stainless steel individually. Decanoic acid recovery was low at low temperatures (26.3% at 5 °C) and increased as the trap temperature increased up to 50 °C, after which recovery (~50%) remained constant. In comparison, the recoveries

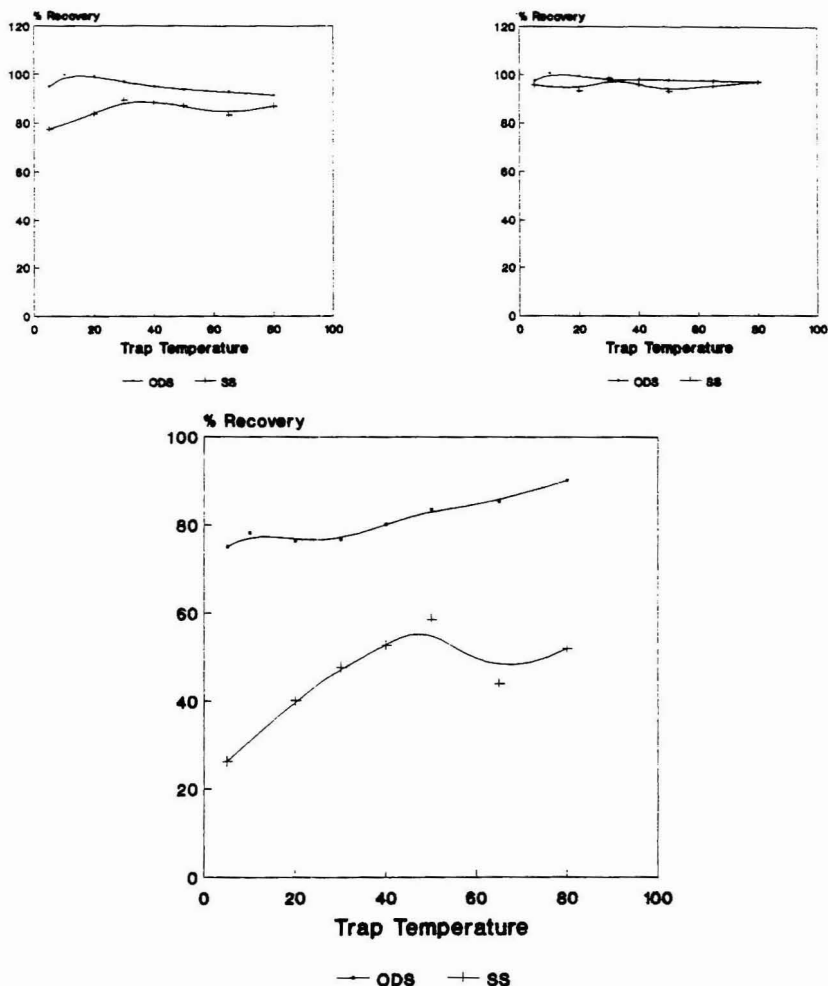


Figure 5. Recovery versus trap temperature for decanoic acid (bottom), 2-naphthol (left), and *n*-tetracosane (right) on stainless steel and ODS traps with pure carbon dioxide.

were generally higher on the ODS phase, indicating that the dispersive interactions between the hydrophobic chain of decanoic acid and the ODS phase contributed to the recoveries obtained. Recoveries of 2-naphthol and *n*-tetracosane on stainless steel were generally high and unchanged with trap temperature, as was also the case for the ODS trap.

Table V shows the recovery profiles for each compound with the stainless steel trap with 1% methanol as the fluid phase. The volatile components are shown as only two points since at trap temperatures greater than 5 °C recoveries of *N,N*-dimethylaniline and acetophenone were 0%. Recoveries of the volatiles were greater at 5 °C with 1% methanol as compared to the recoveries obtained with pure carbon dioxide. This increase in recovery is probably due to the formation of a thin film of methanol which is physisorbed to the stainless steel surface. The recovery of decanoic acid followed the same trend as seen before, with increased recovery as trap temperature increased. Recoveries were constant from 5 to 40 °C at 70–75% for both naphthol and *n*-tetracosane. Both of these compounds are fairly nonpolar and therefore do not

Table V. Percent Recovery for Components of Polarity Mix with 1% Methanol-Modified CO₂ on Stainless Steel

trap temp (°C)	aceto-phenone	<i>N,N</i> -dimethyl-aniline	decanoic acid	2-naphthol	<i>n</i> -tetra-cosane
5	61.3	46.3	32.6	68.5	72.8
20	0	0	45.0	69.3	72.8
30	0	0	50.0	71.0	74.1
40	0	0	56.6	76.7	79.6
50	0	0	67.0	92.9	100.2
65	0	0	69.7	91.7	96.2
80	0	0	71.6	91.7	95.5

trap as efficiently in the thin film of methanol suspected to lie on the stainless steel surface as the polar analytes do. However, as the trap temperature was increased, the amount of methanol on the solid surface decreased, and the recovery of both compounds increased to the 90–100% range.

Because the only compounds to be significantly affected by 1% methanol were the volatiles, recoveries of only the volatiles were determined with 2% and 4% methanol as the

fluid phase at a trap temperature of 5 °C. When 2% methanol was used, the recoveries of the volatiles were lower than those obtained with pure carbon dioxide. The greater concentration (71%) of methanol apparently forms a thicker film that can be mechanically pushed through the trap by the decompressed carbon dioxide. The volatile components are believed to dissolve in and travel with the methanol and exit the trap, resulting in lower recoveries. At a methanol concentration of 4%, recoveries of acetophenone and *N,N*-dimethylaniline were negligible. The maximum recoveries for the volatiles on the other hand occurred with 1% methanol rather than pure CO₂ which gives credence to the idea that these analytes were trapped in a thin film of methanol that coated the stainless steel beads.

CONCLUSIONS

The effect of methanol on trapping efficiency of solid surface and sorbent traps was found to vary greatly with methanol concentration. For methanol concentrations of 2% or less on the ODS trap, it was not necessary to maintain the trap temperature above the boiling point of the methanol. For methanol concentrations above 2% on the ODS trap, low trap temperatures resulted in inefficient trapping due to the presence of condensed methanol on the stationary phase. Recovery maxima were obtained in the 30–50 °C range, depending on the methanol concentration. For the nonvolatile compounds trap temperature had no effect on recovery when 1% and 2% methanol was used. However, when greater concentrations of methanol were used, trap temperatures of at least 40–50 °C were required to obtain efficient trapping. For efficient recovery of the volatile compounds on the stainless steel trap, the addition of a modifier to establish a thin film on the surface drastically improved recovery.

However, the addition of too great a concentration of modifier allowed for mechanical rinsing of the trap. For the nonvolatile compounds high recovery could generally be obtained when methanol was in the fluid phase if trap temperatures exceeded 40 °C.

Several things should be kept in mind in order to view these data practically. Although the compounds in the test mix were referred to as volatiles and nonvolatiles in this text, all of the compounds were GC detectable. During an actual extraction, if acetophenone and *N,N*-dimethylaniline were the analytes of interest, it is likely that pure carbon dioxide and an ODS trap would be used. Modifiers are generally used in dealing with more polar or higher molecular weight compounds. With these types of compounds it would be reasonable to expect behavior closer to that of C₂₄. It is obvious from this work that the addition of modifier can have drastic effects on the ability of a solid-phase trap to function. The vapor pressure of the components, their solubility in the modifier, and the type of trap material must all be considered in order to successfully trap extracted components.

ACKNOWLEDGMENT

We acknowledge Hewlett Packard, specifically William Pipkin, for the loan of the extractor. We also acknowledge Joe Hedrick and Dale Messer for their valuable discussions regarding this work. We thank Air Products and Chemicals, Inc. and Scott Specialty Gases for financial support.

RECEIVED for review February 12, 1992. Accepted July 6, 1992.

Registry No. CO₂, 124-38-9; methanol, 67-56-1; stainless steel, 12597-68-1.

Processing Analytical Data Obtained from Second-Order Reactions by Using Continuous Reagent Addition

Antonio Velasco, Manuel Silva, and Dolores Pérez-Bendito*

Department of Analytical Chemistry, Faculty of Sciences, University of Córdoba, E-14004 Córdoba, Spain

This paper reports a new approach to second-order kinetic analyses based on the continuous addition of the reagent to the analyte solution at a constant rate. A mathematical model was developed to study the kinetics of the process. Methods for the determination of the analyte and the second-order rate constant were developed and tested experimentally. The Fe(II)/SCN⁻ system in the presence of hydrogen peroxide as analyte was used as the model reaction. The methods for the determination of hydrogen peroxide thus developed are compared by using a least-squares fit procedure; those used to obtain the second-order rate constant perform quite well with relative standard deviations between 2-5%.

INTRODUCTION

The significance of kinetic approaches to analytical chemistry has been widely recognized^{1,2} and emphasized in recent reviews.^{3,4} In the last few years, new techniques for the kinetic determination of first- and general-order direct reactions have been developed.⁵⁻⁸ In this work we developed a novel approach to processing analytical data from second-order reactions by using a mathematical treatment that relates kinetic parameters with the experimental variables involved in an open system based on the continuous addition of a reagent solution at a constant rate to another solution containing the analyte to be determined. This mathematical treatment also allows the second-order rate constant of the system to be determined. The chief advantages of this approach lie in the fact that it allows the kinetic response curve to be readily obtained from both slow and fast reactions (for which the first-order condition is commonly used) with straightforward instrumentation since the reaction is made second-order.

Two unconventional analytical kinetic methods and five procedures for determining the second-order rate constant by using the above-mentioned treatment are presented and discussed. The Fe(II)/SCN⁻/H₂O₂ system was chosen to illustrate the applicability of this new approach.

THEORETICAL BASIS OF THE METHOD

For a second-order irreversible reaction such as that shown in



where A is the analyte, R the reagent, and P the product

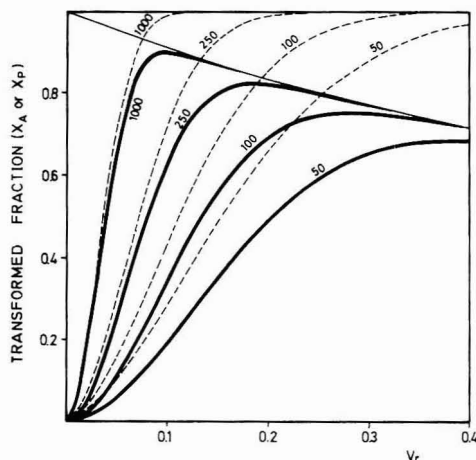


Figure 1. Simulated plots of transformed fraction vs volumetric ratio of added reagent for the hypothetical second-order reaction of eq 1 at different γ values, with reaction monitoring via (—) the product or (---) the analyte. Curve (—) corresponds to the dilution process. These curves also correspond to the variation of the addition rate for 3, 12, 30, and 60 mL/min and γ between 1000 and 50, respectively. ($k = 1.0 \text{ s}^{-1} \text{ M}^{-1}$, $[R]_0 = 1.0 \text{ M}$, and $V_0 = 50 \text{ mL}$).

formed, the reaction rate can be written as

$$-\left[\frac{d[A]}{dt}\right]_{\text{reaction}} = k[A][R] \quad (2)$$

where k is the second-order rate constant. If a solution of a reagent at a concentration $[R]_0$ is added at a constant rate u to a volume V_0 of a solution containing the analyte, its concentration can be expressed by

$$[R] = [R]_0 \frac{ut}{V_0 + ut} - \left(\frac{[A]_0 V_0}{V_0 + ut} - [A] \right) \quad (3)$$

If $[R]_0 \gg [A]_0$ and the addition rate is such that throughout the amount of reagent consumed is very much smaller than that which is added, this equation can be simplified to

$$[R] = [R]_0 \frac{ut}{V_0 + ut} \quad (4)$$

The dilution rate of the analyte A is given by

$$-\left[\frac{d[A]}{dt}\right]_{\text{dilution}} = [A] \frac{u}{V_0 + ut} \quad (5)$$

and the overall rate is found to be

$$-\frac{d[A]}{dt} = k[A][R]_0 \frac{ut}{V_0 + ut} + [A] \frac{u}{V_0 + ut} \quad (6)$$

(1) Mottola, H. A. *Kinetic Aspects of Analytical Chemistry*; Wiley: New York, 1988.

(2) Pérez-Bendito, M.; Silva, M. *Kinetic Methods in Analytical Chemistry*; Ellis Horwood: Chichester, U.K., 1988.

(3) Pardue, H. L. *Anal. Chim. Acta* 1989, 216, 69.

(4) Mottola, H. A.; Pérez-Bendito, D.; Mark, H. B. *Anal. Chem.* 1990, 62, 441R.

(5) Laios, I.; Fast, D. M.; Pardue, H. L. *Anal. Chim. Acta* 1986, 180, 429.

(6) Sarson, J. A.; Pardue, H. L., *Anal. Chim. Acta* 1989, 224, 289.

(7) Fitzpatrick, C. P.; Pardue, H. L. *Anal. Chem.* 1989, 61, 2551.

(8) Schechter, I. *Anal. Chem.* 1991, 63, 1303.

the integrated form of which is

$$\ln \frac{[A]}{[A]_0} = -k[R]_0 t + \frac{k[R]_0 V_0}{u} \ln \left[\frac{V_0 + ut}{V_0} \right] - \ln \left[\frac{V_0 + ut}{V_0} \right] \quad (7)$$

In order to simplify the above expressions we can define the following dimensionless variables:

$$X_A = 1 - \frac{[A]}{[A]_0} \quad V_r = \frac{ut}{V_0} \quad \gamma = \frac{k[R]_0 V_0}{u} \quad (8)$$

where X_A is the transformed fraction of A, which is a concentration fraction instead of a molar fraction. From this, the concentration of A at any time can be calculated from $[A] = [A]_0(1 - X_A)$. V_r is the volumetric ratio of the added reagent, which is a temporary variable, and γ is a parameter directly related to the second-order rate constant. By substitution of these variables into eq 7, this can be rewritten as

$$\ln(1 - X_A) = -\gamma[V_r - \ln(1 + V_r)] - \ln(1 + V_r) \quad (9)$$

or, in an exponential form

$$X_A = 1 - \exp(-\gamma V_r)(1 + V_r)^{\gamma-1} \quad (10)$$

If the reaction is monitored via the product formed, the concentration fraction of A transformed in product, $X_P = [P]/[A]_0$, must be used in order to obtain a dependence similar to that of eq 9, $[P]$ being the concentration of product formed at any time. This concentration can be expressed as

$$[P] = \frac{[A]_0 V_0 - [A]V}{V} = \frac{[A]_0 V_0 - [A]V_0(1 + V_r)}{V_0(1 + V_r)} \quad (11)$$

because the volume at any time can be expressed as $V = V_0 + ut = V_0(1 + V_r)$. Rearrangement of eq 11 yields

$$[P] = [A]_0 \left[X_A - \frac{V_r}{1 + V_r} \right] \quad (12)$$

$$X_P = 1 - \exp(-\gamma V_r)(1 + V_r)^{\gamma-1} - \frac{V_r}{1 + V_r} \quad (13)$$

Plots of X_A or X_P as calculated from eqs 10 and 13 as a function of V_r at different γ values are shown in Figure 1. The γ values used in both equations lay in the same range as their typical experimental counterparts. The shape of these curves depends directly on the γ value; therefore, for a given chemical system, this behavior is also closely related to the selected addition rate. These curves show three distinct zones: the initial and final portions which are concave and convex, respectively, and a virtually linear zone which is of great analytical interest. On comparison of the two types of dependency obtained by monitoring the process via analyte or the product, it is seen that the straight portion is larger in the former case (in the latter, the maximum rate is followed by a decrease resulting from the dilution of the product). Such a decrease conforms to $V_0/V = 1/(1 + V_r)$. Obviously, these differences increase with decreasing γ . The plots shown in Figure 1 are in fact kinetic curves because V_r , X_A , and X_P depend linearly on time and the analytical signal, respectively. The dependencies of X_A and X_P are commented on below.

Let us again consider the second-order irreversible reaction of eq 1 with, for instance, photometric detection, in which only the analyte and product absorb at the wavelength where the reaction is monitored. At time $t = 0$, the absorbance (the analytical signal, S_0) can be expressed as $S_0 = \epsilon_A[A]_0$, where ϵ_A is the molar absorptivity of the analyte and l the path length (generally 1 cm). After a reaction time t the absorbance can be expressed as $S = \epsilon_A[A] + \epsilon_P[P]$ where ϵ_P is the

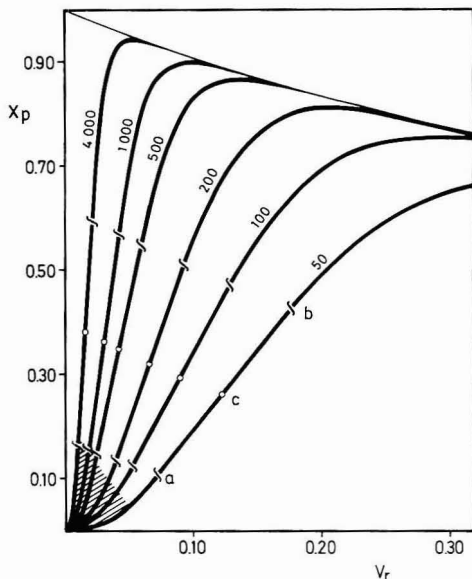


Figure 2. Typical X_P vs V_r plots obtained at different γ values. The a-b segments correspond to the useful zone for application of the maximum reaction method, while the shaded portion corresponds to the initial reaction method. c's are inflection points.

Table I. Effect of the Variability of Experimental Parameters on the Performance of the Analytical Methods

exp param	actual value obtained for an n-fold change in the corresponding exp param			
	max reactn (dX/dV _r) _m	initial reactn dX/d(V _r ²)	γ	t_m
$[R]_0$	\sqrt{n}	n	n	$1/\sqrt{n}$
u	\sqrt{n}	n	$1/n$	$1/\sqrt{n}$
V_0	$1/\sqrt{n}$	$1/n$	n	\sqrt{n}
k	\sqrt{n}	n	n	$1/\sqrt{n}$
$[A]_0$	n	n	1	1

molar absorptivity of the product at the same wavelength. Thus, the difference between both signals will be

$$\Delta S = S - S_0 = [A]_0 \left[(\epsilon_P - \epsilon_A) X_A - \epsilon_P \frac{V_r}{1 + V_r} \right] \quad (14)$$

taking into account the $[A]$ and $[P]$ values stated above. If the product does not absorb at this wavelength, then eq 14 can be written as

$$-\Delta S = \epsilon_A [A]_0 X_A \quad (15)$$

whereas, if the product is the only absorbing species, then

$$\Delta S = \epsilon_P [A]_0 X_P \quad (16)$$

taking into account the ratio between X_A and X_P . Equations 15 and 16 show the linear relationship between the analytical signal and the initial analyte concentration.

Analytical Methods. Two methods were developed using two different regions of the kinetic response (Figure 1). They relate the measured parameter with the analyte concentration and are described in detail below.

Maximum Reaction Method. The unconventional kinetic profiles shown in Figure 1, have an inflection point at which the slope (reaction rate) is maximal and is bounded by a

straight portion. The following mathematical treatment supports application of this methodology.

The slope of the X_A vs V_r plots can be obtained by taking the derivative of eq 10

$$\frac{dX_A}{dV_r} = (1 + \gamma V_r) \exp(-\gamma V_r) (1 + V_r)^{\gamma-2} \quad (17)$$

The V_r value corresponding to the inflection point (maximum reaction rate) can be obtained by imposing the condition $d^2X_A/dV_r^2 = 0$, so

$$(V_r)_m = \frac{\sqrt{\gamma-1}-1}{\gamma} \quad (18)$$

By combining eqs 10 and 17, the maximum reaction rate can be written as

$$\left[\frac{dX_A}{dV_r} \right]_m = (1 - X_A)_m \frac{1 + \gamma(V_r)_m}{1 + (V_r)_m} \quad (19)$$

The value of $(1 - X_A)_m$ in the above equation ranged between 0.60 and 0.57 for γ values over a wide range (20 000–100). Taking into account that γ is generally much greater than 1, the $(V_r)_m$ value can be simplified to $(V_r)_m \approx \gamma^{-0.5}$. Thus, the maximum reaction rate can be written as

$$\left[\frac{dX_A}{dV_r} \right]_m \approx 0.6\gamma^{0.5} \quad (20)$$

and, by substituting for dX_A and dV_r , it becomes

$$-\left[\frac{dS}{dt} \right]_m \approx 0.6\epsilon_A[A]_0 \left[\frac{k[R]_0\mu}{V_0} \right]^{0.5} \quad (21)$$

Similar expressions can be obtained if the reaction is monitored via observation of product formation. Equation 21 shows the linear relationship between the maximum reaction rate and the analyte concentration. An important aspect of this methodology is that it reduces errors due to between-run variations in the second-order rate constants, owing to the square root dependency between the reaction rate and the rate constant according to this equation.

In order to determine the interval over which the X_A or X_P vs V_r plots are linear (the slope will be proportional to the analyte concentration), we assumed the linear zone should encompass a region where the slope yields a relative average deviation with respect to the maximum reaction rate (measured at the inflection point) that is not greater than 5%. Thus, at any point along this portion, the relative deviation of its slope (reaction rate) with respect to the maximum reaction rate will be

$$\delta_r = \frac{(dX/dV_r) - (dX/dV_r)_m}{(dX/dV_r)_m} \quad (22)$$

where the subscripts of X have been removed since this expression holds whether the reaction is monitored via analyte or the product. By application of the average-value theorem, the relative average deviation can be expressed by

$$\bar{\delta}_r = \frac{\bar{\delta}}{(dX/dV_r)_m} = \frac{1}{(V_r)_f - (V_r)_i} \int_{(V_r)_i}^{(V_r)_f} \delta_r dV_r \quad (23)$$

where $\bar{\delta}$ is the average deviation. If the $\bar{\delta}_r$ value is fixed at 0.05 (i.e. a 5% relative average deviation), the corresponding $(V_r)_i$ and $(V_r)_f$ values can be calculated from eq 23 and be used in turn to determine the X_A and X_P values from γ using eqs 10 and 13. These portions are marked in the plots shown in Figure 2 which shorten slightly as γ decreases; however, this zone is wide enough so that even at smaller γ values (e.g. for $\gamma = 50$), the useful portion lies between 11 and 43%

transformed fraction. The linearity of these portions was also checked by calculating their respective regression coefficients, which were $r^2 \approx 0.9998$ in all cases.

Initial Reaction Method. The application of this method is based on the use of kinetic data acquired at the reaction start. Under these conditions, eqs 10 and 13 can be expanded in series

$$X_A = V_r + \frac{\gamma-2}{2!} V_r^2 - \frac{5\gamma-6}{3!} V_r^3 - \frac{3\gamma^2-26\gamma+24}{4!} V_r^4 + \dots \quad (24)$$

$$X_P = \frac{\gamma}{2} V_r^2 - \frac{5\gamma}{3!} V_r^3 - \frac{3\gamma^2-26\gamma}{4!} V_r^4 + \dots \quad (25)$$

and, under these initial conditions, i.e. when V_r is smaller than $0.5(V_r)_m$ (see Figure 2), only the first few terms in the series are significant. This simplification reduces eq 25 to

$$X_P \approx 0.5\gamma V_r^2 \quad (26)$$

Taking into account the relationship between the analytical signal and the transformed fraction of the product, eq 26 can be written as

$$\Delta S = 0.5\epsilon_P\mu V_0^{-1} k[R]_0[A]_0 t^2 \quad (27)$$

This equation shows the linear dependence between the analytical signal and t^2 in the initial step of the reaction and allows the initial analyte concentration to be determined from the slope. When the reaction is monitored via the analyte, the initial reaction method can also be applied, though with some constraints because the initial portion of the X_A vs V_r plot cannot be transformed to a linear form, since the first two terms of the expanded series are required from eq 24. In this case, depending on the γ value, these terms can be similar (γ ca. 50–100) or the second term may feature a greater contribution ($\gamma \geq 1000$). In the latter case, the initial reaction method can be applied to the analyte with minimal errors. By using a treatment similar to that of the maximum reaction method, one can also determine the X_P values at which this method is applicable. Such values (marked in Figure 2), range between 5 and 17% of the transformed fraction of product for γ between 50 and 4000.

On comparison of the two methods it is seen that the maximum reaction method is subject to errors smaller than those of the initial reaction method, which however, is affected less by side reactions since measurements are performed during the initial step of the reaction. On the other hand, the two methods show a different dependence in the second-order rate constant (see eqs 21 and 27). Thus, if two analytes yield the same product with different second-order rate constants, the initial reaction method allows greater discrimination between them thanks to the linear dependence between the analytical signal and k (in the maximum reaction method, the analytical signal is related to $k^{1/2}$). This behavior can be exploited for the resolution of mixtures of these species by using a differential kinetic method based on a combination of both methodologies. In addition, these methods allow application of the corresponding fixed-time approach—and other kinetic methodologies—which involves measuring the reactant concentration at a preset time from the reaction start.

Variability of the Experimental Parameters. The X vs V_r profiles and the maximum and initial reaction methods are affected by various experimental parameters such as the addition rate, initial volume in the reaction vessel, initial concentration of reagent and analyte, and second-order kinetic constant. The influence of these parameters on γ , maximum and initial reaction methods, and t_m (time corresponding to

Table II. Useful Expressions for the Determination of γ

method	monitoring the reactant via the analyte	monitoring the reactant via the product
Recording of the Full Kinetic Curve		
integrated equation	$\gamma = -\frac{\ln \left[\frac{S - S_\infty}{S_0 - S_\infty} (1 + V_r) \right]}{V_r - \ln(1 + V_r)}$	$\gamma = -\frac{\ln \left[1 - \frac{S_d(1 + V_r)}{S_d(1 + (V_r)_d)} \right]}{V_r - \ln(1 + V_r)}$
inflection point	$\gamma \approx (V_r)_m^{-2} - 2(V_r)_m^{-1} - 2$	$\gamma \approx (V_r)_m^{-2} - 2(V_r)_m^{-1} + 1$
half-reaction time	$\gamma = \frac{\ln 2 - \ln(1 + (V_r)_{1/2})}{(V_r)_{1/2} - \ln(1 + (V_r)_{1/2})}$	$\gamma = \frac{\ln 2 - \ln(1 - (V_r)_{1/2})}{(V_r)_{1/2} - \ln(1 + (V_r)_{1/2})}$
Recording of Only a Portion of the Kinetic Curve		
max reactant	$-\frac{dS}{dt} = m_A \epsilon_A [A]_0 \mu V_0^{-1} \gamma^{0.5}$	$\frac{dS}{dt} = m_P \epsilon_P [A]_0 \mu V_0^{-1} \gamma^{0.5}$
initial reactant		$\gamma = \frac{2S}{\epsilon_P [A]_0 (V_r)^2}$

$(V_r)_m$ is illustrated in Table I, which shows how an n -fold change in each parameter affects the performance of the method. Thus, if the addition rate is doubled, the maximum reaction is increased by a factor of $\sqrt{2} = 1.41$ and the initial reaction by 2.0, while γ is decreased by a factor of 2.0 and the t_m by $\sqrt{2} = 1.41$. This table is of great interest for practical application of this approach.

Comparison with Pseudo-First-Order Methods. The performance of this approach with second-order reactions in which the reagent is added at a constant addition rate to a reaction vessel containing the analyte solution can be compared with that of first-order methods in which solutions of the analyte and excess reagent are mixed simultaneously.

If the proposed approach is applied at the start of a reaction monitored via the product, the analytical signal at any time can be expressed by

$$S_2 = 0.5\epsilon_P k_2 [R][A]_0 t \quad (28)$$

where k_2 is the second-order rate constant, $[A]_0$ is the initial concentration of analyte, and $[R] = [R]_0 \mu t / V_0$, provided dilution phenomena are negligible.

When the reaction in eq 1 develops under first-order conditions, the analytical signal at any time can be written as

$$S_1 = \epsilon_P [P] = \epsilon_P [A]_0 [1 - \exp(-k_1 t)] \quad (29)$$

where k_1 is the pseudo-first-order rate constant and $[A]_0$ is the initial concentration of the analyte under these conditions. If the analytical signal is monitored at the start of the reaction, the term in brackets in eq 29 can be simplified to $k_1 t$ and hence this equation can be written as

$$S_1 = \epsilon_P [A]_0 k_1 t \quad (30)$$

If we assume the initial analyte concentration to be the same in both situations, by combining eqs 28 and 30 and taking into account that $k_1 = k_2 [R]$, the relationship between the analytical signals will be $S_2 = 0.5S_1$. Thus, if the same reaction is developed by this continuous-addition-of-reagent technique, the average reaction rate at the start of the reaction (time at which the initial rate method was applied for pseudo-first-order kinetics) would be half that obtained when the analyte and excess reagent are mixed simultaneously. This behavior is of great interest to the monitoring of fast reactions since the use of this approach slows down these reactions.

Determination of the Second-Order Rate Constant. As stated above, the second-order rate constant is directly related to γ , so we developed several methodologies to determine it. Two situations were considered according to

whether the reaction was monitored via the analyte or the product: one in which the full curve was recorded and the other in which only a portion (useful for slow reactions) was recorded.

By using full plots of the transformed fraction vs volumetric ratio of reagent added we developed three methods.

(a) The first is based on the integrated eq 9, into which the relations between X_A and X_P and the analytical signal (absorbance) are substituted. In the final expressions obtained (Table II), S_0 is the absorbance at time $t = 0$, and S_∞ is the final absorbance (both for the analyte), S_d is any value of absorbance for the product measured in the dilution zone (see Figure 1) after the maximum of the plot, which corresponds to a V_r value $(V_r)_d$, and S is the absorbance at time t (both for the analyte and the product).

(b) The second method uses the relation between $(V_r)_m$ and γ at the inflection point according to eq 18. In this case, by using the plot for the analyte, the $(S_0 - S_\infty)$ difference yields $(S_0 - S_\infty)$, at the inflection point because the $(S_0 - S_\infty)/(S_0 - S_m)$ ratio is virtually constant. Such a ratio ranged between 2.55 and 2.69 for the analyte and between 2.53 and 2.54 for the product for γ values over a wide range (20 000–100). Once $(S_0 - S_m)$ is known, $(V_r)_m$ can be readily calculated, and so can γ by using the expressions listed in Table II. An iteration procedure can be used in order to increase the accuracy of this method.

(c) The third method is based on a very useful parameter for kinetic measurements, viz. the half-reaction time, which is directly related to $(V_r)_{1/2}$. This volumetric ratio of reagent added corresponds to the $X_A/2$ or $X_P/2$ values and to an analytical signal of $(S_0 - S_\infty)/2$ and $S_d(1 + (V_r)_d)/2$ for the analyte and product, respectively. By substituting these conditions into eq 9, one can obtain the expressions listed in Table II.

Application of the proposed methods to the determination of γ does not require ϵ_A , ϵ_P , or $[A]_0$ to be known, and in all cases, the γ values can be obtained from the slope of the linear regression of the corresponding expressions.

The methods based on recording only a portion of the typical plot supported by this approach can be useful for slow reactions, in which recording the full curve can be time-consuming. The first proposed method is based on the dependency between the maximum reaction rate and γ , as shown in eq 20, which can be expressed in a general form by $(dX_A/dV_r)_m = m\gamma^{1/2}$, m being a parameter ranging between 0.60 and 0.57 for the analyte and between 0.60 and 0.49 for the product for γ values over a wide interval (20 000–100). By measuring the maximum reaction rate, it is very easy to

Table III. Effects of the Experimental Variables on the Maximum and Initial Reaction Methods, as Well as on γ Values

variable	regression	slope \pm SD	intercept \pm SD	std error of the estimate	regression coeff
iron(II)	$\Delta A/\Delta t$ vs $[C_{Fe}]^{1/2}$	$(1.55 \pm 0.06) \times 10^{-1}$ (A L ^{1/2})/(s mol ^{1/2})	$(-1.4 \pm 0.7) \times 10^{-3}$ A/s	7.3×10^{-4} A/s	0.9956 ($n = 7$)
	$\Delta A/t^2$ vs C_{Fe}	$(4.5 \pm 0.1) \times 10^{-2}$ (A L)/(s ² mol)	$(1.4 \pm 2.0) \times 10^{-5}$ A/s ²	3.1×10^{-6} A/s ²	0.9979 ($n = 7$)
	γ vs C_{Fe}	$(4.4 \pm 0.2) \times 10^5$ L/mol	$(1.6 \pm 0.2) \times 10^2$	50	0.9947 ($n = 7$)
addition rate	$\Delta A/\Delta t$ vs $u^{1/2}$	$(7.8 \pm 0.1) \times 10^{-2}$ A/(s ^{1/2} mL ^{1/2})	$(1.8 \pm 0.8) \times 10^{-3}$ A/s	1.5×10^{-3} A/s	0.9980 ($n = 16$)
	$\Delta A/t^2$ vs u	$(1.02 \pm 0.01) \times 10^{-1}$ A/(s mL)	$(1.0 \pm 0.6) \times 10^{-4}$ A/s ²	1.5×10^{-4} A/s ²	0.9990 ($n = 16$)
	γ vs u^{-1}	84.1 ± 0.7 mL/s	58 ± 25	90	0.9995 ($n = 16$)

determine γ from the expression listed in Table II. An iteration procedure can also be used here to achieve increased accuracy.

The second method is based on measurements at the start of the reaction and on plotting X_P as $(V_t)^2$ according to eq 26 (see final expression in Table II) or using an alternative involving the plot of $2X_P/(V_t)^2$ against V_t , the intercept of which allows γ to be obtained. As stated above, this method is only useful when the reaction is monitored via the product.

Application of these methods requires the product $[A]_{\infty}$ or $e_P[A]_0$ to be known depending on whether the analyte or product is used to monitor the reaction. These values can be obtained from the final absorbance of the reaction.

EXPERIMENTAL SECTION

Reagents. Sodium thiocyanate (Merck), 30% hydrogen peroxide (Merck), and ammonium iron(III) sulfate (Merck) were of reagent grade and used without further purification. Distilled water was used to prepare all solutions except for the Mohr salt solution, which was made in 0.05 M sulfuric acid.

Apparatus. A Metrohm Model 662 spectrophotometer furnished with an immersion probe for measuring the transmittance or absorbance in the visible region and a Metrohm Dosimat Model 665 automatic buret was used to develop and monitor the acid oxidation of iron(II) by peroxide and the subsequent complex formation with thiocyanate. The spectrophotometer output was interfaced to a Hewlett-Packard 98561AE computer for data acquisition, storage, and analysis. All computations and simulations were performed on this processor by using software written in Basic 4.0 language.

Kinetics Measurements. Solutions of 5 M NaSCN, 9×10^{-3} M ammoniumiron(II) sulfate, and 2.94×10^{-3} M H₂O₂ were freshly prepared. The automatic buret was loaded with ferrous reagent solution, and the reaction vessel with hydrogen peroxide standard solution (0.44–4.4 μ mol), 6 mL of sodium thiocyanate solution, and 0.05 M sulfuric acid up to 60 mL. The reaction was developed by continuous addition of iron(II) solution at a rate of 5.0 mL/min, with stirring at 200 rpm, and the increase in the absorbance at 460 nm was monitored for 60 s. The temperature was kept constant at 20 ± 0.1 °C throughout the analysis. Each data set was stored for subsequent retrieval, analysis, and display.

RESULTS AND DISCUSSION

The main objective of this study was to evaluate the major features of the proposed approach by applying the maximum and initial reaction methods to the determination of an analyte and using the above described procedures for the calculation of the second-order rate constant. The oxidation of iron(II) added from the autoburette by hydrogen peroxide in the presence of thiocyanate yielding the classical iron(III)/thiocyanate red complex was chosen as the chemical system, with hydrogen peroxide as the analyte. The involvement of two consecutive reactions (oxidation and complex formation) in this chemical system allows the variation of γ to be monitored over a wider range, which is of great interest in order to obtain a more thorough assessment of the proposed methodology.

Effects of Experimental Variables. So far we have considered the effects of experimental variables, both chemical and instrumental, upon measured rates (maximum and initial) as well as one the γ values.

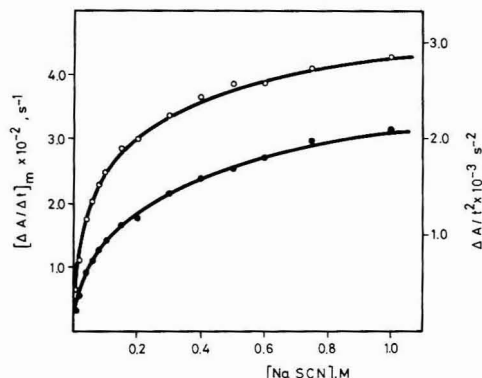


Figure 3. Effect of sodium thiocyanate on the results obtained by using (O) the maximum and (●) the initial reaction method.

Several chemical variables such as pH and iron(II) and sodium thiocyanate concentration affect the development of this system. The pH was adjusted in all experiments with 0.05 M sulfuric acid since, according to the literature,⁹ this is a suitable medium for the iron(III)/thiocyanate complex to be formed. The concentration of iron(II) added from the automatic buret, C_{Fe} , was varied between 1.79×10^{-3} and 2.86×10^{-2} M. According to expressions 21 and 27, a linear dependency was found both by the maximum and by the initial reaction method. A similar behavior was observed when γ values were plotted against the iron(II) concentrations. The first three rows of Table III show the linear regression parameters found for these dependencies. We chose an iron(II) concentration of 8.95×10^{-3} M (500 μ g/mL) for subsequent experiments.

The influence of the sodium thiocyanate concentration was assayed over a wider range (between 0.01 and 1.0 M). In this case, as is shown in Figure 3, there was a logarithmic relationship between the concentration of this species and the measured rates (and γ). The effect of this chemical could be directly related to the reactions involved in this system. In fact, as the concentration of thiocyanate increases, both measured rates increase as a result of the higher degree of formation of the iron(III)/thiocyanate complex upon oxidation of the iron(II) added from the autoburette by hydrogen peroxide. However, at higher concentrations, thiocyanate can also react appreciably with iron(II) (the formation constant of the iron(III)/thiocyanate complex is only 50-fold that of the iron(II) complex), so the effective iron(II) concentration in the reaction vessel decreases. We selected a 0.5 M concentration of sodium thiocyanate as optimal for further experiments, this concentration lay in a dependency region in which minimal variations in its concentration resulted in no appreciable error in the measured rates.

The rate of addition of the iron(II) solution, u , the most important instrumental variable, was studied over a wide

(9) Willis, B. G.; Bittikofer, J. A.; Pardue, H. L.; Margerum, D. W. *Anal. Chem.* 1970, 42, 1340.

Table IV. Regression Data and Analytical Features of the Determination of Hydrogen Peroxide Using Different Determinative Methods

param	kinetic determinative method		
	max reacn	initial reacn	fixed time
linear range, M	7.35×10^{-6} – 7.35×10^{-5}	7.35×10^{-6} – 7.35×10^{-5}	7.35×10^{-6} – 1.03×10^{-4}
slope	$(4.16 \pm 0.06) \times 10^2$ (A L)/(s mol)	12.8 ± 0.2 (A L)/(s ² mol)	$(6.18 \pm 0.07) \times 10^3$ (A L)/mol
intercept	$(9.2 \pm 2.8) \times 10^{-4}$ A/s	$(2.0 \pm 0.1) \times 10^{-6}$ A/s ²	$(7.6 \pm 4.2) \times 10^{-3}$ A
RSD of the estimate	4.0×10^{-4} A/s	1.4×10^{-5} A/s ²	7.3×10^{-3} A
regression coeff	0.9991	0.9988	0.9993
detection limit, M	1.35×10^{-6}	2.27×10^{-6}	1.94×10^{-6}
precision, RSD, %	±1.02	±1.70	±1.38

range (between 0.5 and 55 mL/min). Increasing rates of addition linearly increased the measured rates and decreased γ , consistent with the behavior predicted by eqs 8, 21, and 27. These dependencies are quantified in the data in rows 4–6 in Table III. A rate of addition of 5 mL/min was selected.

Some other instrumental variables were also investigated. The stirring speed (65–250 rpm) did not significantly affect the measured parameters, so 200 rpm was selected. The influence of the initial sample volume, V_0 , was studied between 50 and 80 mL at a constant concentration of added iron(II). The dependencies found were consistent with the dilution or concentration phenomena involved. An initial sample volume of 60 mL was thus selected.

From this study of variables one can conclude that the most appropriate conditions include using a high γ value and a measurement time that is neither too long (otherwise the method would be rather tedious) nor too short (which would call for a highly efficient agitation system to ensure thorough mixing and avoid bubble formation).

Approaches to the Analyte Determination. The absorbance vs time curves recorded under the selected experimental conditions for different amounts of analyte (hydrogen peroxide), were analyzed by using three approaches, viz the maximum and initial reaction methods and the classical fixed-time methodology (measurement time, 24 s). Data relevant to these calibration graphs are summarized in Table IV. The detection limit, calculated on the basis of the variation of the analytical response at low concentrations,¹⁰ and the precision, RSD, calculated from 11 samples containing 4.45×10^{-5} M hydrogen peroxide each, are also shown in Table IV for the three methods. As can be seen, all of the approaches are useful for the determination of hydrogen peroxide; however, the initial reaction methodology performs slightly worse because of its very nature. To further evaluate the consistency between results obtained with the maximum and initial reaction methods, which are the two main approaches proposed in this work, the results yielded by both were subjected to a least-squares fit. The regression equation and statistics were

$$IR = (0.996 \pm 0.017)MR + (0.017 \pm 0.075) \times 10^{-5} \\ S_e = 0.110 \times 10^{-5} \quad r = 0.9989$$

where IR and MR denote the initial and maximum reaction method, respectively, and S_e the standard error of the estimate. Both the standard deviations of the slope and intercept, the standard error of the estimate, and the correlation coefficient confirm the high degree of correlation between the two methods.

Determination of Second-Order Rate Constant. The methods described above for the determination of γ (see Table II) were tested by using the selected chemical system. The results found are shown in Table V. The integrated equation, inflection point, and half-reaction time methods provided smaller relative standard deviations than the others, even

Table V. Statistical Results for the Determination of γ Using the Proposed Methods

method	$\bar{\gamma}$	SD	RSD, %
integrated equation	802.8	26.6	3.3
inflection point	774.7	19.8	2.6
half-reaction time	801.4	27.2	3.4
max reacn	829.8	38.5	4.7
initial reacn	825.5	44.3	5.3

though the differences were very small. This can be attributed to the fact that the former methods are based on the recording of the full kinetic curve, whereas the latter rely on only a portion of it. On the other hand, the integrated equation method, because of its very nature, is a multipoint method, whereas the other can be applied by means of a simple graphical treatment of the kinetic curve (all of them, however, perform similarly). The integrated equation method can be the method of choice for the determination of the second-order rate constant on account of its multipoint nature.

In order to check the applicability of the proposed methods for the determination of second-order rate constants, the experimental and simulated kinetic curves shown in Figure 4 were obtained. The γ value used to generate the simulated curve was that obtained by using the integrated equation method (see Table IV). The fit was very good, which supports the theoretical assumptions made above.

Taking into account that the chemical system used in this work involves two chemical reactions, viz. oxidation of iron(II) by hydrogen peroxide and subsequent formation of a complex between iron(III) and thiocyanate, the value of the second-order rate constant found corresponds to the overall reaction $[(1.25 \pm 0.04) \times 10^2 \text{ L}/(\text{mol s})]$ as calculated by using the integrated equation method].

CONCLUSIONS

Second-order kinetic data were processed by using a mathematical treatment that describes the kinetics involved in adding a reagent continuously at a constant rate to a

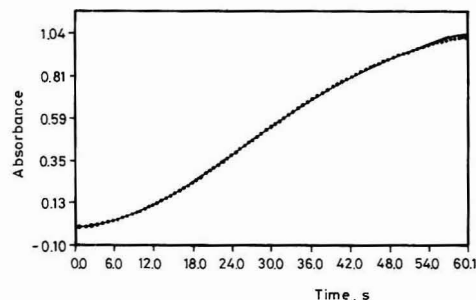


Figure 4. Simulated data (—) compared with the analytical working curve (○). $\gamma = 802.8$; $[\text{Fe(II)}] = 8.95 \times 10^{-3} \text{ M}$; $[\text{SCN}^-] = 0.5 \text{ M}$; $[\text{H}_2\text{O}_2] = 5.88 \times 10^{-5} \text{ M}$; $u = 5 \text{ mL/min}$.

reaction vessel containing the analyte. According to the results obtained, the maximum reaction method is the better of two proposed in this paper. In addition, it offers the following advantages over pseudo-first-order initial rate methods: (a) it is less sensitive to between-run variations in the rate constant since the measured parameter is a function of $k^{1/2}$; (b) it allows a much wider linear portion of the kinetic curve to be used, which avoids errors arising from measurements made at the reaction start in the traditional initial rate methods; (c) it permits rate measurements to be made in a region of smaller instrumental errors. The above advantages arise from the special manner in which the sample and reagent are mixed, which allows kinetic data to be obtained for a wide variety of reactions and is particularly useful for rapid

reactions, which can be addressed with much more straightforward instrumentation than is normally required (the stopped-flow technique). In addition, the proposed technique allows the rate of a given reaction to be altered not only through the reagent concentration, but also through the rate of addition.

ACKNOWLEDGMENT

We are grateful to the DIGICyT for financial support received.

RECEIVED for review October 25, 1991. Accepted June 30, 1992.

Use of Spherical Targets To Minimize Effects of Neutron Scattering by Hydrogen in Neutron Capture Prompt γ -Ray Activation Analysis

Elizabeth A. Mackey^{*,†} and Glen E. Gordon[‡]

Department of Chemistry and Biochemistry, University of Maryland, College Park, Maryland 20742

Richard M. Lindstrom

Inorganic Analytical Research Division, National Institute of Standards and Technology, Gaithersburg, Maryland 20899

David L. Anderson

Division of Contaminants Chemistry, U.S. Food and Drug Administration, Washington, D.C. 20204

For hydrogenous targets that are thinner than they are wide, element sensitivities (counts·s⁻¹·mg⁻¹) for determining concentrations of elements by neutron capture prompt γ -ray activation analysis (PGAA) are enhanced relative to sensitivities obtained from measurements on nonhydrogenous materials. These enhancements are caused mainly by elastic neutron scattering by H, which changes the average neutron fluence rate within the matrix. The magnitude of the effect depends on the macroscopic scattering and absorption cross sections and on the size, shape, and orientation of the target with respect to the neutron beam. Sensitivities increase linearly with H density for thin targets of constant size and shape and also vary with target shape. Theoretical work was shown that element sensitivities for hydrogenous targets in the form of spheres are least affected by neutron scattering. Methods were devised for creating solid spheres and for containing liquids in spherical shapes. Element sensitivities were determined for spheres and disks of several hydrogenous materials. For H, B, Cl, K, Br, and Cd, sensitivities for spheres were found to be less affected by neutron scattering. Exceptions were Sm and Gd sensitivities measured in liquids contained in quartz globes.

INTRODUCTION

For neutron capture prompt γ -ray activation analysis (PGAA), the sensitivity for a given element (where sensitivity is the slope of the analytical response curve, counts·s⁻¹·mg⁻¹) depends on the average neutron fluence rate (ϕ) within the target. Therefore, determinations of element concentrations are valid only if ϕ is the same for the standard and unknown matrix, or if appropriate correction factors are used to account for any differences. Assuming that the incident fluence rate (ϕ_0) is constant, the two processes that affect the average fluence rate within the target are neutron absorption and neutron scattering. In matrices containing large concentrations of absorbing nuclides, a decrease in the overall fluence rate is due to neutron absorption within the target. This self-shielding effect is well understood theoretically and, for simple geometries, can be corrected by application of an

absorption law.¹ The effects of neutron scattering on the average fluence rate cannot, in general, be accounted for by simple correction factors. For several target shapes, results obtained using the University of Maryland and National Institute of Standards and Technology (UM/NIST) PGAA facility^{2,3} showed that when hydrogen, a strong scatterer, is present in the matrix, element sensitivities are enhanced relative to those obtained from nonhydrogenous materials. As the neutron beam at this facility is well thermalized, the sensitivity enhancements are unlikely to be significantly affected by inelastic neutron scattering or neutron moderation.

Theoretical work using Monte Carlo methods to calculate the probability for neutron absorption within a scattering matrix has shown that these enhancements are largely the result of elastic scattering.^{4,5} Elastic neutron scattering affects absorption reaction rates (or sensitivities) by altering the average distance traveled by the neutrons within the target or, equivalently stated, by altering the average neutron fluence rate. The magnitude of the effect is dependent on the size and shape of the target and on the density of the scattering and absorbing nuclides comprising the matrix. Depending on the size and shape of the target, absorption reaction rates may be either increased or decreased relative to those obtained from materials possessing much smaller scattering cross sections. This problem has been studied experimentally using the UM/NIST PGAA facility^{2,3} and theoretically using Monte Carlo methods.^{4,5} Results from Monte Carlo calculations for disks showed the same trends that were observed experimentally.⁶ Similar enhancement effects were recently reported by researchers at the Center for Nuclear Research in Strasbourg, France, but those authors attribute the enhancements to inelastic scattering.⁷

Researchers using the UM/NIST facility obtain accuracy in the analysis of hydrogenous materials by carefully matching the target shape and matrix of test materials and standards.

(1) Fleming, Ronald F. *Int. J. Appl. Radiat. Isot.* 1982, 33, 1263-1268.

(2) Mackey, Elizabeth A.; Gordon, Glen E.; Lindstrom, Richard M.; Anderson, David L. *Anal. Chem.* 1991, 63, 288-292.

(3) Mackey, Elizabeth A. Ph.D. Thesis, University of Maryland, Department of Chemistry and Biochemistry, 1991.

(4) Copley, John R. D.; Stone, Craig A. *Nucl. Instrum. Methods Phys. Res.* 1989, A281, 593-604.

(5) Copley, John R. D. *Nucl. Instrum. Methods Phys. Res.* 1991, A307, 389-397.

(6) Mackey, Elizabeth A.; Copley, John R. D., submitted to *J. Radioanal. Nucl. Chem.*

(7) Trubert, Didier; Duplatre, G.; Abbé, Jean-Charles *Int. J. Radiat. Appl. Isot.* 1991, 42A, 699-705.

[†] Present address: Inorganic Analytical Research Division, Chemical Science and Technology Laboratory, National Institute of Standards and Technology, Technology Administration, U.S. Department of Commerce.

[‡] Deceased.

For example, Anderson et al.⁸ described a procedure for the analysis of hydrogenous materials in which element standards of varying H concentrations are used to determine element sensitivities as a function of the mass of H, to yield accurate results from analyses. Enhancements due to other scatterers commonly present in biological materials, e.g. C, N, O, have not been observed in PGAA measurements, probably because of the lower scattering cross sections of these elements.

In previous study, we showed that the use of spheres largely eliminates the effects of neutron scattering on H sensitivity.² In that study, only one element in one matrix (paraffin) was determined. Hydrogen sensitivities remained constant over the range of sphere sizes measured, whereas sensitivities for disks of the same material (over the same range of mass) showed increasing sensitivity with decreasing disk thickness. Theoretical work has shown that, for targets having a given scattering and absorption cross section, sensitivities for spheres should be least affected by neutron scattering.^{5,6} To determine if the use of spheres would eliminate enhancements for elements in addition to H in other matrices, we have measured sensitivities for several elements in various hydrogenous materials. For this work, methods were devised for preparing solid spheres and for containing liquids in quartz spheres. Element sensitivities were measured for both liquid and solid materials that had been studied in other geometries so that comparisons could be made and the magnitude of the effects of scattering could be assessed.

EXPERIMENTAL SECTION

Test Sample Preparation. A series of disks of constant 1.27-cm diameter and varying thicknesses and a series of spheres of varying diameters were prepared from each of the following substances: urea [6.71% (w/w) H], tris(hydroxymethyl)aminomethane [THAM, 9.15% (w/w) H], NIST Standard Reference Material (SRM) 1570 spinach leaves [5.57% (w/w) H], SRM 1577a bovine liver [6.98% (w/w) H], SRM 1632a bituminous coal [3.85% (w/w) H]. Disks were formed from powders of each substance with a commercial stainless steel die and hydraulic press. For each material, up to 14 disks were prepared ranging in thickness from approximately 1 to 12 mm.

Spheres of the same materials were formed using steel dies. Six dies, capable of forming spheres of diameters 4.76, 6.35, 7.94, 9.53, 11.1, and 12.7 mm, were designed and fabricated at NIST. The dies were made by first machining steel into two cylinders that were oil-hardened to withstand the pressures necessary for forming solid spheres from powders. A hemisphere was hollowed into the end of each cylinder by electric discharge machining with carbon electrodes. The two cylinders and a push rod fit into a sleeve so that when the two pieces of the die met to form a spherical cavity, the push rod was flush with respect to the top of the sleeve (Figure 1). Due to difficulties in compressibility or in obtaining uniform density with the use of these dies, some materials were first formed into disks using the standard 1.27-cm-diameter disk-shaped die (described above), carved into roughly spherical shapes using a scalpel and, finally, smoothed into spheres using those dies capable of forming spheres. This procedure often resulted in spheres with diameters not equal to the internal diameter of the die and thus allowed for a greater number of diameters than six (the number of dies). Spheres of urea, THAM, and SRM 1632a were created in this manner. The diameter of each sphere was measured and the density calculated to ascertain the degree of uniformity over the range of sphere sizes used. The average densities of the spheres were 2–4% less than those of the disks of the same material, the exception being average densities for THAM for which the spheres were 5% more dense than the disks. Relative standard deviations of the densities of spheres for each material were about 2–3%. All targets were packaged in bags formed from 0.0025-cm-thick Teflon film.

Hollow, spherical fused-quartz containers, prepared at the glass shop at NIST, were used for irradiation of liquids (Figure 2).

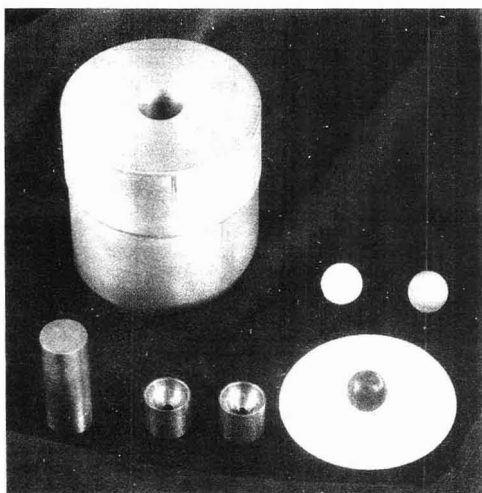


Figure 1. Stainless steel die used to prepare 1.27-cm-diameter spheres from powders and spheres of THAM, SRM 1577a, and SRM 1632a formed using this die.

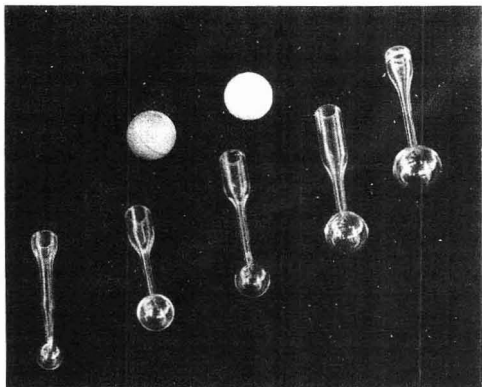


Figure 2. Quartz globes used to contain liquid matrices and two solid 1.27-cm-diameter spheres (THAM and SRM 1570).

External diameters were measured with a micrometer, and internal diameters (5.40, 7.54, 8.22, 10.1, 11.7 mm) were determined based on the volume of H₂O that each could contain. Differences between the external and internal diameters yielded approximate thicknesses of the walls of the globes which ranged from 0.5 to 0.7 mm. Irradiation of empty globes (blanks) showed that the quartz was slightly contaminated with B, and to a lesser extent with Na, but were otherwise very clean. The count rates for B and Na measured in the globe blanks were about 2–3 times greater than the count rates obtained during irradiation of Teflon bag blanks. Data from measurements on materials containing B were corrected for the presence of B and Na in the quartz. The globes were filled using a syringe and placed in Teflon bags to facilitate positioning in the neutron beam. For these experiments, sensitivities for eight elements in 100% H₂O, four elements in 100% D₂O, and five elements in 50% solutions of H₂O and D₂O were measured. Compositions of the 25 solutions are listed in Table I.

PGAA Method, Data Reduction, and Analysis. Most experiments were carried out at a reactor power of 20 MW, which corresponds to a neutron fluence rate at the target position of

(8) Anderson, David L.; Cunningham, W. C.; Mackey, Elizabeth A. *Biol. Trace Elem. Res.* 1990, 27, 613.

Table I. Compounds and Element Concentrations for Stock Solutions 1-8

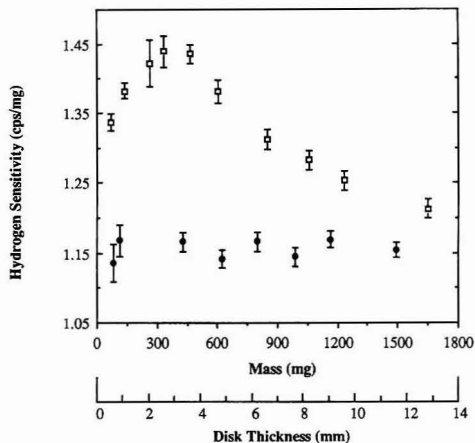
solution	element	compound	solution A (mg/mL) H ₂ O	solution B (mg/mL) D ₂ O	solution C (mg/mL) H ₂ O/D ₂ O
1	H	(H ₂ O)	111.9		50.74
2a	B	H ₃ BO ₃	5.291	5.462	
2b	B	H ₃ BO ₃	1.334	1.097	
2c	B	H ₃ BO ₃	0.533	0.483	
3	Cl	NaCl	58.68	58.75	58.69
4	K	KCl	90.59		
	Cl	KCl	82.15		
5	Br	NaBr	119.9		
6	Cd	CdCl ₂	0.577	0.523	0.576
7a	Sm	Sm ₂ O ₃ in 1 M HNO ₃	0.561		0.588
7b	Sm	Sm ₂ O ₃ in 1 M HNO ₃	0.927		
7c	Sm	Sm ₂ O ₃ in 1 M HNO ₃	1.961		
8a	Gd	Gd ₂ O ₃ in 2 M HCl	0.272	0.205	0.331
8b	Gd	Gd ₂ O ₃ in 2 M HCl	0.541		

approximately $3.3 \times 10^8 \text{ cm}^{-2} \text{ s}^{-1}$.⁹ Disks were placed at an angle of 45° to the neutron beam, and the γ -ray spectra were obtained during irradiations. The UM/NIST PGAA facility is described in detail elsewhere.^{9,10} Targets were suspended in the central, uniform portion of the neutron beam. Liquids, urea and tris(hydroxymethyl)aminomethane (THAM), were irradiated for ≤ 30 min, and the SRMs were irradiated from 5 to 12 h, depending on the counting statistics desired. γ radiations over an energy range of approximately 100 keV to 8 MeV were observed using a germanium detector (27% efficiency relative to a 7.6- \times 7.6-cm NaI crystal) with a Nuclear Data (ND) 16K-channel analog-to-digital converter (ADC). The ADC was connected to a ND9900 Workstation through a ND Ethernet multichannel analyzer.

Data reduction was accomplished using a VAX 11/730 computer. Nuclear Data programs PEAK and PILEUP and a code, SUM, written by one of us (Lindstrom) were used for data reduction. All data were corrected for the effects of the pileup of pulses at high count rates,¹¹ for temporal variations in neutron fluence rate, and for neutron self-shielding¹ except where noted otherwise. A Ti foil (12.7-mm diameter, 139.8 mg) was irradiated, and its γ -rays were observed before and after irradiations to monitor temporal variations of the neutron fluence rate. Over a typical 5-week fuel cycle, the fluence rate varied by $\pm 1.5\%$. Additional corrections were applied to H and B data to account for the presence of these elements in the background. When measured during the irradiation of a Teflon bag blank, neutron capture reactions in the shielding materials produce background equivalent to approximately 4 mg of H and 0.5 μg of B at the target position. When scattering materials are irradiated, these count rates are enhanced as a result of the increased number of neutrons that are scattered into the surrounding shielding and support structures.^{3,12}

RESULTS AND DISCUSSION

Solid Disks and Spheres. Element sensitivities were measured for disks and for spheres of five hydrogenous materials: urea, THAM, SRM 1632a bituminous coal, SRM 1570 spinach leaves, and SRM 1577a bovine liver. Sensitivities for H were measured in all materials, sensitivities for K were measured in the three SRMs, and sensitivities for six additional elements were measured in SRM 1632a. For urea and THAM, H sensitivities were calculated using the nominal H concentration; for the SRMs, element sensitivities were calculated using the certified values, when available. Ele-

**Figure 3.** Hydrogen sensitivities measured in disks (□) and spheres (●) of THAM.**Table II. Average H and K Sensitivities for Spheres of Urea, THAM, Paraffin, and SRMs 1570, 1577a, and 1632a**

material	number of spheres	H sensitivity ^a (counts·s ⁻¹ · mg ⁻¹)	K sensitivity ^a (counts·s ⁻¹ · mg ⁻¹)
SRM 1570	6	1.170 ± 0.033	0.183 ± 0.0062
SRM 1577a	13	1.307 ± 0.017	0.189 ± 0.0067
SRM 1632a	12	1.312 ± 0.028	0.182 ± 0.0096
THAM	8	1.160 ± 0.013	
urea	6	1.180 ± 0.009	
paraffin	12	1.180 ± 0.014	

^a Uncertainties represent one standard deviation of the average sensitivity.

ments for which these materials were not certified include H for all SRMs and B, Si, Cl, Sm, and Gd for SRM 1632a; concentrations for these elements were taken from a compilation of literature values.¹³

Generally, measurements on disks showed the same trends that have been previously observed for disks of paraffin and of SRM 1571 orchard leaves,² i.e., element sensitivities increased with increasing disk thickness over the range of 0–2 mm and beyond 2 mm decreased with increasing thickness. On the average, element sensitivities measured in disks of 2- and 12-mm thickness (of the same material) differed by about 15%. For most materials, the sensitivities for disks for which thicknesses were approximately equal to the diameter (i.e., targets for which the shapes were closest to spherical) agreed best with those for spheres.

Sensitivities for H in disks and spheres of THAM are shown in Figure 3. For spheres of all sizes, sensitivities remained constant within the errors shown which include the uncertainties associated with counting statistics, background subtraction, and fluence-rate normalization factors. Similar results were obtained for H sensitivities from measurements on the other materials; as shown in Table II, H sensitivities for spheres of a given material were constant within $\pm 2\%$. Average sensitivities in spheres of urea, THAM, and SRM 1570 spinach leaves agree within one standard deviation of the average value. However, average H sensitivity values were greater for SRMs 1577a and 1632a than for the other materials, probably due to insufficient drying of these

(9) Failey, Michael P.; Anderson, David L.; Zoller, William H.; Gordon, Glen E.; Lindstrom, Richard M. *Anal. Chem.* 1979, 51, 2209–2221.

(10) Anderson, David L.; Failey, Michael P.; Zoller, William H.; Walters, William B.; Gordon, Glen E.; Lindstrom, Richard M. *J. Radioanal. Chem.* 1981, 63, 97.

(11) Lindstrom, Richard M.; Fleming, Ronald F. *Proceedings of the 4th International Conference on Nuclear Methods in Environmental and Energy Research*; Vogt, J. R., Ed.; University of Missouri: Columbia, 1980; p 25.

(12) Anderson, David L.; Mackey, Elizabeth A., submitted to *J. Radioanal. Nucl. Chem.*

(13) Gladney, Ernest S.; Burns, C. E.; Perrin, D. R.; Roelands, I.; Gills, Thomas E. *National Bureau of Standards Special Publication No. 260-88*; U.S. Government Printing Office: Washington, DC, 1984; p 9.

materials. (The disks and spheres were stored in a desiccator over P_2O_5 ; however, the powdered SRMs were not dried prior to forming disks and spheres.)

Similar results were obtained from measurements of K sensitivities in disks and spheres of the three SRMs. Average values for K sensitivity in spheres, listed in Table II, are the same (within uncertainties listed) as those measured in a solid disk of KNO_3 , 0.185 ± 0.002 counts \cdot s $^{-1}$ \cdot mg $^{-1}$. That the value of the average K sensitivity for spheres is the same within error as that measured in a nonhydrogenous disk-shaped standard indicates that the use of spheres eliminated sensitivity enhancement. Enhancements have not been observed for matrices containing other (weaker) scatterers such as C, N, or O. For example, B sensitivities measured in a graphite matrix (100% C) and in a D_2O matrix (20% D and 80% O) were the same within the errors of the method.⁸

Sensitivities for H and B in disks and spheres of SRM 1632a showed the same trends as those measured in other materials. Sensitivities for S, Cl, K, Si, Ti, Sm, and Gd were also measured in disks and spheres of SRM 1632a. For some of these elements, the trends were less clear due to the lower H concentration in this material (so that less enhancement was expected) and due to lower sensitivities (S, Si, K), or lower concentrations of the elements (Ti, Sm, Gd), causing uncertainties associated with counting statistics to be appreciable ($\geq 2.5\%$). However, the sensitivity averages and standard deviations of the averages for these elements were greater for disks than for spheres.

Liquids Contained in Globes. We previously measured element sensitivities in liquid matrices to determine the magnitude of enhancement as a function of H concentration.² Liquid H_2O and D_2O matrices provided a wide range of H concentrations and ensured homogeneity. For this work, aqueous solutions contained in quartz globes were used to determine whether the use of spheres would eliminate enhancements for liquids. Similar matrices were used (100% H_2O , 100% D_2O , and 50% H_2O /50% D_2O) so that results from previous measurements on liquids contained in Teflon bags could be compared with results from spheres.

Element sensitivities for B, Cl, Cd, and Gd were measured in all three matrices; H and Sm sensitivities were measured in 100% H_2O and in the 50/50 mixture, and those for K and Br were measured in 100% H_2O . The values for the macroscopic absorption cross section, Σ_a , ranged from approximately 0.01 to 0.25 cm $^{-1}$. These values are defined as: $\Sigma_a = \sum N_i(\sigma_a)_i$, where N_i is the number of atoms of element i per unit volume and σ_a is the cross section for neutron absorption. Values for the macroscopic scattering cross section, Σ_s , are controlled largely by the amount of H present and are estimated by $\Sigma_s = \sum N_i(\sigma_s)_i$, using $\sigma_s = 80b$ (the bound atom cross section) for H, and the free atom σ_s values for all other elements.¹⁴ Values for Σ_a ranged from approximately 5 cm $^{-1}$ for 100% H_2O solutions to 0.0004 cm $^{-1}$ for 100% D_2O solutions. The average sensitivity and standard deviation (for five spheres) for each element in each matrix are listed in Table III.

Results of measurements on aqueous boric acid solutions (contained in quartz globes) for three different H concentrations are compared in Figure 4 with those from previous measurements² on boric acid solutions (ranging in H concentration from 0 to 11%) contained in pillow-shaped Teflon bags. The three sensitivity values for spheres represent the average of the five spheres of different sizes measured for each value of H concentration (0, 5.6, and 11.2% H), and the uncertainties shown represent one standard deviation of this average. The data shown for solutions contained in Teflon

Table III. Sensitivities (counts \cdot s $^{-1}$ \cdot mg $^{-1}$) for Elements Measured in Aqueous Solutions Contained in Quartz Globes

element, E_γ (keV)	solution	sensitivity in			standards ^a (0% H)
		100% H_2O	50% H_2O	100% D_2O	
H (2223)	1c	1.24 ± 0.01	1.18 ± 0.02		
B (477)	2c	730.3 ± 9.3	732.2 ± 8.7	715 ± 9.1	714 ± 14
Cl (787)	3	1.94 ± 0.04	$1.91 \pm .01$	1.90 ± 0.03	1.89 ± 0.03
Cl (787)	4	2.01 ± 0.05			
K (770)	4	0.195 ± 0.010			0.185 ± 0.002
Br (245)	5	0.298 ± 0.007			0.308 ± 0.005
Cd (558)	6	219.2 ± 3.2	212.4 ± 2.4	211.4 ± 3.2	245 ± 5
Sm (334)	7a	851 ± 4	860 ± 6		
Gd (182)	8a	1034 ± 17	960 ± 14	948 ± 8	

^a Nonhydrogenous standards used: B_2C , NaBr, NaCl, KCl, KNO_3 , and $CdCl_2$ in D_2O ; uncertainties represent the standard deviation of the average of as many as six measurements.

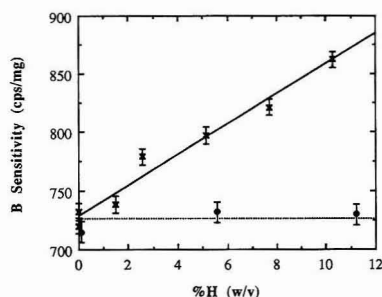


Figure 4. Boron sensitivities measured in boric acid solutions contained in Teflon bags (X) and in quartz globes (●). The dotted line represents the average sensitivity of the three values for the globes, 726 cps.

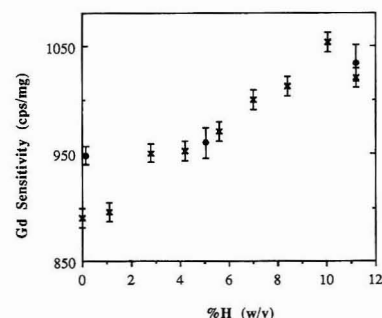


Figure 5. Gadolinium sensitivity measured in aqueous solutions contained in Teflon bags (X) and in quartz globes (●). Data were corrected by f_a .

bags represent single portions, and the uncertainties shown represent the propagated uncertainties associated with counting statistics and background subtraction. Sensitivities remained constant for spheres, as reflected by the small relative standard deviations in Table III, but increased with increasing H concentration for the pillow-shaped bags. Similar results were obtained from measurements on aqueous solutions containing Cl. However, Gd sensitivities measured in spheres showed enhancements similar to those measured in Teflon bags (Figure 5). Sensitivities were constant for the five spheres; the average of the five for each of the three matrices is plotted.

Sensitivities for most elements (H, B, Cl, K, Br, Cd) were constant over the range of sphere sizes studied (Table III). For each of these elements, the standard deviation of the average of the five values (for a given matrix) is approximately

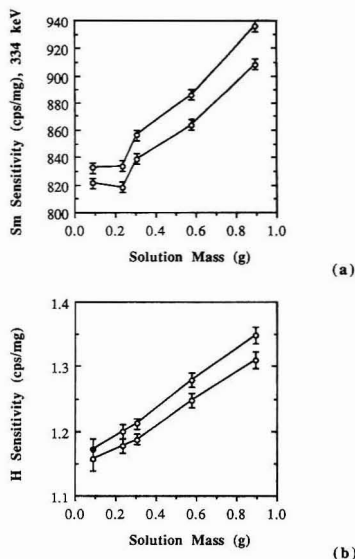


Figure 6. Samarium (a) and hydrogen (b) sensitivities measured in stock solution 7c. The upper curves in a and b represent data that were corrected by f_a and the lower represent uncorrected data.

$\pm 2\%$, which is greater than the uncertainties associated with counting statistics, but much less than the magnitude of sensitivity enhancements observed for nonspherical targets, up to 25%. The exceptions were Sm and Gd sensitivities measured in aliquots of solutions 7b and 7c, and 8b, respectively. Sensitivities for these elements increased with increasing sphere size (constant H concentration). Hydrogen sensitivities measured in these solutions showed the same trends as those of the analytes, i.e., H sensitivities increased with increasing sphere size for three solutions containing Gd and Sm, but were constant for the solutions containing B, Cl, or Cd. Results for Sm and H sensitivities measured in aliquots of solution 7c are shown in parts a and b of Figure 6, respectively. That the analyte and H sensitivities showed the same trends indicates that any change in the neutron distributions within these targets affects both elements in the same manner, regardless of differences in the absorption cross-section curves. However, sensitivities for these same elements (Sm and Gd) measured in solutions 7a and 8a, which were more dilute than solutions 7b and 7c, and 8b, were constant over the range of sphere sizes studied, suggesting that the effect might be dependent on the concentration of absorber.

To determine whether the amount of absorber would affect sensitivities, B sensitivities were measured over a wider range of Σ_a . Boron sensitivities were constant as a function of sphere size for each of three H_2O solutions, and the average sensitivities for each matrix were the same within 1.2% (Table IV). These solutions were more strongly absorbing than solutions 7b, 7c, and 8b, for which sensitivity enhancements were observed, so the concentration of absorber is probably not the cause of the observed enhancements for Sm and Gd.

Both Gd and Sm possess isotopes for which the absorption cross-section curves include broad (full widths at half-maximum of about 0.08 eV), low-energy neutron capture resonances (at energies of about 0.03 and 0.1 eV, respectively). No enhancements were observed for the ^{149}Sm nuclides. A resonance might increase the effective absorption cross section

Table IV. Boron Sensitivities (counts \cdot s $^{-1}$ \cdot mg $^{-1}$) for Several Aqueous Solutions of Varying B Concentrations Measured in Quartz Globes

boric acid stock solution	Σ_a (cm $^{-1}$)	B sensitivity ^a corrected by f_a	not corrected by f_a
H_2O matrix			
solution 2a	0.2475	759.5 \pm 9.12	702.0 \pm 9.24
solution 2b	0.0946	753.4 \pm 2.70	730.9 \pm 7.32
solution 2c	0.045	750.6 \pm 5.67	739.8 \pm 6.57

^a Boron sensitivity at 0% H is 730 \pm 9 (counts \cdot s $^{-1}$ \cdot mg $^{-1}$).

for that element, causing more self-shielding, or cause a decrease in the number of neutrons within a given energy range, i.e., spectral softening or hardening. However, any of these effects would decrease the average fluence rate within the target. We know of no mechanism by which the presence of isotopes possessing absorption resonances might increase sensitivities. Although all resonances enhance scattering as well as absorption, the scattering cross sections at thermal neutron energies are about 2 orders of magnitude smaller than the absorption cross sections; the contribution from Sm or Gd to the macroscopic scattering cross section for the solutions measured is negligible.

The relative importance of any energy-dependent process depends on the details of the energy distribution of the neutron beam and the values of the relevant cross sections for that particular energy distribution. Copley and Stone⁴ have shown that elastic scattering alone can account for sensitivity enhancements of the magnitude observed at the UM/NIST PGAA facility. The extent to which inelastic scattering affects sensitivities is not known. The neutron beam at this facility is well thermalized⁵ so that inelastic scattering should not be a large factor in sensitivity enhancement. However, for elements that possess low energy neutron absorption resonances, changes in the energy spectrum of the neutron beam may be important. Further work is necessary to determine the energy spectrum of the neutron beam and the effect of any changes in the energy distribution on element sensitivities for scattering matrices.

Data shown in the preceding figures and tables have been corrected by a factor, f_a , which accounts for the decrease in the neutron fluence rate caused by absorption within the target. (The measured count rates are divided by f_a to correct for neutron absorption). The value of f_a depends on the target shape and on the amount of absorber present. As defined in ref 1, for spheres, $f_a = 3/x^3[x^2/2 - 1 + (1+x)e^{-x}]$ where $x = \Sigma_a r$ and r = sphere radius, and for disks the approximation $f_a = 1/x[1 - e^{-x}]$, where $x = \Sigma_a(t/\cos 45^\circ)$ and t = disk thickness, was used. This factor is appropriate for pure absorbers, but does not account for any changes in the average fluence rate caused by neutron scattering. The general correction factor that accounts for both scattering and absorption of neutron is $f = \phi/\phi_0$.^{5,6} (If the material is a pure absorber, then $f = f_a$). Scattering may either increase or decrease the average neutron fluence rate, so the appropriate correction factor may be either greater or less than f_a . Theory predicts that, all other factors being equal, spheres will be least affected by neutron scattering, but not necessarily unaffected.^{5,6} For most of the solid spheres studied, element sensitivities were constant within $\pm 2\%$. These materials encompass a broad range of values for Σ_a (from approximately 0.5–5 cm $^{-1}$) but only a relatively small range of Σ_a values (approximately 0.02–0.05 cm $^{-1}$). Corrections for neutron self-shielding were typically $\leq 3\%$.

To determine whether the correction factors required to account for both scattering and absorption (f) are greater or less than those required for pure absorbers (f_a), apparent correction factors, i.e., the factors that would be required to

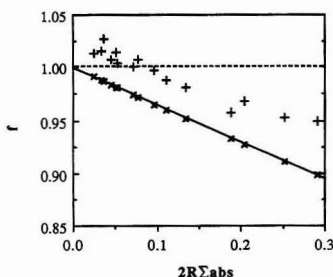


Figure 7. Self-shielding (X) and apparent (+) correction factors for data obtained from measurements of B in boric acid solutions contained in quartz globes.

correct the measured sensitivity to the sensitivity obtained from measurements on nonhydrogenous materials, were compared with the calculated self-shielding factors (f_a) for the same targets. Results from measurements on boric acid solutions of varying concentrations contained in quartz globes showed that the correction factors required for spheres that both scatter and absorb neutrons are greater than those required for purely absorbing spheres (Figure 7). (That is, because the value of the apparent correction factor is greater, the percent by which the values are corrected is less.) This finding indicates that, for spheres, neutron scattering counteracts the effects of neutron absorption; thus, the use of neutron self-shielding factors alone to correct data would overestimate the true correction factor that accounts for the effects of both scattering and absorption. This finding is not consistent with theoretical work^{5,6} that predicts that correction factors for spheres that scatter and absorb will be less than those that only absorb.

CONCLUSIONS

In general, to ensure accuracy in the analysis of hydrogenous materials (of any size or shape), analytical portions and standards should be matched with respect to size, shape, and matrix, where "matrix" refers to the concentrations of individual elements. Using this method, element sensitivities for the (hydrogenous) standards and analytical portions will be enhanced relative to those obtained from nonhydrogenous standards, so that a new set of standards must be prepared for each type of matrix and target shape analyzed. Sensitivity enhancements were not observed in conjunction with other scatterers commonly present in biological materials (C, N, O) so that, in most cases, it is sufficient to match portions and standards with respect to H concentration, size, and shape. To eliminate the need to prepare a different set of standards for each matrix, spheres may be employed as, in many cases, the use of spheres will eliminate sensitivity enhancements.

(15) Reynolds, Samuel A.; Mullins, W. Thomas. *Int. J. Appl. Radiat. Isot.* 1963, 14, 421.

For materials that are both strongly scattering and absorbing (especially hydrogenous materials containing large amounts of Gd or Sm), standards and analytical portions should be closely matched with respect to element composition (as well as size and shape).

Although measurements using instrumental neutron activation analysis (INAA) were not performed for this work, enhancement of INAA sensitivities for hydrogenous materials have been reported twice, and those investigators attributed the observed enhancements to neutron moderation.^{7,15} According to theory, little or no enhancement should be observed for INAA or for in-reactor PGAA in which irradiations in a nearly isotropic neutron field are used.⁵

Theoretical work^{4,5} and comparison of theoretical and experimental data⁶ indicate that the sensitivity enhancements observed using the UM/NIST PGAA facility are large the result of elastic neutron scattering by H. However, it is unlikely that the anomalous results from measurements on spheres containing Sm and Gd solutions can be accounted for by this model. As discussed above, these results suggest a possible role of low-energy neutron absorptions resonances, which are quite strong in both elements, but a mechanism by which the presence of a resonance might increase sensitivities for all elements in the matrix is not known.

ACKNOWLEDGMENT

We gratefully acknowledge the cooperation of the NIST reactor staff during these experiments. We thank Dick Turner of the NIST machine shops for his time and effort in the fabrication of the dies used for creating solid spheres and Jeff Anderson of the NIST glass shop for his time and effort in creating the quartz globes. We also wish to thank John R. D. Copley for his interest and advice in this work. This work was supported in part by the National Institute of Standards and Technology through Grant/Cooperative Agreement 70NANB9H0903 to the University of Maryland. This work was taken from the dissertation submitted by E.A.M. to the Graduate School of Arts and Sciences at the University of Maryland in partial fulfillment of the requirements for a Ph.D. degree in Chemistry. Certain commercial equipment, instruments, or materials are identified in this paper in order to specify the experimental procedures in adequate detail. Such identification does not imply recommendation or endorsement by the National Institute of Standards and Technology nor does it imply that the materials or equipment identified are necessarily the best available for the purpose. Contributions of the National Institute of Standards and Technology are not subject to copyright.

RECEIVED for review February 25, 1992. Accepted June 30, 1992.

Registry No. THAM, 77-86-1; H, 1333-74-0; B, 7440-42-8; Cl, 7782-50-5; K, 7440-09-7; Br, 7726-95-6; Cd, 7440-43-9; Sm, 7440-19-9; Gd, 7440-54-2; urea, 57-13-6; quartz, 60676-86-0; neutron, 12586-31-1.

Steady-State Voltammetry of Strong and Weak Acids with and without Supporting Electrolyte

Malgorzata Ciszewska and Zbigniew Stojek

Department of Chemistry, University of Warsaw, ul. Pasteura 1, 02-093 Warsaw, Poland

Susan E. Morris and Janet G. Osteryoung*

Department of Chemistry, North Carolina State University, Raleigh, North Carolina 27695-8204

Voltammetric reduction of perchloric, phosphoric, acetic, and ascorbic acid was investigated under steady-state conditions at platinum- and gold-disk microelectrodes. The dependence of the wave height of proton in perchloric acid on the concentration of supporting electrolyte (lithium perchlorate) was compared with the theory for currents limited by migration and diffusion. The wave height depends linearly on hydrogen ion concentration without and with supporting electrolyte up to 0.04 and 0.08 M, respectively. Also, acetic and ascorbic acids exhibit linear calibration plots with current proportional to concentration of undissociated acid up to 0.1 M. This is as would be predicted for reduction of proton subsequent to fast dissociation of the acid. The fairly well-defined limiting current for dihydrogen phosphate indicates that weak acids with pK_a in excess of 7 are accessible to voltammetric investigation.

about $1 \times 10^{-4} \text{ cm}^2 \text{ s}^{-1}$). This makes it attractive for examination of the effects of ionic strength on mass transport properties. The diffusion coefficient of proton is well-known for many different experimental conditions. Thus diffusion-limited current for steady-state reduction of proton at a disk can be compared with the value predicted by

$$i_d = 4nFDc_r \quad (1)$$

where r is the electrode radius, to test the fidelity of the actual electrode to the presumed shape and size.

The first objective of this work is to explore these aspects of proton reduction at platinum and at gold embedded circular microelectrodes. Also considered is the relation between the proton concentration as determined voltammetrically and the pH. In particular, the voltammetric reductions of phosphoric, ascorbic, and acetic acids are compared with that for perchloric acid.

INTRODUCTION

Microelectrodes of some geometries, for example, the embedded circular geometry, yield steady-state currents at fairly short times.¹ For example, an embedded circular electrode of diameter 25 μm exhibits a chronoamperometric current within 5% of the steady state for times greater than 0.8 s for $D = 10^{-4} \text{ cm}^2 \text{ s}^{-1}$. In the mass-transport-limited range of potential, this current is independent of charge-transfer kinetics and of surface properties of the electrode. This suggests that voltammetric monitoring of proton concentration under these conditions could be useful analytically. Examples in which this approach could be competitive with potentiometric measurements employing the glass electrode include measurements in media containing charged colloidal particles (where standard pH electrodes cannot be used²), probing proton concentrations in a small region (e.g., near a large electrode), or any situation where one cannot wait for the potential of a pH electrode to stabilize. Other approaches have also recognized the need for nonpotentiometric pH sensors.³

Reduction of hydrogen ion also has the potential to be an excellent test system for electrochemical examination of microelectrodes. We have employed perchloric acid as a test system because it does not contaminate the cell. That is, both H_3O^+ and ClO_4^- are easily rinsed from most surfaces, and carry-over perchlorate would not interfere in most electrode reactions. The sensitivity for proton reduction is large due to the high value of the diffusion coefficient (usually

EXPERIMENTAL SECTION

All reagents were used as received. Volumetric dilutions to 0.05 M stock solutions were made from perchloric acid (9.2 M, puriss, Fluka) and acetic acid (glacial, reagent grade, J. T. Baker). All further dilutions were made from the same 0.05 M stock solution. Electrolyte concentrations were adjusted with lithium perchlorate (Aldrich) or sodium acetate (Sigma) prepared by weight in the appropriate acid solutions. Ultrapure water (Milli-Q, Millipore Corp.) was employed in all solutions and in rinsing. Cyclic staircase and square-wave voltammetries were applied with a Model 273 potentiostat (EG&G PARC) and controlled via software on a PDP8/e minicomputer (Digital Equipment Corp.). A BAS-100 electrochemical analyzer was also used. Except as specified, the experiments were performed in a jacketed cell (25 °C) enclosed in a solid aluminum Faraday cage. Solutions were deoxygenated before voltammetric scans and then blanketed with a stream of water-saturated argon.

A platinum-wire counter electrode and a SCE reference electrode were used. The reference junction was isolated from the low-electrolyte solutions with an auxiliary Vycor-tipped bridge containing 0.01 M HClO_4 . Electrodes were supported via press-fitting into holes drilled in a neoprene-disk cell cap. Working microelectrodes were 11.25- μm -radius Pt and 12.5- μm -radius Au (Project Ltd., Warsaw, Poland). The electrodes were initially polished to mirror finish with 1- μm alumina on a very wet pad (Buehler Ltd.). Subsequently, the surface was renewed before voltammetric scans by polishing briefly with 0.05- μm alumina on a wet pad. The electrode was rinsed to remove alumina with a direct stream of water from a wash bottle impinging on the electrode surface. Water was wicked from the surface using a dry tissue. Bulk viscosities of solutions of LiClO_4 were measured at 25 °C using an Ostwald-type viscometer.

Even with repeated rinses, electrolytes and particulates carry over on the electrode surface from polishing and wiping and contribute to irreproducibility of initial scans in solutions with extremely low concentration of supporting electrolyte. Reproducibility of plateau currents for initial scans is improved by allowing the electrode to remain at the open circuit potential in

(1) Wightman, R. M.; Wipf, D. O. In *Electroanalytical Chemistry*; Bard, A. J., Ed.; Marcel Dekker: New York, 1989; Vol. 15, p 267.

(2) Morris, S. E.; Osteryoung, J. In *Electrochemistry in Colloids and Dispersions*; Mackay, R., Texter, J., Eds.; VCH: New York, 1992.

(3) Hickman, J. J.; Ofer, D.; Laibinis, P. E.; Whitesides, G. M.; Wrighton, M. S. *Science* 1991, 252, 688.

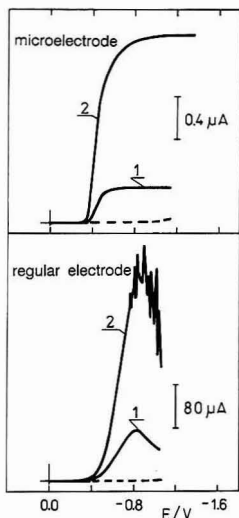


Figure 1. Voltammetric waves for reduction of proton at a microelectrode (11.25- μm -radius Pt disk, top) and at a conventional electrode (0.15-cm-radius Pt disk, bottom). Conditions: linear scan voltammetry, 20 mV s^{-1} ; $T = 20^\circ\text{C}$; supporting electrolyte, 1 mM LiClO_4 . HClO_4 : 0.005 M (1), 0.025 M (2).

solution before voltammetric scans for 3–5 min, which allows electrolyte on the surface of the electrode to disperse in the bulk acid solution. Rinsing after polishing with 0.5 M HClO_4 and then with H_2O accomplishes the same purpose, indicating that alumina particles carried over from polishing are a primary source of the adventitious electrolyte. The best results are obtained when the electrode is maintained for 3–5 min at +0.2 V vs SCE in the acid solution. During that period electrolyte is dispersed and adsorbed oxygen species also are reduced and their products dispersed before the voltammetric scan is begun.

For an appropriately prepared surface, initial scans exhibit a steeply sloped wave with a well-defined plateau. The plateau level is maintained on subsequent scans, but the slope of the wave decreases.

RESULTS AND DISCUSSION

Voltammograms for reduction of proton at an electrode of conventional size and at a microelectrode are compared in Figure 1. The purpose of this comparison is to demonstrate that oscillations related to formation of bubbles at the electrode surface appear at much lower concentrations at the larger electrode. This is despite the fact that the current density at the Pt-microdisk electrode is about 1 order of magnitude higher than at the conventional disk electrode. Apparently, larger bubbles are not formed easily at the microelectrode. We attribute this to faster removal, in the spherical diffusional field, of the hydrogen formed in the reaction.⁴

Linear scan voltammetry of proton at platinum electrodes in nonaqueous solution has been suggested for analytical purposes.⁵ However the linear range of the i vs C relationship was reported to terminate at 4 mM. At higher concentrations the current dropped. That report is consistent with our findings. Formation of gaseous hydrogen at a conventional

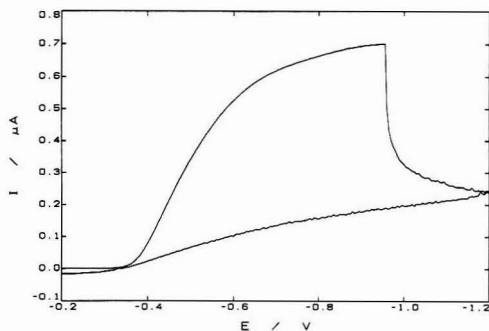


Figure 2. Cyclic staircase voltammogram of 0.01 M HClO_4 at a Pt microelectrode distorted by formation of a bubble. No electrolyte was added. Conditions: $\Delta E_s = 5 \text{ mV}$, $f = 4 \text{ Hz}$.

disk has also been investigated recently by the electrochemical microbalance method.⁶

Curve 2 in the bottom part of Figure 1 reflects consecutive formation of many bubbles. At a microelectrode one bubble can kill the current, and a bubble once started grows very fast. The average rate of growth for the radius of a bubble is estimated to be $12.2 \mu\text{m s}^{-1}$. It is assumed that bubbles form at the electrode surface and are anchored there. An example of the resulting behavior is given in Figure 2. Note that the proton concentration for Figure 2 is less than that for curve 2 of Figure 1. The formation of bubbles depends on concentration but also on the state of the electrode surface. A "properly polished" microelectrode can be used at much higher concentrations than 0.01 M, the concentration of Figure 2, with no evidence of bubbles. After formation of a bubble, the microelectrode usually needs repolishing or washing in a sharp stream of water.

Influence of Supporting Electrolyte. The curves presented in Figure 1 were obtained in solutions containing 1 mM LiClO_4 as supporting electrolyte. Under conditions in which supporting electrolyte is not in excess, the limiting current is determined by both diffusion and migration. This behavior of proton (or other reducible cations) has been known in electrochemistry for a long time.⁷ Rigorous theoretical treatments of microelectrode voltammetry with little supporting electrolyte have appeared in the literature recently.^{8–10}

The dependence of the height of the wave for reduction of 9.14 mM hydrogen ion on the concentration of the supporting electrolyte (lithium perchlorate) is given in Table I. The large concentration of proton was chosen to ensure a good starting point, that is, a high ratio of the concentration of proton to that of other adventitious cations, and to eliminate possible change in the wave height due to reduction of traces of dissolved oxygen, which produces hydroxide. In order to compare the data of Table I with the predictions of theories^{9,10} the currents are corrected for the change in solution viscosity and for change in activity coefficient.

Relative viscosity for solutions of LiClO_4 varies linearly with concentration in the range 1–2 M, with slope equal to 0.106 M^{-1} and intercept equal to 0.966. Below 1 M, relative viscosity values depart positively from the line and approach

(6) Carr, M. W.; Hillman, A. R.; Lubetkin, S. D.; Swann, M. J. *J. Electroanal. Chem. Interfacial Electrochem.* 1989, 267, 313.

(7) Heyrovsky, J.; Kuta, J. *Principles of Polarography*; Academic Press: New York, 1966; p 68.

(8) Oldham, K. B. *J. Electroanal. Chem. Interfacial Electrochem.* 1988, 250, 1.

(9) Amatore, C.; Fosset, B.; Bartlett, J.; Deakin, M. R.; Wightman, R. M. *J. Electroanal. Chem. Interfacial Electrochem.* 1988, 256, 255.

(10) Baker, D. R.; Verbrugge, M. W.; Newman, J. J. *Electroanal. Chem. Interfacial Electrochem.* 1991, 314, 23.

(4) Bockris, J. O'M.; Reddy, A. K. N. *Modern Electrochemistry*; Plenum: New York, 1970; Vol. 2, p 1250.

(5) Nelson, R. C.; Adams, R. N. *J. Electroanal. Chem. Interfacial Electrochem.* 1968, 16, 437.

Table I. Influence of Concentration of LiClO₄ on Limiting Current for Reduction of Proton^a

$C_{\text{LiClO}_4}/\text{M}$	$i/\mu\text{A}$	$C_{\text{LiClO}_4}/\text{M}$	$i/\mu\text{A}$
(0) ^a	0.734	0.0633	0.356
0.0002	0.663	0.180	0.340
0.0022	0.538	1.00	0.264
0.0041	0.494	1.11	0.257
0.0079	0.451	1.25	0.250
0.0149	0.417	1.43	0.240
0.0277	0.390	1.67	0.227
0.0474	0.371	2.00	0.209

^a 10 mM HClO₄. No electrolyte added; the background concentration may be as large as 10^{-6} M; Pt microelectrode ($r = 11.25 \mu\text{m}$).

a value of 1.0 in very dilute solutions of LiClO₄. The limiting current value is multiplied by the relative viscosity for the appropriate LiClO₄ concentration to adjust all currents to those which would be obtained in dilute solution. The maximal value of η/η_0 is 1.178.

A linear variation of ionic diffusion coefficient with the square root of ionic strength is expected¹¹ as a result of change in activity coefficient. In this medium with only univalent salts, we assume

$$D = D^\circ(1 - 0.512C^{1/2}/2) \quad (2)$$

where D is the value of diffusion coefficient in solution with electrolyte concentration C . Limiting currents for high electrolyte concentration ($C > 1$ M), where transport is purely diffusional, are normalized by the relative viscosity and plotted vs $C^{1/2}$. The slope and intercept are respectively $-91.1 \text{ nA M}^{-1/2}$ and 375 nA , with the standard error of estimate $s_y = 1.42 \text{ nA M}^{-1/2}$ and the coefficient of correlation $r = -0.996$. These values, together with eq 1, yield values of D° of 0.90 and $0.94 \times 10^{-4} \text{ cm}^2 \text{ s}^{-1}$, respectively, which agree reasonably well with the value $0.93 \times 10^{-4} \text{ cm}^2 \text{ s}^{-1}$ for D° in water from limiting conductivity at infinite dilution.¹² Normalized values of diffusion-limited current, i_d' , for intermediate concentrations of electrolyte are obtained from this plot.

The data of Table I are used to test theoretical predictions by comparing experimental and theoretical values of the ratio $(i_\infty/\eta_0)/i_d'$ for various values of $\log \gamma$, where γ is the ratio of excess electrolyte, $C_{\text{LiClO}_4}/C_{\text{HClO}_4}$.

To summarize, we compare currents corrected to infinite dilution for changes in viscosity but not corrected to infinite dilution for changes in activity coefficient. The reason for this mixed procedure is that it allows us to separate the effects of changes in viscosity and activity and, thereby, to test directly the reasonableness of the assumption that eq 2 is appropriate. We emphasize that the changes in viscosity are quite large (here about 20%) and need to be taken into account to reach reasonable agreement with theory.

As seen in Figure 3, deviations between the theory and the experiment are small. One theory⁹ assumes both substrate and product are soluble with equal diffusion coefficients. Another theory¹⁰ applies where the substrate is soluble and charged, whereas the product is neutral and insoluble, consistent with a process such as electrodeposition or evolution of a gas. While these assumptions differ, no difference is seen in the predictions of migrational currents by the two theories for the reduction of a univalent cation in a 1:1 indifferent electrolyte, which is shown by the continuous curve of Figure 3. It is not surprising that predictions concerning the transport-limited current are insensitive to the assumptions made about the transport of product. Reduction of

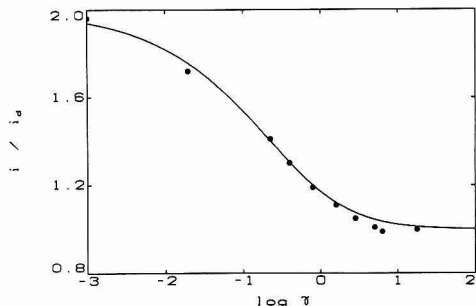


Figure 3. Limiting current ratio $(i_\infty/\eta_0/i_d')$ as a function of the ratio of supporting electrolyte to proton concentration (γ). Data are from Table I. Values of i_d' are obtained as described in the text.

proton comes close to the assumptions of ref 8. Solubility of hydrogen in water is reported to be $1.91 \text{ cm}^3/100 \text{ cm}^3$ ¹³ which corresponds to 0.8 mM. A certain amount of H₂ must dissolve in platinum. The diffusion coefficient of H₂ in water is $(3.43\text{--}7.07) \times 10^{-5} \text{ cm}^2 \text{ s}^{-1}$.¹⁴ The value of D_{H_2} in water from limiting conductivity at infinite dilution¹¹ is $9.3 \times 10^{-6} \text{ cm}^2 \text{ s}^{-1}$, whereas the value is $7.45 \times 10^{-6} \text{ cm}^2 \text{ s}^{-1}$ in 1 M KCl.¹⁴

It is possible that H₂ can form an oversaturated solution in the diffusion layer, which would narrow the gap between the theoretical assumptions and the real experimental situation. To test this point, the ratio of currents measured in the presence and the absence of supporting electrolyte was measured also for 1 mM acid solution. The values obtained agree with the data of Figure 3 within 2%.

We examined the semilogarithmic plot $(\log ((i_d - i)/i) \text{ vs } E)$ for the curves obtained in the absence and the presence of supporting electrolyte and found that the slopes at the wave foot were similar, 59 and 56 mV, respectively. For higher parts of the waves the semilogarithmic plot displayed two points of curvature to give two successively larger values. It has been remarked by Swan¹⁵ that multiple waves may be observed for reduction of proton on platinum microelectrodes. Because the relative heights of these poorly resolved waves depend on electrode radius, electrode activation (preparation), and potential scan rate, it was speculated that the waves reflect differing contributions to the current from two mechanisms for proton reduction on the platinum surface. The diffusion-limited current for the overall process, reduction of proton to hydrogen, is not sensitive to the surface kinetic process, so the height of the wave at steady state is unaffected. We did not examine more closely the kinetics of this process.

The amplitude of the wave for proton reduction depends linearly on concentration both with and without added electrolyte, as shown in Figure 4. The range of linearity is limited by the formation of bubbles at sufficiently high concentration. In the absence of deliberately added electrolyte the linear range extends from 0.01 to 40 mM. The correlation coefficient for this line is 0.99994, and the detection limit is estimated as 0.01 mM.

Absence of supporting electrolyte is a very demanding condition, as was described in the Experimental Section. Addition of supporting electrolyte at the 0.1 M level is advantageous for a variety of reasons. First, the linear range of i vs C is wider, extending up to 0.1 M. Second, the reproducibility of the waves is enhanced. Third, as shown in

(11) Bockris, J. M.; Reddy, A. K. N. *Modern Electrochemistry*; Plenum: New York, 1970; p 384.

(12) *CRC Handbook of Chemistry and Physics*; CRC Press: West Palm Beach, FL, 1978-9.

(13) *Encyclopedia of Electrochemistry of the Elements*; Bard, A. J., Ed.; Marcel Dekker: New York, 1982; Vol IX, Part A, p 407.

(14) Koryta, J.; Dvorak, J.; Bohackova, V. *Lehrbuch der Elektrochemie*; Springer Verlag: Wien, 1975.

(15) Swan, D. N. Ph.D. Thesis, University of Southampton, 1980.

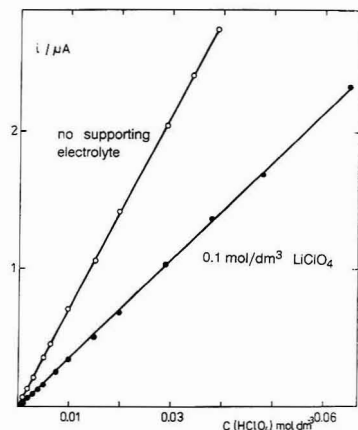


Figure 4. Limiting current for reduction of proton vs concentration of HClO_4 at an 11.25- μm -radius Pt disk.

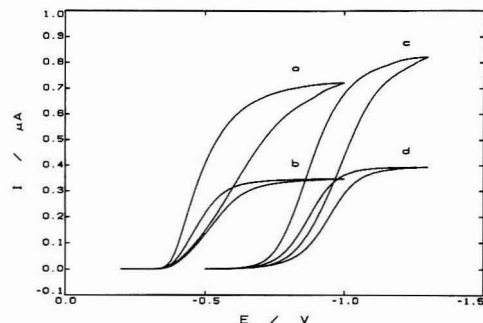


Figure 5. Cyclic staircase voltammograms obtained in 0.01 M HClO_4 at 11.25- μm -radius Pt disk (a, b) and 12.50- μm -radius Au disk (c, d). Concentration of supporting electrolyte: 0 M (a, c), 0.1 M (b, d). Conditions: $\Delta E_s = 5$ mV, $f = 4$ Hz.

Figure 5, the current plateau is well developed at a less extreme potential, which makes measurements faster and more simple.

Referring once again to Figure 3, note that the limiting current depends only weakly on the ratio of supporting electrolyte to proton concentration when that ratio is much larger than unity or much less than unity. The data of Figure 4 are for $\log \gamma = 1$ and $\log \gamma = -3$ (nominal), respectively. It might be expected that in the intermediate range, say $0 \leq \log \gamma \leq -2$, there would be experimental problems with generating acceptable calibration curves, because it would be difficult to maintain $\log \gamma$ constant while the concentration of proton varied. We did not test our patience by exploring this point experimentally. In related work we have obtained satisfactory analytical results by obtaining a matrix of points at various values of γ and C and effectively interpolating to obtain a calibration curve at fixed γ .²

Reduction of Proton at a Gold Microelectrode. Usually, the overpotential for cathodic reduction of proton at gold is not much larger than that at platinum.¹⁶ It depends strongly, however, on the current density. Typical cyclic staircase voltammograms obtained at the gold microelectrode are compared with those obtained at the platinum microelectrode in Figure 5. For these conditions, the current densities were in the range of 0.1 A cm^{-2} , that is, rather high. Both with and

without added supporting electrolyte the voltammograms on gold are shifted substantially toward more negative potential. Under the conditions of Figure 5 the shift is 0.40 V. The heights of the waves at the gold electrode are directly proportional to acid concentration and should be as useful for analytical purposes as those obtained at platinum electrodes.

Reduction of Weak Acids. Weak acids also are reduced at a platinum microelectrode. In our study we chose ascorbic, acetic, and dihydrogen phosphate acids ($\text{p}K_a = 4.17, 4.8$, and 7.21 , respectively). There is no doubt that the reduction process in solutions of these acids is the reduction of proton. The height of the wave in each case diminished gradually with addition of NaOH and disappeared completely when the amount of NaOH equivalent to titration of one proton per molecule was added. In the case of ascorbic acid, which also can be oxidized in a two-electron process at $+0.40 \text{ V}$,¹⁷ the ratio of anodic to cathodic wave height was very close to 2. (The cathodic wave is located at -0.52 V). Ascorbic and acetic acids dissociate negligibly in water, so wave heights are virtually independent of the supporting electrolyte concentration. That is, the diffusing species is neutral, so the current limited by transport of reactant is unaffected by migration. (The limiting current for reduction of acetic acid depends on concentration of sodium acetate in the range 0 – 0.5 mM . We are currently investigating this behavior.)

Reduction of proton from acetic acid follows the reaction¹⁸



Proton is reduced at a potential similar to that for perchloric acid, but the limiting current is controlled by the diffusion coefficient for acetic acid. As an example of the CE kinetic case, it can be seen from a comparison of the reaction layer thickness with the diffusion layer thickness that the diffusion control observed is reasonable. Consider the experimental conditions of a 5-mV step height at 4 Hz . The limiting current is measured about 30 s into the scan (the deviation from steady state is about 5%). The steady-state diffusion layer thickness is given approximately by $l = \pi r/4 = 8.8 \times 10^{-4} \text{ cm}$. The reaction layer thickness is given by $\mu = (D_{\text{HA}}/k_{-1})^{1/2}$. With $k_b = 4.2 \times 10^{10} \text{ M}^{-1} \text{ s}^{-1}$ ¹⁸ and $C_A = 0.1 \text{ M}$, $k_{-1} = k_b C_A = 4.2 \times 10^9 \text{ s}^{-1}$, and with $D = 10^{-5} \text{ cm}^2 \text{ s}^{-1}$, $\mu = 4.9 \times 10^{-8} \text{ cm}$. Thus $\mu/l = 6 \times 10^{-5}$, or the current is controlled by diffusion of the undissociated acid.

A somewhat more sophisticated treatment takes into account the diffusion of H^+ , but assumes k_b is large and the bulk concentrations have the relation $[\text{H}^+] \ll [\text{HA}] \ll [\text{A}^-]$. For spherical diffusion the result is¹⁸

$$i/i_{\text{HA}} = [1 + D_{\text{HA}}(C_A/k_b D_{\text{H}})^{1/2}/K_A r]^{-1} \quad (5)$$

where i is the observed current and i_{HA} is the putative steady-state current for direct reduction of HA . Thus for $i = i_{\text{HA}}$ it must be the case that $K_A \gg D_{\text{HA}}(C_A/k_b D_{\text{H}})^{1/2}/r$. Using the nominal values given above, the condition is $K_A \gg 2 \times 10^{-6} \text{ M}$.

Calibration curves for strong and weak acids in 0.1 M LiClO_4 are linear up to 0.1 M , as shown in Figure 6. The diffusion coefficient values, calculated using these data and eq 1, for acetic and ascorbic acids are $(1.08 \pm 0.03) \times 10^{-5}$ and $(5.7 \pm 0.1) \times 10^{-6} \text{ cm}^2 \text{ s}^{-1}$, respectively. Reported values under similar

(16) Kuhn, A. T.; Byrne, M. *Electrochim. Acta* 1971, 16, 391.

(17) *Organic Electrochemistry*, 2nd ed.; Baizer, M.; Lund, H., Eds.; Marcel Dekker: New York, 1983.

(18) Fleischmann, M.; Lasserre, F.; Robinson, J.; Swan, D. J. *Electroanal. Chem. Interfacial Electrochem.* 1984, 177, 97.

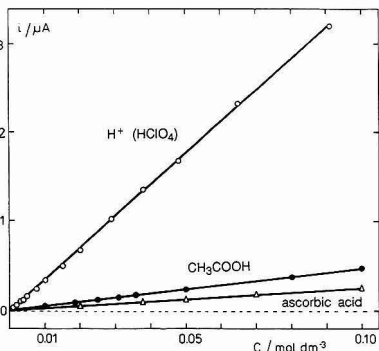


Figure 6. Limiting current vs acid concentration for acetic, ascorbic, and perchloric acids at 20 °C.

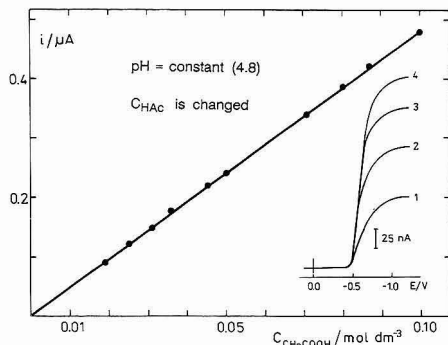


Figure 7. Limiting current for reduction of acetic acid vs concentration of acetic acid at constant pH of 4.8. $C_{\text{HAC}} =$ (1) 0.019 M (2), 0.031 M, (3) 0.042 M, (4) 0.050 M.

conditions of concentration and temperature are $1.2 \times 10^{-5} \text{ cm}^2 \text{ s}^{-1}$ for acetic acid¹⁹ and $5.7 \times 10^{-6} \text{ cm}^2 \text{ s}^{-1}$ for ascorbic acid.²⁰ These values are sufficiently close to the values determined here from the slopes of the calibration plots to suggest that the rates are controlled by diffusion of the undissociated acid.

Several experiments were done for acetic acid in solutions buffered with sodium acetate. Upon a change in NaOAc concentration from 0.01 to 0.1 M the slope of the calibration plot decreased by 8.1%, while the half-wave potential shifted from -0.54 to -0.64 V. Typical waves for reduction in solutions of acetic acid are presented in Figure 7, where also the wave height is plotted versus the concentration of HOAc at constant pH (pH 4.8, i.e., equal concentrations of HOAc and NaOAc).

To explore the limit of acid dissociation constant for which these simple relations obtain, we investigated the reduction of dihydrogen phosphate ion, which has $\text{p}K_A = 7.21$ (25 °C). A wave at -0.65 V is observed for reduction of proton on Pt in 10 mM solution of H_2PO_4^- , without added supporting electrolyte. The wave is progressively less well defined with increasing concentration of electrolyte. The wave is poorly resolved from the background (reduction of H_2O), and the limiting current is somewhat irreproducible. These phenomena appear to be related, that is, the irreproducibility results from the difficulty of subtracting the background

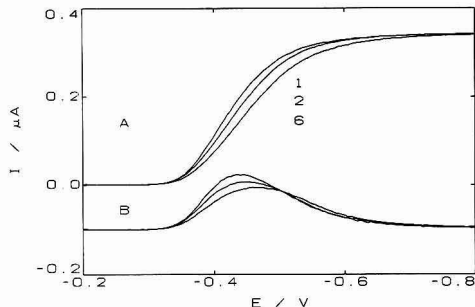


Figure 8. First, second, and sixth scans obtained for reduction of 0.01 M proton (HClO_4) in 0.1 M LiClO_4 : (A) steady-state curves; (B) net current in SWV, net currents offset by -0.1 μA . Conditions: $\Delta E_s = 5 \text{ mV}$, $E_{\text{sw}} = 25 \text{ mV}$, $f = 2 \text{ Hz}$.

current. A diffusion coefficient value calculated from the limiting current is $6.3 \times 10^{-6} \text{ cm}^2 \text{ s}^{-1}$. In the case of reduction of a singly charged anion, the limiting value of i_l/i_d is 0.85 in the absence of supporting electrolyte.⁹ Thus the diffusion coefficient is calculated from eq 1 using $i_l/0.85$ for i_d . Direct titration of the proton from H_2PO_4^- with base yields a linear decrease of limiting current to zero, with an end point corresponding within 3.5% to the titration of one proton. Therefore diffusion-controlled limiting currents for reduction of HA occur up to at least $\text{p}K_A = 7.2$ under these conditions.

The development of eq 5 ignores diffusion of A^- , which should be taken into account to describe our results in more detail. The simple requirement $K_A \gg D_{\text{HA}}(C_A/k_b D_A)^{1/2}/r$ is, for these conditions, $K_A \gg 1.4 \times 10^{-8} \text{ M}$. Since K_A for H_2PO_4^- is $6.2 \times 10^{-8} \text{ M}$, the approximate treatment of eq 5 is in reasonable accord with the results.

Square-Wave Voltammetry. The net current in SW voltammetry has the virtue of providing sensitivity and good rejection of background and unwanted signal.²¹ For totally irreversible systems, the sensitivity is less because there is no backward reaction. Substantial increase in the pulse amplitude will increase the peak amplitude at the expense of a broader peak.²¹ The cathodic reduction of proton is totally irreversible. Furthermore, the wave has a tendency to decrease in slope in consecutive scans, as shown in Figure 8A. Therefore the net current decreases in consecutive runs, as shown in Figure 8B. However, the height of the forward current plateau, at a frequency low enough to produce the steady state, is as stable in time as that for linear scan or staircase voltammetry, that is, the choice of the technique employed to achieve the steady state does not influence the result.

Voltammetry in a Mixture of a Strong and a Weak Acid. The half-wave potentials of HClO_4 and acetic acid differ in value by approximately 100 mV, which is not sufficient to resolve the waves. After differentiation the voltammogram exhibits two peaks corresponding to two acids. However, this procedure can be applied only for a qualitative treatment, since the sensitiveness of the slopes of both steady-state waves to kinetic factors, as described above, leads to unacceptable variations in the magnitude of the differential curve.

CONCLUSIONS

The steady-state transport-limited current for reduction of proton in solutions of strong acids with excess supporting

(19) Gostiša-Mihelčić, V. B.; Vielstich, W. *Ber. Bunsen-Ges. Phys. Chem.* 1973, 77, 476.

(20) Gillam, W. S. *Ind. Eng. Chem., Anal. Ed.* 1945, 17, 217-221.

(21) Osteryoung, J.; O'Dea, J. J. In *Electroanalytical Chemistry*; Bard, A. J., Ed.; Marcel Dekker: New York, 1986; Vol. 14, p 209.

electrolyte obeys quantitatively the equation for steady-state diffusion at a disk. It is useful therefore not only for analytical purposes but also for testing microelectrodes. The same reaction examined over a range of concentrations of supporting electrolyte yields a limiting current which varies from the value of the predicted diffusion-limited current at high electrolyte concentration to a value about twice as large as the predicted diffusion-limited current at low electrolyte concentration. The limiting current is affected strongly by changes in both viscosity and activity coefficient. These changes must be taken into account in order to compare the experimental results with theoretical predictions. With this limitation in mind it is possible also to test microelectrodes by measuring the transport-limited current over the entire range of electrolyte concentration. The analytical application, which can rely on calibration rather than absolute measurements, applies over the entire range as well.

The reduction of weak acids also is useful analytically. Neutral weak acids display diffusion-limited steady-state currents over a wide range of electrolyte concentration. An acid as weak as the dihydrogen phosphate ion ($pK_A = 7.2$) displays a reasonably well-defined limiting current which appears to be diffusion-controlled.

In mixtures the quantity measured is proportional to the sum of the products of diffusion coefficients and concentrations for all of the strong and weak acids present. Because the current response depends on both diffusional and concentrative properties, it is not a useful direct measure of total acidity in the case of mixtures. However, it is an excellent signal for detection of the end point in an amperometric acid-base titration. The ill-defined kinetic properties of the charge-transfer process make it impossible to resolve the reduction process associated with the weak acids from the direct reduction of proton.

ACKNOWLEDGMENT

This work was supported in part by the U.S. National Science Foundation under Grant Nos. CHE9024846 and CHE9208987, and by Project 12-501/III/BST-83/91, University of Warsaw, Poland.

RECEIVED for review March 3, 1992. Accepted July 10, 1992.

Data-Processing Method To Reduce Error Coefficients for Membrane-Based Analytical Systems. 1. Amperometric-Based Sensor Evaluated for Quantification of Oxygen

Christopher E. Uhegbu and Harry L. Pardue*

Department of Chemistry, 1393 BRWN Building, Purdue University, West Lafayette, Indiana 47906-1393

This paper describes the use of a predictive, curve-fitting method to reduce the effects of experimental variables on results obtained with membrane-based devices. Multipoint data from the transient regions of responses are used with suitable models and curve-fitting methods to predict the signal that would be measured for the system at equilibrium. The resulting equilibrium response usually is much less dependent on experimental variables than the transient responses used to predict it. The approach is evaluated for the membrane-based amperometric electrode for oxygen. Current vs time data are used to predict the equilibrium current expected when oxygen concentrations are the same on both sides of the membrane. Predicted equilibrium currents vary linearly with oxygen concentration. Relative to the more common steady-state method, the sensitivity of the predictive method is about 5-fold higher, the measurement time is about 17-fold shorter and the dependencies on membrane thickness and stirring rate are 125- and 8-fold lower, respectively. Pooled standard deviations ($n = 40$) correspond to uncertainties in oxygen concentration of about 0.009 mmol L⁻¹.

An amperometric electrode¹ coupled with an oxygen-selective membrane is one of many types of membrane-based devices²⁻⁴ used in analytical chemistry. As with most such devices, what is usually measured with the oxygen-selective electrode is a nonequilibrium steady-state response,^{5,6} i.e., a response that remains constant with time even though the system is not at equilibrium. For the oxygen-selective device, the steady-state response corresponds to a situation in which the rate of mass transfer to and across the membrane is exactly equal to the rate of mass transfer from the membrane to the surface of the sensing electrode where oxygen is reduced as rapidly as it reaches the electrode surface. Analogous types of rate processes control steady-state responses frequently measured with other types of membrane-based devices.

Because rate processes usually depend more on experimental variables than equilibrium conditions, methods based on nonequilibrium steady-state responses from membrane-based devices usually have large dependencies on experimental variables. This means that variables must be controlled within much tighter tolerances to achieve the same levels of reliability that would be possible with an equilibrium-based method. For example, the oxygen-selective device used

in the steady-state mode is very dependent on variables such as stirring rate and the properties of the membrane that isolate the working electrode from the bulk solution.^{5,6}

One way to reduce variable dependencies and improve the ruggedness of such devices is to use measurement and data-processing approaches that depend on equilibrium conditions rather than rates of mass transfer or chemical reactions. One such approach developed for the oxygen-selective device has been to equilibrate the electrode/membrane system with each test solution and to measure the initial rate of the current-time response.^{5,6} The rationale for this approach is that the measured rate represents a near-equilibrium condition in terms of the oxygen concentration on either side of the membrane. This approach was shown to be effective in reducing effects of membrane thickness and stirring rate in the external (sample) solution on results for oxygen concentration.^{5,6} However, this approach obviously replaces one set of rate processes for another which could be subject to influences from other types of variables. Also, the approach is applicable only to membrane-based systems in which there is a rate process that is directly related to the equilibrium condition.

This paper describes an alternative measurement/data-processing approach for membrane-based devices that offers the reduced variable dependencies demonstrated for the initial rate methods^{5,6} without the potential limitations mentioned above. The objective for the proposed approach is to obtain a signal corresponding to an equilibrium condition between solutions on either side of the membrane. This is accomplished by fitting suitable models to time-dependent (transient) data in a manner such that signals corresponding to equilibrium conditions can be predicted. This is an extension of a general approach developed initially for chemical kinetic processes^{7,8} and subsequently called a *predictive kinetic method*.⁹

We used the oxygen-selective device¹ as a model for this initial study of the general approach. The electrode was first immersed in the sample solution long enough to permit equilibration between oxygen concentrations inside and outside the membrane. The polarizing voltage was applied across the electrode and time-dependent current values were measured for a predetermined time period and stored in a computer. Then a suitable model was used to extrapolate the data current vs time to $t = 0$. The initial current, I_0 , should represent the equilibrium condition and therefore should be independent of variables that influence rate processes.⁷⁻⁹ Effects of membrane thickness and stirring rate are evaluated and compared for the conventional steady-state and proposed predictive methods.

(1) Hitchman, H. L. *Measurement of Dissolved Oxygen*; Wiley: New York, 1978.

(2) Bright, F. V.; Betts, T. A.; Litwiler, K. S. *Anal. Chem.* 1990, 62, 1065-1069.

(3) Bruckenstein, S.; Symanski, J. S. *Anal. Chem.* 1986, 58, 1766-1770.

(4) Melcher, R. G. *Anal. Chim. Acta* 1988, 214, 299-313.

(5) Mancy, K. H.; Okun, D. A.; Reilly, C. N. *J. Electroanal. Chem.* 1982, 4, 65-92.

(6) Wang, H. Y.; Li, X. *Biosensor* 1989, 4, 273-285.

(7) Mielsing, G. E.; Pardue, H. L. *Anal. Chem.* 1978, 50, 1611-1618.

(8) Mielsing, G. E.; Pardue, H. L.; Thompson, J. E.; Smith, R. A. *Clin. Chem. (Winston-Salem, NC)* 1979, 25, 1581-1590.

(9) Pardue, H. L. *Anal. Chim. Acta* 1989, 216, 69-107.

EXPERIMENTAL SECTION

Instrumentation. The oxygen-selective device (Model 5331, Yellow Springs Instrument Co., Yellow Springs OH 45387) was used with different thicknesses (25, 50, 75 μm) of Teflon membranes (YSI 5775, 25 μm thick, Yellow Springs Instrument Co.). A low-impedance electronic power supply was connected by a high-quality mechanical switch to the working electrodes. The polarizing voltage was 0.80 V for all results reported here.

Electrolysis current was measured with an operational-amplifier system with a current-to-voltage converter input stage with current offset and one stage of voltage amplification. A gain setting of 5 V/ μA was used for these studies.

The amplified signal was interfaced (Lab Master, Scientific Products, Corp., Cleveland, OH 44139) to a microcomputer (PC6300, AT&T, Iselin, NJ 08830). Data were transferred from the microcomputer to a supermicrocomputer (MC 550 workstation, Massachusetts Computer Corp., Westford, MA 01886). The computer system¹⁰ and data-processing algorithms^{8,9,11,12} have been described previously. All measurements were made at 25 °C. Samples were equilibrated in a water-jacketed cell through which water was circulated from a temperature-controlled water bath.

Procedures. Oxygen-free water was prepared by bubbling oxygen-free nitrogen through distilled deionized water.¹³ Measured aliquots of oxygen-free water were placed in the temperature-controlled sample compartment and a stream of oxygen-free nitrogen blanketed the solution in the cell at all times. After the oxygen-selective device was immersed in the oxygen-free sample, measured volumes of air-saturated water (0.26 mmol L⁻¹ oxygen) were added and sufficient time (~30 s) was allowed for the oxygen content inside and outside the membrane to equilibrate. Then potential (0.80 V vs Ag/AgCl) was applied across the electrodes and current was measured at two data rates for about 4 s. The first 100 points were collected at intervals of 0.0006 s/point and the last 150 points were collected at intervals of 0.027 s/point.

RESULTS AND DISCUSSION

All imprecisions are reported at the level of one standard deviation (± 1 sd) unless state otherwise.

Equilibration Time. It is important that the equilibration time be long enough that oxygen concentrations inside and outside the membrane become the same but short enough that the oxygen content of the sample does not change significantly. Figure 1 shows response curves for different time periods between the time when the air-saturated oxygen sample is added and the time when polarizing voltage is applied (at $t = 0$); the solutions were stirred continuously throughout the delay and measurement periods. The peak current continues to increase with the waiting period up to the longest period (30 s) included on the plot. Longer waiting periods would have given more complete equilibration between oxygen concentrations inside and outside the membrane; however, substantially longer waiting periods would have been required to improve the equilibrium condition by significant amounts. Accordingly, we chose a waiting period of 30 s as a compromise between the need to reach equilibrium and the need to avoid significant losses of oxygen to the nitrogen stream over the samples.

All results reported below were obtained with a waiting period of 30 s between addition of air-saturated samples to the well-stirred blank in the sample compartment and application of the polarizing voltages.

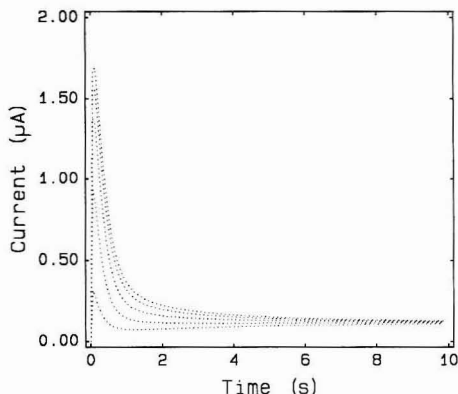


Figure 1. Effects of delay time on current vs time responses. Conditions: $C_{O_2} = 0.16$ mmol L⁻¹; polarizing voltage, 0.80 V vs Ag/AgCl; membrane thickness, 25 μm ; delay time (bottom to top) 5, 10, 15, 20, 30 s.

Response Curves. Figure 2A shows a typical set of response curves for different oxygen concentrations. The origin, $t = 0$, corresponds to the point at which potential is applied across the reference and working electrodes. Because of the faster data rates used during the early parts of the responses, the rising portions appear as solid lines. In all cases, currents rise very quickly when potential is applied, pass through smooth maxima, and then decay toward the steady-state values that are usually measured.

Most responses require about 30 s to reach steady state.¹³ The smooth maxima likely result from uncompensated iR drops and interactions between charging and electrolysis currents. These interactions make it virtually impossible to measure the equilibrium current at $t = 0$ directly. Our goal was to fit a suitable model to the current-time profiles in order to extrapolate each profile back to $t = 0$.

Our first problem was to select a model that would fit the data satisfactorily. Although a theoretical model has been developed for the transient response of this device,⁵ we were unable to obtain satisfactory fits with that model. Accordingly, we tested three empirical models, namely a first-order model,^{8,9} a parallel first-order model,¹¹ and a variable-order model.¹²

To test these options, data from 0.33 to 4.1 s after application of the polarizing voltage were fit with each model. A starting point of 0.33 s was used to reduce complications caused by curvature at the peak maxima. Although all the models fit the data reasonably well, best fits were obtained with the first-order model. Accordingly, unless state otherwise, data reported below were obtained by using a first-order model to fit the data.

Figure 2B shows fits of the first-order model to data in Figure 2A. Experimental and fitted data are virtually superimposed from about 0.2 s to the end of the range for which data were recorded. Rate constants for the first-order model were reasonably consistent for different concentrations. For five replicate runs on eight different concentrations between 0.05 and 0.26 mmol L⁻¹, apparent first-order rate constants varied from 2.6 s⁻¹ at the lowest concentration to 2.1 s⁻¹ at the highest concentration with a pooled standard deviation of 0.05 s⁻¹. The average of all the rate constants ($n = 40$) was 2.3 ± 0.2 s⁻¹. There were significantly larger variations among rate constants that gave best fits for the other two models.

Apparent first-order rate constants were virtually independent of membrane thickness. For membrane thicknesses

(10) Skoug, J. W.; Weiser, W. E.; Cyljak, I.; Pardue, H. L. *Trends Anal. Chem.* 1986, 5, 32-34.

(11) Willis, B. G.; Woodruff, W. H.; Frysinger, J. R.; Margerum, D. W.; Pardue, H. L. *Anal. Chem.* 1970, 42, 1350-1355.

(12) Larson, J. A.; Pardue, H. L. *Anal. Chim. Acta* 1989, 224, 289-303.

(13) Uhegbu, C. E.; Pardue, H. L. *Anal. Chim. Acta* 1990, 237, 413-420.

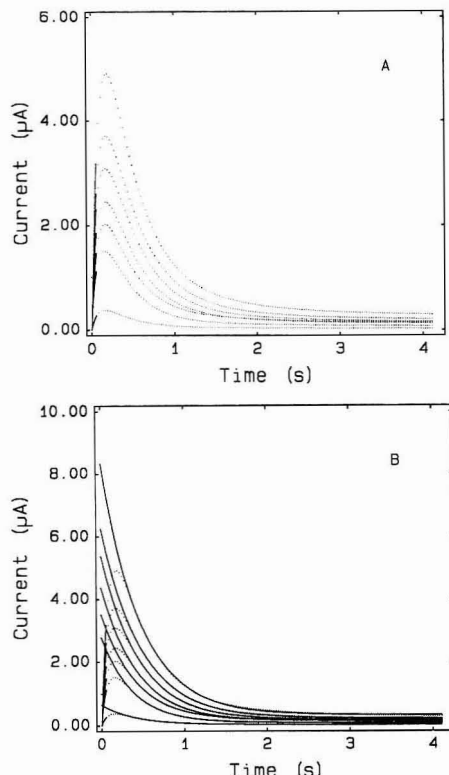


Figure 2. Response curves for different concentrations of oxygen: (A) experimental responses (---); (B) experimental (---) and fitted (—) responses, first-order model. Conditions as in Figure 1 except as follows: equilibration time, 30 s; concentration (bottom to top) 0.0, 0.05, 0.11, 0.13, 0.16, 0.21, 0.26 mmol L⁻¹.

of 25, 50, and 75 μm , average ($n = 5$) apparent rate constants were 1.8 ± 0.03 , 2.0 ± 0.02 , and $1.9 \pm 0.002 \text{ s}^{-1}$, respectively.

Concentration Dependence. Initial currents, I_0 , obtained by extrapolating data for current vs time to $t = 0$, as illustrated in Figure 2B, varied linearly with oxygen concentration for the full range examined (0.0–0.26 mmol L⁻¹). Linear least-squares statistics for results obtained by each of the three models for different fitting ranges are summarized in Table I.

The first-order model gives the best and most consistent values of least-squares statistics. Except for the shortest fitting range, the parallel first-order model gives results consistent with those for the first-order model. For example, when the slope for the 0.3–1.7-s fitting range is dropped, the average value of the remaining three slopes is $29.4 \pm 0.5 \mu\text{A}/(\text{mmol L}^{-1})$ relative to the value of $28.9 \pm 0.2 \mu\text{A}/(\text{mmol L}^{-1})$ for the first-order model. The parallel first-order model requires data over wider ranges to take adequate account of the slower component. The variable-order model gave the poorest and least-consistent values of least-squares statistics. At first glance, this may be a surprising result because the added flexibility of this model is expected to give better fits. However, as noted earlier,¹² the model is undefined for first-order processes; this process appears to be too close to first order for the variable-order model to be used successfully.

All the models and data ranges have intercept values of about 1 μA on the current axis. The intercept values are quite consistent and probably result from the charging current when the potential is first applied across the electrodes. Whatever the source of the intercept, it is just slightly smaller than the extrapolated Faradaic value for the lowest concentration (0.05 mmol L⁻¹) examined (0.7 μA vs 2.5 μA).

In light of the fact that good results are obtained for fitting ranges as short as 1.7 s and that 30 s is required for most responses to reach steady state,¹³ it follows that the measurement time is about 18-fold shorter for the predictive method than for the steady-state method.

Reproducibility. Pooled standard deviations for five runs at each of nine concentrations (including zero) are included as the last column in Table I. With one exception (shortest fitting range for parallel first-order model), the pooled standard deviations are consistent at about 0.25 μA . This represents a concentration uncertainty of about $0.25 \mu\text{A}/28.9 \mu\text{A}/(\text{mmol L}^{-1}) = 0.009 \text{ mmol L}^{-1}$. Under the assumption of a Gaussian distribution, this would correspond to an uncertainty of about 0.02 mmol L⁻¹ at the 95% confidence level.

Effects of Variables. The primary driving force for this study was the possibility of reducing effects of experimental variables relative to effects with the more conventional steady-state measurement approach. We used membrane thickness and stirring rate as the variables to test our hypothesis that this approach would reduce effects of such variables.

Data such as those shown in Figure 2 were used to compare effects of these variables on results obtained by the steady-state and proposed predictive methods. To quantify effects of variable dependencies, we introduce the concept of error coefficients. The error coefficient, EC, is defined as the concentration change, ΔC , per unit change in the variable of interest, ΔV . This is expressed as

$$\text{EC} = \Delta C / \Delta V \quad (1)$$

For systems such as this in which the measured signal varies linearly with concentration ($S = a + bc$), it is easily shown that the error coefficient is given by

$$\text{EC} = (S_2 - S_1) / b(V_2 - V_1) \quad (2)$$

where S_2 and S_1 are signal values for values V_1 and V_2 of the variable of interest and b is the slope of a calibration plot of signal (current in this case) vs concentration. This error coefficient is used below to compare effects of membrane thickness and mixing rate on results by the steady-state and predictive options.

Membrane Thicknesses. Responses similar to those in Figure 2 were obtained for membrane thicknesses of 25, 50, and 75 μm by using one, two, and three thicknesses of the 25- μm membrane. Results obtained by both the steady-state and predictive methods are compared in Figure 3. The plot, which compares the ratios of values for 50- and 75- μm thicknesses to that at 25 μm , shows that the relative change in steady-state current between 25- and 50- μm thicknesses is much larger than that for the predictive method.

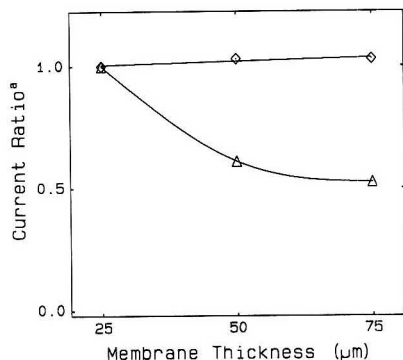
These differences can be quantified by computing error coefficients as described above. For a change in membrane thickness from 25 to 50 μm , the error coefficients for the steady-state and predictive methods are -0.099 and $0.00078 \text{ mmol L}^{-1} \mu\text{m}^{-1}$, respectively. Thus, the steady-state method is 125-fold more dependent on membrane thickness than the predictive method in the 25–50- μm range (see Figure 3). The difference is smaller between 50- and 75- μm thickness.

Stirring Rate. Figure 4 shows effects of different stirring rates on results by the steady-state and predictive methods. At the lower stirring rates, the predictive option is much less dependent on stirring rate than the steady-state option. In

Table I. Linear Least-Squares Statistics for Current vs Oxygen Concentration* for Predictive Method with Different Δ and Fitting Ranges

and Fitting ranges							
range (s)	slope ($\mu\text{A}/(\text{mmol L}^{-1})$)		intercept (μA)		std error of estimate (μA)	corr coeff (r)	pooled st dev (μA)
	value	std dev	value	std dev			
First-Order Model							
0.3–1.7	28.9	0.95	0.77	0.15	0.47	0.98	0.25
0.3–2.5	29.1	0.92	0.74	0.14	0.45	0.98	0.25
0.3–3.3	29.1	0.91	0.73	0.14	0.45	0.98	0.26
0.3–4.1	28.6	0.87	0.69	0.13	0.43	0.98	0.24
av	28.93	0.22	0.73	0.03			
Parallel First-Order Model							
0.3–1.7	24.9	1.9	1.00	0.29	0.93	0.90	0.85
0.3–2.5	28.9	1.0	0.78	0.16	0.51	0.98	0.26
0.3–3.3	29.9	0.96	0.78	0.15	0.48	0.98	0.26
0.3–4.1	29.3	0.95	0.78	0.15	0.47	0.98	0.25
av	28.25	2.3	0.84	1.1			
Variable-Order Model							
0.3–1.7	24.3	0.83	0.65	1.13	0.41	0.98	0.24
0.3–2.5	24.8	0.84	0.66	0.13	0.41	0.98	0.24
0.3–3.3	27.0	1.0	−0.03	0.16	0.52	0.97	0.33
0.3–4.1	23.7	1.0	0.70	0.16	0.51	0.96	0.33
av	24.95	1.4	0.51	0.3			

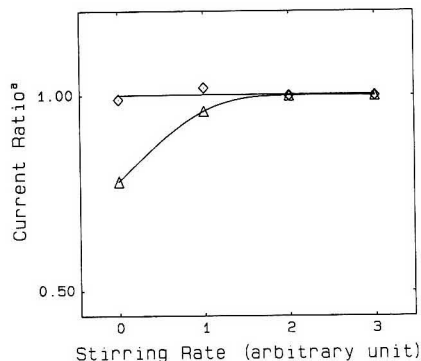
* Average of five runs.

**Figure 3.** Effects of membrane thickness on steady-state (Δ) and predicted initial (\diamond) currents. Ordinate is ratio of currents at 50 and 75 μm to that at 25 μm . Currents at 25 μm : steady state, 0.23 μA ; predicted, 3.21 μA .

this range, the error coefficients for the steady-state and predictive method are 0.081 and 0.0099 (mmol L^{-1})/arbitrary unit, respectively. The predictive method is 8-fold less dependent on stirring rate than the steady-state method.

DISCUSSION

Results presented here show that the predictive method represents a viable option for processing data from the membrane-based oxygen-selective device and that it offers some advantages relative to more common steady-state methods. Advantages include increased sensitivity, reduced measurement time, and reduced dependence on experimental variables. Although reduced variable dependencies were evaluated for membrane thickness and stirring rate, it should be apparent that the approach can also compensate for other variables that would influence the rates of mass transfer to and across the membrane. For example, the approach should compensate for changes in permeability that could result from adsorption of protein or other species onto the surface of the membrane. Another feature of the predictive method is higher sensitivity relative to the steady-state method. Examination of Figure 2 shows that the equilibrium current at $t = 0$ is

**Figure 4.** Effects of stirring rate on steady-state (Δ) and predicted initial (\diamond) currents. Ordinate is ratio of currents at other stirring rates to that at speed 3. Currents: steady-state 0.23 μA ; predicted, 2.53 μA .

about 5-fold higher than the steady-state current. Whether this 5-fold increase in sensitivity is or is not advantageous depends upon other features.

For the oxygen-selective device, the principal limitation of the present approach to the predictive method is the effect of charging current. This would not be a problem for many other types of membrane-based devices that do not involve amperometric or voltammetric measurements. Also, there is at least one alternative approach for the oxygen-selective device. If one were to deplete the oxygen concentration inside the membrane before immersing the electrode in the sample solution, then one could monitor the approach to equilibrium and achieve advantages analogous to those illustrated for prediction of the initial current for a preequilibrated electrode. The approach to equilibrium would be about 10-fold slower, giving more time to compensate for effects of charging current.

Finally, we reemphasize that the oxygen-selective device, though important in its own right, is used as an illustrative

(14) Smart, R. B.; Dormond-Herrera, R.; Mancy, K. H. *Anal. Chem.* 1979, 51, 2315–2319.

(15) Dormond-Herrera, R.; Mancy, K. H. *Anal. Lett.* 1980, 13 (A7), 561–576.

example of many analogous devices that involve mass transport across membranes. It is probable that analogous measurement and data-processing approaches can offer similar advantages for other analytes quantified with this electrode system^{14,15} as well as for other membrane-based systems.²⁻⁴

ACKNOWLEDGMENT

This work was supported in part by Grant No. 13326-24 from the National Institutes of Health.

RECEIVED for review April 6, 1992. Accepted July 6, 1992.

Recognition of Chemical Markers in Chromatographic Data by an Individual Feature Reliability Approach to Classification

Rachhpal S. Sahota[†] and Stephen L. Morgan^{*}

Department of Chemistry and Biochemistry, University of South Carolina, Columbia, South Carolina 29208

A discriminant analysis algorithm based on the classification reliability of individual features was applied to GC and GC-MS data. Two feature selection methods were investigated in which feature weights were defined either by Fisher ratios or by classification accuracy in single feature dimensions. The discriminant function employed was a linear function of these feature weights where the coefficients of summation were reliability values, ranging from -1 to +1, measuring the confidence with which classification can be made on the basis of that feature alone. The two feature selection methods used in combination with this classifier were competitive with the classical discriminant approach of Fisher on the data sets tested. This approach provides information useful for the recognition of unique chemical markers characteristic of particular groups of samples. The emphasis on chemical markers is important because wider use of pattern recognition with GC and GC-MS requires understanding the chemical basis for discrimination.

INTRODUCTION

Computer-controlled instrumentation usually generates multidimensional data that are difficult to visualize and interpret. Even single runs from chromatographic or spectroscopic instruments can generate enormous amounts of data. Whether the analytical data (characterizing a sample or object) represent a chromatogram or a spectrum or some other set of measurements, the resulting pattern can be represented as a row vector of signal intensities, \mathbf{x} :

$$\mathbf{x} = (x_1, x_2, \dots, x_n) \quad (1)$$

where n is the number of features (peak areas, spectral wavelengths, etc.), and the value of x_i represents the measured signal intensity for the i th feature. For example, the raw data defining a chromatogram might consist of signal intensities measured every tenth of a second for 20 min. Even if the raw data are processed to a peak area report, the chemist may have to deal with several dozen peak areas for each chromatogram. When multiple samples are analyzed, the manual comparison of so many peaks across more than a few chromatograms becomes quite difficult. The difficulty of visualizing data in higher than three dimensions also limits the usefulness of graphical data display.

Pattern recognition has a long and successful history of application in analytical chemistry.¹⁻⁶ Two fundamentally different approaches to pattern classification—unsupervised

and supervised learning—are common. *Unsupervised learning* attempts classification based on the inherent relationships among objects without prior assumptions about the structure or clustering of the data. Unsupervised methods often involve either the discovery of natural groupings in the data (e.g., cluster analysis⁷) or the mapping of higher dimensional data sets into a lower number of dimensions for display (e.g., nonlinear⁸ or principal component mapping⁹). *Supervised learning* develops rules for classification of unknown samples on the basis of samples whose classification is known in advance. A training set is used to define the classes of interest via mathematical models derived from the variables relevant to classification. Discriminant analysis is a supervised technique that attempts to differentiate groups of samples by deriving classification rules based on the probability distribution of the data (parametric) or based on other methods that do not assume any particular underlying distributions (nonparametric).

Recognizing whether a unique feature (e.g., a chromatographic peak or spectral wavelength) or a small subset of features distinguishes one pattern from another is often a major goal for the chemist. Such discriminating features may be indicative of the presence of a chemical marker that is unique to a particular group of samples. Multivariate classification approaches often confound individual features (e.g., as eigenvectors in principal component analysis). The significance of a feature in determining a classification decision is usually a function of how that feature varies with other features, as in Fisher's discriminant function. This gestalt treatment of multivariate data, though undoubtedly more powerful than the more easily comprehensible "one factor at a time" approach, has an inherent problem—simple qualitative interpretation of these combined features, in chemical terms, may be difficult. This lack of amenability to chemical interpretation makes these techniques less appealing to many investigators.

Many pattern recognition techniques use some collective function of all the features to assign class membership to a pattern. Often (especially in linear discriminant analysis), a feature with larger feature value contributes more to the final discriminant score than a feature with smaller feature value, even when the two features have equal discriminating abilities. This is an undesirable outcome when discriminating chemical markers are represented by very small feature values (e.g., small chromatographic peaks).

The objective of the classification approach described here is to recognize more clearly the classification ability of individual features. Since weights are assigned on the basis

^{*} To whom correspondence should be addressed.

[†] Current address: Research & Development, Procter & Gamble Pharmaceuticals, P.O. Box 191, Norwich, NY 13815-0191.

(1) Kowalski, B. R.; Bender, C. F. *J. Am. Chem. Soc.* 1972, 94, 5632-5639.

(2) Harper, A. M.; Dwyer, D. L.; Kowalski, B. R.; Fasching, J. L. In *Chemometrics: Theory and Application*; ACS Symposium Series 52; Kowalski, B. R., Ed.; American Chemical Society: Washington, DC, 1977; pp 14-52.

(3) Jurs, P. C. *Science* 1986, 232, 1219-1224.

(4) Jurs, P. C.; Isenhour, T. L. *Chemical Application of Pattern Recognition*; Wiley-Interscience: New York, 1975.

(5) Sharaf, M. A.; Illman, D. L.; Kowalski, B. R. *Chemometrics*; John Wiley: New York, 1986.

(6) Massart, D. L.; Vandeginste, B. G. M.; Deming, S. N.; Michotte, Y.; Kaufman, L. *Chemometrics, A Textbook*; Elsevier: Amsterdam, 1987.

(7) Massart, D. L.; Kaufman, L. *The Interpretation of Analytical Chemical Data by the Use of Cluster Analysis*; R. E. Krieger: Malabar, FL, 1989.

(8) Sammon, J. W., Jr. *IEEE Trans. Comput.* 1969, C-18, 401.

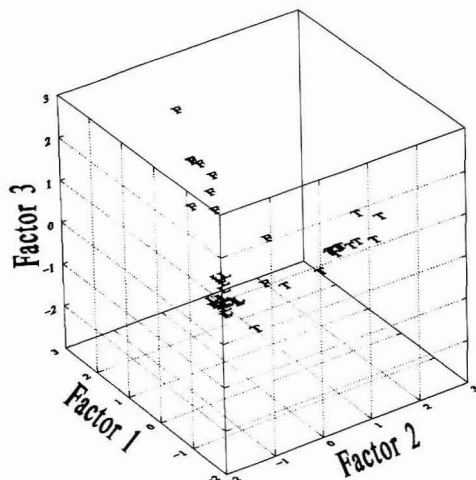


Figure 1. Projection of 43 data points in the space of the first three principal components for data set 1. Symbols: L, *Legionella*; T, *Tatlockia*; F, *Fluoribacter*.

of the discriminating potential of each feature taken by itself, we call this method the "individual feature reliability approach to classification" (IFRAC). The performance of the classifier and the weights assigned to features are compared with results from the classic linear discriminant method of Fisher.^{9,10}

METHODS AND TERMINOLOGY

Computing and Plotting. Programs were written in Turbo Pascal version 5.5 (Borland International, Scotts Valley, CA) and QuickBASIC version 4.5 (Microsoft Corp., Seattle, WA), compiled, and executed on IBM PC compatible computers. Principal component analysis and graphics were performed using SYSTAT version 5.0 (SYSTAT Inc., Evanston, IL). Graphics were plotted on a LaserJet Series II printer (Hewlett-Packard Co., Palo Alto, CA). Copies of data sets and programs used in this work are available from the authors.

Data Sets. Four data sets, referred to as data sets 1–4, respectively, were used to test classification algorithms.

Data set 1 was based on 43 capillary gas chromatograms representing carbohydrate profiles of bacteria.¹¹ Twenty of these chromatograms were carbohydrate profiles of *Legionella pneumophila* samples, 13 samples were *Tatlockia micdadei*, and the remaining 10 samples were *Fluoribacter bozemanii* samples. Each chromatogram consisted of quantitated amounts of eight sugars (Rhamnose, fucose, ribose, mannose, two isomeric aminodeoxyhexoses, muramic acid, and glucosamine) derivatized to alditol acetates. Figure 1 presents a projection of the 43 data points, without normalization or autoscaling (explained later), onto the first three principal components (showing 84% of the total variation in the data). Three different dichotomies of this data set were employed for testing classification algorithms. Data set 1A consisted of all 43 samples with the objective of classifying *L. pneumophila* samples from the combined *Tatlockia* and *Fluoribacter* groups. Data set 1B is data set 1A with two samples

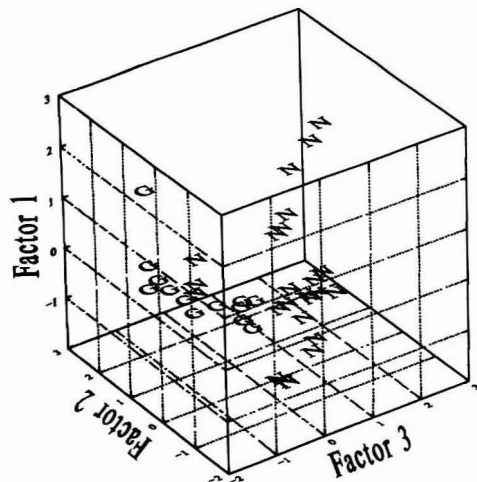


Figure 2. Projection of 37 data points in the three-dimensional space of the first three principal components for data set 2. Symbols: G, carbohydrate containing galactose; N, carbohydrate not containing galactose.

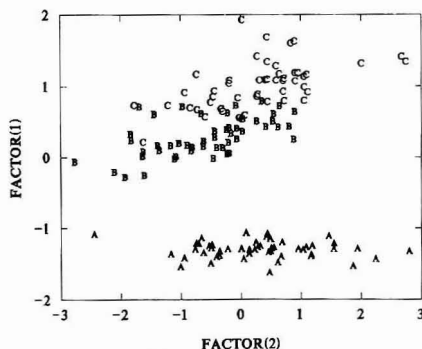


Figure 3. Projection of 150 data points onto the plane of the first two principal components for data set 3. Symbols: A, *Iris setosa*; B, *Iris versicolor*; C, *Iris virginica*.

deleted for reasons described below. Data set 1C consists of the 13 samples of *T. micdadei* plus the 10 samples of *F. bozemanii*; discrimination between these two groups was the objective.

Data set 2 was based on 37 pyrograms obtained by pyrolysis-gas chromatography (Py-GC) of 15 different sugars dissolved in boric acid.¹² Each pyrogram consisted of 16 GC peak heights. All but two sugars were pyrolyzed in duplicate or triplicate. Of the 15 monosaccharides, disaccharides, and trisaccharides, five contained a galactose moiety and the other 10 did not. The classification objective was to discriminate 13 pyrograms of sugars containing galactose from the other 24 pyrograms of sugars not containing galactose. A plot showing the projection of these data points, without normalization or autoscaling, in the space of the first three principal components (explaining 82% of the variation in the data) is shown in Figure 2.

Data set 3 is Fisher's *Iris* data set.⁹ This data set has measurements from three classes of *Iris* flowers (*Iris setosa*, *Iris versicolor*, and *Iris virginica*). The data set includes 50

(9) Fisher, R. A. *Ann. Eugenics* 1936, 7, 179–188.

(10) Green, P. E. *Analyzing Multivariate Data*; The Dryden Press: Hinsdale, IL, 1978.

(11) Fox, A.; Lau, P. Y.; Brown, A.; Morgan, S. L.; Zhu, Z. T.; Lema, M.; Walla, M. In *Proceedings of the Second International Symposium on Legionella*; Thornsberry, C.; Ballows, A.; Feeley, J. C.; Jakubowski, W., Eds.; American Society of Microbiology: Washington, DC, 1984; p 71–73.

(12) Morgan, S. L.; Jacques, C. A. *Anal. Chem.* 1982, 54, 741–747.

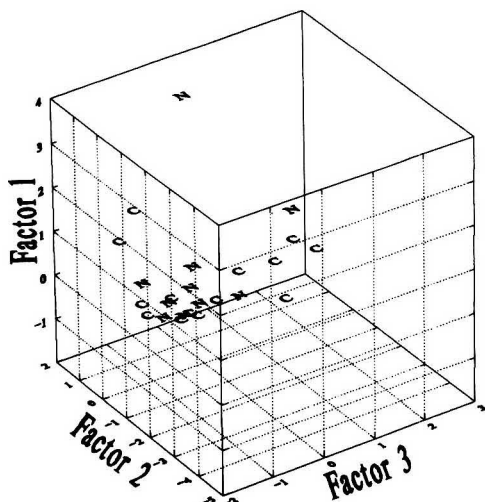


Figure 4. Projection of 24 data points in the three-dimensional space of the first three principal components for data set 4. Symbols: C, transformed malignant cells; N, normal cells.

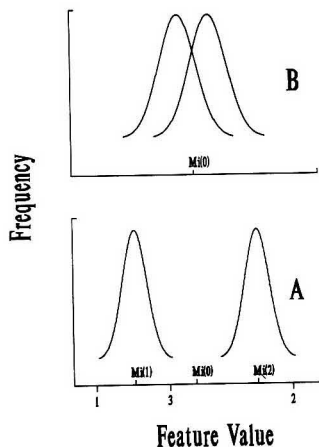


Figure 5. Distributions of feature values for a single feature in a training data set showing (A) two well-separated classes and (B) two overlapped classes.

observations on each class and each observation has four dimensions (sepal length, sepal width, petal length, and petal width). Figure 3 shows a projection of the 150 data points onto the plane of the first two principal components (showing 96% of the variation in the data). The data set denoted 3A contained 100 samples from the two groups *I. setosa* from *I. versicolor*. Data set 3B consisted of the 100 samples from groups *I. setosa* and *I. virginica*. Data set 3C consisted of the 100 samples from the groups *I. versicolor* and *I. virginica*. In each case the objective was to discriminate between the two *Iris* species in the given group.

Data set 4 consists of Py-GC/mass spectrometric (MS) data obtained from 24 different samples of mouse fibroblast cells representing two classes (normal cells and malignant cells transformed with Moloney murine sarcoma virus).¹³ The data consists of the total ion integrated area for 36 different chromatographic peaks. A plot showing the projection of these data points, without normalization or autoscaling, in the three-dimensional space of the first three principal

```

if (( $M_i(1) > M_i(0)$  and  $x_i > M_i(0)$ )
or if ( $M_i(1) < M_i(0)$  and  $x_i < M_i(0)$ )) then
    if  $x_i \geq M_i(1)$  then  $R_i = 1$ ;
    else  $R_i = (M_i(0) - x_i) / (M_i(0) - M_i(1))$ ;
else if (( $M_i(1) > M_i(0)$  and  $x_i < M_i(0)$ )
or if ( $M_i(1) < M_i(0)$  and  $x_i > M_i(0)$ )) then
    if  $x_i < M_i(2)$  then  $R_i = -1$ ;
    else  $R_i = -(M_i(0) - x_i) / (M_i(0) - M_i(2))$ ;
Else  $R_i = 0$ ;

```

Figure 6. Algorithm to compute the reliability function, $R(x_i, M_i(1), M_i(2))$ (abbreviated R_i below), for the i th feature given the value for this i th feature in an unknown sample is x_i . $M_i(1)$ is the mean of the i th feature in group 1, $M_i(2)$ is the mean of the i th feature in group 2, and $M_i(0)$ is the midpoint of the two group means.

components (explaining 66% of the variation in the data) is shown in Figure 4.

Normalization. Normalization of chemical data to a constant sum over all features within each pattern vector (e.g., chromatogram) is a common practice. For example, chromatograms might exhibit variations in peak height or areas because of variations in sample amount. Normalization removes this bias in feature magnitudes that may arise as a result of experimental variations. Effects of normalization on feature selection and classification have been documented often.¹⁴⁻¹⁸ Unfortunately, normalization makes the data "closed": since the sum of the feature values is a constant, when the value of a large feature goes up, values of other features must go down. To minimize this closure effect, Johanson et al.¹⁸ recommend applying normalization over only a subset of the features. Although as many features as possible should be included in this subset, features that differ substantially from other features in their means and/or standard deviations are excluded from the sum to be held constant. Selective closure was applied to two of four data sets included in the study, as discussed later.

The data sets were normalized before computing weights or obtaining classification results with the two IFRAC methods described below. This normalization involved dividing every feature value by the sum of the retained feature intensities. Since, in every case, Fisher's discriminant function performed better with nonnormalized data, the original data were used with that algorithm.

Fisher's Linear Discriminant Method. Fisher's approach to discrimination uses a linear function of feature values and weights:^{9,10}

$$t(\mathbf{x}) = w_1x_1 + w_2x_2 + \dots + w_nx_n = \mathbf{w}'\mathbf{x} \quad (2)$$

where \mathbf{w}' is the transpose of $\mathbf{w} = (w_1, w_2, \dots, w_n)$, and $n \times 1$ row vector of weights, and $\mathbf{x} = (x_1, x_2, \dots, x_n)$ is an $n \times 1$ row vector of feature values. The weight vector \mathbf{w} is defined as

$$\mathbf{w} = \mathbf{C}_w^{-1}\mathbf{d} \quad (3)$$

where \mathbf{d} is the $n \times 1$ vector of differences between the two $n \times 1$ group mean vectors \mathbf{m}_1 and \mathbf{m}_2 , and the $n \times n$ matrix

(13) Sahota, R. S.; Morgan, S. L.; Creek, K.; Pirisi, L. Unpublished work.

(14) Eshuis, W.; Kistemaker, P. G.; Meuzelaar, H. L. C. In *Analytical Pyrolysis*; Jones, C. E. R., Cramers, C. A., Eds.; Elsevier: Amsterdam, 1977; pp 151-156.

(15) Klee, M. S.; Harper, A. M.; Rogers, L. B. *Anal. Chem.* 1981, 53, 801-805.

(16) Marcuson, R.; Burbeck, S. L.; Emond, R. L.; Latter, G. I.; Aberth, W. *Clin. Chem.* 1982, 28, 1346-1348.

(17) Harper, A. M.; Meuzelaar, H. L. C.; Metcalf, G. S.; Pope, D. L. *Numerical techniques for processing pyrolysis mass spectral data. In Analytical Pyrolysis: Techniques and Applications*; Voorhees, K. J., Ed.; Butterworths: New York, 1983.

(18) Johanson, E.; Wold, S.; Sjodin, K. *Anal. Chem.* 1984, 56, 1685-1688.

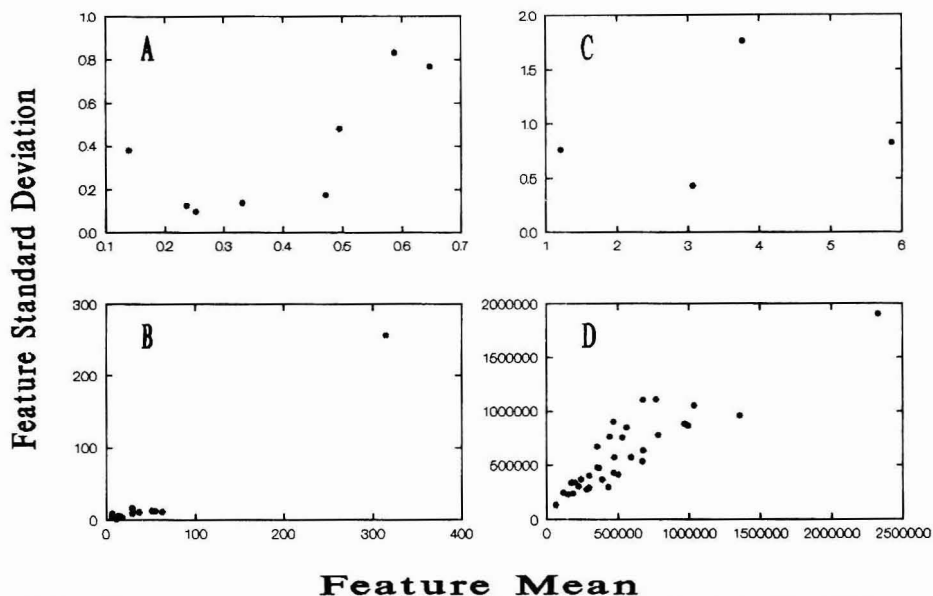


Figure 7. Plots of feature means versus feature standard deviations for (A) data set 1, (B) data set 2, (C) data set 3, and (D) data set 4.

C_w is the within-groups covariance matrix given by

$$C_w = p_1 C_1 + p_2 C_2 \quad (4)$$

where C_1 and C_2 are the $n \times n$ covariance matrices for groups 1 and 2 and p_1 and p_2 are the a priori probabilities for classes 1 and 2.

Mean discriminant scores t_1 and t_2 for the two groups are computed using

$$t_1 = \mathbf{w}'\mathbf{m}_1 \quad \text{and} \quad t_2 = \mathbf{w}'\mathbf{m}_2 \quad (5)$$

The classification threshold, t_c , is computed as the weighted average of the mean discriminant scores of groups 1 and 2:

$$t_c = p_1 t_1 + p_2 t_2 \quad (6)$$

Alternatively, the threshold, t_c , can be specified as the product of the weight vector and \mathbf{M} , the $n \times 1$ vector of overall feature means:

$$t_c = \mathbf{w}'\mathbf{M} \quad (7)$$

The threshold value t_c represents the discriminant function value at the overall feature mean. If the variance of each feature is the same within each group and there is no covariance among the features (zero off-diagonal terms in the within-groups covariance matrix), computing the discriminant function for a particular data point is equivalent to projecting that point onto the line connecting the two group means. Data points that have a smaller value of the discriminant function lie to one side of the overall mean (mean of the entire data set) and belong to group 1. Similarly, data points that project onto this line on the opposite side of the overall mean will have a discriminant function value larger than the threshold value and are classified in group 2. When the features have different variances, the discriminant line is weighted toward the feature with smaller variance. Covariance between features also affects the orientation of Fisher's discriminant line (eq 3). In this work, Fisher's method was applied without feature selection to reduce the number of features.

Feature Selection Method 1. With the IFRAC algorithm two feature selection methods were investigated. In the first method, each feature is assigned a weight on the basis of the difference in the two group means compared to the within-group variance. More specifically, w_i , the weight for the i th feature is given by

$$w_i = (M_i(1) - M_i(2))^2 / (p_1 s_1^2 + p_2 s_2^2) = d_i^2 / (p_1 s_1^2 + p_2 s_2^2) \quad (8)$$

where $M_i(1)$ and $M_i(2)$ are the group means and s_1^2 and s_2^2 are the group variances for the i th feature for groups 1 and 2 and p_1 and p_2 are the a priori probabilities for groups 1 and 2. These weights, often termed the Fisher ratios,⁵ have a lower bound of zero and are not bounded at the upper extreme. If the group means are well separated and/or the samples are tightly clustered within each group, the Fisher ratio will be large, signifying a discriminating feature. The Fisher ratios of eq 8 are univariate measures of discrimination ability whereas the weights of Fisher's discriminant function defined in eq 3 are multivariate measures involving covariances as well as variances of features. Fisher ratios have been employed for transforming data prior to discriminant analysis or nonlinear mapping¹⁹ and have been used for evaluating the importance of single features in other analytical chemical data.²⁰

A subgroup of features that gives a minimum number of misclassifications on cross-validating the training data set is chosen in the following manner. Initially, the subset contains only the feature with the highest weight. The feature with the next highest weight is added to this subgroup, one at a time. At each stage, cross-validation of the training data set is performed to record the number of misclassifications. On the last iteration, the subgroup includes all n features. The features in the first subset producing a minimum number of misclassifications are retained for further classification. Features of lower weight that were added following this subgroup are dropped from further consideration. Thus, the

(19) Ting, K. L. H.; Lee, R. C. T.; Chang, C. L.; Guarino, A. M. *Comput. Biol. Med.* 1975, 4, 301-332.

(20) Duerwer, D. L.; Kowalski, B. R. *Anal. Chem.* 1975, 47, 526-530.

selected set of features includes the fewest number of features that give the lowest number of misclassifications. Other feature combinations were not investigated, as the goal of finding features with individually high discriminating abilities had priority over achieving the best classification performance. The discriminant algorithm defined by the use of this feature selection method, in combination with the individual feature reliability function described below, is designated "IFRAC-1".

Feature Selection Method 2. The second feature selection method evaluated with the IFRAC algorithm is philosophically different from that of method 1. Rather than looking at the distance two groups are separated relative to their dispersion, method 2 looks simply at classification accuracy in each individual feature. Let the total number of cases in the training sets for class 1 and class 2 be m_1 and m_2 , respectively. Figure 5 displays two simulated distributions of feature values for a single feature. The midpoint, $M_i(0)$, of the two group means is used as a decision point. This midpoint will differ from the overall mean in that feature if the two groups have a different number of samples. Let z_1 and z_2 be the number of cases in classes 1 and 2, respectively, that are classified correctly by this single feature alone. The ratios

$$R_i(1) = z_1/m_1 \quad (9)$$

$$R_i(2) = z_2/m_2 \quad (10)$$

are calculated. If either $R_i(1)$ or $R_i(2)$ is less than a predetermined threshold T_R (the same for every feature), then feature i is excluded from further consideration. Otherwise, the feature is assigned a weight equal to its classification ability, given by the ratio

$$w_i = (z_1 + z_2)/(m_1 + m_2) \quad (11)$$

For the i th feature to be assigned a maximum weight of 1.0, both $R_i(1)$ and $R_i(2)$ must equal 1. The threshold T_R (with a value between 0.5 and 1.0) is determined by minimizing the number of misclassifications obtained on cross-validation of the training set.

In summary, this second method of assigning feature weights calculates the weight for the i th feature, w_i , as follows:

$$\text{If } (z_1/m_1) \text{ or } (z_2/m_2) < T_R \text{ then } w_i = 0$$

$$\text{else } w_i = (z_1 + z_2)/(m_1 + m_2) \quad (12)$$

These weights can range from 0 to 1. This feature selection method, in combination with the reliability function described below, is designated "IFRAC-2".

Individual Feature Reliability Classifier. The present classification method differs from most existing methods of discriminant analysis in that classification of an n dimensional distribution is treated as a combination of n separate and independent univariate distributions. The classification function is based on an additive combination of the classifying ability of individual features. Treating features independently in this way does not entirely ignore covariance between features because prior normalization of the data set takes into account how features collectively vary with one another.

We propose the following discriminant function:

$$t(\mathbf{x}) = w_1 R[x_1, M_1(1), M_1(2)] + w_2 R[x_2, M_2(1), M_2(2)] + \dots + w_n R[x_n, M_n(1), M_n(2)] \quad (13)$$

where $\mathbf{w} = (w_1, w_2, \dots, w_n)$ is vector of individual feature weights for each feature x_i . The reliability function for each feature, $R[x_i, M_i(1), M_i(2)]$, takes values from -1 to +1.

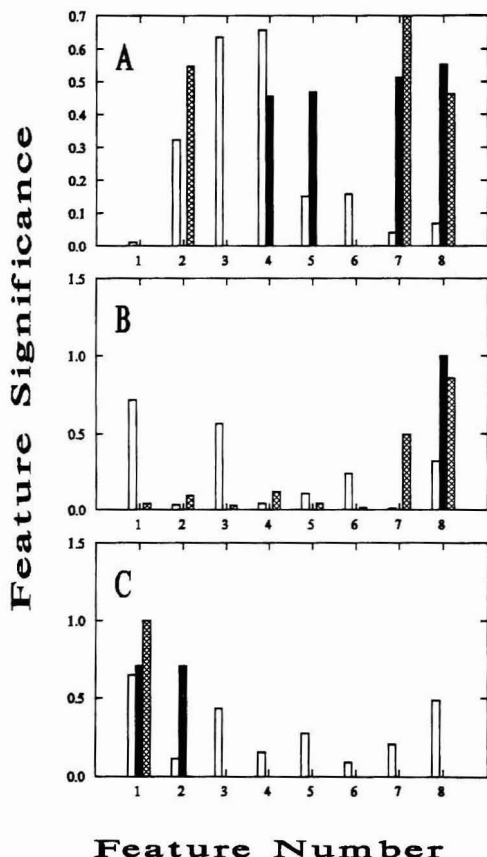


Figure 8. Feature significance (see text for definition) accorded to features by three classification algorithms for (A) data set 1A, (B) data set 1B, and (C) data set 1C. Open histogram bars represent results from Fisher's discriminant method, cross-hatched bars represent results from algorithm IFRAC-1, and solid bars represent results from algorithm IFRAC-2.

Although not necessary, the two hypothetical distributions of values of a single feature x_i shown in Figure 5 are assumed to be Gaussian for simplicity in perception. The lines marked $M_i(1)$ and $M_i(2)$ represent the feature means for class 1 and 2 respectively and the line marked $M_i(0)$ represents the midpoint of the two group means for that feature. In Figure 5A, the two class means are well separated relative to the variability of each group; no samples are misclassified using the midpoint of the two group means as the decision point. Such a feature is considered ideal for classification. Figure 5B shows two class distributions that overlap significantly. Such behavior in training makes this feature less significant for classification and such a feature may be deleted by the feature selection process.

The design of the reliability function, $R[x_i, M_i(1), M_i(2)]$, can be understood in reference to Figure 5A. Let us assume that this i th single feature is adequate for discriminating between the two classes (as shown). If the value of this feature for an unknown sample lies to the left of the mean, $M_i(1)$, for group 1 (e.g., at point 1 in figure 5A), we can assign that unknown to class 1 with highest reliability. In this situation, the reliability function is set to the maximum allowable value of 1. Similarly, if the unknown feature value lies to the right of the mean, $M_i(2)$, for group 2 in this feature (e.g., at point

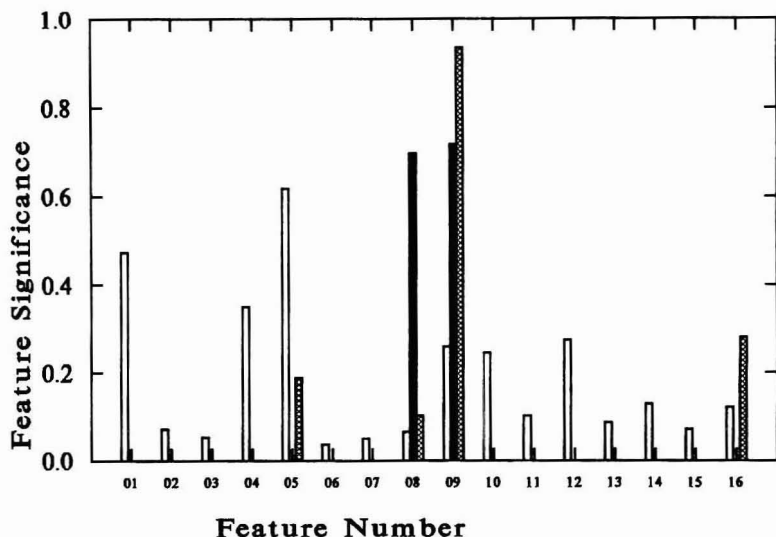


Figure 9. Feature significance (see text for definition) accorded to features by three classification algorithms for data set 2. Open histogram bars represent results from Fisher's discriminant method, cross-hatched bars represent results from algorithm IFRAC-1, and solid bars represent results from algorithm IFRAC-2.

2 in Figure 5A), the reliability function will also be set to a value of 1. Since, the reliability in making a class assignment decreases as the value of the i th feature in the unknown moves closer to $M_i(0)$ (e.g., at point 3 in Figure 5A), the absolute value of the reliability function decreases linearly from 1 to 0 as the feature value changes from $M_i(1)$ (or from $M_i(2)$) to $M_i(0)$. The reliability function is assigned a negative sign when $M_i(1)$ and the value of feature i in the unknown are either both greater than or both less than $M_i(0)$. The sign of the reliability function is positive otherwise. This sign assignment gives the reliability function for the i th feature a negative value when that feature classifies an unknown sample in group 1 and a positive value when that feature classifies the unknown in group 2. The complete algorithm used to compute the reliability function for the i th feature is summarized in Figure 6. An unknown sample is assigned to class 1 if the value of $t(x)$, the discriminant function over all features (eq 13), is negative and to class 2 if this value is positive. A zero value of the discriminant function is indecisive.

Validation Methods. The IFRAC classifier with each of the two feature selection methods was tested by (1) cross-validation and (2) training with one data set and testing with another. Cross-validation involved leaving each observation out, one at a time, from the training set and building a classifier from the remaining observations; the classifier was then used to classify the deleted observation. The second validation method involved dividing each data set into two halves. One half was used for training and the other half for testing. The performance of IFRAC was also compared with classification results and feature weights from Fisher's discriminant method.

RESULTS AND DISCUSSION

Selective Normalization. Plots of the feature standard deviations against the feature means for the four data sets are shown in Figure 7. In Figure 7A, the feature means and standard deviation for the *Legionella* sugar profiling data (data set 1) are plotted. No single feature stands out as unusual in this plot, and normalization of the data set included

Table I. Comparison of the Classification Performance of the IFRAC-1 and IFRAC-2 Algorithms with Fisher's Discriminant Function When Cross-Validation Is Performed*

data set	no. of features	no. of data points	no. of misclassifications		
			Fisher	IFRAC-1	IFRAC-2
1A	8	43	4	6	4
1B	8	41	3	2	1
1C	8	23	0	0	0
2	16	37	0	1	0
3A	4	100	0	0	0
3B	4	100	0	0	0
3C	4	100	4	5	3
4	36	24	11	2	2

* Data sets and algorithms are described in the text.

all eight features. Figure 7C for the *Iris* data also reveals that all four features in data set 3 have similar means and standard deviations; normalization included all four features for this data set. Parts B and D of Figure 7 for data sets 2 and 4, respectively, show features with means and standard deviations that differ significantly from the rest of the features. In Figure 7B for the Py-GC carbohydrate data, a single feature (feature 9) has a higher mean and higher variability than the other 16 features. The data in this set were selectively normalized by dividing each feature value in the chromatogram by the sum of all features in the chromatogram excluding feature 9. Figure 7D shows a similar effect in the Py-GC/MS mouse fibroblast data set (data set 4): a single feature (feature 16) was therefore excluded from the feature sum for normalization, as described. With the IFRAC-1 and IFRAC-2 algorithms raw peak intensities were always normalized before feature selection. Fisher's discriminant method invariably performed better without normalization and thus raw peak intensities were employed in Fisher's method.

Classification Results and Features Significance. Table I presents a comparison of the cross-validation classification performance for the two algorithms, IFRAC-1 and IFRAC-2, with results from Fisher's discriminant method. The number of misclassifications for all four data sets are

Table II. Comparison of the Classification Performance of the IFRAC-1 and IFRAC-2 Algorithms with Fisher's Discriminant Function When Half the Data Set Is Used for Training and Half Used for Testing*

data set	no. of features	no. of data points	no. of misclassifications		
			Fisher	IFRAC-1	IFRAC-2
1A	8	21	1	1	1
1B	8	20	0	0	1
1C	8	11	0	0	0
2	16	18	0	1	0
3A	4	50	0	0	0
3B	4	50	0	0	0
3C	4	50	3	4	2
4	36	12	5	1	3

* Data sets and algorithms are described in the text.

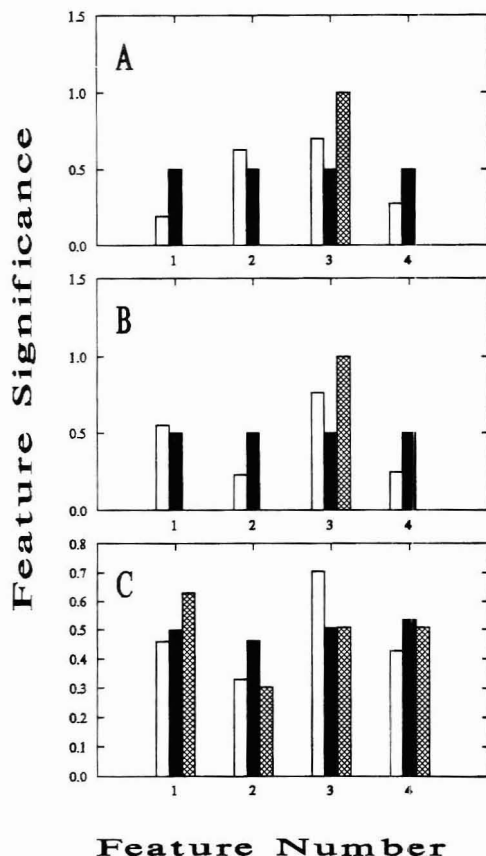


Figure 10. Feature significance (see text for definition) accorded to features by three classification algorithms, for data set 3A (A), data set 3B (B), and data set 3C (C). Open histogram bars represent results from Fisher's discriminant method, cross-hatched bars represent results from algorithm IFRAC-1, and solid bars represent results from algorithm IFRAC-2.

tabulated for each algorithm in the three right-hand columns. Table II shows a similar comparison of the three algorithms for all four data sets when the data sets are split into training and testing halves.

The relative significance of the features in determining classification is shown for the four data sets in Figures 8–11. Feature significance in the case of the IFRAC algorithms was determined by the weight assigned by eq 8 (for IFRAC-1) or

eq 12 (for IFRAC-2) in combination with the feature selection process. That is, if a feature is excluded during feature selection, its weight is set to zero. For Fisher's discriminant method, feature significance was determined by multiplying the feature weights assigned by eq 3 with the value of the mean in each feature. Since the absolute values of the feature weights varied among the data sets and algorithms, these weights were normalized for comparison by dividing by the square root of the sum of the squares of the weights for all features. In all cases the feature weights were computed from all samples in the respective data sets.

Data Set 1. The classification results for data set 1A are shown in Tables I and II, and the feature significance values are plotted in Figure 8A. In discriminating *L. pneumophila* from the other two groups of *Legionella*-like organisms, cross-validation performance was not perfect. This was expected because the principal component map of Figure 1 shows the points representing *Legionella* samples surrounded by the *Fluoribacter* and *Tatlockia* samples. IFRAC-1 assigns weights to three features (features 8, 2, and 7 in order of increasing significance). IFRAC-2 assigns weights to four features (features 4, 5, 7, and 8 in order of increasing significance). All other features were deleted from consideration by the feature selection process in IFRAC-1 or IFRAC-2. Fisher's method assigns high weights to features 2, 3, and 4 but still assigns small weights to the other features. Examination of the data set revealed that two samples of *F. gormanii* contained much more glucosamine than the other samples of *Fluoribacter*, for which the glucosamine levels were very low. These two samples were excluded from data set 1A to create data set 1B. The classification performance, as shown in Tables I and II, increased significantly. As shown in Figure 8B, IFRAC-2 now recognizes that only a single feature, the amount of the sugar glucosamine, is required to distinguish between the remaining species of *Fluoribacter* and *Tatlockia* from those of *L. pneumophila*. Although IFRAC-1 assigns finite weights to all eight features, only two features (7 and 8) are given high weights.

The three classifiers were also used to classify *Tatlockia* from *Fluoribacter* species with the results shown as data set 1C in Tables I and II. There are wide differences between the chromatograms of these two classes, and perfect classification was achieved with all three algorithms, as could be expected from Figure 1. The feature significance plot for the IFRAC-1 and IFRAC-2 algorithms shown in Figure 8C indicate that these two genera can be separated from each other on the basis of only the first two sugars, rhamnose and fucose. IFRAC-1 selects only the first feature, the amount of rhamnose. IFRAC-2 gives equal weight to rhamnose and fucose and, in this case, either peak discriminates *Tatlockia* from *Fluoribacter*. The feature significance values for Fisher's method are scattered over all features with the highest weight also given to the first feature, rhamnose.

The feature significances noted here for data set 1 agree with those previously reported¹¹ with only one exception: discrimination between *L. pneumophila* and the other organisms by the relative amount of glucosamine had not been noted.

Data Set 2. Classification performance for the Py-GC carbohydrate data set is shown in Tables I and II, and feature significance values are plotted in Figure 9. Both cross-validation and test data set validation show only one misclassification with the IFRAC-1 algorithm. IFRAC-1 selects, in order of increasing significance, features 8, 5, 16, and 9 as the features best discriminating galactose-containing sugars from those not containing galactose. IFRAC-2 selects features 8 and 9 and achieves 100% classification. Fisher's method, as before, spreads its weights around all the features, with the highest weight assigned to feature 5. The ability of feature 9 in these pyrograms to discriminate between galactose

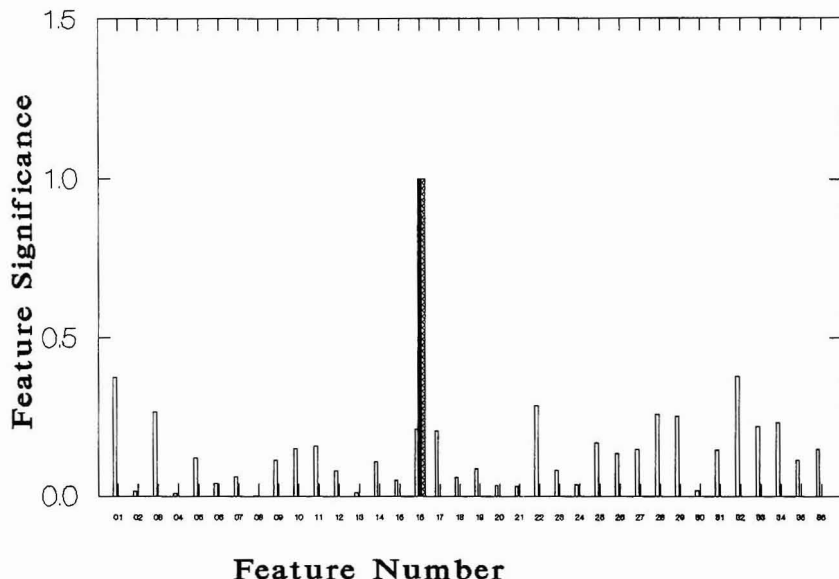


Figure 11. Feature significance (see text for definition) according by Fisher's discriminant algorithm, to features in data set 4.

and glucose was previously noted: for a typical galactose pyrogram this single peak height is about 63% of the peak height sum for the 16 peaks while for glucose the same peak is only 38% of the peak height sum.¹² Although Fisher's discriminant method performs well as a classifier, the weights do not identify this prominent chemical marker in this data set. In the three-dimensional principal components plot of Figure 2, it is the third factor that tends to separate the two groups; the eigenvector for this third factor is dominated by feature 9.

Data Set 3. Fisher's *Iris* data was partitioned in three different ways to test the discrimination of each combination of two groups. As seen in Tables I and II, *I. setosa* samples were discriminated from both *I. versicolor* and *I. virginica* (data sets 3A and 3B) with 100% accuracy by all three algorithms. The other two classes, *I. versicolor* and *I. virginica*, resemble each other more closely, and several misclassifications occurred with all three algorithms during both cross-validation and testing-training. These results are consistent with the principal components plot of this data shown in Figure 3. The feature significance plots in Figure 10A,B reveal that IFRAC-1 achieves its 100% classification between *I. setosa* and either *I. versicolor* or *I. virginica* with only one feature, feature 3 (petal length). IFRAC-2 assigns equal weights to all four features but can achieve 100% classification between these groups with any one of the four features. This observation is often neglected in many presentations of discriminant analysis applied to Fisher's *Iris* data. The feature significance plot for the discrimination between *I. versicolor* and *I. virginica* (Figure 10C) does not emphasize any one of the features.

Data Set 4. With the Py-GC/MS data on mouse fibroblast cells, the IFRAC-1 and IFRAC-2 algorithms outperform Fisher's discriminant method in cross-validation by producing fewer misclassifications (better than 90% accuracy). Fisher's classifier performs very poorly, giving 11 misclassifications out of a total of 24 patterns. One reason for this poor result is that Fisher's discriminant function depends upon the covariance structure of the data set and 24 observations are inadequate for determining the covariance matrices required

for the purpose. The principal components plot of Figure 4 does not show clear separation of the two groups of samples. Feature significance values for Fisher's discriminant method and the two IFRAC algorithms are shown in Figure 11. The performance of both IFRAC algorithms was better than that of Fisher's discriminant method [two versus 11 misclassifications in cross-validation (Table I)]. Fisher's discriminant weights do not identify any particular feature as discriminating. What is surprising is that only one feature, feature 16, was retained by the two IFRAC algorithms. This single discriminating feature was identified as furfuryl alcohol, which has been previously noted as a prominent pyrolysis product from DNA.²¹ DNA is present at higher levels in malignant cells²² and the significance of this result is discussed in another paper.¹³

Effect of Normalization. As noted above, normalization is performed to compensate for variations in sample amounts. Normalization expresses each feature intensity as a fraction of the total pattern intensity. Normalization is employed (e.g., with chromatographic or mass spectral data) when the sum of the feature intensities should be constant but is not; if the weights of replicate samples vary, there will be differences in the absolute peak intensities or areas but not in the relative amounts of the peaks.

On all the four data sets tested here, Fisher's discriminant function performed better with raw data (not normalized), in contrast to the two IFRAC algorithms that gave better results when the data were normalized. These results were expected. Fisher's discriminant function depends upon covariance relationships between features, and normalization disturbs this relationship. Feature selection and the reliability function used in the IFRAC algorithms depend upon the scalar distances of feature values from the midpoint of the two group means. Normalization scaling of these distances is required for IFRAC to function properly. Using normalization can be dangerous when one or more features dominate the patterns,

(21) Eudy, L. W.; Walla, M. D.; Hudson, J. R.; Morgan, S. L.; Fox, A. *J. Anal. Appl. Pyrol.* 1985, 7, 231-247.

(22) Popescu, N. C.; DiPablo, J. A. *Cancer Res.* 1990, 50, 1316-1323.

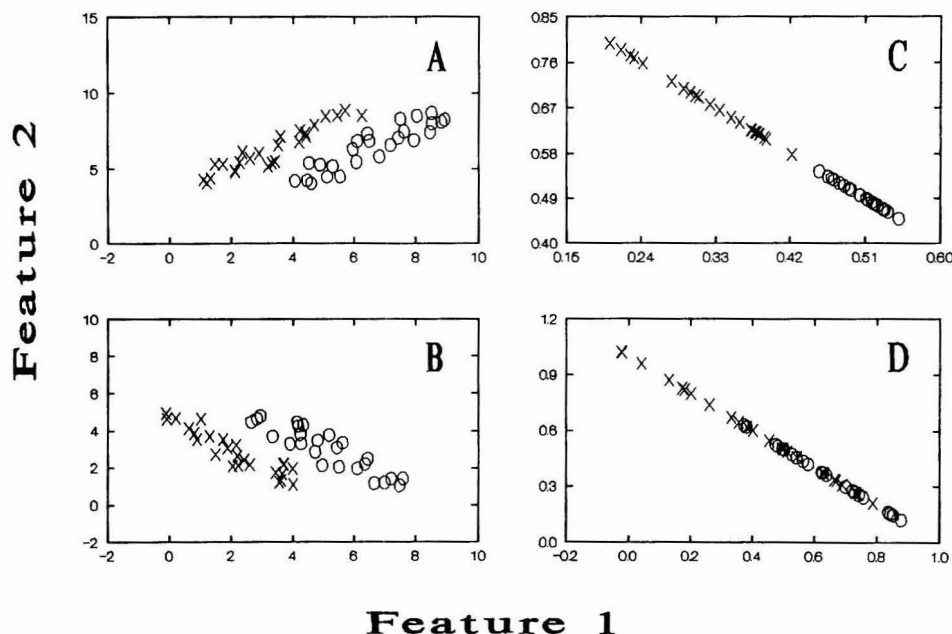


Figure 12. Plots of feature 1 against feature 2 for two simulated data sets: (A) data set with positive correlation between features; (B) data set with negative correlation between features. (C) and (D) are the normalized versions of the data in (A) and (B), respectively. The two groups are represented by crosses and circles.

Table III. Comparison of the Classification Performance of the IFRAC-1 and IFRAC-2 Algorithms with Fisher's Discriminant Function When Cross-Validation Is Performed on the Simulated Data (50 Data Points) of Figure 12

	feature significance			no. of misclassifications		
	Fisher	IFRAC-1	IFRAC-2	Fisher	IFRAC-1	IFRAC-2
Data Set A						
raw data	0.682 ^b	0 ^b	0.564 ^b	0	9	18
normalized data	0.732 ^c	1 ^c	0.826 ^c	a	1	1
	a ^b	0 ^b	0.707 ^b			
	a ^c	1 ^c	0.707 ^c			
Data Set B						
raw data	0.736 ^b	0 ^b	0.564 ^b	0	10	1
normalized data	0.677 ^c	1 ^c	0.826 ^c	a	16	16
	a ^b	0 ^b	0.707 ^b			
	a ^c	0 ^c	0.707 ^c			

^a Fisher's discriminant method weights are unstable because of ill-conditioning. ^b Feature significance for feature 1. ^c Feature significance for feature 2.

as pointed out previously.¹⁸ Selective normalization alleviates this adverse effect by excluding features exhibiting extreme feature values, but does not completely solve the scaling problem.

When high correlation exists among two features important to classification, both features together may provide separation of groups while the two features taken individually may not. Parts A and B of Figure 12 show two simulated data sets (50 data points each) illustrating high correlation. Parts C and D of Figure 12 show the same data after normalization. Normalization tends to smooth out variations induced by differences in sample amount that are reflected in positive correlations among the features, such as seen in Figure 12A. Since the sum of the feature values is made constant by normalization, the two feature values after normalization must be negatively correlated. The effect of normalization is to project the data onto a diagonal line along a direction of negative correlation. This is seen clearly in the plot of the normalized data (Figure 12C,D). If the two classes are separated as in Figure 12B, the projection of the space

between the two clusters of data overlaps with projections of points from both classes. In this case normalization has an adverse effect on the separability of classification.

These two simulated data sets were classified before and after normalization by the three algorithms with the results listed in Table III. On cross-validation, Fisher's algorithm classified the two groups perfectly using the raw (not normalized data) data. IFRAC-1 and IFRAC-2 algorithms showed a classification accuracy of 82% and 64%, respectively, with the data set plotted in Figure 12A. When the data were normalized, classification accuracy of both the IFRAC-1 and IFRAC-2 algorithms improved to 98%. With the data set of Figure 12B, the classification accuracy of IFRAC-1 and IFRAC-2 was 80% and 98%, respectively. After normalization, the classification accuracy of both the algorithms dropped to 68%.

Effect of Autoscaling. Autoscaling, or subtracting the mean and dividing by the standard deviation of each feature, converts each feature in the data set to having a mean of zero and a standard deviation of one. This common data trans-

formation removes inadvertent weighting caused by different means or different magnitudes of variation in each pattern dimension. The effect of autoscaling was tested for each algorithm on each data set. Autoscaling does not have a significant effect on the classification performance or feature weights of Fisher's discriminant method. This makes sense because calculation of covariance matrices involves subtracting the mean from the data. For the two IFRAC algorithms, autoscaling decreased classification performance, and normalizing before autoscaling did not improve results. If a chemical marker is present in a data set, autoscaling tends to reduce its prominence. Autoscaling had no effect on the performance of the IFRAC algorithms on the simulated data set of Figure 12 because no single discriminating feature is present.

CONCLUSIONS

Achieving statistical significance in multivariate classification is often suggested to require a number of samples much larger than the number of features.^{3,4,23-25} This requirement is difficult to satisfy with chromatographic or mass spectral data sets where the dimensionality (number of chromatographic peaks or number of masses) is high. Ritter and Woodruff²⁶ point out that the critical factor for linear separability of groups is not the number of features measured but is the intrinsic dimensionality of the data, given by the number of orthogonal dimensions spanned by the data. Principal components analysis is often used to reduce the dimensionality of the data prior to discriminant analysis.²⁷ However, eigenvectors determined by principal components analysis are orthogonal directions of maximum variability and specifically targeted groups in the data may not necessarily separate along these directions. For example, Figure 4 does not clearly reveal separation of groups for data set 4.

The individual feature reliability classifier discussed here treats n dimensional data sets as n independent dimensions. This important characteristic of our approach helps to alleviate the "curse of dimensionality". Data set 4, with only 24 samples in 36 dimensions, is particularly illustrative in this regard. One reason for the better performance of the IFRAC algorithms on this data set is that feature selection deleted variables contributing only noise to the data set. Even when all features were retained, the accuracy of the IFRAC-1 algorithm on data set 4 remained high at 80% correct classifications. Independent verification confirms that the feature assigned a high weight by the IFRAC algorithms (feature 16) is a discriminator having biological significance.¹³

Classification performance of both classifiers was compared for normalized versus nonnormalized data. Data normalization is a prerequisite for the IFRAC methods described here. Fisher's discriminant function performed better with the original data in contrast to the IFRAC classifiers that gave better results with normalized data.

The two feature selection methods used here with IFRAC differ from each other in that the feature weights assigned by IFRAC-2 are affected to a lesser extent by the within-group variances. For example, let a and b represent two features, each of which can discriminate between the two groups with 100% accuracy. If feature a has a large within-group variance and/or smaller difference in group means as compared with feature b , it will be assigned a lower weight than feature b by IFRAC-1. IFRAC-2 on the other hand will assign equal weights to the two features, because both features

can independently discriminate between the two groups. For that reason, IFRAC-2 assigns equal weights to all the four features for classification of the *Iris* data in data sets 3A and 3B (Figure 10A,B).

Both IFRAC algorithms show classification performance competitive with Fisher's discriminant function. The IFRAC algorithms presented here do not require the large number of samples generally required for data with a large number of features. The simplicity and efficiency of not having to compute or invert covariance matrices can be important with a large number of features and close-to-singular covariance matrices (as was the case in data set 4). When covariance matrices are ill-determined, it may not be possible to compute the inverse, or round-off error becomes significant. Because covariance matrices or inverses need not be computed, the algorithmic efficiencies of the IFRAC classifiers discussed here are high. Feature extraction procedures that combine original features to form more discriminating features are not required. Information on the individual discrimination significance of the original features is retained. Transforming a feature value into a reliability function ensures that the contributions of small but well-discriminating features are not overlooked simply because of the size of their feature values.

Features with the highest weights given by IFRAC and Fisher are different. Even though IFRAC selects a different set of features (usually fewer) than Fisher, the classification performance is comparable to Fisher on the data sets tested. IFRAC provides additional information that the selected features are individually important for classification. The chemist is ultimately interested in translating a statistical discrimination between two groups of samples into actual chemical differences. The search for unique chemical markers for different classes of chemical and biological materials represents an extension of the same goal. The optimal set of features for discriminating among two groups, in a multivariate sense, may not correctly project features that can individually provide best discrimination among these given groups in the sense of chemical markers.

Ultimately, the chemist is interested in interpreting the statistical achievement of discrimination in terms of chemical markers. The individual feature reliability approach to classification described here provides a powerful and effective method of realizing that goal.

ACKNOWLEDGMENT

This work was supported by Grant IN107 from the American Cancer Society, by Contract DAAL03-88-K-0075 from the U. S. Army Office of Research, and by a grant from the Department of Defense Research Instrumentation program. The assistance of K. E. Creek and L. Pirisi (Department of Chemistry & Biochemistry, and School of Medicine, University of South Carolina) with the culturing of mouse fibroblast cells, of Pauline Lau (Boehringer-Mannheim Diagnostics, Indianapolis, IN) and Alvin Fox (School of Medicine, University of South Carolina) with microbial carbohydrate analyses, and of C. A. Jacques (Amway Corp., Ada, MI) with Py-GC is acknowledged. The donation of the HP Pascal programming system from the Hewlett-Packard Co. (Palo Alto, CA) is also acknowledged.

- (23) Derde, M. P.; Massart, D. L. *Anal. Chim. Acta* 1989, 223, 19-44.
- (24) Lavine, B. K.; Jura, P. C.; Henry, D. R. *J. Chemom.* 1988, 2, 1-10.
- (25) Devijver, P. A.; Kittler, J. *Pattern Recognition: A Statistical Approach*; Prentice-Hall International: Englewood Cliffs, NJ, 1982.
- (26) Ritter, G. L.; Woodruff, H. B. *Anal. Chem.* 1977, 49, 2116-2118.
- (27) Yendle, P. W.; MacFie, H. J. H. *J. Chemom.* 1989, 3, 589-600.

RECEIVED for review July 13, 1992. Accepted July 20, 1992.

Flow Determination of Dissolved Inorganic Carbon Using the Alternate Washing System Equipped with a Potentiometric Gas Electrode

Hirokazu Hara,* Yohzoh Okabe, and Tomoko Kitagawa

Department of Chemistry, Faculty of Education, Shiga University, Otsu, Shiga 520, Japan

The alternate washing system equipped with a potentiometric carbon dioxide sensitive gas electrode was prepared for the determination of dissolved inorganic carbon. The design of this system is based on the alternate introduction of a sample solution and a washing stream into a flow cell by means of a four-way valve controlled by a microcomputer. This enables simple, quick, and selective determination of dissolved inorganic carbon in discrete samples. The limit of linear response was ca. 2×10^{-4} M. Determination at pH 5 is proposed because the interference from various volatile weak acids such as nitrite, sulfide, or hydrogen sulfite can be much reduced without sacrificing sensitivity. This system was applied to natural water analysis, and the results were compared with those of alkalinity.

INTRODUCTION

Dissolved inorganic carbon (DIC) is one of the major anionic components in natural waters in addition to sulfate and chloride. Although its form can be varied according to the sample pH, bicarbonate is believed to be the major component in natural waters having neutral or slightly alkaline pH values. The concentration of DIC is related to the activity of photosynthesis of phytoplanktons or the respiratory activity of microorganism. The equilibrium concentration of DIC in pure water is about 1.5×10^{-5} M ($1 \text{ M} = 1 \text{ mol dm}^{-3}$) due to the dissolution of carbon dioxide from the air,¹ while the concentration of DIC in river water lies in the range of (2–20) $\times 10^{-4}$ M in the Shiga prefecture.

Carbon dioxide sensitive gas electrodes have been utilized for the determination of DIC in various samples such as power station water,² sea water,³ pond water used for a growth experiment of phytoplanktons,⁴ and others.^{5–7} Though this type of gas sensor has a perfect selectivity against ionic species due to the microporous hydrophobic membrane, some volatile inorganic and organic acids are reported to cause interference. The interference has been examined from the viewpoint of a steady-state model⁸ or a dynamic response.⁹

Recently, we developed a new design of a flow analysis system called the alternate washing method.¹⁰ With this system, we demonstrated that the selectivity of an ammonia gas electrode for some volatile amines was improved because the so-called pseudoequilibrium potentials were measured.

In this paper, this method was used in the determination of DIC using a carbon dioxide gas electrode. The interference from six inorganic and organic acids was examined and compared with the results from the conventional continuous-flow method. Although the pH of a sample solution was found to be the most important factor in reducing the interference, the alternate washing principle was also effective in reducing the interference in some cases. The system was applied to the analysis of natural water samples.

EXPERIMENTAL SECTION

Apparatus. The body of an ammonia gas electrode (Orion 95-12) equipped with a flow-through cap (Orion 95-12-25) and a PTFE membrane (Orion 95-12-04) was used as a carbon dioxide gas sensor. The internal filling solution was a mixture of 0.001 M sodium bicarbonate and 0.019 M potassium chloride and was saturated with silver chloride. For the measurement of a sulfide solution, silver chloride was not added in order to avoid the reaction between a silver ion and dihydrogen sulfide. Potentials at $25 \pm 1^\circ \text{C}$ were measured by a digital ion meter (Orion 701A) and were transmitted every 0.6 s into a microcomputer (NEC PC8801 MkII) through an 8-bit parallel I/O interface.¹⁰ The general I/O port of the microcomputer was used to send an on-off signal to an automatic four-way valve (Kusano Kagakukikai Model KAV-4L) and two pinch valves (Takasago Electric Inc., PK-0305-NC) to control the switchover. The potential values were also recorded by an analog pen recorder (Rikadenki Model R11). The response time, washing time, and their sum (measuring time) were also measured by a microcomputer and recorded with a printer together with measured potentials. Three peristaltic pumps were used to deliver the sample and buffer solutions (Atto Model SJ1211H x2) and the wash solution, i.e., 0.01 M sodium hydroxide (Atto Model AC2110).

In the continuous-flow measurement, the sample and buffer solutions were mixed in a small mixing chamber before transfer into the flow-through cap.

Reagents. Guaranteed reagent-grade reagents were purchased from Nacalai Tesque (Kyoto). Ultrapure water prepared with a Milli-Q Labo purification system (Millipore) was used for the preparation of dilute standard bicarbonate solutions (0.5, 1, and 2×10^{-4} M).

To control the pH of a sample solution, 0.14 M sulfuric acid was used for pH 2 and a mixture of citric acid and disodium hydrogen phosphate (McIlvaine's buffer¹¹) was used to keep the pH at 3, 4, 5, and 6. The actual pH after mixing with sodium bicarbonate standard solutions was found to be 1.96, 3.07, 4.06, 5.07, and 6.05 on the average. The concentrations of citric acid and Na_2HPO_4 are 0.048 and 0.103 M at pH 5 after mixing with

(1) Kolthoff, I. M.; Sandel, E. B.; Meehan, E. J.; Bruckenstein, S. *Quantitative Chemical Analysis*, 4th ed.; Macmillan: London, 1969; p 781.

(2) Midgley, D. *Analyst* 1975, 100, 386–399.

(3) Nagashima, K.; Washio, Y.; Suzuki, S. *Bunseki Kagaku* 1984, 33, T108–T112.

(4) Kawai, T.; Miyamoto, K.; Umezawa, Y. *Bunseki Kagaku* 1990, 39, 649–653.

(5) Takano, S.; Kondoh, Y.; Ohtsuka, H. *Anal. Chem.* 1985, 57, 1523–1526.

(6) Collison, M. E.; Aebli, G. V.; Petty, J.; Meyerhoff, M. E. *Anal. Chem.* 1989, 61, 2365–2372.

(7) Nikolelis, D. P.; Krull, U. J. *Analyst* 1990, 115, 883–888.

(8) Lopez, M. E. *Anal. Chem.* 1984, 56, 2360–2366.

(9) Morf, W. E.; Mostert, I. A.; Simon, W. *Anal. Chem.* 1985, 57, 1122–1126.

(10) Hara, H.; Motoike, A.; Okazaki, S. *Anal. Chem.* 1987, 59, 1995–1999.

(11) Mashiko, Y. *Theory and measurement of pH*; Tokyo Kagaku dojin: Tokyo, 1967; p 67.

a sample solution, which was high enough to keep the pH of all the sample solutions within ± 0.06 .

Scheme of Alternate Washing System. The scheme and operation principle of the system was essentially identical to that described in detail in a previous paper.¹⁰ A sample solution premixed with a buffer and a wash solution was alternately introduced into the flow cell via a four-way valve. The system was modified so that the wash solution returned into the reservoir via the pinch valve at the measuring stage of a sample solution. The flow rates of sample, buffer, and wash solutions were adjusted to 8.0, 0.6, and 15.6 mL min⁻¹ so as to get the maximum sample throughput. The switchover of the four-way valve from sample to wash was programmed to occur when the potential first decreased below the predetermined value, i.e., the measured potential at 5×10^{-3} M minus 10 mV. The switchover of the four-way valve from sample to wash occurred when a potential difference within ± 0.1 mV was observed more than 40 times between two successive measurements. The number 40 was determined by the preliminary experiments at pH 5 so that the measured potentials reached at least 97% of the final equilibrium potential in the concentration range of 2×10^{-4} and 1×10^{-2} M. The time difference between the switchovers from wash to sample was defined as the response time, that from sample to wash was defined as the washing time, and the sum, the measuring time, was the time required for one measurement.

Selectivity. The interference from nitrite, hydrogen sulfite, sulfide, acetate, formate, and benzoate was evaluated by the selectivity coefficient calculated from the following equation:

$$K^{pot} = [(10^{(E_i - E_b)/S}) - 1] \times 10^{-3} / C_i \quad (1)$$

where E_i and E_b are the measured potentials for a 10^{-3} M sodium bicarbonate solution with and without an interferent of concentration C_i . The slope S was calculated from the linear portion of a calibration curve, i.e., 2×10^{-4} to 1×10^{-2} M. If the difference between E_i and E_b was equal to or less than ± 1.0 mV, the value of K^{pot} was defined to be zero.

Alkalinity. The pH 4.8 alkalinity was measured according to the testing method for industrial water.¹² A 100-mL portion of sample solutions was titrated with sulfuric acid to pH 4.8. The pH 4.3 alkalinity was also measured for comparison.¹³

RESULTS AND DISCUSSION

Optimization of the System. The effect of the flow rate of sample solutions on the measuring time was examined with 1×10^{-4} M and 1×10^{-2} M bicarbonate solutions at pH 2. The flow rates were varied from 4 to 8 mL min⁻¹; the ratio of flow rates of the sample and wash solutions were kept constant. The response time at 1×10^{-2} M was almost independent of the flow rate, while the response time at 1×10^{-4} M decreased with increasing flow rate. The washing time at 1×10^{-2} M decreased with increasing flow rate, while the washing time at 1×10^{-4} M was independent of the flow rate. Consequently, the measuring time became minimum at the highest flow rate tested at both concentrations.

Nagashima et al. recommended using a 0.1 M sodium hydroxide solution as a wash solution in their flow system for the DIC measurement in sea water.³ In our experiment, distilled water was not effective as a wash solution probably because of the slow dissolution rate of carbon dioxide. Though the blank level of DIC in ultrapure water was less than that in distilled water, the washing time became rather long in comparison with that of a sodium hydroxide solution. The best concentration of sodium hydroxide was determined to be 0.01 M based on ease of treatment and experimental cost.

As an internal filling solution, three compositions were tested: (1) 1×10^{-2} M NaHCO₃ + 1×10^{-2} M KCl, (2) 1×10^{-3} M NaHCO₃ + 1.9×10^{-2} M KCl, and (3) 1×10^{-4} M

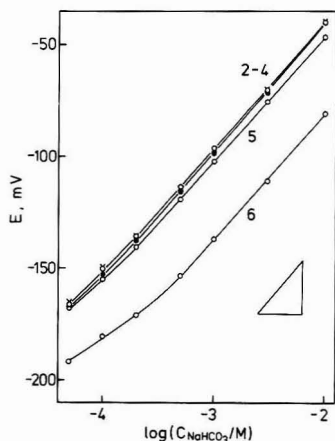


Figure 1. pH dependence of the calibration curves. The curves were measured at pH 2 (O), 4 (X), 5, and 6. The small triangle shows the Nernstian slope.

NaHCO₃ + 1.99×10^{-2} M KCl. In order to stabilize the potential of the internal silver/silver chloride reference electrode, these solutions were saturated with silver chloride. In the calibration graphs at pH 2, the abnormally low peak potential at 10^{-4} M bicarbonate solution was observed with internal filling solution 1, probably due to the very slow response. Although the response speed was normal, the slope of the calibration curve was rather small ($48\text{--}53$ mV decade⁻¹) with solution 3. A Nernstian slope was obtained with solution 2, which was used for further experiments.

pH Dependence of the Calibration Graph. The form of DIC changes according to the sample pH. Below pH 4.4, the DIC should mainly exist as carbonic acid (or aqueous carbon dioxide). The ratio of bicarbonate increases at higher pH values, but this is believed to cause a decrease in sensitivity.^{3,4} Figure 1 shows the pH dependence of the calibration curves. At pH 2–4, the three calibration curves were almost identical. The linear response range was from 1×10^{-2} M down to 2×10^{-4} M. At pH 5, a linear response down to 2×10^{-4} M was also obtained; however, the potentials at each concentration decreased 2–6 mV. This linear response range was sufficient for natural water analysis.

At pH 6, the potentials decreased so much that a linear response was observed only down to 5×10^{-4} M. Further experiments were performed at pH 5, considering the improved selectivity as shown later.

Performance of the System at pH 5. Figure 2 shows the dynamic response time curves for standard sodium bicarbonate solutions. A potential undershoot was observed in the washing process in the low concentration ranges. The reproducibility of two peaks was usually within 1 mV. The reproducibility of the mean value of two peaks for two runs was 0.9, 1.5, 1.9, 3.1, 3.2, and 3.8 mV for 30, 10, 5, 2, 1, 0.5×10^{-4} M solutions, respectively. This result shows the existence of carry over, which seems to be a weak point of the gas electrode. It is usually the best way to reduce carry over by repeating the measurement of the same solution.¹⁰ For example, the error caused by carry over from 1×10^{-2} to 1×10^{-3} M was +15% on the average of 15 independent data (range: 9.9–20.4%), and five repeated measurements of 1×10^{-3} M were enough to eliminate carry over.

(12) Japan Industrial Standards: Testing Methods for Industrial Water K0101, 1986.

(13) Han'ya, T.; Ogura, N. *Examination of water quality*, 2nd ed.; Maruzen: Tokyo, 1985; p 244.

(14) Fiedler, U.; Hansen, E.H.; Růžická, J. *Anal. Chim. Acta* 1975, 74, 423–435.

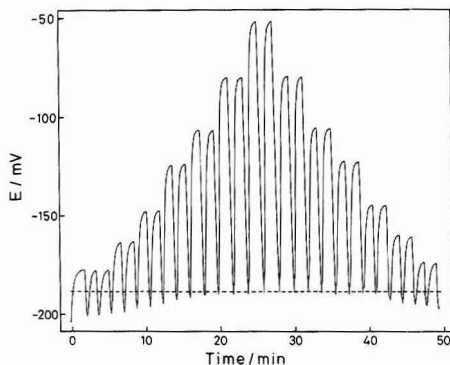


Figure 2. The potential response curve for sodium bicarbonate standard solutions at pH 5. The concentrations of bicarbonate corresponding to each pair of peaks are increasing in the order of 5×10^{-5} , 1×10^{-4} , 3×10^{-4} and 1×10^{-2} M, then decreasing in the reverse order. The first peak measured for 5×10^{-5} M bicarbonate was necessary for the determination of the base potential (shown by the broken line).

Table I. Dynamic Response Characteristics of the System at pH 5

[NaHCO ₃], M	response time, s		washing time, s		measuring time, s	
	mean ^a	std dev	mean ^a	std dev	mean ^a	std dev
10^{-4}	72.2	7.38	20.1	5.92	92.4	11.4
10^{-3}	76.1	6.99	39.9	13.4	116.1	18.7
10^{-2}	75.2	7.90	68.3	19.1	143.9	24.0

^a Results of 12 independent measurements. Two peaks of each concentration were used for calculation.

Table II. Repeatability of 20 Successive Measurements at pH 5

[NaHCO ₃], M		std dev	% rel std dev	% error
amt added	found (mean)			
2×10^{-4}	2.03×10^{-4}	0.0297×10^{-4}	1.5	1.5
5×10^{-4}	5.34×10^{-4}	0.0888×10^{-4}	1.7	6.8
10^{-3}	1.07×10^{-3}	0.0096×10^{-3}	0.9	6.5
3×10^{-3}	3.14×10^{-3}	0.0724×10^{-3}	2.3	4.7
10^{-2}	1.01×10^{-2}	0.0169×10^{-2}	1.7	0.6

Table I summarizes the response time, washing time, and measuring time from 12 independent measurements. Interestingly, the concentration dependence of the response time was insignificant, while the washing time strongly depended on the concentration of bicarbonate. As a result, the measuring time became longer as the concentration increased. It can be concluded that the measuring time for one sample was 1.5–3 min in the concentration range examined. (It is noteworthy that the measuring time of a sample of a certain concentration depends on the concentration of the base solution.)

Table II gives the results of 20 successive measurements performed after one set of a calibration run from 5×10^{-5} to 1×10^{-2} M (and several repeated measurements of 1×10^{-3} M for 2 and 5×10^{-4} M solutions in order to reduce the effect of carry over). Concentration of each peak was calculated by the equation of the regression line obtained from the linear part of a calibration graph (2×10^{-4} to 1×10^{-2} M). As judged from the relative standard deviation of 20 peaks, the repeatability is fairly good. However, a positive drift in peak potentials was observed at 3×10^{-3} M. Carry over is also the reason of the positive error at 5×10^{-4} and 1×10^{-3} M.

Nonetheless, the error was within 7% in all cases listed, which was not very bad, considering the logarithmic character of the sensor.

Selectivity. Lopez studied the selectivity of the potentiometric carbon dioxide gas-sensing electrode.⁸ Her important conclusion was that the selectivity is governed primarily by the acidity rather than the volatility of the interferents. Among the interferents she tested, six substances which are sources of the possible interference in natural water analysis were selected. Table III gives the apparent selectivity coefficients for six interferents at pH 2 and 5 by the continuous flow method and the alternate washing method. The reproducibility of these values is rather poor as judged from the standard deviation, partly because they are rather sensitive to the slight variation of the slope of a calibration graph. Nevertheless, several conclusions can be deduced from the table.

First, the pH is of primary importance relative to the selectivity coefficient obtained by both methods. Only benzoate showed little interference at both pHs, probably because of the low vapor pressure of benzoic acid.⁸ The percentage of undissociated species versus the total concentration can be calculated using the pK_a values given in the table. At pH 2, over 95% of these ions exists in undissociated form except HSO₃⁻ (about 37%). On the contrary, the percentage decreased to 2%, 0.06%, 37%, and 5% for nitrite, hydrogen sulfite, acetate, and formate at pH 5. This is the reason for the remarkable decrease in the selectivity coefficient at pH 5. Only sulfide exists in undissociated form even at pH 5. The decrease in interference from sulfide at pH 5 cannot be explained by the difference in the degree of dissociation at each pH.

Morf et al. reported that the sharp increase and the subsequent gradual decrease in potential could be expected after the step change from a 10^{-4} M CO₂ sample to a 10^{-2} M solution of H₂S with a CO₂ gas electrode having a silicone rubber membrane.⁹ However, the time response curve was monotonous in every continuous-flow measurement including the case of sulfide, although the rapid increase in potential was observed in some cases. Further examination will be necessary to understand the interfering behavior of sulfide when the microporous PTFE membrane is used.

When the results of the alternate washing method (AWM) are compared with those of the continuous-flow method (CFM), the interference can be said to decrease at both pHs, except for the cases when the interference is very large. In the AWM, the pseudoequilibrium potential, which was usually smaller than the equilibrium potential obtained by the CFM, was measured. It is natural that the apparent selectivity coefficient of the AWM was usually smaller than that of the CFM. This is the significant feature of the AWM: the ability to measure a signal that is transient but very near to the true equilibrium for a standard bicarbonate solution and relatively far from the equilibrium for solutions containing the interfering substance. In the AWM, the interference at pH 5 was almost completely removed for all interferents tested except sulfide at least in the concentration range below 10^{-4} M.

The observed sequence of the interference at pH 2 was as follows: hydrogen sulfite > nitrite > sulfide > formate > acetate > benzoate. This sequence is in accordance with that of the pK_a only for hydrogen sulfite and nitrite and for formate and acetate. This result seems to be in conflict with the conclusion of Lopez, at least for sulfide and benzoate. However, part of the discrepancy with the results of Lopez may be ascribed to differences in the experimental conditions such as the concentration of NaHCO₃ in the internal filling solution (0.01 M was used), the concentration of the inter-

Table III. Selectivity Coefficient for Volatile Interferents

interferent	pK _a	concn, M	apparent selectivity coefficient ^a			
			at pH 2		at pH 5	
			AWM ^b	CFM ^c	AWM ^b	CFM ^c
nitrite	3.29	10 ⁻⁵	0	700 ± 200 (n = 4)	0	0
		10 ⁻⁴	1000 ± 100 (n = 4)	1000 ± 200 (n = 4)	0	1 ± 0.9 (n = 4)
		10 ⁻³	800 ± 100 (n = 3)	800 ± 200 (n = 4)	0.1 ± 0.05 (n = 4)	10 ± 2 (n = 4)
hydrogen sulfite	1.76	10 ⁻⁵	20 ± 10 (n = 6)	2000 ± 1000 (n = 3)	0	0
		10 ⁻⁴	5000 ± 700 (n = 3)	5000 ± 1000 (n = 3)	0	0
		10 ⁻³	4000 ± 400 (n = 4)	4000 ± 500 (n = 3)	-0.1 ± 0.02 (n = 6)	4 ± 2 (n = 4)
sulfide	7.0	10 ⁻⁵	0	30 ± 10 (n = 4)	0	10 ± 1 (n = 3)
		10 ⁻⁴	2 ± 0.4 (n = 6)	100 ± 40 (n = 4)	0.6 ± 0.1 (n = 4)	2 ± 2 (n = 4)
		10 ⁻³	300 ± 100 (n = 4)	300 ± 100 (n = 6)	0.3 ± 0.05 (n = 6)	0.6 ± 0.4 (n = 6)
acetate	4.76	10 ⁻⁴	<0.1	2 ± 1 (n = 3)	0	0
		10 ⁻³	<0.1	20 ± 6 (n = 4)	0	1 ± 0.4 (n = 4)
		10 ⁻²	0	3 ± 1 (n = 4)	0	0
formate	3.75	10 ⁻⁴	0	100 ± 50 (n = 4)	0	0
		10 ⁻³	<0.1	1 ± 0.8 (n = 3)	0	0
		10 ⁻²	0	0.3 ± 0.2 (n = 3)	0	0

^a Mixed solution method was used for 10⁻³ M sodium bicarbonate. Mean ± SD is shown with number of data. ^b Alternate washing method. ^c Continuous-flow method.

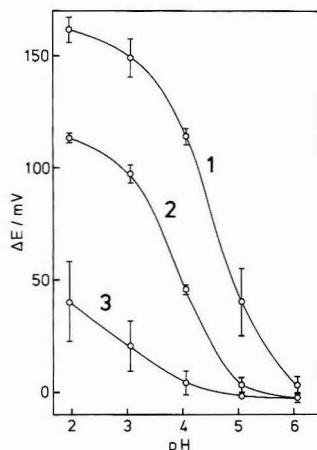


Figure 3. pH dependence of the interference from nitrite. The potential difference between the two 10⁻³ M bicarbonate solutions with and without 10⁻³, 10⁻⁴, and 10⁻⁵ M sodium nitrite (curves 1, 2, and 3, respectively) is plotted against the pH of a sample solution after mixing with a buffer stream. The error bar corresponds to the standard deviation of four independent data of the continuous flow method.

ferents and the difference in the method used to obtain the selectivity coefficient (a separate solution method was used⁹).

Among the interferents tested, nitrite is most important for river water analysis because its concentration in polluted river waters sometimes exceeds 1×10^{-5} M in the Shiga prefecture. The effect of the coexistence of nitrite was examined by the continuous-flow method and the results are shown in the following two figures. Figure 3 shows the pH dependence of the increase in potential caused by the coexistence of sodium nitrite in sodium bicarbonate solution. The interference almost disappeared at pH 5 for 1×10^{-4} M nitrite solution (curve 2) even in the continuous-flow measurement. Figure 4 shows the time response curves of a mixture of nitrite and bicarbonate at each pH. In the AWM, the potential value is recorded after 40 occasions in which the potential difference of two successive measurements every 0.6 s was within ± 0.1 mV. This means that the maximum potential change during 24 s should be below 4 mV (i.e., $dE/dt < 10$ mV min⁻¹) for the switchover. If the rate of potential

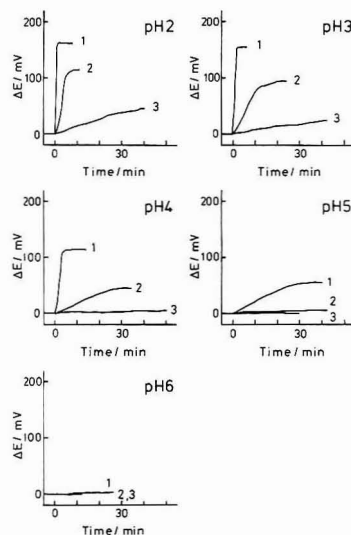


Figure 4. The time response curves of 10⁻³ M bicarbonate solution in the presence of 10⁻³, 10⁻⁴, and 10⁻⁵ M sodium nitrite (curves 1, 2, and 3, respectively) measured by the continuous flow method at each pH.

change is very fast (see curve 1 at pH 2, 3, or 4), the potential of the horizontal part is also recorded in the AWM as in the CFM. However, potential values much nearer to that of the 10⁻³ M bicarbonate solution are measured in the AWM, if the rate of potential change is slower than 10 mV min⁻¹ as was the case for curve 3 at pH 2. Thus, the method of potential measurement in the AWM is useful for improving the apparent selectivity.

Natural Water Analysis. Table IV shows the results of the DIC measurement for natural water samples. The alkalinities of pH 4.8 and 4.3 are included in the table because these values have often been used as a measure of the DIC in aquatic chemistry.

The interference from volatile inorganic and organic species was concluded to be negligible because the values with the pH 2 buffer agreed with those with the pH 5 buffer very well

Table IV. Results of Natural Water Analysis

sample	DIC, ^a × 10 ⁴ M		alkalinity, × 10 ⁴ equiv L ⁻¹	
	pH 2	pH 5	pH 4.8	pH 4.3
pond water	2.36	2.28	2.11	2.62
Lake Biwa	6.62	6.89	6.04	6.57
river 1	2.39	2.29	2.36	2.81
2	5.68	5.62	5.14	5.62
3	5.96	5.93	5.31	5.82
4	7.23	7.19	6.49	6.97
5	9.92	9.63	7.92	8.47
6	9.96	9.91	8.15	8.69

^a Dissolved inorganic carbon measured by the alternate washing method with the buffer of pH 2 or 5.

(correlation coefficient $r = 0.9986$). The concentration of nitrite was below 1×10^{-6} M in all samples.

The alkalinity was obtained by titration with a sulfuric acid solution. Both the pH 4.8 alkalinity and the pH 4.3 alkalinity are often used as a measure of the concentration of bicarbonate. Although the correlation between the DIC

values measured with the pH 5 buffer and the alkalinity was very high ($r = 0.996$ for the pH 4.8 alkalinity and $r = 0.997$ for the pH 4.3 alkalinity), the slopes of the regression lines are 0.78 and 0.79, respectively. This result means that the alkalinity is not directly correlated with the DIC measured in this method. On the other hand, Kuwaki et al.¹⁵ reported that the DIC values in natural waters measured by a gas diffusion/flow injection analysis with a photometric detection system agreed well with the results obtained by indirect photometric ion chromatography (the error was within $\pm 2.2\%$ for five river water samples). Because their system used also the gas diffusion principle, the DIC values measured in our system may correspond to the total concentration of carbonate species. The reasonable interpretation of the alkalinity is beyond the scope of this paper and will require further studies.

ACKNOWLEDGMENT

A part of this work was financially supported by Mitsubishi Heavy Industries, Ltd.

RECEIVED for review March 23, 1992. Accepted July 20, 1992.

Registry No. Water, 7732-18-5; carbon, 7440-44-0; sodium bicarbonate, 144-55-8.

(15) Kuwaki, T.; Tōei, K.; Akiba, M.; Oshima, M.; Motomizu, S. *Bunseki Kagaku* 1987, 36, T132-T135.

Theory of the Interfacial Potential Distribution and Reversible Voltammetric Response of Electrodes Coated with Electroactive Molecular Films

Christopher P. Smith and Henry S. White*

Department of Chemical Engineering and Materials Science, University of Minnesota, Minneapolis, Minnesota 55455

An analytical expression for the interfacial potential distribution at metal electrodes coated with monolayer and submonolayer films of electroactive molecules is reported. The driving force for reversible electron transfer between the metal and electroactive adsorbate is calculated from the interfacial potential distribution and is used to predict the current-voltage wave shape in cyclic voltammetric experiments. The shape of the voltammetric wave and the potential at which it is observed are shown to be functions of the thickness and dielectric constant of the adsorbate film, the surface concentration of electroactive adsorbate, the concentration and type of supporting electrolyte, the solvent dielectric constant, and the potential of zero charge (E_{PZC}). An analytical expression is also presented for the capacitance of adsorbate-covered electrodes.

INTRODUCTION

Cyclic voltammetry is the most frequently used electrochemical method for investigating the structure and electron-transfer dynamics of redox species that are adsorbed or covalently attached to an electrode surface. The established theory¹ of the voltammetric response of an electrode coated with a molecular film containing a reversible electroactive couple, O°/R^{\bullet} ,



yields three major predictions concerning the shape of the voltammetric wave: (i) the maximum value of the voltammetric current (i.e., the peak current) is directly proportional to the total surface concentration of redox centers, Γ_T (mol m^{-2}), and occurs at the standard redox potential, E° , of eq 1; (ii) the voltammetric wave is symmetric about the peak current and has a width of 90.6 mV/n, where $n = z_O - z_R$; and (iii) the position of the voltammetric wave and its width are invariant with Γ_T . These predictions are frequently not born out in experimental results. In particular, voltammetric waves of the adsorbed redox species are usually significantly broader than predicted. Electrochemical investigations of self-assembling redox films²⁻⁹ (e.g., alkanethiols derivatized with a pendant ferrocene group^{2,3}), also show an unusual dependence of the apparent E° on Γ_T ^{3,7} in addition to the usual wave

broadening. Excluding the effects of slow electron transfer (which introduce an asymmetry in the wave shape and can readily be diagnosed as such), these nonideal behaviors are frequently attributed to one or more of the following: surface activity effects,^{10,11} inhomogeneities in the chemical structure of the film,^{3,12} an oxidation state dependence of the redox species' permanent dipole,¹³ and ion pairing between the redox film and electrolyte counterions.^{2,7} Various models based on these effects have been developed to predict the nonideal voltammetric response which, under favorable circumstances, allows one to extract empirical fitting parameters from the data (e.g., "interaction parameters"). While these parameters characterize the departure of the experimental voltammogram from ideal behavior, they cannot be derived from the molecular properties of the film in a straightforward manner.

In addition to the heuristic nature of the above mentioned models, a significant omission of each is that they do not consider the effects of the interfacial potential distribution on the energetics of the electron-transfer reaction. Consider, for instance, Figure 1, which schematically depicts the structures of two electroactive films. In each case, the redox center of the molecule is assumed to be located at a finite distance from the electrode surface, corresponding to the plane of electron transfer (PET). If ions are unable to penetrate into the molecular film, the interfacial potential profiles that we anticipate to find in these systems are characterized by a linear potential distribution between the electrode surface and the PET and a nonlinear potential decay in the solution phase, Figure 1A. If a portion of the molecule extends beyond the redox centers, Figure 1B, then a second linear potential drop is introduced between the redox center and the solution.

A dependence of the reversible voltammetric response on the interfacial potential distribution can be anticipated by considering the factors controlling the driving force for the electron-transfer reaction. From Figure 1, it is clear that only a fraction of the total interfacial drop ($\phi_M - \phi_S$) occurs between the electrode surface and the PET. Thus, it immediately follows that the surface concentrations of O° and R^{\bullet} will be governed by an equilibrium electrode potential that is a function of the electrostatic potential at the PET, ϕ_{PET} . In turn, this potential will be a function of the molecular structure of the film and any parameter of the electrochemical cell that affects the potential distribution (e.g., solvent dielectric constant). In addition, if the electrostatic charges of the redox couple (z_O and z_R) are not the same, as in most experimental systems, ϕ_{PET} will also be a function of the oxidation state of the film. Consequently, the driving force for electron transfer will continuously vary during the voltammetric experiment in a manner that is not intuitively

(1) Bard, A. J.; Faulkner, L. R. *Electrochemical Methods*; J. Wiley: New York, 1980.

(2) Creager, S. E.; Rowe, G. K. *Anal. Chim. Acta* 1991, 246, 233. Rowe, G. K.; Creager, S. E. *Langmuir* 1991, 7, 2307.

(3) Chidsey, C. E. D.; Bertozzi, C. R.; Putviniski, T. M.; Muijs, A. M. *J. Am. Chem. Soc.* 1990, 112, 4301.

(4) Lee, K. A. B. *Langmuir* 1990, 6, 709.

(5) De Long, H. C.; Buttry, D. A. *Langmuir* 1990, 6, 1319.

(6) Collard, D. M.; Fox, M. A. *Langmuir* 1991, 7, 1192.

(7) Acevedo, D.; Abruna, H. D. *J. Phys. Chem.* 1991, 95, 9590.

(8) Diaz, A.; Kaifer, A. E. *J. Electroanal. Chem.* 1988, 249, 333.

(9) Bae, I. T.; Huang, H.; Yeager, E. B.; Scherson, D. A. *Langmuir* 1991, 7, 1558.

(10) Brown, A. P.; Anson, F. C. *Anal. Chem.* 1977, 49, 1589.

(11) Matsuda, H.; Aoki, K.; Tokuda, K. *J. Electroanal. Chem. Interfacial Electrochem.* 1987, 217, 15.

(12) Alberty, W. J.; Boutelle, M. G.; Colby, P. J.; Hillman, A. R. *J. Electroanal. Chem. Interfacial Electrochem.* 1982, 133, 135.

(13) Gerischer, H.; Scherson, D. A. *J. Electroanal. Chem. Interfacial Electrochem.* 1985, 188, 33.

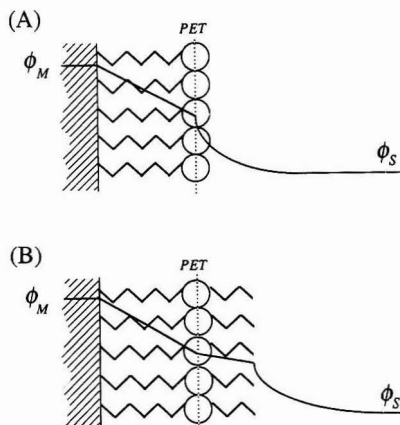


Figure 1. Schematic drawing of irreversibly adsorbed electroactive films in contact with an electrolyte solution. The electroactive O/R centers are indicated by open circles and are separated from the surface by a dielectric film (zig-zag lines) of finite thickness. In A and B, the interfacial potential profile (solid line) is linear across the dielectric region between the metal and the PET. In B, a second dielectric layer extends a finite distance beyond the PET introducing a second linear potential decay. For both A and B, the potential profile in the solution phase is nonlinear.

straightforward. In this paper, we show how the effects of the interfacial potential distribution can account for typical voltammetric behaviors reported in the literature.

RESULTS AND DISCUSSION

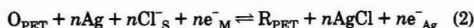
The concepts introduced above are developed in the following order. In Section I, we provide explicit definitions of the equilibrium electrode potential in terms of the surface concentrations of O^s and R^s and the electrostatic potential at the PET. The underlying assumptions of our model are presented in this section, allowing the problem to be posed mathematically. In Section II, an electrostatic model of the interface is introduced and general analytical expressions are developed for the interfacial potential distribution. These results are used in Section III to derive the potential profile and the general current-voltage (i - E) response expected in a cyclic voltammetric experiment. Finally, in Section IV, we calculate the theoretical voltammetric response for two redox systems and qualitatively compare the results to data in the literature.

I. Definition of the Equilibrium Electrode Potential for an Irreversibly Adsorbed Film. In a voltammetric experiment, the instantaneous faradaic current (i) at a specified electrode potential (E) is determined by the surface concentrations of O^s and R^s , hereafter referred to simply as O and R . Thus, to calculate the voltammetric response for a reversible electrode reaction (eq 1), it is first necessary to establish the relationship between the equilibrium surface concentrations (Γ_O and Γ_R) and the electrode potential. To avoid the concept of an absolute interfacial potential, it is convenient to cast the discussion of the thermodynamics of eq 1 in terms of a complete cell. Thus, consider the electrochemical cell



where the left-hand electrode, M , represents a metal electrode that is coated with a molecular film containing the O/R redox couple (e.g., Figure 1) and immersed in an aqueous solution containing Cl^- ions. The right-hand electrode represents an ideally nonpolarizable $Ag/AgCl$ electrode ($AgCl + e^- \rightleftharpoons Ag$

+ Cl^-). Combination of the reference electrode reaction and eq 1 yields the overall cell reaction



where M and Ag represent the left- and right-hand electrodes, respectively, and S represents the bulk solution phase. At equilibrium

$$\mu_O^{PET} + n\mu_{Ag}^S + n\mu_{Cl^-}^S + n\mu_e^- = \mu_R^{PET} + n\mu_{AgCl}^S + n\mu_e^-_{Ag} \quad (3)$$

where μ_i^j represents the electrochemical potential of species i in phase j . Employing the standard thermodynamic definitions and relationships ($\mu_i^j = \mu_i^0 + RT \ln(a_i^j) + z_i F \phi^j$; a_i^j = activity of ion i in phase j ; $\Delta G^0 = \sum \nu_i \mu_i^0$, where ν_i is the stoichiometric coefficient; and $\Delta G^0 = -nFE^0$) and noting that $(\phi_M - \phi_{Ag}) = E$, yields

$$E - E^0 - (\phi_{PET} - \phi_S) = (RT/nF) \ln [(a_O^{PET}) / (a_{Cl^-}^S)^n / (a_R^{PET})] \quad (4)$$

where F , R , and T are Faraday's constant ($C \text{ equiv}^{-1}$), the molar gas constant ($J \text{ mol}^{-1} K^{-1}$), and the absolute temperature (K), respectively, and ϕ_S is the electrostatic potential in the bulk solution (Figure 1). Approximating the activities of O and R by their respective surface concentrations, Γ_O and Γ_R , and assuming $a_{Cl^-}^S = 1$ for simplicity, yields the following relationship between the equilibrium surface concentrations of O and R :

$$E - E^0 - (\phi_{PET} - \phi_S) = (RT/nF) \ln [\Gamma_O / \Gamma_R] \quad (5)$$

Thus, to determine Γ_O / Γ_R , it is necessary to explicitly specify a value of $(\phi_{PET} - \phi_S)$. Since $(\phi_{PET} - \phi_S)$ is an electrostatic quantity, its value will depend on the particular model chosen to evaluate the interfacial potential distribution (Section II).

It is useful at this point to examine a limiting case of eq 5. Keeping in mind the physical pictures drawn in Figure 1, consider a situation in which all of the potential drop across the interface ($\phi_M - \phi_S$) occurs within the film between the metal surface and the redox centers at the PET. Then $\phi_{PET} = \phi_S$, and the left-hand side of eq 5 simplifies to $(E - E^0)$, yielding the Nernst equation. This approximation is assumed in developing the ideal Nernstian voltammetric response of monolayer films,¹ as well as in all existing models that attempt to account for nonideal behavior. However, it is clear from Figure 1 that the quantity $(\phi_{PET} - \phi_S)$ must be known to accurately predict the i - E response.

The criterion for irreversible adsorption follows directly from eq 5 and the preceding discussion. If the adsorbed redox couple (O_{PET} and R_{PET}) is in equilibrium with the solution phase containing the same, but dissolved, redox pair (O_S and R_S), the solution concentrations of O_S and R_S far from the electrode surface will adjust their values in accordance with the electrode potential (E) specified in eq 5, as dictated by the conditions of equilibrium ($\mu_O^{PET} = \mu_O^S$ and $\mu_R^{PET} = \mu_R^S$). Since the thermodynamic properties depend only on the initial and final states of the system, eq 5 will again reduce to the Nernst equation (i.e., $\phi_{PET} = \phi_S$) where the surface concentrations of O and R are replaced by the concentrations of O and R in the bulk solution. In practice, equilibrium between the surface and dissolved species may occur by rapid adsorption and desorption of the redox species or by electron transfer reactions (e.g., $R_S + O_{PET} \rightleftharpoons O_S + R_{PET}$). Thus, a simple experimental criterion for the condition of irreversible adsorption is that (i) the redox couple is not present in the bulk solution phase (or is present at such low concentrations that electron-transfer reactions between bulk and surface species are negligible) and (ii) the total surface concentrations of redox species ($\Gamma_T = \Gamma_O + \Gamma_R$) does not vary during the timescale of the experiment. These conditions are frequently

met, or closely approximated, in voltammetric experiments reported in the literature.

II. Interfacial Potential Distribution. Figure 2 shows the model system used to compute the interfacial potential distribution across the electroactive film shown in Figure 1B. It consists of a planar metal electrode of area A at $x = 0$ covered by two dielectric films of thickness d_1 and d_2 with dielectric constants ϵ_1 and ϵ_2 , respectively, corresponding to the portions of the molecule surrounding the redox center at the PET at $x = d_1$. The outer surface of the film-coated electrode at $x = d_1 + d_2$ is in contact with an electrolyte solution that has a dielectric constant of ϵ_3 and contains a symmetric z:z electrolyte.

Assuming that there is no charge in the film except that associated with the redox centers at the PET, the potential decays linearly from ϕ_M to ϕ_{PET} and from ϕ_{PET} to ϕ_F . In the solution phase ($x > d_1 + d_2$), the potential distribution is assumed to be governed by the Gouy-Chapman model and decays to ϕ_S in the bulk solution¹

$$\tanh(ze(\phi_X - \phi_S)/2kT) = \frac{\tanh(ze(\phi_F - \phi_S)/2kT) \exp(-\kappa(x - d_1 - d_2))}{1} \quad (6)$$

where ϕ_X is the potential (V) in the electrolyte solution at position x , κ is the inverse Debye length (m^{-1}) given by $\kappa = ze(2n^\circ/\epsilon_0\epsilon_3kT)^{1/2}$, e is the charge of an electron (C), n° is the number concentration of the ions in the electrolyte (m^{-3}), ϵ_0 is the permittivity of free space ($C^2 N^{-1} m^{-2}$), and k is Boltzmann's constant ($J K^{-1}$).

In addition to assuming that the only charge in the film is associated with the redox centers at the PET, we also make the following simplifying assumptions:

- (1) Charges on the metal surface (at $x = 0$) and on the redox centers (at the PET) are delocalized (i.e., discreteness of charge is ignored).
- (2) The electrolyte ions approach the film no closer than $d_1 + d_2$ (or d_1 when $d_2 = 0$).
- (3) The contribution to the interfacial potential from molecular dipoles is negligible.

The model we have described is purely electrostatic in nature. The potential profile through the interface can be expressed simply in terms of the electric fields and charge densities throughout the system. With the potential distributions defined above, the magnitude of the electric field ($|E| = -dV/dx$) in each region of Figure 2 is given by eq 7

$$|E| = \begin{cases} 0 & \text{(by definition)} & x < 0 \\ (\phi_M - \phi_{PET})/d_1 & & 0 < x < d_1 \\ (\phi_{PET} - \phi_F)/d_2 & & d_1 < x < (d_1 + d_2) \\ \kappa(2kT/ze) \sinh(ze(\phi_X - \phi_S)/2kT) & & x > (d_1 + d_2) \\ 0 & & x \rightarrow \infty \end{cases} \quad (7)$$

Without specifying exact values, the charge densities ($C m^{-2}$) on the electrode surface (σ_M), at the redox plane (σ_{PET}), and in the solution (the diffuse layer) (σ_{dif}) are given by eq 8

$$\sigma = \begin{cases} \sigma_M & x = 0 \\ \sigma_{PET} & x = d_1 \\ \sigma_{dif} & (d_1 + d_2) < x < \infty \end{cases} \quad (8)$$

Since the volume charge density in the solution, $\rho(x)$ ($C m^{-3}$), varies with distance according to the Boltzmann distribution, σ_{dif} refers to the net charge density of the entire diffuse layer, i.e., $\sigma_{dif} = \int_{d_1+d_2}^{\infty} \rho(x) dx$.

The electric fields and the charge densities are related through Gauss' law. It is convenient to use the boxes shown in Figure 2 to enclose the charges of interest. For the assumed planar geometry, the electric field passes only through the

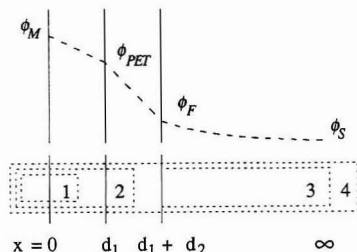


Figure 2. Model system used to calculate the potential profile across the adsorbed redox film.

faces of the boxes parallel to the electrode surface. Thus

$$Q_{enclosed} = \epsilon_0 \int_{surface} \vec{E} \cdot d\vec{a} = A(\epsilon_1 \epsilon_0 |E|_+ - \epsilon_0 |E|_-) \quad (9)$$

where the subscripts "+" and "-" corresponds to the right and left ends of the boxes, respectively. Applying Gauss' law to the four boxes shown in the lower half of Figure 2 yields the following system of equations relating the charge densities ($\sigma = Q_{enclosed}/A$) and interfacial potentials

$$\sigma_M = \epsilon_0 \epsilon_1 (\phi_M - \phi_{PET})/d_1 \quad \text{(box 1)} \quad (10a)$$

$$\sigma_M + \sigma_{PET} = \epsilon_0 \epsilon_2 (\phi_{PET} - \phi_F)/d_2 \quad \text{(box 2)} \quad (10b)$$

$$\sigma_{dif} = -\epsilon_0 \epsilon_3 \kappa (2kT/ze) \sinh(ze(\phi_F - \phi_S)/2kT) \quad \text{(box 3)} \quad (10c)$$

$$\sigma_M + \sigma_{PET} + \sigma_{dif} = 0 \quad \text{(box 4)} \quad (10d)$$

When $d_2 = 0$ (Figure 1A), a similar set of equations can be derived, but the result can be obtained from eq 10 by omitting eq 10b and replacing ϕ_F with ϕ_{PET} . In either case, three of the unknowns must be specified to obtain a solution since there are three more unknowns than there are equations.

Equation 10 is perfectly general, subject to the limitations imposed by the initial assumptions of the model. Although it was derived with an electrochemical system in mind, where σ_{PET} is determined by an applied electrode potential (vide infra), the equations contain no assumptions regarding the redox properties of the film. In fact, the results could even be applied to an electrochemically inert film.

III. Potential Distribution and Voltammetric Response. Using eq 10, it is possible to describe the interfacial potential distribution as a function of the applied potential and redox parameters (e.g., E° , z_R , etc.). It is convenient to describe the potential distribution in terms of the oxidation state of the film.¹⁴ Defining the fraction of molecules in the oxidized state as $f = \Gamma_O/\Gamma_T$ (where $\Gamma_T = \Gamma_O + \Gamma_R$), and using $E = \phi_M - \phi_{Ae}$, eq 5 may be rewritten as

$$\phi_M - \phi_{PET} = E^\circ - E_{PZC} - (RT/nF) \ln [(1-f)/f] \quad (11)$$

where the quantity E_{PZC} ($= \phi_S - \phi_{Ae}$) is equivalent to the potential of zero charge of the uncoated electrode, in the absence of specific ion adsorption, measured with respect to the reference electrode.¹ Substituting eq 11 into eq 10a yields an expression for the charge density on the metal, σ_M ,

$$\sigma_M = (E^\circ - E_{PZC} - (RT/nF) \ln [(1-f)/f]) \epsilon_0 \epsilon_1 / d_1 \quad (12)$$

(14) Equation 10 must be solved iteratively if E is used as the independent variable instead of f .

The charge density at the PET, σ_{PET} , is given simply by eq 13

$$\sigma_{\text{PET}} = F\Gamma_T(z_0f + z_R(1-f)) \quad (13)$$

For a given value of E_{PZC} and f and the corresponding values of σ_M and σ_{PET} , the potentials $E_F = \phi_F - \phi_{\text{Ag}}$, $E_{\text{PET}} = \phi_{\text{PET}} - \phi_{\text{Ag}}$, and $E = \phi_M - \phi_{\text{Ag}}$ may be calculated from eq 10, by working from the last equation to the first, using the identity $\sinh^{-1}[u] = \ln[u + (u^2 + 1)^{1/2}]$ to solve eq 10c.

The total voltammetric current that is measured as a function of applied electrode potential is the sum of the charging (i_c) and faradaic (i_f) currents:

$$i_t = i_c + i_f \quad (14)$$

If the electrode potential is scanned at a constant rate ν (V s⁻¹), the charging current is

$$i_c = \nu AC_T \quad (15)$$

where C_T is the total interfacial capacitance (F m⁻²). For an electroinactive film, the reciprocal capacitance of the interface, C_T^{-1} , is given by the sum of the reciprocal capacitances of the film and the solution,¹⁵

$$C_T^{-1} = \begin{cases} C_1^{-1} + C_2^{-1} + C_{\text{dif}}^{-1} & \text{for } d_2 \neq 0 \\ C_1^{-1} + C_{\text{dif}}^{-1} & \text{for } d_2 = 0 \end{cases} \quad (\text{electroinactive film}) \quad (16)$$

where C_1 and C_2 represent the capacitances of the film to the left and the right of the PET in Figure 2, respectively, and C_{dif} is the potential-dependent diffuse layer capacitance:

$$C_1 = \epsilon_0 \epsilon_1 / d_1 \quad (17a)$$

$$C_2 = \epsilon_0 \epsilon_2 / d_2 \quad (17b)$$

$$C_{\text{dif}} = \epsilon_0 \epsilon_3 \cosh [ze(\phi_F - \phi_S)/2kT] \quad (17c)$$

Equation 16, however, is not generally valid for an electroactive film. The correct expression can be obtained by using the formal definition of the total interfacial capacitance: $C_T = \partial\sigma_M/\partial E$.¹ Differentiating eq 10 with respect to E (with $\partial\phi_M/\partial E = 1$) yields the following system of four equations in five unknowns, written in terms of the capacitances defined in eq 17:

$$C_T = C_1(1 - \partial\phi_{\text{PET}}/\partial E) \quad (18a)$$

$$C_T + \partial\sigma_{\text{PET}}/\partial E = C_2(\partial\phi_{\text{PET}}/\partial E - \partial\phi_F/\partial E) \quad (18b)$$

$$\partial\sigma_{\text{dif}}/\partial E = -C_{\text{dif}}\partial\phi_F/\partial E \quad (18c)$$

$$C_T + \partial\sigma_{\text{PET}}/\partial E + \partial\sigma_{\text{dif}}/\partial E = 0 \quad (18d)$$

The fifth equation is obtained by using the following definition for $\partial\sigma_{\text{PET}}/\partial E$:

$$\partial\sigma_{\text{PET}}/\partial E = (\partial\sigma_{\text{PET}}/\partial\sigma_M)(\partial\sigma_M/\partial E) = (\partial\sigma_{\text{PET}}/\partial\sigma_M)C_T \quad (19)$$

where the dependence of σ_M on σ_{PET} is found by differentiating eqs 12 and 13 with respect to f to give

$$\partial\sigma_{\text{PET}}/\partial\sigma_M = (\partial\sigma_{\text{PET}}/\partial f)/(\partial\sigma_M/\partial f) = (n^2F^2\Gamma_T/RTC_1)f(1-f) \quad (20)$$

Solving eqs 18 and 19 for C_T yields the correct potential-

dependent interfacial capacitance of the system:

$$C_T^{-1} = \begin{cases} C_1^{-1} + (C_2^{-1} + C_{\text{dif}}^{-1})(1 + \partial\sigma_{\text{PET}}/\partial\sigma_M) & \text{for } d_2 \neq 0 \\ C_1^{-1} + C_{\text{dif}}^{-1}(1 + \partial\sigma_{\text{PET}}/\partial\sigma_M) & \text{for } d_2 = 0 \end{cases} \quad (\text{electroactive film}) \quad (21)$$

The variation of σ_{PET} with σ_M reduces the effective capacitance of the layers beyond the PET by the quantity $(1 + \partial\sigma_{\text{PET}}/\partial\sigma_M)$. As the film becomes either fully reduced ($f \rightarrow 0$) or oxidized ($f \rightarrow 1$), $\partial\sigma_{\text{PET}}/\partial\sigma_M \rightarrow 0$ and eq 21 reduces to eq 16. Equation 21 also reduces to eq 16 if the film is electroinactive (in which case $\partial\sigma_{\text{PET}}/\partial\sigma_M = 0$) or if $\partial\sigma_{\text{PET}}/\partial\sigma_M \ll 1$ (i.e., $n^2F^2\Gamma_T/4RTC_1 \ll 1$).

Before proceeding to derive the faradaic current, it is instructive to note that the total interfacial capacitance, C_T , given by eq 21, is a function of two potential-dependent quantities: C_{dif} and $\partial\sigma_{\text{PET}}/\partial\sigma_M$. The importance of these two quantities can be demonstrated by the following example. Consider a monolayer redox film with $d_2 = 0$, $d_1 = 1$ nm, $\epsilon_1 = 4$, and $\Gamma_T = 10^{-10}$ mol cm⁻², immersed in an aqueous solution ($\epsilon_3 = 78$) containing a 1 M 1:1 electrolyte. Equation 21 becomes

$$C_T^{-1} = d_1/\epsilon_0\epsilon_1 + (\epsilon_0\epsilon_3 \cosh [ze(\phi_F - \phi_S)/2kT])^{-1}(1 + (n^2F^2\Gamma_T/RTC_1)f(1-f))$$

Evaluating the diffuse layer capacitance at its minimum value (i.e., at $\phi_F = \phi_S$) and $\partial\sigma_{\text{PET}}/\partial\sigma_M$ at its maximum value (which occurs when the film is half-oxidized, i.e. $f = 1/2$) yields

$$C_T^{-1} = 28.3 + 0.439(1 + 26.5) \text{ m}^2 \text{ F}^{-1}$$

In itself, the term resulting from the diffuse layer capacitance ($C_{\text{dif}}^{-1} = 0.439$) is insignificant relative to the term from the film capacitance ($C_1^{-1} = 28.3$), but since $(1 + \partial\sigma_{\text{PET}}/\partial\sigma_M)$ is large near $f = 1/2$, the diffuse layer capacitance significantly affects the total interfacial capacitance. Furthermore, even if it is assumed that the diffuse layer capacitance is constant (see, for example, the analysis in ref 15), it is clear from the preceding example and eq 21 that the total interfacial capacitance will vary with potential, with the largest variation occurring near potentials corresponding to $f = 1/2$ (i.e., near the voltammetric peak). Since the charging current is directly proportional to the total interfacial capacitance (eq 15), the voltammetric charging current may not be constant (as is generally assumed). The variation of this "baseline" current near the voltammetric peak potential will be discussed later with the numerical results. The effect that the variation of C_{dif} has on the voltammetric wave shape is further discussed in the Appendix.

In addition to the charging current, electrons will flow between the electrode and the redox centers to maintain the chemical equilibrium dictated by eq 5. This faradaic current is computed in terms of the rate of change of the oxidized or reduced species as¹

$$i_f/nFA = \partial\Gamma_O(t)/\partial t = -\partial\Gamma_R(t)/\partial t = \Gamma_T \partial f/\partial t \quad (22)$$

Differentiating eq 11 with respect to time, solving for $\partial f/\partial t$, multiplying by Γ_T , and using the equalities $\partial\phi_M/\partial t = \partial E/\partial t = \nu$ and $\partial\phi_{\text{PET}}/\partial t = (\partial\phi_{\text{PET}}/\partial E)(\partial E/\partial t)$, yields the following relationship between the faradaic current and the oxidation state of the film:

$$i_f = (n^2F^2/RT)\nu\Gamma_T f(1-f)(1 - \partial\phi_{\text{PET}}/\partial E) = (n^2F^2/RT)\nu\Gamma_T f(1-f)C_T/C_1 \quad (23)$$

where the equivalence of $(1 - \partial\phi_{\text{PET}}/\partial E)$ and C_T/C_1 is derived from eq 18a.

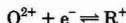
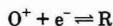
Substituting eqs 15 and 23 into eq 14 and using the definition of eq 20 yields the reversible voltammetric response

(both faradaic and charging currents) for an irreversibly adsorbed redox species

$$i_c = \nu A (1 + \partial \sigma_{PET} / \partial \sigma_M) C_T \quad (24)$$

where the potential-dependent quantities, C_T and $\partial \sigma_{PET} / \partial \sigma_M$, are given by eqs 20 and 21. The voltammetric current, i_c , can be specified by the following independent parameters: z , ($E^0 - E_{PZC}$), and $\epsilon_0 \epsilon_3 / d_2$ (when $d_2 \neq 0$); the two dimensionless groups $F^2 \Gamma_T / \epsilon_0 \epsilon_3 kRT$ and $\epsilon_1 / \epsilon_3 d_1 k$; and the usual voltammetric variables: z_0 , z_R , T , Γ_T , ν , and A .

IV. Computational Results. In this section, we examine the voltammetric behavior of the two redox systems



Since electron-transfer reversibility is assumed, cathodic and anodic currents are the mirror image of each other. Only anodic currents (positive ν) will be shown in the figures. All currents are normalized to $(F^2 \Gamma_T / RT) \nu A \Gamma_T$, and both E and E^0 are referenced to E_{PZC} .

As alluded to earlier, the interfacial capacitance of the film, C_T , is not constant as is usually assumed in analyzing experimental data, so the charging current (eq 15) varies as a function of the film oxidation state.¹⁶ Often, background subtraction is used to remove the charging current from the total voltammetric current. There are situations, however, corresponding to reasonable values for system parameters, where the charging current displays a pronounced minimum at potentials near the peak potential, and a simple background subtraction of the charging current would lead to a large underestimation of the redox activity of the film. In all the voltammograms, both the total current (eq 24) and the charging current (eq 15) are plotted to show when a simple background subtraction is and is not warranted.

All results presented in the figures and in the text were calculated using $T = 298$ K and $z = 1$ (corresponding to a 1:1 electrolyte).

Results for $d_2 = 0$. Figure 3 shows the voltammetric behavior for the $O^+ + e^- \rightleftharpoons R$ system as a function of E^0 , $\epsilon_1 / \epsilon_3 d_1 k$, and $F^2 \Gamma_T / \epsilon_0 \epsilon_3 kRT$. Voltammograms and charging currents are plotted for $0.01 \leq \epsilon_1 / \epsilon_3 d_1 k \leq 10$ and $1 \leq F^2 \Gamma_T / \epsilon_0 \epsilon_3 kRT \leq 10$, which include, but are not limited to, combinations of the following ranges of physical parameters: $5 \leq \epsilon_1 \leq 20$, $0.5 \leq d_1 \leq 2$ nm, $20 \leq \epsilon_3 \leq 80$, $0.1 \leq c \leq 1$ M (c is the supporting electrolyte concentration), and $0.1 \leq \Gamma_T \leq 10 \times 10^{-10}$ mol cm⁻². In examining the results, it is useful to have a specific reference set of physical parameters in mind that correspond to the dimensionless groups. For this purpose, $\Gamma_T = 0.61 \times 10^{-10}$ mol cm⁻², $\epsilon_1 = 5$; $d_1 = 2$ nm; $\epsilon_3 = 78$; and $c = 1$ M correspond to $\epsilon_1 / \epsilon_3 d_1 k = 0.01$ and $F^2 \Gamma_T / \epsilon_0 \epsilon_3 kRT = 1.0$.

The voltammograms are arranged in the following way. Columns correspond to values of $E^0 = \pm 0.2$ V vs E_{PZC} , while the rows correspond to different values of $\epsilon_1 / \epsilon_3 d_1 k$. For given E^0 and $\epsilon_1 / \epsilon_3 d_1 k$, a set of voltammograms are presented that are a function of $F^2 \Gamma_T / \epsilon_0 \epsilon_3 kRT$.

The effect of the four experimental variables (E^0 , Γ_T , ϵ_1 / d_1 , or ϵ_3) on the voltammetric response can be deduced from Figure 3. For example, to examine the effect of changing Γ_T , compare voltammograms within a given family of curves. To examine the effect of changing ϵ_3 , which is proportional to $(\epsilon_3 k)^2$, compare voltammograms for which the parameters $\epsilon_1 / \epsilon_3 d_1 k$ and $F^2 \Gamma_T / \epsilon_0 \epsilon_3 kRT$ change by the same factor, e.g., to see the effect of decreasing ϵ_3 by a factor of 100, compare $F^2 \Gamma_T /$

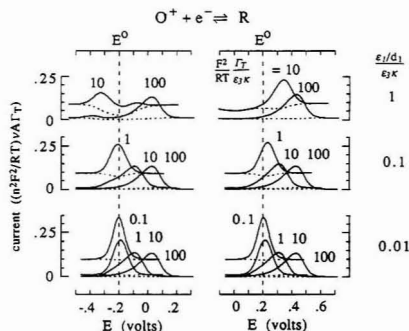


Figure 3. Voltammetric behavior for an electroactive film ($d_2 = 0$) which undergoes the reaction $O^+ + e^- \rightleftharpoons R$. The six sets of voltammograms are arranged in two columns and three rows. The columns correspond to values of $E^0 = \pm 0.2$ V (indicated by the vertical dashed lines). The rows correspond to values of $\epsilon_1 / \epsilon_3 d_1 k$. Voltammograms within each set (for a given E^0 and $\epsilon_1 / \epsilon_3 d_1 k$) are plotted as a function of $F^2 \Gamma_T / \epsilon_0 \epsilon_3 kRT$. The solid lines (—) correspond to the total voltammetric current (both faradaic and charging components) calculated from eq 25. The dashed lines (---) correspond to the charging current (eq 15). Both E and E^0 are reported with respect to E_{PZC} . Values of $T = 298$ K and $z = 1$ were used for each voltammogram.

$\epsilon_0 \epsilon_3 kRT = 0.1$, $\epsilon_1 / \epsilon_3 d_1 k = 0.01$ with $F^2 \Gamma_T / \epsilon_0 \epsilon_3 kRT = 1$, $\epsilon_1 / \epsilon_3 d_1 k = 0.1$. Figure 3 cannot be used to determine the dependence of the voltammograms on the independent variables T or z .

The O^+ / R electroactive film exists in an essentially uncharged state when $E \ll E^0$ or in a charged state when $E \gg E^0$. The maximum charge density at the PET is FT_T . For small values of both $F^2 \Gamma_T / \epsilon_0 \epsilon_3 kRT$ and $\epsilon_1 / \epsilon_3 d_1 k$ (bottom row of Figure 3) the faradaic component of the voltammetric wave approaches that expected in the absence of interfacial potential effects. As either $F^2 \Gamma_T / \epsilon_0 \epsilon_3 kRT$ or $\epsilon_1 / \epsilon_3 d_1 k$ increases, the maximum current decreases, the wave shifts toward more positive potentials, and the peak broadens and becomes more asymmetric. For instance, for the above mentioned set reference parameters ($\epsilon_1 / \epsilon_3 d_1 k = 0.01$; $F^2 \Gamma_T / \epsilon_0 \epsilon_3 kRT = 1$), the faradaic peak current is ca. 20% less than that predicted by assuming that $\phi_{PET} = \phi_s$, the peak width is correspondingly wider, and the peak position is shifted slightly positive of E^0 by ca. 15 mV for both positive and negative values of E^0 . These effects may result from increasing the surface coverage, decreasing the electrolyte concentration, increasing ϵ_1 / d_1 , or using a solvent with a lower dielectric constant.

A physical interpretation for the origin of the nonideal voltammetric shapes can be obtained by examining the potential distribution across an electroactive film as a function of the applied potential. In Figure 4, a representative example of the interfacial potential distribution is shown. While most of the potential drop occurs within the film, there is a small drop in the solution phase (i.e., $\phi_{PET} \neq \phi_s$). For the particular case shown in Figure 4, the potential at the film/electrolyte interface ϕ_{PET} increases by ca. 40 mV between the reduced and oxidized state. Figure 5 shows the continuous variation of the potentials at the metal electrode surface and the PET as a function of the applied electrode potential (vs E_{PZC} of the uncoated electrode). As the film is oxidized, the potential drop in the solution phase ($\phi_{PET} - \phi_s$) increases, reducing the driving force for electron transfer defined by eq 5. At potentials near E^0 , $\partial \sigma_{PET} / \partial E$ is large as a consequence of the change in the charge density at the PET, resulting in the asymmetric, drawn out shape of the voltammetric wave.

Several of the voltammograms in Figure 3 have background currents which vary significantly near the peak current. In these cases (e.g., $F^2 \Gamma_T / \epsilon_0 \epsilon_3 kRT = 1$, $\epsilon_1 / \epsilon_3 d_1 k = 0.1$), surface coverages calculated from the area under the linear back-

(16) Although this variation in the charging current results from faradaic chemistry, C_T is a true interfacial capacitance that can be calculated at all potentials from eq 21, not a "pseudocapacitance" associated with the instantaneous flow of faradaic current.

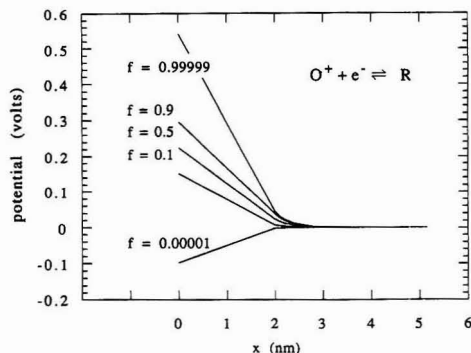


Figure 4. Interfacial potential profile as a function of the oxidation state, $f = \Gamma_{O^+}/\Gamma_T$, for an electroactive film ($d_2 = 0$) which undergoes the reaction, $O^+ + e^- \rightleftharpoons R$. The parameters used for the calculation were $\epsilon_1/\epsilon_3 d_1 \kappa = 0.019$; $F^2 \Gamma_T / e_0 \epsilon_3 \kappa RT = 1.6$; $E^0 = 0.2$ V vs E_{PZC} (corresponding to, for example, $\epsilon_3 = 80$, $c = 1$ M, $d_1 = 2$ nm, $\epsilon_1 = 10$, $\Gamma_T = 10^{-10}$ mol cm^{-2}). The potentials are reported with respect to E_{PZC} .

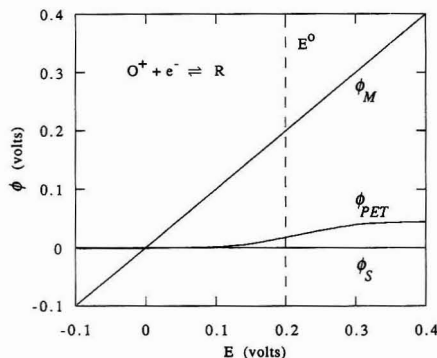


Figure 5. Plot of the electrostatic potentials ϕ_M , ϕ_{PET} , and ϕ_S (vs ϕ_S) as a function of the applied electrode potential E (vs E_{PZC}) for the data in Figure 4.

ground-subtracted current would be too small. If either of the following two conditions is met, the background current may be successfully subtracted from the total current: (i) the charging current is insignificant compared to the faradaic current, or (ii) the charging current is relatively constant during the oxidation of the film. The first condition is met when $i_f/i_c \gg 1$. Taking the ratio of eqs 15 and 23 and using $f = 1/2$ yields $i_f/i_c = n^2 F^2 \Gamma_T d_1 / e_0 \epsilon_1 4 RT$ (which is also the ratio of the dimensionless parameters used in Figure 3, divided by 4). Thus, the faradaic current becomes less significant, relative to the charging current, as the film capacitance ($C_1 = e_0 \epsilon_1 / d_1$) increases. The second condition is met when the total interfacial capacitance (C_T , eq 21) is relatively independent of the electrode potential. For $d_2 = 0$, this condition requires that $C_1^{-1} \gg C_{diff}^{-1} (1 + \partial \sigma_{PET} / \partial \sigma_M)$ which, using the smallest value of C_{diff} and the largest value of $\partial \sigma_{PET} / \partial \sigma_M$, yields the condition that $F^2 \Gamma_T / e_0 \epsilon_3 \kappa RT \ll 1$ and $\epsilon_1 / \epsilon_3 d_1 \kappa \ll 1$, i.e., both of the dimensionless variables used in Figure 3 are small.

Shifts in the apparent E^0 for a reversible electroactive monolayer have been observed by Chidsey et al.³ in their studies of mixed monolayers composed of ω -((ferrocenylcarbonyl)oxy)alkanethiol (an O^+/R redox couple) and n -alkanethiols. In their experiments, the electroinactive n -alkanethiols act as spacers between the ω -((ferrocenylcarbonyl)oxy)alkanethiol molecules, reducing interactions between ferrocene groups. The experimental parameters

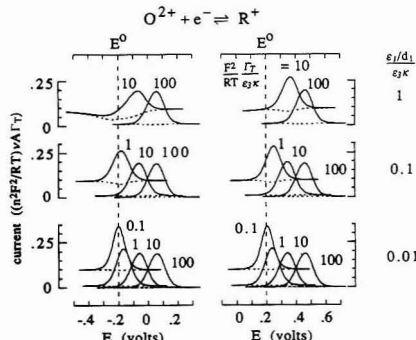


Figure 6. Voltammograms for an electroactive film ($d_2 = 0$) which undergoes the reaction, $O^{2+} + e^- \rightleftharpoons R^+$. The six sets of voltammograms are arranged in two columns and three rows. The columns correspond to values of $E^0 = \pm 0.2$ V (indicated by the vertical dashed lines). The rows correspond to values of $\epsilon_1/\epsilon_3 d_1 \kappa$. Voltammograms within each set (for a given E^0 and $\epsilon_1/\epsilon_3 d_1 \kappa$) are plotted as a function of $F^2 \Gamma_T / e_0 \epsilon_3 \kappa RT$. The solid lines (—) correspond to the total voltammetric current (both faradaic and charging components) calculated from eq 25. The dashed lines (---) correspond to the charging current (eq 15). Both E and E^0 are reported with respect to E_{PZC} . Values of $T = 298$ K and $z = 1$ were used for each voltammogram.

reported by Chidsey et al. ($\Gamma_T = (0.8-5) \times 10^{-10}$ mol cm^{-2} , $\epsilon_1 \approx 7$, $d_1 \approx 2.2$ nm, $[HClO_4] = 1$ M, $\epsilon_3 = 78$, yielding $\epsilon_1/\epsilon_3 d_1 \kappa \approx 0.01$ and $F^2 \Gamma_T / e_0 \epsilon_3 \kappa RT \approx 1-10$) correspond to the set of voltammograms in the lower right corner of Figure 3. For $F^2 \Gamma_T / e_0 \epsilon_3 \kappa RT \approx 1-10$, our results predict that the voltammetric wave should have a nearly ideal shape at low coverages ($\Gamma_T < 1 \times 10^{-10}$ mol cm^{-2}) and be centered at E^0 , be broadened and shifted to potentials slightly positive of E^0 at intermediate surface coverages ($\Gamma_T \approx 3 \times 10^{-10}$ mol cm^{-2}), and develop a shoulder and shift positive of E^0 by ca. 0.1 V at high surface coverages ($\Gamma_T \approx 6 \times 10^{-10}$ mol cm^{-2}). These behaviors are in semiquantitative agreement with the experimental results, although the shoulder predicted at high surface coverages is less pronounced than observed in the experiment. Note that the results in Figure 3 indicate that the voltammograms for $\epsilon_1/\epsilon_3 d_1 \kappa \approx 0.01$ are essentially independent of E^0 . Thus, the above comparison with experimental data does not require a precise knowledge of E_{PZC} .

It is possible to see two current peaks in the voltammogram for the O^+/R couple when $\epsilon_1/\epsilon_3 d_1 \kappa \approx 1$, $F^2 \Gamma_T / e_0 \epsilon_3 \kappa RT \approx 10$, and $E^0 = -0.2$ V (e.g., $\Gamma_T = 1.4 \times 10^{-10}$ mol cm^{-2} , $\epsilon_1 = 20$, $d_1 = 0.34$ nm, $\epsilon_3 = 78$, $c = 0.1$ M). The voltammetric peaks occur at positive and negative potentials of E^0 and have relative magnitudes that depend on the value of $F^2 \Gamma_T / e_0 \epsilon_3 \kappa RT$. At $F^2 \Gamma_T / e_0 \epsilon_3 \kappa RT = 10$, the voltammetric peak at $E < E^0$ is greater than the peak at $E > E^0$; when $F^2 \Gamma_T / e_0 \epsilon_3 \kappa RT = 100$, the more negative peak has nearly disappeared. In the results we have examined, this is the only system and value of E^0 and $\epsilon_1/\epsilon_3 d_1 \kappa$ that exhibits twin peaks, although a shoulder on the wave can be seen for many of the voltammograms in Figure 3. There is also a minimum in the voltammetric current near $E = 0$ for $\epsilon_1/\epsilon_3 d_1 \kappa = 1$, $F^2 \Gamma_T / e_0 \epsilon_3 \kappa RT = 10$, $E^0 = 0.2$ V, but this results from a minimum in the diffuse layer capacitance, not a minimum between faradaic peaks. We were unable to obtain an analytical criterion to predict when double peaks will appear, but we are able to say that they are not predicted if one erroneously uses a potential-independent diffuse layer capacitance (Appendix).

Figure 6 shows the voltammetric behavior for the $O^{2+} + e^- \rightleftharpoons R^+$ system. The O^{2+}/R^+ electroactive film always exists in a charged state. When $E \ll E^0$ the charge density at PET is $F \Gamma_T$, and when $E \gg E^0$ the charge density is $2F \Gamma_T$. The voltammetric behavior of this system is similar to that of the

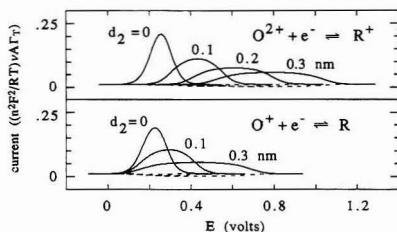


Figure 7. Voltammetric response of electroactive films (top, $O^{2+} + e^- \rightleftharpoons R^+$; bottom, $O^+ + e^- \rightleftharpoons R$) in which the redox center is embedded between two dielectric films (Figure 1B). The redox center is positioned at a distance d_2 from the end of a 2-nm-thick film (i.e., $d_1 + d_2 = 2$ nm). The solid lines (—) correspond to the total voltammetric current (both faradaic and charging components) calculated from eq 24. The dashed lines (---) correspond to the charging current (eq 15). $\epsilon_1 = \epsilon_2 = 10$; $\epsilon_3 = 80$; $c = 1$ M; $E^0 = 0.2$ V; $\Gamma_T = 10^{-10}$ mol cm^{-2} . Both E and E^0 are reported with respect to E_{PZC} . Values of $T = 298$ K and $z = 1$ were used for each voltammogram.

O^+/R system except that the peaks are more symmetric because the relative change in the charge density at the PET upon oxidation is smaller. The double peaked voltammogram in Figure 3 ($\epsilon_1/\epsilon_3 d_{1K} = 1$, $F^2 \Gamma_T / e_0 \epsilon_3 kRT = 10$, $E^0 = -0.2$ V) and the diffuse layer minimum in Figure 3 ($\epsilon_1/\epsilon_3 d_{1K} = 1$, $F^2 \Gamma_T / e_0 \epsilon_3 kRT = 10$, $E^0 = 0.2$ V, near $E = 0$) are no longer visible in this system because the magnitude of the charge density at the PET when $f = 1/2$ is approximately 3 times greater than for the O^+/R couple. (Recall that for the O^+/R couple the average charge per molecule at $f = 1/2$ is $1/2$, while in the O^{2+}/R^+ system the average charge is $3/2$.) The potential profile and the variation of potentials with the electrode potential for this system (not shown) are qualitatively similar to those shown for the O^+/R couple in Figures 4 and 5, respectively.

Acevedo and Abruña have studied the reversible, one-electron oxidation of $[Os(bpy)_2(dipy)Cl]^+$ (an O^{2+}/R^+ couple where $bpy = 2,2'$ -bipyridine and $dipy = 4,4'$ -trimethylenedipyridine) as a function of the dielectric constant of the electrolyte solvent (ranging from 8 to 78) and the surface coverage of the electroactive molecule (range $(0.1-1.1) \times 10^{-10}$ mol cm^{-2}).⁷ Except in very low dielectric solvents in which ion-pairing is suspected, the voltammetric peak position, E_p (and, thus, the apparent E^0), shifts to positive potentials as the surface concentration of adsorbate increases. Using the variation of E_p with Γ_T and extrapolating back to $\Gamma_T = 0$ (where they postulate that ion pairing is least important), they show that E_p shifts to more negative potentials in solvents with larger dielectric constants. These findings are in good accordance with the model presented here.

Results for $d_2 \neq 0$. The voltammetric response of electroactive films in which the redox center (i.e., the PET) is positioned between two dielectric regions of the molecule is shown in Figure 7 for both the O^+/R and the O^{2+}/R^+ couples (corresponding to the schematic in Figure 1B). Voltammograms are shown for films of constant total thickness ($d_1 + d_2 = 2$ nm) as a function of the distance between the PET and the film/solution interface (other parameters are stated in the figure caption). The effect of the outer dielectric region of the molecule on the voltammetric behavior is dramatic, shifting the potential of the peak current from E^0 by 600 mV (for the O^{2+}/R^+ couple) when $d_2 = 0.3$ nm. For comparable values of d_1 and d_2 ($d_1 \approx d_2 \approx 1.0$ nm), the voltammetric waves are broadened and shifted to the extent that they are no longer recognizable as such.

The interfacial potential distribution across the electroactive film comprised of the O^+/R couple with $d_1 = 1.7$ nm, $d_2 = 0.3$ nm is shown in Figure 8 as a function of the oxidation state. In contrast to the potential profile when $d_2 = 0$ (Figure 4), a large increase in ϕ_{PET} occurs as the film passes from the

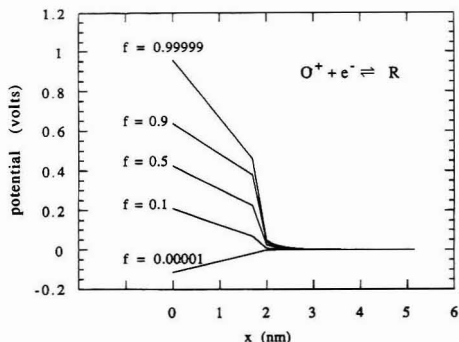


Figure 8. Interfacial potential profile as a function of the oxidation state, $f = \Gamma_O/\Gamma_T$, for an electroactive film ($d_1 = 1.7$ nm; $d_2 = 0.3$ nm) which undergoes the reaction, $O^+ + e^- \rightleftharpoons R$. Other parameters used are the same as in Figure 7. The potentials are reported with respect to E_{PZC} .

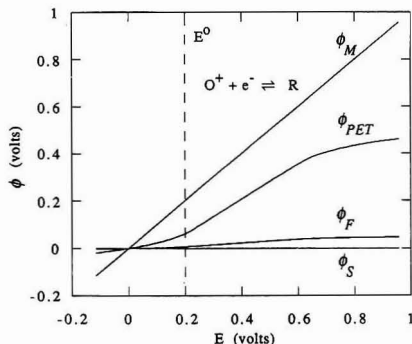


Figure 9. Plot of the electrostatic potentials ϕ_M , ϕ_{PET} , and ϕ_S (vs ϕ_S) as a function of the applied electrode potential E (vs E_{PZC}) for the data in Figure 8.

reduced to oxidized state. The dependence of ϕ_M , ϕ_{PET} , and ϕ_F on the electrode potential are shown in Figure 9, where it is evident that the variation in E near E^0 is nearly matched by an increase in ϕ_{PET} , i.e., $\partial \phi_{PET} / \partial E \rightarrow 1$. This reduces the effective electrode potential ($E - (\phi_{PET} - \phi_S)$, eq 5) and faradaic current (eq 23) near E^0 . Figure 9 also shows that most of the potential drop occurs within the film (i.e., $\phi_F \approx \phi_S$). The changes in ϕ_F in this system for $d_2 \neq 0$ are comparable to those for which $d_2 = 0$ (e.g., Figure 5).

The unusually strong dependence of the voltammetric wave shape on the thickness of the outer dielectric portion of the molecule, d_2 , challenges our assumption that electrolyte ions may be described as point charges having a closest approach of d_1 when $d_2 = 0$ (Figure 1A). In many situations, the electrolyte ions will be prevented from approaching the molecular film closer than a few tenths of a nanometer due to the finite size of the solvated ions and redox centers. Thus, even if the PET is positioned at the outer edge of the film, the film structure shown in Figure 1B may be a better approximation of the interfacial structure where d_2 is interpreted as being the closest approach of ions.

Although we are not aware of any study in which these details of the interfacial structure are known, the extreme sensitivity of the wave shape to changes in d_2 suggests that the effect of a finite distance of closest approach of the electrolyte ions could be measured by varying d_2 or by using ions of different dimensions. Rowe and Creager,² for instance,

have studied mixed monolayers comprised of ca. 30% ferrocene-*n*-hexanethiols and 70% *n*-alkanethiols. As the length of the *n*-alkanethiol exceeds the length of the ferrocene-*n*-hexanethiol, the voltammetric wave is significantly broadened and shifted toward positive potentials (ca. 200 mV). Although the authors attribute this behavior to stabilization of the ferrocene by the alkane environment, we note that the portion of this *n*-alkanethiols extending past the ferrocene redox center may exclude electrolyte ions, giving rise to behavior expected of a film with a portion of a molecule extending past the PET (Figure 1B).

The fact that voltammograms as broad as those in Figure 7 are not usually observed experimentally may indicate that ions permeate into the film to the PET. Indeed, unless counterions intervene, the electrostatic repulsion between charged species would be very large. Chidsey et al.¹⁷ have shown that ion-permeation increases as the field within an adsorbed film reaches a critical value of ca. 10^7 V/cm. This suggests that at sufficiently high fields, our model for $d_2 \neq 0$ will break down.

CONCLUSIONS

We have presented a simple electrostatic model that qualitatively explains many of the nonideal voltammetric behaviors associated with electroactive films which undergo reversible electron transfer reactions. The effect of the interfacial potential distribution is significant and should be included in analyzing the voltammetric behavior of electroactive films unless it can be reasonably assumed that the entire interfacial potential drop occurs within the adsorbed film between the electrode and the PET.

It is frequently assumed in the analyses of self-assembling monolayers that the diffuse layer capacitance, C_{diff} , is a potential-independent parameter that is large relative to the film capacitance. Our results have shown that although C_{diff} is typically much larger than the film capacitance, it is not constant, even in relatively concentrated solutions (e.g., >0.1 M). In addition, the large variation of the charge at the PET amplifies the variation of the diffuse layer capacitance near the peak potential, causing a distortion of the voltammetric wave from its normal symmetric shape. The large variation of the charge at the PET may also cause a significant minimum in the charging current near the peak potential (if $n^2 F^2 \Gamma_T d_1 / \epsilon_0 \epsilon_1 4RT$ is not much greater than 1), making the separation of the faradaic and charging components of the voltammetric current impossible, as discussed previously. In such cases, it is equally impossible to estimate the charging current near the peak potential in a separate experiment in which the redox-active film is replaced by a structurally similar, electroinactive film. The voltammetric response from the latter will obviously not display a minimum in the charging current near the peak potential since its oxidation state does not change.

Many of the concepts contained in this paper are similar to those developed by Frumkin^{1,18} in correcting kinetic rate constants of irreversible electron transfer reactions involving a soluble redox species (the " ϕ_2 -correction"), and later employed by Lane and Hubbard¹⁹ in a similar treatment of the redox kinetics of adsorbed redox species. Here, we have shown that the voltammetric response of a reversible redox couple is affected by irreversible adsorption. The results serve as a reminder that the observed response of a reversible electron-transfer process is affected by the reversibility of all preceding and following steps in the overall reaction.

Finally, our electrostatic model can be readily modified to describe the voltammetric response of redox reactions or film

structures not considered here. For instance, the voltammetric behavior of reversible electron-transfer reactions involving protons would require simple inclusion of the concentration of protons in equilibrium with the electrostatic potential at the PET. Similarly, extension of the electrostatic model to bilayer or multilayer redox films of any general configuration should be routine using the procedure outlined in Section II. These subjects will be considered in future papers.

ACKNOWLEDGMENT

We gratefully acknowledge stimulating discussions with John Norton, Stephen Feldberg, Steven Crockett, Hector Abreuña, and Allen Bard. This research was supported by the Office of Naval Research and the Department of Energy.

APPENDIX

If one assumes that the capacitance of the diffuse layer is constant, the voltammograms would appear symmetric about the peak current located at the potential corresponding to $f = 1/2$, since $E(f = 1/2) - E(f) = E(1 - f) - E(f = 1/2)$ and $i_t(f) = i_t(1 - f)$ for all f . That the peak is located at $f = 1/2$ may be determined by finding where the change in the current with respect to the potential is zero. Differentiating eq 24 with $\rho \equiv \partial \sigma_{PET} / \partial C_M$ yields

$$\partial i_t / \partial E = (\partial i_t / \partial f) (\partial f / \partial E) = (C_T \partial \rho / \partial f + (1 + \rho) \partial C_T / \partial f) (nF/RT) f(1 - f) C_T / C_1 \quad (A1)$$

where, differentiating eqs 20 and 21 (with $\partial C_{diff} / \partial f = 0$),

$$\partial \rho / \partial f = (n^2 F^2 \Gamma_T / RT C_1) (1 - 2f) \quad (A2)$$

$$\partial C_T / \partial f = -C_d^2 (C_1^{-1} + C_{diff}^{-1}) \partial \rho / \partial f \quad (A3)$$

Substituting eqs A2 and A3 into eq A1 and rearranging yields

$$\partial i_t / \partial E = (n^3 F^2 \Gamma_T / R^2 T^2 C_1) (C_T - (1 + \rho) C_{diff}^2 (C_1^{-1} + C_{diff}^{-1})) (1 - 2f) f(1 - f) C_T / C_1 \quad (A4)$$

which may be zero only when $f = 0, 1/2$, or 1, since neither C_T nor the second term in parentheses can be zero. (It may not be obvious that the second parenthetical term may never be zero, but setting it to 0 and rearranging yields the condition, $C_T^{-1} = (C_1^{-1} + C_{diff}^{-1})(1 + \rho)$ which is inconsistent with the definition of C_T in eq 21.) Only $f = 1/2$ corresponds to a maxima in the current since $f = 0$ and $f = 1$ correspond to the physically unattainable limits of $E = -\infty$ and $E = +\infty$, respectively. Thus, only a single peak in the current-voltage relationship would be calculated if one assumes that C_{diff} is constant in eq 21. Therefore, the double peaks seen for the O⁺/R system in Figure 3 at $\epsilon_1 / \epsilon_3 d_{1,K} \approx 1$, $F^2 \Gamma_T / \epsilon_0 \epsilon_3 kRT \approx 10$, and $E^\circ = -0.2$ V must result from the combined effect of the varying charge at the PET and the varying capacitance of the diffuse layer.

When the variation of C_{diff} is included in the differentiation of eq 21 to obtain eq A3, eq A4 becomes unwieldy. For this reason we are unable to present a tractable expression that can be used to predict the position of the current maximum (or maxima). By using the approximation presented above, however, it is possible to calculate potentials that are within 30 mV of the true peak positions for all voltammograms presented in this paper except for those exhibiting more than one peak (i.e., the voltammograms for the O⁺/R couple at $\epsilon_1 / \epsilon_3 d_{1,K} = 1$, $E^\circ = -0.2$ V, Figure 3). This approximate peak potential is calculated from eq 10 with values of σ_M (eq 12) and σ_{PET} (eq 13) corresponding to $f = 1/2$.

(17) Chidsey, C. E. D.; Loiacono, D. N. *Langmuir* 1990, 6, 682.

(18) Frumkin, A. F. *Z. Physik. Chem.* 1933, 164A, 121.

(19) Lane, R. F.; Hubbard, A. T. *J. Phys. Chem.* 1973, 77, 1411.

Voltammetric Sensor for Determination of Water in Liquids

Huiliang Huang and Purnendu K. Dasgupta*

Department of Chemistry and Biochemistry, Texas Tech University, Lubbock, Texas 79409-1061

Thin-film perfluorosulfonate ionomer (PFSI) sensors overcoated with cellulose triacetate, polyvinyl alcohol (PVA)-H₃PO₄, or PVA-PFSI-H₃PO₄ composite films operated in a pulsed voltammetric mode are described. With the proper choice of the protective film, attractive performance in terms of low limits of detection and good quantitative reproducibility are possible in solvents ranging in polarity from saturated hydrocarbons such as hexane, aromatic hydrocarbons such as toluene, and halogenated solvents such as dichloromethane to modestly polar solvents such as diethyl ether and higher polarity solvents such as acetone or acetonitrile. They are not satisfactory for use in very high polarity solvents, e.g., methanol, dimethylformamide (DMF), dimethyl sulfoxide (DMSO), etc. Water activity of the sample equilibrates with the sensing film between the analyzing pulses, and the accumulated water is then electrolyzed by the pulse. The response current shows more than a first-order dependence on water concentration, especially in nonpolar solvents over a large range of concentration.

In two previous papers, we have described PFSI¹ and hybrid PFSI-P₂O₅² thin film amperometric sensors for the determination of water in the gas phase. The determination of water in liquid samples is in general a more challenging task. A survey of the literature indicates that the present practice is dominated by the Karl Fischer method³ while capacitive sensors based on controlled pore aluminum oxide and silicon dioxide are being increasingly used in on-line applications.⁴ More recently Chen and Fritz⁵ have developed a spectrophotometric method capable of determining trace quantities of water based on a shift in the acid-catalyzed equilibrium involving cinnamaldehyde, methanol, water, and cinnamaldehyde dimethyl acetal. This detection method is ideally coupled to chromatography, and a variety of applications have been demonstrated.⁶

There is nevertheless a need for simple inexpensive sensors that perform reliably, especially for process applications. If the PFSI thin-film sensors described previously for gas-phase applications are directly deployed for measurement of water in liquids, limited success is achieved at best. First, physical integrity of the sensing film and electrode-film contact is adversely affected by many solvents that swell the film. Second, experience indicates that adventitious impurities are present in many real liquid samples. Some of these impurities partition into the film and eventually poison the electrodes or the sensing film through electropolymerization or redox conversion. Third, in the continuous amperometric mode used with the gas-phase sensors, the operating voltage is maintained sufficiently high such that the current is essen-

tially limited by the diffusion of water vapor into the film. Liquid-phase diffusion is slow and only limited sensitivity is attainable by this mode. Additionally, too large an applied voltage causes an unacceptably large background current in many solvents, even when essentially no water is present. Presumably, electrochemical breakdown of the solvent occurs and this results in poor detection limits for water.

The above problems can be addressed by (a) utilizing a second electrochemically stable polymer along with the PFSI, either as a protective external film or in a homogeneous mixture with the PFSI. This may serve the dual roles of a confining, swell-inhibiting element that maintains structural integrity and of a selective molecular barrier that allows water transport while inhibiting the transport of other, larger molecules. They can also be addressed by (b) operating in the pulsed voltammetric mode such that the water content of the sensing film comes to equilibrium with the water activity of the solvent in between the pulses, thus improving sensitivity. Experimental investigation of these strategies has led to a class of new sensors that can be utilized in a variety of solvents and are described in this paper.

EXPERIMENTAL SECTION

Reagents. Nafion PFSI was obtained as a 5 wt % solution (equivalent weight (EW) 1100, in a medium of 90% lower alcohols/10% water) from Aldrich Chemical Co. or as tubing from PermaPure Products (Raritan, NJ). The Dow PFSI, 1,1,2,2-tetrafluoro-2-((trifluoroethenyl)oxy)ethanesulfonic acid (EW 850), was obtained as a 2.5 wt % solution in alcohol from the Dow Chemical Co., Freeport, TX. All concentrations given in percent or ppm are compositions by weight. Platinum and rhodium wires (in diameters ranging from 25 to 200 μ m) were obtained from Aesar Inc. Stainless steel needle tubing (Type 304) and rod were obtained from Small Parts Inc. (Miami, FL).

Cellulose triacetate (CTA) was obtained as a powder from Eastman Organic Chemicals. A 1% CTA solution was made by dissolving it in glacial acetic acid or a mixture of 30:70 (v/v) ethanol:chloroform. In acetic acid solution, CTA was stable for several months; solutions in other solvents must be freshly prepared. Eastman AQ 55D was obtained as a 28% aqueous dispersion (Kodak) and was diluted with deionized water to form a 1% solution. A 1% solution of silicone rubber was made by dissolving household silicone rubber adhesive (General Electric) in either ethylene dichloride or toluene. A 1% solution of Nylon was made by dissolving monofilament fishing line (STREN, duPont) in boiling formic acid.

Poly(acrylic acid) (PAA) and PVA (100% hydrolyzed powder from poly(vinyl acetate)) were obtained from Scientific Polymer Products (Ontario, NY). A 2% PVA solution was made by dissolving it in boiling water and was then mixed 1:1 with a 2% K₂S₂O₈ solution. A mixture of 2% PVA and 4% H₃PO₄ was made by dissolving PVA in a boiling aqueous solution of H₃PO₄. A blend of 1% PVA, 1% Dow PFSI and 4% H₃PO₄ was made by dissolving 1 g of PVA in 60 mL of boiling water containing 4.7 g of 85% H₃PO₄ and adding 40 g of the 2.5% Dow PFSI solution; after cooling to room temperature, enough deionized water was added to make the total weight 100 g.

Instrumentation. A simple inexpensive dedicated voltammetric analyzer was constructed for the present sensor application. The schematic diagram of the analyzer is shown in Figure 1. Operational amplifier A₁, capacitor C₁, and the resistor R₂ constitute an integrator, with a scanning rate given by $-dV/dt$

- (1) Huang, H.; Dasgupta, P. K. *Anal. Chem.* 1990, 62, 1935-1942.
- (2) Huang, H.; Dasgupta, P. K. *Anal. Chem.* 1991, 63, 1570-1573.
- (3) Scholz, E. *Karl Fischer Titration*; Springer Verlag: Berlin, 1984.
- (4) Carr-Brion, K. *Moisture Sensors in Process Control*; Elsevier: New York, 1986.
- (5) Chen, J.; Fritz, J. S. in *Advances in Ion Chromatography*; Jandik, P., Cassidy, R. M., Eds.; Century International: Medford, MA, 1990; Vol. 2, pp 73-91.
- (6) Fritz, J. S.; Chen, J. *Am. Lab.* 1991, 23 (11), 24J-24Q.

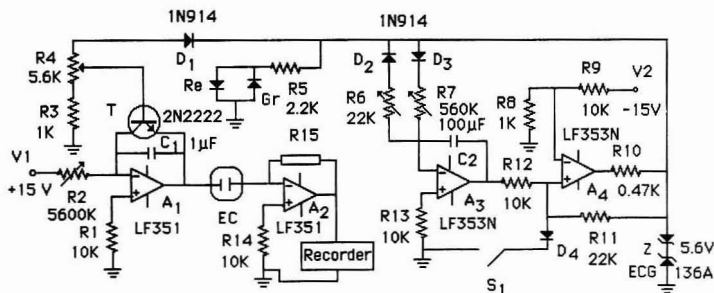


Figure 1. Schematic of the analyzer.

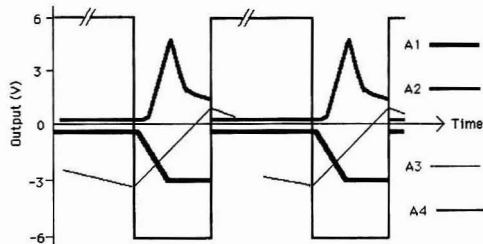


Figure 2. Output of the individual amplifiers of the instrument in Figure 1. The outputs of the individual operational amplifiers A1–A4 are indicated.

$= V_1/R_2C_1$, variable from 0.2 to 6.0 V/s by means of varying input voltage V_1 or resistance R_2 . The output of the integrator applies the desired voltage to the sensor. The sensor output is monitored by operational amplifier A2 functioning as a current \rightarrow voltage converter and is registered on a strip chart or an X–Y recorder. The output of A2 can be varied by the switch-selectable gain resistor R_{15} (0.1–200 k Ω). Operational amplifiers A3 and A4 were respectively used as triangular and square-wave generators. When A4 output reaches about +6 V (limited by the zener diode Z), the red light emitting diode (LED) Re is lit. During this time, A1 output is –0.46 V (limited by transistor T), because diode D1 is reverse biased and does not conduct. The period over which –0.46 V is applied to the sensor depends on the integrating capacitor C_2 and the resistor R_7 . At the end of this period, comparator A4 switches and this output swings to –6 V (limited by the zener diode Z) and a green LED, Gr, is illuminated. Diode D1 is now forward biased and T conducts, causing integrator A1 to begin scanning. The maximum output of A1 is limited by the base voltage of T, this can be adjusted by potentiometer R_4 . Thus a scanning voltage is applied to the sensor. The scanning time is dependent on resistor R_4 and the integrating capacitor C_2 . Together, V_2 , R_8 , and R_9 provide comparator A4 with a reference voltage. Switch S_1 provides for manual operation. When activated, a scanning voltage is applied to the sensor. When the switch is open, the operation is fully automatic and cyclic. Typically, the following preset values were used: scanning time 2 s (including the time at the applied voltage limit), scan limit –4.00 V, scan rate 3.00 V/s, initial voltage –0.46 V, and 60 s between pulses. The outputs of the individual amplifiers are depicted in Figure 2. It is important to note that the voltages cited above are the outputs of the amplifiers vs the common power supply ground and not absolute potentials in the electrochemical sense. Some experiments were conducted with sensors containing a third electrode, a chloridized silver wire, to function as a reference along with appropriately modified electronics. The signal to noise ratios were consistently poorer than those from the two electrode systems and this avenue was not further pursued.

Sensor Fabrication. A number of different sensor configurations were explored; two are described below. The first design contains a cylindrical ceramic element (6.3-mm diameter) on which two rhodium wires (200- μ m diameter, 200 mm long) are wound in parallel on precut threads without contacting each other

(center to center spacing 320 μ m). The base material for this device was obtained from EG&G Inc., Chandler Engineering Division (Tulsa, OK). A variation of the above design utilized 7-mm-diameter threaded (64 or 46 threads/in., double lead, center to center spacing 400 or 550 μ m, respectively) Nylon rods on which electrode wires (typically Pt, 25–200- μ m diameter, 250 mm long) were wound in parallel without contacting each other. The film was formed on these sensors by dip coating the polymer. After the solvent was evaporated at room temperature, the film was thermally cured at 80–120 $^{\circ}$ C for 4 h. Without the thermal curing step, the sensor behavior changed with time. Sensors with increasing film thickness were fabricated by repeating the steps of dip coating, room temperature evaporation, and heat curing.

In the second design, referred to as the coil sensor, a 0.8-mm-i.d. and 1.0-mm-o.d. Nafion tube segment (20 mm in length) was swelled in methanol and then slipped over a 0.9-mm-diameter stainless steel rod segment (7 cm in length). After thermal treatment at 120 $^{\circ}$ C, 20 cm of 200- μ m-diameter Pt wire was wound on the membrane with a turn spacing of \sim 300 μ m. The excess lengths of the platinum wire and the stainless steel rod were respectively insulated with an encapsulating Teflon tube and Teflon tape.

Test Arrangements. To determine sensor performance, the sensor was affixed to a cap which in turn was sealed to the vial containing the liquid sample. The entire assembly was enclosed in a glovebox (Dri-Lab HE 113, Vacuum Atmospheres, Los Angeles, CA). The lead wires of the sensor passed through sealed conduits to the outside of the drybox and connected to the analyzer electronics.

The moisture level in the drybox was maintained well below 100 ppm water by means of nitrogen gas circulated through a drying train by a blower integral to the drybox. The dry train was periodically regenerated by the passage of a gas mixture containing 10% hydrogen and 90% nitrogen while the train was heated.

Samples. Solvents tested as sample matrices were generally purchased in the driest grade available (typically in septum-sealed bottles packed under nitrogen and opened only inside the drybox) and in other cases were dried in-house by distilling over molecular sieves, metallic sodium or magnesium, and anhydrous K_2CO_3 , etc., following procedures outlined in reference compilations.⁷ Relatively high concentrations of water standards were prepared gravimetrically by adding known amounts of water to the dry solvents. In solvents in which water solubility is limited, saturated solutions of water in the solvent were prepared; saturated water concentrations in such solvents have been reported in the literature.⁸ Microaliquots of these high-concentration standards were added with a microliter syringe to the known amount of the sample contained within the test vial. All manipulations were conducted within the drybox. Incremental additions were made, and the data were interpreted following

(7) Perrin, D. D.; Armarego, W. L.; Perrin, D. R. *Purification of Laboratory Chemicals*, 2nd ed.; Pergamon: New York, 1990.

(8) Sorensen, J. M.; Arit, W. *Liquid-Liquid Equilibrium Data Collection. Binary Systems*; Chemistry Data Series; Deutsche Gesellschaft für Chemisches Apparatewesen: Dechema, Frankfurt, Germany, 1979; Vol. V, Part I.

standard addition procedures. It is important to note that for many of the test solvents, significant amounts of water remain in the solvent despite best efforts to dry it. Standard addition is therefore the only means to judge the true response of the sensor to water in the particular sample matrix.

RESULTS AND DISCUSSION

Estimation of Sensor Film Thickness. In the cylindrical sensors, the PFSI film is formed not only on the span of the wire electrodes (0.5 and 1 cm, respectively for the ceramic and Nylon substrate sensors), the active region of the sensor, but also above and below this region. Consequently, the mean film thickness in the active region is difficult to estimate. Based on microscopic examination, we estimate that from 70% to 80% of the applied PFSI occupies the active region. On the basis of gravimetric measurements and a polymer density⁹ of 2 g/cm³ and under the assumption of a uniform film, a sensor with three dip coatings has a ~4-μm film when coated thrice with the 2.5% solution of the Dow PFSI and a ~8-μm film when coated thrice with a 5% Nafion solution. If sensors of similar film thickness but composed of the two different PFSI materials are compared, the Dow PFSI sensors bearing the lower EW polymer show higher response. However, the latter polymer is not commercially available and Nafion can be substituted for the Dow PFSI in all the recipes given here with only a marginal loss of sensitivity at identical film thickness.

Film thicknesses of other composite films or polymer film overcoats were similarly estimated from gravimetric measurements and polymer density. Typically, a single coat of CTA, PVA-H₃PO₄, and the PVA-H₃PO₄-PFSI composite (vide infra), respectively, produced approximately 2-, 3-, and 1.5-μm-thick films.

Protective and Composite Membranes. As previously mentioned, bare PFSI sensors are generally impractical for long-term use. Even when swelling-induced loss of integrity is not a problem, intrusion of undesirable species can foul the measurement system. For example, in the early stages of these studies it was discovered that drying of acetone by molecular sieves leached some material from the desiccant that results in a slow discoloration of the PFSI film. This darkening is accompanied by a decrease in sensor sensitivity. Furthermore, a bare PFSI sensor may have a large enough response to many of the more polar test matrices to make any meaningful measurement of water impractical at low levels.

If the sensing film can be protected by a barrier that has a greater selectivity for water transport, the detection limit for water can be effectively improved. The absolute current levels in the PFSI sensors operated in the pulsed voltammetric mode are relatively large; consequently, the absolute sensitivity can be substantially sacrificed if the discrimination against the matrix can be increased.

However, an acceptable compromise between overall transport efficiency and transport selectivity is not obtained with any arbitrarily chosen barrier layer. When an 8-μm PFSI sensor was coated by a single dip in 1% AQ 55D, the decrease in response was acceptable (~40% of original) but it provided little protection against transport of the matrix solvent. At the other extreme, if coated with 28% AQ 55D solutions, the matrix transport was inhibited but the sensor essentially lost its response to the analyte as well. Barrier layers of silicone rubber and Nylon were largely unusable for similar reasons. PVA or PVA-PAA layers cured by initiating cross-linking with UV irradiation of the persulfate-containing solutions produced the only overcoats among the above to resist swelling by high polarity solvents like methanol, DMF, or DMSO.

Unfortunately, it also reduced the response of the underlying PFSI film to water by a factor of 1000. Thinner films of such material may be more useful. Nonetheless, an appropriate overcoat on the PFSI or a composite sensing film does produce attractive sensors; these are described below in more detail.

Cellulose Acetate Protective Film. It is well recognized that CTA films can be subjected to controlled hydrolysis to govern the effective size cutoff of molecules that permeates the film.^{10,11} Wang and Tuzhi¹² have shown that determinations of small analyte molecules in complex matrices with Nafion-coated electrodes are simplified by an overcoat of a hydrolyzed CTA film. Our experience indicates that unhydrolyzed CTA films are the best for discriminating against the relatively small solvent molecules of major concern to us. Barrier layers of CTA over PFSI have been found to be particularly well suited for use in polar solvents such as acetone, acetonitrile, and diethyl ether and nonpolar solvents such as toluene. We have also found that CTA films formed from ethylene dichloride or chloroform solutions swell easily and lose integrity in a variety of organic solvents. When formed from the solutions prescribed in the experimental section and cured for 2–4 h at 80–90 °C, the CTA films formed are vitreous and resist solvent-induced swelling. If cured at 120 °C for 2–4 h, the film becomes dark brown and is accompanied by a further increase in swelling resistance and discrimination against solvent transport, albeit at the expense of sensor sensitivity. For either cure protocol, two dip-cure cycles are recommended for use in polar solvents such as acetonitrile or acetone that exhibit large background current levels with a bare PFSI sensor. The sensors cured at higher temperature are profitably used in acetone and acetonitrile while those cured at lower temperature are well suited for lower polarity solvents, e.g., diethyl ether, toluene, etc. CTA-overcoated sensors cannot be used in halogenated organic solvents, DMF and DMSO; these solvents destroy the film.

PVA-H₃PO₄ Film. An electrically conductive water-soluble complex of PVA and H₃PO₄ was reported by Polak et al.¹³ Oxygenated anions with multiple -OH functionalities such as borate or silicate rapidly cross-link PVA; pedagogic demonstrations based on these reactions are widely used.^{14–17} We have found that if PVA is dissolved in boiling dilute H₃PO₄ and such a solution is used to form a barrier layer by dip coating, followed by curing at 80–90 °C, such a film is not only insoluble in DMF or DMSO, it is unaffected by boiling methanol or water. Equilibration of such a film with the water activity of the surrounding medium is slow, however; films thicker than 5 μm require ≥10 min to reflect the sample water content. Films of ~3-μm thickness produce response times acceptable for most applications—approach to equilibrium with different barrier layers/sensing films is illustrated in Figure 3. Response time also appears to depend on the tested solvent and is generally somewhat larger in less polar solvents.

The PVA-H₃PO₄ overcoating is the only protective membrane that fully resists dissolution and excessive swelling by highly polar solvents such as methanol, DMF, DMSO, etc. However, even for this film, the response signal ratio to water relative to DMF, DMSO or methanol is <100 and measurement of water below the percent level is impractical. The

(10) Wang, J.; Hutchins, L. D. *Anal. Chem.* 1985, 57, 1536–1541.

(11) Wang, J.; Hutchins-Kumar, L. D. *Anal. Chem.* 1986, 58, 402–407.

(12) Wang, J.; Tuzhi, P. *Anal. Chem.* 1986, 58, 3257–3261.

(13) Polak, A.; Petty-Weeks, S.; Beulher, A. J. *Chem. Eng. News* 1989, 63 (48), 28.

(14) Casassa, E. Z.; Sarquis, A. M.; Van Dyke, C. H. *J. Chem. Ed.* 1986, 63, 57–60.

(15) Sarquis, A. M. *J. Chem. Ed.* 1986, 63, 60–61.

(16) Sarquis, M. *Instructor* 1985, No. 10, 142.

(17) Burke, B. A.; Haworth, D. T.; Raab, M. F. *J. Chem. Ed.* 1988, 65, 895.

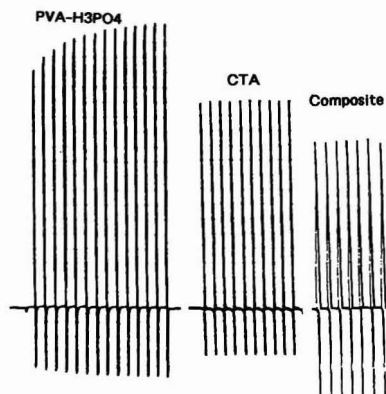


Figure 3. Speed of sensor response to water in acetonitrile with different overcoats: (a) PVA- H_3PO_4 , (b) CTA, (c) composite film. The analyzer pulses are 60 s apart. Note the slower approach of the PVA- H_3PO_4 film to equilibrium.

discrimination against ethanol is somewhat better, and the response current is linearly related to water content in ethanol above a concentration of 2000 ppm.

PVA- H_3PO_4 -PFSI Composite Sensing Films. As indicated above, the utility of PVA- H_3PO_4 barriers are compromised by their slow equilibration. We have found that PFSI can be incorporated in the PVA- H_3PO_4 solution to form a polymer composite that resists swelling. Because the PFSI network is present throughout, only limited protection against matrix solvent penetration is afforded, however. Nevertheless, it has been found that very useful sensors are formed by (a) dip coating thrice with a 5% Nafion solution, allowing solvent to evaporate between coats, (b) coating again with a blend containing 1% PVA, 1% PFSI, and 4% H_3PO_4 , (c) thermally curing at 80–90 °C for 2–4 h, and (d) repeating steps b and c twice more. These sensors can be used in nonpolar solvents like hexane, benzene, or toluene, and halogenated solvents with dichloromethane. They withstand polar solvents such as acetone or acetonitrile, but since they offer little discrimination against the solvent matrix, they are useful in such solvents primarily for the measurement of relatively high water levels; the upper measurement limit extends to several percent water. The overall permeability of the composite polymer overcoat to water is only slightly lower than a CTA overcoat; this is illustrated in Figure 4 for the measurement of water in hexane. (The plotted ordinate value is the observed peak current less the peak current observed before the deliberate addition of water, hence designated as delta current.)

Sensor Performance, Response Behavior, and Parametric Effects. *Dependence of the Response on the Solvent Polarity.* The first step in sensor operation is the partitioning of water from the sample to the sensing film:

$$[\text{H}_2\text{O}]_{\text{film}} = K_D [\text{H}_2\text{O}]_{\text{sample}} \quad (1)$$

where K_D is a distribution constant that is dependent on the sample matrix. The value of K_D is expected to be higher for solvents with low water affinity, e.g., hexane, relative to samples of high water affinity, e.g., acetonitrile. At the same concentration, water activity is higher in low polarity solvents, resulting in correspondingly larger sensor currents. This is illustrated in Figure 5 for a 50(Pt)-400-8(N)-Comp sensor (this abbreviated designation, followed hereinafter, indicates 50- μm Pt electrodes with 400- μm spacing, an 8- μm film of

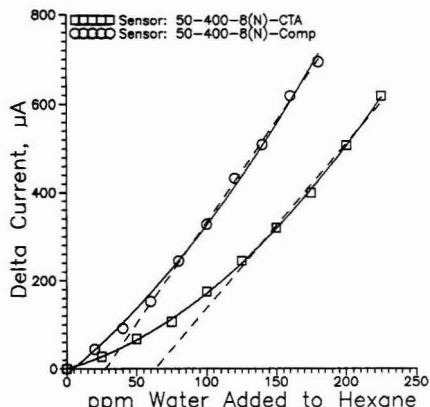


Figure 4. Response of CTA and composite film coated sensor to water added to hexane.

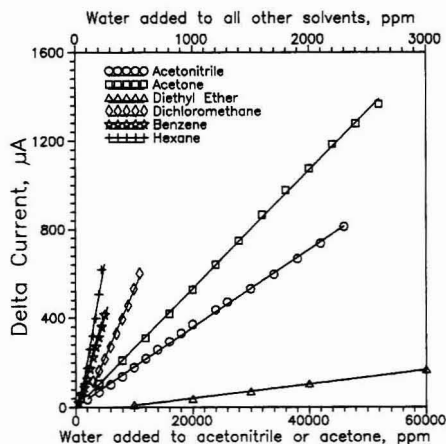
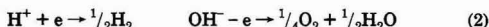


Figure 5. Response of a 50(Pt)-400-8(N)-Comp (see text) sensor to water in various solvents. Scan -0.5 to 4.0 V at 3.0 V/s.

Nafion (N, the Dow PFSI is represented by D), overcoated by the composite membrane) operated under a scanning protocol of 0.5/4.0/3.0 (scanned from -0.5 to -4.0 V at 3.0 V/s) deployed in six different solvents. The ratio of the best-fit slopes for the linear portion of the response region for acetonitrile:acetone:ether:dichloromethane:benzene:hexane in Figure 5 is 1:1.5:3.6:69:100:170.

Linearity of Response. During the application of the analyzing pulse, H^+ and OH^- formed from the dissociation of water in the film are respectively reduced at the cathode and oxidized at the anode:



The linearity of the overall current response as a function of the sample water content may depend on a number of factors. Many of these are interrelated and the contribution of individual causes cannot generally be isolated. The ohmic resistance of the sensing film itself is dependent on $[\text{H}_2\text{O}]_{\text{film}}$, and the resistance can be high in relatively dry nonpolar solvents. Consequently, the actual electrode potentials at any given applied voltage may become dependent on the sample water content in such situations. In the example shown in Figure 4, although the response over the entire

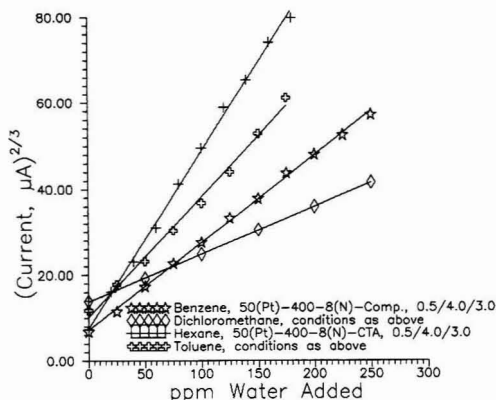


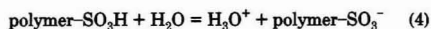
Figure 6. Relationship between $i^{2/3}$ and [water] is linear at low concentrations of water in nonpolar solvents. The inset gives sensor and scan protocols (see text). Different y intercepts indicate varying initial water content of the different samples.

concentration range shown is certainly nonlinear, it is readily apparent that a linear equation will adequately predict the response at the higher concentration end. This may be rationalized in terms of the relatively low importance of the iR drop as the solvent becomes wetter and the film becomes more conductive. An alternative and equally plausible explanation of the observed response behavior is that in eq 1, K_D is truly constant for a given solvent system only if the concentration terms written are replaced with activity terms. For nonpolar solvents, the nature of the nonlinear relationship between water concentration and water activity at least qualitatively predicts the same type of nonlinear response behavior as shown in Figure 4. The solubility of water in hexane at room temperature is ≤ 400 ppm.

In nonpolar solvents at water concentrations low enough to be substantially below saturation (where the nonlinearity of the concentration-activity relationship may not have become pronounced), we have consistently made the observation that the peak current is approximately proportional to the 1.5th power of the concentration of water. A preferred way of looking at such a response behavior is to plot $i^{2/3}$ against the added water concentration; this approach eliminates the necessity of precisely knowing the water concentration of the original "dry" solvent, and the abscissa intercept permits the estimation of the original water content of the sample, in the typical manner standard addition computations are made. Such a plot is shown in Figure 6 for four different low-polarity solvents at relatively low water concentrations. The excellent linear fits shown may not be entirely fortuitous. Consider the following: The current is likely proportional to the product of the concentration of the principal charge carrier (which is most probably H_3O^+ for apolar solvents that cannot effectively solvate the proton) and the mobility of the carrier:

$$i \propto [H_3O^+] \lambda_{H_3O^+} \quad (3)$$

where $[H_3O^+]$ and $\lambda_{H_3O^+}$ are the concentration and the mobility. If we recognize that in the highly apolar environment, the PFSI may only be weakly ionized



then

$$[H_3O^+]^2 = K[\text{polymer-SO}_3\text{H}][\text{H}_2\text{O}] \quad (5)$$

where K is the equilibrium constant for eq 4 and [polymer-

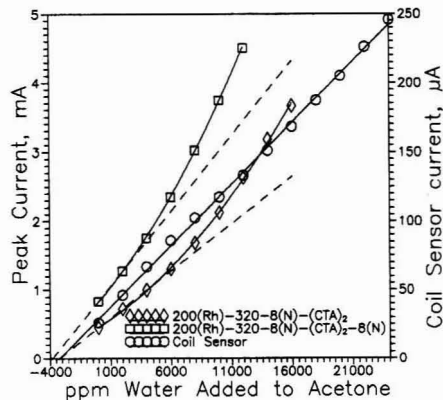


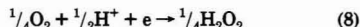
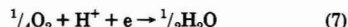
Figure 7. Response to water added to acetone for different sensors (see text). Scan protocols were 0.5/3.0/3.0 for the cylindrical sensors and 0.5/6.0/3.0 for the coil sensor.

$\text{SO}_3^-] = [\text{H}_3\text{O}^+]$. If the PFSI is in excess and the above equilibrium proceeds only weakly to the right

$$[\text{H}_3\text{O}^+] \propto [\text{H}_2\text{O}]^{0.5} \quad (6)$$

If we make the assumption that the mobility of H_3O^+ in the film is linearly related to the water content of the film, eq 3 will indeed predict that $i \propto [\text{H}_2\text{O}]^{1.5}$.

Response Linearity in Polar Solvents. Film Thickness and Interelectrode Separation. When data over a large concentration range are considered, response nonlinearity is also observed with polar solvents. This appears to be more related to the precise nature of the sensor and the scan protocol under which it is operated. The reason for this nonlinearity may have an altogether different reason from those cited above. The water formed at the anode can both diffuse back into the bulk solvent or reenter the electrolytic cycle. Similarly, if the anodically formed O_2 can diffuse to the cathode, it may be reduced to water and/or H_2O_2 ; both may reenter the electrolytic cycle:



The extent to which this happens is likely to be dependent on the thickness of the sensing film, interelectrode distance (for the fixed thread geometry of the cylindrical sensors, the interelectrode distance effectively decreases with increasing wire diameter), and the permeability of the overlaid membrane to the anodic products. These factors affect the probability of diffusion of the anodic products to the cathode relative to the bulk solvent. (Note that the uptake of the anodic products by the solvent at the solvent-sensor interface may also be influenced by the nature of the solvent, i.e., its affinity for water or O_2 . A nonlinear dependence of i on C is thus more likely with low-polarity solvents from this aspect as well).

Figure 7 shows the results for the measurement of added water to "house" acetone. Data are shown for a CTA-coated cylindrical sensor with an 8- μm Nafion film and after coating again with 7-8- μm Nafion, and for a coil type sensor. Quadratic fits are shown as the solid lines, while dashed lines are extrapolated linearly from the lower portion of each response curve to determine the water content of the original sample. Within limits of experimental error and

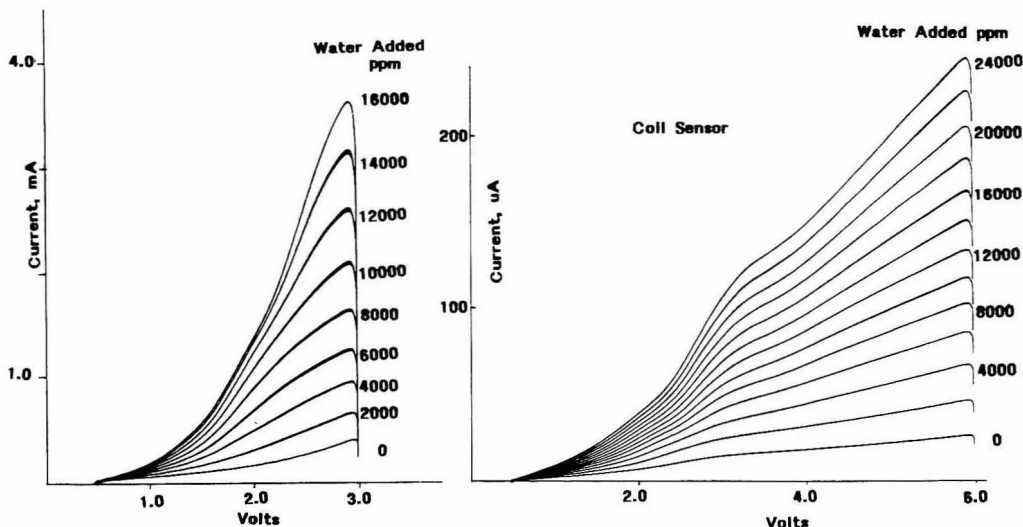


Figure 8. Voltammograms for the data shown in Figure 7.

sample-to-sample variation, essentially the same water content of the original sample is predicted; this validates the applicability of linear extrapolation over a small range.

It is notable that in the same water concentration range, the coil sensor (with no protective membranes and the anode in direct contact with the sample) displays very good linearity ($r = 0.9994$), even though a higher scan limit was used for this experiment and this would normally tend to induce greater response nonlinearity (vide infra). Figure 8 shows the voltammograms for (a) the 8- μm film cylindrical sensor and (b) the coil sensor; the nonlinear i - C response of the first device is very clearly seen.

The thickness of the film in the cylindrical sensors is an important factor. In acetone, a 200(Rh)-320-4(D)-(CTA, 105 °C, 2h)₂ sensor exhibited a linear response ($r = 0.9991$ – 0.9995) up to 9000 ppm added water under a variety of experimental conditions—initial water contents ranging from <300 ppm (dried with 4-Å molecular sieves) to ~1700 ppm and varied scan rates (0.5–4.0 V/s). Nonetheless, the same thin sensing film cannot produce a linear response in a low-polarity solvent like toluene (linear $r < 0.975$).

Nonlinear behavior is thus predictably more commonly observed with larger wire electrodes. Although the absolute level of the response current decreases substantially, more linear sensors result with thinner electrodes. Fabrication is difficult, however, with the very fragile 25- μm wires; we have chosen to perform most of our work therefore with 50- μm -diameter electrodes and these are recommended.

Influence of the Scan Conditions. The scan protocol can influence both the magnitude and the linearity of response. At least in polar solvents, where a thin film sensor, e.g., 200(Rh)-320-4(D)-(CTA, 105 °C, 2h)₂, exhibits linear response to water, the linearity is unaffected by changes in the scan rate. Further, in such solvents the peak current is proportional to the square root of the scan rate over a large range of water concentrations. The peak current from the above sensor was linearly related ($r = 0.9997$ – 0.9998) to (scan rate)^{1/2} over scan rates 0.2–6.0 V/s at water levels <300 to several thousand ppm in acetone. Extending the scan limit increases the peak current, as shown in Figure 9 for a 50-400-6(N)-PVA/H₃PO₄ sensor in acetonitrile. As long as the scan limit is sufficiently high, the initial water content predicted by linear extrapo-

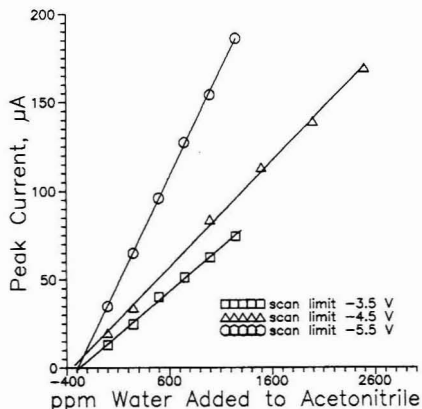


Figure 9. Effect of scan limits, 50-400-6(N)-PVA/H₃PO₄ sensor.

lation also remains independent of the scan rate, as Figure 9 indicates. The i - C response of a sensor can become more linear with a decrease in the scan limit, whether due to lower iR drops or less electrolytic product formation. The nonlinear behavior of the sensor 200(Rh)-320-8(N)-(CTA)₂ (see Figure 7) is significantly changed when the scan limit is reduced to -2.4 V; the linearity of response up to 12 000 ppm added water is excellent ($r = 0.9995$). Attempting to obtain linear response simply by reducing the scan limit is fraught with peril, however; the overall signal decreases, and the contribution of the charging current (which we have thus far neglected) becomes large enough such that the water content of the original sample is seriously overestimated by the standard addition approach.

In our judgment, it is not especially productive to try to obtain a linear sensor response over a large range of water concentration. Over a small range, i.e., with small amounts of water added to perform standard addition, linear extrapolation to determine the initial water content is acceptable and the response curve over a large range is always well predicted by a quadratic response equation. In over 50

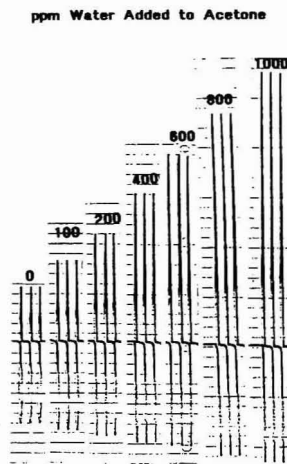


Figure 10. Reproducibility of successive measurements in acetone. Sensor 200(Rh)-320(D)-CTA, scan protocol 0.5/4.0/4.0. The peaks are 60 s apart, and the peak current is 0.3 mA at the highest concentration.

Table I. Detection Limits and Applicable Range

solvent	sensor overcoat	ppm water	
		studied range	LOD
acetone	CTA	100–20 000	3
acetone	composite	1000–52 000	50 ^a
acetonitrile	CTA	100–20 000	5
acetonitrile	composite	1000–85 000	100 ^a
acetonitrile	PVA-H ₃ PO ₄	70–2500	<1
diethyl ether	CTA	100–4000	9
diethyl ether	composite	200–9000	30 ^a
toluene	CTA	20–400	2
toluene	composite	20–500	3
hexane	composite	20–250	5 ^a
dichloromethane	composite	25–600	3
benzene	composite	20–500	2

^a Lower LOD's may be possible. The cited values are largely limited by the water content of the original sample.

experiments in 7 different solvents with more than 25 individual sensors of different types and a variety of experimental conditions, a second degree equation always satisfactorily described the response behavior (quadratic $r = 0.9993$ – 1.0000 , mean 0.9998). For nonpolar solvents at low levels of water, the preferred ordinate plotted is $i^{2/3}$.

Reproducibility and Detection Limits. The response reproducibility of the sensors with repeated analyzing pulses is generally excellent, especially considering the difficulty of measuring low levels of water. An example is shown in Figure 10 for acetone. Detection limits were calculated on the basis

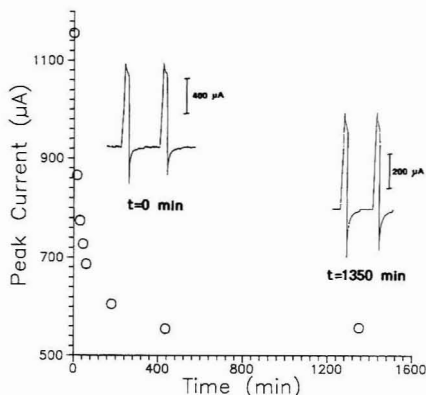


Figure 11. Monitoring the temporal profile of acetone desiccation by molecular sieves. The insets show the peak profiles at 0 and 1350 min. The designation indicates 50- μ m Pt electrodes with 400- μ m spacing and an 8- μ m film of Nafion (N, Dow PFSI is abbreviated D) overcoated by a composite membrane.

of 3 times the standard deviation of the blank and the linear slope at the low end of the water content. These are shown for different solvents and sensors in Table I. In all cases, the cited detection limits are substantially below the minimum water levels that we could experimentally attain; it is therefore especially important to point out that these detection limits are estimated from data at substantially higher concentrations.

Finally, an application of the sensor toward the desiccation of solvents, conceived and carried out at Shell Development, is shown in Figure 11. A flow-through cell was designed to accommodate the sensor and was connected to a sequential analysis injection system.¹⁸ At desired intervals, the sinusoidal pump aspirated a sample from a reservoir containing the sample under desiccation and then pushed it into the sensor cavity. The data shown are for the desiccation of acetone by molecular sieves. Measurements were made in replicate each time and resulted in relative standard deviation values ranging from 0.13 to 1.01%.

ACKNOWLEDGMENT

The cooperation and enthusiasm of Larry A. Spino and Don C. Olson (Shell Development Co., Houston, TX) and Steve Gluck (Dow Chemical, Midland, MI) are greatly appreciated. The expert machining assistance of Kevin Morris is gratefully acknowledged. This research was supported in part by EG & G Inc. (Chandler Engineering Division, Tulsa, OK) and in part by the U.S. Department of Energy, Office of Basic Energy Sciences, through Grant DE-FG05-84ER13281. However, this manuscript has not been subject to review by the DOE and no endorsement should be inferred.

RECEIVED for review May 29, 1992. Accepted July 20, 1992.

(18) Ruzicka, J.; Gübeli, T. *Anal. Chem.* 1991, 63, 1680–1685.

Use of a Laser/Photodiode Array Detector System To Study Mass Transport across Membranes

Shu-Ling Liao, Richard A. Couch,[†] and Carter L. Olson*

College of Pharmacy, The Ohio State University, Columbus, Ohio 43210

A new instrument has been developed to rapidly measure the rate of mass transport across interfaces or membranes without the need for sample extraction. This instrument utilizes a pulsed laser as the light source and a photodiode array as the detector, together with a specially designed diffusion cell to acquire spatially resolved data. Measurements are made in quiet solutions where the concentration gradients on one or both sides of an interface or a membrane are viewed by the diode array detector. Greater sensitivity compared to traditional spectrophotometric measurements can be achieved because the material crossing the barrier is not diluted into the bulk solution for measurement. The system is automated to measure concentration-distance profiles at program-controllable times. After mounting the membrane and loading the solution, there is almost no manual involvement. Concentration-distance profiles of ferricyanide ion developed during electrolysis in the solution above a graphite electrode were acquired as a function of time. The experimental results are in agreement with theoretical results predicted by the Cottrell equation. The permeability of methyl orange across Nucleopore membranes was determined in less than 3 min with a 128-element diode array detector. The mass transport of 4-nitrophenol across silicone rubber membranes was quantified within 15 min with an improved 512-element array detection system. Conventional diffusion studies take much longer for completion.

INTRODUCTION

The in vitro methods commonly used to study mass transport generally involve the use of diffusion cell assemblies composed of two half-cells separated by the membrane of interest. The compound of study is added to the donor half-cell, and both solutions are stirred to facilitate mass transport. At predetermined times, samples are drawn from the bulk solution of one or both of the compartments and assayed, often spectrophotometrically, chromatographically, or by liquid scintillation counting. On the basis of Fick's diffusion laws and if "sink conditions" hold in the receiver compartment, at steady state, the rate of mass transport is constant and equal to PSC_d , where P is the permeability coefficient of the compound across the membrane, S is the cross-section area of the membrane, and C_d is the bulk concentration in the donor.¹ Because both S and C_d are known quantities, P is obtainable from the slope of the linear portion of a plot of the amount of diffusant transported vs time. Due to the slow nature of the diffusion process, the times involved in collecting such experimental data can range from hours for thin artificial membranes to days for skin.

A new instrument has been developed that is capable of simultaneously measuring the concentration-distance profiles

developed in quiet solutions on one or both sides of an interface or a membrane without the need for sample extraction. The instrument provides an instantaneous measurement or "snapshot" of the amount of a substance that has left one side of a membrane and appeared on the other side. Greater sensitivity compared to traditional spectrophotometric measurements can be achieved because the material crossing the barrier is not diluted into the bulk solution for measurement as in a stirred compartment. The system is automated to measure concentration-distance profiles at program-controllable times. After the membrane is mounted and the solution is loaded, there is almost no manual involvement. The permeability of methyl orange across Nucleopore membranes was determined in less than 3 min with a 128-element diode array detector. The mass transport of 4-nitrophenol across silicone rubber membranes was quantified within 15 min, whereas conventional diffusion studies take much longer for completion.

INSTRUMENTATION AND CELL DESIGN

Instrumentation Overview. The laser/photodiode array detector system developed is schematically depicted in Figure 1. The detection is based on absorption spectroscopy. A Moletron DL-II tunable dye laser, pumped by a Moletron UV-22 (Moletron Corp., Sunnyvale, CA; presently Laser Photonics, Orlando, FL) pulsed nitrogen laser, is used to provide a source of highly monochromatic and parallel light of a selected wavelength. The light is filtered down to the desired intensity level and expanded. Originally, a set of biconvex lenses of focal lengths 4.06 and 34.54 cm were used to expand the laser beam from 0.25- to 2.13-cm diameter. In the new and improved system, a Newport (Fountain Valley, CA) Model 910 spatial filter (2.9-mm microscope objective and 5- μ m pinhole) along with a plano-convex lens (75.6 mm) achieves a more uniform beam expansion. The beam then passes through a slit and travels normal to the diffusion cell to minimize light refraction. The variable slit allows the width of the beam to be decreased reducing the possibility of stray light reaching the detector from the sides and also provides another means of controlling the power of the beam. With a nitrogen laser pulse width of 10 ns, the dye laser has a nominal pulse width of 6-8 ns. With such short light pulses, the energy absorbed by the solution is not enough to cause temperature differences that might induce convection. A photodiode array, arranged orthogonal to the interface and beam, serves as the detecting unit. To minimize light diffraction off the membrane, which would complicate positional intensity measurements, the detector is positioned within 1 cm of the diffusion cell. This approach of using a photodiode array to acquire spatially resolved absorption measurement is similar to those described by Fukunaka et al.² and McCreery and co-workers^{3,4} for imaging the elec-

* To whom correspondence should be addressed.

[†] Present address: Pharmavene, Inc., Gaithersburg, MD 20878.

(1) Martin, A. *Physical Pharmacy: Physical Chemical Principles in the Pharmaceutical Sciences*; Lea & Febiger Philadelphia: Philadelphia, 1983; Chapter 15.

(2) Fukunaka, Y.; Dempo, K.; Iwata, M.; Maruoka, K.; Kondo, Y. *J. Electrochem. Soc.* 1983, 130, 2492-2500.

(3) Jan, C. C.; McCreery, R. L.; Gamble, F. T. *Anal. Chem.* 1985, 57 (8), 1763-1765.

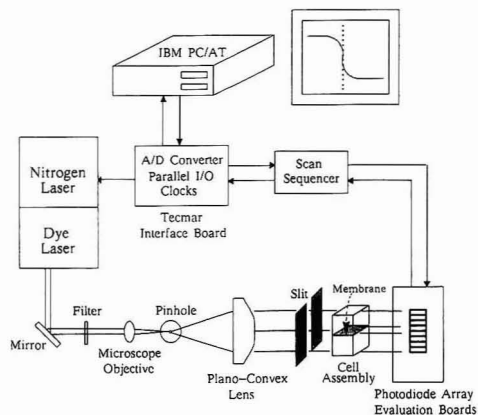


Figure 1. Schematic diagram of the laser/photodiode array system.

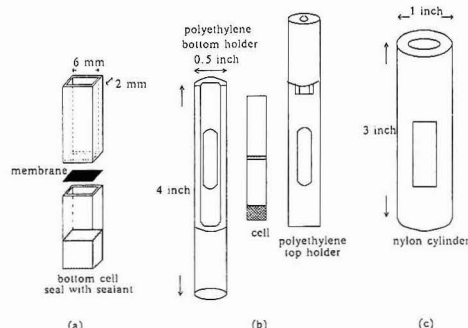


Figure 2. (a) Diffusion half-cells (0.9-mm wall thickness) and membrane. (b) Polyethylene diffusion cell holder. (c) Nylon cylinder.

trochemical diffusion layer at a solid electrode and by Harrison et al.⁵ for measuring the concentration profiles inside a nitrite ion selective electrode membrane.

Because these "quiet solution" studies are very sensitive to convection, all of the equipment is located on a floating optical table (Newport) to isolate the equipment from room vibrations which would otherwise limit acquisition times to perhaps less than 1 min at a typical lab bench. An IBM-PC equipped with a Tecmar LabMaster data acquisition subsystem (Scientific Solutions, Inc., Solon, OH) is used to control laser pulsing, acquire data from the photodiode array, and analyze, display, and store the data. Initial processing of the diode array video signal is accomplished by a home-built circuit board called a scan sequencer, through which the computer controls the diode array and collects the data. Software has been developed to set up and coordinate the tasks necessary to run and evaluate an experiment.

Diffusion Cell Assembly. The diffusion cell shown in Figure 2a is made of two pieces of rectangular bore glass tubing, 2-mm by 6-mm inner dimensions (Wilma WR-0206). The ends that make contact with the membrane are polished to a high degree of smoothness and flatness. While the top compartment remains open, the bottom compartment is sealed with clear silicone Windshield Glass Seal (General Electric, Waterford, NY). Bottom cells of various depths were made. The membrane of study is cut to cover the

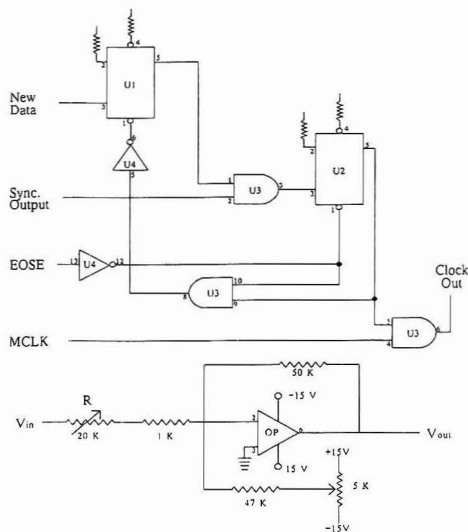


Figure 3. Scan sequencer circuit board design. Key: U1, U2, 7474 dual D-type flip-flops; U3, 7408 quad two-input AND gate; U4, 7414 hex inverter; OP, 741 operational amplifier.

opening, but not stick out over the edges. Two blackened polyethylene pieces (b) were made to hold the two half-cells together with the membrane sandwiched in between and apply even tension in the vertical direction to prevent leakage. This assembly is inserted into a hollow Nylon cylinder (c), which has two screws on the side to secure the assembly in place. Windows were milled out in the holder to allow light passage through the diffusion cell. The diffusion cell is always assembled with the bottom half filled with solution and the membrane in place. After the cell is positioned, the top compartment is filled with solution through a hole drilled through the center of the polyethylene top holder. The diffusion cell assembly is housed in a cuvette holder which is mounted against a kinematic mirror mount so that the tilt of the cell, if any, can be corrected. The kinematic mirror mount is in turn mounted on a rotation stage, which helps position the cell normal to the light beam. Three miniature translational stages stacked under the rotation stage optimally align the cell with the detector.

Detector and Scan Sequencer. The detector of the original system was an S-series 128-element photodiode array (EG&G Reticon Corp., Sunnyvale, CA) operated by an RC-1024SA evaluation board. The detector chip contains photodiode sensor elements for simultaneous light intensity measurements in 128 planes with a center-to-center spatial resolution of 25 μm . In the improved system, a 512-element array operated by a Reticon RC1000 Mother board and RC1001 Satellite board set⁶ is used. A scan sequencer was built to supply power for the diode array's evaluation boards, adjust the video output to be compatible with the LabMaster's A/D converter input, and process the input/output signals of the evaluation boards for total computer control. The circuit diagram is shown in Figure 3. In the lower part circuitry, R is assigned to 14.8 k Ω ; the video output of the array, V_{in} (0–6 V), is thus amplified by a factor of 3.2, which sets the output to 0–19 V. The 5-k Ω variable resistor provides an offset adjustment so that the video output range of the diode array

(4) Wu, H. P.; McCreery, R. L. *Anal. Chem.* 1989, 61 (21), 2347–2352.

(5) Li, X.; Harrison, D. J. *Anal. Chem.* 1991, 63 (19), 2168–2174.

(6) RC1000/RC1001 Operation and Alignment Instructions; EG&G Reticon Corp.: Sunnyvale, CA.

at V_{out} becomes -9.5 to $+9.5$ V. The upper part is the signal processing circuitry that defines the 512 pulses required to trigger the A/D converter for each scan. MCLK is the free-running on-board master clock signal. When a data acquisition request is received from the LabMaster's counter 4 at "New Data", the first in-sequence Sync. Output and EOSE (both output from the evaluation board) allow 512 A/D triggering pulses for the first complete scan of the array to be generated at "Clock Out".

Software. The program is written in Microsoft Quick BASIC using Assembly subroutines to effect rapid data collection. The program sets the integration time of the diode array, programs the counters of the Tecmar LabMaster to trigger the nitrogen laser and the scan sequencer, initializes the A/D converter, and calls the Assembly subroutines to collect data. The program then retrieves data from the Assembly subroutines and performs statistical analysis and data rejection. It also plots, prints, and/or stores the experimental data. Old experimental data can be reviewed as well.

EXPERIMENTAL SECTION

Reagents. Analytical reagent grade chemicals were used without further purification unless otherwise specified. Demineralized double-distilled water was used to prepare all aqueous solutions. Phosphate buffer solutions (0.2 F) of pHs 2.2, 3, 5, 7, and 10 were prepared. The 10 mM $K_3Fe(CN)_6$ (Baker Lot 33407) in 0.2 M KCl/0.02 M HCl stock solution was purged of dissolved oxygen by bubbling (Zn/vanadyl sulfate scrubbed) nitrogen through it for 15 min and then stored away from light. Fresh 4 mM $K_3Fe(CN)_6$ test solutions were prepared upon use. Methyl orange solutions of 5×10^{-4} and 5×10^{-5} M were prepared by serial dilution from the 1 mM stock solution. Yellowish needle crystals of 4-nitrophenol (K & K Laboratories, Inc. 66855X) were obtained by recrystallization from water.

Membranes. Nucleopore membranes (Nucleopore Corp., Pleasanton, CA) were chosen for the preliminary membrane transport studies because they are thin (6–10 μm) yet relatively sturdy, flat, and chemically and biologically inert. The 25-mm disks were presoaked overnight in phosphate buffer before use. Nonreinforced Silastic Medical-Grade silicone rubber sheeting from Dow-Corning (Midland, Michigan) was used in the study of mass transport of 4-nitrophenol. Silastic membrane is permeable to uncharged lipophilic drug molecules and impermeable to charged species. It is homogeneous and inert and has little or no tendency to imbibe water. These characters make it attractive as a membrane for simulation of the drug transport phenomenon. Contrary to this, microporous membranes are not a good model for skin, for example. However, microporous membranes have been used as growth support systems on which cell monolayers have been grown to study transport across cell layers. 4-Nitrophenol was studied because it has been frequently used in diffusion studies, and data pertaining to this system have been reported.⁷ Silastic membrane pieces of 2 cm square were stored in the phosphate buffer to be used for the donor solution after being washed and thoroughly rinsed.

Spectroelectrochemical Study of $K_3Fe(CN)_6$. To evaluate the performance of the laser/photodiode array system for spatially resolved concentration measurements, the formation of an electrochemical diffusion layer was first studied because it is a well-defined system. The concentration-distance profiles developed during electrolysis as a function of time are theoretically predictable.⁸ The potassium ferrocyanide/ferricyanide redox couple was chosen because the reaction is reversible and uncomplicated and the compounds do not adsorb onto the electrode surface. Also the diffusion coefficients of both species are known.⁹ The molar absorptivity of the ferricyanide ion is 1020 (cm M)⁻¹ at 420 nm.

Fine-grain, low-permeability graphite (DFP-1 grade, POCO Graphite Inc., Garland, TX) was used as the working electrode. A graphite rod of 6-mm diameter and 14-mm length was impregnated with Nujol and polished. A 20-gauge silver wire coated with silver chloride served as the reference electrode and was enclosed in a shortened disposable Pasteur pipet. A 31-gauge platinum wire wrapped around the glass-encased Ag/AgCl electrode served as the auxiliary electrode. A piece of polished rectangular borosilicate glass tubing, 2-mm by 4-mm inner dimensions and 2 cm long, was used as the spectroelectrochemical cell. A holder made of three specially machined plastic pieces secured the graphite electrode upright squarely against the polished surface of the bore glass cell. With the vertical tension properly maintained, the graphite surface completely sealed the glass tubing from the bottom. A disposable pipet was used to introduce solution into the cell from the top of the holder through a hole. The reference and auxiliary electrodes also made contact with the solution through this opening.

To perform the experiment, the dark current of each individual diode was recorded. The intensity signal was then measured with the laser beam directed through the clear 4 mM $K_3Fe(CN)_6$ solution to obtain the 100% transmittance values. After the electrode potential was stepped from -0.1 to $+0.6$ V vs Ag/AgCl, the colored oxidation product, $K_3Fe(CN)_6$, started to form at the electrode surface and diffused away. At 1, 5, 9, 17, 25, 33, 49, 65, 97, and 120 s after the potential step, the positionally resolved transmittance of the solution was again measured. Nine scans were averaged per series collection. The diffusion-limited current was simultaneously monitored with an IBM EC/225 voltammetric analyzer interfaced to the IBM-PC.

Transport of Methyl Orange across Nucleopore Membranes. Transport experiments of methyl orange across Nucleopore membranes were conducted to examine the applicability of the laser/photodiode array system in studying the transport process. To restrict mass transport to diffusion, the floating optical table was necessary to reduce room vibrations in the solution cells, the short pulsed dye laser avoided the introduction of heat into the solutions, and migration due to electrical gradients was minimized by using the phosphate buffer, the concentration of which was at least 100 times the species of interest, in both the donor and receiver solutions.

Because both the donor and receiver solutions were initially homogeneous and the diffusion layer developed during the measurement time period would not run into any walls that restricted its growth, the theoretical concentration profiles could be calculated at a selected time and distance away from the interface for a given species with a known diffusion coefficient. The assumption made here was that the concentration of methyl orange at the interface of these two solutions remained constant and equal to half of the initial bulk concentration. The total amount transported at a chosen time, $Q(t)$, was derived to be proportional to $AC_0(D/t)^{1/2}$, where A was the cross-section area for transport, C_0 the initial bulk concentration in the donor cell, and D the diffusion coefficient of the species. When $Q(t)$ multiplied by the square root of time was plotted against time, a linear plot was obtained that had a slope proportional to $AC_0D^{1/2}$. The experimental data could only be evaluated up to 75 μm (three diode elements) of the membrane surface, on each side, due to light diffraction caused by the surface edges of the membrane. Fortunately, when the same restriction was applied to the theoretical data, it still yielded a linear $Q(t) \times t^{1/2}$ plot. By analyzing the slope against $D^{1/2}$, the following equation was derived:

$$\text{measured slope} = 223.5D^{1/2} - 0.1103$$

D thus determined was an "effective" diffusion coefficient (or permeation constant), because the Nucleopore membranes are thin impermeable sheets with pores through which transport occurs. Only a fraction of the total cross-section area is actually available for transport.

To conduct the experiment, the sealed bottom half-cell was filled with phosphate buffer of designated pH, and the membrane was carefully laid on top of the solution without forming any air bubbles. This was placed in the bottom part of the polyethylene holder, and the other empty glass compartment was gently set on top of this. The top polyethylene piece was then closed in to

(7) Jetzer, W. E.; Huq, A. S.; Ho, N. F. H.; Flynn, G. L.; Duraiswamy, N.; Condie, L., Jr. *J. Pharm. Sci.* 1986, 75 (11), 1098–1103.

(8) Bard, A. J.; Faulkner, L. R. *Electrochemical Methods*; Wiley: New York, 1980; Chapters 4 and 5.

(9) Adams, R. N. *Electrochemistry at the Solid Electrode*; Dekker: New York, 1969.

hold the cells together, and the entire assembly was inserted into the Nylon cylinder till the light paths lined up. The top compartment was filled with 100 μ L of the same background solution after the cell was positioned. The dark current and the 100% transmittance signals were recorded first. A syringe was used to introduce 25 μ L of the methyl orange solution into the top compartment. The solution in the top compartment was gently pulled into the syringe and replaced back to the top compartment several times to achieve solution homogeneity in the donor half-cell. At 30, 60, 90, 120, 150, and 180 s after the introduction of methyl orange, the light intensity profiles were measured. Methyl orange transport across 0.2- μ m Nuclepore membranes was measured at pHs 3, 5, 7, and 10. For pHs 5, 7, and 10, 465 nm was the λ_{max} , with a molar absorptivity of 25 200 (cm M^{-1}). At pH 3, λ_{max} was 503 nm and the molar absorptivity 34 300 (cm M^{-1}). Methyl orange transport across Nuclepore membranes of various pore sizes was also measured in pH 7 phosphate buffer.

Transport of 4-Nitrophenol across Silicone Rubber Membranes. 4-Nitrophenol is a weak acid, with a pK_a of 7.15. Flynn et al.⁷ suggested the donor pH be maintained at 2.2 to suppress ionization and the receiver pH be at 10 to best assure sink conditions when the permeation of silicone rubber membranes by 4-nitrophenol is studied. These conditions were mimicked to evaluate the performance of the laser/photodiode array measurement system against the data they reported. At pH 2.2, 4-nitrophenol solution is colorless; at pH 10, the yellow solution has an absorbance peak at 400 nm with a molar absorptivity of 20 200 (cm M^{-1}).

Experiments were first conducted with a 1.8-mm-deep bottom cell filled with pH 10 receiver buffer and the pH 2.2 donor solution (50 mg/100 mL) was introduced into the top compartment at the onset of experiments. Concentration-distance profiles were acquired at 1, 2, 3, 4, 6, 8, 10, 12, and 15 min after the introduction of 4-nitrophenol. It was observed that 4-nitrophenol reached the bottom of the receiver cell after 4 min. An 18-mm receiver cell was then used to allow 4-nitrophenol to diffuse without restriction. A lower bulk concentration of 25 mg/100 mL was used and the profiles were recorded at 2, 4, 8, 13, 20, 30, 40, and 50 min.

The experimental results indicated that quiet solution conditions did not hold as expected, which may be due to density gradient induced turbulence caused by the transport of 4-nitrophenol. The orientation of the diffusion cell was therefore inverted. That is, the bottom cell was filled with the pH 2.2 donor solution, the top compartment was empty when the dark current and the 100% transmittance were measured and pH 10 receiver buffer was introduced into it at the onset of experiments. New membranes were used in all the experiments conducted so far to avoid the time-consuming membrane recovery procedures. However, in final studies, membranes were used over and over with proper recovery treatment between experiments. The bottom cell is again the donor chamber.

RESULTS AND DISCUSSION

Spectroelectrochemical Results for $K_3Fe(CN)_6$. The results of the $K_3Fe(CN)_6$ measurements are shown in Figure 4. The intensity data collected at 9, 25, 49, and 97 s as well as the dark current and the 100% transmittance are shown in (a). The fluctuations observed (except the dark current) may be due to intensity variations inherent in the laser beam and differences in the gains of the individual diodes. The pattern is reproducible as this figure shows. The positional absorbance (b) is derived by applying the equation, $A = -\log_{10}(I/I_0)$, to each individual diode, where I is the intensity measured at various times and I_0 is the intensity of 100% transmittance. Both I and I_0 are dark current corrected. It is evident that the systematic noise is largely eliminated after conversion. These measured profiles are in good agreement with the theoretically predicted values, where the diffusion coefficients of $K_3Fe(CN)_6$ and $K_4Fe(CN)_6$ are 7.63 and $6.5 \times 10^{-6} \text{ cm}^2/\text{s}$, respectively.⁹ This indicates that the laser/photodiode array system functions well as a spatially and temporally resolved spectrophotometer.

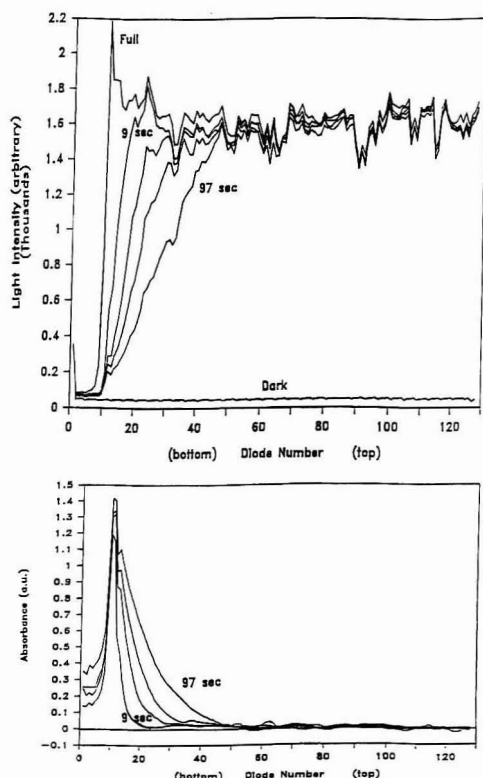


Figure 4. Positional (a, top) intensity and (b, bottom) absorbance measurement of $K_3Fe(CN)_6$ at times 9, 25, 49, and 97 s.

Transport Measurement Results for Methyl Orange. The results for the transport of methyl orange across a Nuclepore membrane of 0.2- μ m pore size at pH 7 are shown in Figure 5. The initial bulk concentration is $1 \times 10^{-4} \text{ M}$, and the concentration in (a) is a fraction of this value. Plot b depicts the amount (integration of concentration starting from 75 μ m of the membrane surface) of methyl orange which leaves the donor compartment and that which appears in the receiver compartment at various times. Both curves should be the same and are in fact reasonably close. The difference between these two curves (shown near the baseline) may be due to the material within the membrane and near the membrane in a "detector hidden" area. When the integrated amount at a given time is multiplied by the square root of time and plotted against time (c), linear plots in agreement with diffusion theory are obtained. The slopes are 0.361 and 0.382 and the effective diffusion coefficients are 4.45×10^{-6} and $4.85 \times 10^{-6} \text{ cm}^2/\text{s}$ on the basis of the measurements in the receiver and donor compartments, respectively. It is believed that the results based on the measured amount of methyl orange that leaves the donor compartment are more dependable because the material in the membrane and detector hidden area is "invisible".

Permeation constants at pHs 3, 5, and 10 are found to be 4.85, 4.32, and $4.25 \times 10^{-6} \text{ cm}^2/\text{s}$, respectively. The variations could be due to actual differences in the diffusion coefficients at the different pH values or to experimental variability. It is found that the permeation constant is unchanged over a concentration range of 1×10^{-6} to $2 \times 10^{-4} \text{ M}$ for pHs 5, 7,

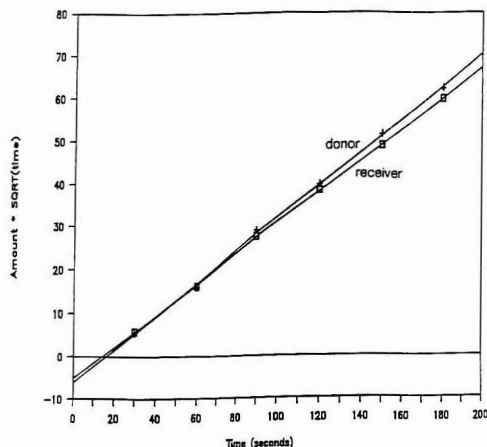
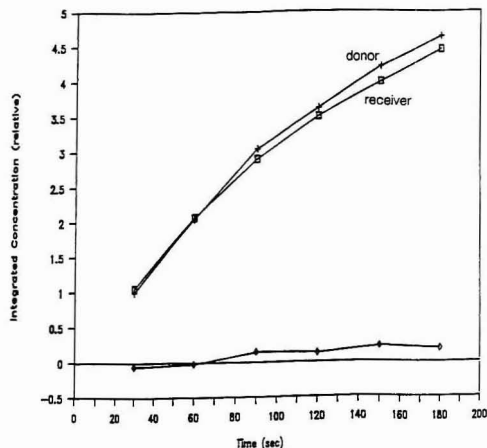
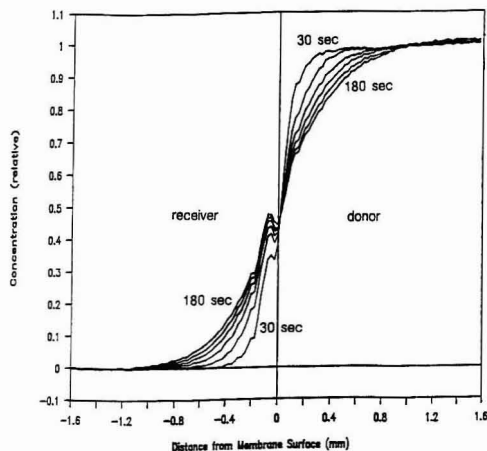


Figure 5. (a, Top) concentration-distance profiles, (b, middle) flux, and (c, bottom) flux $\times t^{1/2}$ for the transport of methyl orange across a Nuclepore membrane of 0.2- μm pore size at pH 7.

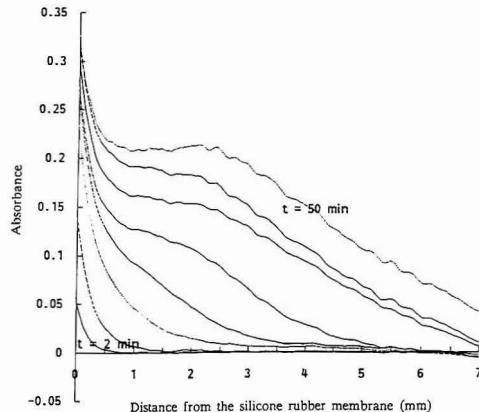


Figure 6. Concentration-distance profiles of 4-nitrophenol in an 18-mm-deep bottom compartment.

and 10. At pH 3, however, the transport of methyl orange is concentration dependent between 5×10^{-5} and 1×10^{-4} M. The reasons were not pursued. The permeation constant is also found to generally increase with membrane pore size and pore area.

Transport Measurement Results for 4-Nitrophenol.

Figure 6 shows the part of the concentration-distance profiles that were viewed by the diode array when an 18-mm-deep bottom cell was the receiver. Distance zero is the position of the first measurable diode outside the diffraction limited region. In a diffusion-controlled transport system like this, the diffusion layer thickness should be proportional to the square root of time. It is observed that the diffusion layer does not grow with time as theoretically predicted throughout the experiment. In this example, the diffusion layer increases with the square root of time for the first 8 min, after which, the diffusion layer thickness becomes larger than expected. The profiles go beyond the view window of the diode array after 20 min. The humps observed indicate that the solution is no longer under quiet conditions after 8 min and induced stirring/mixing of the solution occurs. This phenomenon is repeatedly observed, but the onset and extent of mixing differs from one experiment to another. To quantify the amount of 4-nitrophenol transported, the concentration profiles have to be completely within view and shorter receiver cells are thus required.

When the amount of 4-nitrophenol transported vs time is compared among experiments, it is found that data are reasonably consistent for the first few minutes, then the rate of mass transport starts to vary. A permeability coefficient of $29.2 (\pm 4.2) \times 10^{-3}$ cm/h is derived from the slopes of the linear portions. A lag time of about 1 min is also determined by extrapolating the linear portions of the curves to the time axis. It is suspected that the transport of 4-nitrophenol causes density gradient induced turbulence which is highly irreproducible and uncontrolled so that the rate of mass transport differs from one experiment to another.

These assumptions are confirmed by the data obtained (Figure 7) when the cell orientation is inverted. Although the receiver solution is 20 mm high in the top compartment, the profiles stay within 3 mm of the silicone rubber membrane throughout the experiment (15 min). The membrane/receiver solution interface is located to the right in Figure 7. When the diffusion layer thickness is plotted against the square root of time, linearity is observed which implies that mass transport in this inverted configuration is diffusion-controlled.

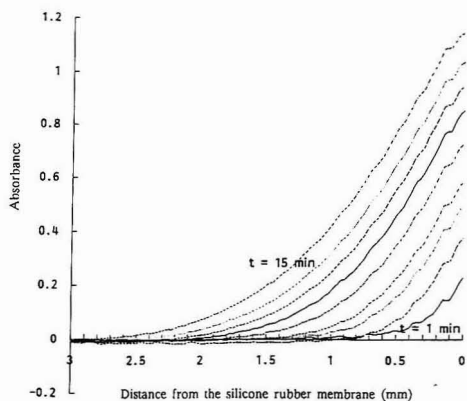


Figure 7. Concentration-distance profiles of 4-nitrophenol in a top compartment.

It is therefore determined that for the remainder of the experiments the top compartment should be the receiver to minimize the density gradient induced turbulence caused by 4-nitrophenol. When the amount transported vs time is analyzed, the lines seem more linear and better defined. However, the results are not very reproducible among experiments. The permeability coefficient ranges $(19.7\text{--}28.7) \times 10^{-3}$ cm/h, with a standard deviation of 14%. The averaged value, 23.7×10^{-3} cm/h, is 20% smaller than that obtained with the bottom cell being the receiver. The lag time previously observed is no longer detectable. That is because the membrane has been laid on top of the donor solution for minutes before the receiver buffer is injected. The membrane is already saturated with 4-nitrophenol when the experiment starts; there is no breakthrough time.

Because the diffusion cell is very small, with a cross-section area of 0.12 cm^2 , membrane inhomogeneity may be observed that was unnoticed by others who used larger membranes in their studies (e.g., 10.4 and 2.10 cm^2 in refs 10 and 11). Thus measurement reproducibility may depend upon the homogeneity of the stock material the small membranes are cut from. Experimental results (Figure 8) show that the transport of 4-nitrophenol is very reproducible when the same piece of membrane is used repeatedly for a series of experiments. The line separated from the others is obtained after the used membrane was recovered by soaking in pH 10 instead of pH 2.2 buffer overnight. Under that circumstance, a small initial amount of 4-nitrophenol in the donor is ionized and diffusion is delayed upon contacting the membrane; a lag time is therefore observed. However, the linear portion after the breakthrough has essentially the same slope as the other measurements. The permeability coefficients derived from these slopes vary between 23.1 and 23.4×10^{-3} cm/h, with a standard deviation of less than 1%. The permeability coefficients of another membrane also repetitively used are 26.8 , 25.8 , and 26.5×10^{-3} cm/h, with a standard deviation of less than 2%. Although highly reproducible results are obtained from both membranes, their permeability coefficients are quite different (23.2 vs 26.4×10^{-3} cm/h). It is concluded that the photodiode array system makes reproducible measurements, but that the silicone rubber sheeting is not very homogeneous. The standard deviation of the data

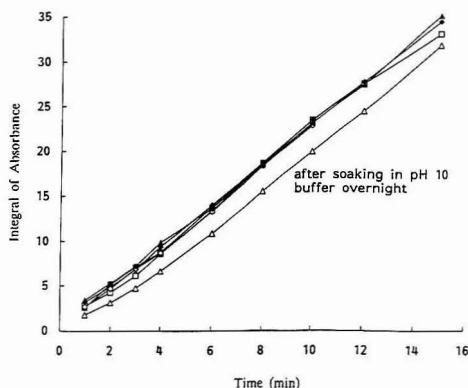


Figure 8. Amount of 4-nitrophenol transported across a membrane used repetitively.

collected by using a new membrane for each experiment ranges from 13 to 15%, which may very well index the inhomogeneity of the sheeting.

CONCLUSION

From the spectroelectrochemical data, it can be stated that the laser/photodiode array system performs well as a spatially resolved spectrophotometer that can measure concentration as a function of both time and distance. The measured results are in agreement with those theoretically predicted. The technique is also applicable to the measurement of transport of methyl orange across Nuclepore membranes. The measurement system is useful in determining the permeability coefficient of 4-nitrophenol at pH 2.2/10 as well. The permeation was quantified within 15 min, whereas conventional diffusion studies take much longer for completion. The permeability coefficient determined is 23.7×10^{-3} cm/h, which is somewhat smaller than 34.7×10^{-3} cm/h reported by Flynn et al.⁷ This may be because they used a 37°C water bath for their diffusion cell and the solutions were stirred, whereas our measurements were taken in quiet solutions at room temperature. Diffusion is known to increase $\sim 1\text{--}2\%$ per degree increase in temperature.

This instrument is expected to be useful for studying mass transport across skin and other biological and pharmaceutical membranes, in which somewhat slower or comparable diffusion is expected. However, this technique is limited to the study of compounds that absorb light. The photodiode array is subject to thermally generated dark current and its associated statistical fluctuations (noise). Dark current buildup imposes a limit upon the integration time allowed, which in turn limits the sensitivity of the measurement system. Because the dark current is halved for each 6.7°C reduction in temperature, sensitivity of this measurement system could be dramatically improved by cooling the array. In addition, with a cooled detector, integration time can be increased permitting the use of much more stable but lower energy conventional light sources.

ACKNOWLEDGMENT

Financial support from the IBM Corp. and Smith Kline & Beecham Pharmaceuticals is gratefully acknowledged.

(10) Garrett, E. R.; Chemburkar, P. B. *J. Pharm. Sci.* 1968, 57 (6), 944-948.

(11) Patel, D. C.; Fox, J. L.; Higuchi, W. I. *J. Pharm. Sci.* 1984, 73 (8), 1028-1034.

Refractory Behavior of Lead in a Graphite Furnace When Palladium Is Used as a Matrix Modifier

Robert W. Dabeka

Food Research Division, Bureau of Chemical Safety, Food Directorate, Health Protection Branch, Health and Welfare Canada, Ottawa, Ontario, Canada K1A 0L2

Using platform atomization with a 0-s ramp to temperatures above 2300–2400 °C, lead appears to form a refractory species in the presence of palladium and graphite. Evidence for this was the appearance of two lead absorption peaks when atomizing above 2700 °C. The refractory behavior was so great that the absorbance maximum of the second lead peak occurred even after those of chromium and molybdenum atomized under the same conditions. Also, a portion of lead was retained on the platform even after ashing at 2400 °C for 15 s with the inert gas flow on. Hydrogen, if present during atomization, caused an enhancement of the refractory peak. Also, the refractory peak was more prominent when uncoated or impregnated graphite platforms, as opposed to pyrolytic ones, were used. It is hypothesized that the refractory behavior of lead is caused by high-temperature formation of a species comprised of lead, carbon, and palladium. The refractory behavior can cause analytical errors in graphite-furnace atomic absorption spectrometry when palladium is used as a matrix modifier for lead and atomization temperatures of 2400 °C or greater are used.

INTRODUCTION

Palladium is widely used in graphite furnace atomic absorption spectrometry as a modifier for many elements.^{1–5} In the case of lead determinations, palladium substantially reduces lead volatility during the ashing step, shifting the lead absorption^{1,6,7} or emission⁸ peak to later times. The modifier mechanism appears to involve three steps: (a) reduction of palladium salts to the metal,^{1,2} (b) palladium-induced low-temperature reduction of PbO to metallic lead,⁹ and (c) formation of lead–palladium intermetallic compounds. Evidence for the latter is Pb–Pd bond formation revealed by X-ray photoelectron spectroscopy⁷ and X-ray diffraction identification of the intermetallic compounds Pd₃Pb and Pb₃Pd.¹⁰ Pb₃Pd₂ was stable only at temperatures below about 1470 °C, while Pd₃Pb was stable above 1370 °C and decomposed above 1770 °C into liquid components.¹⁰ Thermal stabilization of lead during ashing is achieved because the formation of intermetallic compounds lowers the vapor pressure of lead.¹⁰

This study describes hitherto unobserved lead refractory behavior in the presence of palladium. This behavior appears unrelated to previous investigations because the effects occur only at temperatures well above those at which known Pb–Pd intermetallic compounds are stable.

EXPERIMENTAL SECTION

Apparatus. Except where indicated otherwise, measurements were made on a Perkin-Elmer HGA-400 graphite furnace with an AS-60 autosampler mounted on a Varian Model 775-ABQ spectrometer. Pyrolytically coated and uncoated graphite tubes and pyrolytic graphite L'vov platforms were purchased from the manufacturer. Impregnated (proprietary technique) tubes and platforms were purchased from Delta Scientific Co., Ottawa. Uncoated graphite platforms were prepared by machining an uncoated graphite tube into an approximate platform shape. Platforms were placed loosely in each tube rather than using tubes with the platforms fixed in grooves.

Reagents. Deionized water was of ASTM Type III quality. Lead solutions were prepared from lead nitrate, NIST SRM No. 928. Acids were subboiling distilled. The palladium solution was prepared from the metal by dissolution in concentrated nitric acid containing a minimum of hydrochloric acid. After dissolution, most of the additional hydrochloric acid was removed by boiling with excess nitric acid. All other reagents were of analytical reagent quality or better, and none contributed any measureable blank. Graphite powder, "F" purity, was purchased from Ultra Carbon Corp., Cat. No. UCP-3-325.

Procedures. Unless otherwise indicated, the conditions and procedures outlined below were followed. The standard furnace temperature program used was that described in Table I. The actual temperatures referred to are those produced by the atomizer without additional calibration. The gas flow was stopped 5 s preceding atomization and during the full atomization period. The inert gases used were argon and 8% hydrogen in argon.

Lead, cadmium, chromium, and molybdenum measurements were made at 283.3, 228.8, 357.9, and 313.3 nm, respectively. Aliquot volumes of 10 µL of standard, 2 µL of 2% nitric acid as a pipet rinse, and 4 µL of modifier (Pt, Pd, or blank solutions) were pipetted into the furnace for each atomization. Deuterium-continuum background correction was used throughout. All measurements were evaluated for the potential contribution of background and blanks.

Ashing temperature studies were performed by changing the atomization step in Table I to an ashing step. This was accomplished by deleting the clean-out step and leaving the gas flow on throughout the cycle. After the temperature program had finished, the third drying step (300 °C) was converted to an atomization step (2800 °C, 0-s ramp with gas flow off, read), and the temperatures of the first and second drying steps (200 °C and 250 °C) were reduced to 40 °C. The furnace was then started manually and turned off manually after atomization. A manual clean-out step was then included.

RESULTS AND DISCUSSION

Refractory Behavior of Lead and Parameters Affecting It. Figures 1 and 2 illustrate the behavior of lead in the HGA-400 graphite furnace using an atomization temperature

- (1) Retberg, T. M.; Beach, L. M. J. *Anal. At. Spectrom.* 1989, 4, 427–432.
- (2) Voth-Beach, L. M.; Shrader, D. E. J. *Anal. At. Spectrom.* 1987, 2, 45–50.
- (3) Beach, L. M. *Spectroscopy* 1987, 2, 21–23.
- (4) Schlemmer, G.; Welz, B. *Spectrochim. Acta* 1986 41B, 1157–1165.
- (5) Fagioli, F.; Locatelli, C.; Vecchiotti, R.; Torsi, G. *Appl. Spectrosc.* 1991, 45, 983–985.
- (6) Hinds, M. W.; Katyal, M.; Jackson, K. W. J. *Anal. At. Spectrom.* 1988, 3, 83–87.
- (7) Shan, X.-Q.; Wang, D.-X. *Anal. Chim. Acta* 1985, 173, 315–319.
- (8) Sturgeon, R. E.; Willie, S. N.; Luong, V. T.; Berman, S. S. J. *Anal. At. Spectrom.* 1991, 6, 19–23.
- (9) Volynsky, A.; Tikhomirov, S.; Elagin, A. *Analyst* 1991, 116, 145–148.
- (10) Wendl, W.; Muller-Vogt, G. J. *Anal. At. Spectrom.* 1988, 3, 63–66.

Table I. Graphite Furnace Temperature Program

step	temp, °C	ramp time, s	hold time, s	gas flow
1, drying	200	1	20	on
2, drying	250	1	10	on
3, drying	300	1	7	on
4, ashing	400	1	20	on
5, cool-down	40	1	15	on
6, atomization	2800	0	7	off
7, cool	40	1	10	on
8, clean-out	2800	0	7	on

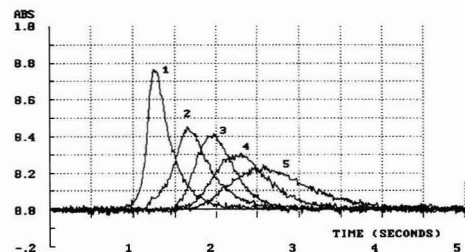


Figure 1. Influence of platinum concentration on the absorption profile of 1 ng of lead in 2% nitric acid using a new impregnated graphite tube and platform, 8% hydrogen in the inert gas, and an atomization temperature of 2000 °C. Amounts (micrograms) of platinum present were (1) 0.0, (2) 0.2, (3) 1.0, (4) 5.0, and (5) 20.

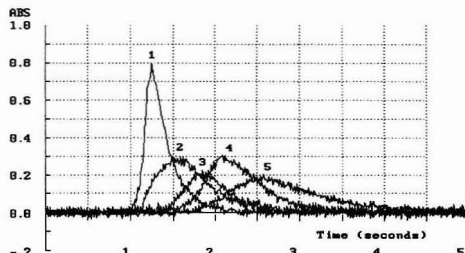


Figure 2. Influence of palladium concentration on the absorption profile of 1 ng of lead in 2% nitric acid using a new impregnated graphite tube and platform, 8% hydrogen in the inert gas, and an atomization temperature of 2000 °C. Amounts (micrograms) of palladium present were (1) 0.0, (2) 0.2, (3) 1.0, (4) 5.0, and (5) 20.

of 2000 °C and show how the position of the lead peak, a function of the kinetics of lead volatilization from the surface, shifts to longer times in the presence of increasing amounts of platinum or palladium. Shifts caused by identical amounts of platinum and palladium are approximately the same although the shape of the absorption curves differ substantially. In all cases, however, only a single absorption peak is present. Figure 3, taken with the same tube, platform, and conditions as Figures 1 and 2 except for a 2800 °C atomization temperature, shows the appearance of one lead peak in the presence of 5 or 20 µg of platinum, and two lead peaks in the presence of 5 or 20 µg of palladium. The second lead peak (Figure 3), with an absorbance maximum almost a full second later than the first, reflects unusually high lead thermal stability and is the subject of this investigation.

Double lead absorption peaks in the absence of palladium have been observed previously¹¹⁻¹⁷ and have been attributed

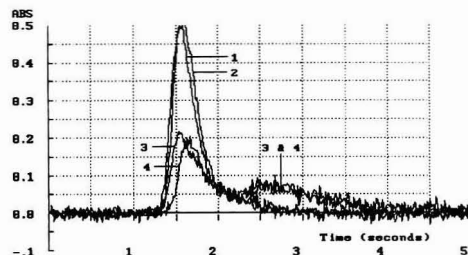


Figure 3. Influence of platinum and palladium concentration on the absorption profile of 1 ng of lead in 2% nitric acid using a new impregnated graphite tube and platform, 8% hydrogen in the inert gas, and an atomization temperature of 2800 °C. Amounts of platinum or palladium present were (1) and (3) 5.0 ng, and (2) and (4) 20 µg.

to either physical artifacts, such as uncorrected background¹¹ or partial occlusion of lead within the sample matrix,¹² or to the simultaneous presence on the atomizer surface of two or more lead compounds, e.g. Pb and PbO,^{13,18} having different volatility.^{13-17,19} Examination of absorbance and background signals under a wide range of conditions in the presence and absence of palladium, platinum, lead, and cadmium revealed that the second lead peak in Figure 3 reflected true lead absorption and was not caused by any of the following potential artifacts: uncorrected background, tube emission, palladium absorption, and readsorption of lead atoms on cooler surfaces followed by a second atomization. Thus, the presence of two absorption peaks in the presence of palladium (Figure 3) appears to be due to volatilization from the platform of two lead species which have different volatility.

The positions of the first lead peaks were approximately identical irrespective of whether platinum or palladium was used as a modifier (Figure 3). The shifts of first peaks to later atomization times with increasing concentrations of platinum or palladium suggest that the vaporization mechanism is diffusion of lead dissolved in a surface-deposited metallic modifier. The greater the volume of palladium, the longer the time for diffusion of lead from the liquid. (Palladium is assumed to be in the liquid state during lead atomization because, under the same conditions, absorption of 1 µg of palladium is observed during the full time interval of both lead peaks.)

The second lead peak observed with palladium modification (Figure 3) appeared to be an element-specific surface interaction between the two elements because (a) the second peak was absent when platinum was used instead of palladium (Figure 3) and (b) only one cadmium peak was observed when cadmium was substituted for lead in the presence of palladium (not illustrated).

The close agreement in peak areas (all within 7%) taken over the full atomization period for the four absorption profiles in Figure 3 suggests that the second lead peak is not due to reatomization of lead which had been atomized and then deposited on a cooler area of the furnace, a potential artifact observed for manganese in the Philips SP9 atomizer.²⁰ Confirmation of the absence of this artifact is the observation of two lead peaks at 217.0 nm using the Perkin-Elmer Model 4100-ZL spectrometer with Zeeman background correction

(11) Manning, D. C.; Slavin, W. *Anal. Chem.* 1978, 50, 1234-1238.
 (12) Karwowska, R.; Jackson, K. W. *J. Anal. At. Spectrom.* 1987, 2, 125-129.
 (13) Sturgeon, R. E.; Mitchell, D. F.; Berman, S. S. *Anal. Chem.* 1983, 55, 1059-1064.

(14) McLaren, J. W.; Wheeler, R. C. *Analyst* 1977, 102, 542-546.
 (15) Regan, J. G. T.; Warren, J. A. *Anal. Chem.* 1978, 50, 89-90.
 (16) Imai, S.; Hayashi, Y. *Anal. Chem.* 1991, 63, 772-775.
 (17) Salmon, S. G.; Davis, R. H., Jr.; Holcombe, J. A. *Anal. Chem.* 1981, 53, 324-330.
 (18) Sabbatini, L.; Tessari, G. *Ann. Chim.* 1984, 74, 779-793.
 (19) Bass, D. A.; Holcombe, J. A. *Anal. Chem.* 1987, 59, 974-980.
 (20) Chaudhry, M. M.; Littlejohn, D.; Whitley, J. E. *J. Anal. At. Spectrom.* 1992, 7, 29-34.

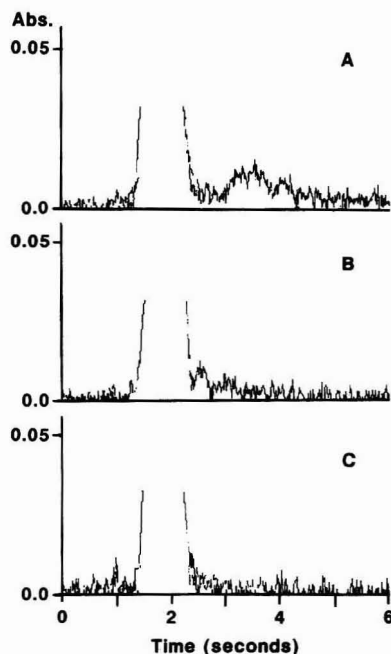


Figure 4. Effect of added graphite on 2 ng of lead in 5% nitric acid. Results obtained using the THGA furnace with pyrolytic graphite cuvette at 2600 °C atomization temperature and 8% hydrogen in argon gas: (A) 10 µg of palladium with approximately 10 mg of graphite powder added to the platform; (B) 10 µg of palladium with no added graphite; (C) 9 µg of platinum with added graphite.

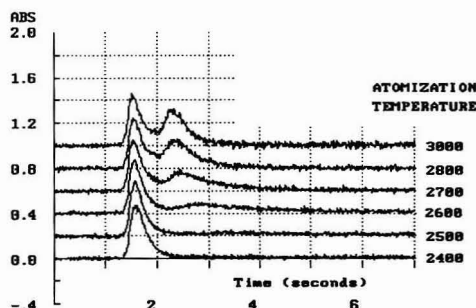


Figure 5. Effect of atomization temperature on atomization profile of 1 ng of lead in a matrix of 8 µg of Pd and 1% nitric acid using an old impregnated graphite platform in a new tube.

and transverse-heated graphite atomizer (THGA) (Figure 4). The integrated-contact cuvette of the THGA does not have cooler ends upon which condensation can occur. Two lead peaks in the presence of palladium were also observed when a Varian GTA-95 furnace on a Varian model 875-ABQ spectrometer was used with an atomization temperature of 2800 °C, a plateau-type pyrolytically coated tube, and a pyrolytic graphite platform. However, unlike the data from HGA-400, the two peaks were clearly separated in time (not illustrated).

Figure 5 illustrates the effect of atomization temperature on the double peak formation in the presence of palladium. At 2400 and 2500 °C, only a single lead peak was present. The reason for this is that only the nonrefractory lead is observed.

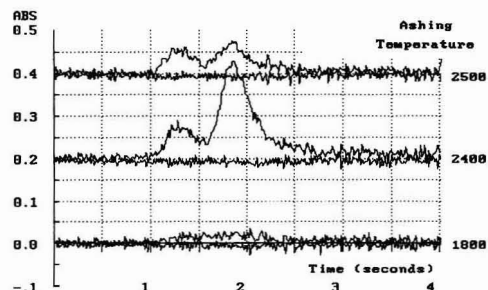


Figure 6. Effect of ashing temperature on the amount of residual lead left on the platform after ashing 10 ng of lead with 8 µg of palladium for 15 s with full gas (8% hydrogen in argon) flow during ashing and 0-s ramp to the ashing step. Absorption and background peaks were simultaneously recorded using a 2800 °C atomization temperature.

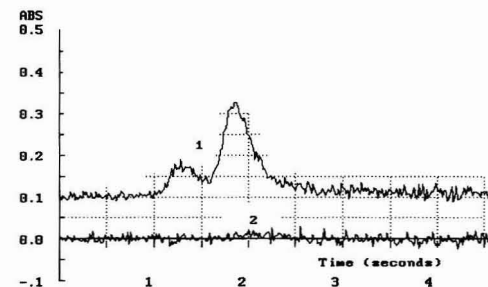


Figure 7. Effect of ramp time during the ashing step on the amount of residual lead left on the platform after ramp and ashing times of (1) 0 and 15 s, and (2) 2 and 10 s at an ashing temperature of 2400 °C. Ten nanograms of lead and 8 µg of palladium were ashed using an old impregnated graphite platform with full gas (8% hydrogen in argon) flow. Absorption peaks were recorded at 2800 °C atomization temperature.

At these temperatures, the refractory lead species is so involatile that lead is volatilized much slower from the platform than its diffusion from the furnace. As a result, the concentration of lead released from the refractory species is too low to give a noticeable absorbance. As the atomization temperature increased, the second lead peak appeared and became more prominent because of more rapid release of lead from its refractory form.

The thermal stability of 10 ng of lead on the platform in the presence of 8 µg of Pd was examined by varying the ashing temperature using a 0-s ramp and a 15-s hold time with the inert gas flow on. After the ashing step, the temperature sensor was set to 2800 °C, and atomization was carried out to check for the presence of residual lead. Figure 6 illustrates that a small trace of lead remained on the platform after ashing at 1800 °C for 15 s. However, when the ashing temperature was increased to 2400 °C, the amount of residual lead increased. This unusual behavior indicates that the refractory lead species requires a high temperature (2400–2500 °C) for its formation. At lower ashing temperatures lead is lost from the furnace. Confirmation of this is illustrated in Figure 7 where the effect of ashing temperature ramp time on the retention of lead on the platform is examined. If a 0-s ramp time followed by a 15-s hold time is used, then a significant amount of lead is retained on the platform. If a 2-s ramp time followed by a 10-s hold time is used, then, even though the total heating time is 3 s less than with a 0-s ramp, most of the lead is lost from the furnace, i.e., the lead is lost during the ramping process before it has a chance to form a refractory species.

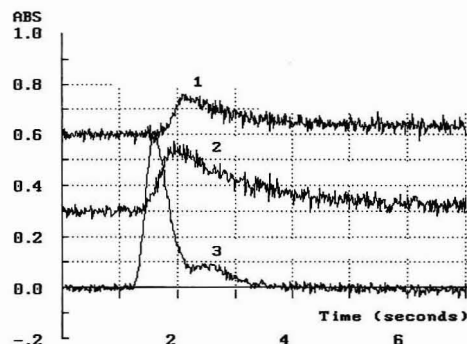


Figure 8. Relative position of the refractory peak (1.4 ng of lead with 8 μ g of palladium) (3) compared with peaks from 0.5 ng of chromium in 1% nitric acid (1) and 2 ng of molybdenum in 10% nitric acid (2). Measurements were made under the same conditions using a new impregnated graphite tube and platform, 8% hydrogen in argon, and an atomization temperature of 2800 $^{\circ}$ C.

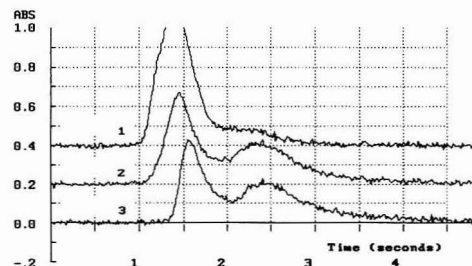


Figure 9. Effect of palladium concentration on absorption profiles of 1.4 ng of lead in 2% nitric acid. Atomization was conducted at 2800 $^{\circ}$ C in an old impregnated graphite platform and tube. Palladium amounts present were (1) 0.08 μ g, (2) 0.8 μ g, and (3) 8 μ g.

The refractory nature of the second lead peak can be qualitatively judged from Figure 8 where a comparison is made with molybdenum and chromium absorption profiles taken under the same conditions with the same tube and platform. The maximum of the second lead peak actually occurred after the maxima of the chromium and molybdenum peaks, indicating an unusually high thermal stability of the refractory lead species. Confirming this conclusion, at an atomization temperature of 2700 $^{\circ}$ C the absorption maximum of 1 ng of palladium in 10% nitric acid using an old impregnated platform precedes that of the second lead peak by about 0.1 s (not illustrated).

Increasing the amount of palladium from 0.08 to 0.8 μ g resulted in an increase in the second absorption peak and a corresponding decrease in the first one (Figure 9). Thus, at least at the low lead concentrations used in this study, a large excess of palladium is needed to maximize the percent of deposited lead forming the refractory species. Once the percent of lead in its refractory form reaches some maximum, however, the addition of more palladium does not substantially alter the magnitude or position of the second lead peak (Figure 9). The insensitivity of the position of the second lead peak to the amount of added palladium suggests that the lead is present as a distinct species prior to release from the surface. Figure 9 also indicates that the refractory peak was not due to artifactual atomic absorption by palladium because increasing the amount of palladium from 0.8 to 8 μ g did not change the magnitude of the second lead peak.

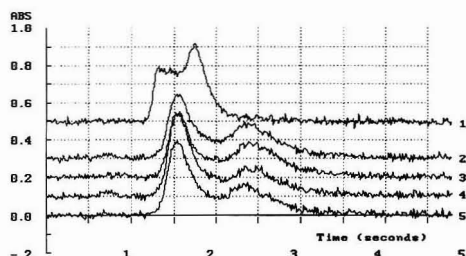


Figure 10. Effect of 4 μ L of different acids on the absorption profile of 1.4 ng of lead with 8 μ g of palladium: (1) 10% sulfuric acid, (2) 1% perchloric acid, (3) 20% hydrochloric acid, (4) 70% nitric acid, and (5) 2% nitric acid. An impregnated graphite platform and tube were used with an atomization temperature of 2800 $^{\circ}$ C and inert gas containing 8% hydrogen in argon.

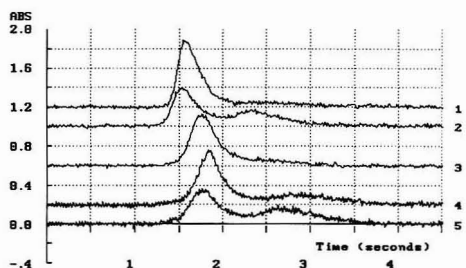


Figure 11. Effects of hydrogen and graphite on the absorption profile of 1.4 ng of lead and 4 μ g of palladium in 2% nitric acid. (1) Uncoated graphite platform and tube in the absence of hydrogen and (2) in the presence of 8% hydrogen in argon. (3) Pyrolytic graphite platform and pyrolytically coated tube with 8% hydrogen in argon. (4) Impregnated graphite platform and tube in the absence of hydrogen and (5) in the presence of 8% hydrogen in argon.

The second lead peak was sensitive to the presence of different chemicals, and the addition of 4 μ L of 15% citric acid, 1% magnesium nitrate or 1% ammonium dihydrogen phosphate caused its disappearance as well as a corresponding increase in the integrated absorbance of the first peak. The addition of 4 μ L of 70% nitric acid or 1% perchloric acid did not significantly affect the magnitude of the second lead peak (Figure 10). Four microliters 10 M hydrochloric acid caused a slight enhancement, while 4 μ L of 10% sulfuric acid resulted in two peaks, both of which appeared before the refractory peak (Figure 10).

Graphite played a role in formation of the second peak. Using the THGA, no second peak was observed unless graphite was actually added to the platform (Figure 4), suggesting that the pyrolytic graphite used for construction of the THGA cuvettes is sufficiently inert to prevent noticeable interaction of the graphite with lead and palladium. On the HGA-400 atomizer, going from an impregnated or uncoated graphite tube and platform to a pyrolytic graphite platform and pyrolytically coated tube in the presence of hydrogen depressed the refractory peak (Figure 11). The magnitude of the second peak depended only on the platform material and did not change when impregnated, uncoated, and pyrolytically coated tubes were interchanged. The shift of both the first and second lead peaks with changes in tube and platform types was likely due (a) to observed slower heating of the uncoated and pyrolytically coated tubes as compared with the impregnated one, and (b) to an additional delay in heating the pyrolytic platform because of its greater mass (0.070 vs 0.077 g for the impregnated one).

Hydrogen played a major role in the formation of the refractory species. Figure 11 shows that for both uncoated and impregnated graphite platforms, the magnitude of the second peak decreased noticeably when no hydrogen was present. Prereduction of palladium by hydrogen during the ashing step does not appear to be the reason for enhancement because neither tube pretreatment (at 450 °C with 8% hydrogen) with palladium nor ashing (at 450 °C with 8% hydrogen) followed by atomization in pure argon enhanced the second peak. Conversely, ashing in pure argon followed by atomization in the presence of 8% hydrogen caused no reduction in the magnitude of the second lead peak when compared with ashing and atomizing in the presence of 8% hydrogen. Thus, enhancement of the refractory peak by hydrogen was only observed when hydrogen was present during the atomization step.

The reduction in lead volatility in the presence of hydrogen is unusual because hydrogen in the absence of palladium usually increases lead volatility, shifting the lead absorption peak to earlier times^{21,22} and facilitating atomization at temperatures as low as 950 °C.²² The opposite effect is observed here, and it is hypothesized that hydrogen is catalytically activating the high-temperature formation of the refractory species.

Importance. The refractory behavior of lead is of importance from two viewpoints. First, the gain in thermal stability for lead is sufficiently high to provide an interesting starting point for material sciences investigations.

Second, the phenomenon is of importance in analytical applications. Reduced palladium has been proposed as a matrix modifier for many elements, including lead.¹⁻³ If this modifier is coupled with the availability of multielement spectrometers, for which atomization temperatures above 2400 °C are not uncommon,^{23,24} then conditions for analytical errors related to the effect are created. For example, at atomization temperatures of 2400–2500 °C, lead absorption reaches an apparent baseline level within about 2.5–3.5 s (Figure 5). Cutting the integration time at this point would result in failure to measure about 50% of the lead present (less if higher atomization temperatures or pyrolytic graphite platforms are used). Also, failure to extend the total heating time (at the atomization temperature) to beyond about 10 s would result in retention of a small portion of lead on the platform so that the integrated absorbance of the next measured solution would be higher than that of the first solution. Finally, it is conceivable that if palladium is used as a matrix modifier, the lead sensitivity in samples and standards will differ because the samples may have constituents (e.g., traces of citrate, phosphate, or magnesium nitrate) which prevent formation of the refractory species.

An example of the above factors is illustrated in Figure 12. Atomizations 1–10, 21–30, and 41–50, performed in the absence of ammonium dihydrogen phosphate, show a generally low integrated absorbance with a gradual increase with each subsequent atomization. These effects appear to be caused by retention and gradual accumulation of a portion of the refractory species on the platform. Atomizations 11–20, 31–40, and 51–60, performed in the presence of ammonium dihydrogen phosphate, show a sharp increase in the integrated absorbance with initial introduction of the phosphate, e.g.,

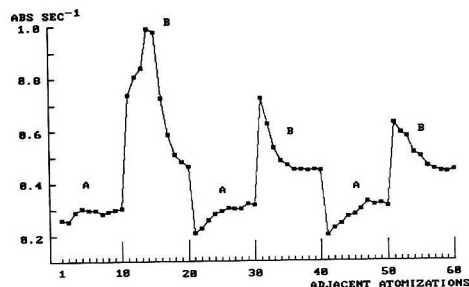


Figure 12. Effect of the analytical sequence on changes of integrated absorbance of 1.8 ng of lead with 4 μ g of palladium in 2% nitric acid atomized at 2400 °C using an older impregnated graphite platform with a 0-s ramp time and 5-s hold time. No clean-out step was incorporated. Atomizations falling under groups B contained 4 μ L of 1% ammonium dihydrogen phosphate, while those in groups A contained none. All the illustrated atomizations were run sequentially using the same tube and platform.

replicate 31 in Figure 12, followed by a gradual decrease to stable readings, e.g., replicates 36–40. The stable readings, however, are at least 30% higher than most readings taken in the absence of the phosphate. As mentioned previously, ammonium dihydrogen phosphate prevents formation of the refractory species. When it is first introduced, it not only prevents formation of the refractory species for the added lead, it also releases some of the refractory lead previously accumulated on the platform, thus explaining the initial high readings and subsequent decrease.

The increasing and decreasing trends have practical analytical importance only if a high-temperature clean-out step to remove accumulated refractory lead is not incorporated in the furnace temperature program. However, in the presence of palladium, even with a clean-out step, the integrated absorbance differences between pure lead solutions and those containing ammonium dihydrogen phosphate (or other chemicals which prevent formation of the refractory species) will remain a source of analytical error. Thus, palladium should not be used as a matrix modifier for lead in situations where the lead refractory species may form.

Explanation of the Refractory Behavior. No definitive conclusion can be reached about the nature of the refractory behavior. On the basis of the data presented, however, the phenomenon appears to be caused by high-temperature formation of a labile refractory species composed of lead, carbon, and palladium.

The major supporting evidence for this, although indirect, is (a) the presence of the refractory behavior on three different models of atomizer, (b) the enhancement of the effect when the surface area of the platform graphite was greatest (uncoated anisotropic graphite or old impregnated graphite), (c) the appearance of the effect in the THGA only after graphite powder was added to platform, (d) the absence of a second peak when platinum was substituted for palladium or when cadmium was substituted for lead in the presence of palladium, (e) the insensitivity of the refractory peak position to palladium concentration, and (f) increased retention of lead on the platform when the ashing temperature with a 0-s ramp time was raised from 1800 to 2400 °C.

Future Studies. Numerous questions about the effect remain unclear: (a) reasons for the strong enhancing effect of hydrogen when it is added to the inert gas during the atomization step; (b) whether or not traces of hydrogen are actually necessary for formation of the species; (c) the stability of the refractory species at various temperatures; (d) the

(21) Ni, Z.-m.; Han, H.-b.; Le, X.-c. *J. Anal. At. Spectrom.* 1986, 1, 131–134.

(22) Gilchrist, G. F. R.; Chakrabarti, C. L.; Byrne, J. P. *J. Anal. At. Spectrom.* 1989, 4, 533–538.

(23) Harnly, J. M.; Miller-Ihni, N. J.; O'Haver, T. C. *Spectrochim. Acta* 1984, 39B, 305–320.

(24) Lundberg, E.; Frech, W.; Harnly, J. M. *J. Anal. At. Spectrom.* 1988, 3, 1115–1119.

activation energy of the refractory species as well as its composition; and (e) the nature of the species, i.e., whether the species is a solid-phase solution or crystal structure and whether chemical binding is involved.

Suggestions as to future experimental approaches include (a) X-ray diffraction and X-ray photoelectron spectroscopy; (b) the use of capacitive discharge or metal-tube atomizers to effect more rapid heating and cooling in the presence of a platform; and (c) the use of thinner platforms to effect more rapid heating and cooling.

ACKNOWLEDGMENT

Thanks are due to B. Marchand, L. Bigras, and C. G. Gillette-Welling of the Medical Services Branch, Health and Welfare Canada, for the use of their Perkin-Elmer Model 4100-ZL spectrometer and THGA furnace.

RECEIVED for review March 3, 1992. Revised manuscript received June 30, 1992. Accepted July 23, 1992.

Registry No. Lead, 7439-92-1; palladium, 7440-05-3; graphite, 7782-42-5.

Determination of Inorganic Halogen Species by Liquid Chromatography with Inductively Coupled Argon Plasma Mass Spectrometry

Valeri V. Salov,[†] Jun Yoshinaga, Yasuyuki Shibata, and Masatoshi Morita*

National Institute for Environmental Studies, 16-2 Onogawa, Tsukuba, Ibaraki 305, Japan

An analytical procedure based on inductively coupled argon plasma mass spectrometry and high-performance liquid chromatography is developed for a determination of six inorganic halogen anions IO_3^- , BrO_3^- , Cl^- , ClO_3^- , Br^- , I^- . Absolute detection limits for I^- , Br^- , and Cl^- species are 25 pg, 0.8 ng, and 36 ng, respectively. The injection volume can be changed in the interval 1–25 μL . The method has been applied to the analysis of drinking water, "Miso" soup, and human urine. Three unidentified halogen compounds are detected in human urine by the developed method. Limits of detection and a sensitivity of the procedure are discussed.

INTRODUCTION

Halogens are important elements in the chemical industry. Many industrial materials contain and are produced from halogen compounds. Halogen compounds are also important in life processes as osmolytes, for maintaining ion balance, hormonal function, etc. Trace analysis of halogen species is thus important for industrial purposes, for understanding geochemical cycles of the elements and for the understanding of their nutritional and toxicological implications. Recently developed inductively coupled plasma mass spectrometry (ICP-MS) is known to be an extremely sensitive method for the analysis of metals^{1–8} and nonmetallic elements.^{1,7,9} Bromine and iodine are elements that can be sensitively determined by ICP-MS.¹⁰

Combining ICP-MS or atomic emission spectrometry with modern liquid chromatographic techniques is an effective method of speciation analysis.^{1,9,11} The present paper is devoted to the application of high-performance liquid chromatography (HPLC) with ICP-MS detection to the trace determination of halogen species in aqueous samples.

EXPERIMENTAL SECTION

Reagents. Potassium iodide, iodate, bromide, bromate, chloride, chlorate, and perchlorate ("G" grade) were obtained from Kanto Chemical Co. Inc., Japan. Potassium periodate and ammonia solution ("AAS" grade) were obtained from Wako Pure Chemical Industries, Ltd., Japan. Tetramethylammonium hydroxide (TMAH) and malonic acid ("GR" grade) were supplied

by Nacalai Tesque, Inc., Japan. The reagents were used without further purification. Other reagents were of the highest grade commercially available.

Standard Solutions. Stock solutions (0.0500 M) for each anion were prepared. A working Standard Solution (mixture of 5×10^{-5} M IO_3^- , I^- , 5×10^{-4} M BrO_3^- , Br^- , and 5×10^{-3} M Cl^- , ClO_3^-) was prepared each week from stock solutions.

Sample Preparation. A sample (8 mL) of "Miso" soup was centrifuged and filtered (Minisart NML, 0.45 μm , Sartorius GmbH, Germany). Other samples were used without any preparation.

HPLC. A Perkin-Elmer 410 Bio LC system was used with HPLC columns GS-220M, GS-220H, and GS-220 (gel-permeation, 7.6-mm i.d. \times 100, 250, and 500 mm, respectively; Asahi Chemical Industry Co., Ltd., Japan). The column outlet was connected by a short Teflon tube (i.d. 0.25 mm) to the inlet of the pneumatic nebulizer. The eluent flow rate was 1 mL/min. Samples (aqueous solutions) were injected with a 25- μL syringe (Hamilton).

ICP-MS. The operation conditions of the ICP-MS (PMS-2000, Yokogawa Electric, Japan) were as follows: Ar flow rate nebulizer 0.78 L/min, auxiliary 0.5 L/min, plasma 13 L/min; sampling height, 4.5 mm from top of the induction coil; power, 1.3 kW; spray chamber cooling temperature, 5 °C.⁹ The following isotopes were monitored: $^{127}\text{I}^+$, $^{79}\text{Br}^+$, $^{35}\text{Cl}^+$.

Calculations. The chromatogram peak areas and retention times were calculated by using PMS-2000 Yokogawa software and an NEC PC-9801RA computer with an Intel 80386 CPU. Special simulation and statistics programs in C were developed by means of Borland C++ software (Borland International). The PC-8041 computer with Intel 80386 CPU (Sharp Co.) was used for these calculations.

RESULTS AND DISCUSSION

Separation of Halogen Anions. Iodine is the most interesting halogen for ICP-MS since it can be very sensitively determined. The chromatographic behavior of IO_3^- and I^- has been described.^{12–14} In order to establish appropriate separation conditions, an ion chromatographic procedure¹² was examined. By this method, however, the adsorption isotherm for I^- already showed a nonlinear shape at 10^{-5} M. It was also noted that the retention time was long (more than 30 min) and depended on the concentration. For these reasons, it was considered not appropriate to apply these chromatographic conditions to low-concentration analysis. During the search for good separation conditions, it was found that the use of an Asahipak GS-220 gel permeation column with 0.025 M TMAH, 0.025 M malonic acid buffer solution adjusted to pH 6.8 by NH_4OH made it possible to separate IO_3^- and I^- . Using a 500-mm length column, the total analysis time was about 25 min. In order to reduce retention times, 36 TMAH-malonic acid-ammonia buffer solutions with different compositions and 3 columns with different lengths

[†] Visiting scientist from Vernadsky Institute of Geochemistry and Analytical Chemistry, ul. Kosygina 19, 117975 GSP-1, Moscow, Russia.

(1) Thompson, J. J.; Houk, R. S. *Anal. Chem.* 1986, 58, 2541–2548.

(2) Gray, A. L. *Spectrochim. Acta, Part B* 1985, 40B, 1525–1537.

(3) Douglas, D. J.; Houk, R. S. *Prog. Anal. At. Spectrosc.* 1985, 8, 1–18.

(4) Fassel, V. A. *Fresenius' Z. Anal. Chem.* 1986, 324, 511–518.

(5) Vaughan, M. A.; Horlick, G. *Appl. Spectrosc.* 1986, 40, 434–460.

(6) Houk, R. S. *Anal. Chem.* 1986, 58, 97–105.

(7) Date, A. R.; Cheung, Y. Y.; Stuart, M. E. *Spectrochim. Acta, Part B* 1987, 42B, 3–20.

(8) Houk, R. S.; Thompson, J. J. *Mass Spectrom. Rev.* 1988, 7, 425–461.

(9) Shibata, Y.; Morita, M. *Anal. Sci.* 1989, 5, 107–109.

(10) Olivares, J. A.; Houk, R. S. *Anal. Chem.* 1986, 58, 20–25.

(11) Morita, M.; Uehiro, T. *Anal. Chem.* 1981, 53, 1997–2000.

(12) Oikawa, K.; et al. *Ion Chromatography*; Kyoritsu Shuppan: Tokyo, 1988 (in Japanese).

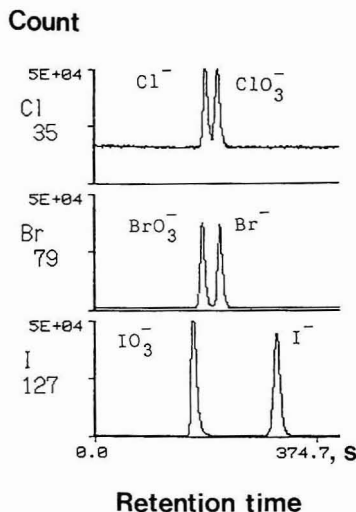
(13) Mullins, F. *Analyst* 1987, 112, 665–671.

(14) Ito, K.; Shoto, E.; Sunahara, H. *J. Chromatogr.* 1991, 549, 265–272.

Table I. Retention Times (s) of Investigated Species, $p = 0.95^a$

species	GS-220M	n	GS-220	n
IO_3^-	166.1 \pm 0.4	6		
IO_3^-	166.1 \pm 0.1	32		
BrO_3^-	180.4 \pm 0.5	23	781 \pm 13	2
Cl^-	186.4 \pm 0.6	12	829 \pm 5	3
ClO_3^-	207.7 \pm 0.5	12		
Br^-	210.9 \pm 0.8	23	958 \pm 4	3
I^-	304.8 \pm 0.2	32	1462 \pm 6	3
I compound	199.5 \pm 1.4	7	not detected	3
Br compound-1			701 \pm 12	3
Br compound-2	171.4 \pm 0.7	21	748 \pm 3	3

^a The total extra column delay 7.9 \pm 1.6 s is not subtracted from the retention time.

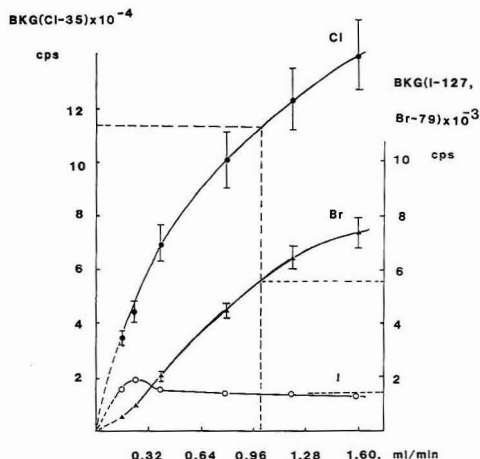
**Figure 1.** Separation of six halogen anions (GS-220M, 10 μL of the mixed solution containing 5×10^{-3} M Cl^- , ClO_3^- , 5×10^{-4} M BrO_3^- , Br^- , and 5×10^{-5} M IO_3^- , I^-).

were investigated. The retention mechanism of the 7 anions under investigation was considered to be an ion pair/hydrophobic interaction.

For the simultaneous and quick (5-min) determination of six anions (IO_3^- , BrO_3^- , Cl^- , ClO_3^- , Br^- , I^-), 0.05 M malonic acid + 0.0375 M TMAH buffer solution and a GS-220M column were used (Table I, Figure 1). These conditions were a compromise between the number of determinants and the analysis time. The total analysis time could be reduced to 2.5 min, if it was required to determine IO_3^- and I^- only.

Background. The background count directly influences the limit of detection in ICP-MS. It depends on many factors including possible ultratrace concentrations of halogen species in pure water and reagents, spectral interference by molecular ions and photons, memory effects, and so on.

The background count from pure water depends on the flow rate, as shown in Figure 2. The data were obtained by use of the Yokogawa PMS-2000 instrument's own peristaltic pump. In the present work, it was observed that the background standard deviation depended linearly on the total count. One equation could be applied to all three halogens: $\text{SD}_{\text{Bkg}} (\text{cps}) = (0.094 \pm 0.004) \text{Bkg} (\text{cps}) - (68 \pm 197)$; $n = 18$; $r = 0.997$; $s_0 = 332$ (the intercept is simply zero).

**Figure 2.** Dependence of the background count from pure water on the flow rate.

Background signals decreased in the order $^{37}\text{Cl} \gg ^{35}\text{Cl} \gg ^{81}\text{Br} > ^{79}\text{Br} > ^{127}\text{I}$. When we consider that the isotope abundance of ^{35}Cl is higher than ^{37}Cl and that of ^{79}Br is almost the same as ^{81}Br , spectral interferences at $m/e = 37$ and 81 can be present.

Pure water or 1 N nitric acid were used to wash the ICP-MS tube connections to suppress memory effects. There was no difference between them if the concentration of the iodine species was less than 5×10^{-5} M. Chromatographic memory effects tended to appear if the columns were not used for several days. In this case 3–4 h of blank operation was needed to wash the columns.

Calibration Curves. Calibration curves for six ion species were straight lines. The chemical form of the element had no influence on the ICP-MS response; i.e. the response (peak area) was the same for the element within each of the following pairs (IO_3^- , I^-), (BrO_3^- , Br^-) and (Cl^- , ClO_3^-). The data for each pair were therefore combined, and three calibration curves for I, Br, Cl were obtained (the second strings for I and Br and a string for Cl in the Table II). With 60 points covering large concentration intervals (0.0002–0.5 nmol) the calibration curve was linear with a small negative intercept for I. This was critical for low-concentration determinations. To obtain more accurate results, it was better to use different calibration curves for low and high concentrations. The situation was the same for Br. For iodine the concentration range (0.0002–0.03 nmol) of the calibration was better suited to trace-level determinations. The injection volume could be changed within the range 1–25 μL without altering retention times and peak widths.

Sensitivity. The measure of the sensitivity is the slope of the calibration curve. Other conditions being equal, it depends on the number density of the detected ions in the plasma.¹⁵ The degree of ionization α can be used for relative sensitivity estimations. The α values for 79 elements at $T = 7500$ K, and electron density $n_e = 10^{15} \text{ cm}^{-3}$ have been calculated⁶ from the Saha equation.¹⁵ Expected relative sensitivities for I, Br, and Cl did not match the observed

(15) Boulos, M. M.; Barnes, R. M. In *Inductively Coupled Plasma Emission Spectroscopy*; Boumans P. W. J. M., Ed.; John Wiley & Sons: New York, 1987; Part 2, pp 289–352.

(16) Korn, G. A.; Korn, T. M. *Mathematical Handbook for Scientists and Engineers*; McGraw-Hill Book Co.: New York, 1968.

Table II. Used Calibration Line Parameters, Y (Peak Area Count) = bX (mol) + a , $p = 0.95^a$

atom	a	10^{-12b}	n	r	s_0	interval, nmol
I	248 ± 169	1030 ± 20	42	0.999	436	0.0002–0.03
	–1777 ± 1308	1174 ± 8	60	1.000	4583	0.03–0.5
Br	50 ± 290	62 ± 1	30	0.999	539	0.002–0.5
	–1531 ± 779	67.6 ± 0.4	42	1.000	2168	0.5–5
Cl	21 ± 2382	6.05 ± 0.09	24	0.999	4243	2–3000

^a n = number of points, r = correlation coefficient, s_0 = standard deviation from line.**Table III.** Analyzed Samples

no.	sample	place or man	date	time of sampling	analysis time
I	drinking water	National Institute for Environmental Studies, Tsukuba	91.12.17	7:15 p.m.	7:32 p.m.
II	drinking water home	Tsukuba, Ibaraki 305	91.12.18	8:00 a.m.	10:50 a.m.
III	Japanese soup "Miso"	Institute Restaurant	91.12.18	0:15 p.m.	2:20 p.m.
IV	human urine	girl	91.12.18	9:30 a.m.	11:20 a.m.
		1 year and 5 months			
V	human urine	boy	91.12.17	10:05 p.m.	1:10 p.m.
		3 years and 2 months			next day
VI	human urine	man	91.12.17	8:15 p.m.	8:30 p.m.
		31 years			

sensitivities quantitatively, but there was a qualitative agreement.

Limits of Detection. Limits of detection may be determined by peak height or peak area. The conventional way of defining the detection limit from the peak height is to use S/N (signal height to noise level) = 2. Very small peaks with $2\sigma_{Bkg}$ height from I, Br, and Cl can be detected if these elements are present in absolute amounts 0.2 pmol, 10 pmol, and 1 nmol and 25 pg, 0.8 ng, and 36 ng respectively.

Peak area detection limits could be determined as peak width $\times 3\sigma_{Bkg}$ (at flow rate 1 mL/min, σ_{Bkg} for I, Br, and Cl were 73, 449, and 10 550 cps, respectively; Figure 2 and the above-mentioned σ_{Bkg} (Bkg) dependence). By using 12 s for peak width (in this experiment, a condition was selected in which 30% of the total time was spent monitoring each of the three elements while the remaining 10% was spent switching the mass condition from one element to the next), we obtained a detection limit peak area count of 788 (I), 4849 (Br), and 113 940 (Cl). This corresponded to detection limits for I, Br, and Cl of 0.52 pmol, 77 pmol, and 19 nmol and 66 pg, 6.2 ng, and 0.67 μ g, respectively.

Calibration line parameters can be used for the estimation of detection limits.¹⁷ This method gave values between those described above.

Application. Several samples were analyzed (Tables III–V). Drinking water contains a small amount of IO_3^- but not I^- . Iodate may be present as the result of purification of water (chlorination). The dominant existence of IO_3^- is also found in German mineral water.¹⁸ In soup prepared from drinking water (sample III) we found I^- but not IO_3^- . Long heating with "organic" compounds may cause the reduction of $IO_3^- \rightarrow I^-$. The total amount of iodine in sample III is more than that in sample I. Bromide was found in high concentrations. The excess amount of Br⁻ was considered to come from food materials.

The concentrations of halogen species in human urine can depend on the water and food consumed, the time of the day the sample was taken, urine volume, and many other factors. Br⁻ and I⁻ concentrations in urine in this experiment were

Table IV. Concentrations of Different Species in the Analyzed Samples, $n = 6$, $p = 0.95$

sample no.	$IO_3^- + IO_4^-$ $10^6 C$, M (ppb)	I^- $10^6 C$, M (ppb)	Br ⁻ $10^6 C$, M (ppm)	Cl ⁻ $10^6 C$, M (g/L)
I (20)	4.1 ± 0.5 (5.2 ± 0.6)	not found	not found	0.918 ± 0.001 (3260 ± 4) × 10 ⁻⁵
II (20)	2.5 ± 0.5 (3.2 ± 0.6)	not found	not found	0.780 ± 0.001 (2734 ± 4) × 10 ⁻⁵
III (5)	not found	9.3 ± 1.8 (12 ± 2)	7.38 ± 0.07 (5.90 ± 0.06)	150 ± 2 (5.33 ± 0.08)
IV (5)	not found	33 ± 2 (42 ± 1)	6.35 ± 0.05 (5.08 ± 0.04)	107 ± 2 (3.81 ± 0.06)
V (5)	not found	26 ± 2 (34 ± 2)	4.87 ± 0.02 (3.90 ± 0.02)	78 ± 1 (2.78 ± 0.04)
VI (5)	not found	83 ± 1 (106 ± 1)	17.59 ± 0.06 (14.07 ± 0.05)	270 ± 4 (9.6 ± 0.1)

Table V. Concentrations (ppb) of Unidentified Compounds in the Analyzed Samples, $p = 0.95$

sample no.	I Compound	n	Br compound first	Br compound second	n	column
IV (25)	not detected	3	60.8 ± 10	184 ± 7	3	GS-220
			total			
IV (25)	2.0 ± 0.5	8	357 ± 40		4	GS-220M
V (5)	not detected	6	285 ± 48		6	GS-220M
VI (5)	not detected	6	1611 ± 20		6	GS-220M

Table VI. Molar Concentration Relations for Some Species

sample	Cl ⁻ :Br ⁻	Br ⁻ :I ⁻	Cl ⁻ :I ⁻	Br ⁻ :(unknown, 1 + 2)
III	2.03 × 10 ⁴	794	1.62 × 10 ⁶	not found
IV	1.69 × 10 ⁴	192	3.24 × 10 ⁶	16.5
V	1.60 × 10 ⁴	187	3.00 × 10 ⁶	17.1
VI	1.53 × 10 ⁴	212	3.25 × 10 ⁶	8.7

similar to reported data.¹⁹ It is interesting to note that the ratio of Cl⁻, Br⁻, and I⁻ seems rather constant (Table VI).

Unidentified Compounds. With the GS-220M column, a peak was observed close to the bromate peak in urine samples IV–VI (Table I). From statistical analysis of repeated retention time measurements, it was shown that the peak was not bromate. This was further checked and proved by

(17) Doerfel, K. *Statistika v analiticheskoj Khimii*; Moskva: Mir: Moskva, 1969 (in Russian).

(18) Heumann, K. G.; Seewald, H. *Fresenius' Z. Anal. Chem.* 1985, 320, 493–497.

(19) Iyengar, G. V.; Kollmer, W. E.; Bowen, H. J. M. *The Elemental Composition of Human Tissues and Body Fluids*; Verlag Chemie: New York, 1978.

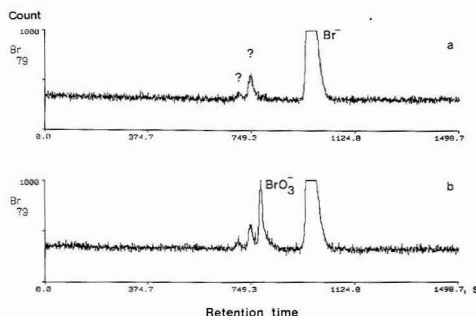


Figure 3. Separation of Br compounds (GS-220, 25 μ L): (a) sample IV; (b) sample IV containing 7.5×10^{-6} M added BrO_3^- .

use of a longer column. With a long column, the "unknown" peak was shown to be composed of at least two different compounds (Figure 3). When the injection volume was increased to 25 μ L, a very small but definite "unknown" peak appeared in the iodine window (Figure 4). Concentrations were estimated on the basis that an "unknown" molecule contained one iodine or bromine atom (Table V). The identification of these compounds is a subject of further study. The present method will have a wide range of applications in the fields of biological and environmental science.

CONCLUSION

Inorganic halogen species can easily be determined by ICP-MS coupled with liquid chromatography. The sensitivity of the ICP-MS detector is very high and greater than that of other detectors¹²⁻¹⁴ for Br and I. Halogens are selectively determined by ICP-MS. They can be rapidly separated and analyzed with minimal preparation procedures.

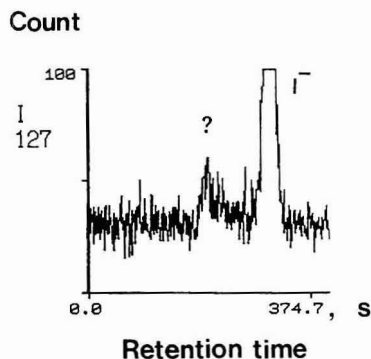


Figure 4. Chromatogram of the sample IV (GS-220M, 25 μ L).

ACKNOWLEDGMENT

V.S. thanks the Science and Technology Agency of Japan, Japan Research Development Co., and Japan International Science and Technology Exchange Center for financial support in the form of a postdoctorate research fellowship. We thank Dr. N. Furuta for discussion about plasma equilibria and Dr. T. Uehiro for the consultations dealing with the NEC graphics adapter.

RECEIVED for review March 10, 1992. Accepted June 22, 1992.

Registry No. IO_4^- , 15056-35-6; IO_3^- , 15454-31-6; BrO_3^- , 15541-45-4; Cl^- , 16887-00-6; ClO_3^- , 14866-68-3; Br^- , 24959-67-9; I^- , 20461-54-5; H_2O , 7732-18-5.

Photoacoustic Spectroscopy and the Effect of Amplified Spontaneous Emission

Gregory L. Klunder, Robert J. Silva,[†] and Richard E. Russo*

Lawrence Berkeley Laboratory, MS 90-2024, Berkeley, California 94720

Amplified spontaneous emission (ASE), which results from dye fluorescence, causes pulsed dye lasers to produce an output that is spectrally impure. The effect of such an output can create inaccurate analytical information, particularly in absorption and photothermal spectroscopies. The spectral output of laser dye LD-466 has been characterized. ASE was shown to have a broad-band spectral output, 445–495 nm, and was most intense when lasing was inefficient, on the edges of the dye gain curve. A 10^{-3} M Pr^{3+} solution produced similar photoacoustic waveforms from lasing and ASE. Linear calibration curves were generated with the laser tuned to 468 and 495 nm. At 495 nm Pr^{3+} has no absorbance and the photoacoustic signals were produced from ASE.

INTRODUCTION

The ability to select lasing wavelengths over a broad spectral range makes dye lasers versatile light sources for the analytical chemist. Laser dyes are available which cover wavelengths from around 400 nm to greater than 900 nm with some individual dyes spanning as much as 80 nm. In high-gain short-pulse dye lasers the broad tuning range of the dye can result in an output which is not spectrally pure.¹ Amplified spontaneous emission (ASE), a broad-band spectral background resulting from the dye fluorescence, exhibits laserlike properties (e.g. low divergence and spectral narrowing),² reduces the laser efficiency, and increases background noise in the laser output.^{2–7} Dye lasers operate most efficiently at the maximum of the dye gain curve. As the laser is tuned toward the extremes of the dye gain curve, the lasing efficiency is reduced and the amount of ASE increases. Minimization of ASE can be attained by reducing the number of amplifier stages in the laser cavity with a trade-off of reduced power.

Many studies have concentrated on the fundamentals of ASE without much focus on its effect on analytical experiments.^{1–6,8} Nogar and Keller⁹ described the effects of laser sidebands on resonant ionization mass spectroscopy of lutetium. Their study concentrated on a narrow bandwidth (50 cm^{-1}) around the laser line. In ours and other laboratories,^{10–13} a pulsed dye laser is routinely used to perform

photoacoustic spectroscopy. Spectra of the analyte under different matrix conditions are collected and used to determine complexation information. Thus, a nonspectrally pure output of the dye laser could alter the spectra. In this study, we examined the spectral output for a laser dye, LD-466, over the operating range of the dye. The ASE is shown to generate a photoacoustic signal and provide a linear calibration curve similar to a lasing line.

EXPERIMENTAL SECTION

Dye Laser Spectra. The experimental setup used to study the spectral output of the dye laser is shown in Figure 1. A pulsed (20 pulses/s) Nd:YAG laser (Spectra Physics, Model DCR-3) was used to pump a tunable dye laser (Spectra Physics, Model PDL-2). The Spectra Physics dye laser has separately transverse-pumped oscillator, amplifier, and preamplifier cells. Wavelength selection is achieved in the oscillator by changing the angle of a grating (600 lines/mm) which is in the Littrow configuration and is fully illuminated with a prism beam expander. Each dye cell increases the output power, but will also add to the amount of ASE. The major contribution to ASE was from the preamp. In studies where the preamp of the dye laser was not involved, the Nd:YAG pump beam was blocked from irradiating the preamp dye cell instead of removing it from the optical path, assuring the same alignment of the laser. A grating acting as the back mirror of the laser cavity determines the output wavelength. The dye laser spectral output should be Lorentzian with a line width of 0.07 cm^{-1} .

The dye laser beam was scattered off of a diffuser and the image of the scattered beam was aligned slightly off center of the entrance slits (20 μm) of the 0.85-m double monochromator (SPEX Model 1404, 1800 lines/mm grating) to avoid saturation of the PMT. Two neutral density filters (ND 1 and 2, optical density 1 and 3, respectively) were also needed when scanning the laser line (as in Figure 2) to avoid saturation of the PMT. An optical density of 1 (ND 1) was used to study the ASE with the preamplifier stage in the dye laser. Scattered light off the prism was observed by a fast photodiode (United Detector Technology, Model PIN-10DFP) which was used to monitor fluctuations in the pulse power of the dye laser. A gated integrated boxcar averager (Stanford Research Systems, Model SR250, 50- Ω input impedance) was used to acquire the signal from the photodiode. The width of the boxcar was 6 ns, which is approximately the width of the laser pulse. An IBM-PC recorded the measurements on a pulse-by-pulse basis with an A/D board (Data Translation, Model DT-2801A). At each wavelength, 50 pulses were averaged to yield the laser output spectra.

Photoacoustic Spectroscopy (PAS). The photoacoustic spectroscopy setup has been described previously.¹³ Briefly, the tunable pulsed dye laser beam passes through a rectangular cuvette containing the analyte solution. A piezoelectric crystal attached to the bottom of the cuvette monitors the amplitude of the thermal expansion pulse generated by the optical absorption and nonradiative relaxation of the analyte species. In these experiments praseodymium was chosen as the analyte. Laser

[†] Lawrence Livermore National Laboratory, L-234, Livermore, CA 94550.

(1) Przybylski, M.; Otto, B.; Gerhardt, H. *Appl. Phys. B* 1989, 49, 201–203.

(2) Ganiel, U.; Hardy, A.; Neumann, G.; Treves, D. *IEEE J. Quantum Electron.* 1975, 11, 881–892.

(3) Nair, L. G.; Dasgupta, K. *IEEE J. Quantum Electron.* 1985, 21, 1782–1794.

(4) Haag, G.; Munz, M.; Marowsky, G. *IEEE J. Quantum Electron.* 1983, 19, 1149–1160.

(5) Lowenthal, D. D.; Eggleston, J. M. *IEEE J. Quantum Electron.* 1986, 22, 1165–1173.

(6) Dujardin, G.; Flamant, P. *Opt. Commun.* 1978, 24, 243–247.

(7) Johnston, T. F., Jr. *Encyclopedia of Physical Science and Technology*; Academic: New York, 1987; Vol. 14, pp 96–141.

(8) Allen, L.; Peters, G. T. *Phys. Lett. A* 1970, 31, 95–96.

(9) Nogar, N. S.; Keller, R. A. *Anal. Chem.* 1985, 57, 2992–2993.

(10) Schrepp, W.; Stumpe, R.; Kim, J. I.; Walther, H. *Appl. Phys. B* 1983, 32, 207–209.

(11) Beitz, J. V.; Bowers, D. L.; Dextader, M. M.; Maroni, V. A.; Reed, D. T. *Radiochim. Acta* 1988, 44/45, 87–93.

(12) Pollard, P. M.; Liezers, M.; McMillan, J. W.; Phillips, G.; Thomason, H. P.; Ewart, F. T. *Radiochim. Acta* 1988, 44/45, 95–101.

(13) Torro, R. A.; Palmer, C. E. A.; Baisden, P. A.; Russo, R. E.; Silva, R. J. *Anal. Chem.* 1990, 62, 298–303.

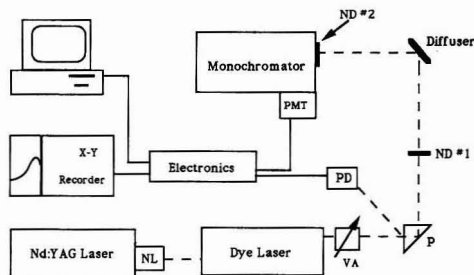


Figure 1. Experimental setup for measuring ASE. Key: ND = neutral density filters, PD = photodiode, NL = nonlinear crystals, VA = variable attenuator, PMT = photomultiplier tube, P = prism (ASE experiments) or photoacoustic cell (PAS experiments).

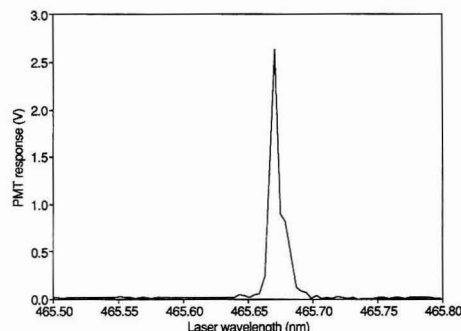


Figure 2. Laser scan in 0.005-nm increments with monochromator set at 466 nm with two neutral density filters, OD 1.0 and 3.0.

dye LD-466 (Exciton) with an operating range from 445 to 495 nm was found to be suitable to overlap the 468- and 481-nm absorption bands of praseodymium. The dye was prepared in 1 L of methanol with 1 g of DABCO¹⁴ added to extend the lifetime of the dye. A high-power variable attenuator (NRC Model 935-5) was placed between the dye laser and the cuvette to control the laser power. The average laser power was measured with a power meter (Scientech 365 with a Model 380101 head).

Conventional Spectroscopy. The absorbance spectrum of praseodymium was obtained using an IBM Model 9420 UV/vis spectrophotometer. A 0.04 M Pr³⁺ in 0.1 M HClO₄ sample was referenced with a 0.1 M HClO₄ solution.

Reagents. A 1000 ppm stock solution of Pr³⁺ was prepared from the chloride salt (Fisher Scientific) in 0.1 M perchloric acid. A series of analyte solutions were prepared from the stock solution.

RESULTS AND DISCUSSION

To demonstrate the influence of ASE on photoacoustic spectroscopy, the spectral output over the lasing profile of the dye, LD-466, was characterized. A series of wavelength scans was recorded, first by tuning the dye laser with the monochromator at a fixed wavelength (Figures 2 and 3) and then by scanning the monochromator with the laser at a fixed wavelength (Figure 4). These results provide information as to where in the dye gain curve ASE starts to appear and the spectral range that it covers. The broad-band spectral output from the ASE is expected to follow the gain curve (fluorescence) of the dye. Thus, as the dye laser is tuned to wavelengths on the ends of the dye gain curve (less efficient lasing), the ASE can be observed by setting the monochromator to a wavelength in the center of the gain curve.

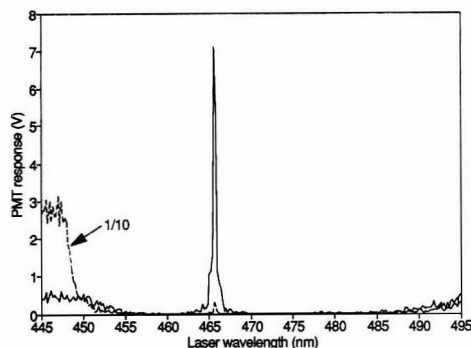


Figure 3. Laser scan in 0.2-nm increments with monochromator set at 466 nm, without (solid) and with (dashed) the preamplifier in the dye laser and a neutral density filter (OD = 1).

For Figure 2, the monochromator was set to 466 nm and the dye laser was tuned over this region with the smallest allowable increments of the dye laser grating, 0.005 nm. The spectrum shows that the 466-nm dye laser peak actually appears at 465.67 nm and has a fwhm of 0.007 nm with a shoulder on the red side of the peak. The wavelength mismatch is due to the laser scanning controls being slightly out of calibration; however, this has no significant effect on the results. The specifications for the PDL-2 indicate the line width should be 0.07 nm (0.0015 nm at 466 nm) and have a Lorentzian profile. The monochromator band-pass (20 μ m slits, 0.2 cm⁻¹, 0.004 nm at 466 nm) and scanning increments of the dye laser contribute to the measured line width and the shoulder. Two neutral density filters which reduced the total intensity by 4 orders of magnitude were used to prevent saturating the PMT. In the narrow spectral region around the 466-nm laser line, the peak of the dye gain profile, amplified spontaneous emission does not seem to be present in any significant amount due to the high efficiency of lasing.

The 466-nm wavelength was monitored over the operating range of LD-466; the dye laser was tuned from 445 to 495 nm in 0.2-nm increments with the monochromator at 466 nm (Figure 3). When the laser is not tuned to 466 nm, the light that is recorded by the PMT is strictly due to ASE. The ASE starts to appear when the dye laser is tuned to wavelengths less than 455 and greater than 485 nm. The spectrum represented by the dashed curve was obtained with 5 mW of average lasing power (measured at the peak lasing wavelength, 466 nm) without the preamplifier cell in the dye laser. The solid curve represents the spectrum with the preamp in the laser and using the same power. In the latter case a neutral density filter (OD = 1) was required to prevent the ASE at the shorter dye laser wavelengths from saturating the PMT. Without the preamplifier, no neutral density filter was needed. Including the preamplifier increased the amount of ASE at 445-nm dye laser wavelength by 60-fold. The true magnitude of the laser line was shown in Figure 2 and is not represented here due to inexact overlap of the monochromator wavelength with the dye laser scan rate. In obtaining these spectra, the neutral density filters which were used for obtaining the data in Figure 2 have been eliminated. The actual magnitude of the laser line would be 3 and 4 orders of magnitude larger than is shown with and without the preamp, respectively. The laser line width appears to be broad with a shoulder on the blue side of the peak, again due to the band-pass of the monochromator and the tuning of the dye laser.

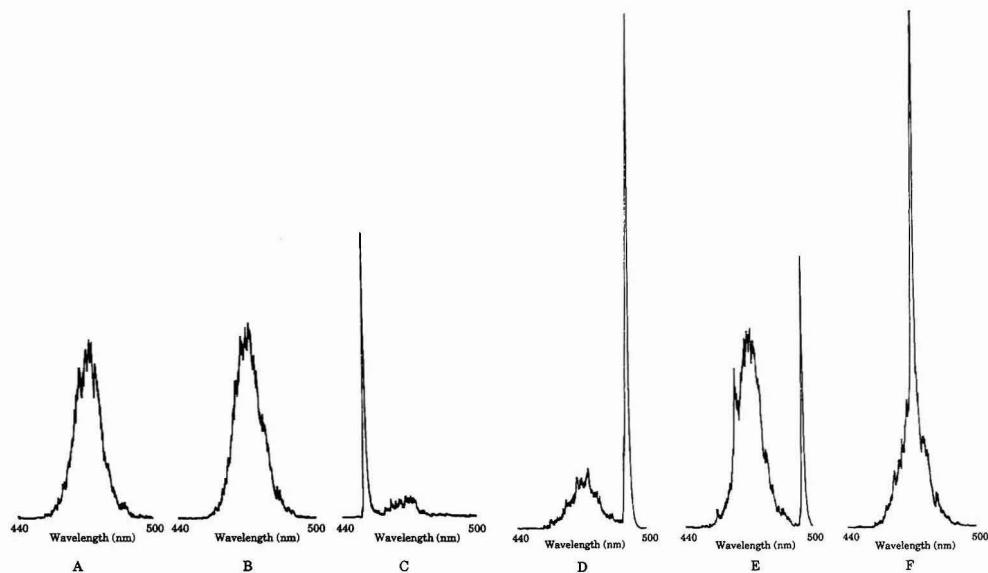


Figure 4. Spectra obtained by scanning the monochromator with the dye laser set at fixed wavelengths: (A) 440 nm, (B) 445 nm, (C) 450 nm, (D) 490 nm, (E) 495 nm, (F) 500 nm.

To show the broad-band output of the ASE, the dye laser was set at a wavelength while the monochromator was scanned from 440 to 500 nm; several spectra are presented in Figure 4. These spectra were obtained without the preamplifier cell in the dye laser (minimal ASE) and by keeping all the recording settings constant. With the laser at 440 or 445 nm (A, B), no lasing was observed and the ASE has a noisy spectral output that spans from 445 to 495 nm, i.e. the gain profile of the LD-466 dye. Setting the laser to 450 nm (C), lasing was observed and ASE was still present, although reduced significantly. On the high end of the dye gain curve, a similar trend was expected as the dye laser was set to nonlasing wavelengths. In Figure 4D, with the dye laser set at 490 nm, a strong lasing line with a small amount of broad-band ASE was present. When the dye laser was set further out on the dye gain curve at 495 nm (E), a weak lasing line and increased amount of ASE were observed. With the dye laser set to 500 nm, off the dye gain curve, it was expected that a large amount of ASE and no lasing would be present. As seen in Figure 4F, a surprise lasing line appeared at 472 nm, in the middle of the broad-band ASE. This anomaly has been attributed to a "grating ghost" which diffracts light at 472 nm when the grating is tuned to 500 nm, as well as light at 500 nm. Gratings which have been mechanically ruled are prone to imperfections, resulting in grating ghosts. The ghost wavelength is much weaker than the desired wavelength and is offset by some increment, in this case approximately 28 nm. In Figure 4E, a peak appears on the blue side of the broad-band ASE at 467 nm, which is 28 nm less than the 495 nm to which the dye laser is tuned. When the dye laser is tuned to 500 nm (F), the 472-nm ghost increases the efficiency of the laser cavity at that wavelength to the point where lasing is stimulated. Spectra obtained with the preamplifier cell in the dye laser showed the ASE to have similar spectral characteristics with increased intensity.

Pulse-to-pulse variations of the laser intensity during experiments are monitored with a fast photodiode which has a flat response ($\pm 7\%$) over a spectral range of 450–950 nm. The response of the photodiode will be the sum of all the light in the wavelength response range, which includes both

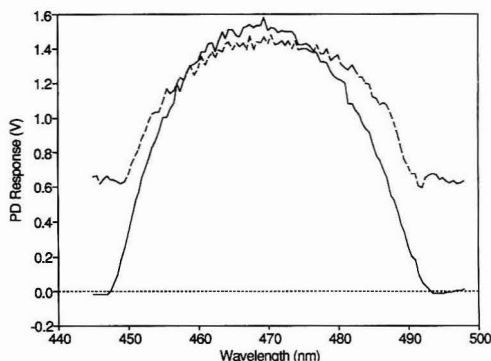


Figure 5. Photodiode response with (dashed) and without (solid) the preamplifier in the dye laser.

ASE and lasing, similar to using a power meter. With the laser beam blocked, the response of the photodiode was offset to a value of zero. Figure 5 shows the photodiode response as the dye laser is scanned from 445 to 498 nm. For both spectra, the dye laser output was adjusted to an average power of 5 mW at 466 nm. Without the preamp (solid curve), the photodiode response has a maximum around 466 nm and goes to zero at the extremes of the dye gain curve. When the preamp is in the dye laser (dashed curve), the photodiode response is broader and is nonzero at the extremes. Even when the laser is tuned below 450 nm, where the response of the photodiode falls off by 50%, the signal is approximately 0.6 V. The photodiode is responding to the broad-band ASE and not the wavelength set by the laser. Although the photodiode provides a good measure of the relative intensity of all the light as seen by the sample, the actual intensity at the wavelength indicated by the laser grating position may be misrepresented.

Figure 6 shows the absorbance spectra for a 0.04 M Pr^{3+} solution in 0.1 M HClO_4 using the IBM spectrophotometer.

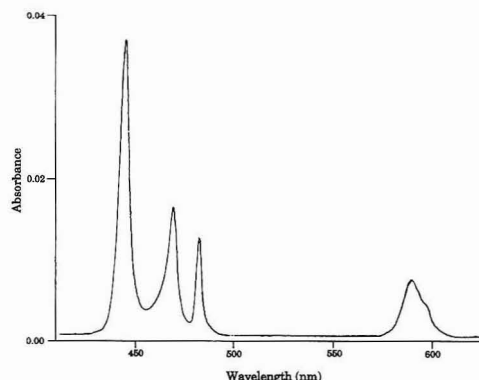


Figure 6. Absorbance spectra of 0.04 M Pr^{3+} in 0.1 M HClO_4 .

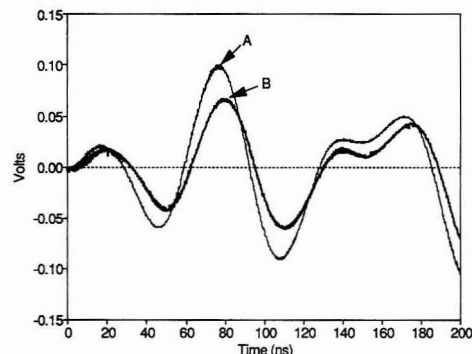


Figure 7. Oscilloscope traces of the photoacoustic waveforms: (A) lasing, (B) ASE.

The spectrum shows the bands at 468 and 481 nm that can be excited by the LD-466 dye. In photoacoustic spectroscopy, pulsed light passing through the cuvette will be absorbed by the analyte and will generate a thermoelastic expansion pulse which is monitored by the piezoelectric transducer. Oscilloscope traces of the transient photoacoustic waveforms generated from ASE and lasing are very similar, as seen in Figure 7. The PAS signal is obtained by gating a boxcar and measuring the amplitude of the second peak as a function of wavelength. To obtain the photoacoustic spectrum, which is identical to an absorption spectrum, the intensity of the peak is plotted versus dye laser wavelength. Curve A is the acoustic waveform generated with the laser tuned to the 468-nm peak of Pr^{3+} and an average power of 20 mW. When the laser grating was tuned to 495 nm (weak lasing, strong ASE) and the average power adjusted to 20 mW (preamp in cavity), ASE generated the photoacoustic waveform in curve B. Although ASE is more intense when the laser is at 445 nm, we chose to use 495 nm where Pr^{3+} has no absorption. The delay in the signal, approximately 20 ns, is most likely due to a slight change in the position of the laser beam in the cuvette. The 20 ns time delay may correspond to a shift in position of only 10^{-4} cm, which may be due to adjusting the grating in the dye laser.

Table I presents the measured photoacoustic amplitude at different laser wavelengths with approximately the same photodiode (PD) response, i.e. same average power. With the laser set at 468 nm (no ASE), a strong photoacoustic signal was observed, as expected. In the absence of lasing,

Table I. Photoacoustic Response (PAS) for Selected Dye Laser Wavelengths and Photodiode Signals (PD)

	laser wavelength (nm)	PD (V)	PAS (V)	ratio PAS/PD
10^{-3} M Pr^{3+}	445	0.53	1.15	2.17
	450	0.42	0.85	2.02
	468	0.53	1.92	3.62
	495	0.51	0.23	0.45
	500	0.51	1.96	3.84
H_2O blank	445	0.51	0.07	0.14
	468	0.40	0.07	0.18

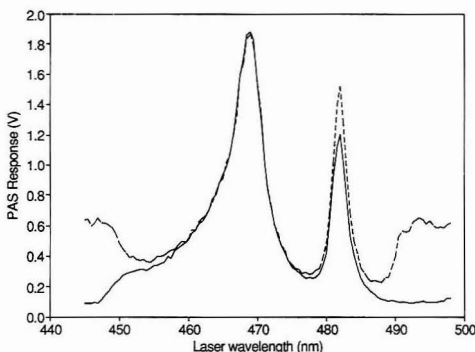


Figure 8. Photoacoustic spectra of Pr^{3+} with (dashed) and without (solid) the preamplifier in the dye laser.

at 445 nm, a relatively strong PAS response was also recorded which occurred strictly from the ASE. At 450 nm where lasing is observed (see Figure 4C), the PAS signal is smaller due to a reduction of the ASE intensity, even though there is a small amount of absorption of the Pr^{3+} from lasing at 450 nm contributing to the PAS response. The ASE intensity was less at longer wavelengths (see Figure 2), and this is reflected in the PAS response at 495 nm. Although lasing is present at 495 nm, there is no Pr^{3+} absorption and the weak PAS signal is due to ASE. The anomaly observed in Figure 4F with the laser set to 500 nm is also reflected in the observed PAS signal. Compared to a laser setting of 468 nm, the PAS response is larger than would be expected given the PD response. The ASE and the lasing observed in Figure 4F both overlap the absorption spectra of Pr^{3+} and contribute to the PAS signal.

Photoacoustic spectra of Pr^{3+} obtained with (dashed curve) and without (solid curve) the preamplifier are presented in Figure 8. The data were collected simultaneously with the photodiode responses shown in Figure 5. In both spectra the 468-nm band has the same shape and amplitude; however, the absorption band at 481 nm is larger with the preamp. When normalized to the PD response, the peak amplitudes are the same. The major differences in the two spectra appear on the ends where ASE is more prevalent. Below 450 nm, the PAS signal should start to increase due to the large Pr^{3+} absorption band at 446 nm. Without the preamp, the PAS signal decreases due to inefficient lasing. With the preamp, the signal begins to increase as expected; however, this is due to the absorption of the broad-band ASE and not lasing below 450 nm. Above 490 nm (weak lasing but no Pr^{3+} absorption), a strong PAS signal is generated with the preamp, whereas, without the preamp the photoacoustic spectrum closely resembles the absorption spectrum. With the preamp in the laser cavity, the ASE significantly alters the Pr^{3+} spectrum. Normalization of these spectra near the ends is not possible due to the near zero division without the preamp. Note that

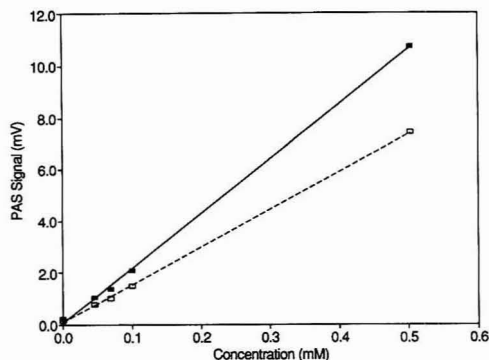


Figure 9. Calibration curves produced from lasing at 468 nm (solid) and ASE with the laser tuned to 495 nm (dashed).

ASE is still present without the preamp, although the effects are not as noticeable.

Calibration curves shown in Figure 9 were generated with the laser set at 468 (solid) and 495 nm (dashed). In both cases, the laser was adjusted to yield an average output power of 20 mW. The calibration curve for 495 nm is due to the

broad-band ASE absorption. In a separate experiment, a solution of Nd^{3+} was scanned using laser dye LD-466. Neodymium has absorption bands at 510 and 521 nm and no absorption in the 445–495-nm range. Only the water background was measured, indicating that the ASE must overlap an absorption band of the analyte to generate a PAS signal.

CONCLUSIONS

In this study, we have demonstrated that the impure spectral output of dye lasers can play an important role in photoacoustic spectroscopy. ASE may also effect other analytical techniques, in particular, other photothermal spectroscopies.

ACKNOWLEDGMENT

We acknowledge others who have been a part of this project, Pat Grant, Rich Torres, and Cindy Palmer. This work was prepared by Yucca Mountain Site Characterization Project (YMP) participants as part of the Civilian Radioactive Waste Management Program. The YMP is managed by the Yucca Mountain Site Characterization Project Office of the U.S. Department of Energy, Las Vegas, NV.

RECEIVED for review March 16, 1992. Accepted July 23, 1992.

Acrylamide Polymerization Kinetics in Gel Electrophoresis Capillaries. A Raman Microprobe Study

Tracey L. Rapp, Will K. Kowalchuk, Kevin L. Davis, Elizabeth A. Todd, Kei-Lee Liu, and Michael D. Morris*

Department of Chemistry, University of Michigan, Ann Arbor, Michigan 48109-1055

The formation of 3.5% T, 3.3% C cross-linked polyacrylamide is monitored in 75- μ m-i.d. electrophoresis capillaries by Raman microprobe spectroscopy. The disappearance of the acrylamide 1292-cm⁻¹ band is followed with 60-s time resolution for 30 min, and 2-4 min resolution for up to 10 h. Polymerization is 98% complete in 1.5 h and greater than 99% complete after 2 h. In the 900-1700-cm⁻¹ region no bands attributable to cross-linking are observable. Reaction in the capillary follows second-order kinetics. The reaction is faster in the bulk system because heat dissipation is not sufficient to maintain a constant temperature.

INTRODUCTION

Capillary gel electrophoresis (CGE) is an attractive complement to slab gel electrophoresis. CGE was first developed by Cohen and Karger for the separation and molecular weight determination of peptides and proteins.¹ The capillary inner diameter dimensions of less than 100 μ m permit efficient heat removal and facilitate the use of high field strengths. The technique is increasingly used in gene sequencing by the Sanger dideoxy chain extension method.^{2,3} Pulsed field capillary gel electrophoresis for separation of large nucleic acid fragments has been demonstrated,^{4,5} and the benefits of capillary gel affinity electrophoresis, with separation in a buffer containing an intercalator, have also been shown.⁶

While the utility of CGE is clear, column lifetime is a significant problem. At high field strengths (typically greater than 300 V/cm), or after repeated use, gel performance deteriorates. Analyte mobilities increase, resolution decreases, and sometimes the gel fails completely.^{2,7} Bubble formation in the capillary during polymerization of the gel or during later use is one catastrophic failure mode. However, little is known about the gel structure in the capillaries and the processes which cause the slow deterioration. As the first step in a study of capillary gel structure and dynamics, we report the intracapillary polymerization kinetics of cross-linked polyacrylamide. In doing so, we also investigate the utility of Raman microprobe spectroscopy for measurement of intracapillary gel properties.

The Raman microprobe provides spectra with 1-10- μ m spatial resolution.^{8,9} The microprobe retains the well-known strengths of Raman spectroscopy, including easy applicability

to aqueous systems. Raman microscopy is routinely used in polymer film and fiber production for the identification of impurities. It has also been successfully used to identify local differences in crystallinity and local concentration of copolymers in polymer processes.⁹ As evidenced by its use for these applications, Raman microprobe spectroscopy could also provide a direct method for monitoring gel structure and chemistry within an electrophoresis capillary.

The Raman spectra of polyacrylamide gels have been reported by Bansil and Gupta,^{10,11} who assigned most bands. SERS spectra of polyacrylamide have been reported by Suh and Michaelian.¹² Ahern and Garrell¹³ used SERS to probe polymerization on a silver colloid. There is general agreement on the assignment of major bands in the region 900-1700 cm⁻¹, but there is disagreement on whether Raman spectroscopy can detect polybisacrylamide sequences in cross-linked polyacrylamide gels, especially with a low percentage of cross-linker (%C). Gupta and Bansil attribute bands at 1035, 1063, and 1075 cm⁻¹ to the skeletal (-C-C-C-) stretches of the cross-linked polymers and 418, 441, and 462 cm⁻¹ to the (-C-C-C-) bending vibration of the gel.¹¹ Ahern and Garrell could not find any of these bands but did observe a band at 705 cm⁻¹ which could possibly be attributed to the polybisacrylamide. They also observed that monomeric bisacrylamide itself has a peak at 705 cm⁻¹ and left this band unassigned.¹³

Polymerization of cross-linked and linear polyacrylamide gels has been monitored in bulk by various methods such as viscosity measurements,^{14,15} titration of unreacted monomer,¹⁶ UV absorption,¹⁷ Tyndall effect (increase in light scattering due to gel formation),¹⁸ and NMR spectroscopy.¹⁹ However, there have been no attempts to study the polymerization kinetics of linear or cross-linked polyacrylamide gels in the environment of the microbore fused-silica capillary.

EXPERIMENTAL SECTION

Raman spectra were obtained with a modified Spex 1877 triple spectrograph fitted with either an 1200-groove/mm or 1800 groove/mm grating in the spectrograph stage and a Photometrics series 200 cryogenically cooled CCD detector.²⁰ The light source

- (1) Cohen, A. S.; Karger, B. L. *J. Chromatogr.* **1987**, *397*, 409-417.
- (2) Drossman, H.; Luckey, J. A.; Kostichka, A. J.; D'Cunha, J.; Smith, L. M. *Anal. Chem.* **1990**, *62*, 900-903.
- (3) Sverdlow, H.; Zhang, J. Z.; Chen, D. Y.; Harke, H. R.; Grey, R.; Wu, S.; Dovichi, N. J.; Fuller, C. *Anal. Chem.* **1991**, *63*, 2835-2841.
- (4) Heiger, D. N.; Cohen, A. S.; Karger, B. L. *J. Chromatogr.* **1990**, *516*, 33-48.
- (5) Demana, T.; Lanan, M.; Morris, M. D. *Anal. Chem.* **1991**, *63*, 2795-2797.
- (6) Guttman, A.; Cooke, N. *Anal. Chem.* **1991**, *63*, 2038-2042.
- (7) Karger, A. E.; Harris, J. M.; Gesteland, R. F. *Nucl. Acids Res.* **1991**, *19*, 4955-4962.
- (8) Clark, R. J. H.; Hester, R. E., Eds. *Advances in Infrared and Raman Spectroscopy*; Heyden and Son: London, 1980; Vol. 7, pp 223-282.

- (9) Gardiner, D. J.; Graves, P. R., Eds. *Practical Raman Spectroscopy*; Springer-Verlag: Berlin, 1989; pp 119-151.
- (10) Gupta, M. K.; Bansil, R. *J. Polym. Sci.: Polym. Phys. Ed.* **1981**, *19*, 353-360.
- (11) Gupta, M. K.; Bansil, R. *J. Polym. Sci.: Polym. Lett. Ed.* **1983**, *21*, 969-977.
- (12) Suh, J. S.; Michaelian, K. H. *J. Raman Spectrosc.* **1987**, *18*, 409-414.
- (13) Ahern, A. M.; Garrell, R. L. *Langmuir* **1988**, *4*, 1162-1168.
- (14) Ghormley, V. F.; Galperin, N. I.; Osmanov, T. O.; Khomikovskii, P. M.; Abkin, A. D. *Eur. Polym. J.* **1980**, *16*, 529-535.
- (15) Feng, X. D.; Guo, X. Q.; Qiu, K. Y. *Makromol. Chem.* **1988**, *189*, 77-83.
- (16) Bosio, A. B.; Loehlein, C. B.; Snyder, R. S.; Righetti, P. G. *J. Chromatogr.* **1980**, *189*, 317-330.
- (17) Pegon, Y.; Quincy, C. *J. Chromatogr.* **1974**, *100*, 11-18.
- (18) Gelfi, C.; Righetti, P. G. *Electrophoresis* **1981**, *2*, 213-219.
- (19) Gromov, V. F.; Bogachev, Y. S.; Bune, Y. V.; Zhuravleva, I. L.; Teleshov, E. N. *Eur. Polym. J.* **1991**, *6*, 505-508.

was a frequency-doubled CW Nd-YAG laser, 532 nm (ADLAS DPY 305 c/315) providing 30–40 mW of power at the sample. The spectrograph slit width was adjusted to maintain 5- or 8-cm⁻¹ resolution. Illumination and back-scattered light collection were through an Olympus, IMT-2 inverted research microscope using a 20X/0.4 NA ultralong working distance objective for bulk measurements or a 20X/0.7 NA objective for intracapillary measurements. Capillaries were held stationary by a locally constructed Delrin stage to prevent heat loss to the metal of the microscope frame.

A 3.5% T/3.3% C polyacrylamide gel was prepared by combining 1.4 mL of 50% stock solution made from solid acrylamide and *N,N'*-methylenebisacrylamide monomer (Sigma) with 4.00 mL of 5 X Tris-borate-EDTA (TBE) and 420 μ L of 3% ammonium persulfate (BioRad) diluted to 20.00 mL. The stock solution was deoxygenated by bubbling N₂ through for 2–3 min. The TBE was prepared by mixing 0.5 M EDTA (Mallinckrodt), Tris base (Boehringer), and boric acid (Baker).

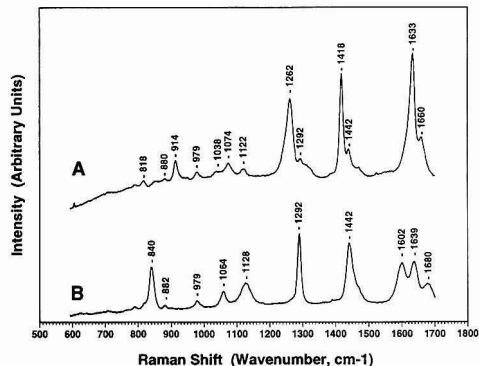
Fluorocarbon-coated fused silica capillary (Polymicro Technologies) with 75- μ m i.d. and 360- μ m o.d. was cut to 30-cm total length. The inner capillary walls were cleaned with 1 M HCl, 1 M KOH, and methanol. To bind the gel to the walls, a 1:1 mixture of methanol and 3-(trimethoxysilyl)propyl methylacetate (Aldrich) was pumped into the capillary and allowed to stand for a minimum of 4 h. Polymerization was initiated by mixing 5 μ L of TEMED (Life Technologies, Inc.) with the 20 mL of monomer solution described above. The mixture was then pumped through the capillary for 1 min, after which time the pumping was stopped and Raman spectra were collected. The time between addition of the catalyst and the start of Raman data collection did not exceed 2 min. Bulk solutions were prepared in the same manner as the solutions used in the capillaries. The reaction was monitored in a 20-mL aliquot contained in a 25-mL glass sample vial placed on the Delrin microscope stage.

Reaction-monitoring spectra were obtained with an integration time which varied during the course of the reaction. During the first 15 min, a 30-s integration was used. For the second 15 min a 2-min integration time was employed. For later spectra (30 min to 10 h) a 5-min integration time was used. By increasing the integration time as the reaction proceeded, we were able to monitor small amounts of starting material late in the reaction without undue compromise in time resolution. All reactions were performed at room temperature (approximately 24 °C). Temperature inside the bulk reaction vessel was monitored using a type k thermocouple (Omega). The signal was amplified with a low-noise amplifier constructed locally.

To derive kinetic information, band intensities were taken as areas under bands, calculated with the integration routines in Spectra-Calc (Galactic Industries). Reactions were followed as the attenuation of the acrylamide C–H bending vibration at 1292 cm⁻¹. For presentation, all spectra were subjected to a Savitsky-Golay quadratic-cubic smooth ($n = 9$) using the routines in Spectra-Calc. For the extraction of kinetic data, however, only simple background subtraction or ratioing was employed. Second-order kinetic fits were performed using DeltaGraph (DeltaPoint).

RESULTS AND DISCUSSION

Figure 1 shows the Raman spectra of bulk solution samples of the reaction starting materials: 5.0% by weight acrylamide and bisacrylamide. The band positions agree well with those reported by others.^{10,12} Figure 2 shows spectra obtained during the bulk and capillary polymerization of a 3.5% T/3.3% C gel. Representative curves early (2 min) and late (32 min) in the reaction are shown. For the bulk sample, a spectrum of completely polymerized (10.5 h) monomer is also shown. There is little difference between the corresponding spectra of the bulk and capillary samples. The corresponding band positions are identical within experimental error (± 1 –2 cm⁻¹), and in both cases the observed band positions are in agreement with literature values.



disappearance or growth of others can be understood by comparison of the observed bands with literature band assignments.

At the high-frequency end of the monomer spectrum (or the spectrum 2 min after initiation), the three bands at 1680, 1639, and 1602 cm^{-1} are assigned to C=O stretching (amide I), C=C stretching, and NH_2 bending (amide II) vibrations, respectively. The 1639- cm^{-1} band disappears as the C=C double bond is broken during the course of the polymerization. The 1680- and 1602- cm^{-1} amide bands undergo small to moderate frequency shifts to 1690 and 1615 cm^{-1} in response to the changing environment. An intense peak at 1442 cm^{-1} in the monomer spectrum is assigned to the superposition of a CH_2 bending mode and a C-N stretching mode (amide III). After polymerization, these two bands are observed at the shifted frequencies of 1462 and 1435 cm^{-1} , respectively. Another intense monomer peak in the spectrum is the vinylic C-H bending mode at 1292 cm^{-1} . This band disappears during the course of the reaction. In its place, a broad aliphatic C-H bending vibration in the polymerized gel appears at 1329 cm^{-1} . This is an expected frequency shift when a C=C bond is broken.

Two partially unresolved peaks at 1223 and 1187 cm^{-1} grow in as the polymerization progresses. These two bands are assigned to a NH_2 wag and a polymer skeletal vibration. A strong, broad peak around 1128 cm^{-1} from a C-C skeletal stretching mode in the acrylamide monomer can also be observed. This asymmetric band moves to a lower frequency of 1114 cm^{-1} upon polymerization. Weak bands at 1083 and 1064 cm^{-1} in the initial polymerization spectra (2 min after initiation) can still be observed after 32 min in the polymerized gel spectrum. These two weak bands are no longer visible approximately 2 h (± 15 min) after the initiation of the reaction when polymerization is 99% complete. Another weak band in the monomer spectrum at 979 cm^{-1} which is assigned to an out of plane HC-CH bend disappears during the initial stages of polymerization. During the later stages of the polymerization, a new band at 987 cm^{-1} may be attributed to the same vibration in the polymer.

In the region between 1000 and 1100 cm^{-1} , Gupta and Bansil¹¹ have assigned three bands (1075, 1063, 1035 cm^{-1}) to different C-C skeletal stretching vibrations which may arise from structurally different forms of highly-branched polyacrylamide. These bands were absent in the spectra of completely reacted cross-linked polyacrylamide reported by Ahern and Garrell.¹³ There are several reasons why Gupta and Bansil may have observed these unconfirmed bands. Percent conversion (polymerization efficiency) drops as the concentration of TEMED (reaction catalyst) is increased. Feng et al.¹⁵ reported only a 95% conversion for the concentration of TEMED used by Gupta and Bansil. Also, Bosio et al.¹⁶ found that at high bisacrylamide concentrations (>20% C) only an 80% polymerization was observed after 1 h. However, if the system was left standing overnight, 96% conversion was achieved. Gupta and Bansil reported spectra after 8 h of polymerization. Therefore, it is possible that they may have been observing incompletely polymerized gels containing free monomer.

We observe only two bands, at 1083 and 1064 cm^{-1} , in the 1000–1100- cm^{-1} region. The 1083- cm^{-1} band is from the initiator ammonium persulfate and is easily observed in solutions even as dilute as 3×10^{-3} M. The 1064- cm^{-1} vibration is found in the monomer spectrum of acrylamide (Figure 1B). These assignments are reasonable because both bands eventually disappear from the completely polymerized gel spectrum. We concur with Ahern and Garrell,¹³ who concluded that at low cross-linker concentration, this region of the Raman

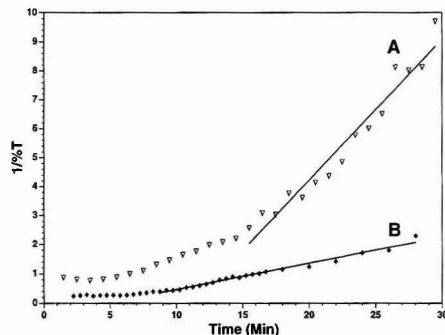


Figure 3. Reaction kinetic plots for $T = 3.5\%$, $C = 3.3\%$ polymerizations (A) in bulk and (B) in an electrophoresis capillary. Acrylamide reciprocal concentration is plotted in units of $1/(\%T)$.

spectrum is not especially sensitive to the presence of cross-linking.

We have investigated the feasibility of time-resolved Raman microscopy for kinetic studies of the polymerization of acrylamide. We have chosen to follow the disappearance of the acrylamide C-H bending vibration at 1292 cm^{-1} . The intensity of this bending vibration and other weaker bands should not be affected by the potential problem of the Tyndall effect. Gelfi and Righetti¹⁸ reported only a 5% transmission loss by scattering for gels containing 3% C. Therefore the Tyndall effect in our gels should be negligible. The use of an array detector allows us to simultaneously monitor several bands in the spectrum, but we are constrained by the length of the spectral window (approximately 280 cm^{-1} with an 1800 grooves/mm grating).

The bands chosen for kinetics should be intense and well-resolved from nearby strong bands. In the 800–1700- cm^{-1} interval, there are several strong monomer bands, including those at 1292, 1442, and 1639 cm^{-1} . The 1442- cm^{-1} band was excluded because of the presence of polyacrylamide bands at 1435 and 1462 cm^{-1} which appear as the reaction proceeds. Similarly, the 1639- cm^{-1} region was rejected because of the proximity of amide I and II bands at 1680 and 1602 cm^{-1} . Therefore, the C-H bending region was employed. The C-H bending mode of acrylamide at 1292 cm^{-1} was monitored for the disappearance of monomer. The growth of the 1329- cm^{-1} polymer band could also be monitored in this spectral window, but because this band is weaker than the monomer band, intensities could not be measured with adequate accuracy for kinetic studies.

The lowest detectable amount of unreacted monomer was determined by measuring the integrated peak areas under the 1292- cm^{-1} band for a series of unpolymerized acrylamide/bisacrylamide solutions. The total monomer concentrations (%T) of the solutions were varied while the bisacrylamide content (%C) remained constant. We obtained a linear calibration curve ($r = 0.9995$) with a detection limit of 0.035% T, or 1.0% of the 3.5% T initial concentration used in the kinetics experiments.

Second-order kinetics for acrylamide polymerization have been reported by Gelfi and Righetti¹⁸ and by Chen and Crambach.²¹ Figure 3A,B demonstrates that the reactions in the bulk and capillary have different behaviors. After an initial induction period of about 7 min, the capillary polymerization follows the expected second order kinetics. We can fit to a second order rate constant of $1.5 \times 10^{-3} \text{ } \text{T}^{-1} \text{ s}^{-1}$ out

to about 28 min. Beyond this time the acrylamide concentrations are too low for a reliable fit.

In the bulk, however, we find a limiting rate constant of about $8.1 \times 10^{-3} \text{ T}^{-1} \text{ s}^{-1}$ over the period 16–30 min, which corresponds to the interval of maximum temperature (see below). After the induction period of 5 min, short sections of earlier parts of the curve can be fitted to second-order kinetic equations, but we find such agreement fortuitous because the system is not at constant temperature. We do observe an induction period of about 6 min before measurable decrease in acrylamide Raman intensity begins.

Thirty minutes after initiation, the polymerization was 97% complete in the bulk and 88% complete in the capillary. The reaction was >98% complete after 1.5 h in both the bulk and the capillary. These times are longer than the times reported by Gelfi and Righetti¹⁸ for 5% T/3% C gels (95% complete after 12–15 min). However, slower reaction rates are expected for gels with total monomer content below 5% T because of the lower availability of the acrylamide monomer to the growing polymer chain.¹⁸

The identity of the Raman spectra at intermediate points during the reaction strongly suggest that the reaction mechanisms and final products are similar in the 75- μm -i.d. capillary and bulk solution. However, the kinetics differ significantly. It has been reported that as the polymerization temperature is increased, the reaction rate increases and the induction period decreases.^{22,23} Therefore, the rate constants and induction periods for the bulk and capillary polymerizations should be identical only if the reactions proceed at the same temperature.

We have made thermocouple measurements of the temperature rise in the bulk system during the course of the polymerization (Figure 4). For the first 8–9 min, i.e. during the induction period, the temperature remains at the initial temperature, 23–24 °C. It then rises 5.0–5.5 °C to about 29 °C over 6–7 min and then drifts slowly downward as the reaction rate declines. The laser wavelength (532 nm) is far removed from any acrylamide absorption bands; therefore, laser-induced heating should be negligible. To test this assumption, we have made temperature measurements with and without laser illumination. Comparison of Figure 4A (laser on) and B (laser off) shows that laser heating does not contribute to the observed temperature change.

In the bulk polymerization, the induction period is 2 min shorter and the final rate constant is 5 times larger than observed inside the capillary. The entire edifice of capillary electrophoresis is built upon the observation of good heat dissipation in 100- μm -i.d. and smaller capillaries. The 5 °C temperature rise accompanying the exothermic reaction in the bulk polymerization system would be expected to be smaller in the capillary. This difference in thermal environments accounts for the apparent difference in reaction rates between the bulk and the capillary. The good adherence to second-order kinetic equations in the capillary implies that the temperature change is under 1 °C. It has been suggested that the resulting cross-linked polymer structure is a function

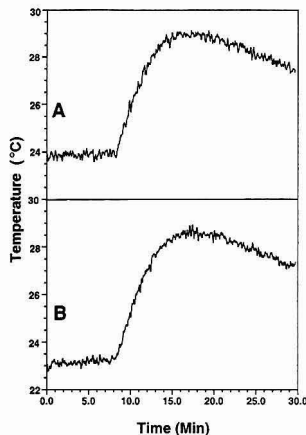


Figure 4. Temperature rise during bulk polymerization of T = 3.5%, C = 3.3% (A) with 30 mW of 532-nm illumination and (B) without laser illumination.

of polymerization temperature.¹⁸ We propose that conclusions about polyacrylamide chemistry and structure from experiments in bulk solution cannot be applied uncritically to the chemistry and structure of the stoichiometrically equivalent gels in electrophoresis capillaries.

CONCLUSIONS

Raman microprobe spectroscopy has been shown to be a useful tool for probing structures of molecules within an electrophoresis capillary. Our system is based on a modified f/9 spectrograph. An optimized instrument could easily have 10 times better throughput. In that case, it should be possible to observe changes in Raman spectra under electrophoresis working conditions with an acquisition time of 1–3 s. Even more information should be obtainable at low (50–500- cm^{-1}) frequencies, where vibrational modes of the polymer backbone are observed. Recently developed holographic beam splitters allow high throughput Raman microscopy in this region²⁴ and should allow Raman probes of polyacrylamide conformation under field-free or biased conditions. Finally we note that anti-Stokes Raman intensities measure thermal population of vibrational excited states and have long been used for temperature measurement. Anti-Stokes Raman microscopy may prove useful as a direct probe of intracapillary temperatures during electrophoresis. Experiments toward these goals are underway in our laboratories.

ACKNOWLEDGMENT

This work was supported in part by NIH Grant GM-37006 and in part by DOE Grant DE-FG02-89ER13996.

RECEIVED for review April 1, 1992. Accepted July 24, 1992.

Registry No. Acrylamide, 79-06-1; *N,N'*-methylenebisacrylamide, 110-26-9.

(22) Gelfi, C.; Righetti, P. G. *Electrophoresis* 1981, 2, 220–228.

(23) Gressel, J.; Rosner, A.; Cohen, N. *Anal. Biochem.* 1975, 69, 84–91.

(24) Pallister, D.; Liu, K.-L.; Morris, M. D.; Owen, H. *Appl. Spectrosc.*, in press.

Fiber-Optic Ammonia Sensor for Measuring Synaptic Glutamate and Extracellular Ammonia

Satyajit Kar and Mark A. Arnold*

Department of Chemistry, University of Iowa, Iowa City, Iowa 52242

A fiber-optic ammonia gas sensor designed for neurochemical applications is presented. Parameters evaluated in terms of effect on the steady-state and dynamic response of this sensor include the indicator dye, concentrations of indicator and total ammonia nitrogen in the internal solution, volume of the internal solution, structure of the gas-permeable membrane, and temperature. The final ammonia sensor responds over the concentration range from 7 to 3000 nM with a limit of detection of 7 nM and response times ranging from 2 to 5 min. Glutamate oxidase is immobilized at the tip of this ammonia sensor to provide a glutamate biosensor with a detection limit of 0.1 μ M when operated at pH 7.8. In addition, this ammonia sensor is used to measure extracellular ammonia levels in perfused retinal and eye-cup tissue preparations. These measurements indicate a calcium-dependent, potassium-evoked release of ammonia during these depolarization conditions.

INTRODUCTION

We are interested in developing biosensors for the primary amino acid neurotransmitter glutamate.¹⁻⁴ One strategy is based on the immobilization of glutamate oxidase at the tip of an ammonia gas sensing probe. This enzyme selectively catalyzes the oxidative deamination of glutamate according to the following reaction:

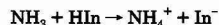


The steady-state production of ammonia at the probe tip is detected and related to the amount of glutamate in the sample solution.

Others have recently reported the general analytical properties of glutamate biosensors based on immobilized glutamate oxidase in combination with the detection of either oxygen or hydrogen peroxide.⁵⁻⁹ Guilbault and co-workers have discussed the potential of a glutamate biosensor based on the amperometric detection of hydrogen peroxide for neurochemical experiments.¹⁰ They concluded that interference by easily oxidizable endogenous species such as ascorbate and tyrosine is the major limitation of this approach.

The limit of detection for glutamate at neurochemically relevant pH values is the critical issue for our approach based on the detection of ammonia. In this regard, the detection limit of the internal sensing element for ammonia is the key parameter. Extracellular glutamate concentrations range from 1 to 10 μ M during typical neurochemical experiments.¹¹ At physiological pH, only a small fraction of the total ammonia nitrogen generated from the glutamate oxidase catalyzed reaction will be in the detectable form of ammonia. For example, the physiological pH for the photoreceptor cells within the toad retina is 7.8.¹² Only 3.4% of the total ammonia nitrogen is ammonia at pH 7.8, where as nearly 97% is in the form of the undetectable ammonium ion. Under ideal circumstances where glutamate is quantitatively converted to ammonia at the sensor tip, 1 μ M glutamate requires the ability to measure 34 nM ammonia. Such low detection limits are not possible with conventional gas-sensing technology.

We report here our success in developing a fiber-optic ammonia sensor (FOAS) with nanomolar detection limits. This sensor is constructed by trapping a thin layer of an internal indicator solution between a microporous Teflon membrane and a fiber-optic probe. Ammonia from the sample solution diffuses across this membrane, enters the internal solution and reacts with the indicator dye in the following manner:



The nonprotonated form of the indicator is detected by a fluorescence measurement through the fiber-optic probe. Nanomolar detection limits are possible with this sensor design because of the inherent sensitivity of fluorescence measurements and because ammonia is trapped by the indicator dye. During operation, ammonia continues to enter the indicator solution until the ammonia partial pressure is equivalent on both sides of the gas-permeable membrane. A majority of the ammonia that enters the indicator solution is converted to ammonium ions which results in an accumulation of the detected nonprotonated indicator species and an enhancement in the detection limit. The extent of this enhancement is governed by the pK_a and concentration of the indicator dye.¹³

The analytical properties are reported for our FOAS and the corresponding glutamate biosensor. The ammonia sensor possesses a detection limit of 7 nM with response times ranging from 2 to 5 min. The detection limit for the corresponding glutamate biosensor is 0.1 μ M when operated at pH 7.8. The FOAS has been used to measure extracellular ammonia levels in eye-cup and retinal tissue preparations. Extracellular ammonia has been measured to establish the feasibility of monitoring glutamate superimposed on a basal level of ammonia. We expected to find low background ammonia

- (1) Wang, A. J.; Arnold, M. A. *Anal. Chem.* 1992, 64, 1051-1055.
- (2) Kaitenbach, M. S.; Arnold, M. A. *Mikrochim. Acta*, in press.
- (3) Arnold, M. A. In *Immunochemical Assays and Biosensor Technology for the 1990s*; Nakamura, R. M., Kasahara, Y., Rechnitz, G. A., Eds.; American Society for Microbiology: Washington, DC, 1992; Chapter 16.
- (4) Arnold, M. A. *Proc. SPIE-Int. Soc. Opt. Eng.* 1988, 906, 128-133.
- (5) Chen, C. Y.; Su, Y. C. *Anal. Chim. Acta* 1991, 243, 9-15.
- (6) Dremel, B. A. A.; Schmid, R. D.; Wolfbeis, O. S. *Anal. Chim. Acta* 1991, 248, 351-359.
- (7) Wollenberger, U.; Scheller, F.; Pawlowa, M.; Muller, H. G.; Risinger, L.; Gorton, L. In *GBF Monograph*; Schmid, R. D., Scheller, F., Eds.; VCH Publishers: New York, 1989; Vol. 13, pp 33-36.
- (8) Hale, P. D.; Lee, H. S.; Okamoto, Y.; Skotheim, T. A. *Anal. Lett.* 1991, 24, 345-356.
- (9) Yau, T.; Yamamoto, H.; Wasa T. *Anal. Chim. Acta* 1990, 236, 437-440.
- (10) Villarta, R. L.; Cunningham, D. D.; Guilbault, G. G. *Talanta* 1991, 38, 49-55.

- (11) Shank, R. P.; Campbell, G. L. In *Handbook of Neurochemistry*; Lajtha, A., Ed.; Plenum Press: New York, 1983; Vol. 3, Chapter 14.
- (12) Miller, R. F.; Slaughter, M. M. In *Retinal Transmitters and Modulators: Model for the Brain*; Morgan, W., Ed.; CRC Press: Boca Raton, FL, 1985; Vol. II.
- (13) Rhines, T. D.; Arnold, M. A. *Anal. Chem.* 1988, 60, 76-80.

levels that did not vary during the experiment.^{14,15} Surprisingly, we measured a calcium-dependent, potassium-evoked release of ammonia from both the isolated retinal tissue and the intact eye-cup. The ramifications of this finding are discussed with an emphasis on the potential analytical utility of this FOAS for neurochemical investigations.

EXPERIMENTAL SECTION

Apparatus and Reagents. Fluorescence measurements were made with a fiber-optic spectrometer. The light source consisted of a 100-W tungsten-halogen lamp maintained in an Oriel Model 66184 illuminator housing and powered by an Oriel Model 6393 transformer. Light from the source first passed through an IR-blocking filter and then a 490-nm interference filter before being focused into a bundle of quartz optical fibers by an Oriel Model 77800 fiber-optic input assembly. The fiber bundle directed the light into a home-built light-tight box that contained the sensor, chopper, and detector optics. Light exiting the bundle was collimated before passing through an EG&G PAR Model 197 mechanical chopper which was operated at a frequency of 1.995 kHz. The chopped radiation was focused into a set of plastic optical fibers. This set of plastic fibers directed the excitation radiation to the internal solution at the tip of the gas sensor. A second set of plastic optical fibers collected a portion of the luminescence from the internal solution and directed this light to the detector optics. Light from the sensor tip was first collimated and then passed through a 540-nm interference filter to isolate the fluorescence radiation. Finally, the filtered light was focused onto the face of a photomultiplier tube (PMT) which was operated at 650 V. An EG&G PAR Model 5209 lock-in amplifier was used to measure the PMT current. Data were stored on an 8088-based IBM personal computer with a National Instruments Model GPIB IEEE interface between the lock-in amplifier and the computer.

5-Carboxy-4',5'-dimethylfluorescein (CDMF) and 2,7-bis(2-carboxyethyl)-5-carboxyfluorescein (BCECF) were used as received from Molecular Probes, Eugene, OR. All other solutions were made with reagent grade chemicals that were obtained from common commercial suppliers. All solutions were made with distilled-deionized water that was prepared immediately before use by passing the house-distilled water through a Milli-Q three-house water purification unit. Toads of the type *Bufo marinus* (5.5–6.0 in.) and *Bufo americanus* (2.0–2.5 in.) were purchased from Charles D. Sullivan Co., Nashville, TN.

Procedures. Sensor Construction. Ammonia sensors were constructed by trapping a small volume of the internal solution between a gas-permeable membrane and a fiber-optic probe. The fiber-optic probe was fabricated by inserting 17 individual plastic optical fibers into a custom made glass tube and securing these fibers with an adhesive sealant. The glass tube was prepared by grinding the closed end of a common glass capillary tube to a thin, flat surface and then polishing this surface to a smooth, optically transparent finish. The plastic optical fibers were type Super ESKA Ek-10 from Mitsubishi Rayon America, Inc., with a numerical aperture of 0.47 and an outer diameter of 250 μm . The fiber-optic probe was inserted into a conical-shaped plastic tube and held in place by an adhesive sealant. A small reservoir was created at the tip by slightly recessing the fiber-optic probe relative to the outer edge of the tube. The outer diameter of the resulting sensor tip was 2 mm and the volume of the reservoir was less than 1 μL . The internal solution and gas-permeable membrane were added by inverting the sensor body, applying approximately 1 μL of solution to the reservoir, stretching a small square of membrane over the solution and holding the membrane in place with a plastic O-ring. The internal solution contained 0.115 M sodium chloride, 0.100 M ammonium chloride, and 50 μM CDMF, unless stated otherwise. Gas-permeable membranes were microporous Teflon membranes from Gore and Associates, Elkton, MD. Unless stated otherwise, all membranes had an average pore size of 1.0 μm .

Glutamate biosensors were constructed by immobilizing a thin layer of glutamate oxidase on the outer surface of the Teflon

membrane of the FOAS. Glutamate oxidase was immobilized by physically entrapping approximately 0.02 mg (0.04 units) of enzyme with a cellulose diacetate dialysis membrane.

Sensor Characterization and Ammonia Calibration Curves. Unless stated otherwise, measurements were made in thermostated glass jacketed cells and the temperature was maintained at 25 °C with a Fisher Model 80 water bath. Two procedures were used to collect data for sensor calibration curves. In the first procedure, the sensor tip was initially immersed in a 10.00-mL aliquot of the working buffer to which ammonium chloride had been added to give a total ammonia nitrogen concentration of 2 μM . The working buffer was composed of 10.0 mM Trizma base, 100 mM sodium chloride, 5 mM glucose, and 0.005% 5-fluorouracil (added as an antimicrobial agent) adjusted to pH 7.8 with 6 M hydrochloric acid. Various ammonia concentrations were then generated by adjusting the pH of this solution with either acid or base. The solution pH was measured continuously with a Ross-type combination pH electrode (Orion No. 810200) in conjunction with a Beckman Model 71 pH-mV⁻¹ meter. In the second procedure, the sensor tip was immersed in a 10.00-mL aliquot of a 0.01 M sodium hydroxide solution that contained 0.105 M sodium chloride. Various ammonia concentrations were obtained by making microliter additions of an ammonium ion standard. In both cases, the sensor response was collected as a function of time until a steady-state value was identified. Calibration curves were constructed by plotting the steady-state response as a function of ammonia concentration. Response times were measured as the time required to achieve 95% of the overall change in response.

Extracellular Ammonia Measurements. Extracellular ammonia concentrations were measured in perfusion buffers in contact with either retinal tissue from *B. marinus* or complete eye-cups from *B. americanus*. In both cases eyes were removed from toads that were first anesthetized by submersion in ice for 1 h. Eye-cup preparations were prepared by dissecting the eye and removing the lens. Freshly prepared eye-cups were perfused with generous portions of a pH 7.8 Ringer's buffer solution. After removing the lens from the eyes of the *B. marinus* toads, the retinal tissue was isolated by touching and then lifting a square of absorbant paper to the vitreal surface of the eye-cup preparation. The retinal tissue adhered to the paper and was removed as a single-layer sheet from the underlying pigment epithelium. The retinal tissue was maintained in the pH 7.8 Ringer's buffer throughout. The time required to isolate the retinal tissue was approximately 45 min.

Depolarization experiments were carried out with either half of a retinal tissue or a complete eye-cup. In both cases, the preparation was incubated in a series of buffer solutions at room temperature in the dark. The buffer volume was 1.5 and 1.0 mL for the retinal tissue and eye-cup preparations, respectively, and the incubation time was 15 min throughout. Initially, preparations were incubated in a normal Ringer's buffer (2.5 mM potassium). Next, the cells were depolarized with a high-potassium Ringer's buffer (56.0 mM potassium). Calcium-dependent release processes were then blocked with a cobalt-containing, normal potassium Ringer's buffer (4.0 mM cobalt and 2.5 mM potassium). Finally, the preparations were incubated with a cobalt-containing, high-potassium Ringer's buffer (4.0 mM cobalt and 56.0 mM potassium). After incubation, each sample was carefully removed by aspiration and stored frozen at -25 °C until it could be analyzed. Preparations were rinsed with the next buffer between steps.

Ammonia concentrations were determined by either a calibration curve or standard addition procedure. In the first case, an ammonia calibration curve was constructed over the 50–300 nM concentration range in a 0.5-mL aliquot of the corresponding working buffer. The sensor was then immersed in a fresh 0.5-mL aliquot of this buffer in order to reestablish the baseline condition. A small volume of the sample was then added and the sensor response was monitored. If the detected ammonia concentration was less than 50 or greater than 300 nM, then the volume of sample added was adjusted and the measurement repeated. The required sample volumes ranged from 25 to 200 μL . In the standard addition procedure, the sensor was initially immersed in a fresh 0.5-mL aliquot of the working buffer to establish the baseline response. Two standard additions of a 10 μM ammonia solution were added sequentially and the corre-

(14) Cooper, A. J.; Plum, F. *Physiol. Rev.* 1987, 67, 440–514.

(15) Benjamin, A. M. In *Handbook of Neurochemistry*; Lajtha, A., Ed.; Plenum Press: New York, 1982; Vol. 1, Chapter 4.

sponding sensor responses were recorded. An appropriate volume of the sample was then added, and the sensor response was again recorded. The volumes of standard and sample were adjusted such that the final concentration of ammonia from all additions did not exceed 300 nM. All measurements were made at 25 °C. In addition, each measurement was made by using a working buffer that matched the buffer used to collect that particular sample.

RESULTS AND DISCUSSION

Responses of fiber-optic gas sensors depend on several nonspectroscopic parameters which include pK_a , stability, and concentration of the indicator dye, concentration of ammonium chloride in the internal solution, volume of the indicator solution, properties of the gas-permeable membrane, and temperature. We have systematically examined these parameters with the goal of nanomolar detection of ammonia.

Sensor Parameters. CDMF was selected as the indicator for this sensor because of its acid-base properties and stability compared to other fluorescein derivatives. Initially, a pK_a of 7.0 was identified by our previously reported simplex optimization routine¹³ as the ideal indicator pK_a for a sample ammonia concentration range from 2 to 200 nM. Of the fluorescein derivatives commercially available, BCECF and CDMF were selected as potential indicator dyes because their pK_a values are reported to be 7.0.¹⁶ Stability tests revealed that BCECF was less stable both thermally and photochemically compared to CDMF. A second factor in favor of CDMF is its larger Stokes shift. Finally, BCECF is significantly more expensive.

Spectroscopically, CDMF is characterized by a molar absorptivity of $6.23 (\pm 0.03) \times 10^4 \text{ M}^{-1} \text{ cm}^{-1}$, a high quantum efficiency and wavelengths of maximum excitation and emission of 505 and 538 nm, respectively. The effective pK_a for CDMF was measured by titrating the indicator in a solution with an ionic strength of 0.115 M at 25 °C. These are the same conditions used in the internal indicator solution. The titration was monitored by measuring the fluorescence of the nonprotonated form of the indicator. The pK_a was 6.95 ± 0.01 under these conditions which corresponds to an effective equilibrium constant of 159.3 ± 3.7 for the reaction with ammonia based on a value of 9.1522 ± 0.0006 for the pK_a of ammonium ions at 25 °C and an ionic strength of 0.11 M.¹⁷

The total dye concentration has a dramatic effect on both the steady-state and dynamic response properties of the sensor. These effects were examined by monitoring the sensor response to an ammonia concentration step from zero to 200 nM for a series of sensors with CDMF concentrations ranging from 10 to 70 μM . The results from this experiment are plotted in Figure 1. As the concentration of the indicator dye increases, more ammonia must enter the internal indicator solution in order to establish the steady-state condition. As such, larger amounts of dye provide higher signals, which propagates into greater sensitivity and lower detection limits. The response begins to level-off at high dye concentrations because of self-absorption by the indicator. In terms of the dynamic response, high dye concentrations have an adverse effect on response times. The need for more ammonia requires more time to establish the steady-state condition. In this case, response times become insensitive to the amount of indicator when the concentration of CDMF drops below 20 μM . The ideal indicator concentration can be identified by plotting the ratio of the response magnitude and the response time as a function of dye concentration. The inset in Figure

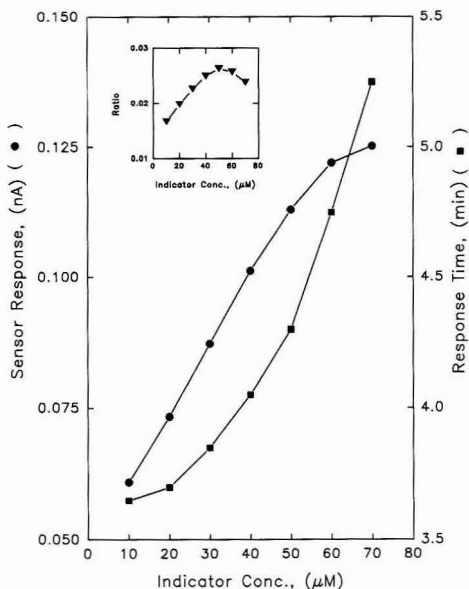


Figure 1. Effect in indicator concentration on the (●) magnitude of response and (■) response time. The inset shows the ratio of the magnitude of response and response time as a function of indicator concentration.

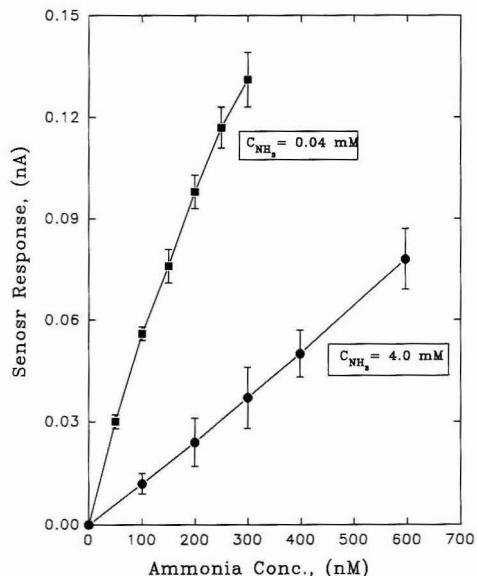


Figure 2. Ammonia response curves with total ammonia nitrogen concentrations in the internal solution of (■) 0.04 mM and (●) 4.0 mM.

1 shows this plot from which 50 μM is clearly identified as the optimum concentration of CDMF.

The total ammonia nitrogen concentration in the internal solution (C_{NH_3}) also has a major impact on the sensor response. The effect of C_{NH_3} on the steady-state response is illustrated in Figure 2 where responses for sensors with 4 and 0.04 mM C_{NH_3} are presented. A high C_{NH_3} results in an increase in

(16) Haugland, R. P. *Molecular Probes: Handbook of Fluorescent Probes and Research Chemicals*; Molecular Probes, Inc.: Eugene, OR, 1989; pp 86-94.

(17) Bates, R. G.; Pinching, G. D. *J. Am. Chem. Soc.* 1950, 72, 1393-1396.

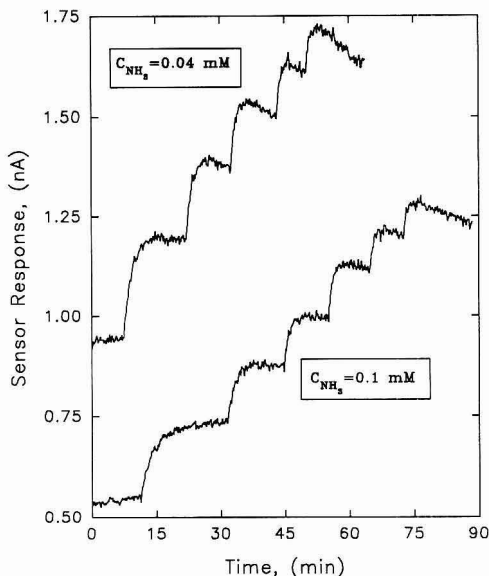


Figure 3. Time-dependent responses for sensors with total ammonia nitrogen concentrations in the internal solution of 0.04 and 0.1 mM.

linearity over the entire concentration range with a corresponding decrease in both sensitivity and limit of detection. A low C_{NH_3} , on the other hand, provides superior sensitivity at low concentrations but levels off rapidly to provide limited sensitivity at high concentrations. Such responses are predictable.¹³

The C_{NH_3} also has an effect on the stability of the steady-state signal. Figure 3 shows typical intensity-time profiles for sensors with C_{NH_3} levels of 0.04 and 0.1 mM. This figure shows that the steady-state signal slowly degrades with time at higher sample ammonia concentrations. This degradation in signal is faster with lower C_{NH_3} and it can be essentially eliminated by decreasing the intensity of the incident radiation. These results are consistent with photobleaching of the nonprotonated form of the indicator being responsible. With lower C_{NH_3} , larger amounts of the nonprotonated form of the indicator are generated, thereby increasing the photobleaching process.

The volume of the indicator solution affects both the magnitude of response and response times. Responses to ammonia concentration steps from 0 to 200 nM were monitored for a series of sensors with different volumes of internal solutions. Volumes were varied by altering the depth of the reservoir into which the internal solution was placed. With our sensor geometry, an increase in solution volume also results in an increase in the optical path length. Figure 4 summarizes the effect of solution volume on both the steady-state and dynamic properties of the sensor. As expected, increasing the optical path length provides larger signals up to the point where the path length no longer increases as the depth of the reservoir is increased. The sensor response is independent of sample volume above 0.5 μL , which corresponds to a 0.1-mm-thick solution, thereby indicating that our fluorescence measurements are only capable of sensing the first 0.1 mm of the internal solution. In regards to the dynamic response, sensor response times increased with respect to solution volume, as more ammonia is needed to equilibrate larger volumes. These results indicate that mass transport within the internal solution is rate limiting under these conditions. Extrapolation to zero volume gives the

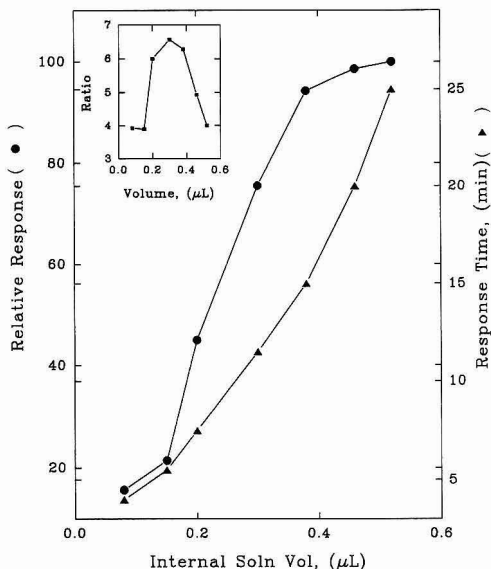


Figure 4. Effect of internal solution volume on the (●) magnitude of response and (▲) response time. The inset shows the ratio of magnitude of response and response time as a function of internal solution volume.

minimum response time possible based on sensor components other than the internal solution, such as type, porosity, and thickness of the gas-permeable membrane.

The effect of the gas-permeable membrane on the fluorescence measurement has been evaluated by comparing fluorescence signals measured with and without the Teflon membrane in place. In this experiment, the tip of a sensor without a membrane was immersed in a 0.13 M phosphate buffer that contained 50 μM CDMF. The concentration of the nonprotonated form of the indicator was controlled by adjusting the pH of this solution. These measurements were repeated with the same sensor and optics, but with the membrane in place. In this latter case, the indicator solution reservoir was filled with the pH-adjusted 50 μM CDMF solution and the fluorescence intensity was measured after immersing the sensor tip into a solution that was identical to this internal solution. Overall, the membrane provided a 1.5-fold enhancement in the sensitivity of the measurement. Diffuse reflectance off the membrane surface enhances both the intensity of the excitation radiation and the amount of emitted radiation captured by the collection fibers.

Sensors constructed with different gas-permeable membranes were evaluated in order to identify gross effects caused by membrane parameters. In all cases, microporous Teflon membranes were used; however, a complete series of membranes was not available, thereby making it impossible to perform a systematic study of these parameters. Nevertheless, sufficient membrane types were available to demonstrate that the sensor response is relatively insensitive to membrane parameters in comparison to parameters involving the internal indicator solution.

The examined membranes were composed of either plain microporous Teflon or microporous Teflon with a laminated layer of polyethylene. Table I summarizes the results in terms of the relative magnitude of response and response times obtained from sensors responding to a 0–200 nM ammonia concentration step. Plain and laminated membranes with average pore sizes of 1.0 μm resulted in similar response times. The magnitude of response, however, was significantly larger with the plain membrane. The plain membrane is more

Table I. Responses from Sensors with Different Membranes^a

average pore size (μm)	%	membrane			
		plain ^b		laminated ^c	
	porosity	rel response	response time (min)	rel response	response time (min)
1.0	91	100.0 \pm 6.2	4.0 \pm 0.3	51.0 \pm 7.3	5.1 \pm 0.8
0.2	78			89.6 \pm 13.0	7.0 \pm 0.4
0.02	50	79.9 \pm 11.9	10.1 \pm 1.6		

^a Mean \pm 1 standard deviation for four replicate measurements.^b Microporous Teflon. ^c Microporous Teflon with polyethylene lamination.

flexible compared to the laminated membrane which causes it to bow under the weight of the indicator solution. Larger indicator solution volumes with the corresponding longer optical path lengths account for the higher sensitivity. Apparently, the layer of polyethylene slows the rate of ammonia mass transport across the membrane, thereby counteracting the expected advantage of a smaller volume of internal solution in terms of the response time. In fact, response times were slightly longer with the laminated membrane. When the pore size of the laminated membrane was decreased from 1.0 to 0.2 μm , both the magnitude of the response and the response time increased. Presumably, the decrease in porosity lowers the flux across the membrane and increases the response time. The increase in magnitude of response is caused by a significant difference in the texture of these two laminated membranes. The 0.2- μm membrane was shinier than the 1.0- μm membrane which provided higher incident intensity of the excitation radiation due to enhanced reflectance off the membrane surface. Although both membranes were laminated with polyethylene, the structures of these laminated films differ, which accounts for the difference in reflectivity. Decreasing the pore size of the plain membranes from 1.0 to 0.02 μm resulted in longer response times and a lower magnitude of response. Once again, the smaller flux across the membrane as the porosity decreases explains the slower rate of response. In this case, however, the difference in magnitude of response is caused by a difference in rigidity of the membranes. The 0.02- μm membrane is considerably stronger and bows much less than the 1.0- μm membrane which corresponds to a shorter optical path length and smaller responses. Similar results were found when plain membranes were compared for use in ammonia gas sensing electrodes.¹⁸

The final parameter investigated is temperature. For the most part, the application dictates the temperature of the measurement. Nonetheless, the temperature profile is important because the temperature sensitivity of the sensor dictates the extent to which the temperature must be controlled. Temperature profiles for our FOAS are presented in Figure 5 for both the magnitude of response and the response times. In this experiment, sensor responses were monitored for a 0–200 nM concentration step in a background solution of 0.01 M sodium hydroxide. Both the magnitude of response and response times decrease with increasing temperature over the range from 5 to 45 °C. The highest response to response time ratio is obtained at 20 °C (see Figure 5 inset). The decrease in magnitude of response is consistent with a decrease in the equilibrium constant at elevated temperatures. Shorter response times are provided by faster mass transport processes at the elevated temperatures. The shape of these profiles reveals a large temperature sensitivity which necessitates rigid temperature control during operation.

Response Curves. Ammonia calibration curves are presented in Figure 6 for a FOAS constructed by using a plain

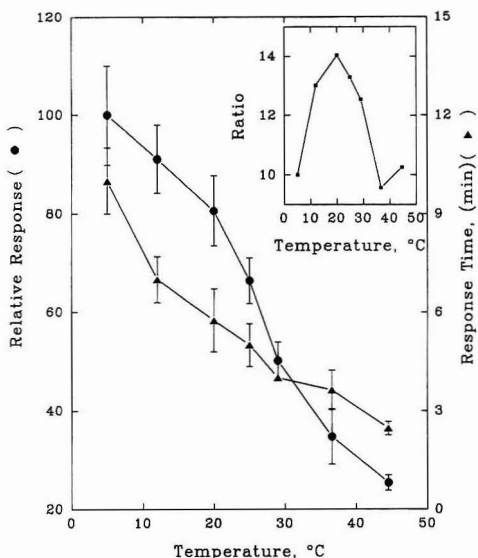


Figure 5. Effect of temperature on the (●) magnitude of response and (▲) response time. The inset shows the ratio of magnitude of response and response time as a function of temperature.

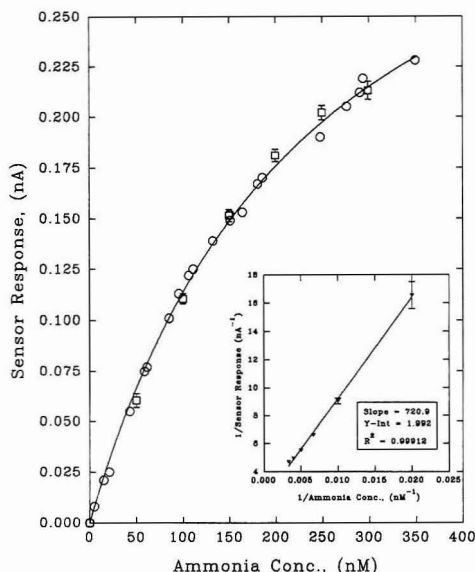


Figure 6. Calibration curve for the fiber-optic ammonia gas sensor showing responses obtained with the (○) pH adjustment and (□) standard addition methods. The inset shows a double reciprocal plot of the data collected with the standard addition method.

microporous Teflon membrane with an average pore size of 1.0 μm and an internal indicator solution composed of 0.115 M sodium chloride, 0.100 mM ammonium chloride, and 50 μM CDMF. Respectively, the open squares and open circles show the responses obtained by using the standard addition and pH adjustment methods described in the Experimental Section. Raw signals from these sensors were normalized in order to account for slight differences in the geometries of

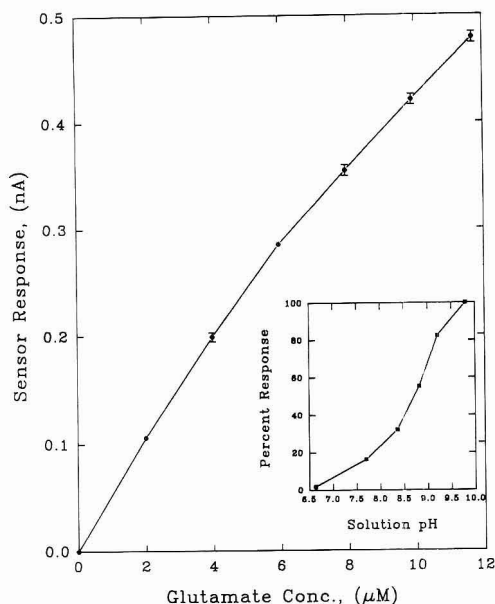


Figure 7. Glutamate calibration curve for the glutamate biosensor based on ammonia detection. The inset shows the pH profile for this biosensor.

individual sensor bodies. After adjustment, the signals overlap throughout the ammonia concentration ranges tested which were from 50 to 300 nM for the standard addition method and from 5 to 294 nM for the pH adjustment method. The solid line was generated by fitting these data to the previously described response function.¹³ This curve shows the expected nonlinear response with a detection limit ($S/N = 3$) of 7 nM. Precision at 50 nM ammonia was found to be 5.8%. Response times ranged from 2 to 5 min with faster responses at higher ammonia concentrations. In terms of sensor stability, photodegradation limited the utility of a given sensor to 1 day. Sensor calibration was accurate throughout this time period with no appreciable drift in the baseline signal.

In addition to the nonlinear response, the response function predicts a linear relationship for a double reciprocal plot of the data ($1/I_p$ vs $1/[NH_3]$). The inset in Figure 6 shows such a plot for this sensor. The transformed data can be modeled by a linear function with a slope of $721 \pm 15 \text{ M}^{-1} \text{ A}^{-1}$, y-intercept of $(2.0 \pm 0.8) \times 10^3 \text{ A}^{-1}$, and a correlation coefficient of 0.9983.

The detection limit for ammonia is below that needed for making glutamate measurements in the 1–10 μM concentration range at pH 7.8. A glutamate biosensor was then fabricated to verify the utility of the FOAS for such an application. Figure 7 shows the resulting glutamate calibration curve which was obtained in a pH 7.8 Ringer's buffer. The expected nonlinear response was observed over this concentration range. The detection limit for glutamate was $0.100 \pm 0.003 \mu\text{M}$. Response times ranged from 8 to 19 min and recovery times were even longer, ranging from 25 to 30 min. The pH profile is shown as the Figure 7 inset. Because the maximum enzyme activity is obtained over the pH range from 7.0 to 8.0,¹⁹ greater sensor responses with increasing pH is caused by the increased sensitivity to ammonia.

Endogenous Ammonia in Retinal and Eye-Cup Preparations. Before the glutamate biosensor can be used for

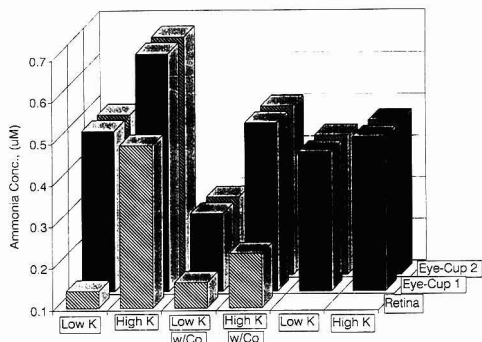


Figure 8. Concentrations of ammonia found in various extracellular fluids during the potassium-evoked depolarization of retinal and eye-cup preparations.

monitoring the synaptic modulation of glutamate in perfusates, endogenous ammonia levels must be established. We expected the ammonia level to be low and constant under our conditions.¹⁴ Ammonia levels detected during potassium-evoked depolarization of cells in our tissue preparations, however, revealed that endogenous ammonia is not constant. Figure 8 summarizes the results obtained. Overall, higher levels of ammonia were measured in the eye-cup preparations because of the larger number and variety of cells present. Potassium-evoked depolarization results in a significant increase in the level of ammonia in the perfusion buffer. The addition of cobalt, which blocks calcium-dependent synaptic events, resulted in less ammonia released during depolarization with elevated potassium. This effect is particularly evident for the retinal tissue preparation where the elevation of ammonia is only 20% of that measured in the absence of cobalt. This result suggests a significant calcium-dependent release of ammonia during potassium-evoked depolarization. After exposure to cobalt, cells associated with the eye-cup no longer responded to depolarization conditions which indicates cellular damage caused by the toxicity of cobalt.

Overall, modulation of ammonia by potassium-evoked depolarization precludes the use of this FOAS as the internal sensing element for a biosensor to measure synaptic glutamate during depolarization experiments. Although a second ammonia sensor could be used to account for extracellular ammonia variations, such an arrangement would be cumbersome and subject to systematic errors based on nonuniform ammonia distribution within the tissue matrix. The important discovery, however, is the apparent modulation of ammonia concentrations during synaptic processes. Of course many more experiments are needed to better define the potential neurochemical role of ammonia, but our results suggest that ammonia is a neurochemically active compound. The low detection limit of our FOAS makes it ideally suited to investigate this exciting phenomenon.

ACKNOWLEDGMENT

This work was funded by grants from the National Institutes of Health (GM-35487) and the National Science Foundation (BNS-8716768). We thank Hitoshi Kusakabe and the Yamasa Shoyu Co. for the generous donation of glutamate oxidase.

RECEIVED for review April 3, 1992. Accepted June 29, 1992.

Registry No. NH_3 , 7664-41-7; glutamic acid, 56-86-0; glutamate oxidase, 39346-34-4; calcium, 7440-70-2; potassium, 7440-09-7.

(19) Kusakabe, H.; Midorikawa, Y.; Fujishima, T.; Kuninaka, A.; Yoshino, H. *Agric. Biol. Chem.* 1983, 47, 1323-8.

Speciation of Mercury and Lead Compounds by Microbore Column Liquid Chromatography-Inductively Coupled Plasma Mass Spectrometry with Direct Injection Nebulization

Sam C. K. Shum, Ho-ming Pang, and R. S. Houk*

Ames Laboratory-U.S. Department of Energy, Department of Chemistry, Iowa State University, Ames, Iowa 50011

Various cationic species of Hg (Hg^{2+} , MeHg^+ , EtHg^+ , and PhHg^+) and Pb (Pb^{2+} , $(\text{Me})_3\text{Pb}^+$, and $(\text{Et})_3\text{Pb}^+$) are separated as ion pairs by reversed-phase liquid chromatography. Lead is detected at ≈ 0.2 pg and Hg at ≈ 7 pg by inductively coupled plasma mass spectrometry. A direct injection nebulizer minimizes band broadening and yields good sensitivity by injecting all the sample into the plasma. Chromatographic conditions such as mobile-phase composition and the compound used for ion pairing are selected based on the mutual requirements of chromatographic performance and detection sensitivity. The inorganic ions Pb^{2+} and Hg^{2+} can be monitored directly in human urine by simply diluting and injecting the liquid sample. The organolead and organomercury ions were not concentrated enough to be seen directly in urine, but good separations were obtained when these compounds were spiked into the sample.

INTRODUCTION

The toxicological and biological roles of trace elements depend on their chemical forms and/or oxidation states.¹⁻⁴ Thus, analytical methodology for measuring trace element speciation is necessary. The atomic spectroscopic methods that are usually used for elemental analysis generally do not distinguish the various species present for each element. However, speciation information can be obtained by coupling chromatographic separations with element-selective detection by atomic spectroscopy.⁵⁻¹⁰ Inductively coupled plasma mass spectrometry (ICPMS) is one of the most attractive detection systems for elemental speciation because of its excellent detection limits, its multielement capability, and its ability to measure isotope ratios.¹¹⁻²⁸

In most experiments with plasma detection for liquid chromatography (LC) separations, the nebulizer is one of the weakest links in the whole process because it causes band broadening and loss of much of the sample.²⁹ Several recent papers^{30,31} describe the basic properties and analytical performance of a new version of the direct injection nebulizer (DIN), originally developed by Fassel and co-workers.^{32,33} The DIN is a microconcentric pneumatic nebulizer placed inside the ICP torch. The DIN has a low dead volume (<2 μL) and produces a mist of fine droplets (1–10- μm diameter).³⁴ Rinse-out times for memory-prone elements such as Hg, I, and B are also reduced greatly compared to those obtained with conventional nebulizers.³⁰ When used for LC-ICPMS of As, Se, and Sn species, the DIN provides absolute detection limits that are superior by 1–2 orders of magnitude to those obtained with conventional nebulizers. In addition, the low dead volume and absence of a spray chamber minimize postcolumn band broadening and facilitate the use of microscale LC columns and liquid flow rates (30–100 $\mu\text{L min}^{-1}$) that are low enough for all the column effluent to be introduced into the plasma.^{24,31}

The present work reports the capabilities of LC-DIN-ICPMS for measuring charged species of Hg and Pb. The species chosen (Hg^{2+} , MeHg^+ , EtHg^+ , PhHg^+ , Pb^{2+} , $(\text{Me})_3\text{Pb}^+$, and $(\text{Et})_3\text{Pb}^+$), where Me = methyl, Et = ethyl, and Ph = phenyl, are known or potential toxins and are of substantial

* Corresponding author.

- (1) Goyer, R. A. In *Casarett and Doull's Toxicology: The Basic Science of Poisons*, 4th ed.; Casarett, L. J., Andur, M. O., Doull, J., Klaassen, C. D., Eds.; Pergamon Press: New York, 1991; Chapter 19.
- (2) Cappon, C. J. *LC/GC* 1988, 6, 584–599.
- (3) Batley, G. E.; Low, G. K.-C. In *Trace Element Speciation Analytical Methods and Problems*; Batley, G. E., Ed.; CRC Press, Inc.: Boca Raton, FL, 1989; Chapter 9.
- (4) Gardiner, P. E. *J. Anal. At. Spectrom.* 1988, 3, 163–168.
- (5) Uden, P. C., Ed. *Element-Specific Chromatographic Detection by Atomic Emission Spectroscopy*; American Chemical Society: Washington, D.C., 1992.
- (6) Krull, I. S., Ed. *Trace Metal Analysis and Speciation*; Elsevier: New York, 1991.
- (7) Keliher, P. N.; Ibrahim, H.; Gerth, D. J. *J. Anal. Chem.* 1990, 62, 184R–212R.
- (8) Harrison, R. M.; Rapsomanikis, S., Eds. *Environmental Analysis Using Chromatography Interfaced with Atomic Spectroscopy*; Ellis Horwood Ltd.: Chichester, U.K., 1989.
- (9) Keliher, P. N.; Gerth, D. J.; Snyder, J. L.; Wang, H.; Zhu, S. F. *J. Anal. Chem.* 1988, 60, 342R–368R.
- (10) Ebdon, L.; Hill, S.; Ward, R. W. *Analyst* 1987, 112, 1–16.
- (11) Thompson, J. J.; Houk, R. S. *J. Anal. Chem.* 1986, 58, 2541–2548.
- (12) Jiang, S. J.; Houk, R. S. *Spectrochim. Acta* 1988, 43B, 405–411.
- (13) Dean, J. R.; Munro, S.; Ebdon, L.; Crews, H. M.; Massey, R. C. *J. Anal. At. Spectrom.* 1987, 2, 607–610.

- (14) Matz, S. G.; Elder, R. C.; Tepperman, K. J. *J. Anal. At. Spectrom.* 1989, 4, 767–771.
- (15) Crews, H. M.; Dean, J. R.; Ebdon, L.; Massey, R. C. *Analyst* 1989, 114, 895–899.
- (16) Beauchemin, D.; Bednas, M. E.; Berman, S. S.; McLaren, J. W.; Siu, K. W. M.; Sturgeon, R. E. *J. Anal. Chem.* 1988, 60, 2209–2212.
- (17) Beauchemin, D.; Siu, K. W. M.; McLaren, J. W.; Berman, S. S. *J. Anal. At. Spectrom.* 1989, 4, 285–289.
- (18) Heitkemper, D.; Creed, J.; Caruso, J.; Fricke, F. L. *J. Anal. At. Spectrom.* 1989, 4, 279–284.
- (19) Sheppard, B. S.; Shen, W.-L.; Caruso, J. A.; Heitkemper, D. T.; Fricke, F. L. *J. Anal. At. Spectrom.* 1990, 5, 431–435.
- (20) Shibata, Y.; Morita, M. *Anal. Sci.* 1989, 5, 107–109.
- (21) Shibata, Y.; Morita, M. *Anal. Chem.* 1989, 61, 2116–2118.
- (22) Suyani, H.; Creed, J.; Davidson, T.; Caruso, J. *J. Chromatogr. Sci.* 1989, 27, 139–143.
- (23) Suyani, H.; Heitkemper, D.; Creed, J.; Caruso, J. *Appl. Spectrosc.* 1989, 43, 962–967.
- (24) Shum, S. C. K.; Neddersen, R.; Houk, R. S. *Analyst* 1992, 117, 571–575.
- (25) Al-Rashdan, A.; Heitkemper, D.; Caruso, J. *J. Chromatogr. Sci.* 1991, 29, 98–102.
- (26) Gercken, B.; Barnes, R. M. *J. Anal. Chem.* 1991, 63, 283–287.
- (27) Bushue, D. S. *Analyst* 1988, 113, 1167–1170.
- (28) Bushue, D. S.; Moody, J. R.; May, J. C. *J. Anal. At. Spectrom.* 1989, 4, 773–775.
- (29) Browner, R. F.; Boorn, A. W. *J. Chem. Phys.* 1984, 56, 786A–798A.
- (30) Wiedner, D. R.; Smith, F. G.; Houk, R. S. *J. Anal. Chem.* 1991, 63, 219–225.
- (31) Houk, R. S.; Shum, S. C. K.; Wiedner, D. R. *Anal. Chim. Acta* 1991, 250, 61–70.
- (32) Lawrence, K. E.; Rice, G. W.; Fassel, V. A. *J. Anal. Chem.* 1984, 56, 289–292.
- (33) LaFreniere, K. E.; Fassel, V. A.; Eckels, D. E. *J. Anal. Chem.* 1987, 59, 879–887.
- (34) Wiedner, D. R.; Houk, R. S. *Appl. Spectrosc.* 1991, 45, 1408–1412.

Table I. Instrument Conditions and Operating Procedures

ICPMS	Sciex Elan Model 250
ICP torch	modified Sciex short torch: injector tube orifice diameter = 1 mm; 6-mm-o.d. × 4-mm-i.d. quartz tee attached at torch base
argon flow rates (L min ⁻¹)	
outer	12* ^a
auxiliary	1*
make-up	0.30* regulated by mass flow controller
nebulizer gas	0.4*
sample flow rate	100 µL min ⁻¹ typical
forward power	1.4 kW*
sampling position	20 mm from load coil, on center*
sampler	Copper, 1.0-mm-diameter orifice
skimmer	Nickel, 0.9-mm-diameter orifice
detector voltage	~4000 V
ion lens setting	
bessel	-19.80 V
plate	-11.00 V
barrel	+5.42 V
photon stop	-7.46 V*
operating pressures	
interface	1.0 Torr
quadrupole chamber	3 × 10 ⁻⁵ Torr

^a Typical values cited. These parameters, marked with an asterisk, were adjusted daily to maximize ion signal (see text) and differed slightly from day to day.

interest in medical and environmental sciences.^{1,35-39} Optimum chromatographic conditions for separating these species as ion pairs by reversed-phase LC are discussed. Finally, application of this methodology for the speciation of Hg and Pb directly in human urine with very little sample preparation is described.

EXPERIMENTAL SECTION

ICPMS and Direct Injection Nebulizer (DIN). The inductively coupled plasma mass spectrometer used was the Elan Model 250 (Perkin-Elmer SCIEX, Thornhill, ON, Canada). The instrumental system and conditions are described in Table I. The plasma and sampling conditions indicated with an asterisk were optimized daily to maximize the signal from the analyte of interest.

The DIN used in this work was similar to one described previously (Figure 1 or ref 30). In order to operate at a liquid flow rate of 100 µL min⁻¹ while maintaining low backpressure (<750 psi), a 50-µm-i.d. × 45-cm-long fused silica capillary was used. In addition, the 50-µm DIN plugged less easily than the 30-µm one used for the previous LC work.²⁴ Tolerance to plugging was necessary for the analysis of urine, since the salt matrix was not removed beforehand. The width of the annular gap between the inner capillary and the nebulizer tip was ≈ 25 µm, the same as in the previous work.

Instrumentation, Columns, and Mobile Phases. A digital LC pump (SSI Model 222D) with a biolean microflow pump head (Scientific Systems, Inc., State College, PA) was employed. Samples were injected using a Rheodyne 7410 microinjector with a 2-µL internal sample loop disk. The analytical column used in most of this work was a 5-cm-long, 1.6-mm-i.d. PEEK column packed with reversed-phase C₁₈ material (CETAC Technologies, Omaha, NE). A similar but longer column (15 cm) was used for Hg speciation in urine. A precolumn filled with Adsorbosil silica (Alltech Association, Inc., Deerfield, IL) was placed between the

pump and the analytical column to saturate the mobile phase with silica and to extend the lifetime of the analytical column. The outlet of the analytical column was connected through a switching valve (Rheodyne 9010) to the DIN with a narrow bore polysil tube (50-µm-i.d. × 5-cm-long, Scientific Glass Engineering, Inc., Austin, TX). The narrowbore connecting capillary minimized extracolumn band broadening.

Standard solutions for optimizing ICPMS conditions were loaded to a 1-mL loop on the switching valve and then injected to the nebulizer. The fused silica capillary of the DIN was connected to the outlet of the switching valve. The outlet of the analytical column was directed to the DIN at all times except during optimization. A solution containing 5 mM ammonium pentanesulfonate in 20:80 v/v acetonitrile (ACN)-water served as the mobile phase. Separations were performed isocratically at a flow rate of 100 µL min⁻¹.

Data Acquisition. New Elan 500 upgraded hardware and software have been installed on this ICPMS. Data were acquired by peak hopping in the multielement monitoring mode using 0.5-s measurement time, a 20-ms dwell time, and 1 measurement per peak. The mass spectral resolution was 0.9 amu at 10% peak height. The most abundant isotopes of Hg* (*m/z* = 202) and Pb* (*m/z* = 208) were monitored. The ICP operating conditions and voltages applied to the ion lenses were optimized to provide maximum signal for inorganic Pb at 100 µg L⁻¹ and inorganic Hg at 250 µg L⁻¹ in 20:80 v/v ACN-H₂O.

Chromatograms were recorded in real time and stored on the hard disk of an IBM PS/2 Model 70 computer. These data (as ASCII files) were then processed using a spreadsheet program. The raw count rates were first smoothed with a five-point Savitzky-Golay routine.⁴⁰ Peak area was determined by summing all the count rates under each peak. The background was measured while nebulizing only the mobile phase by summing the total counts in the particular chromatographic region corresponding to each peak. For this work, the detection limit was defined as the amount of the element necessary to give a peak area equal to three times the standard deviation of the background count rate at each analyte mass.

Reagents and Samples. The mobile phases were prepared as follows. Ion-pairing reagents S5 (0.5 M sodium pentanesulfonate), S7 (0.5 M sodium heptanesulfonate), and S12 (0.5 M sodium dodecane sulfonate) were purchased from Regis Chemical Co. (Morton Grove, IL). Sodium salts in the eluent would be expected to cause plugging of the DIN,²⁴ plugging of the sampling orifice,⁴¹⁻⁴³ and matrix effects (usually suppression) on the signal for Hg* and Pb*.^{42,44-48} Therefore, the ion-pairing reagents were converted to their ammonium salts by passing them through a column filled with cation-exchange resin Dowex 50W-X8 in the ammonium form. The nitrogen and hydrogen present in the ammonium cation did not deposit as solids on the sampler and did not cause serious matrix effects. The resulting stock solutions of ammonium salts of S5, S7, and S12 were then diluted with ACN (HPLC grade) and deionized water (DW). Nitric acid (5%) and ammonium hydroxide (1 M) were added to adjust the pH. All mobile phases were filtered through a 0.45-µm-pore nylon filter and degassed under light vacuum from an aspirator for 10 min. At the end of each working day, the LC system was flushed overnight with 75% methanol in water as instructed by the supplier.

Chloride salts of MeHg*, EtHg*, PhHg*, (Me)₂Pb*, and (Et)₂Pb* were obtained from Alfa Products (Danvers, MA) and were used without further purification. Stock solutions of various Hg and Pb compounds at ≈ 300 mg L⁻¹ each were prepared from the above reagent-grade compounds in DW. Stock solutions of

(35) Cox, C.; Clarkson, T. W.; Marsh, D. O.; Amin-Zaki, L.; Tikriti, S.; Myers, G. G. *Environ. Res.* 1989, 49, 318-332.

(36) Friberg, L.; Vostal, J. *Mercury in the Environment*; CRC Press: Cleveland, 1972.

(37) Grandjean, P. *Biological Effects of Organolead Compounds*; CRC Press: Boca Raton, FL, 1984.

(38) Mahaffey, K. R., Ed. *Dietary and Environmental Lead: Human Health Effects*; Elsevier Scientific: New York, 1985.

(39) Beckock, R. L. *Anal. Chem.* 1986, 58, 274A-288A.

(40) Savitzky, A.; Golay, M. J. E. *Anal. Chem.* 1964, 36, 1627-1639.

(41) Olivares, J. A.; Houk, R. S. *Anal. Chem.* 1986, 58, 20-25.

(42) Jiang, S.-J.; Houk, R. S. *Anal. Chem.* 1986, 58, 1739-1743.

(43) Douglas, D. J.; Kerr, L. A. *J. Anal. At. Spectrom.* 1988, 3, 749-752.

(44) Tan, S. H.; Horlick, G. J. *Anal. At. Spectrom.* 1987, 2, 745-763.

(45) Beauchemin, D.; McLaren, J. W.; Berman, S. S. *Spectrochim. Acta* 1987, 42B, 467-490.

(46) Gregoire, D. C. *Spectrochim. Acta* 1987, 42B, 895-907.

(47) Vandecasteele, C.; Nagels, M.; Vanhoë, H.; Dams, R. *Anal. Chim. Acta* 1988, 211, 91-98.

(48) Crain, J. S.; Houk, R. S.; Smith, F. G. *Spectrochim. Acta* 1988, 43B, 1355-1364.

inorganic Hg and Pb at 100 mg L⁻¹ each were prepared by diluting 1000 mg L⁻¹ standards (PLASMACHEM Associates, Inc., Bradley Beach, NJ) in DW. All standards were prepared fresh daily by diluting stock solutions using DW. ACN was HPLC grade from Fisher Scientific, DW (resistance \approx 18 M Ω) was obtained from a Barnstead Nanopure-II system (Newton, MA), and ethylenediaminetetraacetic acid (EDTA) was reagent grade from Fisher Scientific.

Two urine samples were used. First, a freeze-dried urine standard reference material (SRM 2670, National Institute of Standards and Technology, Gaithersburg, MD) was reconstituted as instructed and used without further dilution for Pb speciation in urine. Second, a 24-h human urine specimen was collected from the first author for Hg speciation.

RESULTS AND DISCUSSION

System Dead Volume and System Variance. The general advantages of microbore columns compared to conventional packed columns include high separation efficiencies, better detection limits, decreased solvent consumption and lower costs, compatibility with on-line detectors like MS, and the possibility of using exotic mobile phases or reagents.^{49,50} However, attention must be paid to the extra-column volumes in connecting tubes, injector devices, and detectors; otherwise, the efficiency of a separation may be compromised by extracolumn broadening.^{51,52} This problem is especially important for microbore columns operated at low liquid flow rates.

In chromatography, peak broadening is often expressed in terms of peak variance.⁵³ In the simplest terms, the total variance of a peak is

$$\sigma^2 = \sigma_{\text{col}}^2 + \sigma_{\text{sys}}^2 \quad (1)$$

where σ_{col}^2 represents the contribution of the analytical column and σ_{sys}^2 is the contribution of the rest of the system (injector, connecting tubing, detector, etc.) to the peak variance. Here σ_{sys}^2 is the juxtaposition of all broadening occurring outside the analytical column. For Gaussian peaks, σ can be calculated from the full width at half-maximum ($W_{1/2}$) of the peak:

$$W_{1/2} = 2.35\sigma \quad (2)$$

In this section, both the system dead volume (μ L) and σ_{sys}^2 (s^2) are estimated to evaluate the contribution of the nebulizer to peak broadening relative to that from the chromatographic column.

The system dead volume was determined by adding known dead volumes and measuring the resulting effect on peak variance. Tubing of different sizes was used to connect the outlet of the analytical column to the switching valve. A 2- μ L sample containing MeHg⁺ (500 μ g Hg L⁻¹) was introduced to the 5-cm-long column. The mobile phase was 20:80 v/v ACN-H₂O, and no pairing reagent was used. Under these conditions, MeHg⁺ was not retained and eluted at the void time.

A plot of σ^2 vs added volume is shown in Figure 1. Extrapolation to $\sigma^2 = 0$ gave the system dead volume. The system dead volume was found to be 1.6 μ L, which was close to the value of 2 μ L estimated previously for the 50- μ m DIN.⁵⁰

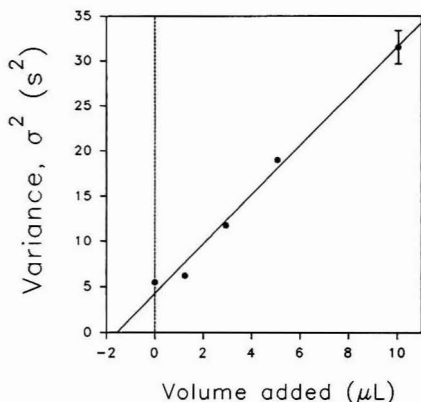


Figure 1. Determination of system dead volume and system variance. The line represents a least squares fit. See text for conditions.

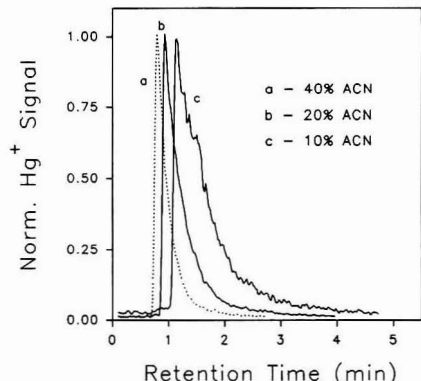


Figure 2. Effect of ACN percentage on peak shape for MeHg⁺. Each peak is normalized to the same maximum value so that the peak widths can be compared readily. See text for conditions.

Two methods were used to estimate the system variance. First, σ_{sys}^2 was estimated from the y-intercept of the plot in Figure 1 and was found to be 4.1 s^2 . Second, σ_{sys}^2 was estimated using flow injection peaks. In this method, the analytical column was removed from the HPLC system; that is, the injector was connected directly to the switching valve (by a polysil tube) which was connected to the DIN. A 2- μ L sample of MeHg⁺ (500 μ g Hg L⁻¹) and AuCl₄⁻ (100 μ g Au L⁻¹) was injected to the plasma. The carrier solvent contained S5 at 5 mM in 20:80 v/v ACN-H₂O. The standard deviations of these measurements were determined by five replicate injections.

The peak asymmetry factors measured at 10% peak height⁵⁴ were 1.3 ± 0.2 for MeHg⁺ and 1.2 ± 0.1 for Au. Thus, the flow injection peaks were approximately Gaussian, and the $W_{1/2}$ values for these flow injection peaks could be used to calculate σ_{sys} and σ_{sys}^2 for MeHg⁺ and Au, respectively. The system variance was found to be $5.0 \pm 0.3 s^2$ for MeHg⁺ and $4.0 \pm 0.2 s^2$ for Au. The chromatographic peak for MeHg⁺ shown subsequently (e.g., Figure 2) had a variance of $\sigma^2 \approx 56 s^2$. Thus, the estimated value of $\sigma_{\text{sys}}^2 = 4-5 s^2$ indicated that

(49) Novotny, M. L. *Mag.* 1985, 3, 876-886.

(50) Guiochon, G.; Colin, H. In *Microcolumn High-Performance Liquid Chromatography*; Kucera, P., Ed.; Elsevier: New York, 1984; Chapter 1.

(51) Saito, M.; Hibi, K.; Ishii, D.; Takeuchi, T. In *Introduction to Microscale High-Performance Liquid Chromatography*; Ishii, D., Ed.; VCH Publishers: New York, 1988; Chapter 2.

(52) Gluckman, J. C.; Novotny, M. In *Microcolumn Separations: Columns, Instrumentation, and Ancillary Techniques*; Novotny, M. V., Ishii, D., Eds.; Elsevier: New York, 1985; pp 57-72.

(53) Fritz, J. S.; Schenk, G. H. *Quantitative Analytical Chemistry*; Allyn and Bacon, Inc.: Newton, MA, 1987; Chapter 21.

(54) Kirkland, J. J.; Yau, W. W.; Stoklosa, H. J.; Dilks, C. H. *J. Chromatogr. Sci.* 1977, 15, 303-316.

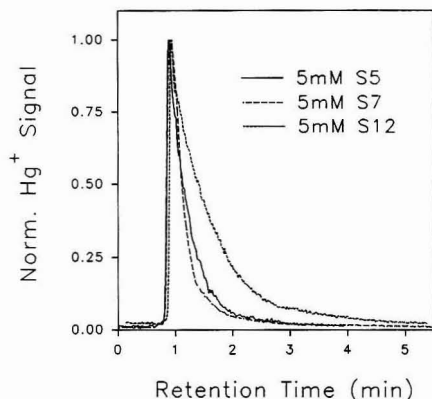


Figure 3. Effect of various ion pairing reagents on peak shape for MeHg^+ . Each peak is normalized to the same maximum value. See text for conditions.

most of the peak broadening was caused by the column, and less than 5% of the peak broadening was caused by the DIN.

Chromatographic Conditions. When coupling HPLC with ICPMS by the DIN, the separation conditions must be carefully selected so that the analytical performance of the nebulizer and plasma are not compromised. The composition and flow rate of the mobile phase are particularly important.^{24,30}

The effect of the ACN concentration (v/v) in the mobile phase on the peak shape was studied. Results for MeHg^+ are given in Figure 2. A 2- μL sample containing MeHg^+ , EtHg^+ , and PhHg^+ (500 $\mu\text{g Hg L}^{-1}$ for each species) was injected to the 5-cm-long column. The pairing reagent used was 5 mM S5. Figure 2 shows that the overall peak broadening and retention time of MeHg^+ were sensitive to the percentage of ACN in the mobile phase. With more ACN present, the MeHg^+ peak became sharper and retention time was reduced. In fact, $W_{1/2}$ increased by 150% from 40% ACN to 10% ACN. Although not shown in Figure 2, the same effect was also found for EtHg^+ and, to a lesser extent, for PhHg^+ .

Figure 3 shows the effect of various ion-pairing reagents on the peak shape of MeHg^+ . Each reagent was present at 5 mM in 20:80 v/v ACN- H_2O . There were no significant differences in peak shapes obtained with S5 and S7. However, S12 broadened the peak greatly, so this reagent was not used further. When the concentration of S5 in 20% ACN (v/v) was varied from 5 to 20 mM, and the pH was varied from 3.0 to 6.5, no significant effect on peak shape was observed.

The effect of the percentage of ACN in the mobile phase on retention time for two trialkyllead and three organomercury compounds was also studied (Figure 4a,b). As expected, the retention decreased as the concentration of the organic modifier increased. In particular, the percentage of ACN exerted a stronger effect on the retention times of the compounds with the large organic groups (i.e., PhHg^+ and $(\text{Et})_3\text{Pb}^+$). In the separation of the organomercury compounds, even though good separations were achieved using 5% ACN, the peaks were broad (Figure 2). On the other hand, sharp peaks were achieved using 40% ACN, when each Hg species was injected individually, but the peaks from the mixture of the three Hg species could not be resolved.

The effect of flow rate and percentage of ACN on ion signal with the DIN has been described elsewhere.²⁴ No green C_2 emission was observed visually from the plasma when the solvent contained less than 50% ACN. The plasma stayed on and remained stable when 75% ACN was nebulized, but

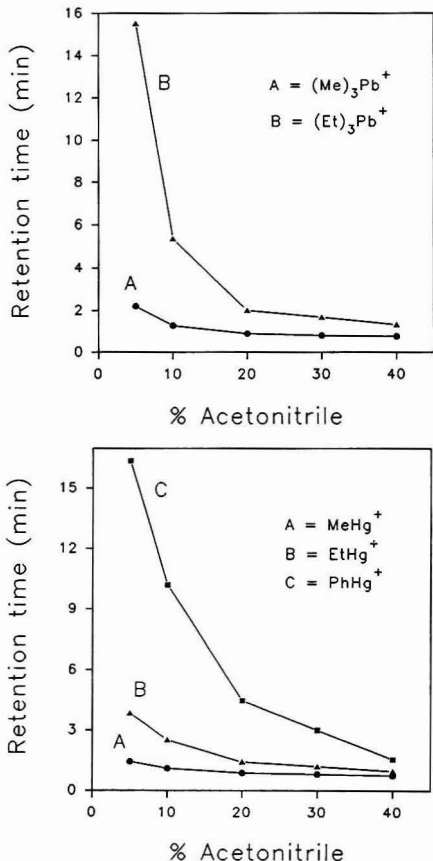


Figure 4. (a) Effect of mobile phase composition on the retention time for $(\text{Me})_3\text{Pb}^+$ and $(\text{Et})_3\text{Pb}^+$. Column, 1.6-mm i.d. \times 5 cm long; flow rate, 100 $\mu\text{L min}^{-1}$; mobile phase, 5 mM ammonium pentanesulfonate in various percentages of ACN (v/v) in water; injection volume, 2 μL ; sample size, 40 pg (as Pb) of each species. (b) Effect of mobile-phase composition on the retention time of MeHg^+ , EtHg^+ , and PhHg^+ . Conditions as in part a. Sample size: 2 ng (as Hg) of each species.

carbon deposition^{55,56} on the sampling cone did cause substantial signal drift. In addition, maximum ion signal was attained when the DIN was operated at a liquid flow rate of $\approx 120 \mu\text{L min}^{-1}$ and when a solvent containing 15–25% ACN was nebulized. Fortunately, this mobile-phase composition also suppressed tailing of the chromatographic peak, as shown in curve b of Figure 2. Finally, at a liquid flow rate of 120 $\mu\text{L min}^{-1}$, the rinse-out time for Hg in 2% HNO_3 was 15 s or less.³⁰

In summary, 5 mM S5 in 20:80 v/v ACN-water at 100 $\mu\text{L min}^{-1}$ was chosen as the optimum mobile phase and liquid flow rate. These conditions represent a compromise between maximum sensitivity, reasonable rinse-out time, reasonable separation time, and resolution. The performance of plasma-based detection methods for LC is generally sensitive to the composition and flow rate of the mobile phase,^{6,11} and ICPMS with the DIN is no exception.

Speciation of Hg and Pb Compounds in a Test Mixture. An aqueous test mixture containing MeHg^+ , EtHg^+ , PhHg^+ ,

(55) Hutton, R. C. *J. Anal. At. Spectrom.* 1986, 1, 259–263.

(56) Hausler, D. *Spectrochim. Acta* 1987, 42B, 63–73.

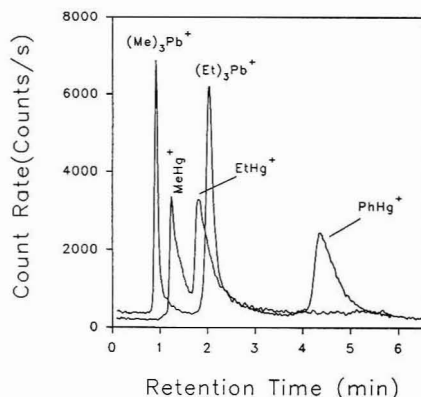


Figure 5. Separation of two trialkyllead and three organomercury species. Column, 1.6-mm i.d. \times 5 cm long; flow rate, 100 μ L min⁻¹; mobile phase, 5 mM ammonium pentanesulfonate in 20:80 v/v ACN-H₂O (pH = 3.4); injection volume, 2 μ L; sample size, 40 pg (as Pb) for (Me)₃Pb⁺, 80 pg (as Pb) for (Et)₃Pb⁺, and 2 ng (as Hg) for each of the organomercury species.

Table II. Analytical Figures of Merit for the Separation of Lead Species

	Pb ²⁺	(Me) ₃ Pb ⁺	(Et) ₃ Pb ⁺
(A) In Aqueous Sample (Figure 5)			
retention time (min)	0.9	2.0	
sensitivity ^a (counts/pg of Pb)	750	730	
RSD ^b (%)	1.7	2.0	
detection limits ^c (pg of Pb)	0.2	0.2	
(μ g L ⁻¹ , ppb)	0.1	0.1	
(B) In Urine (Figure 6)			
retention time (min)	0.6	0.9	2.0
sensitivity ^a (counts/pg of Pb)	850	800	750
RSD ^b (%)	2.8	1.7	2.5
detection limits ^c (pg of Pb)	0.2	0.2	0.2
(μ g L ⁻¹ , ppb)	0.1	0.1	0.1

^a Sensitivity was calculated based on peak area and amount injected. ^b Relative standard deviation of peak area for five replicate injections of 40 pg (as Pb) of each species. See Figure 5 for LC conditions. ^c Detection limit defined as amount of Pb required to yield a net peak that was 3 times the standard deviation of background. Peak areas were used in these calculations. ^d Relative standard deviation of peak area for three replicate injections of SRM 2670 + 40 pg (as Pb) spike of each of the trialkyllead species. See Figure 6 for HPLC conditions.

(Me)₃Pb⁺ and (Et)₃Pb⁺ was prepared. A separation of these species in a single injection is shown in Figure 5. The analytical figures of merit under these separation conditions are shown in Tables II and III.

The peaks for (Me)₃Pb⁺ and (Et)₃Pb⁺ were easily resolved, and the separation was completed in less than 3 min (Figure 5). Peak area measurements indicated that the Pb sensitivity (total counts/pg of Pb) was similar (i.e., within 5%) for the two forms (Table II). Precision based on five separate injections of \approx 40 pg (as Pb) of each species and measurement of peak areas was better than 2% RSD for both species. Calibration curves for each species based on peak areas from injections of 0.04, 0.1, 0.4, and 1 ng (as Pb) were all linear with correlation coefficients of 0.9998 for (Me)₃Pb⁺ and 0.9993 for (Et)₃Pb⁺. Absolute detection limits were \approx 0.2 pg of Pb for both species (Table II). These absolute detection limits were superior by 1–4 orders of magnitude over those obtained

Table III. Analytical Figures of Merit for the Separation of Mercury Species

	Hg ²⁺	MeHg ⁺	EtHg ⁺	PhHg ⁺
(A) In Aqueous Sample (Figure 5)				
retention time (min)	1.2	1.8	4.4	
sensitivity ^a (counts/pg of Hg)	30	35	37	
RSD ^b (%)	2.7	2.8	3.0	
detection limits ^c (pg of Hg)	7	7	6	
(μ g L ⁻¹ , ppb)	4	4	3	
(B) In Urine (Figure 8)				
retention time (min)	1.7	2.8	4.7	
sensitivity ^a (counts/pg Hg)	30	13	16	
RSD ^b (%)	3.7	3.8	4.1	
detection limits ^c (pg of Hg)	7	18	16	
(μ g L ⁻¹ , ppb)	4	9	8	

^a Sensitivity was calculated based on peak area and amount injected. ^b Relative standard deviation of peak area for five replicate injections of 2 ng (as Hg) of each species. See Figure 5 for LC conditions. ^c Detection limit defined as amount of Hg required to yield a net peak that was 3 times the standard deviation of background. Peak areas were used in these calculations. ^d Relative standard deviation of peak area for three replicate injections of diluted urine spiked with Hg²⁺, MeHg⁺, and EtHg⁺. See Figure 7 for HPLC conditions.

previously by electrochemical detection,⁵⁷ UV-vis absorption,⁵⁸ ICPAES,^{26,59} and LC-ICPMS.²⁶ Relative detection limits for Pb species were \approx 0.1 μ g L⁻¹.

In the separation of organomercury species, previous work^{27,60} reported a high background for Hg, presumably due to bleeding of species containing Hg from the column or to memory effects in the spray chamber or desolvation system of the nebulizer. For the present work, the Hg background was \approx 100 counts/s, which was comparable to the background usually seen at $m/z \approx 200$ when the DIN is used with this particular ICPMS device.³⁰ The PEEK column and tubing used and the ability of the DIN to operate without a spray chamber probably helped keep the Hg background at a reasonable level. However, the Hg peaks had longer tails than the Pb peaks, presumably due to some memory for Hg in either the column or the DIN. Despite this tailing, the peaks for MeHg⁺, EtHg⁺, and PhHg⁺ were resolved adequately (Figure 5).

Peak area measurements indicated that sensitivity (total counts/pg of Hg) was similar for all three forms of Hg (Table III). Precision based on five separate injections of \approx 2 ng (as Hg) of each species and measurement of peak areas was \approx 3% RSD for all three species. Calibration curves for each species based on injections of 0.2, 0.5, 2, 5, and 10 ng (as Hg) and peak areas were all linear with correlation coefficients 0.9995 or better. Absolute detection limits were \approx 7 pg of Hg for all three forms (Table III). These absolute detection limits were superior by factors 5–1000 over those obtained previously by LC-cold vapor ICPMS,²⁷ LC-ICPMS,²⁷ and LC-ICPAES.⁶¹ The improvement in absolute detection limits is expected because all of the sample reaches the plasma with the DIN. Relative detection limits for all three forms were \approx 4 μ g L⁻¹, which are comparable to those obtained with conventional nebulizers.

(57) MacCrehan, W. A.; Durst, R. A.; Bellama, J. M. *Anal. Lett.* 1977, 10, 1175–1188.

(58) Blaszkiewicz, M.; Baumhoer, G.; Neidhart, B. *Fresenius' Z. Anal. Chem.* 1984, 317, 221–225.

(59) Ibrahim, M.; Nisamanepong, W.; Hass, H. L.; Caruso, J. A. *Spectrochim. Acta* 1985, 40B, 367–376.

(60) Houk, R. S.; Jiang, S. J. In *Trace Metal Analysis and Speciation*; Krull, I. S., Ed.; Elsevier: New York, 1991; Chapter 5.

(61) Krull, I. S.; Bushue, D. S.; Schleicher, R. G.; Smith, S. B., Jr. *Analyst* 1986, 111, 345–349.

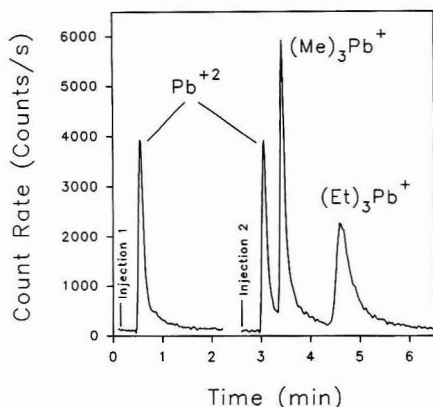


Figure 6. Separation of Pb species in NIST SRM 2670 freeze-dried urine (normal level). Conditions as in Figure 5. EDTA was added to the sample at 10 mg L⁻¹ before injection. Injection 1: NIST SRM 2670 freeze-dried urine (normal level). Injection 2: NIST SRM 2670 freeze-dried urine spiked with 40 µg (as Pb) of each of the trialkyllead species.

Pb Speciation in Freeze-Dried Urine. The proposed method was tested for measurement of Pb and Hg species in human urine. The NIST SRM 2670 freeze-dried urine (normal level) was used for experiments in Pb speciation. Inorganic Pb²⁺ was retained permanently on the column; presumably, the reversed-phase column was not completely end-capped, a problem noted previously.¹¹ The Pb²⁺ was removed by flushing the column with EDTA, which yielded a substantial Pb signal that was well above the Pb background of ~200 counts/s in EDTA. In order to elute the Pb²⁺, excess EDTA was added to the urine sample before injection to ensure a metal to ligand molar ratio of 1:50 or larger. Background was determined by injecting a blank containing the same amount of EDTA as in the urine sample.

Chromatograms for the separation of inorganic Pb and two trialkyllead species spiked into urine are given in Figure 6. Injection 1 shows the peak for Pb²⁺ in NIST SRM 2670 freeze-dried urine (normal level). Only the inorganic peak was found. Using a standard addition method, the sample was found to contain 10.3 µg L⁻¹ of Pb, which is close to the suggested value (10 µg L⁻¹) from NIST.

Since the NIST SRM did not contain measurable levels of (Me)₃Pb⁺ and (Et)₃Pb⁺, these compounds were spiked into the NIST urine to test the suitability of the method for this separation in the presence of a difficult matrix. Injection 2 of Figure 6 shows the separation of all three Pb species. The retention times for the two trialkyllead species remained the same as in their separation from a simple aqueous test mixture (Table II). Peak area measurements showed that sensitivity was similar for all three forms and was comparable (within 10%) to those obtained for Pb species in the test mixture. The reproducibility of the peak areas was better than 3% RSD (*n* = 3). Absolute detection limits were 0.2 pg for all three Pb compounds in urine.

In injection 2, the peak height for Pb²⁺ was the same as that in injection 1. Also, reasonable chromatographic peaks were seen for (Me)₃Pb⁺ and (Et)₃Pb⁺. These observations showed that the use of EDTA to prevent permanent retention of Pb²⁺ did not disturb the relative amounts of the alkyllead ions or perturb their chromatographic behavior. Undesired interconversions between different chemical forms of an element or instability of particular species are common problems in speciation experiments. The simple procedure

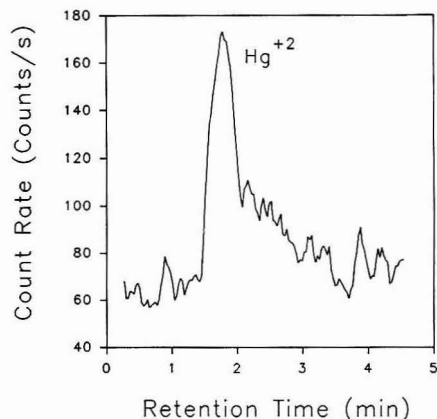


Figure 7. Hg²⁺ in a 24-h human urine specimen. Conditions as in Figure 5. Column: 1.6-mm i.d. × 15 cm long.

for preparing the sample (i.e., mere dilution) also may help prevent problems from interconversion or instability of the species present.⁶²

Hg Speciation in 24-h Human Urine. A 24-h⁶³ urine specimen (~2 L) from the first author was analyzed for Hg species. A chromatogram from one injection of the urine specimen is given in Figure 7. Only the inorganic mercury peak was found. Using a standard addition method, the specimen was found to contain 25 µg L⁻¹ of inorganic mercury. The total mercury content of this urine sample was determined to be 28 µg L⁻¹ by flow injection and standard addition, i.e., no chromatographic column was employed. None of the organomercury ions were present at sufficient concentrations to be observed directly in urine, as was the case for the organolead ions described in the preceding section. A preliminary preconcentration procedure would be required to see these species.⁶⁴

The chromatographic procedure described in the present work was evaluated further by the following spike experiment. Another urine aliquot was diluted by a factor of 10 with deionized water and spiked with 0.75 ng of Hg²⁺ and 2 ng (as Hg) of each of the alkylmercury species. The dilution minimized the matrix effect of Na on Hg signal. A longer column (15 cm) was also required to resolve the Hg²⁺ peak from that for MeHg⁺.

Figure 8 shows the separation of these three Hg compounds in urine. Since a longer column was used, the retention times for MeHg⁺ and EtHg⁺ were almost twice as long as those reported for Hg speciation in the aqueous test mixture. Peak area measurements indicated that the sensitivity for Hg²⁺ was similar to that obtained for the Hg species in the simple aqueous solution. However, the sensitivities for MeHg⁺ and EtHg⁺ were reduced by a factor of 2 in the urine matrix, presumably due to matrix suppression from Na (~1000 ppm Na). With the anionic pairing reagent in the eluent, Na⁺ was weakly retained and eluted at ~2 min after the sample was injected, i.e., after the Hg²⁺ peak but before the subsequent peaks for MeHg⁺ and EtHg⁺. Thus, sensitivity for Hg²⁺ was not affected by the urine matrix, because the Na from the urine had not yet reached the plasma when Hg²⁺ eluted. In

(62) Sheppard, B.; Caruso, J.; Heitkemper, D.; Wolnick, K. *Analyt.* 1992, 117, 971-976.

(63) Jacobs, D. S.; Kasten, B. L., Jr.; Demott, W. R.; Wolfson, W. L. *Laboratory Test Handbook with DRG Index*; Lexi-Comp Inc.: OH, 1984; p 514.

(64) Blaszkiewicz, M.; Baumhoer, G.; Neidhart, B. *Fresenius' Z. Anal. Chem.* 1986, 325, 129-135.

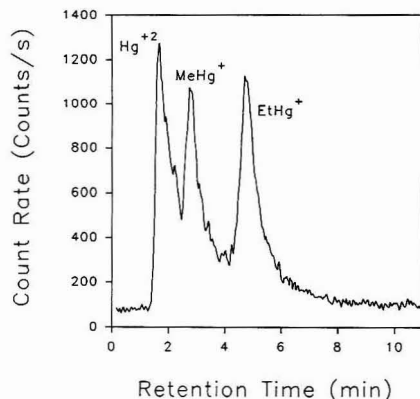


Figure 8. Separation of Hg species in a diluted 24-h human urine specimen. Conditions as in Figure 7. Sample: urine diluted by a factor of 10 with deionized water and spiked with 0.75 ng (as Hg) of Hg^{2+} and 2 ng (as Hg) of each of the organomercury species.

contrast, because of the tail on the Na^+ chromatographic peak, some Na was present in the plasma when MeHg^+ and EtHg^+ eluted. Hence, the Hg^+ signal from these species was diminished by a matrix effect caused by Na. For this separation, the precision was still 5% RSD or better ($n = 3$). Absolute detection limits were 7–18 pg of Hg for the three Hg compounds in urine.

As a final note, the reversed-phase ion-pairing separation reported here proved remarkably robust and resilient even when a difficult matrix (urine) was analyzed. Chromatographic retention times were not affected by repeated injections of the urine matrix. Chromatographic resolution²³ was only slightly poorer in the presence of the urine matrix than that obtained for the test solutions. For example, the resolution between $(\text{Me})_2\text{Pb}^+$ and $(\text{Et})_2\text{Pb}^+$ peaks was 3.7 in Figure 5 (for the test solution) compared to 3.0 in Figure 6 (for the spiked urine matrix).

SAFETY NOTE

The Hg and Pb compounds described in this paper could be severe toxins and should be handled with extreme care. Avoid inhaling the fine droplets produced by the DIN, particularly when these Hg and Pb compounds are present.

ACKNOWLEDGMENT

The columns used were supplied by Daniel R. Wiedner (CETAC Technologies) and Douglas Gjerde (Sarasep, Inc.). Ames Laboratory is operated for the U.S. Department of Energy by Iowa State University under Contract no. W-7405-Eng-82. This work was supported by the Office of Basic Energy Sciences, Division of Chemical Sciences.

RECEIVED for review April 20, 1992. Accepted July 23, 1992.

Selective Detection of Brominated Hydrocarbons by the Photodetachment-Modulated Electron Capture Detector

J. A. Bognar, W. B. Knighton, and E. P. Grimsrud*

Department of Chemistry, Montana State University, Bozeman, Montana 59717

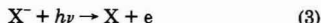
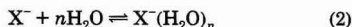
A version of the photodetachment-modulated electron capture detector (PDM-ECD) is described by which the intentional addition of SIF_4 to the detector gas causes selective responses to trace levels of simple brominated compounds, including CF_2Br_2 and CH_2Br_2 , in the presence of simple chlorinated compounds, including CFCl_3 , CHCl_3 , and CCl_4 . These response characteristics are created by the simultaneous occurrence of the following gas-phase processes within the PDM-ECD: electron capture by the halogenated hydrocarbons, RX, to form halide negative ions, X^- ; electron photodetachment of Br^- ions by a broad-band UV light source; and prevention of Cl^- photodetachment by the association of Cl^- with the Lewis acid, SIF_4 , and other fluoroaluminum compounds that result from the addition of SIF_4 to the PDM-ECD detector gas. This device is also shown to provide selective responses to iodinated hydrocarbons in the presence of chlorinated and brominated compounds.

INTRODUCTION

Since its invention about 30 years ago, the electron capture detector (ECD) for gas chromatography (GC) has become invaluable for the trace environmental analysis of a wide range of halogenated compounds.¹ This is because the ECD responds strongly to many halogenated compounds and only weakly or not at all to many other classes of compounds that might also be present in an environmental sample. However, in addressing an increasing array of complex environmental problems that are associated with halogenated hydrocarbons, an even greater level of response specificity than afforded by the conventional ECD is often needed. One example of this concerns the relationship between atmospheric halocarbons and stratospheric ozone. Most of the attention in this area has been directed toward the role of chlorinated compounds, such as CF_2Cl_2 , CFCl_3 , CH_3CCl_3 , CCl_4 , and CH_3Cl .² Since the concentrations of these chlorinated compounds in the lower regions of the atmosphere are in the high ppt (parts per trillion) range, they have been relatively easy to monitor by existing GC-ECD^{3,4} or GC-mass spectrometric^{5,6} techniques, and a great deal is now known about the atmospheric chemistry of chlorinated compounds. It is now thought that brominated compounds, such as CF_3Br , CF_2BrCl , CH_3Br , $\text{CH}_2\text{BrCH}_2\text{Br}$, CHBr_3 , and CH_2Br_2 , may also play an important role in stratospheric ozone depletion.⁷⁻¹² Much less is known about the atmospheric chemistry of the brominated

compounds, however, because their background concentrations in the lower atmosphere are much lower, in the low ppt range, and, therefore, they are much more difficult to detect and quantify. One of the greatest difficulties associated with the trace analysis of brominated compounds in the atmosphere by the GC-ECD approach is presented by the fact that the earth's atmosphere now contains many chlorinated compounds (in addition to the major ones mentioned above) whose individual concentrations are at least in the low ppt range. Therefore, the ECD's sensitive response to these chlorinated compounds confuses the detection and determination of the atmospheric brominated compounds. In order to study the atmospheric chemistry of brominated compounds, it would clearly be desirable to have a GC detector that responds sensitively to the brominated compounds and does not respond at all to the chlorinated compounds.

In a recent report from our laboratory, we described a version of the photodetachment-modulated electron capture detector (PDM-ECD) that responded sensitively to iodinated but not to chlorinated compounds.¹³ The PDM response of this detector was shown to be determined by the following set of gas phase reactions:



Electron capture by chlorinated or iodinated compounds (RX) led to the formation of chloride or iodide ions (X^-), respectively, by reaction 1. With small amounts of water intentionally added to the detector gas, hydration of X^- by reaction 2 was extensive for the chlorinated compounds where $\text{X}^- = \text{Cl}^-$ and was not extensive for the iodinated compounds where $\text{X}^- = \text{I}^-$. The PDM response of this detector was proportional to the rate of photodetachment (PD) as shown by reaction 3 using a 100-W Hg arc lamp as a light source without a monochromator. The UV light of this source caused extensive PD of the I^- ions, but little PD of the Cl^- ions because the Cl^- ions were extensively hydrated through reaction 2. The potential of the H_2O -modified PDM-ECD for providing selective responses to brominated in the presence of chlorinated compounds was also investigated. However, the extent of hydration of Br^- by reaction 2 is significantly greater than for I^- and more closely resembles that of Cl^- . Therefore, it was much more difficult to establish conditions within the

(1) Zlatkis, A.; Poole, C. F. *Electron Capture, Theory and Practice in Chromatography*; Elsevier: New York, 1981.

(2) Prather, M. J.; Watson, R. T. *Nature (London)* 1990, 344, 729-734.

(3) Lovelock, J. E. *Nature (London)* 1971, 230, 379.

(4) Lovelock, J. E.; Maggs, R. J.; Wade, R. J. *Nature (London)* 1973, 241, 194-196.

(5) Grimsrud, E. P.; Rasmussen, R. A. *Atmos. Environ.* 1975, 9, 1010-1013.

(6) Grimsrud, E. P.; Rasmussen, R. A. *Atmos. Environ.* 1975, 9, 1014-1017.

(7) Fabian, P.; Borchers, R.; Penkett, S. A.; Prosser, N. J. D. *Nature (London)* 1981, 294, 733-735.

(8) Rasmussen, R. A.; Khalil, M. A. K. *Geophys. Res. Lett.* 1984, 11, 433-436.

(9) Berg, W. W.; Heidt, L. E.; Pollock, W.; Sperry, P. D.; Cicerone, R. J. *Geophys. Res. Lett.* 1984, 11, 429-432.

(10) Hammit, J. K.; Camm, F.; Connell, P. S.; Mooz, W. E.; Wolf, K. A.; Wuebbles, D. J.; Bamezai, A. *Nature (London)* 1987, 330, 711-716.

(11) Singh, O. N.; Borchers, R.; Fabian, P.; Lal, S.; Subbaraya, B. H. *Nature (London)* 1988, 334, 593-595.

(12) Finlayson-Pitts, B. J.; Livingston, F. E.; Berko, H. N. *Nature (London)* 1990, 343, 622-625.

(13) Arbon, R. E.; Grimsrud, E. P. *Anal. Chem.* 1990, 62, 1762-1768.

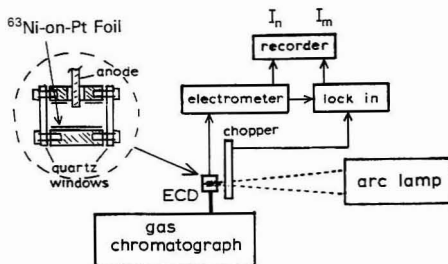
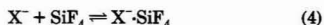


Figure 1. Schematic diagram of the photodetachment-modulated electron capture detector (PDM-ECD) used here. The normal ECD current, I_n , and a PD-modulated component of the ECD current, I_m , are simultaneously monitored. The full intensity of a 100-W Hg arc lamp is used without a monochromator or light filter and is chopped at a frequency of 83 Hz. Detector temperature is 150 °C.

H₂O-modified PDM-ECD in which strong, selective responses to brominated compounds in the presence of chlorinated compounds could be attained.

In the present study we report the use of SiF₄, instead of H₂O, for increasing the selectivity of the PDM-ECD's response to brominated compounds in the presence of chlorinated compounds. Babcock, Taylor, and Herd have previously shown¹⁴ that SiF₄ undergoes a fast Lewis acid-base association reaction (shown generally for a halide anion, X⁻, in reaction 4) with Cl⁻ at room temperature in which the Cl⁻ ion becomes bonded to the electron deficient Si atom to form a penta-coordinate ion complex, Cl⁻·SiF₄.



Babcock et al. also reported that the corresponding reaction of SiF₄ with Br⁻ ion was too slow to be reliably measured by their flowing afterglow technique. The PDM-ECD measurements to be reported here will be accompanied by pulsed e-beam high-pressure mass spectrometry (PHPMS) measurements of reaction 4 in which equilibrium constants for the cases, X⁻ = Cl⁻ and Br⁻, have been determined. Also, the PHPMS measurements will indicate the importance of SiF₄-derived impurities in affecting the responses of the SiF₄-modified PDM-ECD to halogenated compounds.

EXPERIMENTAL SECTION

PDM-ECD. A schematic diagram of the PDM-ECD is shown in Figure 1. Many of its components have been described previously in detail.^{13,15,16} For the present study, the ECD has an internal diameter of 1.0 cm and length of 1.5 cm. Ionization of the atmospheric pressure detector gas is caused by a 15 mCi ⁶³Ni-on-Pt foil that forms the cylindrical internal wall of the ECD. A stainless-steel pin of 1/16-in. diameter protrudes 1/16 in. into one side of the active volume and serves as the anode of the ECD. Pulses of +50-V amplitude, 2.5-μs width, and 3-kHz frequency were continuously applied to the anode. The time-averaged electron current thereby obtained is then amplified by an electrometer. The total emission from a 100-W Hg arc lamp shown in Figure 1 is mechanically chopped at a frequency of 83 Hz and passed through the quartz windows of the ECD. In a single GC analysis by the PDM-ECD, two responses are simultaneously observed at a dual-pen recorder. An normal ECD response (δI_n) is provided at pen 1 by monitoring the decrease in the electrometer current as an EC-active compound passes through the detector. A photodetachment-modulated response

(δI_m) is provided at pen 2 of the recorder by the lock-in amplifier that extracts the 83-Hz component of the electrometer current.

Samples were introduced to the PDM-ECD by a 10-ft × 1/8-in. stainless-steel column packed with 10% SF-96 on Chromosorb W which was maintained at room temperature. Nitrogen carrier gas (30 mL/min) was first passed through oxygen- and water-removing traps prior to the GC. A detector make-up gas (nitrogen, 15 mL/min) was also passed through oxygen- and water-removing traps and then through a 1.35-L stainless-steel exponential dilution vessel prior to mixing with the column effluent at the base of the detector. SiF₄ was added to the make-up gas by its injection into the exponential dilution vessel using a gas-tight syringe. The PDM-ECD was maintained at 150 °C by a pair of cartridge heaters controlled by a thermocouple sensor. A second thermocouple sensor provided an independent measure of the detector temperature.

The halogenated methanes studied here were obtained in pure form from commercial suppliers. Mixtures of these in nitrogen gas were made by successive dilution into gas-tight glass vessels with final storage in a 4.5-L glass carboy. This carboy was pressurized slightly with nitrogen gas, allowing numerous samples to be transferred by a 50-mL syringe to a 1.0-mL gas sampling loop attached to the head of the GC column. The amount of each halogenated compound added to the carboy was adjusted so that the normal ECD responses did not exceed 15% of the total ECD standing current. While two different sources of SiF₄ were tested (Matheson, 99.99% pure, and PCR, 99.5% pure), no significant differences in their effects on PDM-ECD responses were observed.

PHPMS. The pulsed e-beam high-pressure mass spectrometer (PHPMS) has also been previously described in detail¹⁷⁻¹⁹ and was used here with selection of the following parameters: buffer gas, methane; ion source pressure, 4 Torr; temperature, 150 °C; pulse width, 20 μs; pulse repetition rate, 10 s⁻¹. The PHPMS allows identification of the negative ions formed under thermal electron capture conditions and, by use of its temporal measurement capabilities, allows determination of equilibrium constants for ion clustering reactions.¹⁷

RESULTS AND DISCUSSION

In attempting to identify a gaseous Lewis acid that might interact preferentially with Cl⁻ ion versus Br⁻ ion, BF₃ was first tested²⁰ as an additive to the detection gas of the PDM-ECD, and promising results were initially obtained. However, it was also noted that BF₃ tends to adhere strongly to the surfaces of the gas transfer lines and the PDM-ECD, so that many hours were typically required in order to either rid the system of BF₃ or to achieve a stable PDM-ECD response after changing the concentration of BF₃ in the makeup gas. Therefore, when initial experiments with SiF₄ also looked promising and were not accompanied by noticeable memory effects, subsequent attention was devoted entirely to the use of SiF₄.

In Figure 2, the PDM-ECD responses, including a normal response, δI_n , and a PD-modulated response, δI_m , to a multicomponent sample containing CF₂Br₂, CH₃I, CHCl₃, CCl₄, and CH₂Br₂ in pure nitrogen buffer gas is shown. Since all of these halogenated methanes are known to capture electrons rapidly, sensitive δI_n responses to each of them are observed (the first peak shown is due to residual oxygen). Since the total emission from a Hg-arc lamp has been used without a monochromator or filter, δI_m responses are observed for all of the halocarbons.^{13,15} In Figure 3, the same sample has been analyzed after adding 350 ppb (parts per billion)

(17) Knighton, W. B.; Zook, D. R.; Grimsrud, E. P. *J. Am. Soc. Mass Spectrom.* 1990, 1, 372-381.

(18) Knighton, W. B.; Grimsrud, E. P. *Int. J. Mass Spectrom. Ion Processes* 1991, 109, 89-94.

(19) Knighton, W. B.; Grimsrud, E. P. *J. Am. Chem. Soc.* 1992, 114, 2336-2342.

(20) Larson, J. W.; McMahon, T. B. *J. Am. Chem. Soc.* 1985, 107, 766-773.

(14) Babcock, L. M.; Taylor, W.; Herd, C. R. *Int. J. Mass Spectrom. Ion Processes* 1987, 81, 259-272.

(15) Mock, R. S.; Grimsrud, E. P. *Anal. Chem.* 1988, 60, 1684-1694.

(16) Mock, R. S.; Grimsrud, E. P. *J. Am. Chem. Soc.* 1989, 111, 2861-2870.

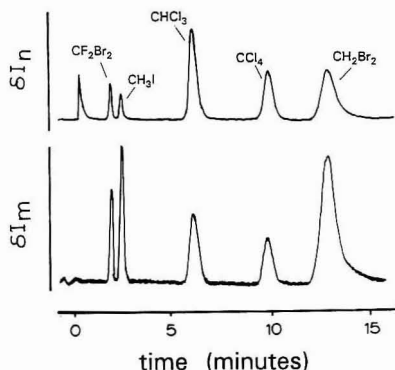


Figure 2. Normal (δI_n) and modulated (δI_m) PDM-ECD responses simultaneously obtained in the GC analysis of a 1.0-mL nitrogen gas sample containing the following amounts of halogenated methanes: 1.6 ppb (parts per billion) CF_2Br_2 , 1.1 ppb CH_3I , 27 ppb CHCl_3 , 4.2 ppb CCl_4 , and 8.3 ppb CH_2Br_2 . In this case, the detector gas is pure nitrogen. The ECD standing current is 4.2 nA.

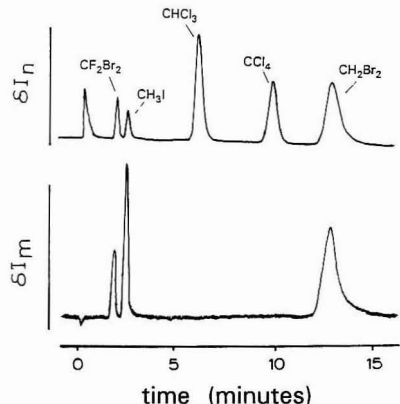


Figure 3. PDM-ECD responses to the sample described in Figure 2 with 350 ppb SiF_4 added to the detector gas supply. The δI_m responses to CHCl_3 and CCl_4 have been eliminated. The ECD standing current is 4.2 nA.

SiF_4 to the detector gas. It is noted that the level of baseline standing current and the normal δI_n responses to all five compounds in Figure 3 have not been changed by the addition of SiF_4 . However, it is also noted that the δI_m responses to the two chlorinated compounds, CHCl_3 and CCl_4 , have been completely eliminated in Figure 3. At the same time, the δI_m response to CH_3I in Figure 3 has been unaffected by the presence of SiF_4 and the δI_m responses of the two brominated compounds, CF_2Br_2 and CH_2Br_2 , remain about two-thirds as great as in Figure 2.

A repeated analysis of the same mixture after the concentration of SiF_4 had been raised to 30 ppm (parts per million) is shown in Figure 4. Even with this relatively large amount of SiF_4 added to the carrier gas, the ECD standing current is diminished by only 15% relative to that in Figure 2 and, the normal δI_n responses to all compounds are not significantly altered. The δI_m response to CH_3I in Figure 4 remains about 65% as great as in Figure 2 while the δI_m response to CH_2Br_2 has been completely eliminated. It is interesting to note, however, that the response to CF_2Br_2 has not been entirely eliminated. This residual level of δI_m response to CF_2Br_2 is presently thought to be related to the fact that electron capture

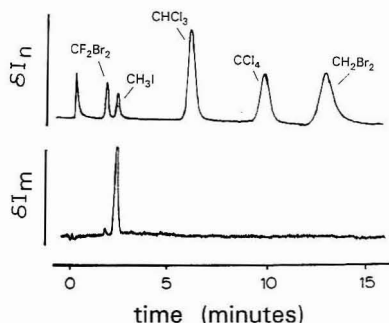


Figure 4. PDM-ECD responses to the sample described in Figure 2 with 30 ppm (parts per million) SiF_4 added to the detector gas supply. The δI_m responses to CHCl_3 , CCl_4 , and CH_2Br_2 have been eliminated. The ECD standing current is 3.6 nA.

by this compound in an atmospheric pressure buffer gas produces about 20% Br_2^- along with the major ion, Br^- , while electron capture by CH_2Br_2 produces only Br^- .²¹ Apparently, under the conditions of Figure 4 photodetachment of the Br^- ions is prevented by its interaction with the detector gas dopant while photodetachment of the Br_2^- ions is not. Another important point illustrated in Figure 4 is that with use of relatively high concentrations of SiF_4 no disturbances of any kind to the PD-modulated signal is observed as the chlorinated compounds pass through the detector. Therefore, a problem previously noted¹³ in which inverse responses to chlorinated compounds were observed when relatively high concentrations of protic clustering agents (water, methanol, and ethanol) were added to the detector gas is absent with use of SiF_4 as a complexing agent.

In order to more completely understand the effects of SiF_4 on the PDM-ECD responses shown above, measurements of the ion-molecule reactions between halide ions and SiF_4 were made with a pulsed e-beam high-pressure mass spectrometer (PHPMs). Using the temporal capabilities of this instrument,¹⁷ equilibrium measurements of reaction 4 for the cases $\text{X}^- = \text{Cl}^-$ and Br^- were obtained by measurements such as the two shown in Figure 5. In part A, Cl^- is first produced following an e-beam pulse by electron capture to CF_2Cl_2 and then undergoes equilibrium reaction 4 with SiF_4 to form Cl-SiF_4 . In part B, Br^- is first produced by electron capture to CH_2Br_2 and then undergoes equilibrium reaction 4 with SiF_4 . In each of these experiments, a constant intensity ratio for the X^- and X-SiF_4 ions is reached very quickly after the e-beam pulse. By assuming that the ion intensity ratios reflect the ion concentration ratios within the source²² and from the known partial pressure of SiF_4 (P_{SiF_4}) in the ion source, the equilibrium constant for reaction 4 is calculated from the relation

$$K_4 = [\text{X-SiF}_4]/[\text{X}^-]P_{\text{SiF}_4} \quad (5)$$

At least five determinations of K_4 were performed for each case, $\text{X}^- = \text{Cl}^-$ and Br^- , using a range of SiF_4 concentrations spanning more than one order of magnitude. K_4 was found to be $2.0 (\pm 0.1) \times 10^7 \text{ atm}^{-1}$ for $\text{X}^- = \text{Cl}^-$ and $2.1 (\pm 0.1) \times 10^8 \text{ atm}^{-1}$ for $\text{X}^- = \text{Br}^-$ at 150 °C. Our determination of K_4 for $\text{X}^- = \text{Cl}^-$ is in excellent agreement with a previous measurement of this system by Larson and McMahon²⁰ who found $K_4 = 1.9 \times 10^7 \text{ atm}^{-1}$ at 150 °C. In an attempt to determine K_4 for the case $\text{X}^- = \text{I}^-$, no cluster ion of the type I-SiF_4 was

(21) Zook, D. R.; Knighton, W. B.; Grimsrud, E. P. *Int. J. Mass Spectrom. Ion Processes* 1991, 104, 63-80.

(22) Kebarle, P. *Annu. Rev. Phys. Chem.* 1977, 28, 445-476.

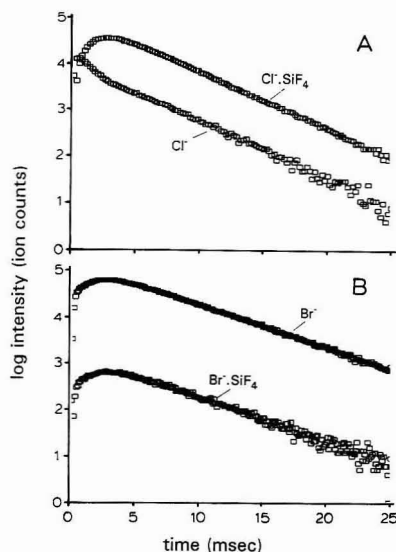


Figure 5. Measurements of the equilibrium constant, K_4 , for the association of SiF_4 with Cl^- and Br^- ions by the pulsed e-beam high-pressure mass spectrometer (PHPMs). In part A, the ion source contains 0.2 mTorr of CF_2Cl_2 , 0.46 mTorr of SiF_4 , and 4.0 Torr of methane. In part B, the ion source contains 0.2 mTorr of CH_2Br_2 , 3.7 mTorr of SiF_4 , and 6.0 Torr of methane. The source temperature is 150 °C.

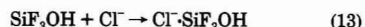
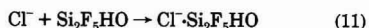
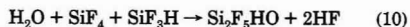
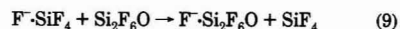
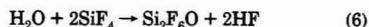
detected. On this basis, K_4 for I^- is estimated to be smaller than $1 \times 10^2 \text{ atm}^{-1}$ at 150 °C.

The results shown previously in Figures 2–4 can now be considered in terms of the K_4 values just determined for reaction 4. In Figure 3, it was shown that the addition of 350 ppb SiF_4 to the detector gas caused the PDM-ECD responses to the chlorinated compounds to completely disappear, while the responses to the brominated compounds decreased by about 33%, and the response to CH_3I was unchanged. Since we now know that $K_4(\text{Cl}^-) \gg K_4(\text{Br}^-) \gg K_4(\text{I}^-)$, the results shown in Figure 3 are at least in qualitative agreement with the possibility that reaction 4, alone, prevents the photodetachment of the X^- ions. Upon closer inspection, however, it will be shown below that processes in addition to reaction 4 are also operative. Under the equilibrium conditions in Figure 3 ($P_{\text{SiF}_4} = 3.5 \times 10^{-7} \text{ atm}$, $K_4(\text{Cl}^-) = 2.0 \times 10^7 \text{ atm}$, and $K_4(\text{Br}^-) = 2.1 \times 10^3 \text{ atm}$), application of eq 5 indicates that about 12% of the total chloride ions would be expected to remain as free Cl^- ions, unbound to SiF_4 , and that 99.9% of the total bromide ions would be expected to remain as free Br^- ion. Therefore, reaction 4, alone, does not appear to adequately account for the complete loss of the PDM response to the chlorinated compounds and the 33% reduction in the PDM response to the brominated compounds in Figure 3. Similarly, the complete loss of the PDM response to CH_2Br_2 observed under the conditions of Figure 4 ($P_{\text{SiF}_4} = 3.0 \times 10^{-6} \text{ atm}$) is not consistent with the prediction by eq 5 that 94% of the total bromide ion would remain as free Br^- ion under these conditions.

Additional evidence for processes other than reaction 4 was also noted in the PHPMs experiments. For example, the full mass spectrum recorded in one of the measurements of K_4 for the Cl^- ion is shown in Figure 6A. In this spectrum, significant intensities are noted for ions in addition to the expected Cl^- and Cl-SiF_4 ions. These additional ions are

thought to be F-SiF_4 , $\text{Cl-SiF}_3\text{OH}$, $\text{F-Si}_2\text{F}_6\text{O}$ and $\text{Cl-Si}_2\text{F}_6\text{O}$. Since $\text{Si}_2\text{F}_6\text{O}$ is known to be a common impurity in SiF_4 ,²³ the $\text{Cl-Si}_2\text{F}_6\text{O}$ ion is thought to be formed by the association of Cl^- with this impurity. A means by which the other unexpected ions are possibly formed is suggested by the mass spectrum shown in Figure 6B which has been recorded under the same conditions as in Figure 6A except that 1.0 mTorr of water vapor has also been added to the ion source. With added water vapor, the relative intensities of the unexpected ions, F-SiF_4 , $\text{Cl-SiF}_3\text{OH}$, and $\text{F-Si}_2\text{F}_6\text{O}$, have been significantly increased. It is also noted in Figure 6B that the intensity of the $\text{Cl-Si}_2\text{F}_6\text{O}$ ion has been decreased and that a new ion, $\text{Cl-Si}_2\text{F}_6\text{HO}$, has been formed. In parallel experiments in which SiF_4 and water vapor, but not CF_2Cl_2 , were present in the methane buffer gas, no negative ions of significant relative intensity were observed.

Most of the synergistic effects of SiF_4 and water vapor on the spectrum in Figure 6B can be explained by reactions 6–11, each of which has precedence in the literature:



By reaction 6, HF is produced from water,²³ along with additional $\text{Si}_2\text{F}_6\text{O}$. While HF will bind strongly to Cl^- by reaction 7,²² the Cl^-HF cluster ion is not observed apparently because it is quickly converted to F-SiF_4 by reaction 8 (from literature data,²⁰ reaction 8 is estimated to be slightly exothermic). The F-SiF_4 ion will tend to be converted to $\text{F-Si}_2\text{F}_6\text{O}$ by F^- transfer to the common impurity $\text{Si}_2\text{F}_6\text{O}$, as shown by reaction 9. SiF_3H is also known to be a common impurity in SiF_4 .²³ In the presence of water, $\text{Si}_2\text{F}_6\text{HO}$ can then be formed by reaction 10, leading to $\text{Cl-Si}_2\text{F}_6\text{HO}$ by reaction 11. Note that the ion $\text{F-Si}_2\text{F}_6\text{HO}$ is not formed by a reaction analogous to reaction 11 because the free F^- ion is not thought to be present. It is also noted in parts A and B of Figure 6 that the intensity of the ion $\text{Cl-SiF}_3\text{OH}$ was increased by the addition of water vapor. This suggests the occurrence of reaction 12 followed by reaction 13. A reaction analogous to reaction 12 has been previously reported for SiCl_4 .²⁴

The full mass spectrum for one of the measurements of K_4 for the Br^- ion is shown in Figure 7A. Even though the partial pressure of SiF_4 used in Figure 7A is 1 order of magnitude greater than for the corresponding experiment involving Cl^- in Figure 6A, it is seen that the fraction of Br^- that is complexed by SiF_4 or impurities in SiF_4 is very small. In Figure 7B, the addition of 1 mTorr of water vapor to the Br^- system is shown to cause a significant reduction in the concentration of free

(23) Reents, W. D.; Wood, D. L.; Mujice, A. M. *Anal. Chem.* 1985, 57, 104–109.

(24) Rand, M. J. *Anal. Chem.* 1963, 35, 2128–2133.

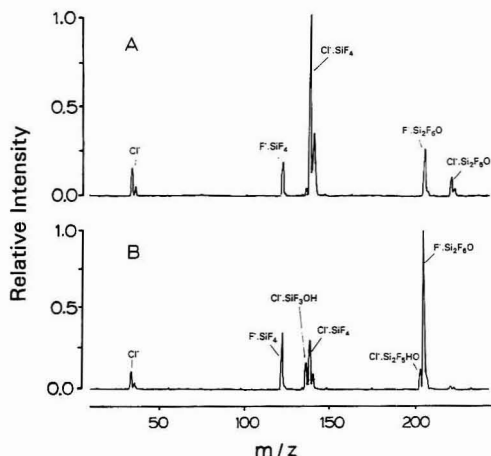


Figure 6. Illustrations of complete mass spectra observed in PHPMs experiments involving Cl^- ion (note that all ions containing Cl^- appear as an isotopic doublet of 3:1 relative intensity). In spectrum A, the ion source contains 0.2 mTorr of CF_2Cl_2 and 0.30 mTorr of SiF_4 in 4.0 Torr of methane buffer gas. In spectrum B, 1.0 mTorr of water vapor has also been added to the ion source. The temperature is 150 °C.

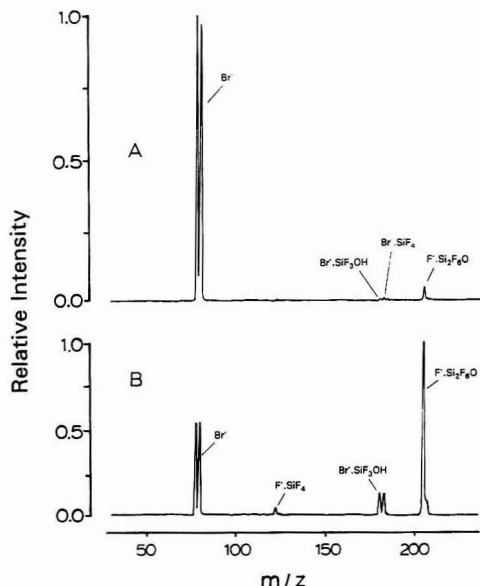


Figure 7. Illustrations of complete mass spectra observed in PHPMs experiments involving Br^- ion (note that all ions containing Br^- appear as an isotopic doublet of 1:1 relative intensity). In spectrum A, the ion source contains 0.2 mTorr CH_2Br_2 and 3.0 mTorr of SiF_4 in 4.0 Torr of methane buffer gas. In spectrum B, 1.0 mTorr of water vapor has also been added to the ion source. The temperature is 150 °C.

Br^- ion and an increase in the concentration of ions F-SiF_4 , $\text{Br-SiF}_3\text{OH}$, and $\text{F-Si}_2\text{F}_6\text{O}$. This indicates that reactions 6–13, which were suggested above to lead to unexpected ions for the Cl^- system, are also operative for the Br^- system. In the PDM-ECD experiments shown previously in Figures 2–4, the presence of approximately 1 mTorr of water vapor in the

atmospheric pressure buffer gas is likely in spite of our best efforts to remove traces of water. Therefore, the greater-than-expected reductions in the PDM-ECD responses to both chlorocarbons and bromocarbons noted previously in Figures 3 and 4 are probably caused by additional reactions of the type shown in reactions 6–13. In corresponding PHPMs experiments involving I^- only one complexing reaction of I^- with either SiF_4 or with the impurities that accompany SiF_4 and water vapor was observed. This reaction produced a small amount (<5% relative intensity) of the complexed ion $\text{I-SiF}_3\text{OH}$ under the conditions described in Figure 7B. Therefore, it seems likely that the impurity SiF_3OH causes the approximately one-third reduction of the PDM-ECD response to CH_3I noted previously in Figure 4.

CONCLUSIONS

A means of obtaining specific PDM-ECD responses to simple brominated compounds in the presence of chlorinated compounds has been demonstrated here. The addition of 350 ppb SiF_4 to the detector gas at 150 °C causes no detectable diminution of the ECD standing current; no detectable effect on normal ECD responses to compounds; the complete removal of PDM-ECD response to chlorinated compounds from which Cl^- is formed by electron capture; and the retention of two-thirds of the PDM-ECD response to brominated compounds from which Br^- is produced upon electron capture. Since SiF_4 does not strongly adhere to surfaces of the detector or the transfer lines, a stable PDM-ECD response is quickly established following either a change in the concentration of SiF_4 in the detector gas or the removal of SiF_4 from the system. By parallel mass spectrometric measurements, it has been shown here that Cl^- bonds much more strongly to SiF_4 than does Br^- , and this undoubtedly accounts for part of the specificity of the PDM-ECD for brominated versus chlorinated compounds. However, the K_4 values and mass spectrometric measurements reported here also indicate that a major portion of the effects of SiF_4 on the PDM-ECD responses is actually caused by impurities in the SiF_4 -doped detector gas. While some of these impurities are known to originate with the supply of SiF_4 , the most chemically active ones are thought to be produced in the ion source by reactions of SiF_4 with residual water vapor. Any future improvements in the elimination or control of these impurities would be expected to lead to even better response specificity for brominated compounds than has been demonstrated here. It has also been shown that the SiF_4 -modified PDM-ECD provides an excellent means of obtaining selective responses to iodinated compounds in the presence of chlorinated and even brominated compounds. Along with standard methods for analyte preconcentration from either air⁸ or water²⁵ samples, the SiF_4 -modified PDM-ECD can be expected to provide a powerful tool for the selective trace analysis of brominated or iodinated compounds in environmental samples.

ACKNOWLEDGMENT

This work was supported by grants from the Idaho National Engineering Laboratory, Idaho Falls, ID, and the National Science Foundation (Grant CHE-9021330).

RECEIVED for review April 28, 1992. Accepted July 23, 1992.

Registry No. SiF_4 , 7783-61-1; CF_2Br_2 , 75-61-6; CH_3I , 74-88-4; CHCl_3 , 67-66-3; CCl_4 , 56-23-5; CH_2Br_2 , 74-95-3.

CORRESPONDENCE

Determination of Amide Hydrogen Exchange Rates in Peptides by Mass Spectrometry

Géraldine Thévenon-Emeric, John Kozlowski, Zhongqi Zhang, and David L. Smith*

Department of Medicinal Chemistry and Pharmacognosy, Purdue University, West Lafayette, Indiana 47907

When proteins are dissolved in D₂O, the amide hydrogens are gradually replaced with deuterium. Some amide hydrogens in proteins exchange within seconds, while others resist exchange for months. The rates at which amide hydrogens in proteins undergo isotopic exchange depend on the secondary and tertiary structures of proteins, as well as on experimental variables such as pH and temperature. Because amide hydrogen exchange rates are sensitive to protein structure, they have been used extensively as probes for detecting and understanding conformational changes in proteins. For example, amide hydrogen exchange rates have been used to investigate binding in enzyme/substrate¹ and antibody/antigen complexes,² to study allosteric changes in hemoglobin,³ and to identify intermediates in protein folding.⁴

A variety of experimental methods of varied simplicity and resolution have been used to quantify the levels of deuterium in proteins. IR⁵ and UV⁶ spectroscopy have proved useful for determining the deuterium content of entire proteins but give no information about the levels of deuterium in specific regions of a protein. Both one- and two-dimensional NMR have been used to follow deuterium exchange at specific sites in small proteins, such as cytochrome c⁷ and bovine pancreatic trypsin inhibitor.⁸ Although exchange rates of specific amide hydrogens can be determined by NMR, this method does require assigning the amide hydrogen resonances and is generally restricted to small, highly soluble proteins. Neutron diffraction has also been used to determine rates of hydrogen exchange in proteins.⁹

A medium-resolution method that is potentially suitable for investigations of large proteins has been described by Rosa and Richards¹⁰ and subsequently refined by Englander et al.¹¹ Their approach involves exchanging tritium into a protein, fragmenting the protein into peptides with acid proteases, isolating peptides, and determining the levels of tritium per molecule of peptide. Englander et al.³ have used this method effectively to investigate allosteric changes in

hemoglobin. The goal of the present study was to determine whether this method could be modified so that the levels of amide deuterium can be quantified by mass spectrometry. To demonstrate the feasibility of this approach, we have used both continuous-flow fast atom bombardment mass spectrometry (CF FABMS) and proton NMR to determine the rates at which two peptides undergo hydrogen exchange under

slow-exchange conditions. The potential for using CF FABMS for determining amide hydrogen exchange rates in proteins is discussed.

EXPERIMENTAL SECTION

Materials. Ile-Ser-bradykinin and bovine hemoglobin were purchased from Sigma Chemical Co. Deuterated water (99.9% deuterium) was purchased from Cambridge Isotope Laboratories. The N-terminal fragment comprising residues 1-14 of the β -chain of hemoglobin was isolated by reversed-phase HPLC from a peptic digest of hemoglobin. The identity of this fragment was established by its FAB mass spectrum (MH⁺ 1494.8) and its E/B linked scan daughter ion mass spectrum.

Isotope Exchange. The test peptides, Ile-Ser-bradykinin and the 1-14 segment of the β -chain of hemoglobin, were dried then dissolved in D₂O (20 °C, pH > 5) and incubated for at least 2 h. This exchange-in solution was placed in an ice bath to lower the temperature to 0 °C, and 20 volumes of exchange-out solvent (H₂O/CH₃CN/trifluoroacetic acid, 90/10/0.1, 0 °C) were added. Aliquots of this solution were removed at intervals of increasing time and analyzed by CF FABMS.

Hydrogen Quantitation. The CF FABMS apparatus used in this investigation consisted of a Kratos MS-50 RF mass spectrometer, a Rainin Instruments gradient HPLC pump system, and a CF FAB probe constructed in our laboratory.¹² Samples were injected into the flowing solvent (H₂O/CH₃CN/glycerol/1-thioglycerol/trifluoroacetic acid, 84/10/3/0.1) via a Rheodyne injector (Model 7520) fitted with a 1- μ L sample loop. Solvent flowed into the mass spectrometer at a rate of 3 μ L/min. The mass spectrometer was operated at a scan rate of 30 s/decade and an accelerating potential of 8 kV. Data were acquired with a Kratos DS-90 system and subsequently analyzed with a Macintosh computer where the number of deuterium atoms per molecule was deduced from the isotope pattern of the protonated molecule ion.

All proton NMR data were obtained on a Varian VXR-500S spectrometer equipped with a 5-mm variable-temperature indirect detection probe. The peptide and the D₂O were cooled to 0 °C prior to mixing and analysis. Each spectrum was a collection of 16 transients where each transient was acquired using a 4- μ s rf pulse (35° tip angle), an 8-kHz spectral width, and 64K data points (4-s acquisition time). A recycle time of 4.5 s/transient

- (1) Brandt, P.; Woodward, C. *Biochemistry* 1987, 26, 3156-3162.
- (2) Paterson, Y.; Englander, S. W.; Roder, H. *Science* 1990, 249, 755-759.
- (3) Ray, J.; Englander, S. W. *Biochemistry* 1986, 25, 3000-3007.
- (4) Roder, H.; Elöve, G. A.; Englander, S. W. *Nature* 1988, 335, 700-704.
- (5) Osborne, H. B.; Nabadryk-Viala, E. *Methods Enzymol.* 1982, 88, 676-680.
- (6) Englander, J. J.; Calhoun, D. B.; Englander, S. W. *Anal. Biochem.* 1979, 92, 517-524.
- (7) Jeng, M. F.; Englander, S. W.; Elöve, G. A.; Wand, A. J.; Roder, H. *Biochemistry* 1990, 29, 10433-10437.
- (8) Wagner, G.; Wüthrich, K. *J. Mol. Biol.* 1982, 160, 343-364.
- (9) Kossiakoff, A. A. *Nature* 1982, 296, 713-721.
- (10) Rosa, J. J.; Richards, F. M. *J. Mol. Biol.* 1979, 133, 399-416.
- (11) Englander, J. J.; Rogero, J. R.; Englander, S. W. *Anal. Biochem.* 1985, 147, 234-244.

- (12) Smith, D. L. In *Continuous-flow Fast Atom Bombardment Mass Spectrometry*; Caprioli, R. M., Ed.; Wiley & Sons: New York, 1990.

gave a total acquisition time of 72 s for each spectrum. Spectra were collected at time intervals ≥ 300 s. The digital integrals and peak intensities of the amide protons were used to follow the displacement of protium with deuterium.

RESULTS AND DISCUSSION

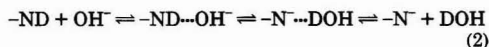
The average m/z of the protonated molecule ion is a direct measure of the total number of deuteriums per molecule of peptide, but gives no information about the locations of the deuterium atoms in the peptide. To determine the number of peptide amide deuteriums from the average m/z , it is essential to prepare samples such that only the peptide amides are labeled. This requirement can be met by exchanging all "exchangeable" hydrogens, followed by removal of rapidly exchanging hydrogens through a back-exchange step, leaving only amide nitrogens deuterated.

Hydrogen exchange in peptides can be either acid- or base-catalyzed. As a result, the rate constant for hydrogen exchange can be written as in eq 1. The rate at which peptide amide

$$k_{ex} = k_{OH}[OH^-] + k_H[H^+] \quad (1)$$

hydrogens undergo isotopic exchange is a minimum around pH 2–3 and increases by a factor of 10 for each pH unit away from this region.¹⁴ Hence, decreasing the pH from 7.5 to 2.5 decreases the rate of hydrogen exchange by approximately 5 orders of magnitude. For the present study, exchange-in was performed around pH 7 where the reaction is base-catalyzed, and the rate of exchange-out (k_{ex}) was determined at pH 2.1 where the acid- and base-catalyzed reactions are approximately equal.

To understand the feasibility and limitations of this sample preparation procedure, it is important to understand the hydrogen-exchange reaction. Steps in base-catalyzed hydrogen exchange are illustrated in eq 2. Small peptides have



little secondary or tertiary structure, allowing their hydrogens to collide and form hydrogen bonds with proton acceptors (OH^-) at the diffusion-limited rate. The intermediate complex can be visualized as two bases, $-N^-$ and OH^- vying for the proton. The partitioning of protons between the two bases is related to the pK_a 's of their conjugate acids. The fraction of complexes proceeding to the right of eq 2 is described by eq 3, where ΔpK is $pK_a(H_2O) - pK_a(-NH)$. With the pK_a 's

$$\text{fraction} = 10^{\Delta pK} / (10^{\Delta pK} + 1) \quad (3)$$

of H_2O and peptide amide $-NH$, 15.7 and approximately 18.5, respectively, it is evident that only one collision in a thousand proceeds to the right in eq 2. The process described in eq 2 illustrates the base-catalyzed removal of a hydrogen from an amide nitrogen. The hydrogen-exchange process is completed by reversing this reaction. The rate of the reverse reaction is usually much faster than the rate of the forward reaction because $[water] \gg [hydroxide]$ and because ΔpK is positive. A more complete discussion of the mechanism of hydrogen exchange has been described by Englander and Kallenbach.¹³

The structure of Ile-Ser-bradykinin is given in Figure 1 to illustrate some of the different types of hydrogens that are present in peptides. The peptide amide hydrogens, which are of principal interest to this study, are located below the peptide backbone. Peptides with a total of m residues and n proline residues have $m - n - 1$ peptide amide hydrogens.

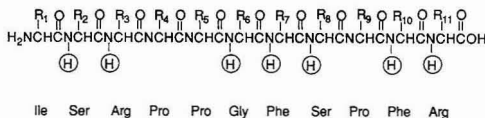


Figure 1. Amino acid sequence of Ile-Ser-bradykinin illustrating different types of hydrogens that undergo isotopic exchange at different rates.

The pK_a 's of hydrogen bound to carbon are generally much larger than 18.5 and effectively do not undergo exchange. In contrast, hydrogens bound to oxygen in Ser, Thr, Tyr, Glu, and Asp have pK_a 's much less than 18 and undergo isotopic exchange much more rapidly than peptide amide hydrogens. Likewise, hydrogens located on the N-terminus ($-NH_2$) and C-terminus ($-OH$), as well as amide hydrogens on asparagine and glutamine exchange rapidly.¹³ These large differences in the exchange rates of different types of hydrogens can be used to ensure that the deuterium content of protonated molecule ions is in fact a direct measure of the number of peptide amide deuteriums.

Two model peptides used in this investigation, Ile-Ser-bradykinin and the 1–14 segment of the β -chain of hemoglobin, were fully deuterated by incubating them in D_2O at high pH (>5) where the exchange rate is fast. The incubation solution was then chilled and diluted 20-fold with acidified H_2O (pH 2.1, 0 °C). The rate of amide hydrogen exchange decreases by approximately a factor of 3 for a 10-deg reduction in temperature.¹⁴ Based on the pK_a 's of the deuterated groups, all but the peptide amide deuteriums were expected to be replaced with hydrogen within seconds.

Aliquots of the exchange-out solution were analyzed by CF FABMS. An example of the isotope pattern of the protonated molecule ion for the deuterated sample is given in Figure 2B. Mass spectra of aliquots of the exchange-out solution were corrected for the natural abundance of isotopes (Figure 2A) to give a more accurate measure of the deuterium content of the peptides (Figure 2C). The number of deuterium atoms per molecule of peptide was determined from the first moment of the corrected isotope pattern. For example, the corrected spectrum in Figure 2C indicates that there are 8.9 deuteriums per peptide. Based on the amino acid composition of this peptide (Figure 2), there are 12 peptide amide hydrogens that could be replaced with deuterium. Although all 12 of these amide hydrogens would have undergone isotopic exchange during the exchange-in step, 3.1 have undergone back-exchange prior to analysis.

Mass spectra similar to the one illustrated in Figure 2C were used to follow hydrogen/deuterium exchange with the time that fully deuterated peptides were incubated in H_2O , as illustrated in Figure 3 for the β 1–14 peptide. Linear regression analysis of three separate sets of data gave the three lines in Figure 3. These results, as well as results obtained with several other peptides, demonstrate that rate constants for isotopic exchange in peptides can be determined with a precision of $\pm 10\%$. Rate constants for hydrogen/deuterium exchange in the β 1–14 peptide and in Ile-Ser-bradykinin were calculated from such plots (Table I).

To verify that the CF FABMS procedure is an accurate measure of the amide deuterium content of peptides, hydrogen/deuterium exchange was determined at the same pH and temperature by proton NMR. The reverse exchange reaction (i.e., replacement of hydrogen with deuterium) was used to facilitate the NMR measurements. Except for isotope effects, which are about 5%, the rate constants for the two isotopic exchange reactions are expected to be the same.¹⁴ Similar results (Table I) were indeed obtained by NMR and CF FABMS. The validity of the present experimental results is also indicated by comparing them to values obtained by

(13) Englander, S. W.; Kallenbach, N. R. *Quart. Rev. Biophys.* 1984, 16, 521–655.

(14) Englander, S. W.; Poulsen, A. *Biopolymers* 1969, 7, 379–393.

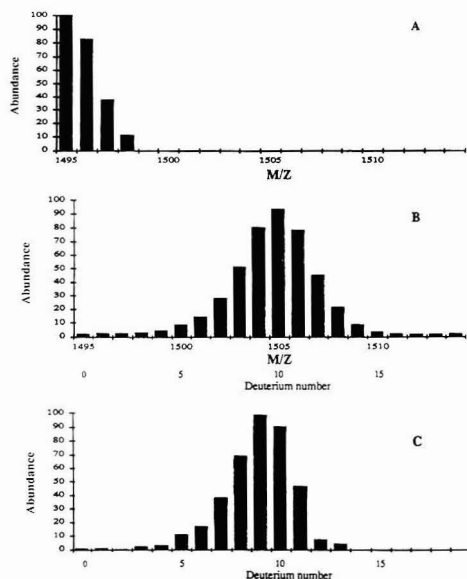


Figure 2. Isotope patterns of the protonated molecule ion of the 1-14 segment of the β -chain of hemoglobin (Val-His-Leu-Thr-Pro-Glu-Gly-Lys-Ser-Ala-Val-Thr-Ala-Leu) obtained by direct injection CF FABMS. (A) Theoretical isotope pattern for a molecular ion with the natural abundance of isotopes. (B) Deuterated sample illustrating the shift in m/z upon deuteration. (C) Spectrum B after removal of contributions from the natural isotopes.

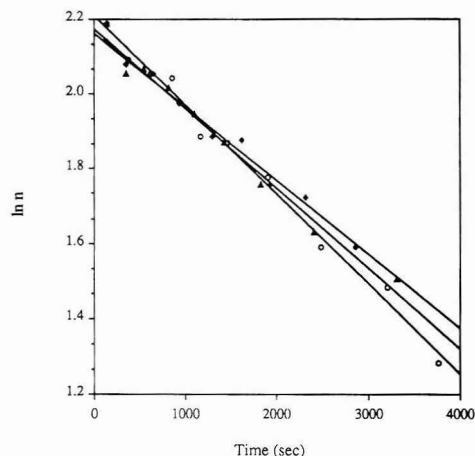


Figure 3. Plot of the deuterium content of the 1-14 segment of the β -chain of hemoglobin versus the deuterium exchange-out time. Results for three analyses are given with lines fitted to each set of data.

semiempirical calculations described by Molday et al.¹⁵ After adjustments for pH and temperature, these calculations suggest that the rate constants for hydrogen exchange in these peptides should be approximately 0.011 min^{-1} , which is in adequate agreement with the present experimental results.

Table I. Rate Constants (min^{-1}) and Half-Lives (min) for Amide Hydrogen Exchange in Ile-Ser-bradykinin and the 1-14 Segment of the β -Chain of Hemoglobin Determined by CF FABMS and Proton NMR

peptide	FABMS		NMR	
	<i>k</i>	half-life	<i>k</i>	half-life
Ile-Ser-bradykinin	0.0186	37	0.0174	40
β 1-14	0.0132	53	0.0120	58

CONCLUSIONS

The present results demonstrate that the amide deuterium content of peptides can be determined by CF FABMS. These measurements are possible because the experiments are performed under slow-exchange conditions (pH 2-3, 0°C), because rapidly exchanging deuteriums are completely exchanged-out in the continuous-flow solvent, and because analyses are performed very rapidly by CF FABMS. The ability to quantitatively determine the number of amide deuteriums in a peptide is relevant to an established method for following hydrogen exchange in proteins, as described previously by Rosa and Richards¹⁰ and Englander et al.¹¹ Proteins are subjected to various tritium exchange-in conditions, followed by transfer into slow-exchange conditions (pH 2-3, 0°C) where they are digested with pepsin. Peptides are isolated and analyzed for isotope content. Since the amount of tritium per peptide is determined from their radioactivity and UV absorbance, peptides must be isolated to relatively high purity, and the isolation procedure must be completed before substantial exchange-out has occurred. Ideally, the entire analysis would be completed within the time equal to 1 half-life for exchange. Analytical methods used to correct for the loss of hydrogen isotopes during the analysis have been described.¹¹

Substituting deuterium for tritium and using directly-coupled HPLC-CF FABMS to determine the deuterium content of peptides may substantially improve this approach for investigating the multidimensional structures of proteins. The most attractive feature relates to the fact that peptide molecular weight maps of proteolytic digests can be made by HPLC-CF FABMS on a time scale that is less than 1 half-life for exchange. Furthermore, the rate at which deuterium is lost from each peptide could be determined as illustrated in Figure 3 and used to correct for the small amount of deuterium that is lost during analysis. Since the number of deuteriums per peptide is determined directly from the mass spectrum, assumptions about the UV extinction coefficient, which was used previously to quantify peptides, are not necessary. Hence, the accuracy with which isotope exchange occurs, and therefore the ability to detect subtle changes in protein structure may be significantly improved by the proposed modification.

ACKNOWLEDGMENT

The authors are grateful to S. W. Englander for helpful discussion in the early stages of this investigation. This investigation was supported through a grant (RO1 GM40384 and P30 AI27713) from the National Institutes of Health.

Outline of a Theory of Focusing in Linear Chromatography

Leonid M. Blumberg

Hewlett-Packard Company, Route 41, P.O. Box 900, Avondale, Pennsylvania 19311-0900

INTRODUCTION

There is renewed interest in chromatographic focusing by simultaneous programming of column parameters in time and distance (along the column).¹⁻⁶ Can such *nonuniform* (coordinate dependent) *time-varying* separation achieve better resolution than the separation in the equivalent *uniform time-invariant* separation? A theoretical solution to the problem was not found in the literature.

Apparently, for any *linear*^{7,8} (independent of a solute concentration) separation, such improvement is not possible.

The purpose of this short communication is to report the major results of the theory which led to that conclusion and to outline the flow of its logic. To stay close to the results of the previous work,⁸ this report, for the most part, is limited to the media where the *distance-based velocity gradients* are nearly constant within a zone. A more general study requires additional development of the theory for the evolution of a zone in a nonuniform medium, and the reexamining of such fundamental concepts as the resolution in a nonuniform separation, etc. These topics go beyond the capacity of a brief report and are being separately prepared for publication. Besides, a nonuniformity where the distance-based velocity gradients are nearly constant within the zones is practically the most important one. (More dramatic nonuniformity can significantly distort the zones or even split them.)

THEORY

Throughout this paper, a chromatographic separation is assumed to be *one-dimensional* (all solutes follow the same path) and *linear*. It is important to emphasize that the properties of the medium where the separation takes place can be **functions of distance and time**.

Consider a migration of two zones of different solutes. Let at a certain time, the distance, l , between the zones be $l = z_b - z_a$ where z_a and z_b are the centers of masses of the zones, and the difference, Δu , between velocities of the zones be $\Delta u = u_b - u_a$. Assume that the solutes are almost identical, so that the zones remain just barely separated having coordinates, z_a and z_b , nearly equal to the coordinate $z = (z_a + z_b)/2$ of the center of mass of both zones. Similarly, the difference of velocities of the zones is so small compared to the average $u = (u_a + u_b)/2$ that both u_a and u_b are nearly equal to u . Finally, both zones have nearly the same variances σ^2 .

The ratio⁹

$$R_s = R_s(z) = \frac{l(z)}{4\sigma(z)} \quad (1)$$

represents the *distance-based resolution* of the zones when

their center of mass is at a coordinate z . The rate

$$R'_s = \frac{dR_s}{dz} = \frac{1}{4\sigma} \left(\frac{dl}{dz} - \frac{l}{\sigma} \frac{d\sigma}{dz} \right) \quad (2)$$

of resolution tells how the separation of the zones evolves during their migration. Substitution of relation $dl/dz = (d/dt)(dt/dz) = \Delta u/u$ and eq 1 into eq 2, and replacement of $d\sigma/dz$ by $(d\sigma^2/dz)/(2\sigma)$ yields

$$R'_s = \frac{\Delta u}{4u\sigma} - \frac{R_s}{2\sigma^2} \frac{d\sigma^2}{dz} \quad (3)$$

In further discussions, a sample introduction is said to be *ideal* if $\sigma^2(0) = 0$. A *basic* separation is a uniform time-invariant one. An *ideal basic* separation is a basic separation with an ideal sample introduction. A separation is *smooth* if within the zones of solutes, the velocities of the solutes are nearly linear functions of distance for any z .

In a basic separation, the velocity of a solute can be viewed as the sole representative of the *identity* of the solute. If Δu_0 is the difference between the velocities of two solutes in a basic separation then the ratio $\delta = \Delta u_0/u$ (the reduced difference in the velocities of the solutes) can be referred to as the *identity gap* between the solutes. Due to the possible nonuniformity of an arbitrary separation, additional difference in the velocities of the zones at a given time can come from the difference of the condition in the medium for the two solutes at that time. The latter can be represented by the local distance-based gradient, $g = g(z)$, of velocity of the solutes at z . The net difference, Δu , between the velocities of the two zones is the sum $\Delta u = \Delta u_0 + gl = \delta u + gl$. Substitution of Δu in eq 3 and taking account of eq 1 yield

$$R'_s = \frac{\delta}{4\sigma} + \frac{gR_s}{u} - \frac{R_s}{2\sigma^2} \frac{d\sigma^2}{dz} \quad (4)$$

Further simplification of this expression is possible due to previous results.⁸ The model and derivations developed in ref 8 lead to the conclusion that for any smooth separation one has $d\sigma^2/dz = H + 2\sigma^2 g/u$. In the rhs of this expression, the first term, $H = H(z)$, is the plate height at z which reflects the dispersion in the medium while the second term reflects the change in σ^2 caused by the deformation of the zone due to the distance-based velocity gradients. Substitution of this expression into eq 4 results in the simpler relation

$$R'_s = \frac{\delta}{4\sigma} - \frac{HR_s}{2\sigma^2} = \frac{\delta}{8\sigma} \left(2 - \frac{4HR_s}{\delta\sigma} \right) \quad (5)$$

The purpose of this study is to compare an arbitrary separation with the appropriately defined equivalent ideal basic separation. Notice that the local properties of a chromatographic medium are completely described by the two parameters⁸ H and u . Two media are *z-equivalent* to each other for a given zone of a solute if for that zone they have the same $H(z)$ and $u(z)$. The values $R_{s0} = R_{s0}(z)$ and $R'_{s0} = R'_{s0}(z)$ are the resolution and its rate in the *z-equivalent* ideal basic separation. For such separation⁹ $l = \delta z$, $\sigma^2 = Hz$.

(9) Giddings, J. C. *Unified Separation Science*; John Wiley & Sons: New York, 1991.

- (1) Rubey, W. A. *J. High Resolut. Chromatogr.* 1991, 14, 542-548.
- (2) Phillips, J. B.; Jain, V. Abstracts of papers presented at the 1991 Pittsburgh conference and exposition on analytical chemistry and applied spectroscopy; American Chemical Society: Washington, DC 1991; p 831.
- (3) Reighetti, P. G.; Gianza, E.; Bianchi-Bosisio, A.; Sinha, P.; Kottgen, E. *J. Chromatogr.* 1991, 569, 197-228.
- (4) Van Puyvelde, F.; Chimovitz, E. H. *J. Supercrit. Fluids* 1990, 3, 127-135.
- (5) Fuggerth, E. *Anal. Chem.* 1989, 61, 1478-1585.
- (6) Schomburg, G.; Roeder, W. *J. High Resolut. Chromatogr.* 1989, 12, 218-225.
- (7) Guiochon, G.; Guillemin, C. L. *Quantitative Gas Chromatography for Laboratory Analysis and on-line Process Control*; Elsevier: Amsterdam, 1988.
- (8) Blumberg, L. M.; Berger, T. A. *J. Chromatogr.* 1992, 596, 1-13.

Substitution of these relations into eqs 1 and 2, yields for R_{so} and R_{so}'

$$R_{so} = \frac{\delta}{4} \sqrt{\frac{z}{H}} = \frac{\delta \sigma}{4H} \quad R_{so}' = \frac{1}{4\sigma} \left(\delta - \frac{\delta z}{2Hz} \right) = \frac{\delta}{8\sigma} \quad (6)$$

These relations suggest that at any z , the specific resolution, R_{so}/δ (the resolution per unit of the identity gap), depends only on $\sigma(z)$ and $H(z)$ while the specific rate of resolution, R_{so}'/δ , depends only on $\sigma(z)$. With R_{so} and R_{so}' , eq 5 can be rewritten as $R_s/R_{so}' = 2 - R_s/R_{so}$, or

$$\frac{R_s}{R_{so}} + \frac{R_s'}{R_{so}'} = 2 \quad (7)$$

Also, let $E = E(z) = R_s/R_{so} - 1$ and $\epsilon = \epsilon(z) = R_s'/R_{so}' - 1$ be excesses (relative to the z -equivalent ideal basic separation) of the resolution and its rate, respectively. Eq 7 becomes

$$E + \epsilon = 0 \quad (8)$$

RESULTS AND DISCUSSION

Equations 7 and 8 represent the main result of the theory. For simplicity in reasoning, the equations were derived for a medium with constant gradients of velocities of the solutes. It can be shown that these equations are valid for arbitrary velocities as well. In the general theory, however, the local values for plate height, the velocity, and its distance-based gradient should be replaced with their aggregate⁶ (effective) counterparts. Also the notion of resolution in a nonuniform separation and the entire strategy of comparison of the quality of a nonuniform separation with that of a uniform separation needs to be more carefully scrutinized. All these developments were beyond this brief report. Nevertheless, in the remaining, it is assumed that eqs 7 and 8 are valid for any linear separation. (The proof of the general case will be submitted for the publication later.)

Equations 7 and 8 have important implications. They indicate that the sum of the reduced resolution, R_s/R_{so} , and the reduced rate, R_s'/R_{so}' , of resolving any two solutes, as well as the sums of the excesses of these quantities are the important invariants of a separation. The sums always remain the same for any separation. Also, the ratios as well as the excesses E and ϵ represent figures of merit for the local qualities of a separation and its evolution.

According to eq 7, resolution of two solutes in any medium evolves in such a way that R_s/R_{so} and R_s'/R_{so}' can never simultaneously exceed unity. If one is larger than unity, the other must be smaller than unity. Thus, at any location, the quality of the resolution and its rate can never simultaneously exceed similar qualities in the z -equivalent ideal basic separation. If one is better than the respective quality in the ideal basic separation, the other must be worse than its ideal basic counterpart.

Similarly, the sum of the excesses of resolution and its rate is an invariant which always remains zero. If at any coordinate, z , resolution is excessive relative to the z -equivalent basic separation, its rate must have a deficiency (a negative excess). Conversely, only when the zones are under-resolved (have a negative excess of resolution) can the rate of their resolution exceed that in the z -equivalent ideal basic separation.

This discussion can be summarized in a form of the law of [an arbitrary] chromatographic separation (uniform or nonuniform, time-varying, or time-invariant).

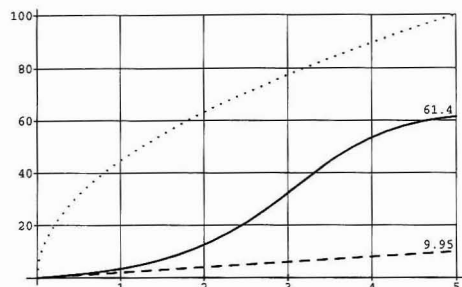


Figure 1. Specific resolution, $4R_s/\delta$, vs coordinate, z (in meters), of the center of mass of two zones. All graphs represent evolving resolution of two solutes with the same identity gap, δ , in a 5-m-long column with $H = 0.5$ mm. The average, u , of velocities of the zones is also the same for all separations and does not change along the column. The dotted line, $4R_s/\delta = z/(H)^{1/2}$, represents the uniform time-invariant separation with the ideal sample introduction. The dashed line, $4R_s/\delta = z/(\sigma^2(0) + Hz)^{1/2}$, also reflects uniform time-invariant separation but with the sample introduction which took 10 times longer than the elution time of a nonretained peak in the previous separation. The solid line represents the separation with the same nonideal sample introduction as in the previous case, and with the focusing by the negative distance-based gradient $g = Cu$ where $C = -1 \text{ m}^{-1}$. The gradient (nonuniformity of the separation) travels along the column with the velocity, u , of the zones. Hence, the zones always "see" the same distance-based velocity gradient. However, at a given distance from the column inlet, the distance-based gradient changes with time providing for the nonuniform time-varying separation.

Consider two one-dimensional linear separations of the same nearly identical solutes: an arbitrary separation *A* and a uniform time-invariant separation *B* with the ideal sample introduction. Let *A* and *B* be z -equivalent at a coordinate z . Then at z , the rate of resolving of the solutes in *A* cannot exceed the rate of resolving them in *B* unless the resolution in *A* is lower than the resolution in *B*.

Simply, no focusing can provide better resolution than the one available from the equivalent ideal basic separation. However, the negative implications of the theory should not be overestimated. While establishing the limits to the focusing, the theory helps to recognize its potential. After all, no separation is ideal and the room for the focusing always exists.

A computer simulation of the focusing after a nonideal sample introduction is shown on Figure 1. Under the conditions of Figure 1, the nonideal sample introduction causes more than the 10-fold loss of the resolution compared to the ideal basic separation. The focusing provides a dramatic (better than 6-fold) recovery from the same nonideal sample introduction.

ACKNOWLEDGMENT

The author is indebted to Terry A. Berger and Raymond D. Dandaneau. Without Terry's assistance in this study and without Ray's support and encouragement, this work would not be possible. The author also appreciates stimulating discussion of chromatographic focusing with Georges Guiochon.

RECEIVED for review March 26, 1992. Accepted July 21, 1992.

TECHNICAL NOTES

Cellulose Acetate-Coated Porous Polymer Joint for Capillary Zone Electrophoresis

Chen-Wen Whang* and I-Chih Chen

Department of Chemistry, Tunghai University, Taichung, Taiwan 40704, Republic of China

INTRODUCTION

Capillary zone electrophoresis (CZE) has become an important separation method as a result of its high resolving power and speed. Separations with more than 10^6 theoretical plates in less than 20 min has been demonstrated.^{1,2} Due to the extremely small volumes of sample zone encountered in CZE, on-column detection, such as UV absorption and fluorescence detection, are the most commonly used methods. On-column detection eliminates zone dispersion owing to the joints, fittings, and connectors that are necessary for conventional off-column detection systems. However, in some applications, such as CZE coupled with off-column electrochemical detection or continuous sample collection, a capillary outlet free from the applied potential field is generally required. To isolate the column end from the high voltage, special devices like a porous glass joint,³ porous graphite joint,⁴ and on-column glass frit⁵ have been applied to create a current-free zone at the capillary outlet, where an electrochemical sensor or a fraction collector is placed. Although these techniques work well with direct electrochemical detection and off-column sample collection, the problem is how to produce such structures reliably and inexpensively.

Recently, Linhares and Kissinger⁶ reported a sample introduction system for CZE based on a bare on-column fracture near the inlet end of the capillary. When a potential is applied between the fracture and the outlet end of the capillary, electroosmotic flow pulls sample into the capillary through the inlet. This sample introduction system can be viewed as an "electroosmotic syringe". The on-column fracture is easy to construct, and it can also be used as a general method to separate the column into two segments. We have tried using this technique to create a current-free segment of capillary for off-column electrochemical detection. However, we did observe some sample leakage through the fracture assembly. This is probably caused by the back-pressure generated inside the shorter segment of capillary because of the laminar type of flow in it, which forces the analyte ions to diffuse through the open fracture.

In this paper, we describe a modified capillary joint for CZE. Instead of using a bare fracture as the coupler, a cellulose acetate (CA) membrane was uniformly coated over the fracture. This design is basically similar to the porous glass joint used by Ewing³ except that a porous polymer joint is created here. CA membranes are known to be permselective primarily based on size; only small molecules (H_2O , O_2) and ions (Na^+ , Cl^- , etc.) can diffuse rapidly through the mem-

brane.^{7,8} Larger analyte and solvent molecules are excluded from permeating through the pores. CA-coated electrodes have been commonly used by electrochemists to build a size-exclusion selectivity into electrochemical detection in static solution⁹ and a flowing stream.¹⁰⁻¹² Problems of electrode poisoning, due to protein adsorption or accumulation of reaction products, can be effectively eliminated. In the present case, the CA-coated fracture will ensure that only small buffer ions and, therefore, current will pass but does not allow the larger analyte ions to pass through it. In comparison with a bare on-column fracture, the CA-coated porous polymer joint provides better efficiency and minimal sample loss. Besides, it has the advantages of long durability, inexpensiveness, and easy construction.

EXPERIMENTAL SECTION

Apparatus. The CZE system was assembled in-house. A high-voltage power supply (Glassman High Voltage, Inc., Whitehouse Station, NJ; Model PS/EH40R2.5) was used to generate the potential across the capillary. Fused-silica capillaries (Polymicro Technologies, Phoenix, AZ) of 50- μm i.d., 360- μm o.d., and 70-cm length were used in this study. After the polymer-coated joint was formed (described below), the capillary was filled with buffer solution. The high-voltage end of the capillary and the buffer reservoir were contained in a Plexiglass cabinet equipped with an interlock for operator safety. Platinum wire was used as the electrode. Detection of UV absorption was performed at 254 nm using an UV detector (Linear Instruments, Reno, NV; Model UVIS 200) equipped with an on-column capillary cell module. The output signal was recorded with either a strip-chart recorder (Pantos, Kyoto, Japan; Model U-228) or an integrator (Shimadzu, Kyoto, Japan; Model C-R3A). In the determination of possible leakage from the porous polymer joint, a constant-flow HPLC pump (Eldex, San Carlos, CA; Model 9600) and a fluorescence spectrophotometer (Hitachi, Tokyo, Japan; Model 160-10S) were used.

Reagents. All chemicals were of analytical-reagent grade. Thiamine, nicotinamide, and riboflavin were obtained from Sigma Chemical Co. (St. Louis, MO). Pyridoxal hydrochloride and sodium fluorescein were purchased from E. Merck (Darmstadt, FRG). Cellulose acetate (39.8% acetyl content) was obtained from Aldrich Chemical Co., Inc. (Milwaukee, WI). A 12% (w/v) cellulose acetate (CA) solution was prepared with HPLC-grade acetone. The electrophoresis buffer was a mixture of 10 mM sodium dihydrogen phosphate and 10 mM sodium tetraborate, pH 9.0. The buffer solution was prepared with distilled-deionized water, obtained using a Sybron/Barnstead (Boston, MA) NAN-

(7) Lonsdale, H. K.; Cross, B. P.; Graber, F. M.; Milstead, C. E. In *Permeable Membranes*; Rogers, C. E., Ed.; Marcel Dekker: New York, 1971; pp 167-187.

(8) Colton, C. K.; Smith, K. A.; Merrill, E. W.; Farrel, P. C. *J. Biomed. Mater. Res.* 1971, 5, 459-486.

(9) Kuhn, L. S.; Weber, S. G.; Ismail, K. Z. *Anal. Chem.* 1989, 61, 303-309.

(10) Sittampalam, G.; Wilson, G. S. *Anal. Chem.* 1983, 55, 1608-1610.

(11) Wang, J.; Hutchins, L. D. *Anal. Chem.* 1985, 57, 1536-1541.

(12) Hutchins, L. D.; Wang, J.; Tuzhi, P. *Anal. Chem.* 1986, 58, 1019-1023.

- (1) Jorgenson, J. W.; Lukacs, K. D. *Anal. Chem.* 1981, 53, 1298-1302.
- (2) Jorgenson, J. W.; Lukacs, K. D. *Science* 1983, 222, 266-272.
- (3) Wallingford, R. A.; Ewing, A. G. *Anal. Chem.* 1987, 59, 1762-1766.
- (4) Yik, Y. F.; Lee, H. K.; Li, S. F. Y.; Khoo, S. B. *J. Chromatogr.* 1991, 585, 139-144.
- (5) Huang, X.; Zare, R. N. *J. Chromatogr.* 1990, 516, 185-189.
- (6) Linhares, M. C.; Kissinger, P. T. *Anal. Chem.* 1991, 63, 2076-2078.

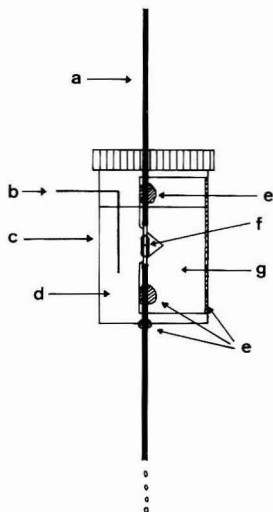


Figure 1. Cellulose acetate-coated fracture assembly and buffer reservoir: (a) fused-silica capillary; (b) platinum-wire electrode; (c) 10-mL plastic vial; (d) buffer solution; (e) epoxy glue; (f) CA-coated fracture; (g) glass plate.

Opure II system. The solution was filtered through a 0.45- μ m membrane filter prior to use.

Cellulose Acetate-Coated Capillary Joint. The procedure for construction of an on-column fracture was similar to that described by Linhares and Kissinger.⁶ A small section (~3 mm) of polyimide coating was burned off 9 cm from the end of a 70-cm-long fused-silica capillary. The capillary was placed over a 2-cm \times 1-cm microscope slide, on which a V-shaped breach (about 4 mm wide and 3 mm deep) was created near the center of one edge. The exposed section of capillary was situated on top of the breach and was glued in place with epoxy glue (Spar Chemical Industry Co., San Francisco, CA) at each end of the exposed region. By using a glass-fiber cleaver (Newport; Fountain Valley, CA), a small scratch was made on top of the uncoated silica. The capillary was then pushed up gently from the bottom, directly under the scratch, with a small pointed stylet thereby forming the fracture. By use of a micropipet tip, a small drop (~3 μ L) of 12% (w/v) CA solution (in acetone) was carefully dripped onto the fracture. Under a gentle stream of air and with slight rotation of the whole microscope slide, a thin film of CA membrane was uniformly coated over the fracture region. After drying in air for 1 h, the film thickness was found to be about 80 μ m, as estimated under a microscope.

The fracture assembly was then placed in a 10-mL plastic vial with a 1-mm hole drilled in the bottom. The microscope slide was vertically glued to the inner wall of the vial with the short section of capillary stretching out of the hole in the bottom. The length of the stretched capillary was about 8 cm. With the capillary in position, the hole was sealed using epoxy glue. The vial was then filled with buffer solution and a platinum-wire electrode was dipped in the solution. This electrode was connected in series to a digital current monitor (Keithley Instruments, Inc., Cleveland, OH; Model 177 DMM) and the ground terminal on the high-voltage power supply. A detailed schematic of the polymer-coated capillary joint is shown in Figure 1.

CZE Procedure. A detection window 4 cm either before or after the capillary joint was formed by burning off a small region of polyimide coating. The capillary was then carefully inserted into the UV detector, and the detection window was aligned with the focusing lens. The capillary was first washed (pressurized flow) with 0.1 M NaOH for 3 min, followed by a 2-min rinse with water and a 2-min flush with the running buffer. Finally, the column was equilibrated with the buffer under an electric field

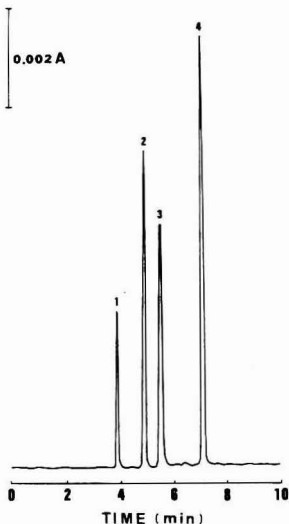


Figure 2. Electropherogram of four vitamins with UV detection 4 cm before the fracture. Conditions: column 50- μ m i.d. \times 360- μ m o.d. \times 70-cm total length, on-column fracture 9 cm from the end of capillary; buffer solution 10 mM phosphate + 10 mM borate, pH 9.0; voltage applied 23 kV (18 μ A) across the anodic end of capillary and the fracture; 5-s gravity injection at 15-cm height; UV detection wavelength 254 nm. Peak identities: (1) thiamine; (2) nicotinamide; (3) riboflavin; (4) pyridoxal.

of 200 V/cm for 1 h. Sample injection was performed by gravity. The capillary inlet was lifted 15 cm higher than the capillary outlet for 5 s.

RESULTS AND DISCUSSION

On a fused-silica capillary with a thick wall (145 μ m in this study), an on-column fracture assembly can be easily constructed following the published procedure.⁶ This fracture functions as a joint connecting two segments of capillary, which is generally required for sample collection, electrochemical detection, or other off-column detection methods in CZE. The fracture created is very fine, and the two sections of capillary are never separated. Since the fracture is so small, minimum bulk flow through the fracture should be expected. However, during a series of CZE experiments using capillaries with the fracture assembly for off-column electrochemical detection, we did observe some leakage of sample components through the fracture.

In order to examine the characteristic of a capillary with a bare on-column fracture, two detection windows were created on the capillary with one at 4 cm before the fracture and the other 4 cm after the fracture. Four water-soluble vitamins, viz., thiamine (vitamin B₁), nicotinamide, riboflavin (vitamin B₂), and pyridoxal (vitamin B₆), were used as test compounds. In a buffer of pH 9.0, nicotinamide behaves as a neutral marker. High voltage was applied between the anodic end of capillary (in a Plexiglas box) and the cathodic end at the fracture assembly. A typical electropherogram of the four vitamins is illustrated in Figure 2. A significant decrease in peak size of the four compounds was observed when the electropherogram obtained after the fracture was compared with that obtained before the fracture. The losses of peak area range from 22% for riboflavin (molecular weight = 376.4) to 38% for nicotinamide (molecular weight = 122.1). The average loss of N (theoretical plate number) is about 20%.

Table I. Migration Times (t_m), Theoretical Plate Numbers (N), and Peak Area (A) of Four Vitamins Detected before and after the CA-Coated Fracture^a

compd	before the fracture			after the fracture		
	t_m , s	$10^4 N$	A	t_m , s	$10^4 N$	A
thiamine	222 (2)	1.08 (0.18)	662 (34)	300 (2)	1.00 (0.23)	590 (31)
nicotinamide	288 (3)	1.71 (0.14)	1271 (100)	372 (3)	1.56 (0.22)	1232 (48)
riboflavin	330 (4)	1.60 (0.21)	1376 (159)	426 (5)	1.53 (0.15)	1316 (102)
pyridoxal	426 (4)	2.04 (0.24)	2635 (50)	546 (3)	1.76 (0.12)	2582 (129)

^a Data are represented as mean (standard deviation); $n = 5$. Experimental conditions as in Figure 2.

Altogether we have tested four capillaries with a carefully constructed on-column fracture; none of them gave a loss of peak area smaller than 18% for nicotinamide, the compound with the smallest molecular weight (and size) in the test sample. We believe this is caused by leakage of sample through the open fracture, with components of smaller size leaking the most. It has been shown that the length of the second capillary behind the joint will have a pronounced effect on the column efficiency.³ This is because the volume of buffer within the second capillary must be driven by the electroosmotic flow generated in the separation capillary. The formed laminar flow of buffer within the second capillary will create a back-pressure which is proportional to the length of the second capillary. The optimal efficiency can be obtained with a short (<2 cm) segment of capillary. However, due to the geometric restriction of the UV detection cell module used here, the detection capillary behind the joint cannot be shortened to less than 9.0 cm without contaminating the optical parts of the detector. The observed sample loss may be caused by the back-pressure generated in the relatively long detection capillary, which forces analyte ions to permeate through the open fracture before entering the detection capillary.

In order to solve the leakage problem, a thin layer of CA membrane was coated over the fracture region. This CA-coated fracture can be viewed as a "porous polymer joint", similar to the "porous glass joint" used by Ewing³ for off-column amperometric detection. Using a CA-coated porous polymer joint, no significant loss of peak size or column efficiency was observed, even with a 9-cm segment of detection capillary behind the fracture. This is to be expected because the CA membrane creates a diffusion barrier which allows only small buffer ions and molecules to pass through it. The larger analyte ions are excluded from permeating through the pores and are pushed downstream into the detection capillary by the electroosmotic flow. In order to quantitatively examine the effect of the CA-coated fracture on the performance of the capillary, five consecutive injections of the four test vitamins were made and were detected 4 cm before and after the fracture. The average migration times (t_m), theoretical plate numbers (N), and peak areas (A), as well as the standard deviations, were calculated. The results are listed in Table I. The relative standard deviations (RSD) of migration times for the four compounds are about 1%. The average loss of peak area is about 5% with a range of 2% for pyridoxal to 9% for thiamine. The average loss of N values (triangular approximation) due to the presence of a porous polymer joint is about 9% with a range of 4% to 14% for the four vitamins tested, which is better than that reported for a porous glass joint with a similar length of detection capillary.³ Basically, the CA-coated porous polymer joint should be expected to have a smaller band-broadening effect. According to Ewing,³ the porous glass joint was constructed by sliding a small section (2–5 mm) of "thirsty glass" tube over the capillary fracture, followed by sealing both ends of the porous glass segment with epoxy glue. The inner diameter of the porous glass tube must be slightly larger than the outer diameter of the fused-silica capillary; therefore, a small dead

volume will form around the fracture region. On the other hand, the CA membrane is tightly adhesive to the fracture region in a porous polymer joint, leaving no stagnant zone formed between capillary surface and membrane. This "zero dead volume" nature probably explains its better performance.

Under conditions of equal capillary length and electrical field strength, the current measured with the CA-coated fracture system was about 10% smaller than that observed with a normal CZE system without fracture. This is probably due to the relatively large size of the borate buffer ions ($B_4O_7^{2-}$), which makes their diffusion through the CA membrane pores more difficult. However, we found that the film thickness of a CA membrane coated over the fracture had no significant influence on the total resistance of the capillary. Under an electrical field of 380 V/cm and with a buffer mixture of 10 mM phosphate and 10 mM borate, changing the film thickness from 60 to ~300 μ m only caused a 7% decrease in current. Although the performance of the CA membrane was not significantly affected by its thickness, the success of preparation of a porous polymer joint was empirically found to be dependent upon the original CA content in acetone. As described in the Experimental Section, the porous polymer joint was formed by dripping a small drop of CA solution (in acetone) onto the capillary fracture and drying it under a stream of air. Because acetone is very volatile, a thin film of CA membrane will rapidly form at the fracture region. With a 10% (w/v) CA solution, the viscosity would be too low and CA molecules could easily penetrate into the fracture before drying, causing blockage of the capillary. If the percent of CA in acetone was raised to 15% (w/v), the solution would be too viscous and the fracture could not be coated evenly. The optimal content was found to be 12% (w/v) CA in acetone. To avoid a change of CA content, the coating procedure should be performed as quickly as possible.

The reliability of the porous polymer joint was tested by connecting the capillary (50- μ m i.d. \times 65-cm length) to an HPLC pump. A CA-coated fracture was constructed 3 cm from the low-pressure end of the capillary. The fracture assembly was placed in a small vial filled with 7 mL of distilled water and an aqueous solution of 20 μ M sodium fluorescein was pumped through the capillary at a constant flow rate. After 20 min the flow was stopped and the solution in the vial was taken out for fluorescence measurement. The sample vial was refilled with fresh distilled water and the HPLC pump was started again with a higher flow rate. The variation of measured fluorescence intensity as a function of flow rate is schematically represented in Figure 3. The CA membrane joint did not leak until the flow rate exceeded 40 μ L/min. The corresponding pressure at this flow rate was about 110 psi. Such a high flow rate (or pressure) was seldom found in normal CZE experiments, even during pressure injection or pressure flushing the capillary with a syringe. The reliability of the porous polymer joint is clearly demonstrated.

One of the problems observed with the porous polymer joint was the rapid loss of membrane integrity in an electrophoresis buffer containing a small amount of acetonitrile (e.g. 15%). This was probably caused by dissolution

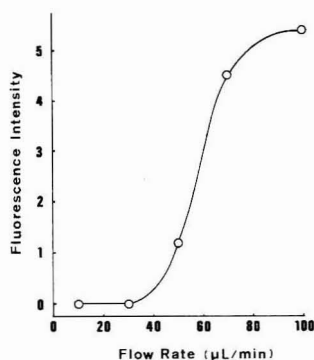


Figure 3. Fluorescence intensity of buffer reservoirs during leak test. Experimental details are described in the text.

of CA in acetonitrile-contained buffer. On the other hand, methanol did not affect the CA membrane. Table II shows the migration times (t_m), the theoretical plate numbers (N), and the peak area (A) of thiamine and nicotinamide obtained during a series of electrophoretic separations using a buffer of 50% (v/v) methanol content. The porous polymer joint was immersed in the methanolic buffer all the time, and a detection window was formed 4 cm behind the joint. No significant losses of efficiency and peak area were observed, even after 65 consecutive injections. The slight increase of migration time was due to column aging because the capillary was not rinsed between injections. If the column had been washed with 0.1 M NaOH for 2 min between injections, almost no change of migration time could be observed.

Another problem found with the joint assembly was the gradual deterioration of epoxy glue in buffer solution. Since the capillary with the joint assembly was affixed to a glass microscope slide with epoxy glue for rigidity (see Figure 1), deterioration of epoxy glue would destabilize the porous polymer joint. This problem can be alleviated by keeping the joint assembly immersed in distilled-deionized water when not in use. Under normal conditions, the porous polymer

Table II. Migration Times (t_m), Theoretical Plate Numbers (N), and Peak Area (A) of Thiamine and Nicotinamide during a Series of Electrophoretic Separations with a 50% Methanolic Buffer^a

no. of injections	thiamine			nicotinamide		
	t_m , s	$10^4 N$	A	t_m , s	$10^4 N$	A
1	282	6.49	672	399	1.18	471
8	285	6.53	663	402	1.17	438
17	286	6.26	687	401	1.12	426
24	292	6.50	630	406	1.17	445
30	294	6.24	633	410	1.20	431
38	300	6.13	638	414	1.20	436
47	298	6.36	647	415	1.17	430
55	301	6.26	670	420	1.13	442
60	303	6.26	641	423	1.14	435
65	304	6.17	653	427	1.12	453

^a Experimental conditions: column 50- μ m i.d. \times 360- μ m o.d. \times 60-cm total length, on-column fracture 9 cm from the end of capillary, detection window 4 cm after the fracture; voltage applied 23 kV (20 μ A); 1-s electromigration injection. Other conditions as in Figure 2.

joint can last for more than 1 week without deterioration.

In conclusion, a porous polymer joint for CZE can be easily constructed by fracturing the capillary followed by covering the fracture with a layer of CA membrane. Unlike the bare on-column fracture, sample loss is minimized with the CA-coated fracture. In comparison with the porous glass joint³ or the porous graphite joint,⁴ the CA-coated porous polymer joint has the advantages of high performance, long durability, inexpensiveness, and easy construction. We believe this joint should be useful in some CZE applications, such as sample introduction by electroosmotic syringe,⁶ continuous sample collection, and off-column electrochemical detection, where a segment of capillary free from the high electrical field is required.

ACKNOWLEDGMENT

Financial support from the National Science Council of the Republic of China is gratefully acknowledged.

RECEIVED for review February 20, 1992. Accepted June 30, 1992.

Synchronization of Timing in Chemiluminescence Thin-Layer Chromatographic System by Coupling Pneumatic Nebulization with Optical Fiber-Based Detection

Nian Wu and Carmen W. Huie*

Department of Chemistry, State University of New York at Binghamton, Binghamton, New York 13902-6000

INTRODUCTION

The peroxyoxalate chemiluminescence (CL) reaction involving the oxidation of oxalate derivatives, typically bis-(2,4,6-trichlorophenyl)oxalate (TCPO) or bis-(2,4-dinitrophenyl)oxalate (DNPO), in the presence of a sensitizer is among the most efficient nonenzymatic reactions known and has been extensively investigated for the postcolumn detection of various fluorophores or compounds derivatized with fluorescent labels in high-performance liquid chromatography (HPLC). For example, peroxyoxalate CL detection in HPLC has been demonstrated to be highly sensitive and selective for the determination of catecholamines,¹ secondary and tertiary amines,^{2,3} polycyclic aromatic amines and hydrocarbons,^{4,5} steroids,⁶ and carboxylic acids.⁷ In addition, HPLC determination of compounds such as choline and acetylcholine using an immobilized enzyme reactor followed by peroxyoxalate CL detection has also been reported.⁸ Recently, a number of dansyl amino acids have been used as model systems for the optimization of CL detection in HPLC based on the oxidation of TCPO or DNPO, and the average detection limit and relative standard deviation on reproducibility were found to be about 200 fmol (0.07 ng) and 4%, respectively.⁹ In contrast, very little work has been reported on the use of CL detection methods for the determination of analytes after separation by thin-layer chromatography (TLC). The reason for this is perhaps in large part related to experimental difficulties encountered in the synchronization of timing between the introduction of the CL reagents onto the TLC plates and detection of the rapidly decaying CL emission generated from the analytes adsorbed on the plate surface. This particular timing problem, however, can be overcome with relative ease in HPLC since all experimental parameters can be controlled with good accuracy.⁹

The use of CL detection in TLC was first demonstrated by Curtis and Seitz involving the measurement of various dansyl amino acids by successively spraying the plate with TCPO and H₂O₂ solutions and subsequently collecting the CL emission with an optical fiber-based detection system.¹⁰ Although in general this CL detection method was shown to be comparable to conventional fluorescence detection, it was found that the CL intensity changed rapidly with time under optimized conditions, leading to loss in sensitivity during a complete scan of the TLC plate. To minimize this problem,

CL detection was coupled with a vidicon rapid scanning spectrometer, since this detection system is capable of simultaneously measuring CL emission from all areas of the plate, thus reducing errors associated with the measurements of the rapidly changing CL signal.¹¹ However, this modification introduced complexity and cost to the CL instrumentation, making it difficult, for example, in the application of CL detection methods for analyses in routine clinical laboratories.

In this note a novel experimental setup involving the use of a pneumatic nebulizer to provide relatively uniform and reproducible spraying of the premixed peroxyoxalate CL reagents (TCPO and H₂O₂) onto the TLC plates and its coupling with an optical fiber to synchronize the timing between chemical excitation and measurement of CL emission is reported. Experimental parameters such as nebulization conditions, positioning and size of the optical fiber, microenvironment of the sample spot, scan speed, and particle size of the TLC plate were optimized to achieve sensitive and reproducible detection of three dansyl amino acids.

EXPERIMENTAL SECTION

Apparatus. Figure 1 shows a diagram of the experimental setup. A commercially available TLC scanner (CAMAG) was modified to serve as a precision two-dimensional stage for scanning the TLC plate in the x-y directions. Situated at a fixed position directly above the translational stage was a pneumatic nebulizer mounted in series with an optical fiber along the x-direction using an aluminum plate (dimensions 1.5 × 6 cm²), which was designed to allow for adjustment of distance between the nebulizer and optical fiber and of their respective heights from the TLC plate. Pneumatic nebulization provides a means by which a steady flow of reactive aerosol is sprayed onto the sample spots that are traveling directly beneath the nebulizer along the x-direction; the optical fiber allows for CL emission generated from the sample spots to be rapidly and reproducibly transported to the detection system in synchronization with chemical excitation.

A concentric pneumatic nebulizer obtained from an atomic absorption spectrophotometer (Model 82-810, Jarrell Ash) was used for the generation of aerosol. As shown in Figure 1, appropriate concentrations of TCPO and H₂O₂ solutions were placed in separate containers and the solutions were forced to move toward the direction of the nebulizer under the influence of pressurized argon gas. A gas flow controller obtained from a gas chromatograph (Model 376000, Varian) and a fine metering valve (Part No. 180502, PGC Scientifics) were placed between the gas flow controller and the CL reagent containers to allow for fine adjustment of the liquid flow rates of TCPO and H₂O₂. These two CL reagents were mixed within a stainless steel tee (1/16-in. Swagelok), and this premixed solution was then delivered to the nebulizer via a 50-cm-long × 75-μm-inner-diameter fused-silica capillary (Catalog No. Tsy-075375, Polymicro Technologies). After the premixed solution entered the nebulizer, an argon gas stream (nebulizing gas) with flow rate controlled by another gas flow controller interacted with the liquid stream of premixed CL solutions, resulting in the formation of aerosol which was sprayed onto the TLC plate. It should be noted that one or more reactive

(1) Kobayashi, S.; Sekino, J.; Honda, K.; Imai, K. *Anal. Biochem.* 1981, 122, 99-104.

(2) DeJong, G. J.; Lammers, N.; Spruit, F. J.; Brinkman, U. A. Th.; Frei, R. W. *Chromatographia* 1984, 18, 129-133.

(3) Kwakman, P. J. M.; Brinkman, U. A. Th.; Frei, R. W.; DeJong, G. L.; Spruit, F. J.; Lammers, N.; Van Den Berg, J. *Chromatographia* 1987, 24, 395-399.

(4) Sigvardson, K. W.; Birks, J. W. *Anal. Chem.* 1983, 55, 432-435.

(5) Sigvardson, K. W.; Kennish, J. M.; Birks, J. W. *Anal. Chem.* 1984, 56, 1096-1102.

(6) Kozlowski, T.; Grayeski, M. L.; Weinberger, R. J. *Chromatogr.* 1984, 317, 355-366.

(7) Grayeski, M. L.; DeVasto, J. K. *Anal. Chem.* 1987, 59, 1203-1206.

(8) Van Zoonen, P.; Gooijer, C.; Velthorst, N. H.; Frei, R. W. *J. Pharm. Biomed. Anal.* 1987, 5, 485-492.

(9) Baeyens, W.; Bruggeman, J.; Dewaele, C.; Lin, B.; Imai, K. J. *Biochem. Biophys. Res. Commun.* 1990, 171, 13-23.

(10) Curtis, T. G.; Seitz, W. R. *J. Chromatogr.* 1977, 134, 343-350.

(11) Curtis, T. G.; Seitz, W. R. *J. Chromatogr.* 1977, 134, 513-516.

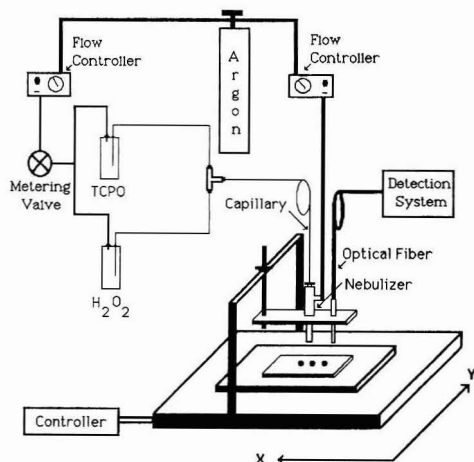


Figure 1. Experimental setup used for the CL detection of dansyl amino acids separated on HPTLC or TLC plates.

intermediates may be formed due to reaction of TCPO with H_2O_2 .¹²

Two types of optical fibers were evaluated for the transport of CL emission to the detection system: an optical fiber bundle, 61-cm long \times 1.6-mm diameter with a numerical aperture of 0.55 and an acceptance angle of 68° (Part No. 77520, Oriel), and a single optical fiber, 50-cm long \times 0.4-mm diameter with a numerical aperture of 0.22 and an acceptance angle of 47.2° (Superguide G, Fiberguide). One end of the optical fiber was placed adjacent to the nebulizer as shown in Figure 1 and the other end was interfaced to the detection system. The CL emission was isolated by a 10-nm band-pass filter centered at 520 nm (Corion) and was then detected by a photomultiplier tube (Model 9558B, EMI) operated at a voltage between 700 and 800 V. The photocurrent was fed to a picoammeter (Model 7080, Oriel) and the signal was recorded on an integrator (Chromjet, Spectra-Physics).

Optimization of Detection Sensitivity. A TLC plate was sprayed successively with a diluted dye solution of rhodamine B to completely wet the plate surface. The dye molecules adsorbed on the silica gel surface were then excited chemically using the aerosol aspirated from the nebulizer to determine the optimum flow rates for the CL reagent solutions and the nebulizing argon gas stream by adjusting the corresponding gas flow controllers and/or fine metering valve and monitoring the characteristics of the CL emission. It was found that at a pressure reading of 20 psi (flow rate: 6 L/min) and 3 psi (flow rate: 0.03 mL/min) for the nebulizing argon gas and CL reagent solution flows, respectively, the aerosol aspirated from the nebulizer appeared to produce a relatively strong and steady electronic signal. This CL emission can also be observed visually from the plate surface as very well-defined luminescence zones. Using this set of optimized flow conditions, the optimum distance between the nebulizer and optical fiber and their respective heights from the plate surface which give the highest CL intensity while maintaining good chromatographic resolution were also briefly investigated. It was found that, for the CL detection of three dansyl amino acids separated on HPTLC plates (vide infra), the optimum distances between these experimental components were as follows: nebulizer and optical fiber = 8 mm; optical fiber and plate surface = 4 mm; tip of nebulizer and plate surface = 5 mm (corresponding to 15 mm from the aerosol exit orifice).

Procedures. Development was carried out in either an acid solvent system of chloroform-ethyl acetate-methanol-acetic acid (9:15:4.5:0.2) or a basic solvent system of methyl acetate-2-

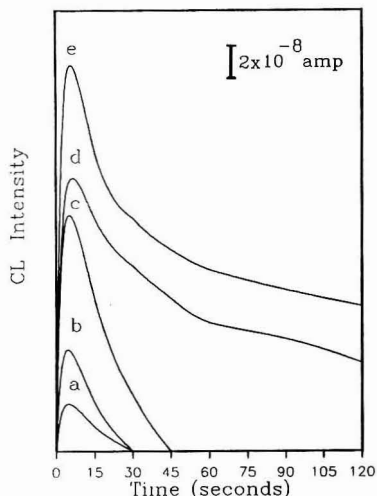


Figure 2. CL intensity-time curves of five sample spots of equal amounts of dansylglycine (3.1 ng/spot) separated on the same HPTLC plate using the acid solvent system. The spots were detected (a) without prespraying with any organic solvent and after prespraying with (b) ethyl acetate, (c) dioxane, (d) Trion X-100/chloroform mixture (1:4 v/v), and (e) liquid paraffin/chloroform mixture (3:2 v/v). TCPO and H_2O_2 concentrations were 3 mM and 0.88 M, respectively.

propanol-aqueous ammonia (9:7:2). The plates were air-dried for a few minutes at room temperature after development. If added, CL enhancers, i.e., various organic solvents, were pre-sprayed onto the sample spots using a compressed gas sprayer (Catalog No. 14654, Alltech) prior to CL measurements. A hand-held UV lamp was used to generate visible fluorescence from the sample spots to aid in the alignment of the sample spots separated on the plate along the x-direction with respect to the position of the nebulizer and optical fiber. Afterward, the plate was sprayed with the aerosol while being scanned along the x-direction at an optimum scan speed of 2 mm/s.

Chemicals and Materials. TCPO was prepared by the procedure described by Mohan and Turro.¹³ Dansylglycine, dansyl-L-arginine, and dansyl-L-leucine were purchased from Sigma. Hydrogen peroxide (30%) and all other chemicals were obtained from Aldrich. The dansyl amino acids were dissolved in a 20% 0.04 M Li_2CO_3 -HCl buffer of acetonitrile and kept at below $0^\circ C$. Stock solutions of TCPO and H_2O_2 with concentrations of 3–5 mmol/L in ethyl acetate and 0.88–1.2 mol/L in acetonitrile, respectively, were used. Separations were performed on either conventional silica gel TLC plates (Whatman LK6) or 5- μm silica gel HPTLC plates (Whatman LHP-K) which were purchased from Alltech.

RESULTS AND DISCUSSIONS

Figure 2a shows a CL emission intensity-time profile of dansylglycine spotted on a HPTLC plate. It can be seen that the CL intensity reached its maximum within ~ 5 s after the sample spot had been sprayed with the aerosol, followed by a rapid decay of the CL signal. This observation is consistent with those obtained by Curtis and Seitz who investigated the effects of TCPO and H_2O_2 concentrations on the CL intensity of dansylglycine adsorbed on silica gel TLC surfaces and found that at high peroxide concentrations, i.e., 0.8–1.2 M, the CL intensity was the highest but lifetime was very short, and the converse was true for low peroxide concentrations.¹⁰ However,

(12) Alvarez, F. J.; Parekh, N. J.; Matuszewski, B.; Givens, R. S.; Hizuchi, T.; Schowen, R. L. *J. Am. Chem. Soc.* 1986, 108, 6435–6439.

(13) Mohan, A. G.; Turro, N. J. *J. Chem. Educ.* 1974, 51, 528–530.

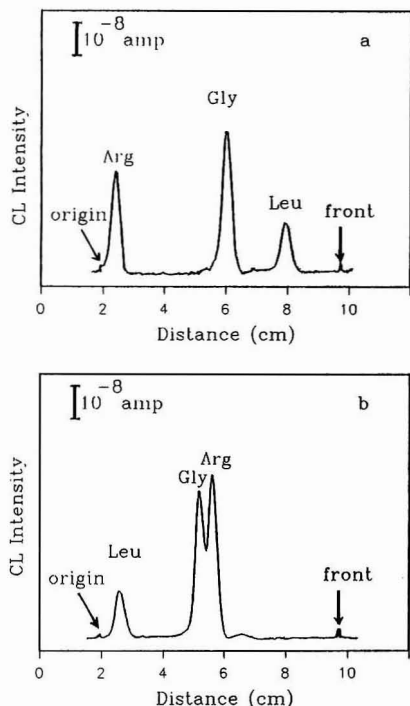


Figure 3. HPTLC chromatograms of three dansyl amino acids (Arg = 4.9 ng of dansyl-L-arginine, Gly = 4.3 ng of dansylglycine, and Leu = 3.8 ng of dansyl-L-leucine) developed in (a) the acid solvent system and (b) the basic solvent system. TCPO and H_2O_2 concentrations were 3 mM and 0.88 M, respectively.

variation in TCPO concentration in the range above 10^{-3} M appeared to have little effect on the CL intensity-time behavior. Using the present experimental setup, rapid and reproducible measurements of the CL emission at the peak maximum region as shown in Figure 2a is possible, thus allowing for significant enhancement in sensitivity and precision for the quantitation of analytes using the peroxalate CL reaction in TLC. At a distance of 8 mm between the nebulizer and optical fiber, a scan speed of 2 mm/s was found to produce the best sensitivity while good resolution was maintained for the detection of three dansyl amino acids separated on a HPTLC plate using an acid solvent system, as shown in Figure 3a. At this scan speed, each sample spot travels past the light collection zone of the optical fiber at ~4 s after it has been sprayed with the aerosol, which happens to fall within the time period at which the peak maximum of CL emission occurs, as shown in Figure 2a. The average limit of detection (LOD) based on a signal-to-noise ratio (S/N) of 3 for the three dansyl amino acids was found to be ~0.45 ng, which is about 1 order of magnitude lower than that reported by Curtis and Seitz (LOD for dansylglycine ~7 ng) using their optical fiber-based detection system.¹⁰ Relative standard deviation ($n = 6$) for dansylglycine (3.1 ng/spot) was found to be ~6%, which could arise from inconsistency in the manual spotting of the small volume (0.10–0.50 μ L) of samples onto the HPTLC plates using a 1- μ L syringe and/or variations related to chemical excitation, e.g., CL efficiency. Calibration plots of dansylglycine indicated linear response from LODs up to 0.1 μ g ($r = 0.995$). Figure 3b shows a HPTLC chromatogram of the three dansyl amino acids obtained under the same experimental conditions as in Figure 3a except using

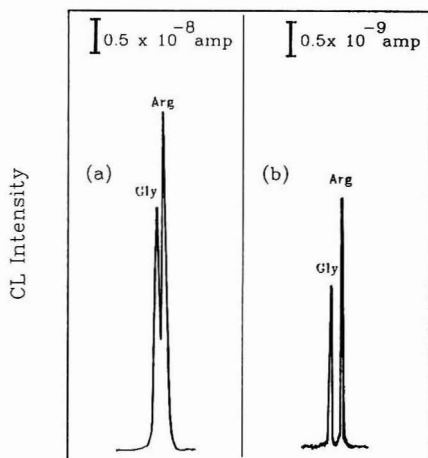


Figure 4. HPTLC chromatograms of two dansyl amino acids (Arg = 4.9 ng of dansyl-L-arginine and Gly = 4.3 ng of dansylglycine) developed in the basic solvent system and detected using (a) an optical fiber bundle and (b) a single optical fiber. TCPO and H_2O_2 concentrations were 3 mM and 0.88 M, respectively.

a basic solvent system for development. It can be seen that significant peak overlap occurs between dansylglycine and dansyl-L-arginine. To minimize the extent of this overlap, higher resolution was obtained by employing an optical fiber with significantly smaller core diameter as the light guide while other experimental conditions were kept the same. Parts a and b of Figure 4 compare the resolution and sensitivity of the two dansyl amino acids separated on the same HPTLC plate using an optical fiber bundle and a single optical fiber, respectively. It is clear that significant enhancement in resolution was achieved by employing the optical fiber with the smaller core diameter, but this gain in resolution was accompanied by a loss in sensitivity.

It has been demonstrated that luminescence intensity of certain amino acid derivatives generated by conventional TLC fluorescence detection methods can be enhanced by ~100-fold after the plate has been sprayed with a viscous and nonvolatile organic solvent system containing liquid paraffin or Triton X-100.¹⁴ Thus, it seems that further gain in sensitivity for the CL detection of dansyl amino acids separated on TLC plates may be achieved by exploiting the capabilities of the present experimental setup to detect CL signals enhanced by prespraying the sample spots with organic solvent systems having appropriate physical properties. Interestingly, parts a and b of Figure 2 indicate that the CL intensity of dansylglycine was slightly higher when the sample spot has been presprayed with ethyl acetate; however, when compared to Figure 2c which shows the effect of prespraying dioxane onto the sample spot, enhancement in CL intensity is even higher. This observation was surprising since it is well-known that CL intensity is greatest in ester and ether solvents. A similar observation has also been reported by Curtis and Seitz, who suggested that when compared to ethyl acetate, the stronger interaction of dioxane with the TLC plate may play an important role in providing greater CL intensity for the dansyl amino acids.¹⁰ Perhaps more interestingly, parts d and e of Figure 2 show that a CL intensity-time profile of dansylglycine changed significantly, i.e., increased in peak intensity and lifetime, after the sample

(14) Uchiyama, S. Uchiyama, M. *J. Liq. Chromatogr.* 1980, 3, 681–691.

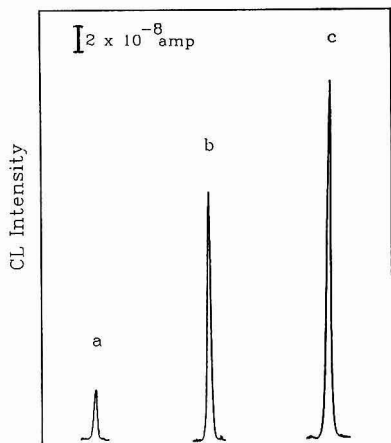


Figure 5. Relative CL intensity of three sample spots of equal amounts of dansylglycine (3.1 ng/spot) separated on the same HPTLC plate using the acid solvent system. The spots were detected (a) without prespraying with any organic solvent and after prespraying with (b) Triton X-100/chloroform mixture (1:4 v/v) and (c) liquid paraffin/chloroform (3:2 v/v). TCPO and H_2O_2 concentrations were 5 mM and 1.2 M, respectively.

spots were presprayed with two different viscous and non-volatile organic solvent systems.

To evaluate the gain in detectability of dansylglycine after treatment with the viscous and nonvolatile organic solvent systems, parts a–c of Figure 5 show the relative CL intensity

of three equal amounts of dansylglycine samples eluted simultaneously on the same HPTLC plate and detected with the present experimental system at identical R_f values. It can be seen that the Triton X-100/chloroform and liquid paraffin/chloroform solvent systems enhanced the CL intensity ~5- and 7-fold, respectively, which yield corresponding average LODs ($S/N = 3$) of about 0.10 and 0.08 ng, respectively. The average relative standard deviation ($n = 6$) on reproducibility using both solvent systems was ~4% (3.1 ng/spot). Lastly, the detectability of dansyl amino acids separated on HPTLC plates as compared to conventional TLC plates was also briefly investigated. It was found that without the influence of any organic enhancers, the average LOD ($S/N = 3$) obtained for the CL detection of the three dansyl amino acids separated on TLC plates was ~0.80 ng, which is only slightly higher than that found on HPTLC plates (~0.45 ng).

More detailed studies are necessary for the further optimization of various experimental parameters to achieve better analytical figures of merit. To this end, a better understanding of the fundamental processes involved in the chemical excitation of analytes adsorbed on the plate surface and of the physicochemical basis for the increase in CL observed when plates treated with a viscous and nonvolatile solvent are used is essential; of particular interest would be a comparison study of CL intensity–time behavior of analyte and background signals generated from the plate surface, since the kinetics of these signals have been shown to be different when CL detection is performed in HPLC, which leads to significant improvement of detection limits of the analytes.¹⁵

RECEIVED for review April 13, 1992. Accepted July 23, 1992.

Registry No. Dansylglycine, 1091-85-6; dansyl-L-arginine, 28217-22-3; dansyl-L-leucine, 1100-22-7.

(15) Hanaoka, N.; Tanaka, H.; Nakamoto, A.; Takada, M. *Anal. Chem.* 1991, 63, 2680–2685.

Tissue Bioreactor for Eliminating Interferences in Flow Analysis

Joseph Wang* and Najih Naser

Department of Chemistry, New Mexico State University, Las Cruces, New Mexico 88003

INTRODUCTION

Immobilized enzyme reactors are gaining considerable importance in flow analysis.¹⁻⁵ Such reactors serve mainly to facilitate the analyte conversion into a detectable species. Indeed, of all the conversion methods used in flow injection analysis (FIA), biocatalytic reactors are by far the most common. Three types of biocatalytic reactors have thus been used: the packed bed, open tubular and single string reactors. Such reactors often require high enzyme loadings and very stable preparations, and may suffer from the build-up of back-pressure under continuous use.^{1,2} Significant amounts of time and resources are thus being invested for optimizing enzyme reactors for maximum efficiency.

The present note describes the utility of tissue bioreactors for the elimination of potential interferences in FIA. Enzyme reactors have been used previously for the removal of interferences in connection with electrochemical monitoring of flow stream.^{6,7} Tissues possess several advantages over their enzymatic counterparts, including improved stability, higher biocatalytic activity, and low cost. Such advantages have received considerable attention in connection with the preparation of electrochemical biosensors.^{8,9} However, little attention has been given to the use of plant tissues (in place of isolated enzymes) as reactor columns in flow analysis. A kidney reactor was employed in flow measurements of glutamine, with a downstream potentiometric detection of the generated ammonia.¹⁰ Unlike substrate measurements (for which low conversion efficiencies are sufficient), the destruction of interferences requires high enzymatic loadings, as provided by cellular materials. In particular, on-line degradation of surface-active proteins and electrooxidizable interferants (e.g. ascorbic acid and acetaminophen) is accomplished in the present work by exploiting the rich papain, ascorbic acid oxidase (AAO), and polyphenol oxidase activities of the papaya, zucchini, and potato tissues, respectively. The optimization and characterization of these low-cost and yet highly efficient tissue-eliminator bioreactors are reported in the following sections.

EXPERIMENTAL SECTION

Apparatus. Amperometric measurements were performed with an EG&G PAR Model 264A voltammetric analyzer, the output of which was displayed on a X-Y-t recorder (Bioanalytical Systems (BAS), Model RXY). The flow injection system consisted of a 50-mL syringe/carrier reservoir, held by the syringe pump (Model 341B, Sage), interconnecting Teflon tubing, a Rheodyne Model 5020 injection valve (20- μ L loop), the tissue reactor, and a carbon paste thin-layer detector (Model TL-4, BAS). The Ag/AgCl reference electrode and the counter electrode were located in a downstream compartment (Model RC-2A, BAS).

The tissue reactor consisted of a polyethylene cartridge (usually of 5.0-cm length and 1.0-cm i.d.), filled with the desired tissue.

A central hole (usually of 1.0- or 2.0-mm diameter) was made, with a cork borer, in the tissue cylinder to obtain a desired open tubular reactor configuration. Luer fittings (to the connecting Teflon tubing) served for the solution inlet and outlet.

Reagents. All solutions were prepared with doubly distilled water. The supporting electrolyte was 0.05 M phosphate buffer (pH 7.4). Acetaminophen, dopamine, casein, bovine albumin (Sigma), potassium ferrocyanide, and ascorbic acid (Baker) were used without further purification. The plants used in this study were purchased from a local grocery store.

Procedure. Amperometric detection proceeded under flow injection conditions. The working potential (usually +0.60 V) was applied, and transient currents were allowed to decay to a steady-state value. All measurements were performed at room temperature.

RESULTS AND DISCUSSION

The use of tissue reactors as effective matrix isolation tools in flow analysis offers the advantages of high activity and stability, self-supported rigidity, and extreme simplicity. Such unique application was examined and demonstrated in connection with amperometric measurements at a thin-layer detector. Passage of the samples through the biocatalytic reactors was used to alleviate two major interferences characteristic of amperometric monitoring, including biofouling and overlapping signals.

For example, tissue reactors can circumvent protein passivation effects and hence impart high stability during amperometric detection. Such prevention of biofouling is illustrated in Figure 1 utilizing a papaya reactor. The papain enzyme, present in the papaya reactor, rapidly cleaves proteins into smaller peptide fragments^{11,12} that do not passivate the detecting electrode. When the protein-rich ferrocyanide (A) and acetaminophen (B) solutions bypass the papaya reactor (top), a rapid decrease of the flow injection response of these analytes is observed (up to 68 and 60%, respectively). This passivation problem is eliminated by passing the samples through the papaya reactor (bottom). No loss of the amperometric response is observed throughout these prolonged series (RSD of 1.7 (A) and 1.2% (B)). Note also that the speed inherent to the flow injection operation is not compromised by the use of the tissue reactor (i.e. sharp peaks with no dispersion).

Ascorbic acid is an easily oxidizable endogenous compound which exists in relatively high concentrations in most biological fluids. Hence, amperometric assays of such fluids often suffer from a large ascorbic acid response which masks the peaks of interest. The high enzymatic (AAO) activity of the zucchini tissue¹³ can greatly facilitate the elimination of the ascorbic acid interference, in accordance to eq 1:

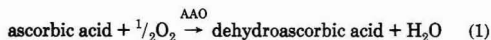


Figure 2 (bottom) demonstrates the interferant-removal efficiency obtained with the zucchini reactor. It shows amperometric peaks for a 1×10^{-5} M ascorbic acid solution obtained with (B) and without (A) passage through the reactor.

(11) Hill, R. In *Hydrolysis of Proteins*; Anfinsen, C. B., Anson, M. L., Edsall, J. T., Richard, F. M., Eds.; Advances in Protein Chemistry; Academic Press: New York, 1965; Vol. 20.

(12) Wang, J.; Wu, L. H.; Martinez, S.; Sanchez, J. *Anal. Chem.* 1991, 63, 398.

(13) Wang, J.; Naser, N.; Ozsoz, M. *Anal. Chim. Acta* 1990, 234, 315.

- (1) Bowers, L. D. *Anal. Chem.* 1986, 58, 513A.
- (2) Cliffe, S.; Filippini, C.; Schneider, M.; Fawer, M. *Anal. Chim. Acta* 1992, 256, 53.
- (3) Yao, T.; Akasaka, R.; Wata, T. *Electroanalysis* 1989, 1, 413.
- (4) Masoom, M.; Townshend, A. *Anal. Chim. Acta* 1986, 179, 399.
- (5) Almuhaideb, A. M.; Townshend, A. *Anal. Proceedings* 1989, 26, 56.
- (6) Adams, R. N.; Bradberry, C. W. *Anal. Chem.* 1983, 55, 2439.
- (7) Risting, L.; Yang, X.; Johansson, G. *Anal. Chim. Acta* 1987, 200, 313.
- (8) Rechnitz, G. A. *Science* 1981, 214, 287.
- (9) Wang, J. *Electroanalysis* 1991, 3, 255.
- (10) Mascini, M.; Rechnitz, G. A. *Anal. Chim. Acta* 1980, 116, 169.

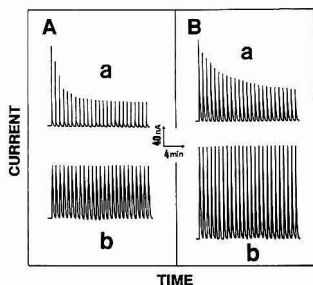


Figure 1. Amperometric response to repetitive injections of 1×10^{-4} M ferrocyanide (A) and 4×10^{-4} M acetaminophen (B) solutions containing 500 ppm casein and albumin, respectively, without (a) and with (b) passage through the papaya reactor. Operating potential, +0.50 V; flow rate, 1.0 mL/min; carrier/electrolyte, phosphate buffer (pH 7.4). Reactor length and inner diameter, 5 cm and 1 mm, respectively.

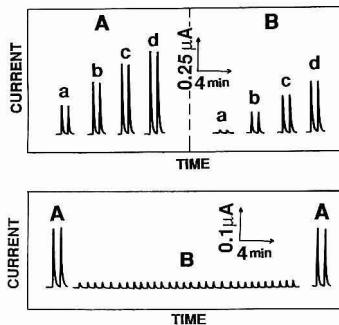


Figure 2. Bottom: flow injection amperometric peaks for 1×10^{-5} M ascorbic acid, with (B) and without (A) passage through the zucchini reactor. Top: response to 1×10^{-5} M ascorbic acid solutions, containing 0 (a), 1×10^{-5} M (b), 2×10^{-5} M (c), and 3×10^{-5} M (d) dopamine, with (B) and without (A) passage through the zucchini reactor. Operating potential, +0.60 V; reactor length and inner diameter, 4 cm and 1 mm, respectively. Carrier/electrolyte and flow rate, as in Fig. 1.

The short (4-cm) tissue reactor results in more than 90% diminution of the ascorbic acid response. The biocatalytic degradation capability is maintained throughout this prolonged series of 30 repetitive injections. Following this operation, the zucchini reactor was bypassed, and the resulting peaks were similar to those recorded in the beginning of the experiment.

The bioanalytical utility of the ascorbic acid destruction process is also illustrated in Figure 2 (top), using the common interference of ascorbic acid on measurements of catecholamine neurotransmitters. This figure displays flow injection peaks for ascorbic acid solutions containing increasing level of dopamine. An additive response, that precludes the measurement of dopamine, is observed without passage through the plant reactor (A). In contrast, the 94% removal of ascorbic acid when the sample mixture is flowing through the reactor permits a nearly selective quantitation of dopamine (B).

Crucial to the successful use of a tissue-eliminator reactor is appropriate optimization of experimental conditions for maximum conversion efficiency (R , i.e., the fraction of substrate consumed). Figure 3A shows the dependence of R upon the volume flow rate for different reactor lengths. As the residence time of an element of solution within the zucchini

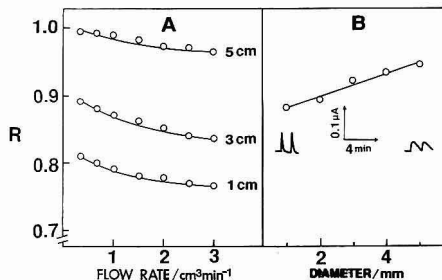


Figure 3. Dependence of the degree of conversion upon the volume flow rate (A) and tube diameter (B). Injections of a 1×10^{-5} M ascorbic acid solution. Zucchini reactor of 1-mm tube diameter (A) and 3-cm length (B); flow rate, 1.0 mL/min. Carrier/electrolyte and potential, as in Figure 2.

reactor increases (i.e. slower flow rates or longer reactors) the conversion efficiency increases. For the 1–5-cm-long reactors, at 0.33–3.0 mL/min rates, the conversion efficiency ranges between 0.76 and 0.99. The attainment of such high efficiencies (at moderate flow rates or reactor lengths) is attributed to the rich AAO activity of the tissue. (It should be pointed out that the use of the pure enzyme for the same task would be extremely expensive, as 1 mg of AAO, containing only 700 units, costs \$70!). The inner diameter of the open-tubular reactor is another parameter affecting its efficiency. Figure 3B shows the dependence of R upon the diameter for a 3-cm-long reactor. R increases (from 0.88 to 0.94) by increasing the reactor diameter between 1 and 5 mm. Note also the broadening of the FIA peaks (i.e. increased dispersion) associated with the increasing diameter. Hence, longer (5 cm) reactors of 1-mm diameter were employed for achieving effective interferent elimination while maintaining high sample frequencies.

The high biocatalytic conversion efficiencies are maintained over relatively long periods. No apparent mechanical stability problems were observed with “soft” tissues, e.g. zucchini. Indeed, the same zucchini reactor was operated for a period of 10 days, with no apparent loss in its efficiency (as was indicated daily from the effective removal of 1×10^{-5} M ascorbic acid). Such performance is attributed to the inherent stability of the enzyme within its own natural environment. Considering the broad availability and extremely low cost of plant tissues, they can be easily replaced when needed. The reactor-to-reactor reproducibility was estimated by using six different sections of the zucchini plant (conditions as in Figure 2). The mean conversion efficiency found was 0.91, with a range of 0.89–0.93 and a relative standard deviation of 2.6%.

Effective elimination of phenolic interferants can be accomplished utilizing a potato reactor, which is rich with polyphenol oxidase. In particular, the common analgesic acetaminophen (paracetamol) is easily oxidized and often interferes in amperometric measurements in the anodic region. As illustrated in Figure 4 (bottom), passage of acetaminophen solutions through the potato reactor results in 92% diminutions of the drug response. The potato polyphenol oxidase can facilitate also the biodegradation of catecholamines; ca. 90% decrease of the response for dopamine is indicated from the flow injection peaks displayed in Figure 4 (top). Obviously, the detection of numerous nonphenolic compounds should benefit from such destruction of phenolic interferences.

In conclusion, it has been shown that tissue reactors can be used for the removal of interfering substances, hence imparting high stability and selectivity on flow amperometry. High conversion efficiencies are coupled to extreme simplicity

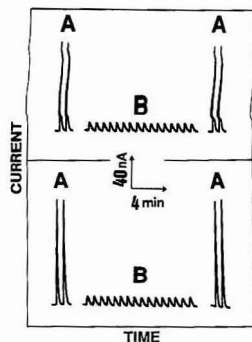


Figure 4. Flow injection amperometric peaks for 1×10^{-5} M dopamine (top) and 1×10^{-4} M acetaminophen (bottom), with (B) and without (A) passage through the potato reactor (5-cm length, 1-mm tube diameter). Other conditions, as in Figure 2.

and low cost (compared to analogous applications of immobilized enzyme reactors). The diversity of cellular materials holds great promise for the removal of other target interferants. While the concept has been illustrated in connection

with amperometric detection for flow injection systems, tissue reactors may benefit other analytical flow systems and detection modes. Additional advantages may be gained by coupling several tissue reactors (for the simultaneous removal of various interferants), or by employing flow reversal schemes (for quantitative conversion with shorter columns). The conversion efficiency should be adjusted to meet the requirement of each sample (with 100% conversions used for a large excess of the interfering species). In addition, periodic calibrations should be employed to detect possible losses in the efficiency. Besides their great analytical utility, tissue reactors may find important environmental applications, i.e., low-cost cleanup of water streams from pollutants (such as phenols or peroxides).

ACKNOWLEDGMENT

This work was supported by the U.S. Environmental Protection Agency (Grant No CR-817936-010). Mention of trade names or commercial products does not constitute endorsement or recommendation by the U.S. EPA.

RECEIVED for review April 30, 1992. Accepted July 20, 1992.

AUTHOR INDEX

- Anderson, D. L., 2366
 Arnold, M. A., 2438
- Blumberg, L. M., 2459
 Bognar, J. A., 2451
 Burns, K. I., 2339
- Chang, C.-J., 2313
 Chen, I.-C., 2461
 Ciszowska, M., 2372
 Cooke, N., 2348
 Cooks, R. G., 2313
 Couch, R. A., 2413
- Dabeka, R. W., 2419
 Dasgupta, P. K., 2406
 Davis, K. L., 2434
 Deinzer, M. L., 2316
 Dubin, P. L., 2344
- Edwards, S. L., 2344
 Elchuk, S., 2339
- García Pinto, C., 2334
 Gordon, G. E., 2366
 Grimsrud, E. P., 2451
 Guttman, A., 2348
- Hara, H., 2393
 Hoke, S. H., II, 2313
 Houk, R. S., 2444
 Hsu, C. S., 2327
 Huang, H., 2406
 Huie, C. W., 2465
- Kaplan, J. I., 2344
 Kar, S., 2438
 Kitagawa, T., 2393
 Klunder, G. L., 2429
- Knighton, W. B., 2451
 Kocher, C. A., 2316
 Kowalchuk, W. K., 2434
 Kozłowski, J., 2456
- Laramée, J. A., 2316
 Li, X.-H., 2313
 Liao, S.-L., 2413
 Lindstrom, R. M., 2366
 Liu, K.-L., 2434
 Lucy, C. A., 2339
- Mackey, E. A., 2366
 Mehta, M. S., 2344
 Moreno Cordero, B., 2334
 Morgan, S. L., 2383
 Morita, M., 2425
 Morris, M. D., 2434
 Morris, S. E., 2372
 Mulcahey, L. J., 2352
- Naser, N., 2469
- Okabe, Y., 2393
 Olson, C. L., 2413
 Osteryoung, J. G., 2372
- Pang, H.-m., 2444
 Pardue, H. L., 2378
 Pérez-Bendito, D., 2359
 Pérez Pavón, J. L., 2334
- Qian, K., 2327
- Rapp, T. L., 2434
 Richheimer, S. L., 2323
 Russo, R. E., 2429
- Sahota, R. S., 2383
 Salov, V. V., 2425
 Shibata, Y., 2425
 Shum, S. C. K., 2444
 Silva, M., 2359
 Silva, R. J., 2429
 Smith, C. P., 2398
 Smith, D. L., 2456
 Stojek, Z., 2372
- Taylor, L. T., 2352
 Thévenon-Emeric, G., 2456
 Timmons, D. W., 2323
 Tinnermeier, D. M., 2323
 Todd, E. A., 2434
 Tomalia, D., 2344
- Uhegbu, C. E., 2378
- Velasco, A., 2359
- Wanders, B., 2348
 Wang, J., 2469
 Whang, C.-W., 2461
 White, H. S., 2398
 Wood, J. M., 2313
 Wu, N., 2465
- Xia, J., 2344
- Yoshinaga, J., 2425
- Zhang, Z., 2456

Analytical Abstracts Now on CD-ROM!



Available in
Macintosh™
and
IBM Compatible
Formats

This valuable source of current awareness information in analytical chemistry is now available on a single SilverPlatter CD-ROM.

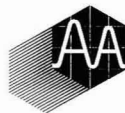
Analytical Abstracts on CD-ROM features:

- Approximately 140,000 items from 1980 onwards
- Easy to use SilverPlatter software
- Quarterly updates with more than 3,000 items
- Unlimited searching – no additional costs

Special Discount for Hardcopy Subscribers

Contact us today for further information and a FREE demo disk.

Judith Barnsby, Royal Society of Chemistry,
Thomas Graham House, Science Park, Milton Road,
Cambridge CB4 4WF, United Kingdom
Tel: +44 (0) 223 420066 Fax: +44 (0) 223 423623
Telex: 818293 ROYAL

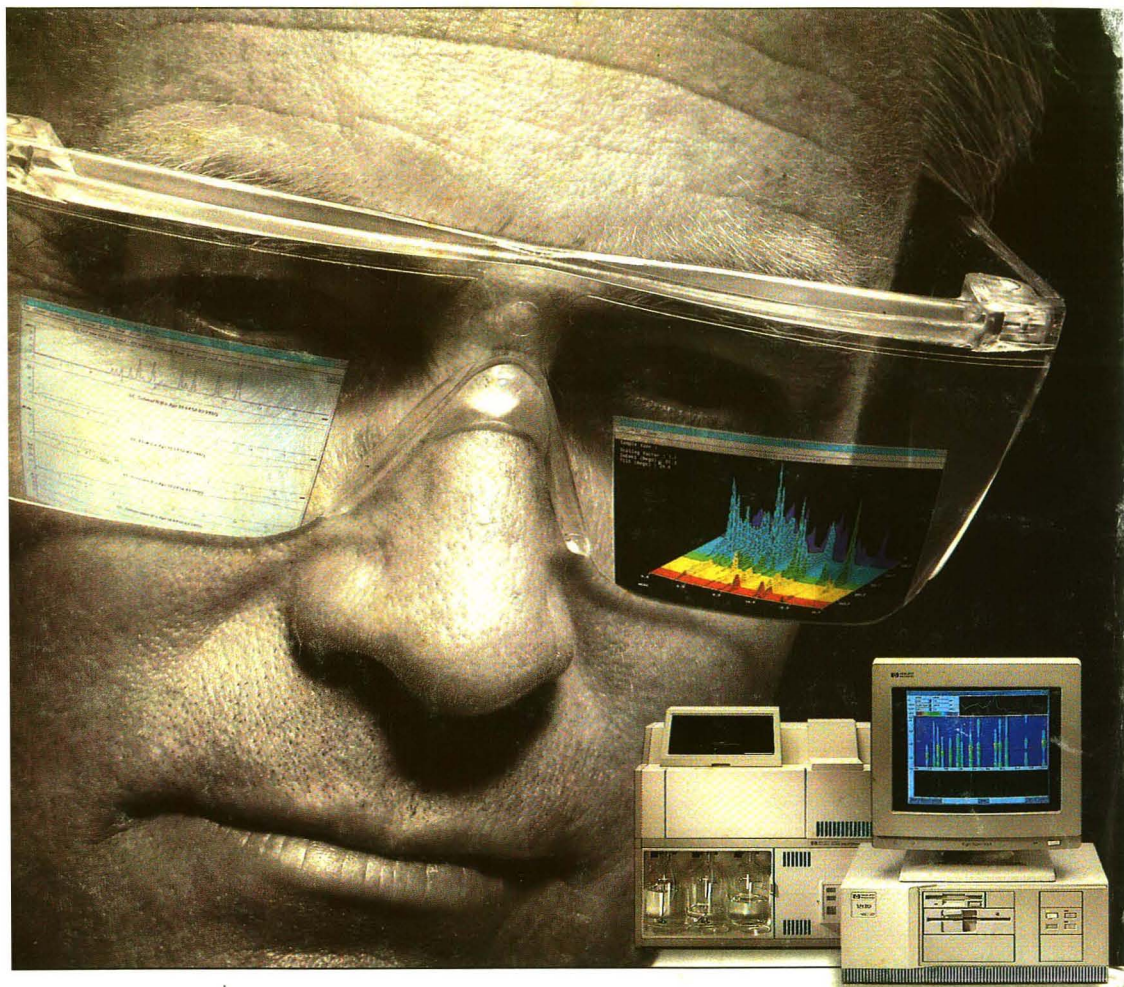


ROYAL
SOCIETY OF
CHEMISTRY



Information
Services

Take a new look at complex LC data with 3-D confidence.



The new HP 1090 Win LC system combines spectroscopy and chromatography under Microsoft® Windows, to meet GLP.

Access the power of the spectral dimension and confirm complex quantification in a single HPLC analysis. With our new PC-based system, now you can acquire and integrate data at multiple wavelengths, run purity checks and search spectral libraries automat-

ically. And control automated fluorescence detection too.

For greater confidence in GLP compliance, conduct system suitability tests, routinely and unattended. A sequence summary report collates all the relevant statistics, while the PC archives the raw data, method, and instrument log for each analysis in one file, testifying to the quality and traceability of your results.

Our 3-D LC software runs on

any standard PC, and links to company-wide systems through the HP Unified Lab. We offer a data-processing-only version too.

The HP 1090 Win LC performs reproducibly from the first elution to the last. And it's backed by HP's first-ranked reliability, service and support. For details on the most advanced HPLC solution for GLP work, call 1 800 334-3110, Ext. 195 today.



**HEWLETT
PACKARD**